CHARACTERISATION OF CELLULAR RESPONSES AND GENE DELIVERY CAPABILITIES WITHIN POROUS AGAROSE SCAFFOLDS

Matthew Scott Sullivan

Submitted in accordance with the requirements for the degree of Doctor of Philosophy

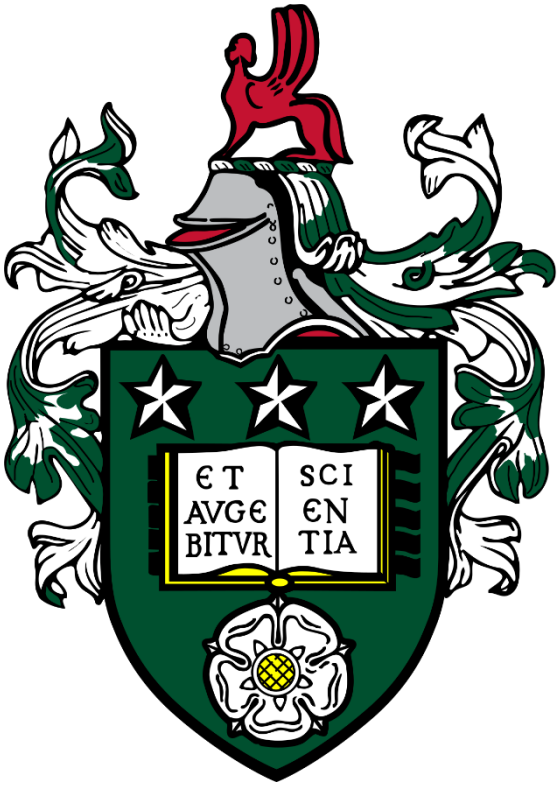

The University of Leeds

Institute of Medical and Biological Engineering

School of Biological Sciences and School of Mechanical Engineering

April 2024

The candidate confirms that the work submitted is his own and that appropriate credit has been given where reference has been made to the work of others.

ACKNOWLEDGEMENTS

Firstly, I'd like to acknowledge the Engineering and Physical Sciences Research Council (EPSRC) for providing the essential funding required for me to complete this PhD research as part of the Centre for Doctoral Training (CDT) in Tissue Engineering & Regenerative Medicine at the University of Leeds.

Secondly, I'd like to pay a huge thanks to my supervisor Dr Hazel Fermor. I will be forever grateful to you for taking over supervision of my PhD project. After Dr G Feichtinger's unexpected move into industry, you crucially stepped up and provided not only the necessary knowledge and expertise, but also rock-solid stability and calmness in a period that I know must have been challenging for all involved. Moving over to FBS was the best decision we made and I'm so glad I became a member of the Fermor lab group. I would also like to thank my wider supervisor team; Prof David Wood and Dr Elena Jones, who have been ever present throughout my time at the University of Leeds, providing vital additional support whenever it was required. Finally, I must say a thank you to Dr Georg Feichtinger, your passion and novel ideas are what first inspired me to take on the challenge that was this PhD.

A further thank you to everyone in both the St James's WTBB and iMBE labs. The hours spent training me on the various equipment and laboratory techniques did not go unnoticed and helped me immensely. With this in mind, a special mention needs to go to Mrs Nicola Conway, Dr Sarah Myers, Dr James Warren, Lucy Ormiston-Lee, and Daniel White. In particular, I'd like to highlight the latter, Danny – our endless chats about agarose, electrophoresis, PhD life and everything in-between made these 4 years an absolute pleasure.

I must also acknowledge that part of the research described in chapter 3 was carried out in partnership with *Daniel White* whose contribution was as follows: to comprehensively characterise the physical and structural properties of *in-situ* synthesised Calcium Phosphate particles as generated using the novel Feichtinger agarose gel electrophoresis system (selection of these results being illustrated in section 3.4.2.1.1). My own contributions to this thesis therefore explicitly cover chapters 1 through 7, excluding section 3.4.2.1.1 of chapter 3.

Away from the lab, I can't go without mentioning the CDT FC group - James, Paddy, Danny, Kern and Simon. So many stories, laughs, movie quotes, krakens, shanked golf shots and one-bounce games shared and played over the years. Leeds wouldn't have been Leeds without all of you.

Lastly, a few words for my family. To my brother Mark, you set the standard for me in so many aspects of life and education is no exception. Unlike on the tennis court or the ski slope, I'm more than happy, if you are, to finally now call this one a draw. And to my parents, Lynn and John, your unwavering support throughout all my years in education has been the backbone to

my success. I cannot thank you enough for all these opportunities I've had in education and in life in general and furthermore instilling in me the drive to be the best I can be.

I dedicate this thesis to my Grandparents, Mollie and Albert. Their love, support and profound interest regarding my research was dearly appreciated. You are both sorely missed.

ABSTRACT

A traumatic osteochondral lesion is a severe type of articulating tissue injury which disrupts and causes damage to both surface cartilage and underlying sub-chondral bone layers. Afflicted patients generally present with early symptoms such as joint discomfort and severe pain which if left untreated can ultimately progress to the pathological disease known as post-traumatic osteoarthritis. At this late stage, the recommended treatment option is total joint replacement surgery; a procedure which is highly invasive and only has a finite functional *in-situ* lifespan. In physically active younger patients, the latter property is sub-optimal and thus more effective early stage interventions are needed to fully repair the osteochondral tissue unit. Gene activated matrices (GAMs) are considered an exciting tissue engineering treatment solution, whereby single or multiple reservoirs of therapeutic DNA payloads are incorporated specifically within a biomaterial matrix to facilitate high quality bone and cartilage tissue formation. However, a limitation of current gene activated matrices is their limited efficacy in gene delivery and lack of spatial patterning during fabrication and incorporation. As osteochondral tissue is complex with gradient-like features, a GAM containing a gradient payload distribution is hypothesised to be more effective than current unpatterned approaches. To achieve this, a novel agarose gel electrophoresis platform was utilised to fabricate porous agarose scaffolds which contained spatially controlled *in-situ* deposited DNA payloads.

Experimentally, this project for the first time sought to comprehensively evaluate and characterise the above platform in terms of its inherent physical biomaterial properties, DNA payload patterning capabilities (DNA-CaP, DNA-PEI), biomaterial adhesion, cytotoxicity profile and 3D transfection performance. To achieve an acceptable osteochondral-like porous biomaterial GAM, it was found that a combination of freeze-drying and higher inherent agarose hydrogel concentrations (>3wt%) were required. Upon conversion into suitably porous scaffolds, the agarose GAM systems were then shown to be cytocompatible but crucially appeared to be lacking inherent 3D cellular adhesion characteristics. Following this major finding, various surface functionalisation methods (fibronectin, LAP-PEO, polydopamine) were tested for scaffold-wide cell adhesion enhancement. The polydopamine coating method appeared remarkably effective in this regard, enhancing C2C12 and Y201 3D cell-scaffold attachment and proliferation specifically after 7 days of seeding. Histological analysis further showed effective differentiation towards osteogenic and chondrogenic lineages when in the presence of respective differentiation media conditions for 4 weeks. 3D transfection analysis revealed, however, that all agarose-polydopamine GAM scaffolds, developed via the electrophoresis patterning platform, failed to induce any tangible gene expression over a 7 day seeding period. Future experimentation is therefore needed to elucidate the exact failure mechanisms shown in this transfection study, with the aim that corrective measures can be generated which can ultimately produce a transfection capable agarose GAM product.

In an additional explorative study, it was also shown that an alternative transfection-capable vector type (CCHLV) could be synthesised from the gene expression cassette region of a plasmid vector. This was significantly aided by the novel use of an ELAN type IIS restriction enzyme synthesis strategy, which could more efficiently produce the final nucleic acid vector product in comparison to current gold standard strategies (ELAN type II). Future experimentation is therefore required to fully characterise these newly developed vectors for its 2D and 3D transfection capabilities.

Overall, huge strides were made in the advancement of a completely novel early stage continuous gradient GAM concept, of which ultimately serves to expand not only the knowledge and understanding of applying agarose DNA electrophoretic patterning in the field of GAM system development and manufacture, but furthermore elucidates the substantial limitations this specific concept inherently possesses which may restrict its adoption as a osteochondral defect regeneration device.

LIST OF FIGURES

LIST OF TABLES

DISSEMINATION OF RESEARCH

Sullivan, M., Jones, E., Wood, D., and Feichtinger, G., 2019. "Characterisation of cellular responses and drug delivery capabilities within mineralised hydrogel scaffolds". At Leeds Institute of Medical Research (LIMR).

Sullivan, M., Jones, E., Wood, D., and Feichtinger, G., 2019. "Characterisation of cellular responses and drug delivery capabilities within mineralised hydrogel scaffolds". At Joint EPSRC TERM CDT Conference (Manchester).

Sullivan, M., Jones, E., Wood, D., and Feichtinger, G., 2019. "Characterisation of cellular responses and drug delivery capabilities within mineralised hydrogel scaffolds". At Biomaterials and Tissue Engineering Group (BITEG).

Sullivan, M., Jones, E., Wood, D., and Fermor, H., 2021. "Creation of a linear Covalently-Closed Hairpin Loop Vector (CCHLV) expression construct capable of effective gene transfer within a gene activated matrix". At Future Leaders in Regenerative Medicine: Joint Conference CDTs and UKSB.

ABBREVIATION LIST

2D	Two dimensional
3D	Three dimensional
ACP	Amorphous calcium phosphate
ADAMTS	A disintegrin metalloproteinase with thrombospondin-like motifs
AGE	Agarose gel electrophoresis
ALK5	Activin receptor-like kinase-5
ALP	Alkaline phosphatase
ANOVA	Analysis of variance
ATCC	American type culture collection
AUC	Area under the curve
BM-MSC	Bone marrow mesenchymal stem cell
BMP	Bone morphogenic protein
BMSCs	Bone marrow-derived mesenchymal stem cells
BMU	Basic multicellular unit
BPB	Bromophenol blue
BS	Basal media scaffolds
CaP	Calcium phosphate
CCHLV	Covalently closed hairpin loop vectors
CG	Chitosan-gelatin
CME	Clathrin-mediated endocytosis
CMV	Cytomegalovirus
CnE	Caged nanoparticle encapsulation
CS	Chondrogenic media scaffolds
CSLM	Confocal laser scanning microscopy
CuAAC	Copper-catalysed azide–alkyne cycloaddition

CvME	Caveolae-mediated endocytosis
DAMPs	Damage associated molecular patterns
DAPI	4' ,6-diamidino-2-phenylindole
ddH_2O	Double-distilled water
DMSO	Dimethyl sulfoxide
DOPA-K	3,4-dihydroxy-L-phenylalanine-lysine
ECM	Extracellular matrix
EDTA	Ethylenediaminetetraacetic acid
EdU	Ethynyl-2'-deoxyuridine
EDX	Energy dispersive x-ray spectrometry
EEO	Electroendosmosis
eGFP	Enhanced green fluorescent protein
ELAN	Enzymatic ligation assisted by nucleases
EthD-III	Ethidium homodimer III
F-AGE-1	Feichtinger-Agarose Gel Electrophoresis-1
FBS	Foetal bovine serum
FDA	Food and drug administration
FITC	Fluorescein isothiocyanate
FN	Fibronectin
GAG	Glycosaminoglycan
GAM	Gene activated matrix
GEC	Gene expression cassette
H&E	Haematoxylin and eosin
HA	Hydroxyapatite
HCl	Hydrochloric acid
HEPES	4-(2-hydroxyethyl)-1-piperazineethanesulfonic acid
hMSC	Human mesenchymal stem cell

HSV	Herpes simplex virus
hTERT	Human telomerase reverse transcriptase
ICRS	International cartilage repair society
IGF	Insulin-like growth factor 1
IL	Interleukin
IL-1R1	Interleukin-1 receptor type 1
ISO	International standards organisation
ITS	Insulin-transferrin-selenium
KOD	Thermococcus kodakaraensis
LAP	Laponite®
LAP-PEO	Laponite-poly(ethylene oxide)
LB	Luria bertani
LDH	Lactate dehydrogenase
LIC	Ligation independent cloning
Met-Luc	Metridia luciferase
MFI	Mean fluorescence intensity
MMP	Matrix metalloproteinase
MRS	Multiple restriction sites
MSC	Mesenchymal stem cells
mTGase	Microbial transglutaminase
N/P	Nitrogen to phosphate ratio
NBF	Neutral buffered formalin
NF_kB	Nuclear factor kappa B
NLS	Nuclear localisation sequence
NPC	Nuclear pore complex
NPT	Neomycin phosphotransferase
OA	Osteoarthritis

OCTE	Osteochondral tissue engineering
OD	Optical density
OPF	Oligo(poly(ethylene glycol) fumerate
OPG	Osteoprotegerin
Ori	Origin of replication
OS	Osteogenic media scaffolds
PBS	Phosphate buffered saline
PCL	Poly(caprolactone)
PCL-PU	Polycaprolactone-polyurethane
PCR	Polymerase chain reaction
PDA	Polydopamine
PDGF	Platelet derived growth factor
pDNA	Plasmid DNA
PEI	Poly(ethylenimine)
PEO	Polyethylene oxide
PGA	Poly(glycolic acid)
PLA	Poly(lactic acid)
PLGA	Poly(lactic-co-glycolic acid)
Poly(A)	Polyadenylation
PTOA	Post-traumatic osteoarthritis
PVA	Poly(vinyl alcohol)
RANKL	Receptor activator of nuclear factor kappa-β ligand
RPM	Revolutions per minute
SDD	Silicon drift detectors
SE	Secondary electron
SEM	Scanning electron microscopy
SFM	Serum free media

SOC	Super optimal medium with catabolic repressor
SV40	Simian virus 40
TAE	Tris base, glacial acetic acid, EDTA
TGF-β	Transforming growth factor-beta
TGFβRII	Transforming growth factor beta receptor type II
TIMP	Tissue inhibitor of metalloproteinase
TJR	Total Joint Replacement
TK	Thymidine kinase
TKR	Total Knee Replacement
TNF	Tumour necrosis factor
VEGF	Vascular endothelial growth factor

LIST OF CONTENTS

CHAPTER 1

INTRODUCTION

1 CHAPTER 1: INTRODUCTION

1.1 General introduction

Osteochondral tissue is a highly organised and complex region of the human body made up of zonally distinct tissue phases, which act synchronously to facilitate the smooth and repeated action of articulating synovial joint movement over a human's entire lifetime. Osteochondral tissues consist of an articular cartilage phase with an underlying subchondral bone phase (Lepage *et al.*, 2019).

As a result of sudden trauma, athletic injury or inherent pathological conditions, early localised osteochondral lesions may manifest, resulting in substantial joint destabilisation, often culminating in downstream effects such as severe pain, impairment of joint function and general poor quality of life (Swieszkowski *et al.*, 2007). Moreover, increased mechanical degradation as a result of poor tribological performance (i.e higher friction) and damage associated inflammatory processes may lead to further joint degradation and progression to osteoarthritis (OA) (Link *et al.*, 2020; Scanzello & Goldring, 2012).

In contrast to subchondral bone, which possesses a certain degree of self-repair capacity, articular cartilage is an avascular tissue, with low self-regenerative abilities (Karuppal, 2017). Because of this, full osteochondral lesions cannot typically heal and thus OA will progress, eventually requiring clinical intervention. Currently, the most common and effective OA treatment is a total joint replacement (TJR). Although TJR's stand as the prevailing treatment option, it may not be the optimal recourse for younger, more physically active patients. TJR's are often not engineered to withstand the sustained, high mechanical loads required from such patients, resulting in early implant failure and the need for more invasive, less functional revisions (Julin *et al.*, 2010). In recent years, an array of alternative joint-preserving treatments has emerged, aimed at postponing the necessity for TJRs, particularly in younger individuals with osteochondral defects. These include mosaicplasty, osteochondral allo/autografts, microfracture, autologous chondrocyte implantation and biomaterial/scaffold-based systems (Redman *et al.*, 2005). The use of basic biomaterial scaffolds to emulate and support the repair of osteochondral tissue is associated with several limitations, most commonly poor reproduction of the functional multi-layered tissue environment (Lesage *et al.*, 2022).

This thesis will explore the potential of an innovative scaffold-based system (known as a gene activated matrix) in addressing substantial osteochondral defects. Through its novel method of action, this medical intervention aims to more effectively repair the complex tissue environment, thereby postponing the need for artificial prosthesis and extending the lifespan of native tissues.

1.2 Osteochondral tissue

1.2.1 Sub-chondral bone

Subchondral bone lies beneath the calcified layer of articular cartilage and has two main roles: as a stress absorber and to support the shape and health of the overlying cartilage (Goldring & Goldring, 2010).

The structure and function of subchondral bone tissue differs across the two distinct regions: the sub-chondral cortical bone plate and the sub-chondral trabecular bone. The sub-chondral bone plate is situated directly below the calcified cartilage layer and is a thin cortical channel of moderate microporosity, thus allowing penetration of nerves as well as arterial and venous blood vessels (Madry *et al.*, 2010). In contrast, the sub-chondral trabecular bone is considerably more porous (macroporous range), is more metabolically active and contains greater levels of blood vessels, sensory nerves and bone marrow. Anatomically, this region of the sub-chondral bone contains trabeculae which are widely spread and organised in alignment to the direction of force, inferring a degree of structural and mechanical anisotropy to the environment (Oftadeh *et al.*, 2015). Trabecular bone performs structurally as a shock absorber and biologically to provide metabolic maintenance to overlying cartilage.

1.2.1.1 Composition

Subchondral bone is composed of a biphasic matrix containing inorganic minerals (65% dry weight), organic components (25% dry weight), and water (10% dry weight). The mineral phase consists of the crystalline calcium apatite known as hydroxyapatite ($Ca_{10}(PO_4)_6(OH)_2$), whilst the organic phase consists of collagen type I, III and V, as well as non-collagenous proteins, proteoglycans, and lipids (Boskey, 2015). At the ultrastructural level, thin triple helical collagen type I molecules form as the main structural unit and are covalently organised into a staggered striated structure known as a collagen fibril (67 nm banding pattern) (Vyas *et al.*, 2020). Within each fibril are interspersed hydroxyapatite crystals approximately 25-50 nm in size, specifically in their platelet conformation (Bocciarelli, 1970). The crystals can be either intra-fibrillar or extra-fibrillar, whereby they associate either in the gap regions between fibrils or are found surrounding the overall structure (Lees & Prostak, 1988; Weiner & Traub, 1986). Through parallel stacking of fibrils, they form mineralised collagen fibril bundles otherwise known as collagen fibres (Figure 1.1). As composite mineralised fibre units have high cross-linking density and dissipation potential, bone tissue is imbued with remarkable tensile strength and toughness (Martin & Ishida, 1989).

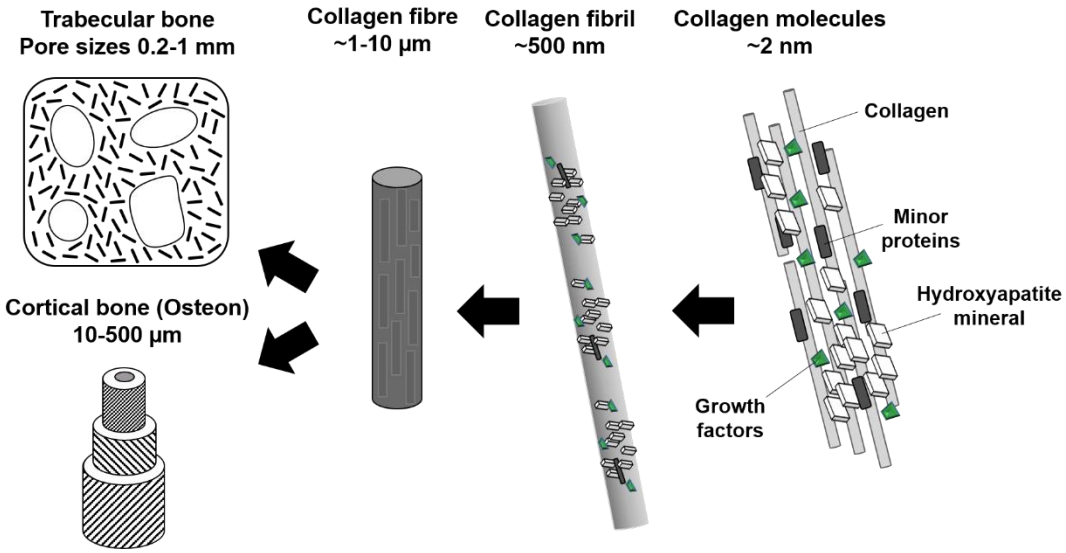

Figure 1.1 – Summary of bone tissue organisation and microstructure from its smallest components (right) to its conformation as part of larger tissues. Adapted from (Kane & Ma, 2013).

1.2.1.2 Bone cells

The maintenance of bone tissue, including its structure, integrity and functional health, is orchestrated by a diverse array of cell types. Among these are osteogenic progenitor cells, osteocytes, bone lining cells, osteoblasts, and osteoclasts.

Osteoprogenitor cells, which are immature Mesenchymal Stem Cells (MSCs), are primarily situated in the inner layers of both the periosteum (the outer membrane of bone) and the endosteum (the lining of the medullary cavity). They serve as a critical supply line for osteoblasts and bone lining cells. Meanwhile, bone lining cells, which assume a flattened and elongated form, reside on the surfaces of quiescent or inactive bone tissue, acting specifically against resorptive activities (Mohamed, 2008). Osteocytes, the most abundant type of bone cell, are situated within the lacunae and canaliculi units of the bone matrix and represent entrapped osteoblasts. These terminally differentiated cells play a pivotal role in localised bone remodelling and mechanotransduction (Goldring, 2015). Osteoblasts, which originate from osteoprogenitor cells, are immature mononuclear cuboidal cells. Their chief function lies in the synthesis of the various components constituting the extracellular matrix (ECM) of bone, this includes the secretion of collagen fibres and further organic elements of the bone matrix. They also regulate mineralisation by releasing enzymes such as tissue-nonspecific alkaline phosphatase (within matrix vesicles) that facilitate the deposition of calcium and phosphate ions, and thus create seeding sites for hydroxyapatite crystal formation (Anderson & Reynolds, 1973; Bottini *et al.*, 2018). Osteoclasts, multinucleated phagocytic cells with origins in the macrophage-monocyte progenitor lineage, are the driving force behind the process of bone remodelling, they respond to growth or changing mechanical stresses experienced by the skeleton. Through attachment to the bone surface (known

as the sealed actin ring), they create acidic microenvironments from which enzymes such as cathepsins and metalloproteinases, as well as the acid itself, can break down mineralised bone matrix components (Lerner, 2012).

1.2.1.3 Bone remodelling

The process of bone remodelling is a sophisticated and indispensable mechanism for upholding the structural integrity of healthy subchondral bone. This intricate cycle encompasses five pivotal stages: activation, resorption, reversal, formation and termination and takes place over the course of 120-200 days (Agerbaek *et al.*, 1991). Orchestrating these stages are specialised entities known as Basic Multicellular Units (BMUs), comprising osteoclasts, osteoblasts, osteocytes and bone lining cells. Furthermore, it is additionally regulated by an array of highly specialised signalling pathways involving RANKL (receptor activator of nuclear factor kappa-β ligand)/RANK/OPG (osteoprotegerin) (Boyce & Xing, 2008).

In the initial phase of activation, an abrupt external stimulus, often arising from microdamage within the tissue, triggers a site-specific response: osteocyte apoptosis (Dallas *et al.*, 2013). This event leads to a localised reduction in the population of osteocytes expressing the OPG regulatory decoy receptor. This reduction results in the diminished inhibitory effect on bone resorption processes. Consequently, with fewer OPG molecules in competition, the RANK cytokine and RANKL receptor find increased opportunities for binding on proximal osteoclasts and osteoblasts (Kennedy *et al.*, 2014). This heightened association between RANK and RANKL initiates a signalling cascade that ultimately upregulates osteoclast genes via the NFATc1 master regulator, driving significant osteoclastogenesis and marking the commencement of the resorption phase (Boyce & Xing, 2007; Kenkre & Bassett, 2018).

These newly formed/differentiated osteoclasts establish multiple sealed actin ring sites at the damaged region, setting the stage for the creation of an acidic resorption environment and the subsequent release of specific enzymes, including Cathepsin-K and matrix metalloproteinase-9 (MMP-9). These enzymatic actions lead to the swift degradation of the damaged bone, generating mineralised matrix components as by-products of the reaction (Dole *et al.*, 2017).

Crucially, to avoid unnecessary or prolonged bone resorption, osteoclasts undergo programmed cell death upon completing the recycling of a sufficient amount of damaged bone (Kenkre & Bassett, 2018). This paves the way for the recruitment of both active osteoblasts and immature mesenchymal stem cells. Through autocrine and paracrine stimulation of TGF-β and BMP growth factors, osteoblast differentiation and proliferation is induced, marking the onset of the reversal stage (Chen *et al.*, 2012). These newly formed osteoblasts embark on the synthesis and deposition of a newly formed, collagen-rich mineralised matrix (Atkins & Findlay, 2012). This

process culminates in the assembly of collagen fibre bundles into structured bone tissue units, either in the form of compact Haversian systems or porous trabeculae.

1.2.2 Articular Cartilage

Hyaline articular cartilage is a layer of tissue found covering the articulating surfaces of bones at joints and functions as a low friction gliding surface, provides resistance to mechanical impacts and shock whilst also minimising peak pressure acting on the underlying sub-chondral bone layers (Buckwalter. J. A, 1998). It is 2-4 mm thick and is absent of blood vessels, nerves or lymphatics (Fox. A, 2009; Shepherd & Seedhom, 1999).

1.2.2.1 Composition

Articular cartilage is described as a gel-like tissue system and is able to lubricate articular joints over a lifetime of movement cycles without succumbing to wear degradation. This can be attributed to its specialised component structure, consisting of chondrocyte cells embedded within a dense ECM. In terms of the cartilage ECM, it is a complex network composed of several specialised components including collagen (15–25% wet weight), water (70–80% wet weight), glycoproteins and proteoglycans (5–10% wet weight), the latter of which are large molecules made up of central proteins linked with negatively charged glycosaminoglycans (GAG) side chains (Cohen *et al.*, 1998). Interestingly, depending on the distance from the articular surface, the composition and structure of the constituents highlighted above changes. Specifically, this takes the form of four distinct morphological zones: the superficial zone, the middle or transitional zone, the deep zone and the calcified zone. The following diagram in **Error! Reference source not found.** illustrates its morphological appearance.

The superficial zone is the first and thinnest layer of articular cartilage (10-20% of thickness). It contains collagen fibres (type II) which are tightly packed and aligned parallel to the articular surface. This zone is densely populated with flattened chondrocytes and is in contact with synovial fluid, thus providing sufficient nutrient supply and protection to the embedded cellular material. This layer is responsible for the tensile properties often associated with cartilage, allowing significant resistance to sheer, tensile and swelling pressure forces imposed through biomechanical articulation (Fox. A, 2009).

Immediately beneath the superficial zone is the transitional zone, which represents the largest proportion of articular cartilage (40-60% volume). This region acts as the functional interface between the superficial and deep zones whilst also conferring added resistance to compressive forces. It is able to achieve this through the presence of large diameter collagen fibrils which are configured in a fairly irregular fashion. Moreover, aggrecan concentration increases in comparison to the previous zone whilst the chondrocyte density decreases and becomes more spheroid-like (Fox. A, 2009).

The deep zone makes up the remaining 30% of the articular cartilage volume and is responsible for providing the greatest resistance to compressive forces – given that the collagen fibrils are at their widest diameter and that their arrangement is perpendicular to the articular surface (Fox. A, 2009). This zone also contains columnar orientated chondrocytes and maintains a high proteoglycan content – a factor which contributes to its load bearing functionalities (Guo & Torzilli, 2016).

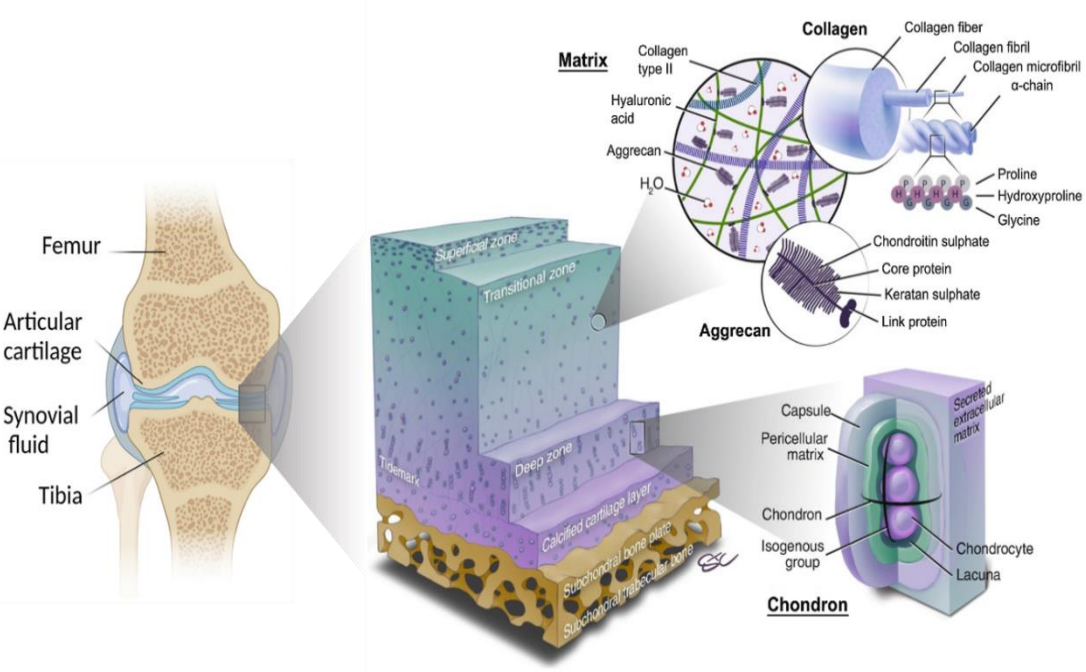

Figure 1.2 - Schematic representation of the larger osteochondral environment with emphasis on the extracellular structure of multi-zonal articular cartilage as well as the individual matrix, collagen, and chondron components. Image adapted from (Nguyen *et al.*, 2021) and (Baumann *et al.*, 2019) under the licence numbers 5778310877830 and 5778700805645.

As shown in **Error! Reference source not found.** the tidemark underlines the boundary between the deep zone and the calcified layer. Within the calcified layer, there is gradual coalition of cartilage tissue with the underlying subchondral bone. This is mainly achieved through the robust anchorage of the collagen fibrils to the bone surface and the conversion of chondrocytes to a hypertrophic phenotype (Fox. A, 2009; Pan *et al.*, 2009). Hypertrophy alters the structure of cartilage through the biomineralisation of hydroxyapatite crystals within vesicles budding from hypertrophic chondrocytes (Orimo, 2010).

On a deeper level, each of the stated zones are comprised of chondron units; which specifically consist of an individual chondrocyte and a pericellular matrix (Fraser *et al.*, 2006). In terms of the pericellular matrix, this is a unique microenvironment comprised of type II and VI collagen, proteoglycans, fibronectin and biglycan, which envelopes the chondrocyte cell (Fraser *et al.*, 2006; Poole *et al.*, 1987). It specifically functions as the critical communication interface between the chondrocyte and the larger surrounding ECM system whilst also mediating cellular

mechanotransduction and the exchange of nutrients, oxygen and signalling molecules (Guilak *et al.*, 2006).

1.2.2.2 Articular cartilage function

Articular cartilage serves as a vital component in efficiently transmitting mechanical loads and enabling smooth frictionless joint motion, which is particularly critical considering that habitual activities such as walking can impose substantial load stresses, reaching up to four times the body weight, on articulating cartilage joint regions like the knee (D'Lima *et al.*, 2012). This tissue's ability to withstand such loads and maintain essential load-bearing capacity is intricately tied to the mechanism of biphasic lubrication.

The biphasic lubrication of articular cartilage is a sophisticated and dynamic process that relies on its unique composition as mentioned previously. Comprising a solid matrix primarily consisting of collagen fibres and proteoglycans, and interstitial water occupying the spaces within this matrix, articular cartilage exhibits biphasic behaviour in response to mechanical forces. When pressure is exerted on the cartilage during activities like walking or joint movement, the interstitial water within its structure is expelled from the compressed regions (Katta *et al.*, 2008). This expulsion creates a pressurised environment within the tissue, counteracting the external load and contributing significantly to its load-bearing capacity. Crucially, biphasic lubrication also plays a pivotal role in minimising friction and reducing wear during joint articulation (Forster & Fisher, 1996). As the interstitial water is forced out during compression, it acts as a lubricant between the sliding surfaces of the joint, facilitating smooth movement. This lubricating effect is essential for preventing detrimental wear that could occur if joint surfaces were to experience direct friction.

Alongside interstitial water, chondrocytes and synovial cells also secrete the glycoprotein lubricin, of which acts as a secondary lubricant specifically coating exposed articular cartilage surfaces and forming a molecular barrier that further reduces friction and prevents adhesion between cartilage surfaces (An *et al.*, 2022). Finally, other lubricants present specifically in the synovial fluid contribute to articular cartilage lubrication. These include free or bound hyaluronic acid, phospholipids, and proteoglycans, which collectively enhance lubrication and provide additional protection to the cartilage surface (An *et al.*, 2022). In the case of hyaluronic acid, this helps maintain the viscosity and lubricating properties of the synovial fluid, while phospholipids and proteoglycans contribute to the formation of boundary layers and reduce friction during joint movement (Lin *et al.*, 2020).

1.2.2.3 Chondrocytes and cartilage homeostasis

Cartilage is sparsely populated with chondrocyte cells (Fox. A, 2009) which are responsible for the synthesis, organisation and turnover of cartilage tissue, specifically with regards to large ECM

components including type II collagen and proteoglycans (Bhosale & Richardson, 2008). Each chondrocyte is embedded within its own localised microenvironment, the chondron, directing specific ECM recycling whilst heavily restricting its own bilateral migration. As a result, cellular turnover and proliferation characteristics remain remarkably low, and therefore act as a significant factor for which cartilage tissue possesses poor repair capacities in response to injury (Fox. A, 2009).

Healthy hyaline cartilage is maintained via a delicate interplay of catabolic and anabolic cell signalling mechanisms, which lead to the controlled degradation and/or synthesis the various ECM components, respectively (Figure 1.3) (Finnson *et al.*, 2012). Chondrocytes continuously monitor the tissue's architecture and biochemical composition, allowing for site-specific adjustments to the cartilage ECM constituents depending on the mechanical and chemical need within the joint space. This allows for the maintenance and replenishment of old with new tissue (Buckwalter. J, 2005). It must be noted however that cartilage remodelling primarily functions to maintain tissue homeostasis with large scale systematic turnover , as seen in bone remodelling, not being possible in this environment (Yokota *et al.*, 2011) For example, when activated by changes to its cellular microenvironment (soluble factors, oxygen levels or mechanical stress), chondrocytes produce inflammatory cytokines and chemokines – specifically interleukins (IL-1β, IL-6), Transforming Growth Factors (TGF-β) as well as matrix degrading enzymes such as metalloproteinases and aggrecanases (A Disintegrin and Metalloproteinase with Thrombospondin motifs; ADAMTS) (Glyn-Jones *et al.*, 2015). Many of these molecules influence vital signalling and transcriptional activities of cartilage maintenance genes within chondrocytes. Specifically, as anabolic and catabolic regulators, cytokines such as IL-1β and TGF-β can directly affect complex signalling pathways resulting in changes in chondrocyte matrix metabolism (Demoor *et al.*, 2014).

IL-1β is synthesized largely by chondrocytes but also by synoviocytes and macrophages within the synovial membrane (having direct influence on locally resident MSC differentiation and lineage commitment) (Goldring & Marcu, 2009). Through binding to its receptor interleukin-1 receptor type 1 (IL-1R1) a signalling cascade is created which ultimately leads to the activation of NF_kB. This transcription factor permits expression of genes encoding matrix metalloproteinase (MMP) enzymes such as the catabolic MMP-13, which actively removes ageing or damaged cartilage matrix by cleavage of non-helical telopeptides of type II collagen (Billinghurst *et al.*, 1997). Crucially, under normal homeostasis, levels of this cytokine importantly remain low and its expression tightly controlled.

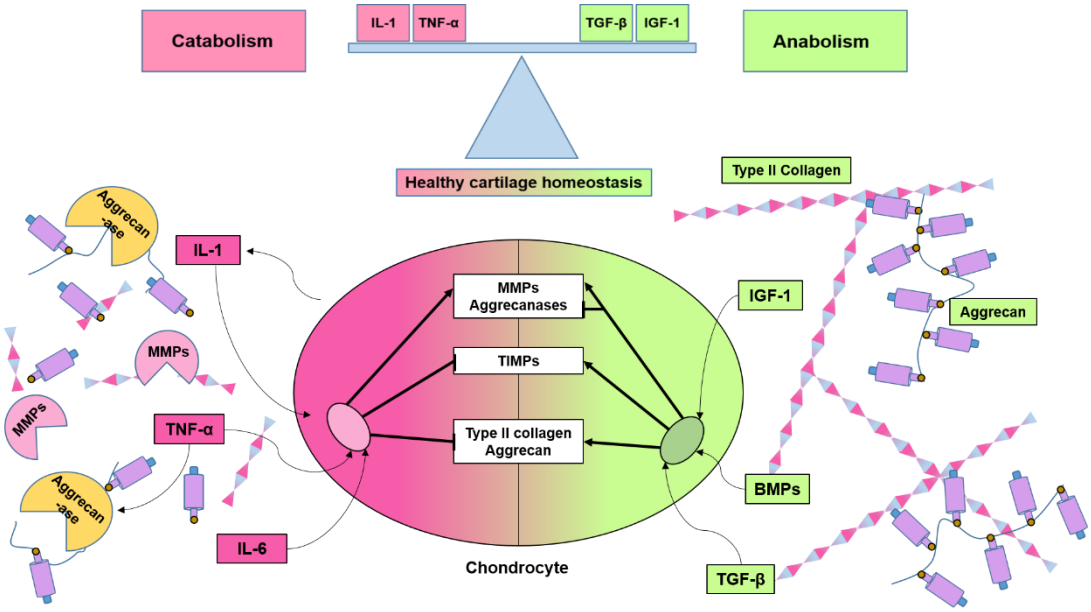

Figure 1.3 – Influence of catabolic and anabolic cellular signalling and growth factors for the maintenance and/or healthy turnover of cartilage tissue. TNF: Tumour necrosis factor, TIMP: Tissue inhibitor of metalloproteinase, IGF: Insulin growth factor. Image adapted from (Demoor *et al.*, 2014).

Due to the mechanosensitive nature of chondrocytes, levels of active TGF-β (converted from its latent form) have been shown to markedly increase when a load is detected by cells (strain below 20%, stress below 18 MPa) (Bougault *et al.*, 2012; Natenstedt *et al.*, 2015). At this point, the associated intracellular signalling pathway is initiated and results in the TGFβ type II receptor (TGFβRII) and activin receptor-like kinase-5 (ALK5) cascade. This leads to downstream translation of genes specific for; ECM component synthesis, articular cartilage maintenance, regulation of other inflammatory cytokines (such as IL-1) and the inhibition of chondrocyte hypertrophy (Finnson *et al.*, 2008).

1.3 Gradients of the osteochondral tissue

As illustrated in sections 1.2.1 and 1.2.2, sub-chondral bone and articular cartilage are two highly distinct and variable tissue types, which possess functionally adapted characteristics at macro, micro, and nanoscale levels. This includes high variability with regards to structural, biochemical (cellular and matrix) and biomechanical properties within each of the tissues. Yet, when amalgamated into one whole tissue system (as the osteochondral tissue unit), they act synergistically, whereby each tissue relies on the other for functionally dependent support. This relationship is achieved and maintained by a number of gradients which will be described in more detail below.

1.3.1 Structural gradients

Osteochondral tissue functions effectively due to the presence of axial gradients along its structure, specifically with regards to natural tissue porosity, pore size and permeability. In the

articular cartilage region, the distinctive composition of collagen and aggrecan ECM proteins create a gel-like tissue with an overall porosity ranging from 60-85%. Here, pore sizes fall within the range of 2-6 nm in diameter, crucially remaining open and interconnected, enabling the diffusion of small-sized nutrients and waste products (Ansari *et al.*, 2019). Despite its low overall permeability, permeability gradients also exist across different cartilage zones. For instance, Boschetti *et al* reported permeability values of $9.33x10^{-16}$, $8.01x10^{-16}$ and $7.11x10^{-16}$ m^4/Ns for the superficial, transitional, and deep articular cartilage zones, respectively (F.Boschetti *et al.*, 2004).

In the subchondral bone region, these axial gradients undergo further modifications. The subchondral bone plate is a highly compact and hard cortical tissue characterized by lower overall porosity (5-30%) and larger pore sizes (0.1-250 μm) compared to the upper articular cartilage region (Ansari *et al.*, 2019). The final trabecular bone layer then exhibits a unique structural composition marked by varying levels of compactness, ranging from 30-90% porosity and pore sizes spanning 5-2000 μm in diameter. This intricate gradient in porosity and pore size ensures optimal nutrient exchange and mechanical support throughout the osteochondral tissue structure (Ansari *et al.*, 2019). Significantly, permeability within such bone regions is also increased to an approximate value of $2\ x10^{-15}$ m^4/Ns (Martin *et al.*, 2007).

1.3.2 Cellular and matrix gradients

Osteochondral tissue contains a variety of cells and matrix components throughout its distinct layers. This includes osteoblasts, osteoclasts, osteocytes, bone lining cells and mineralised type I collagen within the bone layer, hypertrophic chondrocytes and mineralised type II collagen within the calcified cartilage layer, and primary chondrocytes embedded within type II collagen and proteoglycans within the articular cartilage layer (Wang *et al.*, 2022). Significantly, in terms of the transition from trabecular bone to the cortical bone plate, it can be said that no obvious cellular gradient is present. In contrast, within the articular cartilage tissue unit, several gradients exist specifically with regards to cell distribution and size. Firstly, concerning chondrocyte cell density, it has been found that chondrocyte numbers (per unit cartilage volume) decrease markedly when transitioning between the respective superficial, transitional and deep zones (24,000 – 10,300 – 7,700 cells/mm^3) (Quinn *et al.*, 2013). This amounts to a 59% and 67% decrease in overall cell density and is indicative of the zonally specific functional requirements – i.e. higher density regions being more resistive to shear forces whereas low density regions allow for compressive force propagation via the higher proportion of zonally deposited matrix components. Secondly, in addition to cell density changes, there is also graded variation in the size of chondrocytes within

the articular cartilage tissue unit, with cellular dimensions increasing and becoming more elongated from the superficial layer down towards the deep zone (Figure 1.4) (Fox. A, 2009).

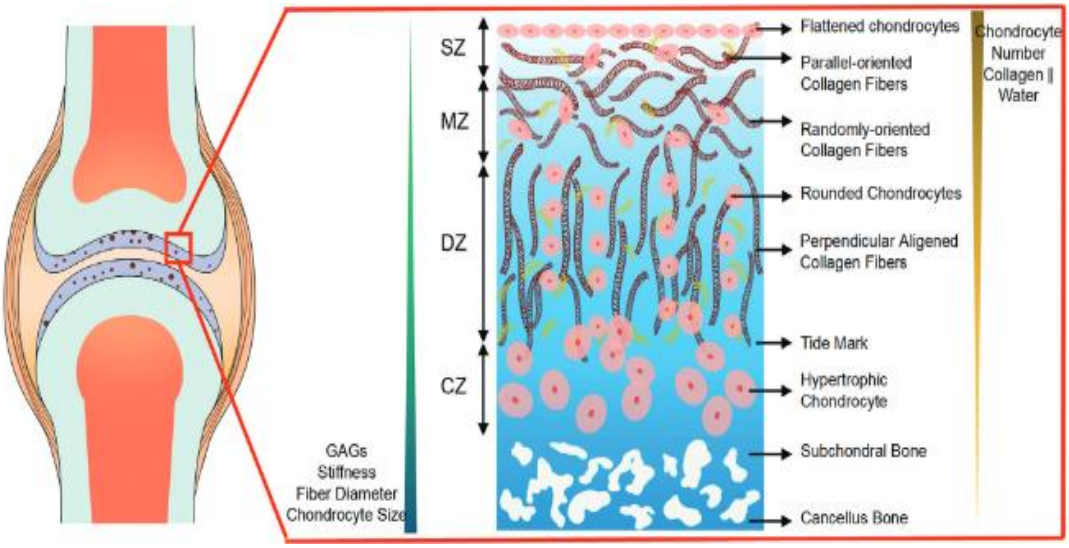

Figure 1.4 – Graphical illustration of the various cellular (chondrocyte) and matrix (collagen fibres, proteoglycans, water) gradients found within the osteochondral tissue compartment. Taken from (Zhou *et al.*, 2020) under licence number 5658290205623

The composition and arrangement of cartilage ECM gradually changes according to proximal location to the articular surface or the inner cortical bone regions. The cartilage fluid phase (interstitial water and electrolytes) shows zonal gradation, with superficial regions possessing upwards of 80% total water content, in comparison to only 67% in the deep zones (Figure 1.4) (Crolla *et al.*, 2022; Maroudas & Venn, 1977). Functionally, this graduated decrease appears inherently linked to the need for extensive cellular nutrient supplies in the upper regions as well as allowing for mechanical load distribution and finally providing lubricative properties. With such properties becoming less essential upon increases to tissue depth, the proportional fluid phase decreases further throughout the calcified cartilage layers and eventually into the subchondral bone region, where water content is as low as 15-25% (Surowiec *et al.*, 2022).

Gradients are present within the solid phase of the cartilage ECM. The superficial cartilage zone contains the highest density of collagen (type II) (86% of the zonal dry weight), and is characterised specifically by the presence of thin component fibrils (30-35 nm in diameter) packed in a dense and parallel orientation (Ansari *et al.*, 2019). This direction determines the greatest tensile and shear strength (Bhosale & Richardson, 2008). Moving into the transitional zone, collagen type II fibril density then decreases, appearing marginally more diffuse over the larger overall zonal area. Furthermore fibril diameter increases with depth whilst assuming a more angular conformation. The deep zone displays a further reduction in collagen type II content, with these fibrils now constituting only 67% of the zonal dry weight. Notably, the collagen fibrils in this zone are the largest, ranging from 40 to 80 nm in diameter. They are arranged perpendicular to the articular surface, with functional emphasis on the reinforcement between

the cartilage and the underlying sub-chondral bone (Figure 1.4) (Ansari *et al.*, 2019). In terms of the calcified cartilage layer, the proportion of type II collagen decreases further in this zone (only 20% zonal dry weight) and furthermore begins transitioning towards a mineralised phenotype (Zhang *et al.*, 2012). At the sub-chondral bone region, no collagen type II is present with bone tissue instead being composed of mineralised collagen type I fibres.

Alongside a gradient in collagen content, it is further found that the proportion of and type of proteoglycans can also differ along the articular cartilage depths. This is illustrated firstly by their apparent zonal dry weight increase from the superficial region to the transitional region (15%-25%) before diminishing marginally in the deep region (20%) (Ansari *et al.*, 2019). The predominant proteoglycans in the superficial zones are the decorin and biglycan subtypes whilst aggrecans are found most concentrated in the deep zone (Alcaide-Ruggiero *et al.*, 2023; Ansari *et al.*, 2019).

1.3.3 Biomechanical gradients

The mechanical properties of the osteochondral tissue also vary because of the structural, cellular and matrix gradients present. The compressive modulus of articular cartilage regions gradually increases from the superficial (0.02 MPa) to the deep zone (6.44 MPa), and the compressive strength increases from 0.005 to 4 MPa. In deeper calcified cartilage layer, a compressive modulus of 6 GPa is exhibited, a clear indication of the mechanical strength imbued by mineralisation processes. The sub-chondral cortical bone plate exhibits a Young's modulus ranging from 16-23 GPa, whereas it falls within the range of 1-2 GPa for the trabecular bone (Augat & Schorlemmer, 2006; Gibson, 1985). Furthermore, the compressive and tensile strength of the cortical bone plate measures 133 MPa and 49-60 MPa respectively, contrasting with 0.5-100 MPa and 1-20 MPa in the trabecular bone layers (Lawson & Czernuszka, 1998; Roeder *et al.*, 2008; Suchanek & Yoshimura, 1998).

1.4 Osteochondral defects and post-traumatic OA

1.4.1 Classification

An osteochondral defect can be defined as a localised lesion in which severe destruction and alteration occurs within both the articular cartilage and sub-chondral bone units of articulating osteochondral tissue (Zhou *et al.*, 2020). Often this can be as a result of sudden stimuli of mechanical origin (hyperphysiological blunt trauma/ repetitive over-use microtrauma) or underlying biological factors (i.e. osteochondritis dissecans or osteonecrosis), and can occur in joints such as knee, ankle and hip (Thomas *et al.*, 2017). Post injury symptoms are generally progressive with pain, swelling, severe inflammation and loss of mobility all classic indicators which materialise quickly after defect creation (Howell *et al.*, 2021).

Given that the symptomatic presentation of osteochondral defects closely resembles that of partial or full-thickness chondral defects (i.e. lesions which stem only as far as the calcified cartilage layer), clinicians utilise macroscopic evaluation techniques in combination with a standardised classification system to fully characterise individual lesion severity (Gorbachova *et al.*, 2018; Mithoefer *et al.*, 2015). The Outerbridge system and the ICRS (International Cartilage Repair Society) grading scale have been used specifically for this purpose – with both generally discriminating on account of lesion size and depth (Slattery & Kweon, 2018). Despite the ICRS system being the most recently formulated grading scale (established by Brittberg and Winalski in 2003 (Brittberg & Winalski, 2003)), it is now widely regarded as a gold standard classifying system, specifically featuring five grading levels ranging from 0 (or normal tissue) to 4 (or severely abnormal) (De Laroche *et al.*, 2018). Examples of these gradings can be found in Figure 1.5. Due to the disruption and destruction to the sub-chondral bone layer, osteochondral defects are defined solely as ICRS grade 4 lesions.

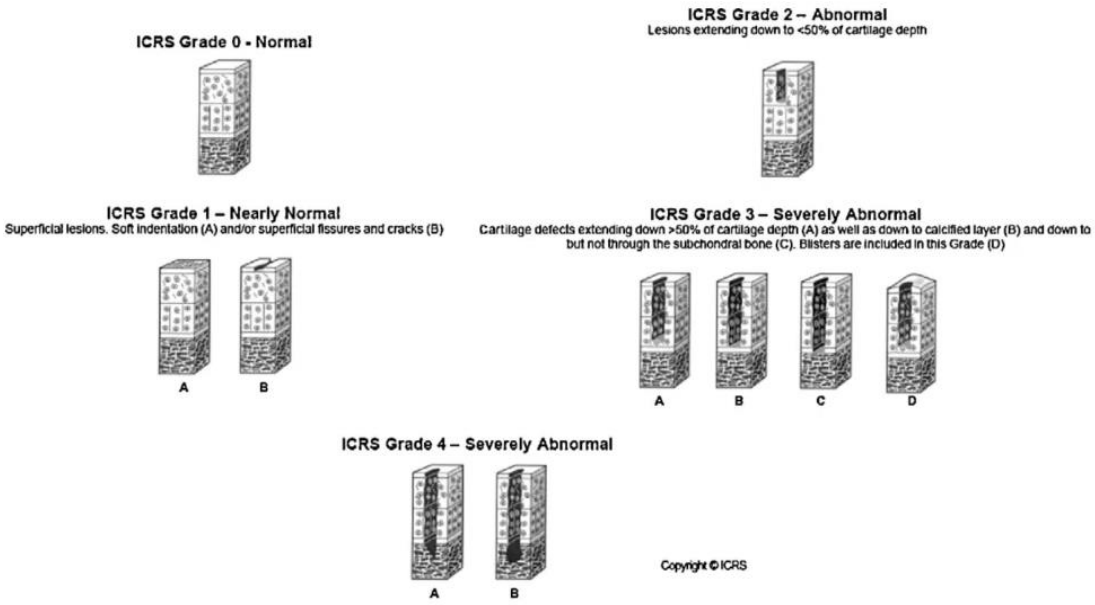

Figure 1.5 – Graphical illustration of various degrees of cartilage and sub-chondral bone lesions according to the ICRS grading system. Taken from the ICRS Cartilage Injury Package.

1.4.2 Post defect tissue response

In previous sections, it was discussed how intricacies in tissue composition and cell signalling of both articular cartilage and sub-chondral bone lead to healthy maintenance and turnover, allowing the articulating joint to remain functional over an entire lifetime. However, upon subjection to a hyperphysiological traumatic stimuli, the delicate homeostasis can become skewed, leading to inappropriate activation of catabolic factors, which induce degradation and lead to system wide loss of function. This runaway effect can ultimately result in the condition known as post-traumatic osteoarthritis (PTOA).

The pathogenic mechanism of PTOA following an osteochondral lesion usually proceeds according to three phases, the immediate phase (relating to the causative mechanistic event), the acute phase (relating to associated cell death and inflammation), and finally the chronic phase (relating to end stage joint pain and dysfunction) (Evers *et al.*, 2022). As such, the acute phase proceeds directly after the supraphysiological trauma, and can be characterised by the significant loss of integrity of chondrocytes within the damaged region (Bajaj *et al.*, 2010). This cellular destabilisation results in an influx of calcium ions into the joint space, leading to substantial waves of adjacent chondrocyte apoptosis (D'Lima *et al.*, 2001). During the apoptosis process, such chondrocytes release unique inflammatory mediators such as IL-16 and IL-1β (He *et al.*, 2018). These bind to their associated receptors on non-apoptotic chondrocytes and begin the previously described NF_kB signalling cascade. The final result being the induction and subsequent expression of catabolic MMP's (MMP3 and MMP13), leading to large scale cartilage matrix breakdown (Klatt *et al.*, 2006; Liacini *et al.*, 2003).

Alongside this, trauma associated damage can also lead to changes to the synovial tissue and sub-chondral bone layers. Here, local chemokines as well as individually released cartilage matrix components such glycoproteins, proteoglycans, or GAGs act as damage associated molecular patterns (DAMPs), and therefore can induce an innate immune response in the form of the polarisation of resident synovial macrophages (Evers *et al.*, 2022). Through toll-like receptor activation, the immune cells upregulate similar inflammatory markers, releasing more or less the same catabolic factors into the region whilst further promoting joint inflammatory processes. Of these, IL-1β particularly has specified roles within the exposed sub-chondral bone layers, whereby its receptor binding with exposed bone cells leads to promotion of osteoclastogenesis (Dilley *et al.*, 2023). As a result, an influx of bone remodelling cells can be observed, with bone resorption presenting as a common early-mid stage PTOA indicator (Figure 1.6).

In the final chronic phase, of which may last months or years, progressive synovitis, hemarthrosis, osteophyte development and fibrosis of the joint capsule are all commonly presented and the causative factors for the severe joint pain and overall dysfunction presented clinically (Dilley *et al.*, 2023).

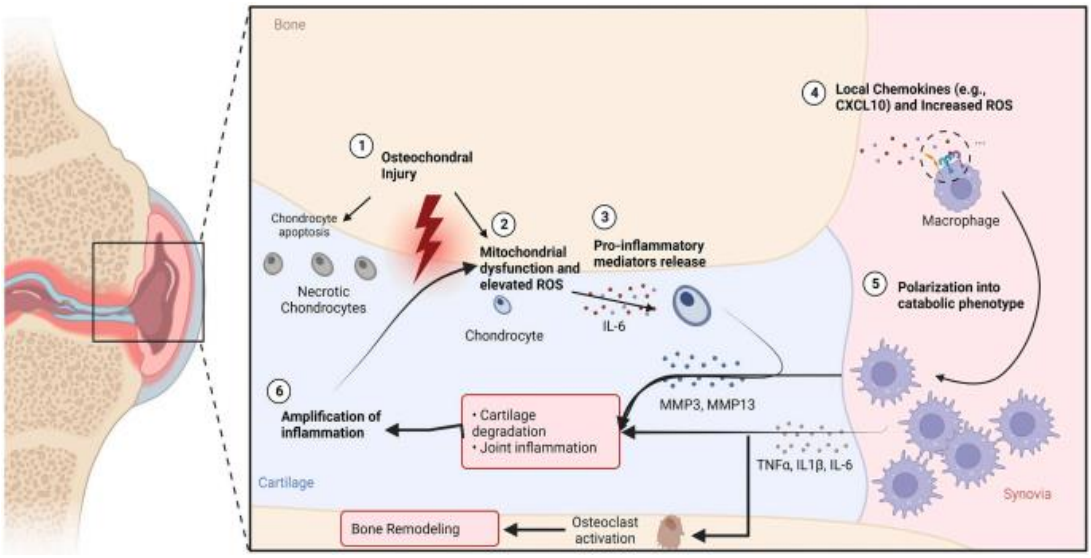

Figure 1.6 – Schematic illustration of the cross-talk between cartilage, sub-chondral bone, and the synovial tissue in the pathogenesis of PTOA. 1) Traumatic injury resulting in the formation of an osteochondral defect. As a result of such injury, large scale chondrocyte apoptosis and necrosis occurs. 2) Mitochondrial dysregulation of adjacent chondrocytes results in the release of inflammatory mediators (IL-6), of which stimulates the production of catabolic MMPs. 4) Simultaneously, trauma associated damage to synovial tissue leads to resident macrophage polarisation 5) of which can cause the production and release of further catabolic factors (TNF-α, IL-1β, and IL-6) into the synovial fluid. Ultimately, the presence of such factors induces wide-scale cartilage degradation as well as the induction of sub-chondral bone remodelling. 6) Extensive cartilage and bone remodelling favours the progression of inflammatory behaviours restricting reparative mechanisms. Taken from (Dilley *et al.*, 2023).

1.4.3 Symptoms of post-traumatic osteoarthritis

In unfortunate individuals who experience severe osteochondral lesions, the pathogenic process outlined above can be considered the most likely disease pathway if interventions are not sought. Characteristically, in these scenarios patients will ultimately present with classical degenerative osteoarthritis symptoms including pain (both activity related and at rest), joint stiffness/instability and reduced overall articulating range of motion (Hunter *et al.*, 2008). In these cases, the pain presents early due to direct exposure of the sub-chondral bone regions and is then further exacerbated upon the triggering of inflammatory processes, synovitis and downstream bone degeneration. Furthermore, through actions of said inflammatory mediators, primary afferent nerves previously considered non-problematic, later become aggravated and highly sensitised, meaning even gentle physical activities elicit discomfort and pain (Hunter *et al.*, 2008).

In contrast, being an aneural tissue, the progressive destruction of the solid phase articular cartilage regions has less significance with regards to the symptomatic pain experienced by patients, however it does play a substantial role in the presented biomechanical tissue dysregulation (Mansour, 2003).

Firstly, as a direct outcome of the hyperphysiological load, the proximal articular cartilage becomes heavily damaged, and as a result assumes a more disorganised and swelled conformational state. At the molecular level, this is characterised by fibrillated ECM networks whereby the collagen fibres appear ruptured and matrix associated GAGs are rapidly cleared (Di

Micco *et al.*, 2004). Crucially, in this state, tensile modulus properties are reduced by up to 90% whilst its compressive modulus is also heavily impacted, thus impairing the tissue's ability to withstand and transmit any additional compressive loads post trauma (Akizuki *et al.*, 1986). Furthermore, load associated chondrocyte apoptosis and the progressive diminishing of local proteoglycans result in heightened collagen type I deposition in comparison to the more functional collagen type II previously found in healthy hyaline articular cartilage, leading to stiffer and thinner matrix being deposited within the injured area, which possesses sub-optimal elastic modulus (Silver *et al.*, 2002). This ultimately means future mechanical loads may not be properly dissipated and in fact are transmitted fully to the sub-chondral bone. As a result, significant structural alterations take place within both the sub-chondral cortical bone plate and underlying trabecular bone layers including bone marrow oedema and the formation of periarticular osteophytes (Goldring & Goldring, 2010; van der Kraan & van den Berg, 2007).

1.5 Current treatments for osteochondral defects

Although epidemiological data is sparse comparing knee, ankle and hip PTOA, it is generally accepted that knee PTOA is the most prevalent of the three worldwide (Maia *et al.*, 2023). Naturally, multiple knee joint specific surgical approaches have therefore been reported which have aimed to treat the condition, at various stages of its disease pathway.

In chronic late stage PTOA cases, in which large scale osteochondral tissue degeneration has occurred, the most appropriate treatment option is a total knee replacement (Schenker *et al.*, 2014). Typically this involves the majority of the articulating joint being replaced with a metal prosthesis being implanted. TKR's have proven to be remarkably successful, especially in older patients (> 70 years old), with significant improvements in knee function and quality of life being observed post operation, whilst significantly its survivorship remains in the region of 95% when collectively analysed after 10 years (Canovas & Dagneaux, 2018; Ho *et al.*, 2023). However, in the case of younger more active individuals who present with late stage osteoarthritis, TKR outcomes have been less favourable, with higher rates of complications and increased risk of revision often observed in the first 5-10 years post operation (Julin *et al.*, 2010). Iterative revision surgery is particularly debilitating with additional bone alterations often required to accommodate occlusion of new implants, leading to substantial bone loss and compromised bone quality. Moreover, revised TKR's may not achieve same level of biomechanical function as the original (Roman *et al.*, 2022). Although several contributing factors have been proposed, the overriding mechanism appears to stem from the higher physical demands placed on the implants by said patients resulting in faster than anticipated failure (Losina & Katz, 2012).

It is therefore recommended that alternative treatments are sought for younger patients, which can be applied in the early stages of the disease timeline, thus delaying the onset of severe degradative pathologies and the consequent necessity for total prosthetic intervention. For

osteochondral defects specifically, such treatments include: microfracture, mosaicplasty and autologous chondrocyte implanation..

1.5.1 Microfracture

The strategy of microfracture was first coined by Steadman *et al.*, who put forward the idea that precise drilling of micro-holes at the site of a small osteochondral lesion could induce a degree of site-specific repair (Steadman. JR, 1997). Specifically, through using an arthroscopic awl, multiple fracture holes roughly 3-4 mm apart can be generated at the lesion site. These cavities penetrate into the sub-chondral bone plate (approximately 4 mm depth), and importantly leads to underlying bone marrow infiltration, without disruption of sub-chondral bone plate integrities, and super-clot formation (Bhosale & Richardson, 2008). In doing so, endogenous bone marrow mesenchymal stem cells (BM-MSCs) contained within the super clot can adhere to and fill the defect, before undergoing differentiation to form new articular cartilage and bone tissue (Figure 1.7).

Despite a healing response being activated via the above process, the resulting neotissue that is deposited is often in the form of fibrocartilage rather than the desired hyaline phenotype, which possesses less durability and is generally considered biomechanically inferior (Bhosale & Richardson, 2008; Howell *et al.*, 2021). Furthermore, the repair tissue possesses homogeneity with no evidence of the cellular, matrix and biomechanical gradients indicative of natural osteochondral tissue. As a result of these two factors, load induced degeneration occurs in the period post-surgery and ultimately the reoccurrence of joint dysfunction (Mithoefer *et al.*, 2009). Furthermore, in the case of the repair of larger osteochondral lesions (between 2-4 cm^2), it has been suggested that microfracture is largely ineffectual (Chimutengwende-Gordon *et al.*, 2020).

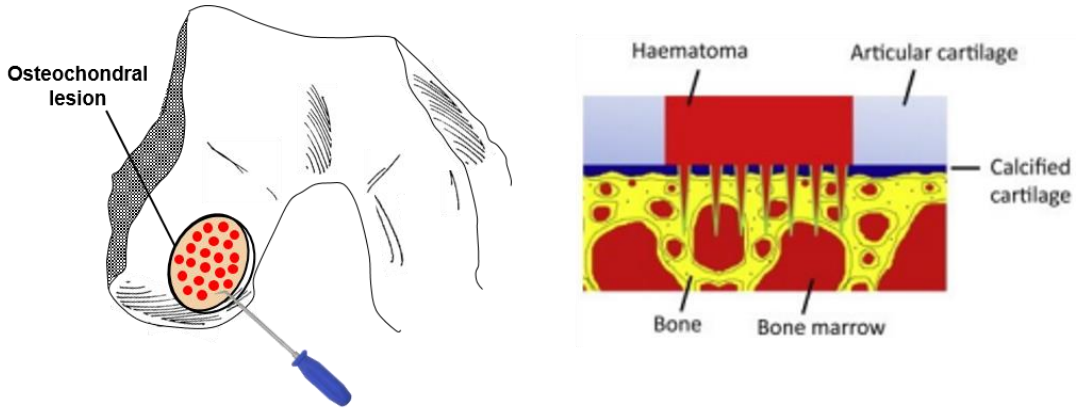

Figure 1.7 – Graphical illustration of the surgical procedure known as microfracture for the repair of osteochondral lesions. (Left image) shows the precise creation of multiple micro-holes within a defect through the use of an arthroscopic awl (and drill). (Right image) demonstrates the formation of a haematoma/super-clot, of which contains reparative bone-marrow derived MSCs. Right image taken from (Hunziker *et al*, 2015) with permission from Elsevier under licence number 5658680567026.

1.5.2 Mosaicplasty

Mosaicplasty was first reported in 1999 by Kish and Hangody as a potential method for the treatment of osteochondral defects (Kish *et al.*, 1999). It utilises the concept of autologous tissue transplantation, whereby cylindrical osteochondral plugs are isolated from a healthy non-weight bearing region of the articulating knee joint and consequently transplanted onto various locations within the defect site (Bhosale & Richardson, 2008). Figure 1.8 provides an example of this procedure. The main benefit of its use includes the vast coverage of a lesion with high quality autologous tissue which possesses natural osteochondral tissue gradients. With the provision of such gradients, functional biomechanical tissue properties (such as compressive strength, viscoelasticity and load transmission) can be critically restored to this defect region (Robert, 2011). Additional advantages include high defect coverage (up to 90% of the defect), stable press-fit of transplanted tissue (without the need for additional attachment additives), and the fact that the operation is a single stage arthroscopic day procedure (Bhosale & Richardson, 2008; Hildner *et al.*, 2011; Shah. M, 2007).

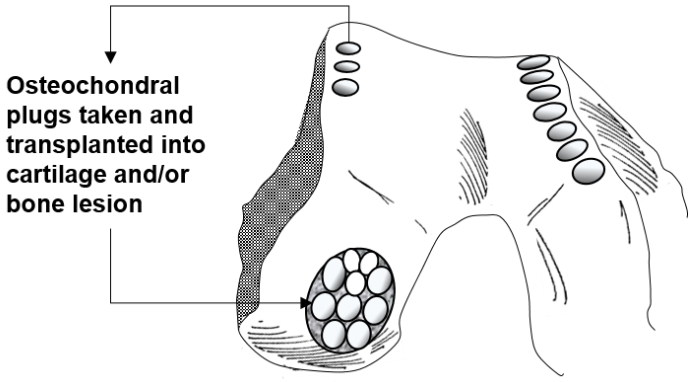

Figure 1.8 – The mosaicplasty surgical concept in which osteochondral plugs are extracted from non-weight bearing regions and implanted into the lesion site. Adapted from (Bartha *et al.*, 2006).

However, considerable amount of the literature also details several adverse consequences associated with this procedure. Firstly, it has been stated that the act of removing osteochondral tissue from healthy non-weight bearing joint sites destroys a comparable amount of healthy tissue the surgeon would be attempting to treat, leading to severe donor site morbidity (Hunziker, 2002). Furthermore, the procedure itself is technically challenging, requiring specialised surgical equipment and can only be used in certain contexts (e.g. patellar defects often untreatable) (Bentley, 2004). In terms of quality of integration and repair, this process is not held in particularly high regard. The mosaic plugs often fail to integrate laterally with native cartilage whilst the space between the plugs is filled with fibrocartilage. Synovial leakage can also occur resulting in cyst formation (Bhosale & Richardson, 2008). Additionally, upon analysis of the donor sites, it has been identified that chondrocytes undergo significant degeneration in the period after surgery whilst formation of osteophytes is also common (Kim *et al.*, 1991).

1.5.3 Autologous chondrocyte implantation

Due to the ability of chondrocytes to deposit new cartilage matrix, a cell based method known as autologous chondrocyte implantation (ACI) was proposed for osteochondral defects. This approach was first reported by Brittberg and can be separated into two distinct stages (Brittberg *et al.*, 1994). The first stage involves the debridement of the osteochondral defect site followed by the harvesting of a 0.5-1 cm non-weight bearing full thickness articular cartilage biopsy. Chondrocytes from this healthy tissue sample are then isolated and expanded *in-vitro* (Bentley *et al.*, 2012). After 3-5 weeks of cell culture (ensuring cell phenotype is maintained), the second stage is carried out. This comprises the re-implantation of chondrocytes into the defect site and either a periosteal autograft or a porcine collagen membrane being applied to enclose the defect. For effective surface fixation, sutures and/or fibrin glue are added around the defect circumference in a final step (Ozmeriç *et al.*, 2014). Under optimum conditions (3-4 weeks unloaded, 6-10 weeks minimal mechanical loading), transplanted chondrocytes gradually deposit cartilage ECM within the osteochondral defect, which can in some cases develop into hyaline-like cartilage tissue (Brittberg *et al.*, 1994). A follow-up study by Ogura *et al* (minimum 2 years) looked at the ability of ACI methods for osteochondral defect repair (chondral lesions 6.0 cm^2, bone defect area of 1.7 cm^2). In the sample set of 15 patients, it was found 83% of patients illustrated complete defect filling (Ogura *et al.*, 2019).

Despite having a relatively high success rate there remains limitations of the use of ACI for large osteochondral defect repair. This includes firstly the requirement of a prolonged treatment process with two major surgical interventions at multiple sites, as standard (Hunziker *et al.*, 2015). Secondly, the long post-operative recovery time (taking 10-21 months for biomechanically stable neotissue to be fully integrated) (Saris *et al.*, 2009). Thirdly the high cost, with a full ACI procedure generally costing upwards of $14,400 per patient (Clar *et al.*, 2005). And finally, the failure to fully reproduce the osteochondral gradient tissue environment. Despite the appearance of hyaline-like cartilage within the central defect, it has been reported fibro-like cartilage can form on the outer edges of the membrane-tissue interface with sub-optimal functional properties (Ozmeriç *et al.*, 2014).

Based on the pre-clinical and clinical outcomes of the three surgical treatment methods discussed in section 1.5, it is clear that a cost-effective, high quality, gradient tissue producing strategy for osteochondral defect repair remains elusive. The approach of tissue engineering offers a promising avenue for overcoming these challenges. By combining biomaterials, cells, and signalling factors, engineered scaffolds can be designed to mimic and facilitate the recapitulation of the native tissue environment, providing a platform for controlled and effective bone and cartilage regeneration. Pursuing tissue engineering strategies holds the potential to address the shortcomings of traditional approaches, offering more reliable, personalised, and durable solutions for the repair of osteochondral defects.

1.6 Osteochondral tissue engineering

The field of tissue engineering was first defined and presented by Robert Langer and Joseph P. Vacanti in their seminal report in 1993 (Langer & Vacanti, 1993). They defined it as an interdisciplinary field combining the ideas of physiology, cell biology & gene therapy with biotechnology and material engineering in the hope of developing medical therapies and innovations which have the capability to restore, maintain, or improve the functional capacity of a tissue or organ. Since then, the field has developed exponentially, with developed approaches following an established paradigm involving the use of biomaterials, cells, and inductive/regulatory stimuli, which work in tandem to bring about a full healing response to an injured region specifically lacking the capacity to spontaneously heal (Figure 1.9) (Parveen *et al.*, 2006).

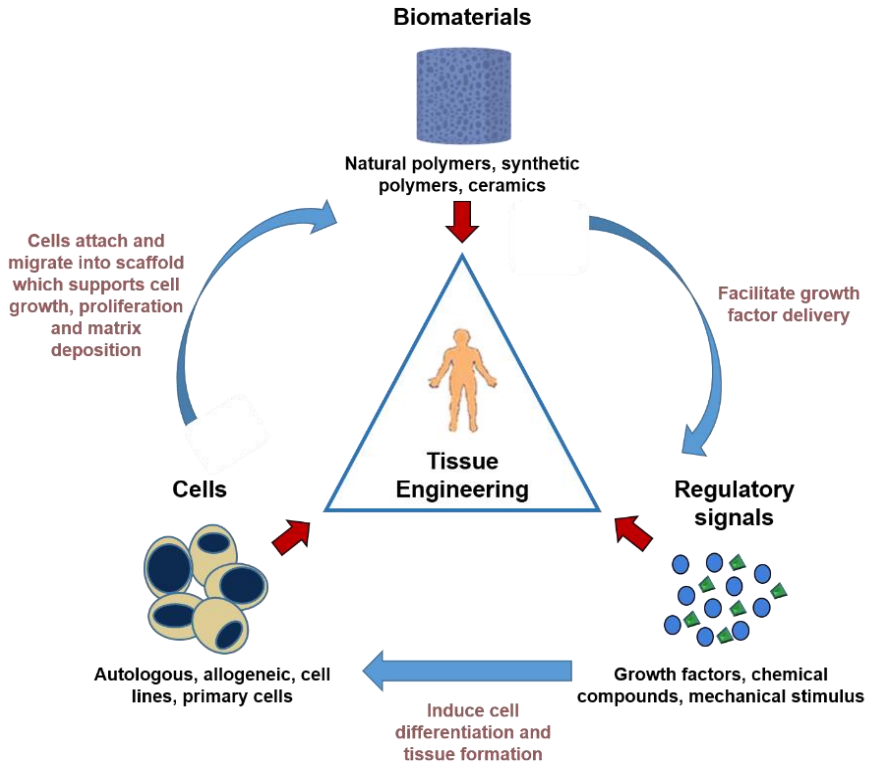

Figure 1.9 – The three interlinked components which encompass the tissue engineering triad. Adapted from (Murphy *et al.*, 2013).

The most common tissue engineering process takes place as follows: 1) a patient presents with a site-specific injury or defect, 2) a cellular sample is obtained from the patient and expanded *in-vitro*, 3) the expanded population is homogeneously seeded throughout a mechanically supportive structure (known as a scaffold), 4) the cell-laden construct is then transplanted directly into the defect site, whereby repair then ensues (Ambekar & Kandasubramanian, 2019). Naturally, variations have been developed, including cell-free and scaffold-free strategies, which may be applied depending on the nature of the defect in question. In terms of this thesis however, cell-free approaches will be particularly acknowledged and discussed in greater detail, specifically for their application in osteochondral defect repair.

1.6.1 Biomaterial composition

As part of the tissue engineering triad, the biomaterial scaffold represents a vital component without which a full and powerful tissue repair response could not proceed. Within the field, they can be represented as 3D sponges, hydrogels, non-woven fibrous constructs, electrospun or woven structures or as 3D printed systems. In terms of their function, these biomaterials inherently provide 3D environments which allow for endogenous cellular recruitment, adhesion, infiltration and growth (Ramzan *et al.*, 2023). Moreover, as a result of their unique natural tissue mimicry (via chemical or mechanical cues), it is possible large and interconnected cell populations can be established, which over time gradually begin to self-organise and differentiate, thus facilitating new healthy bone and cartilage tissue deposition within and surrounding the implanted scaffold system (Berthiaume *et al.*, 2011). Significantly, as such systems would be implanted within a living articulating tissue environment, it is crucial that they possess not only appropriate cell adhesion abilities, but also have a good degree of biomechanical strength/stability, cytoxicity, non-immunogenicity and biodegradability (Dhandayuthapani *et al.*, 2011). Additionally, for the purpose of osteochondral repair, scaffold wide osteoconductivity is considered paramount (Ramzan *et al.*, 2023). Furthermore, structural parameters including pore size, porosity, and geometry must also be considered due to their roles in influencing cellular adhesion, nutrition, behaviour and fate. Such parameters can also affect overall mechanical properties of the scaffold system. This specifically includes the trade-off relationship between porosity and overall mechanical strength, whereby highly porous systems generally have weaker mechanical properties in comparison to an equivalent biomaterial system with lower bulk porosity (Ding *et al.*, 2014), meaning a fine balance must be struck throughout the biomaterial, thus allowing for the ultimate formation of high quality end stage functional repair tissue.

With these factors in mind, various scaffold formulations have been proposed, which are made up of either naturally occurring or synthetically manufactured constituents.

1.6.1.1 Synthetic polymers

Over the last 30 years, many different synthetically formulated polymers have been exploited with remarkable success as medicinal treatments, with several Food and Drug Administration (FDA) approved uses in fields such as orthopaedic fixation, ligament augmentation and as components of vascular stents (Maitz, 2015). Due to possessing a large number of advantageous traits, including strong biocompatibility, biodegradability and scale-up manufacturing potential, many have been recently earmarked for translational use as 3D osteochondral tissue engineering scaffolds (Makadia & Siegel, 2011). Such derivatives include poly(glycolic acid) (PGA), poly(lactic acid) (PLA), poly(lactic-co-glycolic acid) (PLGA), poly(vinyl alcohol) (PVA) and poly(caprolactone) (PCL) (da Silva *et al.*, 2009; Tian *et al.*, 2023; Wei & Dai, 2021).

As α-hydroxy acid containing polymers, PLGA and PLA have undergone considerable testing as potential bone and cartilage scaffold systems, with researchers significantly producing scaffolds with tuneable biodegradation profiles which coincide with cell-laden osteogenic and chondrogenic neotissue formation rates (Atala, 2007). Furthermore, upon the existence of an ester bond linkage within the polymer chains, the biomaterial can be subjected to non-enzymatic hydrolysis, which crucially produces non-toxic degradation products (Place *et al.*, 2009).

Further advantages of synthetic polymers is their tuneability and applicability across a range of fabrication techniques, with polymer blend solutions being highly suitable with systems such as fibre bonding, electrospinning and additive manufacturing (L. Chen *et al.*, 2023; Mikos *et al.*, 1993). In the case of electrospinning, polymer fibrous meshes can be reproducibly manufactured with speed, accuracy and precision, and crucially can be generated to resemble gradient structural architectures of native ECM (Zhou *et al.*, 2018). This includes in some cases the ability to adjust polymer fibre diameter, orientation and overall scaffold pore size – a feature highly relevant when considering the gradient compositions observed in natural osteochondral tissue.

Recent technological advances in additive manufacturing techniques have seen a recent surge in reported examples of synthetic biomaterial scaffolds of which possess truly continuous structural variabilities (Li *et al.*, 2021). One of these methods, 3D printing, has been especially popular, owing to its ability to firstly generate a computer aided predictive digital model of the scaffold in question, which can be easily modified and altered, before then being physically replicated in lab settings via controlled deposition of fluid bioinks. One such example is that reported by Di Luca *et al*, who were able to fabricate 3D printed scaffolds with continuous pore size gradients throughout its entire scaffold bulk (Di Luca, Ostrowska, *et al.*, 2016; Di Luca, Szlazak, *et al.*, 2016). Their unique cylindrical scaffold, formulated via fused deposition modelling of poly(ethylene oxide terephthalate)/poly(butylene terephthalate) block co-polymer, consisted initially of small pore diameters (500 μm fibre spacing) which then gradually increased, for every millimetre of new fibre deposited, up to a final large pore diameter of 1100 μm. Interestingly, following gradient and non-gradient scaffold seeding and culture of hMSCs in osteogenic media, it was found that overall cell differentiation into osteoblasts was enhanced (12 times increase in alkaline phosphatase (ALP)) specifically in favour of the gradiented iteration. Moreover, upon similar culture in chondrogenic media, it was further identified that chondrogenesis could also be increased, but significantly in an inverse direction, whereby smaller pore regions specifically induced the greatest amount of GAG production (Di Luca, Ostrowska, *et al.*, 2016; Di Luca, Szlazak, *et al.*, 2016).

Alternative continuous deposition processes have also been utilised to generate structural gradients, with several commercial or in-house manufactured "gradient makers" being reported. In these examples, a minimum of two separate reservoirs are established which continually feed bio-ink or gelatable solutions into a single joined outlet, of which can then be extruded and cast

within scaffold molds (Li *et al.*, 2021). Significantly, by utilising pumps which control the relative flow rate of each reservoir solution, it is possible to generate highly unique structural gradients over the resulting scaffold bulk, upon its casting. This idea was specifically applied in a clever proof-of-concept report by Constantini and colleagues, of whom developed an adjustable valve-based flow focusing outlet system. Within this system gelatin and nanoHA reservoirs were combined with a controllable air-bubble generating valve, thus allowing the creation of a gradient 3D foam-like scaffold crucially with pores ranging from 80 up to 800 μm diameter. Although biological and mechanical characterisation remains untested as of this thesis, such a uniquely controllable scaffold holds significant potential, allowing for not only structural gradients but also the inclusion of active biologics (Costantini *et al.*, 2019).

However, several drawbacks are present with the use of synthetic scaffold biomaterials, in some cases stopping its wide-spread adoption as a 3D osteochondral scaffold matrix. Firstly, as they are artificial polymers, they are considered mostly bioinert, lacking inherent cellular binding motifs as well as any natural ECM components (R. Y. Chen *et al.*, 2023). Furthermore, polymer chains often possess high hydrophobicity, which when combined with the previous limitations, produces a system which is somewhat restrictive to large scale cell attachment and thus the effective deposition of bone and cartilage matrix (Siddiqui *et al.*, 2018). As a result of this, it is commonly reported synthetic polymers undergoing additional time-consuming modification steps, such as plasma treatment, or simply having them be incorporated as part of a larger composite biomaterial with known cellular adherence capabilities (Yang *et al.*, 2002). Regrettably, one downfall of the continuous structural gradient scaffold approaches described above is their distinct lack of pre-clinical data, with most systems appearing to be at an early proof-of-concept stage with only *in-vitro* cellular and mechanical tests generally being reported.

1.6.1.2 Natural polymers

Given the substantial recent advancement in biotechnological isolation and purification methodologies, it makes considerable sense to formulate reparative scaffold systems from naturally occurring constituents, particularly if possible with those found inherently within the tissue that's aiming to be repaired. For osteochondral tissue engineering, it is therefore common for biomaterial frameworks to contain one or many of the previously described cartilage and bone matrix components, with specific examples including the generation of collagen, hyaluronic acid and hydroxyapatite 3D systems (Asensio *et al.*, 2022; Bernhardt *et al.*, 2018; Magalhaes *et al.*, 2014; Parisi *et al.*, 2020). Additionally, several other natural polymers have been identified for potential use as a scaffold through their high degree of structural symmetry with the natural bone and cartilage ECM environment. This includes polymeric protein and polysaccharide hydrogels such as gelatin, fibrin, alginate, agarose and chitosan, as well as solid scaffolds such as silk and silk-fibroin (Alves da Silva *et al.*, 2010; Li *et al.*, 2017; MacIntosh *et al.*, 2008). Through having

ancestral native/organic chemistry, these polymers primarily offer excellent biocompatibility profiles, with low level cytotoxicity, low immunogenicity and good biodegradability also characteristically observed. Furthermore, they also often possess inherent cellular adherence, whereby cell recognition and attachment motifs are expressed on the scaffold surfaces, allowing for cellular attachment and subsequent differentiation and downstream matrix deposition within the 3D environment (O'Brien, 2011).

Among these, collagen stands out as a highly popular natural polymer for osteochondral tissue engineering approaches. In these examples, purified collagen type I and type II, derived from various sources including mammalian, amphibian, fish, and marine tissues, have been utilised to specifically craft wet hydrogels or 3D nanofibrous frameworks (Jiang *et al.*, 2022). Interestingly, early endeavours with such pure collagen, however, revealed challenges related to scaffold fragility and degradation rates, prompting the incorporation of cross-linking steps into the fabrication processes (Zanetti *et al.*, 2013). Through such modifications (physical or chemical), next generation 3D collagen cross-linked scaffolds have since been formulated with enhanced durabilities and mechanical strengths. When combined with its other inherent properties such as good hydrophilicity, cytocompatibility and the presence of amino acid sequence motifs for cell adhesion, they represent highly promising candidates for tissue repair biomaterials (Dong & Lv, 2016).

Another highly promising avenue involves the use of polysaccharide hydrogels, which are an important class of natural polymeric materials widely found in plants, animals and micro-organisms. They are generally defined as repeating monosaccharides bound by a glycosidic bond and can possess highly variable physicochemical properties, specifically dependent on their inherent organic chemistry and functional groups (Aravamudhan *et al.*, 2014). In the case of tissue engineering hydrogels, examples can be found utilising positively charged chitosan polysaccharides, negatively charged alginate and the electroneutral agarose (Liu *et al.*, 2008). Crucially, each is able to assemble into highly interconnected 3D hydrogel structures from their aqueous solutions, either through ionic, covalent or physical cross-linking processes (Jin *et al.*, 2021). When in their cross-linked gel-state, they are able to mimic the inner environment of the osteochondral ECM, specifically exhibiting not only water swelling and viscoelastic behaviour, but also good biocompatibilities, cellular adherence and favourable porosity. This is significant, as they can all promote and facilitate endogenous cellular retention, adhesion, migration and differentiation (Wu *et al.*, 2023). Additionally, through the presentation of functional groups (-OH, -COOH, -NH_2), the gels are considered a facile platform for additional functionalisation, allowing for instance the encapsulation of several therapeutic drug moieties (Bashir *et al.*, 2020).

1.6.1.2.1 Agarose

Derived from the cell walls of various red algae species of seaweed (*Rhodophyceae*), agarose constitutes a linear polysaccharide composed of repeating agarobiose units, combining D-

galactose and 3,6-anhydro-L-galactopyranose sugars (te Nijenhuis, 1997). Furthermore, it serves as the primary component of agar and can be extracted on a large scale through methods like agaropectin precipitation, ion exchange and ionic liquid mixing. When extracted and processed, agarose subsequently presents as a white powder with a melting temperature of 80–90 °C and a aqueous gelation temperature of 30–40°C, however it is noted that such properties can vary depending on its molecular weight, concentration and number of side groups present (i.e. chemically modified low melting point agarose) (Jiang *et al.*, 2023). Moreover, upon heating, agarose can be easily solubilised in several organic/inorganic solvents and buffers including water and 4-(2-hydroxyethyl)-1-piperazineethanesulfonic acid (HEPES) (Zarrintaj *et al.*, 2018).

In its aqueous form, agarose exhibits unique thermo-responsive reversible gelation behaviours, whereby sequential heating and cooling can result in the spontaneous orientation of helical agarose fibres into a structured 3D hydrogel framework (Figure 1.10). Such frameworks are held together through strong hydrogen bonding between abundant hydroxyl groups present on the agarose chains, and the hydrogen molecules found within water (Jiang *et al.*, 2023). Ultimately, this results in the entrapment of buffer or solvent molecules and the formation of a highly interconnected and nanoporous matrix structure.

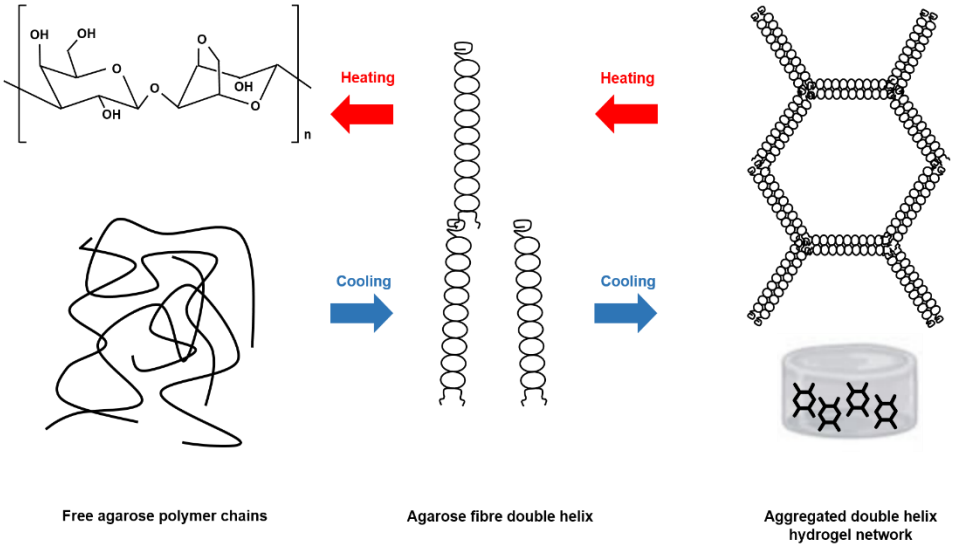

Figure 1.10 – The chemical structure and gelation mechanism of agarose. Adapted from (Jiang *et al.*, 2023).

Interestingly, through modifications to agarose concentration, structural and mechanical properties of such physically cross-linked agarose gels can also be tuned, thus allowing the hydrogels to possess variable properties depending on its functional purpose (Salati *et al.*, 2020). Furthermore, it is also known that increases in agarose concentration can lead to denser or tighter agarose fibre networks, which contain less space and thus smaller pores (pore diameters of 1 wt% and 3 wt% agarose hydrogels = ~500 nm and ~300 nm respectively – as per Maaloum *et al* (Maaloum *et al.*, 1998)). Mechanically speaking, increases in agarose concentration have also

resulted in gels which possess variable elastic modulus, with values of 38, 254 and 929 KPa being reported for 1 wt%, 2.5 wt% and 5 wt% agarose hydrogels respectively (Park *et al.*, 2005).

Owing to its electrostatic neutrality and modifiable porous network, agarose hydrogels have further utility as a filling material for gel electrophoresis (Jiang *et al.*, 2023). In this technique, groups of charged macromolecules (e.g. nucleic acids, proteins, viruses) are induced to migrate through a biomaterial system on account of the generation of an electric potential force (Li & Arakawa, 2019; Tomioka *et al.*, 2022). Moreover, as such mobility within solid matrices is linked directly to its molecular mass, macromolecules of different sizes migrate throughout the agarose hydrogel at markedly different speeds, thus allowing for their effective separation, characterisation and if required purification (Stellwagen & Stellwagen, 2009).

Alongside possessing thermos-responsive self-gelling capabilities and excellent tuneable mechanical properties, agarose hydrogels are also hydrophilic and considered highly biocompatible, inducing low levels of cytotoxicity as well as minimal immunogenic responses when exposed to cellular material (Samrot *et al.*, 2023). This was exemplified by work by Cigan *et al*, who reported the effective encapsulation of human chondrocytes with a 3D agarose matrix. It was shown that over a 1-2 month culture period, cells not only remained viable and proliferated, but also maintained chondrocyte phenotype, thus allowing for effective proteoglycan and GAG deposition. Crucially, upon examination at one month, constructs exhibited near native human cartilage-like functional properties, with compressive Youngs modulus and dynamic moduli of 254 and 945 KPa, respectively (Cigan *et al.*, 2016).

Limitations do however remain with the large-scale use of agarose hydrogels for specific osteochondral tissue engineering purposes. This includes its potentially restrictive biodegradability, which requires agarase enzyme for its unanimous breakdown, not naturally occurring in humans (Ng *et al.*, 2009). Additionally, agarose hydrogels have also been known to lack appropriate cell adhesion motifs, thus chemical, surface, or composite modifications may be required for large scale 3D cell attachment and infiltration (in comparison to cellular encapsulation – which works effectively) (Bloch *et al.*, 2005). Finally, in the case of bone regeneration, the essential requirement of macroporosity often requires additional physical and structural modifications to nanoporous agarose gels – with processes such as freeze-drying, gas foaming, porogen templating used with good success in these cases.

While a range of natural and synthetic polymers currently exist which can be fabricated into 3D biomaterial structures that mimic the natural ECM environment, as illustrated in Figure 1.9, scaffold systems alone may not always be sufficient for effective repair. Supplementation with regulatory signals to fully induce native tissue repair and recapitulation is an emerging approach. The combination of 3D scaffolds with gene delivery therapeutic vectors (gene activated matrix

(GAM)) (Bonadio *et al.*, 1999) is an approach which has potential utility for osteochondral tissue repair.

1.7 Gene therapy

Gene therapy can be defined as the act of transferring genetic material (DNA or RNA) to a patient, leading to durable transgene expression within host cells ultimately curing disease symptoms (Gelehrter *et al.*, 1998). In any successful gene therapy approach, three specific components are required: a therapeutic/corrective gene, an effective expression system and a delivery agent. Specifically for genetic diseases, such as Haemophilia, Cystic Fibrosis & β-Thalassaemia, the above approach must be tailored to induce a permanent alteration in the genetic code in order to bring about the desired cure/treatment – often referred to as a stable gene transfer. Precursor cells or stem cells are targeted in this regard, meaning upon cell division the gene is passed to every daughter cell (post-mitotic, slowly dividing cells may be subjected to this treatment also). In contrast, tissue repair approaches such as osteochondral defect regeneration, require a limited, time-dependent strategy, inducing a powerful yet short-lived reparative effect that diminishes over time. This is termed transient gene transfer (Gelehrter *et al.*, 1998).

As of 2022, a total of 24 gene therapies have been approved for clinical use with the majority utilising a permanent integrating vector strategy. Such diseases which have been treated include familial lipoprotein lipase deficiency, adenosine deaminase (ADA-SCID), haemophilia B and for a range of cancers (bladder, myeloma, lymphoma) (Arabi *et al.*, 2022).

1.7.1 Non-viral expression systems

1.7.1.1 Plasmids

Plasmids (pDNA) are generally accepted as the standard nucleic acid expression vector for non-viral gene therapy strategies. Commonly found in bacteria as small, circular, double stranded DNA, plasmids act as complementary gene reservoirs to bacterial chromosomes, containing additional genetic sequences which often infer a selective advantage, namely antibiotic resistance. Their size can vary from 0.8-120 kb, permitting inclusion and expression of almost any transgene DNA sequence, whilst also allowing its effective replication within bacterial host cells (Linnemann & Krawetz, 2009; Pahle & Walther, 2016).

Structurally, natural bacterial plasmids contain the following components: Origin of Replication (ori), and a minimum of one gene sequence coding for an advantageous gene. The origin of replication acts fundamentally to allow a plasmid to replicate independently within a cell, controlling the host range and copy number of the plasmid. This ability to drive replication stems from its three functional elements (for example in E.coli – oriC); the conserved DNA repeat sequences – termed DnaA-boxes (recognised by DnaA bacterial initiator protein), the adenine and thymine rich DNA unwinding element and further binding sites for replication initiation

proteins (Costa *et al.*, 2013; Leonard & Mechali, 2013). Host replication enzymes are then recruited to begin DNA sequence replication (Wolanski *et al.*, 2015).

Overall, the naturally existing plasmid structure described is sufficient for bacterial function, however to employ plasmids as gene therapy vectors, significant alterations are required. The altered plasmids, known as artificial plasmid vectors, are specifically designed to firstly; introduce foreign DNA into another cell, and secondly express the desired gene for an extended period of time. As such, further sequence components, on top of the ori, are required. Figure 1.11 illustrates a common artificial plasmid vector composition containing these necessary sequences.

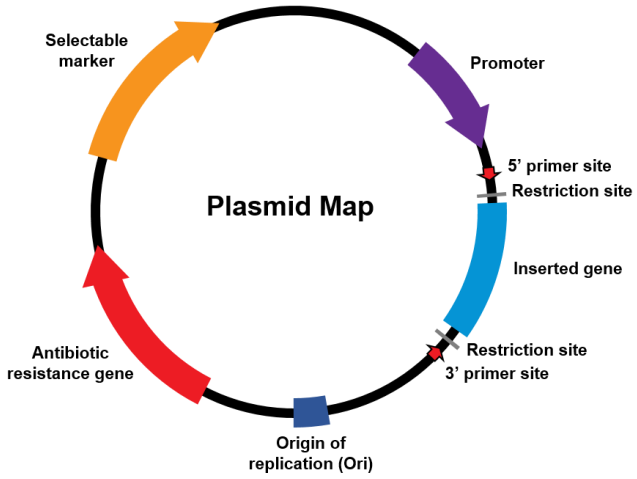

Figure 1.11 – A generalised plasmid map for a standard artificial plasmid gene expression vector.

Firstly, a promoter region (and associated downstream polyadenylation site) is an essential requirement to drive the level of transcription of the transgene, a factor that in the vast majority of vector systems is preferably optimally maximised. Due to this fact, and the variability seen in each promoter sequences strength and duration potential, the selection and suitability of a promoter to the vector application is critical. For example, a Cytomegalovirus (CMV) promoter, which is indicative of a strong, ubiquitous promoter, has only a short expression cycle, whereas tissue specific promoter sequences, known as generally weaker promoters, will produce prolonged, long-term transgene expression (Tolmachov, 2009; Wong & Harbottle, 2013). Multiple restriction sites (MRS) are also vital components frequently incorporated into the plasmid architecture. These short DNA segments are usually located downstream of the promoter sequence and are recognisable by restriction enzymes, thus permitting straightforward DNA insertion. Finally, for the purposes of amplification, identification and selection of plasmids within transformed bacterial cells, artificial plasmids possess a selectable marker gene, usually in the form of antibiotic resistance (e.g. ampicillin or kanamycin).

In short, artificial plasmids have been engineered to generally be a safe, stable, pliable and cheap gene therapy technology, where genes/proteins can either be mass produced or used as a therapeutic platform for gene delivery.

Yet, in terms of its gene therapy potential, specifically the efficiency of delivery/transfer of plasmids into cells, is somewhat limited (Hardee *et al.*, 2017; Mairhofer & Grabherr, 2008). Such inefficiency for gene delivery of plasmids alone stems from the foreign nature of the vector and the mobilisation of innate safety mechanisms and in-built barriers within the body. This includes vector sequestering by first pass organs (lungs and liver) (Sakurai *et al.*, 2001), nucleic acid degradation by resident serum nucleases (Pouton & Seymour, 1998), opsonisation and immune mediated uptake/removal (Vaughan *et al.*, 2006). Furthermore, as the plasmid vector reaches the target tissue, components within extracellular matrix environment (such as exogenous nucleases) or the matrix itself will degrade or prevent tissue diffusion respectively (Escoffre *et al.*, 2010). Moreover, even after entry into target cells, the vector must then progress through more intracellular barriers; the cytoplasmic trafficking to the nucleus (via potentially degradative endosomal vesicles), and entry into the nucleolar compartment (size-mediated nuclear pore complex) (Varkouhi *et al.*, 2011). Due to such obstacles, a number of strategies have been developed to act as vehicles for plasmid delivery, imbuing the vectors with more effective entry mechanisms whilst also permitting greater protection (Holmen *et al.*, 1995; Washbourne & McAllister, 2002).

1.7.2 Methods for plasmid gene delivery

The act of transient cellular transfection can be defined as the process whereby foreign genetic material is deliberately delivered into eukaryotic cells in order to induce a non-permanent gene expression response. Crucially, unlike viral vector systems, non-viral vectors such as plasmids require a large degree of assistance to achieve such a feat. Over recent years, several strategies have been formulated which facilitate this process and thus can be specifically characterised as either physical-based or chemical based approaches.

In the physical transfection approaches, so called "naked" plasmid vectors can be tangibly escorted into cells via the purposeful creation of transient membrane holes or defects (Al-Dosari & Gao, 2009). Such membrane disruption techniques include electroporation (permeability enhancement via short electric pulses) (Escoffre *et al.*, 2009), gene gun (high speed delivery DNA coated gold particles) (Uchida *et al.*, 2009), microinjection (proximal injection of plasmids into individual cells) (Lukacs *et al.*, 2000) and ultrasound/sonoporation (proximal delivery of microbubbles containing plasmids of which burst under sound waves) (Endoh *et al.*, 2002). Although many of these approaches have been successfully utilised in various forms *in-vivo*, they are generally considered impractical for large scale cellular transfection. Moreover, they suffer from particular drawbacks such as low transfection efficiency (particularly in primary cells), high

mortality rates (in the case of high voltage pulses), can be labour intensive, and also require specialist equipment (Kim & Eberwine, 2010).

Chemical transfection methods differ from the above approaches mainly due to the fact that the plasmid DNA, in terms of physical and chemical structure, is actually transiently modified and coupled with specific chemical components into what is known as DNA complexes, which can then facilitate cellular internalisation and the expression of the foreign genetic material. Such chemical vehicles utilised for DNA coupling include inorganic nanoparticles (for example Calcium phosphate (CaP)), cationic polymers (such poly(ethylenimine) (PEI) and poly-L-lysine) and cationic lipids. In all these cases the positively charged chemical compounds listed can form stable electrostatic interactions with negatively charged DNA, leading to a transfection capable complex.

1.7.2.1 Calcium phosphates

CaP nanoparticles are classified within the inorganic mineral non-viral vector sub-set and have been utilised as safe and convenient plasmid delivery agents since the 1970's (Maitra, 2005). As one of the major compounds within calcified tissues, CaP nanoparticles are considered highly advantageous for gene delivery within bone contexts, specifically due to the fact that alongside DNA delivery they can act as excellent nucleation sites for the deposition of hydroxyapatite and large scale biomineralisation (Hou *et al.*, 2022). They are also biocompatible with excellent additional properties including natural biodegradability, low toxicity and non-immunogenicity (Bakan *et al.*, 2017; Pedraza *et al.*, 2008). Furthermore, due to CaP particles possessing an overall positive cationic character, they are distinctly capable of binding with high affinity to negatively charged phosphate groups within DNA molecules, specifically via calcium ion chelation. Crucially, within this chelated conformation it has been found that DNA co-complexes can be largely protected from intracellular nucleases – a previously stated barrier for plasmid based transfection, and thus stimulate transient gene expression (Bakan *et al.*, 2017).

In terms of the formation and synthesis of both CaP nanoparticles and DNA-CaP co-complexes, the most established method is that reported by Graham *et al.* In this method, therapeutic plasmid DNA is mixed initially with a $CaCl_2$ solution, before subsequent additional collaboration with a HEPES phosphate buffer. Through this sequential approach, it was observed that the plasmids were condensed into a heterogeneous population of nano-sized and micron sized DNA-CaP nanoparticle co-complexes, which visually can represent themselves as insoluble precipitate regions (Graham, 1988). Upon the introduction of the DNA-CaP co-complex solution to a cellular culture, the process of transient transfection is initiated.

Generally, the transfection process continues over four established stages; the cellular uptake/endocytosis stage, the endosomal trafficking stage, nuclear entry stage and the gene

expression stage. In the first uptake stage, the positively charged DNA-CaP co-complexes are attracted to the negatively charged cell membrane and are induced to form stable interactions with specific cell surface receptors. Such interactions crucially stimulates the endocytosis signalling response, which can result in one of the following uptake pathways: phagocytosis, clathrin-mediated endocytosis (CME), caveolae-mediated endocytosis (CvME) and micropinocytosis (Sahay *et al.*, 2010). Although marginal differences exist between each individual endocytosis process, the overriding outcome is the engulfment and internalisation of the CaP-plasmid complexes, specifically incorporating them into intracellular vesicles. After entering the cytoplasm within this vesicle (stage 2), the inorganic complexes are specifically trafficked towards the nucleus, gradually transitioning in conformation through endosomal-like compartments until finally maturing into the low pH region known as the late endosome (pH 4-6) (Xu, 2022). In normal circumstances, the endosome, at this stage, begins actively pumping H^+ ions into its own compartment to induce the acidified degradation of foreign material (lysosomal pathway) (Qiao *et al.*, 2015). However, due CaP co-complexes inherent insolubility and alkalinity, such H^+ ion pumps are effectively neutralised. Moreover, this mechanism is additionally coupled with the pH mediated dissolution of free calcium ions away from the co-complex into the endosomal vesicular area, which results in firstly the elevation of its osmotic pressure and thus prompting its eventual swelling (water influx) and bursting (i.e. the reverse salt osmotic effect) (Olton *et al.*, 2011). The end result of this stage is therefore the proximal delivery of DNA-CaP complexes to the nucleolar membrane boundary. In the third step, the DNA is introduced into the nucleus. Crucially, this is governed either by natural cellular division or by nuclear pore complexes (NPCs), which act as filtration channels allowing for the size-dependent transfer of genetic material across the nuclear envelope (Feray, 2017; Lam & Dean, 2010). In the case of CaP co-complexes, the calcium interacts with the NPC and allows for the fast diffusion of nanosized particles. In the final stage, the delivered genetic template is separated fully from the inorganic nanoparticles and is expressed via the initiation of transcription and translation processes. In the case of plasmid vectors, this encompasses initial transcription factor binding to promoter sequences, mRNA production, and finally ribosomal mediated translation (Miller & Dean, 2009).

Of the many properties of CaP nanoparticles which aid in its successful use as a nucleic acid delivery vehicle, it is generally accepted that its inherent particle size is the most significant for the purposes of efficient transfection. One reason for this, stems from distinct criteria surrounding endocytosis mediated payload uptake, such that effective complex internalisation is often capped between the ranges of 20-200 nm in diameter. In the case of nanoparticles payloads above this range, it is evidenced instead that the interaction between the membrane and the particles is weaker, leading to the induction of the less effective phagocytosis internalisation pathways (Han *et al.*, 2012; Xiang *et al.*, 2006). With this in mind, one limitation commonly observed with the Graham and van der Eb aqueous co-precipitation based approach, is the uncontrolled particle aggregation identified during initial process of mineral synthesis and

complexation. As particles are produced in a free-flowing liquid environment, they can be prone to unwanted colloidal behaviours, which can ultimately result in the production of a large number of micron scale CaP co-complex particles. Upon their subsequent application to cells, it was found such colloidal suspensions have severely limited capability for successful vector transfection and downstream gene expression (Dorozhkin, 2010; Welzel *et al.*, 2004).

Crucially, in the last decade, a multitude of approaches have been utilised to either overcome such issues with CaP aqueous nanoparticle synthesis or provide supplementary complex modifications which enhance the entry and trafficking pathway. This includes glycerol shock treatment (transient alteration of cell membrane integrity for DNA-CaP entry) (Jordan *et al.*, 1996), CaP synthesis in the presence of lipid coatings and multi-shell complexes (CaP-DNA-CaP-DNA conformation) (Li *et al.*, 2010; Sokolova *et al.*, 2006). Additionally, a further highly novel approach involving electrophoresis mediated CaP synthesis in agarose hydrogels has also been proposed. This will be discussed in section 1.8.3.1 (Watanabe & Akashi, 2006).

1.7.2.2 Polyethylenimine

Another chemical vehicle utilised in the field of gene therapy is the polymer known as Polyethylenimine (PEI). In terms of its chemistry, PEI consists of repeating units of two aliphatic carbon groups and an amino nitrogen, and is commercially available in a linear or branched polymeric forms (with molecular weights ranging from 200 Da and 1,500 KDa) (Figure 1.12) (Boussif *et al.*, 1995). Although sharing a multitude of similarities, branched PEI differs from linear PEI on account of the fact it contains primary, secondary and tertiary amines, whereas the latter only possesses secondary amines (Hall *et al.*, 2017). It is worth noting through the existence of said protonatable amines, these polymers possess highly desirable traits for nucleic acid delivery vehicles; for example, its naturally high cationic charge density as well as a buffering capacity which maintains pH above that commonly observed in the endo-lysosome (pH 6-7) (Boussif *et al.*, 1995). As such, upon exposure of plasmids to solutions of cationic PEI, the strongly positive charges attract the negatively charged phosphates present within the genetic material, thus inducing wholesale condensation and the eventual formulation of a PEI-DNA complex – or polyplex for short.

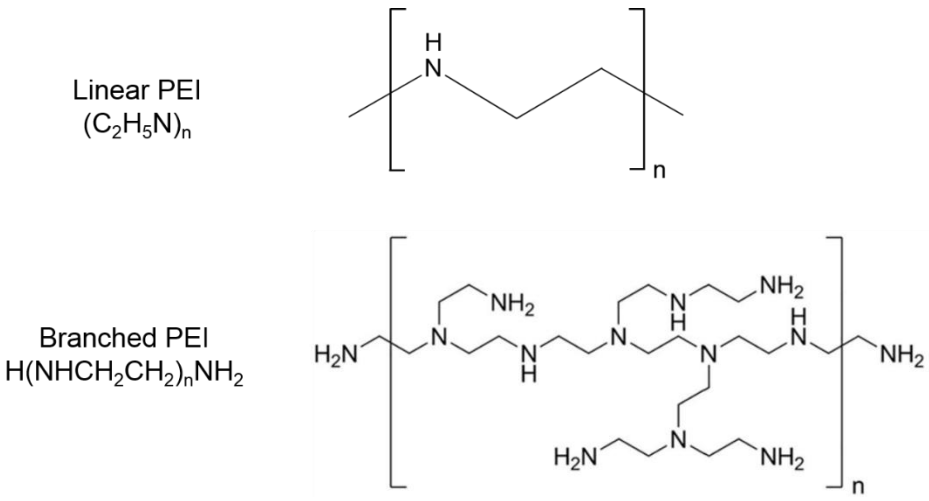

Figure 1.12 – Linear and branched PEI structures.

Interestingly, seminal research has shown that polyplexes generally induce successful transfection of eukaryotic cells in a largely comparable manner to that previously outlined for calcium phosphate complexes, with polyplexes undergoing sequential cellular uptake, endosomal trafficking, nuclear entry and transcription/translation stages (Boussif *et al.*, 1995; Zakeri *et al.*, 2018). The mechanism of vector internalisation is carried out almost identically in the polyplex transfection pathway, with a net-positive charge of DNA-PEI complexes inducing the strong association with the negative cell membrane. Upon successful endocytosis (clathrin mediated), polyplexes are similarly trafficked across the cytoplasm within intracellular endosomal vesicles, yet crucially they utilise a modified mechanistic process for its subsequent escape. The process in question has been termed the proton sponge hypothesis and was introduced in the well-established report by Behr and colleagues (Behr, 1997). In this process H^+ ions are once more pumped into the late endosome for the purpose of lowering the overall compartment pH, in anticipation for lysosomal fusion and foreign cargo degradation. However, due to the remarkable buffering capacity of PEI, the polyplex is able to effectively bind these protons, thereby limiting the acidification process. Due to the pH therefore remaining stable, further protons are translocated into the endosomal compartment and crucially this is partnered with the simultaneous accompaniment of chloride ions (in order to maintain overall charge balance). The final result of this is an unbalanced endosome with very high ionic concentration. The only choice herein is to transport water into the system, which generates an unsustainable osmotic pressure and thus the swelling and rupture of the endosomal vesicle (Vermeulen *et al.*, 2018). Much like the DNA-CaP co-complexes, the polyplexes are subsequently released into the cytosol within a close proximity to the nucleus. By interacting effectively with the NPC, they are able to diffuse into the nucleus and consequently initiate nucleic acid vector transcription and translation – the final stage in the transfection process. A diagrammatic illustration of the above polyplex gene delivery process can be seen below in Figure 1.13 A and B.

Although considered the gold standard nucleic acid delivery vehicle, the transfection efficiency of polyplexes can be highly variable, with *in-vitro* and *in-vivo* performance largely being determined by the hydrodynamic radius, surface charge and shape of the polymeric particles initially synthesised. Crucially, such properties can however be controlled by three main mechanisms in order to maximise transfection. This includes modifications to reaction containment volume, the inherent PEI molecular weight, and lastly the concentration of PEI added. With regards to the latter, this is often referred to as the N/P ratio, whereby a number is given to represent the ratio of the total number of amines in PEI added to a system in comparison to the original number of phosphates present within plasmid DNA (Mahajan & Tang, 2019). As polyplex formation is governed by electrostatic attractive forces, it can therefore be assumed that introducing higher concentrations of cationic PEI to the same quantity of plasmid, results in significantly more effective polyplex condensation and thus particle populations will be synthesised with smaller overall diameters (<200 nm) as well as a larger net positive zeta potential. Ultimately, through the application of these higher N/P ratio polyplexes, it can be observed improvements in cell membrane interactions, enhanced cellular and nuclear uptake efficiencies as well as greater downstream expression characteristics (Oh *et al.*, 2002).

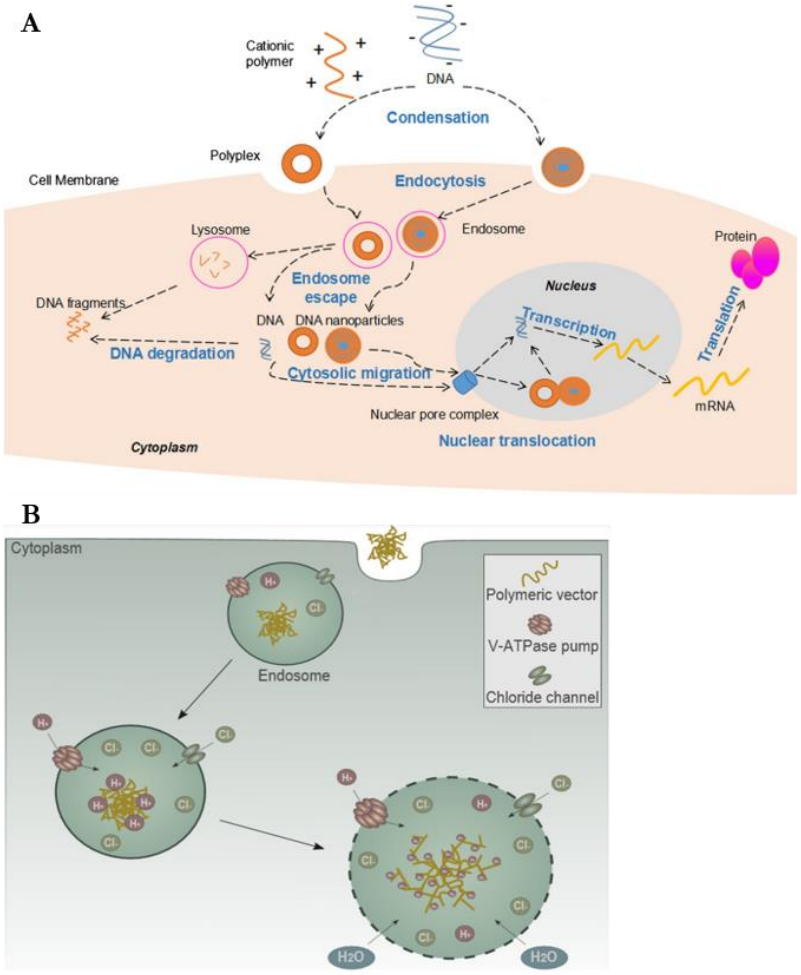

Figure 1.13 (A & B) – Summary of the PEI mediated non-viral gene delivery process (A), including specific diagrammatic illustration of the proton sponge effect (B). Images taken from (Wu *et al.*, 2018) and (Vermeulen *et al.*, 2018) with permission from Elsevier under licence number 5660711238652.

Unfortunately, one limitation with the use of polyplexes with high N/P ratios is the increased prevalence of free unbound PEI within the transfection solution, which possesses cytotoxic potential to eukaryotic cells (Oh *et al.*, 2002). Although the mechanisms remain up for debate, it is hypothesised that in such a conformation, delivery of free PEI can result in not only cell membrane destabilisation and damage, but also induce amplified endosomal and lysosomal compartment rupture (Casper *et al.*, 2023). Through such systemic rupture, degradative lysosomal enzymes and reactive oxygen species can be released into the cytosol, thus inducing cellular stress pathways which can ultimately lead to cellular apoptosis or necrosis (Lin *et al.*, 2012; Moghimi *et al.*, 2005). With this factor in mind, non-viral gene delivery protocols must therefore consider the fine interplay between PEI concentration, polyplex size and surface charge, and associated cytotoxicity, in order to bring about highly effective and successful PEI mediated transfection.

1.8 Gene activated matrices (GAMs)

As briefly stated earlier in this literature review, the concept of a gene activated matrix or GAM is effectively the successful amalgamation of two therapeutic approaches: scaffold-based tissue engineering and gene therapy. Classically, this approach is epitomised by the existence of a 3D biomaterial framework (natural, synthetic or composite scaffolds), which contains a reservoir of therapeutic genetic material (nucleic acid-transfection vehicle complex) (Figure 1.14). Upon subsequent implantation of said system, it is hypothesised that endogenous cellular infiltration into the 3D scaffold will occur, leading to the exposure, release and transfer of the incorporated genetic payload into nearby adherent cells. Such transfer will eventually lead to the existence of a local transiently modified cell population, which expresses a desired therapeutic protein over a sustained time period, thus ultimately facilitating high quality repair of a diseased or injured region. Although the possibilities are vast for the specific protein encoded within the DNA vector, a preference is generally observed towards the use of growth factor or transcription factor based strategies. Through their system wide production, long term phenotypic responses such as cellular differentiation, vascularisation and anti-inflammation behaviours can be achieved.

The concept of a GAM tissue engineering system originated due to several inherent limitations present within previous scaffold mediated tissue engineering systems involving recombinant proteins (i.e. growth factors). These systems were generally found to be sub-optimal due to pre-loaded proteins being highly susceptible to *in-vivo* proteolytic enzymes as well as possessing short half-lives. Moreover, recombinant proteins were also expensive and highly challenging to manufacture at scale (Shi *et al.*, 2014). In contrast, GAM systems containing non-viral plasmid complexes were seen as a promising alternative, whereby proteins can instead be self-produced by locally transduced/transfected cells. Through this mechanism, the necessity for supraphysiological doses of protein is completely negated, with inexpensive low lose plasmids (nanogram-microgram levels) inducing powerful and sustained protein expression in a spatiotemporal manner (Chen *et al.*, 2011). Importantly, through facile scaffold loading of plasmid

vectors, payloads can be gradually released over a period of weeks as opposed to the daily burst release patterns observed with some recombinant protein scaffolds (Laird *et al.*, 2021).

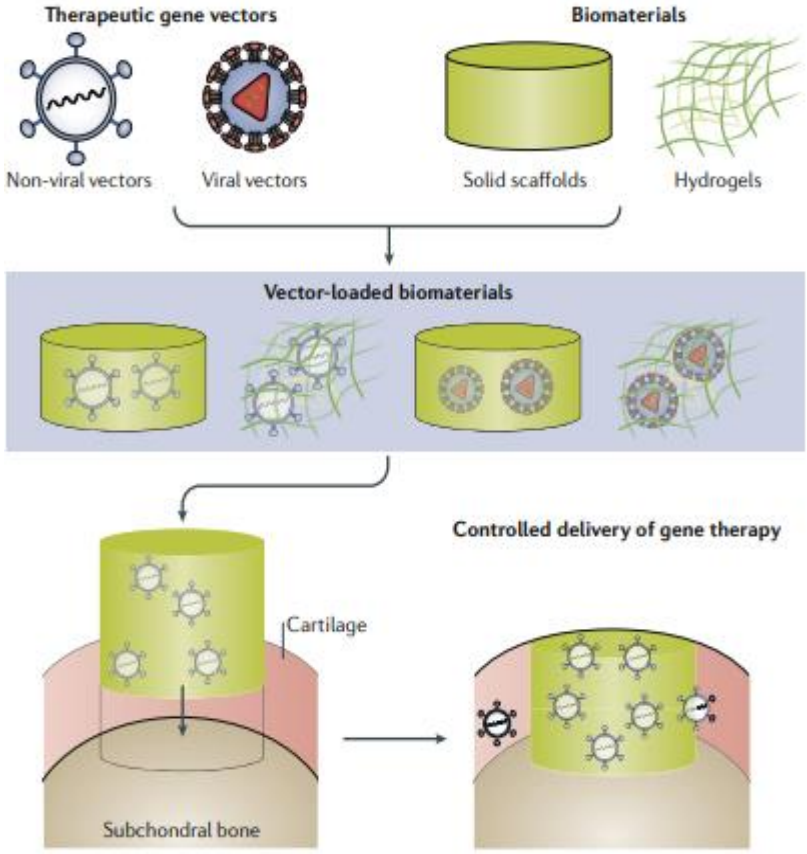

Figure 1.14 – Illustration of the fabrication and implantation process for an osteochondral GAM system. Taken from (Cucchiarini & Madry, 2019) with permission from Springer Nature under licence number 5660830797086.

Development of an osteochondral GAM system involves the fabrication of an ECM-like scaffold analogue which possesses one or multiple osteogenic and chondrogenic gene therapy DNA vectors. Through the expression and production of osteo- and chondro-inductive proteins, growth factors or signalling molecules, it is predicted that high quality gradient-like bone and cartilage tissue would form, upon its implantation within an osteochondral defect.

1.8.1 Candidate transgenes for osteochondral tissue repair

The main function of a DNA loaded scaffold system is to deliver a specific gene of interest to a tissue or specific cells to bring about a desired cellular response or change. The transgene is the singular component within the vector system capable of conveying such a change, and thus a highly important factor of a gene therapy strategy. For an osteochondral GAM strategy, a substantial number of transgenes exist which, upon their expression, induce either osteogenic and chondrogenic cellular signalling and repair pathways. A selection of these genes can be found in Table 1.1.

In terms of monotherapeutic/tissue specific studies, successes have been illustrated regarding the use of plasmid encoding bone morphogenic family members (BMP-2, 7), which in femoral/fibular defect models induced effective osteogenesis and vascularisation (Betz *et al.*, 2013; Loozen *et al.*, 2013). Evidence has also been shown for RUNX2 as an additional osteogenic growth factor regulator (Needham *et al.*, 2014) . Similarly, BMP-6, TGF-β1-3 has been identified as a possible cartilage inducing agents as a result of their ability as differentiation controllers or as anabolic/catabolic regulators, thus allowing for the enhancement or downregulation of healthy or OA phenotypes respectively (U Song *et al.*, 2005).

Table 1.1 – Summary of the potential osteogenic and chondrogenic transgenes which have been utilised in recent GAM approaches. Abbreviations, VEGF: vascular endothelial growth factor, PDGF: platelet derived growth factor, IGF: Insulin growth factor.

Transgene	Gene Function	Therapeutic Response	References
TGF-β1, TGF-β3	Anabolic growth factor	Chondrogenic and differentiation, cartilage matrix synthesis, cellular proliferation	(Lee *et al.*, 2017; B. Li *et al.*, 2014)
BMP-2, BMP-7	Anabolic growth factor	Osteogenic differentiation	(Betz *et al.*, 2013; Loozen *et al.*, 2013)
RUNX2	Transcription factor	Osteogenic differentiation	(Needham *et al.*, 2014)
VEGF, PDGF	Anabolic growth factor	Osteogenic differentiation, cellular proliferation, angiogenesis	(D'Mello *et al.*, 2015)
IGF	Anabolic growth factor	Chondrogenic differentiation	(Leng *et al.*, 2012)
Osterix	Transcription factor	Osteogenic differentiation	(Yang *et al.*, 2015)
SOX-9	Transcription factor	Chondrogenic differentiation	(Ledo *et al.*, 2020; Needham *et al.*, 2014)

1.8.2 Current osteochondral GAM scaffolds

Having discussed the various natural and synthetic biomaterial constituents which may be utilised within osteochondral tissue engineering (OCTE) as well as the fundamental concepts behind gene therapy, the following section will now discuss the current state of GAM approaches utilised for osteochondral defect repair and recapitulation.

In terms of the present generation of acellular OCTE GAM systems, they can generally be seen to follow either a monophasic approach; whereby a single structurally consistent material is produced which possesses one or multiple gene payloads, or it may be multiphasic approach; whereby a collection of different biomaterials are amalgamated, each possess both structural tissue specific cues as well as tissue specific gene payloads (i.e. osteo-inductive or chondro-

inductive). With regards to the latter discrete layered-based approach, layer-layer fusion or cross-linking steps are often required between each biomaterial phase to generate a single facile system, this can be complex, time-consuming, potentially damaging to pre-loaded biological components and may induce mechanical weak spots (Seo *et al.*, 2014).

One of the earliest instances of an osteochondral GAM was the porous bi-layered chitosan-gelatin (CG) scaffold approach reported by (Chen *et al.*, 2011). In this particular example, a chondrogenic CG phase containing pTGF-β1 vectors was combined, via fibrin glue, with an osteogenic CG-HA phase containing pBMP-2 vectors, thus producing full GAM system (Figure 1.15 A). Upon *in-vitro* testing, this scaffold was shown to induce 3D seeded rabbit MSCs to differentiate into either chondrocytes or osteoblasts depending on their proximal region of adherence (upper or lower scaffold regions). Specifically, after two weeks, TGF-β1 and BMP-2 protein production was elevated within distinct regions whilst according to qPCR analysis chondrogenic (aggrecan, collagen II) and osteogenic (osteonectin, osteopontin, collagen I) markers were also upregulated. The scaffolds were also evaluated within an animal defect model, however implantation took place using cell-laden bi-layered GAM constructs as opposed to scaffolds in their acellular form. In this subsequent study, although simultaneous bone and cartilage tissue repair was reported *in-vivo*, it was highlighted that phase separation and mechanical instabilities may exist between the CG layers as a result of the non-permanent use of fibrin glue (Chen *et al.*, 2011). Given this system was only applied in a small sized animal defect model, it therefore remains up for debate whether optimal performance can be maintained in larger more mechanically challenging environments with more expansive defects. It is also puzzling that this report remains the sole osteochondral GAM study found which successfully utilises naked plasmid DNA alone for gene delivery and the induction of osteochondral differentiation. As primary cells such as MSCs are notoriously difficult to transfect, it appears surprising how such powerful cellular responses were achieved without the use of a chemical transfection vehicle in this example (Zhou *et al.*, 2023).

Indeed, new reports have since emerged which employ a more orthodox GAM approach, whereby therapeutic plasmid vectors are utilised in conjunction with previously described chemical transfection vehicles, specifically within a biphasic osteochondral scaffold system. One such example is the collagen type II/I-nHA bi-layered GAM as reported by Lee *et al* (Figure 1.15 B) (Lee *et al.*, 2017). In terms of its structure, multi-shell nanoparticle complexes of CaP/pTGFβ-3/CaP/PEI and CaP/pBMP-2/CaP/PEI were found to be individually incorporated into separately freeze-dried collagen type II and collagen type I-nHA scaffold phases before eventual amalgamation via microbial transglutaminase (mTGase) mediated cross-linking. Once in the form of a single GAM system, the authors were then able to probe not only its mechanical properties but also its 3D *in-vitro* chondrogenic and osteogenic differentiation capability. Crucially, they firstly found that under load, the bi-layered GAM possessed compressive strengths

similar in magnitude to cancellous bone. Furthermore, upon seeding with human mesenchymal stem cells (hMSCs), they secondly illustrated successful and long term therapeutic transgene expression (~28 days), which was followed by the up-regulation of several additional osteochondral genes and the deposition of ECM matrix proteins. As a result, they surmised the developed GAM was capable of discrete chondrogenic and osteogenic differentiation, with a specific dependence on the region of cellular adherence and unique payload uptake. With such potential, the authors believe testing within an *in-vivo* animal model remains the logical next step for such a promising invention (Lee *et al.*, 2017).

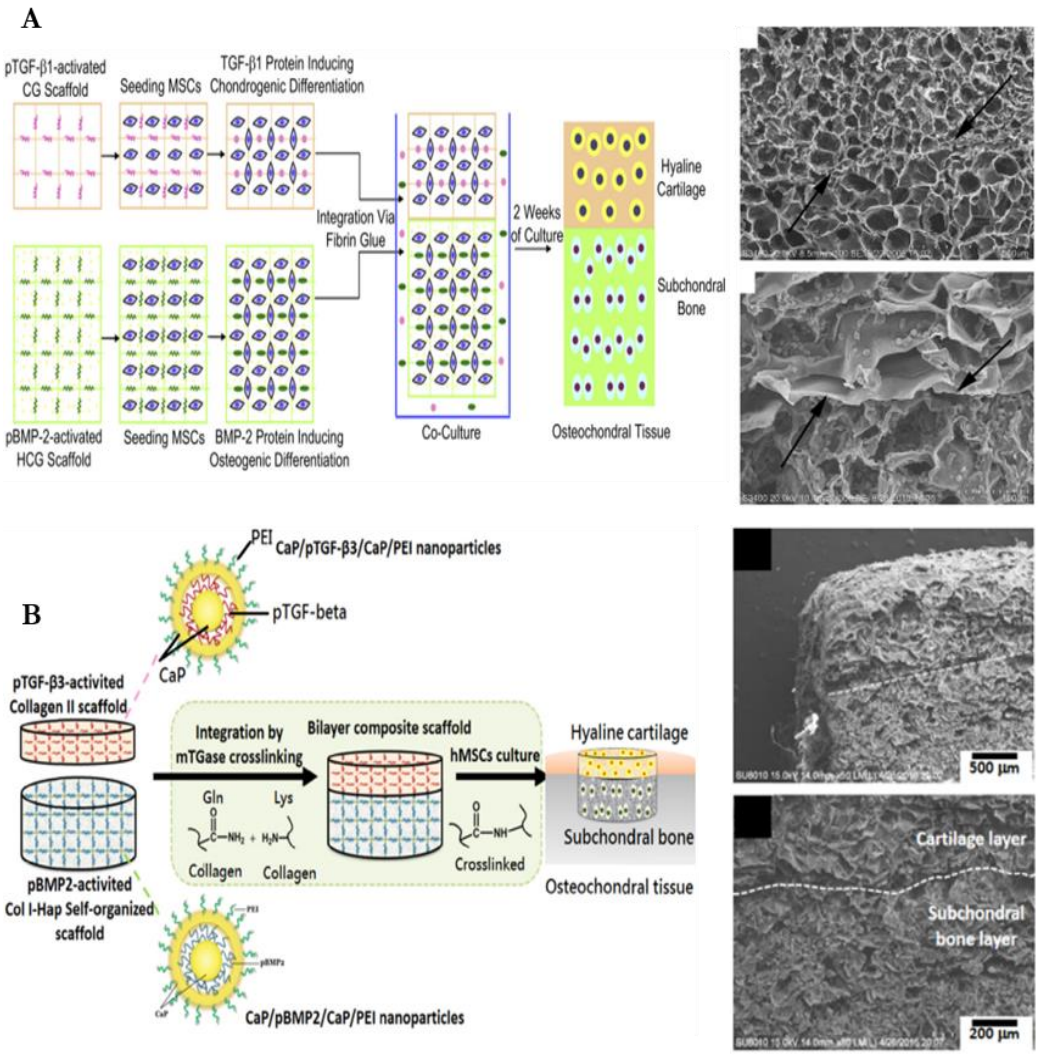

Figure 1.15 (A & B) – Examples of two different bi-layered osteochondral GAM systems which have been incorporated with chondrogenic and osteogenic growth factor encoding plasmid payloads. A: bi-layered chitosan-gelatin (CG) and HA-chitosan-gelatin scaffold by (Chen *et al.*, 2011) which contains respective layers of naked pTGF-β1 and pBMP-2 DNA vectors. SEM micrographs illustrated bi-layered scaffolds possessed a highly porous interconnected, honeycomb-like structure with a pore size range of 50-100 µm (black arrows indicating the integrated scaffold interface). Upon *in-vitro* MSC seeding as well as *in-vivo* implantation, new bone and cartilage tissue was simultaneously deposited. B: A bi-layered composite collagen type II/I-nHA scaffold by (Lee *et al.*, 2017) which contains respective layers of CaP/pTGFβ-3/CaP/PEI and CaP/pBMP-2/CaP/PEI transfection payloads. Despite two different collagen types being utilised, a highly integrated porous scaffold was produced with an average pore size in both phases of 250 µm. Furthermore, upon hMSC cell seeding sustained levels of transfection capable plasmids were released from the GAM, all of which promoted transgene expression and the stimulation of osteogenic and chondrogenic differentiation. Taken from (Chen *et al.*, 2011) and (Lee *et al.*, 2017) with permission from Elsevier under licence numbers 5663671029408 and 5663671263326.

A further osteochondral GAM approach of significant promise was that of Kasper *et al* and Needham *et al*, who developed a series of synthetic bi-layered oligo(poly(ethylene glycol) fumerate) (OPF) hydrogel systems specifically containing plasmids encoding chondrogenic and osteogenic master transcription factors (SOX trio and RUNX2) (Kasper *et al*., 2006; Needham *et al*., 2014). In a similar fashion to Lee *et al*, the hydrogel GAMs developed here contained plasmid vectors complexed with a chemical transfection reagent (branched PEI and hyaluronic acid), thus imbuing plasmids with a clear and viable delivery pathway for downstream protein production. Upon their implantation *in-vivo*, it was shown that scaffold mediated gene delivery was largely successful and could effectively enhance simultaneous bone and cartilage tissue repair within rat osteochondral defects (1.5 mm diameter and 1 mm depth), in comparison to empty hydrogels and monophasic groups. This proved particularly significant given SOX trio-RUNX2 combinations have, in the past, been shown to be sub-optimal for such defect repair applications (a result previously hypothesised to be due to the over-dominant nature of SOX trio expression versus RUNX2) (Cao *et al*., 2011; Jeon *et al*., 2012). In contrast, Needham and colleagues believed the distinct bi-layered nature of the OPF GAMs restricted cellular migration and dual uptake of bone and cartilage inducing payloads, thus allowing for the enforcement of the desired singular transcription factor expression. Despite the obvious evidence of tissue repair, they purport that more effective regenerative responses could have been achieved if the GAM release profiles were optimised (currently 80% plasmid release after 4 days). As hyaline cartilage formation is largely dependent on sub-chondral bone support, they believe a delayed chondrogenic release method would facilitate a more systematic delivery process and thus induce more effective and higher quality overall osteochondral tissue formation (Needham *et al*., 2014).

A further limitation often identified in the *in-vitro* and *in-vivo* application of bi-layered GAMs is the categorical zonal osteogenicity and chondrogenicity observed within 3D cultured scaffolds or repaired defect regions, whereby strict tissue boundaries are often exhibited with little evidence of osteochondral tissue gradients or transitioning (Needham *et al*., 2014; Yu *et al*., 2023). As a result, highly crucial intermediate regions such as the calcified cartilage layer fail to be recapitulated, which can significantly impact downstream processes such as vascular development in neobone tissue as well as the facilitation of an appropriate avascular environment in cartilage zones (Hunziker & Driesang, 2003).

1.8.3 Continuous gradient GAM scaffolds

In response to the limitations and substantial complexities observed in the techniques above, it is the view of the Feichtinger research group at the University of Leeds that in order for truly successful regeneration of native osteochondral tissue, 3D GAM systems should evolve away from the dogmatic concept of a layer-orientated design modality, instead striving to construct a single biomaterial preparation with multiple tissue specific payloads incorporated in subtle gradient-like conformations – i.e. a continuous gradient GAM. In the context of a continuous

gradient osteochondral GAM, this would likely involve the fabrication of a scaffold system containing bi-directional concentration gradients, whereby distal ends contain purely chondro-inducing or osteoinducing genetic payloads whilst the middle portion contains a variable blend. As a result of this novel design standpoint, it is therefore anticipated such systems, upon payload uptake and expression, should allow for enhancements in scaffold wide cellular communication, facilitate more synchronised hierarchical tissue deposition, and ultimately induce the final creation of smooth transitional high quality osteochondral tissue. Additionally, on account of the hypothesised monophasic nature, such gradient GAM systems may hold the potential to mitigate other previously observed bi-layered related issues, such as neo-tissue separation, layer stratification, and scaffold phase instabilities.

Unfortunately, despite the existence of a large number of continuous gradient recombinant protein incorporated scaffold concepts, it is surprising to find no examples currently exist for equivalent continuous gradient GAMs, specifically in the context of full osteochondral tissue (bone and cartilage) repair. Furthermore, in the examples that do currently exist (recombinant protein scaffolds), it appeared the generation of *in-situ* gradients required the application of unique and highly complex additive manufacturing methods including 3D printing, controlled fluid mixing, electrospinning (Bittner *et al.*, 2019; Castro *et al.*, 2015; Dormer *et al.*, 2010; Mohan *et al.*, 2014).

Although the methods above showed considerable promise with regards to inducing more synchronised and hierarchical osteochondral tissue formation, they were generally limited by their high complexities, over-reliance on synthetic bio-ink components and overall unfeasibility for large-scale low cost batch manufacture. Furthermore, it was found issues still existed over the *in-vivo* stability, half-lives and dosage of recombinant growth factor protein payloads, particularly with regards to inducing long term and sustained therapeutic cellular responses in defect sites. Based on these limitations, there is a clear demand for more simplified, low cost methodologies which are capable of generating *in-situ* continuous gradients with the more advantageous gene-based payloads.

1.8.3.1 Concept of electrophoretic spatial patterning

One simple and cost-effective method for generating gene payload gradients is the use of electrophoresis, whereby charged components are spatially distributed within a monophasic 3D hydrogel matrix using attractive electrical force potentials. In such methods, this specifically involves the establishment of positive and negative electrode sites at spatially opposing locations within or adjacent to the biomaterial of interest, thus allowing for the facile movement of charged molecules into and across the 3D system and the eventual formation of a continuous gradient. Theoretically, based on this concept, it would therefore be possible for the spatial orientation of

charged molecules or minerals across the x, y, and even the z directions, depending on the electrophoretic capabilities of the system.

A seminal paper which first describes an iteration of this concept is that of Watanabe and Akashi, who proposed the combined ideological approach of electrophoretic ion migration (within electro-capable hydrogels) in combination with facile mineralisation/crystal synthesis in confinement. As a result of this unique combination, they were able to develop a highly novel system whereby CaP and/or HA particles could be synthesised and subsequently spatially deposited at specific locations within a 3D agarose hydrogel containment system – all via the simple and straightforward use of agarose hydrogels, electrophoretic potentials and salt reservoirs (Watanabe & Akashi, 2006).

Their formative method from 2006, as shown in Figure 1.16, can be described in the following step-wise process. 1) Using a standard horizontal gel electrophoresis tank, a 3 wt% agarose gel was first cast and set up between separate reservoirs of $CaCl_2$ (40 mM) and Na_2HPO_4 (40 mM), which acted as anode and cathode specific loading buffers. 2) Each buffer was then adjusted to approximately pH 7.4 prior to mineral synthesis and patterning. 3) A 100V electrophoretic field potential was finally induced, over a period of 30 minutes, prompting the mobilisation of electro-mobile salt ions (in the form of Ca^{2+}, HPO_4^{2-}, PO_4^{3-}, OH^-) to successfully enter into the hydrogel network. 4) Due to the opposing migration patterns, salt ions were able to interact specifically within the agarose gel matrix, allowing for the *in-situ* synthesis of CaP and HA particles.

Post mineralisation, all gels were submerged in ultra-pure water before then undergoing lyophilisation in preparation for characterisation studies. Ultimately, they found under scanning electron microscopy (SEM) that numerous spatially distinct HA populations of approximately 1 μm diameter were synthesised within said gels (Figure 1.16 B-D) (Watanabe & Akashi, 2006). Significantly, through the capabilities of this agarose gel electrophoresis (AGE) method, as well as a subsequent Watanabe *et al* iteration (electrophoresis with additional alternate soaking), it was confidently purported by the authors that such novel anisotropic CaP and HA agarose gels may hold significant potential as a mineralised bone repair device, and as such the platform described should warrant further study and greater optimisation to achieve this ultimate goal (Watanabe & Akashi, 2006, 2008).

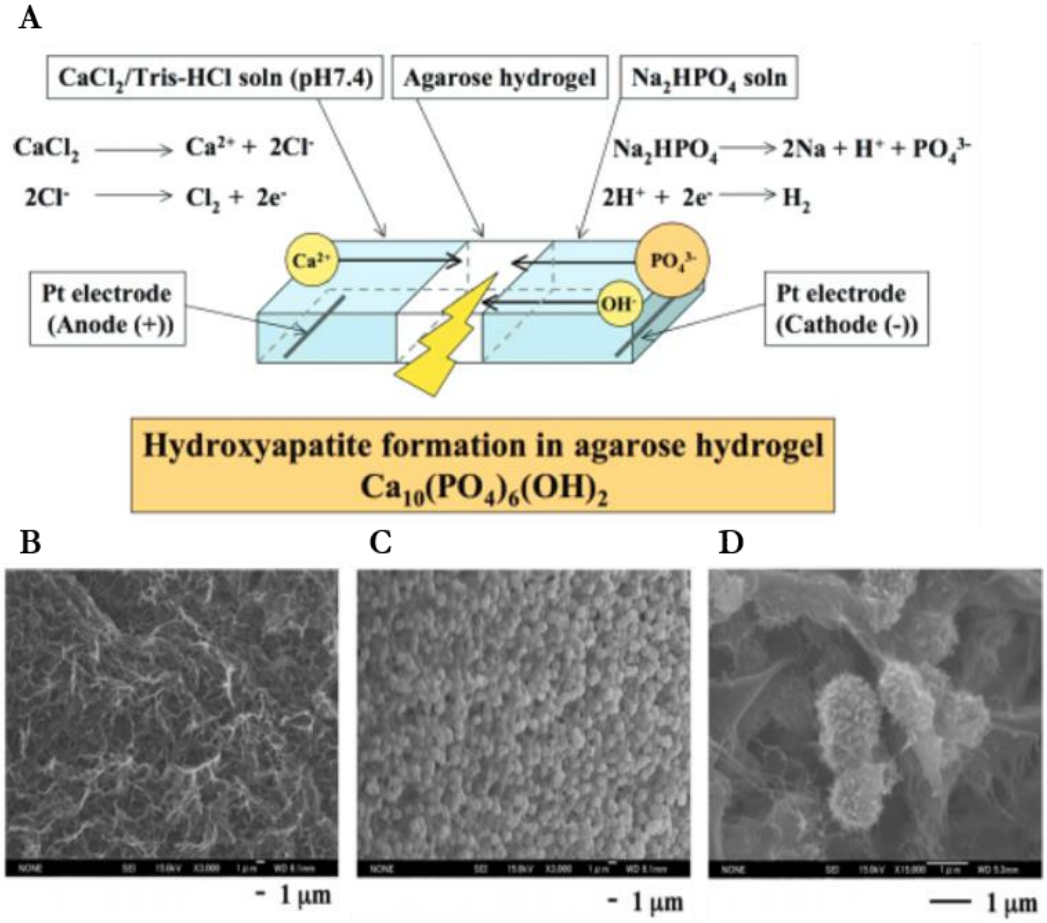

Figure 1.16 (A & B) – Seminal agarose gel electrophoresis methodology for CaP/HA crystal synthesis *in-situ* within 3D agarose hydrogels. A: Schematic illustration of the electrophoresis setup for the formation of CaP/HA in a large 3wt% agarose hydrogel. Through the provision of two different salt solution reservoirs ($CaCl_2$ and Na_2HPO_4) at the anode and cathode regions it was possible to induce electrophoretic ion migration into an agarose gel region. Upon co-localisation within the centre portion, HA precipitate product is formed and deposited *in-situ*. B: SEM image of blank agarose hydrogel. C: Surface imaging of *in-situ* deposited HA precipitates. D: High magnification micrograph of individual HA particles. Figures adapted with permission from (Watanabe & Akashi, 2006) via Copyright 2023 American Chemical Society.

Utilising the core concepts described above, a further research group (Kamitakahara *et al*) reported a modified version of the AGE approach, which specifically sought to speed up the rate of *in-situ* CaP/HA synthesis as well as reduce the excessive salt reservoir volumes previously required (100 mL range) (Kamitakahara *et al*., 2012). Crucially, this was achieved by the formulation of a more facile opposite loading well approach, whereby specific 40 µL cationic (20 mM $CaCl_2$) and anionic (12 mM Na_2HPO_4) salt loading solutions were instead loaded individually into agarose gel wells separated by a width of 48 mm or 15 mm (Figure 1.17 A). This new system also used both 3 wt% and 1 wt% bulk agarose gels as well as a 40 mM Tris buffer (pH 8), which acted as the electrophoresis buffer working solution. Post solution loading, a 100V electrophoretic field potential was again induced, significantly resulting in the appearance of a white precipitate between the wells after only 11 minutes. Unlike Watanabe *et al* however, Kamitakahara and colleagues characterised each of the mineralised 1wt% and 3wt% gel slices via

direct and indirect lyophilisation (with or without submergence ultra-pure water), showing that amorphous CaP particles were generally produced directly after gel synthesis but could be converted into HA through incubation with water. Moreover, in this case of the submerged 1 wt% and 3 wt% gels, upon SEM imaging, the authors also identified distinct populations of 500-600 nm and 300-400 nm spinous HA particles respectively (Figure 1.17 B) (Kamitakahara *et al.*, 2012). This was a significant finding as it led to the proposition that an inverse relationship exists within this approach specifically between agarose percentage and particle diameter, whereby controlling the hydrogel pore characteristics (i.e the rigid nanoporous gel structure) can positively restrict crystal growth and result in the synthesis of small sized *in-situ* mineral populations. As native hydroxyapatite found within mineralised collagen fibrils is generally less than 100 nm, this method holds considerable promise that through further optimisation via agarose type, buffer pH and gel concentration modifications, near native HA populations and/or gradients could feasibly be synthesised, and thus such mineralised gels could be applied within bone repair contexts.

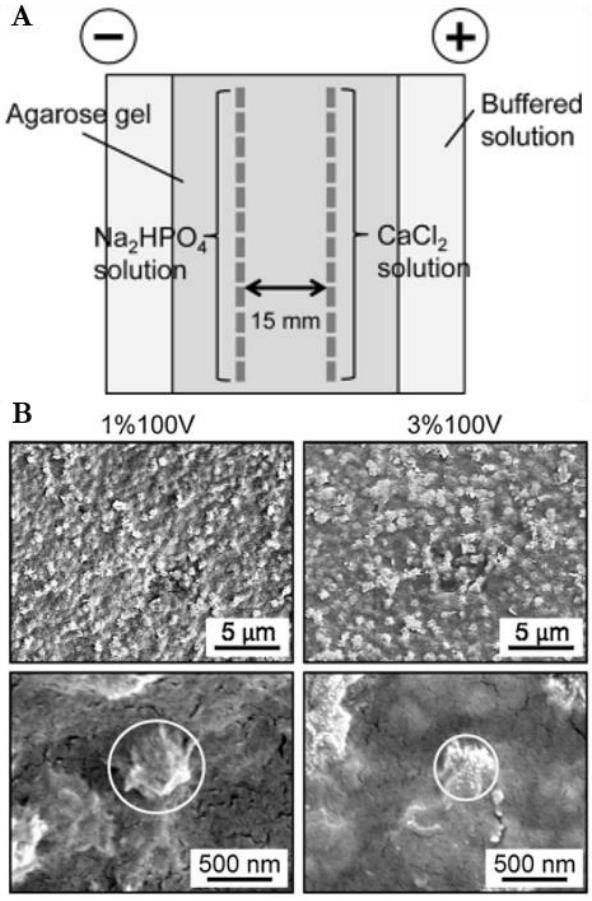

Figure 1.17 (A & B) – Modified agarose gel electrophoresis methodology for CaP/HA crystal synthesis *in-situ* within 3D agarose hydrogels. A: Schematic illustration of the opposite loading electrophoresis setup whereby small volumes of salt solutions were placed into individual gel wells. B: Following electrophoresis, Ca^{2+}, PO_4^{3-}, H^+ ion migration resulted in individual precipitate regions containing either amorphous calcium phosphate or HA nanoparticles. SEM images of HA particles suggest particle size was decreased if agarose percentage was increased. Images taken from (Kamitakahara *et al.*, 2012) with permission from Elsevier under licence number 5659271219293)

In summary, the methods discussed in the section above illustrate a methodology for the joint synthesis and spatial deposition of nanosized CaP/HA containing minerals throughout an agarose hydrogel biomaterial. Through the physical resemblance of the *in-situ* synthesised CaP nanoparticles to near native bone minerals as well as agarose hydrogels possessing structural similarities to the ECM, the seminal authors for this approach believe such a system could be utilised within a multitude of bone related ailments and diseases.

Considering this high degree of promise, it is the belief of Dr Feichtinger and colleagues at the University of Leeds that this platform technology holds several further uses which have currently not been explored in any capacity. One such application, which forms the focus of this PhD, concerns the partial use of this agarose electrophoretic synthesis and patterning system for the creation of continuous DNA-CaP gradient agarose GAMs (Watanabe *et al* patent application: WO2007061001 A1 (Watanabe & Akashi, 2007) – only covers the *in-situ* synthesis of calcium-phosphate nanoparticles and not calcium-phosphate/DNA co-precipitate nanoparticles). The following sections will now discuss in detail the core Feichtinger AGE GAM methodology and how highly novel potential GAM systems can be generated for subsequent application in osteochondral repair contexts.

1.9 Feichtinger AGE GAMs for use OCTE

The controlled induction of inorganic nanoparticle crystallisation within a confined system or biomaterial hydrogel stands as a pivotal process in biomaterials science. It emulates the intricate mineralisation pathways observed in native biomineralisation processes, particularly in bone formation. Intriguingly, when such biomaterials are combined with gene loading strategies, such as those utilised in various GAM systems, it could be hypothesised that a new generation of smart spatially patterned transfection systems could be generated. The research performed in this thesis for the first time seeks to comprehensively explore novel strategies which utilise biomineralisation in confinement concepts (described above in the 2006 and 2008 reports by Watanabe *et al* and Kamitakahara *et al*) alongside standard electrophoretic DNA patterning/migration in the hope that such an amalgamation can produce a continuous gradient GAM system capable of spatial cellular transduction within a 3D cell-laden scaffold construct (Kamitakahara *et al*., 2012; Watanabe & Akashi, 2006).

As such, a brand new electrophoretic nucleic acid payload patterning method has been tentatively proposed for the combined synthesis, co-localisation and spatial patterning of *in-situ* biomineral-DNA complexes, specifically within a single agarose hydrogel system. This approach combines the following scientific concepts; 1) the idea of biomineral crystallisation in confinement and 2) the use of electrophoretic agarose-plasmid patterning for controlling spatial deposition of nucleic acids within a nanoporous hydrogel matrix. It is proposed that such methods can be used to produce a new class of spatially controlled or gradiented GAM which may overcome the previously described limitations found within current bi-layered osteochondral GAM systems.

The minimal proof-of-concept development for this method is detailed in the following sections (with unpublished data from (Feichtinger, 2016)).

1.9.1 Feichtinger-AGE-1 proof-of-concept

Prior to commencement of this thesis, investigations by Dr G Feichtinger and colleagues established an initial unpublished methodology by which inorganic phosphate-nanoparticles (e.g. CaP) and gradient DNA payloads could be spatially patterned within specific regions of 1 wt% agarose gels, using electrophoresis. It was hypothesised that by utilising the dual electrophoretic movement of both particles (CaP-positive charge, plasmid DNA-negative charge) nanoparticle-DNA complexation could be controlled and induced *in-situ*, thus ultimately generating spatially patterned transfection capable therapeutic payloads. This approach was named the Feichtinger agarose gel electrophoresis (or F-AGE-1) method and significantly built on and repurposed several concepts previously reported by the groups Watanabe *et al* and Kamitakahara *et al* - specifically of that relating to use of electrophoresis to control the formation and deposition of calcium-phosphate nanoparticle precipitates (Kamitakahara *et al*., 2012; Watanabe & Akashi, 2006). The F-AGE-1 methodology utilised a conventional horizontal electrophoresis tank and is illustrated in Figure 1.18. Briefly, a 1 wt% agarose gel containing 0.75 mM Na_2HPO_4 and 25 mM HEPES at pH 7.4 was cast specifically containing a single row of 16 wells. A 5 μg plasmid solution with 30% glycerol was loaded into all wells and a 60V electrophoretic potential was applied to load the nucleic acid payload into the gel. After 6 minutes, the potential was removed and $CaCl_2$ solutions (0-225 mM) were added to all wells, followed by reversal of the electric field polarity and the re-application of a 60V potential for a further 6 minutes. Between 2-3 minutes, white precipitates began to appear adjacent to the wells (in the direct vicinity of the previously loaded plasmid vectors), with an intensity dependent on the initial $CaCl_2$ loading concentration.

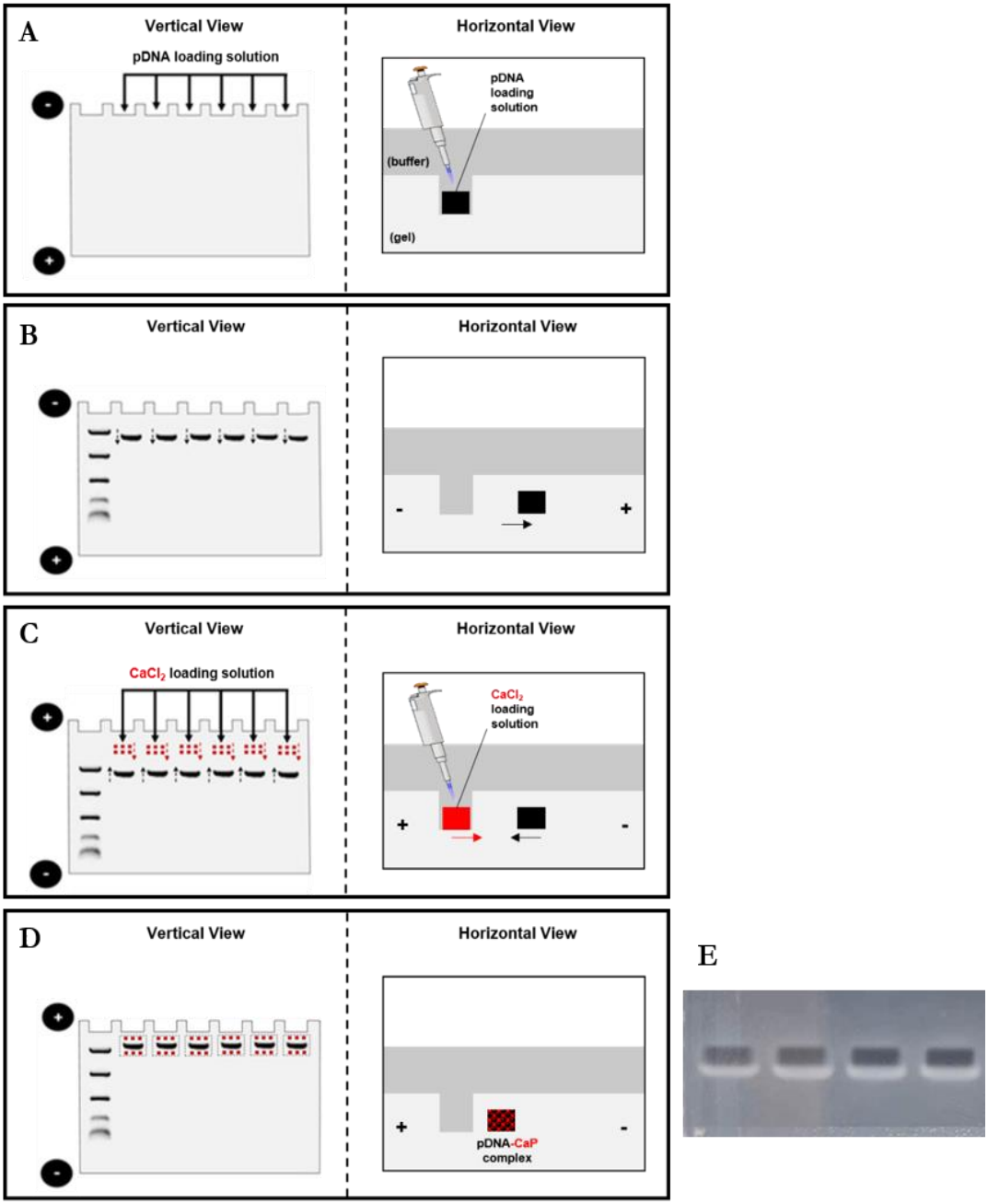

Figure 1.18 (A-E) – Spatial patterning of nucleic acid payloads within 1 wt% agarose gels using the F-AGE-1 approach. A: 25 µL plasmid DNA loading solution pipetted within agarose wells, settling at the bottom under gravity. B: a 60V potential is applied across the gel for 6 minutes, using a - ⟶+ electrode configuration. C: 25 µL $CaCl_2$ loading solution pipetted within agarose wells, settling at the bottom under gravity. D: a 60V potential is applied across the gel for 6 minutes, using a + ⟶- electrode configuration. E: Actual F-AGE-1 agarose gel containing DNA-CaP precipitates (n=4) (225 mM $CaCl_2$ used).

Post precipitation, each individual mineralised gel was either stained to illustrate DNA complexation/encapsulation or directly freeze-dried for nanoparticle SEM (and EDX) analysis (Figure 1.19).

To initially ascertain if successful DNA-CaP co-complexation took place during the F-AGE-1 patterning process, various precipitate containing gel slices (of different $CaCl_2$ concentrations)

were stained with ethidium bromide (EthB), which possessed strong affinities to plasmid DNA. Through imaging in both the EthB filter (Pink colouration) alongside false imaging the opaque precipitates (light blue colouration), a qualitative indication of successful co-localisation was provided. In the case of Figure 1.19 A (F-AGE-1 0-225mM $CaCl_2$ patterning), it was therefore shown that DNA-CaP co-localisation appeared largely successful and was most effective in the highest $CaCl_2$ concentration utilised – 225 mM).

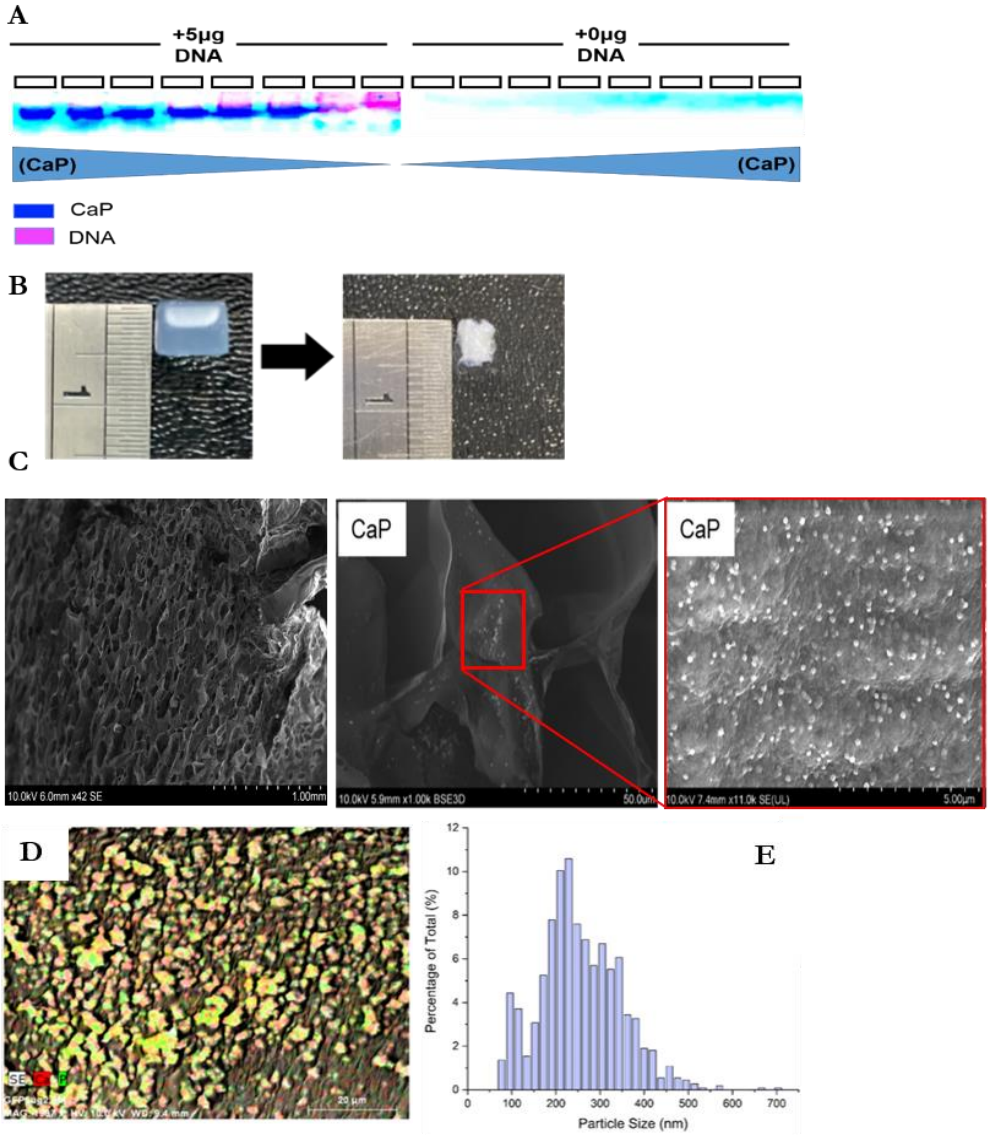

Figure 1.19 (A-E) – A selection of results from the F-AGE-1 proof of concept investigation regarding the synthesis and characterisation of *in-situ* DNA-CaP nanoparticle complexes. A: Confirmation of electrophoretic co-localisation between CaP precipitates and plasmid DNA via EthB DNA staining in combination with false imaging (DNA:pink EthB stain) (CaP: blue false imaging) B: Digital camera image of DNA-CaP gel slice pre and post freeze-drying. C: SEM images of 1 wt% scaffold and pDNA-nanoparticles synthesized in agarose matrix. D: Electron dispersive x-ray scattering (EDX) based analysis of *in-situ* particle composition (calcium = red and phosphate = green). E: Particle size distribution of pDNA-CaP co-precipitate synthesised within 1 wt% agarose gel.

The gel slice containing the optimal co-complexed DNA-CaP nanoparticle precipitate (225 mM $CaCl_2$) was extracted and freeze-dried to produce a macroporous GAM. Based on visual analysis,

it was found that lyophilisation had a substantial effect on these lower percentage agarose gels, whereby a white, glossy, highly porous scaffold was synthesised. Unfortunately, as a result of this process Dr Feichtinger also observed significant alterations to the agarose scaffold structure, with resulting GAM scaffolds exhibiting large-scale mechanical fragility (collapsing under moderate physical handling) as well as considerable bulk surface area shrinkage (Figure 1.19 B). Despite such poor mechanical properties, it was confirmed via SEM (and EDX imaging) that spherical CaP particles had been effectively synthesised and deposited *in-situ* using the F-AGE-1 methodology (Figure 1.19 C and D). Additionally, through extensive high magnification image analysis it was identified that the CaP populations were spherical in nature with a hydrodynamic radius which ranged from 100 – 400 nm.

Importantly, despite multiple variations between the F-AGE-1 methodology versus that previously described by Watanabe *et al* and Kamitakahara *et al*, it was shown in these proof-of-concept investigations that a modified AGE method could be generated which allows for similar synthesis and deposition of CaP nanoparticles *in-situ* within a 3D agarose hydrogel matrix (Kamitakahara *et al*., 2012; Watanabe & Akashi, 2006, 2008). Furthermore, it uniquely shows that it is possible to combine an AGE CaP synthesis approach with a simple electrophoretic plasmid loading strategy, thus allowing for the apparent production of nanosized DNA-CaP co-complexes. As previously discussed in this literature review regarding how the size of DNA-CaP co-complexes severely impacts the efficiency of the CaP mediated transfection process, this novel method holds potential for combatting such a limitation, crucially via the synthesis of DNA-CaP co-complexes in 3D confinement (i.e within a nanoporous agarose hydrogel).

1.9.2 Additional method for producing *in-situ* plasmid gradients

Evidently, in the basic F-AGE-1 methodology described above, only a single DNA loading step was utilised for basic proof-of-concept testing regarding DNA-CaP synthesis and co-localisation. As a result, it can be said that the agarose GAMs generated at this stage were lacking the key gradiented characteristic sought by the Feichtinger research group for osteochondral GAM fabrication. To rectify this issue and allow for the creation of continuous gradients of nucleic acid payloads, the research group proposed one simple modification to the F-AGE-1 methodology. This change specifically included the use of multiple sequential plasmid DNA loading steps (dual or triple DNA loading), prior to the $CaCl_2$ loading step. Through this method, it was hypothesised that multiple DNA payloads could be spatially distributed throughout an agarose hydrogel, crucially in a continuous overlapping gradient conformation. Furthermore, by loading different DNA vectors, each encoding for a specific therapeutic factor (i.e. TGFβ, BMP, SOX, RUNX2), it was proposed that a bone-intermediate-cartilage anisotropic payload gradient would be possible, and thus allow for the facilitation of more native osteochondral tissue formation via the regionally specific DNA payload uptake by cells. To test this hypothesis, an additional proof-of-

concept study was performed whereby plasmids were labelled with different cyanine-dimer dyes (blue - YOYO1, green – POPO3, red – TOTO3) (ThermoFisher) prior to sequential loading into a 1 wt% agarose gel. Crucially, by running the DNA at a constant voltage (60V) with 5 minute intervals per DNA loading, it was possible to generate a highly controlled *in-situ* DNA gradient pattern (Figure 1.20 A & B). Ultimately, through this success, it was envisaged that the F-AGE-1 method would eventually be modified with such sequential loading steps, thus forming a true continuous gradient osteochondral GAM.

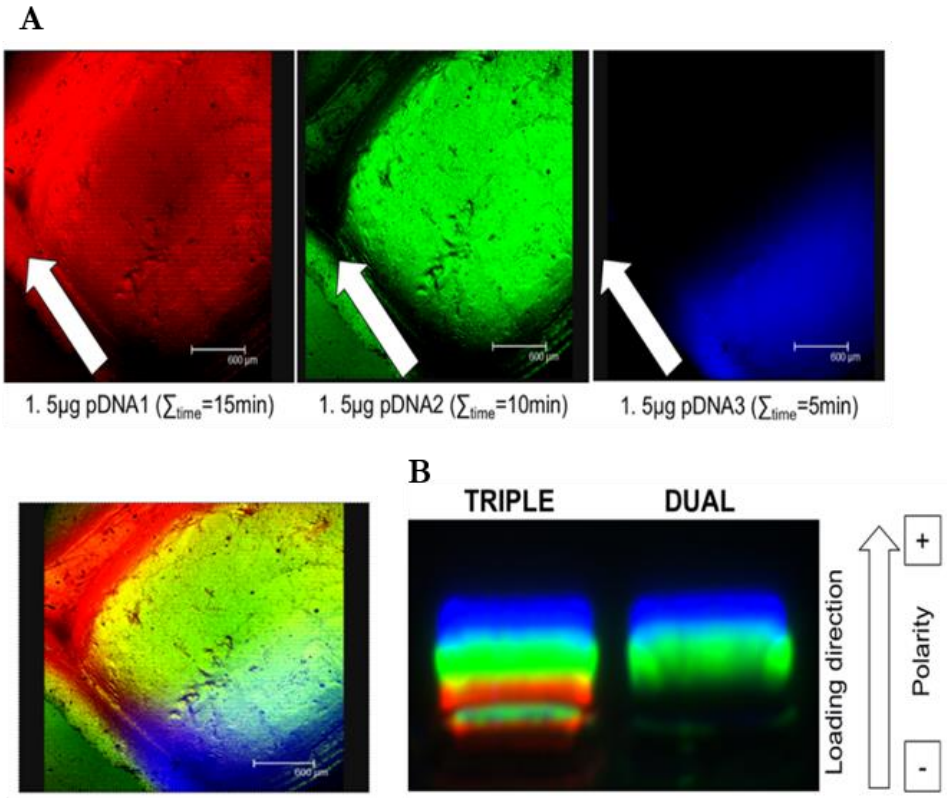

Figure 1.20 (A & B) – Investigation into control of DNA gradients in 1 wt% agarose hydrogels using different cyanine-dimer dye labelled pDNA samples (pDNA1-3) and sequential loading. A: DNA distribution and overlapping gradients as observed by confocal microscopy). B: and in a separate experiment on a BioRad GelDoc imaging station. Control over distribution as well as dependence of dispersion and size of different zones/pDNAs on loading time clearly observable. Scale bars = 600 µm.

1.10 Rationale for spatially patterned GAM systems for osteochondral repair

This review has highlighted a clear imperative for early interventions with regards to the treatment of large scale or severe osteochondral defects. Whilst microfracture, mosaicplasty and other current front-line treatments present reasonable therapeutic profiles, they are somewhat dogged by several innate limitations which restrict their restorative or regenerative power, specifically within complex multi-tissue environments. This includes limited mechanical resilience (in cell therapies), lack of tissue specific morphogenic cues, as well as damaging surgical co-factors such as donor site morbidities (in the case of mosaicplasty). The field of tissue engineering on the other hand showcases several attributes which may allow for the circumvention of said limitations. Frustratingly, despite such potential, translation in recent years has appeared more

challenging than anticipated, with many recombinant protein and bi-layered GAM concepts still falling short in terms of replicating the precise bio-architecture required for adequate repair of the full osteochondral environment (Chen *et al.*, 2011; Lee *et al.*, 2017). This discrepancy can consequently impact key fundamentals within the repair pathway such as healthy long term tissue maintenance as well as biomechanical properties.

The Feichtinger research group anticipate that 3D gene-activated matrix (GAM) systems, featuring electrophoretic patterning gradients, offer a distinctive design ideal for effectively treating severe osteochondral injuries. Through the creation of smart 3D scaffold biomaterials featuring directional gradients of multiple nucleic acid-transfection payloads, it can be anticipated that advanced cellular orchestration can be achieved within distinct regions of biomaterial space, crucially emulating and recapitulating natural tissue morphogenetic processes – much like those seen in embryonic development. The Feichtinger research group hypothesise therefore that upon cell-free implantation of patterned GAM systems (likely in conjunction with microfracture), endogenous cells will infiltrate, populate and therapeutically respond to not only the basic biomaterial framework but also the pre-designed spatial gene payloads distributed within, ultimately directing cells to either osteogenic and chondrogenic lineages, within a single biomaterial system.

1.10.1 Project outline

Specifically, this PhD project aims to build on and advance the small pool of evidence currently acquired regarding a new class of GAM biomaterials developed by the Feichtinger research group (Feichtinger, 2016). Whilst the current unpublished material and early process development data (conference material only) shows promising findings, the overall system remains at a very early stage of development (technology readiness level 1-2), and as such inherently contains systems and processes that remain either untested, require further validation or simply possess direct limitations. For this thesis such factors included:

1) Current biomaterial/hydrogel physical properties unsuitable for application within an osteochondral treatment context (poor physical/structural properties post lyophilisation)
2) Unconfirmed cytotoxicity and long term 3D cellular adhesion of F-AGE-1 agarose GAM scaffolds
3) Full validation required for short and long term 3D gene transfection in relevant cell lines

With such factors in mind, this project will investigate firstly the translation of previously established nucleic acid patterning platform (F-AGE-1) within freeze-dry compatible agarose gels, as well as attempt to further modify the F-AGE-1 methodology with the view of novel

incorporation of cationic polymers such as PEI within said systems. Furthermore, the potential of using freeze-dried agarose scaffolds as 3D gene delivery biomaterials will be studied in greater depth, with particular emphasis on cellular cytotoxicity, 3D cellular adhesion, proliferation and differentiation. Finally, upon provision of an optimally designed adherence capable biomaterial system, short and long term transfection of spatially patterned agarose GAMs will be investigated, with an additional proof of concept study being performed regarding alternative nucleic acid vector systems.

Ultimately, the long-term goal for this construct involves the use of the aforementioned Feichtinger electrophoretic GAM patterning approaches to create a bi-directional gradiented biomaterial system in which numerous therapeutic nucleic acid payloads are spatially patterned and thus capable of directing complex *de novo* tissue formation. However to achieve this final design outcome (Figure 1.21), singular payload patterning and transfection must first be thoroughly established and optimised. As such, for this PhD thesis project, only singular payload patterning using the Feichtinger electrophoretic patterning principles was applied, in a proof-of-concept structure.

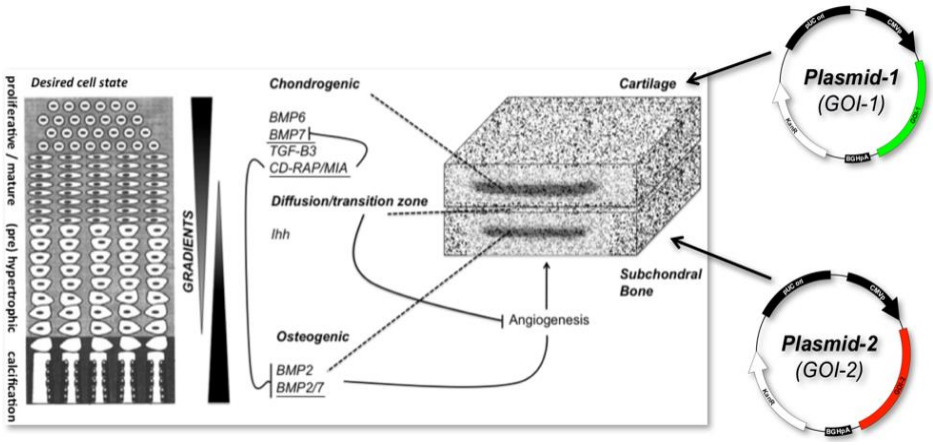

Figure 1.21 – Envisaged final application of the Feichtinger platform technology for musculoskeletal tissue interface regeneration. Inclusion of morphogenic gene therapeutic gradients and scaffold composition mimicking instructive morphogenic gradients for tissue formation and graded mineralisation content provided by phosphate-nanoparticles or cationic polymers.

1.11 Project aims and objectives

The specific aim of this project was to comprehensively characterise and optimise the biological responses and gene delivery capabilities of the developed electrophoretically patterned agarose GAMs.

In order to achieve this aim, the following research objectives were developed.

- To determine the effect of freeze-drying on different agarose formulations.
- To determine if the primary F-AGE-1 agarose gel electrophoresis approach can be successfully translated into higher percentage agarose gels.

- To design and validate a new iteration of the agarose gel electrophoresis approach which could synthesise and spatially deposit pDNA-PEI transfection payloads *in-situ*.
- To determine the biocompatibility of agarose GAM scaffolds.
- To characterise the 3D gene delivery capabilities of developed agarose GAM scaffolds.
- To explore the potential of covalently closed hairpin loop vector (CCHLV) systems as an alternative nucleic acid vector for agarose GAM incorporation.

This thesis is therefore organised into four experimental chapters which chronologically outline the various research methodologies and associated results in relation to the stated research objectives.

Chapter 3 therefore qualitatively and quantitatively investigates the physical and structural differences in 1wt% and 3wt% freeze-dried agarose GAM biomaterial compositions for their specific use in osteochondral defect repair applications, as well as for the first time comprehensively verifying that the F-AGE spatial patterning approach can synthesise and spatially control not only pDNA-CaP payloads *in-situ* but also DNA-PEI polyplexes.

Chapter 4 describes the optimisation of sterility, cytotoxicity and cellular adhesion (cell attachment, viability, 3D infiltration and differentiation) capabilities of agarose scaffolds or GAMs for support of 3D culture of biological relevant adherent cell lines such as L929, C2C12 and Y201. This included the testing and physico-chemical characterisation of three different surface coatings (Fibronectin, Laponite-PEO, Polydopamine.

Chapter 5 describes the optimisation of calcium phosphate (CaP) mediated and polyethylenamine (PEI) mediated 2D cell monolayer transfection protocols for two different cell lines (C2C12 and Y201), the validation of agarose scaffolds acting as adequate surfaces for 3D transfection (control study), and finally the characterisation of gene delivery capabilities of electrophoretically loaded PDA coated agarose GAM scaffolds.

Chapter 6 illustrates the construction and 2D transfection testing of two novel enzymatic ligation assisted by nucleases (ELAN) strategies which allow for efficient synthesis of CCHLV DNA vectors.

CHAPTER 2

GENERAL MATERIALS AND METHODS

2 CHAPTER 2: GENERAL MATERIALS AND METHODS

2.1 Materials

2.1.1 Equipment

All equipment used in this project is tabulated in the Appendix, Table 8.1.

2.1.2 Consumables

All consumables used in this project is tabulated in the Appendix, Table 8.2.

2.1.3 Cell lines

All cell lines used the following cell culture media preparation:

Cell culture medium: Dulbecco's Modified Eagle Medium (DMEM) (Medium-High Glucose), 10% v/v Fetal Bovine Serum (FBS), 100U/mL penicillin/streptomycin (P/S), 2 mM L-Glutamine.

L929 Mouse Connective Tissue Cell Line

Description: L929 cells (NCTC clone 929: CCL 1, American Type Culture Collection (ATCC), Manassas, VA, USA; ECACC No. 88102702, European Collection of Cell Cultures, Salisbury, Wiltshire, SP4 OJG, UK).

Subculture duration: twice weekly (1:5 passage ratio)

Incubation conditions: 37°C, 5% CO_2, humidified environment

C2C12 Mouse Skeletal Myoblast Precursor Cell line

Description: Mouse C3H Muscle Myoblast, purchased from the German collection of microorganisms and cell cultures DSMZ#ACC565 (Braunschweig, Germany).

Subculture duration: twice weekly (1:5 passage ratio)

Incubation conditions: 37°C, 5% CO_2, humidified environment

Y201 Human Telomerase Reverse Transcriptase (hTERT) immortalised human MSC Cell line

Description: Clonally derived primary bone marrow mesenchymal Stem Cells (MSC) manipulated post-isolation using a stable lentiviral hTERT integration system. Kindly donated by Dr Paul Genever (University of York).

Subculture duration: once weekly (1:2 passage ratio)

Incubation conditions: 37°C, 5% CO_2, humidified environment

2.1.4 Chemicals and reagents

All chemicals, stock reagents and restriction enzymes used in this project is tabulated in the Appendix, Table 8.3 and Table 8.4.

2.1.5 Plasmids

The plasmids used in this project are detailed in Table 2.1 and Figure 2.1 and Figure 2.2.

Table 2.1 – Plasmids used in this study.

Plasmids		
Name	**Purpose**	**Manufacturer**
pCAG-d2-eGFP (Figure 2.1)	Primary vector expression system CCHLV gene expression cassette template Enhanced Green Fluorescent Protein (eGFP) Insert	Provided by Dr G Feichtinger and colleagues
pMetLuc2 (Figure 2.2A)	Metridia Luciferase (Met-Luc) Insert	Clontech/TaKaRa (Palo Alto, CA, USA)
pCAG-MetLuc2 (Figure 2.2B)	*Metridia* Luciferase (Met-Luc) Insert Gene insert isolated from pMetLuc2 plasmid Cloned into pCAG backbone using restriction enzyme mediated cloning	In-house production (chapter 5)
pCAG-MetLuc2 (Esp3I)	*Metridia* Luciferase (Met-Luc) Insert Esp3I recognition sites cloned upstream and downstream of gene expression cassette	In-house production (chapter 6)

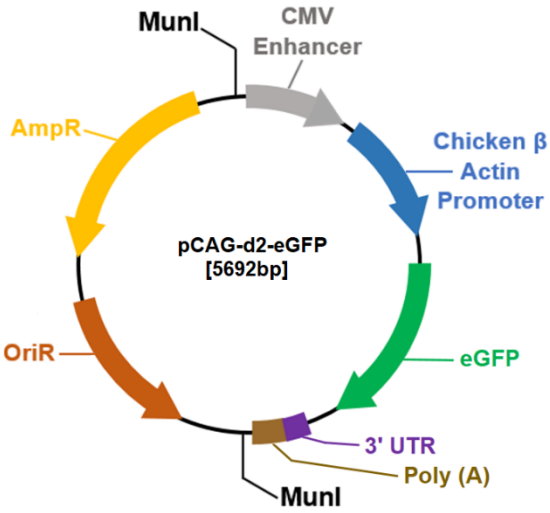

Figure 2.1 – pCAG-d2-eGFP vector map. Cytomegalovirus (CMV) enhancer sequence, chicken β actin promoter, self-replication origin (oriR), Simian virus 40 (SV40) Polyadenylation (Poly(A)) sequence, enhanced Green Fluorescent Protein (eGFP), Ampicillin resistance gene (for selection in E.coli). MunI recognition sites flanking the gene expression cassette region.

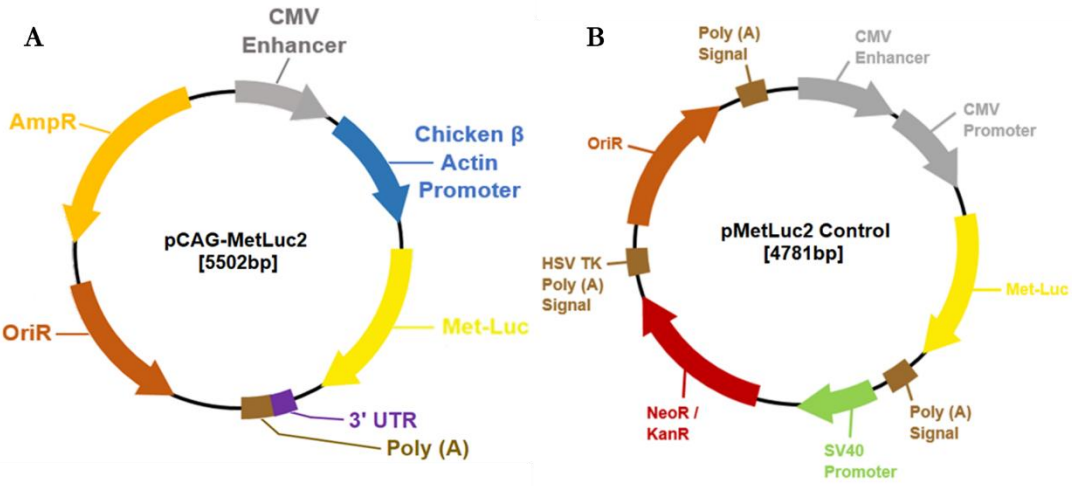

Figure 2.2 (A & B) – pCAG-MetLuc2 and pMetLuc2 Control vector maps. A) CMV enhancer sequence, chicken β actin promoter, self-replication origin (oriR), Simian virus 40 (SV40) Polyadenylation (Poly(A)) sequence, *Metridia* Luciferase gene insert (Met-Luc) , Ampicillin resistance gene (for selection in E.coli). MunI recognition sites flanking the gene expression cassette region. B) CMV enhancer sequence, CMV promoter sequence, self-replication origin (oriR), Herpes Simplex Virus (HSV) thymidine kinase (TK) and SV40 Poly(A) sequences, *Metridia* Luciferase gene insert (Met-Luc), Kanamycin/Neomycin open reading frame.

2.2 Methods

2.2.1 Tissue culture methods

Essential protocols for successful mammalian cell culture were performed in accordance with strict asceptic technique. This importantly included the correct storage and subsequent handling of all pre-sterilised cell culture consumables prior to and then within the confines of a class II ventilated safety cabinet.

2.2.1.1 Cell culture media preparation

For 200 mL of L929, Y201 and C2C12 complete media, 174 mL of DMEM (Sigma) was added to; 20 mL of FBS, 4 mL of P/S (5 mg.mL^{-1}) and 2 mL of L-glutamine (200 mM).

2.2.1.2 Cell counting

A Countess automatic cell counter (Invitrogen) was used to count total cell numbers in a suspension. A 50 µL cell aliquot was initially mixed with an equal volume of trypan blue (1:1 ratio). A Countess disposable slide (Invitrogen) was then loaded with 10 µL cell-trypan blue suspension before insertion and counting within the cell counter chamber. The resulting output determined the proportion of live and dead cells, in cells per mL. The live cell number value, from this output, was then used for cell seeding density calculations.

2.2.1.3 Cell culture resurrection, maintenance and passage

A cryo-preserved cell aliquot was gently warmed to room temperature and its contents transferred to a 15 mL falcon tube. Pre-warmed complete media (5 mL) was added dropwise and the suspension was centrifuged for 10 minutes at 150 g. The supernatant was discarded and the cell pellet reconstituted in 10 mL supplemented cell media. The cell suspension was subsequently seeded into a T-175 tissue culture flask and placed in a humidified incubator (37°C, 5% CO_2).

Samples were incubated for a further 48 hours before the culture media was removed and replenished, a process which also extracts any unbound non-adherent cells from the starting cell aliquot. Depending on cell line proliferation rate, cell culture media was exchanged weekly or twice-weekly until 60-80% confluency was achieved, as seen under light microscopy.

Once 60-80% confluent, cells were passaged. Depleted growth medium was aspirated. Flasks were washed once with sterile PBS (without calcium and magnesium) and 5 mL trypsin/EDTA was added before returning into incubator (37°C, 5% CO_2) for 4-6 minutes. After visual confirmation of cell detachment, the suspension was transferred to a sterile 50 mL falcon tube containing 10 mL supplemented media (FBS presence leading to trypsin inactivation). The cell suspension was centrifuged for 10 minutes, 150xg, the supernatant removed and re-suspended in 5 mL supplemented media to be counted, as per section 2.2.1.2, when necessary. Cell cultures were re-established in new T-175 flasks at the desired passage ratio.

2.2.1.4 Cell freezing

To maintain a good supply of frozen cell stocks, once each cell line progressed successfully through 2-3 rounds of passage and expansion, a proportion of cells were frozen. Specifically, any excess cells not taken forward for continued culture were separated and then centrifuged for 5 minutes, 150xg. The supernatant was removed and the remaining cell pellet was re-suspended in freezing media (10% dimethylsulfoxide (DMSO), 90% FBS) at a desired ratio of 1 mL per $1x10^6$ cells. The cell suspension was then briefly kept on ice before transfer to labelled cryovials within a freezing container. The container was stored in a -80°C freezer for 48 hours before reallocation to liquid nitrogen dewar for long term storage.

2.2.2 Spatial patterning of nucleic acid transfection payloads within agarose hydrogels

Nucleic acid payload patterning was accomplished in each of the following methodologies through the use of a horizontal Sub-Cell GT electrophoresis system (BioRad, Massachusetts, USA) (Figure 2.3). Each method utilised a 3 wt% agarose gel formulated using SeaKem® LE agarose powder (Lonza, UK) in combination with either Buffer A: 0.75 mM Na_2HPO_4 and 25 mM 4-(2-hydroxyethyl)-1-piperazineethanesulfonic acid (HEPES) (pH 7.4) or Buffer B: 25 mM HEPES (pH 8). Molten gels (130 mL) were cast within an in-house produced gel tray of 15 x 15 cm dimensions, alongside in-house produced gel combs, as shown in Figure 2.4.

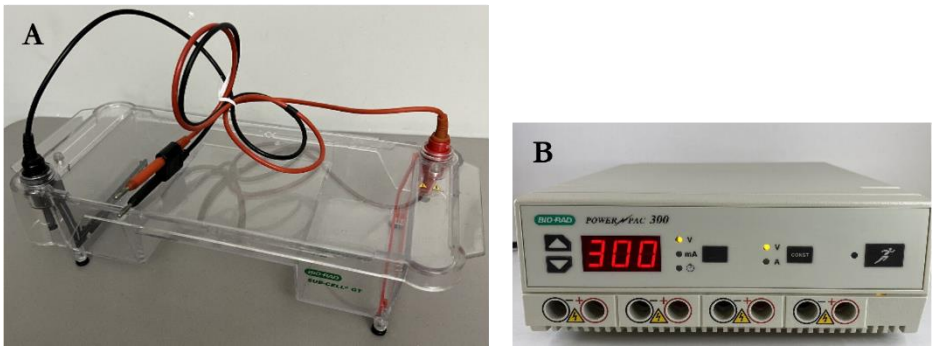

Figure 2.3 – The horizontal Sub-Cell GT electrophoresis system and associated power pack (PowerPac 300, BioRad) used in the F-AGE approaches.

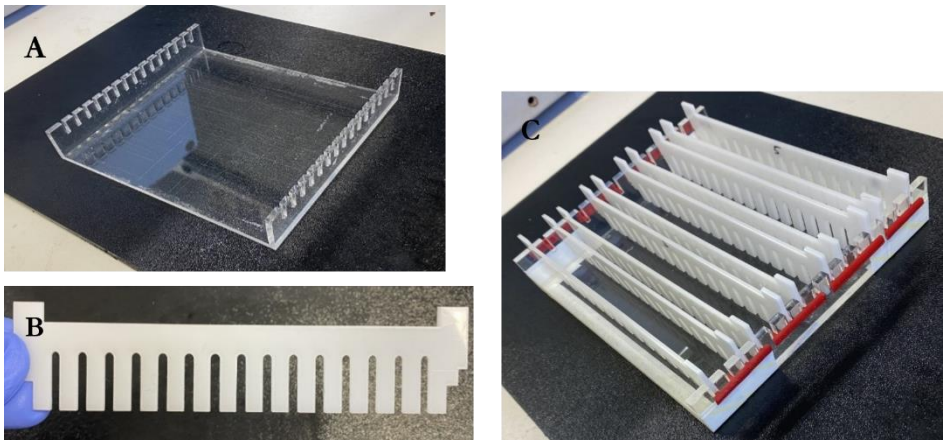

Figure 2.4 – The in-house agarose gel tray and comb developed by the Feichtinger research group for high throughput nucleic acid payload patterning within agarose gels. Each 15 x 15 cm gel tray contains 15 fixed comb positions. Each comb produces 16 possible wells upon agarose gel casting. Total of 240 possible wells per agarose gel.

2.2.2.1 F-AGE-1 nanoparticle approach

The Feichtinger Agarose Gel Electrophoresis (F-AGE-1) nanoparticle approach was a strategy first conceptualised by Dr G Feichtinger as a simple method to spatially control nucleic acid and

nanoparticle deposition within 3D agarose gel matrices, specifically allowing for the *in-situ* co-localisation of nucleic acids with CaP nanoparticles.

2.2.2.1.1 Loading solutions

Master stock loading solutions for both the DNA vectors and the inorganic nanoparticles were prepared as shown in Table 2.2 and Table 2.3. Each master stock solution contained enough volume for 60 individual loading runs, with 25 µL used per well. Once formulated, the mastermixes were stored at -20°C until required.

Table 2.2 – DNA Master stock loading solutions used for the F-AGE-1 method. pCAG-d2-eGFP or pCAG-MetLuc2 was used as the plasmid vectors for all DNA master stocks. FN = Fibronectin.

	Master Stock loading Solution Constituents (Total volume: 1500 µL)			
Master-stock Type	**pDNA (1µg/µL)**	**Glycerol (30%)**	**ddH$_2$O**	**FN (1µg/µL)**
2.5 µg DNA only	150 µL	250.2 µL	1098 µL	N/A
5 µg DNA only	300 µL	250.2 µL	949.8 µL	N/A
10 µg FN Only	N/A	250.2 µL	649.8 µL	600 µL
2.5 µg DNA + FN	150 µL	250.2 µL	498 µL	600 µL
5 µg DNA + FN	300 µL	250.2 µL	349.8µL	600 µL

Table 2.3 – $CaCl_2$ Master stock loading solutions used for the F-AGE-1 method.

	Master Stock loading Solution Constituents (Total volume: 1500 µL)		
Master Mix Type	**$CaCl_2$ (500mM)**	**Glycerol (30%)**	**ddH$_2$O**
0mM	N/A	250.2 µL	1249.8 µL
112.5mM	337.8 µL	250.2 µL	912 µL
162.5mM	487.8 µL	250.2 µL	762 µL
212.5mM	637.8 µL	250.2 µL	612 µL
225mM	675 µL	250.2 µL	574.8 µL

2.2.2.1.2 Buffer and agarose gel solution

The F-AGE-1 method utilised the buffer solution known as Buffer A for agarose hydrogel creation and as a running buffer, as stated in section 2.2.2.

A concentrated stock solution of Buffer A (500 mM HEPES + 15 mM Na_2HPO_4) was formulated as follows; 119.16 g HEPES and 2.129 g Na_2HPO_4 was added to ~1000 mL ddH_2O. After sufficient mixing, the pH of the solution was subsequently brought up to 7.4 using 6M NaOH before storage in the dark.

To achieve a working/running Buffer A solution (25 mM HEPES and 0.75 mM Na_2HPO_4), the concentrated stock was simply diluted 20 fold in ddH_2O to a final volume of 2000 mL. The working stock was then utilised as required.

To generate a 3wt% agarose gel slab, 130 mL working Buffer A was added to 3.9 g agarose powder respectively. Once mixed, the solution was then heated until the agarose had completely dissolved (solution appearing transparent), before then being allowed to cool to 50°C (For analytical agarose gels, SYBR™ Safe DNA Stain (Thermo Fisher) was added at this stage using a dilution factor of 1:10,000). Once cooled, the molten solution was poured into a 15 x 15 in-house gel tray containing appropriate comb inserts. Following this, the loaded gel tray was incubated for 60 mins at room temperature, thus permitting gel solidification. Once hardened the in-house comb inserts were carefully removed, leaving behind intact loading wells.

2.2.2.1.3 Gel loading and electrophoretic patterning

Firstly, master stock loading solutions formulated in section 2.2.2.1.1 were gently thawed on ice. At the same time, the solidified agarose gel slabs made in section 2.2.2.1.2 were carefully placed within a horizontal Sub-Cell GT gel tank before 1800 mL working/running Buffer A was added, ensuring anionic and cationic reservoirs were filled equally. After a subsequent 20 minute gel-buffer equilibration (room temperature), the system was considered ready for nucleic acid payload patterning.

The following protocol was specific to the F-AGE-1 system in which both pDNA and $CaCl_2$ loading solutions were used to induce pDNA-CaP co-localisation (as diagrammatically illustrated in chapter 1, Figure 1.18). For pDNA only controls, or CaP only controls, the same protocol was applied but with only one loading solution used.

Briefly, 25 µL of pDNA master stock was gently applied to a single agarose well using a standard Gilson pipette (stage 1). A 300V potential was then immediately induced across the agarose gel for 5 minutes, inducing negatively charged pDNA molecules to translocate "downwards" towards the positively charged cathode (stage 2). Subsequently, in the same well, 25 µL of a specific $CaCl_2$ mastermix loading solution was then carefully applied (stage 3). Importantly, this was followed by reversal of the electric field polarity. A further 60V potential was then

immediately induced across the gel for 6 minutes, this time inducing the cationic species to translocate in the "upwards" direction (due to switching of the cathode and anode position) towards the previously loaded pDNA (stage 4). Over this 6 minute process, white CaP precipitates materialise within the region directly below the loaded well.

2.2.2.1.4 Gel Excision

After formulation of the F-AGE-1 nucleic acid payloads within the agarose gels, an in-house designed hydrogel excision tool (Figure 2.5) was used to remove each individual hydrogel. The tool was designed similarly to a biopsy punch whereby the cutting element simply slides through the bulk agarose gel, taking up only the small hydrogel of interest. Precise hydrogels of dimensions 6mm by 4.6mm by 5.8mm were formed using this tool, as shown in Figure 2.5 E.

Furthermore, based on the pDNA concentration used and the $CaCl_2$ master mix type, the excised hydrogels were then renamed as individual agarose GAMs as shown in Table 2.4.

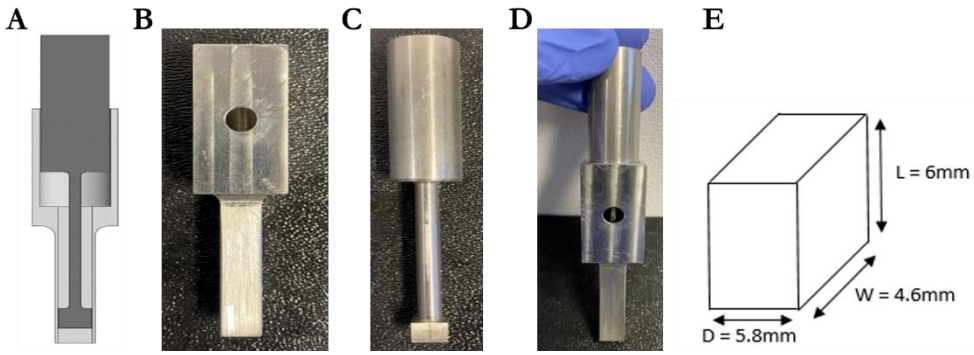

Figure 2.5 (A-E) – The in-house designed hydrogel excision tool developed by the Feichtinger research group. A: SolidWorks model of the combined excision tool, including the cutting element and the removal tool. B: The manufactured steel cutting element. C: The manufactured steel removal tool. D: The combined excision and removal tools. E: Dimensions of the excised hydrogel product post removal.

Table 2.4 – F-AGE-1 Agarose GAM designations after individual gel excision using the in-house excision tool.

DNA Master Stock Used	$CaCl_2$ Master Mix Used				
	0mM	**112.5mM**	**162.5mM**	**212.5mM**	**225mM**
2.5 µg DNA only	AGE1-2.5-0mM	AGE1-2.5-112.5mM	AGE1-2.5-162.5mM	AGE1-2.5-212.5mM	AGE1-2.5-225mM
5 µg DNA only	AGE1-5-0mM	AGE1-5-112.5mM	AGE1-5-162.5mM	AGE1-5-212.5mM	AGE1-5-225mM

2.5 µg DNA + FN	AGE1-2.5FN-0mM	AGE1-2.5FN-112.5mM	AGE1-2.5FN-162.5mM	AGE1-2.5FN-212.5mM	AGE1-2.5FN-225mM
5 µg DNA + FN	AGE1-5FN-0mM	AGE1-5FN-112.5mM	AGE1-5FN-162.5mM	AGE1-5FN-212.5mM	AGE1-5FN-225mM

2.2.2.2 F-AGE polyplex approach

The Feichtinger Agarose Gel Electrophoresis (F-AGE polyplex) approach was a strategy developed by this author and can be considered an amalgamation of the F-AGE-1 methodology and the opposite loading methodology championed by (Kamitakahara *et al.*, 2012). Specifically, this involved the substitution of inorganic nanoparticle salt solutions ($CaCl_2$) for a cationic polymer such as linear PEI. Due to the high charge density of PEI, it was hypothesised that such polymers would be electrophoretically mobile and thus allow for *in-situ* patterning within agarose gels. Moreover, by loading PEI and pDNA in oppositely located agarose gel wells, the components would be able to co-localise to form a polyplex. The following sections describe the F-AGE polyplex approach in a step-wise manner.

2.2.2.2.1 Loading solutions

Linear Polyethylenimine (PEI) (25KDa, Alfa Aesar) was reconstituted to 1 µg/µL according to an established two-step process. Initially, ddH_2O was added to PEI powder followed by dropwise addition of 1M hydrochloric acid (HCl), initiating complete dissolution at approximately pH 2. Using continual stirring, the pH was then raised to 7 through dropwise addition of 1M NaOH. The resulting PEI solution was then filter sterilised through a 0.22 µM filter before aliquotting and storage at -70°C.

The 2.5 µg and 5 µg DNA only master stock loading solutions previously used in the F-AGE-1 approach were also used in the F-AGE polyplex approach (Table 2.2). Additional PEI master stock loading solutions were formulated as per Table 2.5. Each PEI master stock solution contained enough volume for 60 individual loading runs, with 30 µL used per well. Once formulated, all mastermixes were stored at -20°C until required.

Table 2.5 – PEI master stock loading solutions used for the F-AGE polyplex method.

	PEI Master Stock loading Solution Constituents (Total volume: 1800 µL)		
Desired N/P ratio / Master Mix Type	**Linear PEI (1µg/µL)**	**Glycerol (30%)**	**ddH_2O**
N/P0	N/A	250.2 µL	1549.8 µL
N/P8 (2.5µg)	155.4 µL	250.2 µL	1394.4 µL

N/P16 (2.5µg)	310.2 µL	250.2 µL	1239.6 µL
N/P24 (2.5µg)	465.6 µL	250.2 µL	1084.2 µL
N/P40 (2.5µg)	775.8 µL	250.2 µL	774 µL
N/P8 (5µg)	310.2 µL	250.2 µL	1239.6 µL
N/P16 (5µg)	620.4 µL	250.2 µL	929.4 µL
N/P24 (5µg)	930 µL	250.2 µL	619.8 µL
N/P40 (5µg)	1548 µL	250.2 µL	1.8 µL

2.2.2.2.2 Buffer and agarose gel solution

The F-AGE polyplex method utilised the buffer solution known as Buffer B for agarose hydrogel creation and as a running buffer, as stated in section 2.2.2.

A concentrated stock solution of Buffer B (500 mM HEPES) was formulated as follows; 119.16 g HEPES was added to ~1000 mL ddH_2O. After sufficient mixing, the pH of the solution was subsequently brought up to 7.4 using 6M NaOH before storage in the dark at room temperature.

To achieve a working/running buffer B solution (25 mM HEPES), the concentrated stock was simply diluted 20 fold in ddH_2O to a final volume of 2000 mL. The working stock was then utilised as required.

A 3 wt% agarose gel slab was generated using the same protocol stated in section 2.2.2.1.2 with the exception of using a working solution of Buffer B instead of Buffer A.

2.2.2.2.3 Gel loading and electrophoretic patterning

Master Stock loading solutions specific for the F-AGE polyplex method were allowed to thaw gently on ice. Then, as previously described, a solidified agarose gel slab was subsequently inserted into the horizontal Sub-Cell GT tank and equilibrated with running buffer B.

The following protocol was specific to the F-AGE polyplex system in which pDNA and PEI loading solutions were used to generate and deposit pDNA-polyplexes within an agarose gel (as diagrammatically illustrated in Figure 2.6).

Briefly, 25 µL of pDNA master stock was gently applied to a single agarose well using a standard Gilson pipette (stage 1). A 300V potential was then immediately induced across the agarose gel for 20 minutes (stage 2). Subsequently, in the same well 30 µL of a specific PEI mastermix loading solution was added (stage 3). Importantly, electric field polarity was reversed at this stage. A further 300V potential was then immediately induced across the gel for 10 minutes (stage 4). Over this 10 minute process, thin white polyplex deposits materialise within the region between the loaded wells.

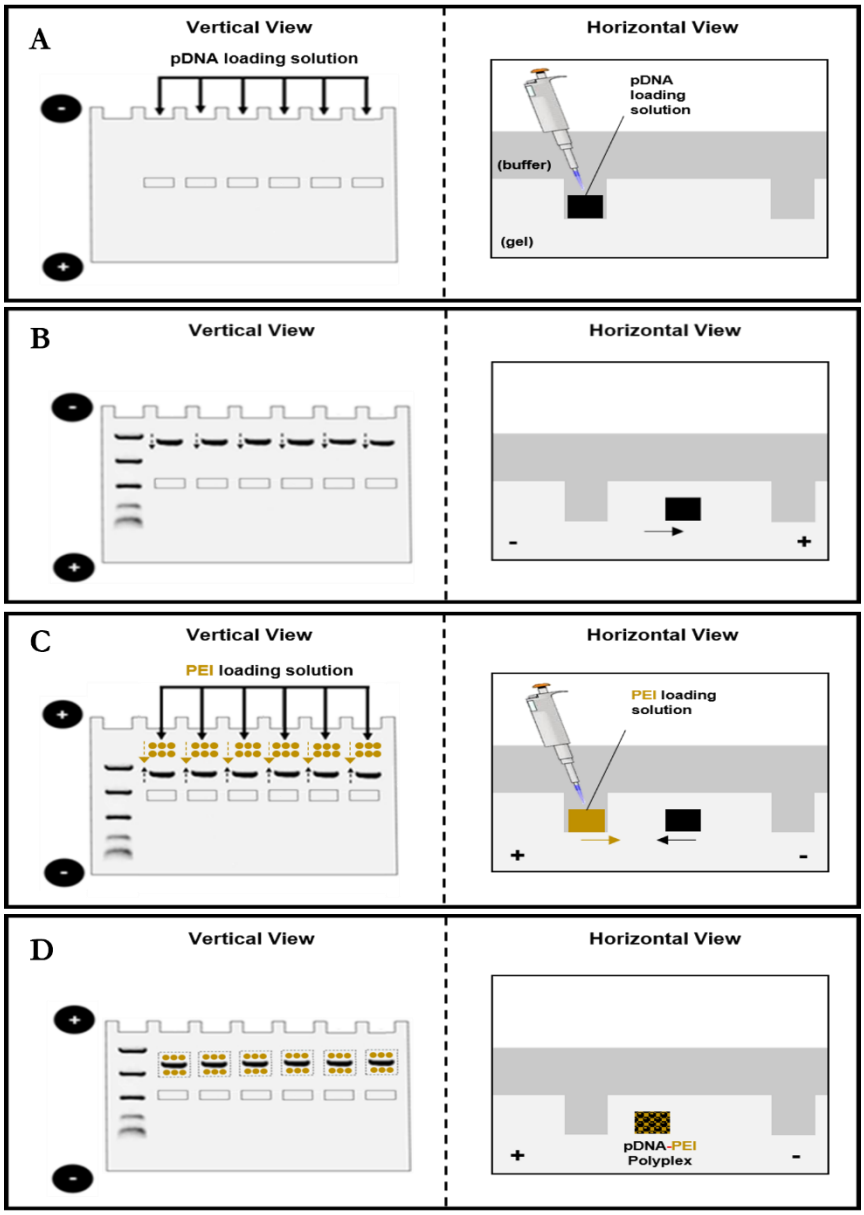

Figure 2.6 (A-D) – Spatial patterning of nucleic acid payloads within agarose gels using the F-AGE polyplex approach. A: 25 µL pDNA loading solution pipetted within "upper" agarose wells. B: a 300V potential is applied across the gel for 25 minutes, using a - ⟶+ electrode configuration. C: 30 µL PEI loading solutions pipetted into the same "upper" agarose wells respectively. D: a 300V potential is applied across the gel for 10 minutes, using a + ⟶- electrode configuration.

2.2.2.2.4 Gel Excision

F-AGE polyplexes were excised as per section 2.2.2.1.4. Based on the pDNA concentration used as well as the N/P master mix type, the excised hydrogels were then independently renamed as individual agarose GAMs as shown in Table 2.6.

Table 2.6 – F-AGE polyplex Agarose GAM designations after individual gel excision using the in-house excision tool.

DNA Master Stock Used	PEI Master Stock Used				
	N/P0	**N/P8**	**N/P16**	**N/P24**	**N/P40**
2.5 μg DNA only	AGE-2.5-N/P0	AGE-2.5-N/P8	AGE-2.5-N/P16	AGE-2.5-N/P24	AGE-2.5-N/P40
5 μg DNA only	AGE-5-N/P0	AGE-5-N/P8	AGE-5-N/P16	AGE-5-N/P24	AGE-5-N/P40

2.2.3 Freeze-drying protocol

Agarose hydrogels or porous scaffolds were transferred to individual wells of a 48 well plate before placement inside a -80°C freezer for 45 minutes. Upon completion, well plates were moved, with speed, to a freeze-dryer (ModulyoD, Thermo Savant), whereby a pre-set programme was initiated. Conditions of this programme included: -45°C chamber temperature, 0.2 mb chamber pressure. Samples were subsequently lyophilised for 12 hours or unless otherwise stated.

2.2.4 Scaffold functionalisation methods

2.2.4.1 Fibronectin surface coating

Bovine plasma fibronectin (FN) (Invitrogen) was reconstituted with 50 μg/mL sodium phosphate buffer pH 7.8 at two different concentrations; 25 μg/mL and 50 μg/mL. Freeze-dried agarose scaffolds were then immersed in either solution for 12 hours, washed in PBS (1 mL) and subsequently freeze-dried overnight. Dry FN coated scaffolds were then washed with 70% ice-cold ethanol (1 mL) before a second freeze-dry step (section 2.2.3).

2.2.4.2 LAP-PEO surface coating

Equal amounts of Laponite® RD (LAP) and Polyethylene oxide (PEO, molecular weight = 10^6 g/mol - Sigma) were added to deionised water and mixed at room temperature for 24 hours, generating final combined LAP-PEO solutions of either 40 mg/mL or 120 mg/mL concentration. Freeze-dried agarose scaffolds were then immersed in these solutions for 4 hours, before undergoing standard additional freeze-drying procedures. The resulting LAP-PEO coated scaffolds were finally washed with 70% ice-cold ethanol (1 mL) before a second freeze-dry step (section 2.2.3).

2.2.4.3 Polydopamine surface coating

Dopamine-HCl (Sigma) was mixed with 10 mM Tris-HCl buffer (pH 8.5) in order to generate either 1 mg/mL or 2 mg/mL fresh dopamine solutions. These solutions were then incubated, under constant mixing conditions using magnetic stirrer, at room temperature for 10 minutes, ensuring an initial colour change from colourless to light orange occurs (initial polymerisation). Freeze-dried agarose scaffolds were then immersed in either of the newly polymerised polydopamine (PDA) solutions and incubated for 4, 8, 12 or 24 hours, over which time further polymerisation occurs (Figure 2.7). Upon completion, scaffolds were removed from solutions and washed overnight in deionised water (room temperature), using an orbital shaker (180 revolutions per minute (rpm)) to remove unbound PDA. Scaffolds were then freeze-dried, followed by ice-cold ethanol sterilisation (1 mL wash) and a second freeze-dry step (section 2.2.3).

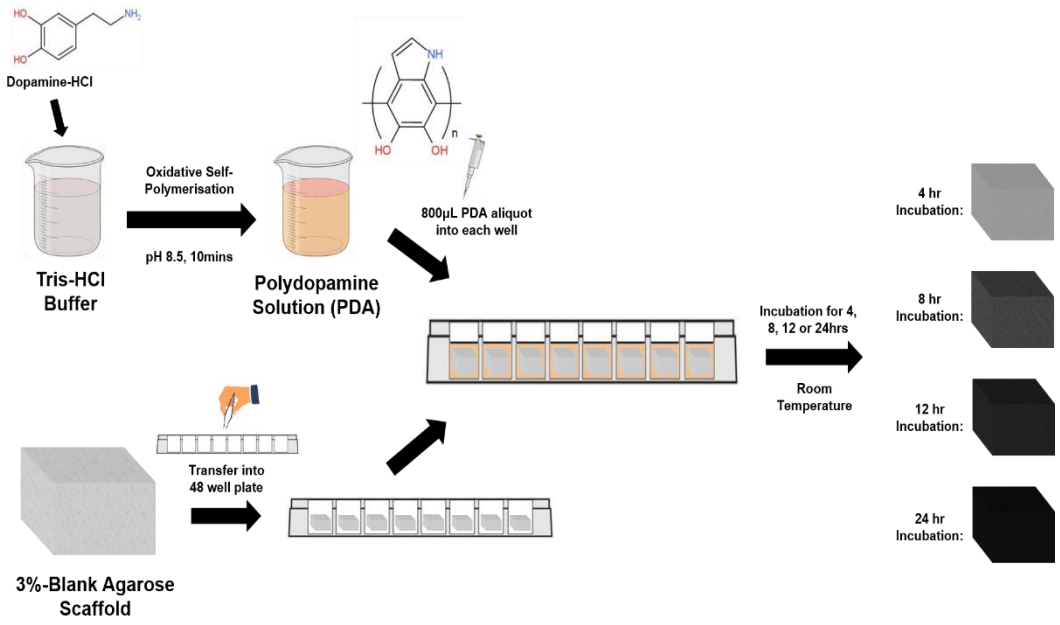

Figure 2.7 – Schematic for the functionalisation of agarose scaffolds using Polydopamine solutions.

2.2.5 3D Cell seeding methods

2.2.5.1 Static Seeding

3D scaffolds were seeded using passive static seeding techniques. Initially, scaffolds were placed inside wells of untreated 48 well plates or treated plates with modifications (Table 2.7). This included deposition of a 3 wt% agarose layer within individual wells (to deter cell-plastic attachment). Additionally, prior to cell seeding, scaffolds were either kept in their non-wetted freeze-dried form, or pre-conditioned with 60 µL complete culture media. For the latter, hydrated scaffolds were incubated for 10 minutes at room temperature. Post conditioning, scaffolds were then partially dehydrated via transfer into a 37°C, 5% CO2 incubator for 1 hour.

At this point, C2C12 or Y201 cells were re-suspended to a total volume of 60 µL per scaffold, at the required cell density. Five 12 µL aliquots were then drop-seeded onto each of the exposed surfaces of the scaffold and placed in an incubator for 2-3 hours to allow sufficient cell attachment. After incubation, 800 µL complete media was applied to enable entire scaffold coverage. Scaffolds were subsequently kept in culture undisturbed, with media changes occurring every 2-3 days or when experimentally required.

Table 2.7 – A range of static seeding conditions utilised during this study.

Static Seeding Conditions	Method 1	Method 2	Method 3	Method 4
Treated 48 well plate	✓	✓	✓	✗
Additional 3wt% agarose layer	✗	✗	✓	✓
Scaffold pre-conditioning	✗	✓	✗	✓

2.2.6 Assessment of 3D cellular attachment & viability

To ascertain the capacity for successful 3D cell growth of agarose scaffolds, cell attachment and viability was monitored visually using a LIVE-DEAD Viability assay (Viability/Cytotoxicity Assay Kit for Animal Live & Dead Cells (30002), Biotium California, USA) in tandem with Confocal Laser Scanning Microscopy (CSLM) techniques. The assay comprised of a LIVE-DEAD cell double stain in which solutions of acetoxymethyl esterase substrate (Calcein-AM) and a plasma membrane-impermeant DNA dye (Ethidium homodimer III (EthD-III)) were used to simultaneously label live and dead cells for fluorescent detection.

In principle, double fluorescent cell labelling simply applies substrates of differing lipophilic/phobic properties to cell material with opposing membrane integrities to bring about a specific fluorescent response. As such, upon entry into live cells, the lipophilic membrane permeable Calcein-AM can be cleaved by residual intracellular esterase enzymes, producing a green-fluorescent calcein product with excitation and emission wavelengths of 494nm and 517nm respectively. In contrast, EthD-III, a lipophobic DNA binding dye, can only produce a fluorescent signal when cell membrane integrity is compromised (i.e in dead cells). Such cell death therefore provides sufficient access to the nucleolar compartment to enable DNA binding, catalysing the production of a red fluorescent signal (25-fold enhancement) with an excitation/emission wavelength of 532 nm/625 nm. Consequently, with the above assay applied, a cultured cell sample will stain live and dead cells green and red respectively. Furthermore, due to overlapping excitation spectra, simultaneous viewing of live and dead cells can be achieved.

A working fluorescent dye solution of 2 μM Calcein-AM and 4 μM EthD-III was prepared according to manufacturer's instructions. In short, stock solutions of 4 mM Calcein-AM and 2 mM EthD-III were warmed to room temperature, of which 5 μL and 20 μL were respectively added to 10 mL PBS. The subsequent solution was vortexed, distributed into sufficient aliquots and stored at -20°C for future use. Cell seeded scaffolds were then removed from culture medium, rinsed briefly with PBS to remove residual serum esterase activity, and placed in a 96 well round bottom plate containing 180 μL aliquots of working LIVE-DEAD solution. Scaffolds were then incubated in the dark for 30-45 minutes at room temperature before transfer onto glass slides. Using a confocal microscope (Leica DM6 CS), samples were observed using fluorescein isothiocyanate (FITC) (excitation filter: 465 – 495 nm, emission filter: 515 – 555 nm) and TexasRed® (excitation filter: 575–600 nm, emission filter: 510–585 nm) detection channels. Images were captured for each scaffold orientation using LAS X, Leica software.

2.2.7 Assessment of 3D cellular proliferation

To further enhance the understanding of 3D agarose cell growth, specifically in the period after initial cell attachment, alamarBlue® cell proliferation agent (BioRad, UK) was applied to the fabricated scaffolds. Although primarily designed for evaluation of cell proliferation within 2D conditions, the assay can be applied to 3D biomaterials with certain modifications.

Specifically, this assay utilises a non-toxic non-fluorescent resazurin ingredient, which can signify cellular metabolic activity and proliferation upon substrate reduction. The principle, as stated in the assay manual, is based on the functional capacity of actively metabolising cells to reduce the blue non-fluorescent resazurin compound into the highly fluorescent and diffusible red product – resorufin. The subsequent accumulation of such product can then be quantitatively measured using absorbance or fluorometric based spectrophotometry.

Biologically, proliferating cells can continuously convert resasurin into resorufin, such that a proportional relationship between amount of fluorescence accumulation and increasing cellular populations is found. In contrast, non-viable, metabolically-deficient cells lose their hydrolysing capability, thus restricting successful resazurin conversion, leading to an overall loss of fluorescent signal.

Consequently, this difference can be utilised effectively for the assessment of 3D scaffold cultures, whereby fluorescence detected in culture medium is proportional to the number of viable cells growing on the fabricated agarose GAMs.

2.2.7.1 Assay Protocol

AlamarBlue® reagent was diluted 1 in 10 in culture medium to generate a working solution. 200 μL was then added in triplicate to sample and controls within round bottom 96 well plates. The

samples were then incubated at 37°C, 5% CO_2 for 4 hours before transfer of all sample supernatent (including blanks) into a black flat bottom 96 well plate. Additionally, a separate sample of alamarBlue working solution was autoclaved at 120°C for 15 minutes to produce a fully reduced positive control. Fluorescence intensity was then measured using a Varioscan Lux microplate reader with appropriate excitation and emission wavelengths set (540 nm/590 nm). Corrected fluorescence values were then generated using the formula below (Equation 2.1).

$$\text{\% Reduction of AlamarBlue®} = \frac{\text{FI590 (test sample)} - \text{FI590 (untreated control)}}{\text{FI590 (Reduced sample)} - \text{FI590 (untreated control)}} \times 100 \qquad \textbf{2.1}$$

2.2.8 Histological evaluation of agarose scaffolds

2.2.8.1 General histological processing

Agarose scaffolds were removed from culture medium, rinsed twice with Phosphate buffered saline (PBS) before being fixed in 10% Neutral buffered formalin (NBF) for 24 hours, inside individual plastic histology cassettes (Thermofisher Scientific). Upon sufficient fixation, cassettes were transferred to an automatic tissue processor where a pre-set programme was initiated. This included a graded series of alcoholic dehydration chambers (70% Ethanol – 2 hours, 90% methylated spirits – 2 hours, 100% methylated spirits - hours 100% methylated spirits – 1 hour, 100% methylated spirits – 2 hours, 100% methylated spirits – 2 hours). This was then followed by 3 separate xylene washes (2 hours) to initiate clearance and finally a 2-step impregnation of molten paraffin wax (3 hours per step). After completion, scaffolds were placed into metal wax-base moulds, filled with excess molten paraffin wax, and subsequently cured using a cold plate. The hardened wax blocks were then removed from the mould and sectioned into 10 μM thick slices representing top, middle, bottom scaffold layers, using a microtome (Leica). Using a water bath (45°C), each section was subsequently placed floating on the surface, allowing wrinkles to gradually disappear, before being positioned onto a superfrost microscope slide (SLS). The sections were then placed overnight on a hot-plate to dry.

2.2.8.2 Haematoxylin & Eosin staining

Haematoxylin and Eosin (H&E) staining was utilised to visualise cellular morphology and histoarchitecture across the full longitudinal plane of a cell seeded agarose scaffold. Sections generated using the methodology outlined in section 2.2.8.1 were initially placed in a slide rack before undergoing a common sequential H&E staining protocol. The samples were first de-waxed in xylene (10 minutes – xylene I, 10 minutes – xylene II), then dehydrated in a graded sequence of ethanol chambers (3 minutes - 100% ethanol I, 2 minutes – 100% ethanol II, 2 minutes – 100% ethanol III, 2 minutes – 70% ethanol), followed by a rehydration rinse step in

tap water (3 minutes). The sections were next submerged in Mayer's haematoxylin (Atom Scientific) for 1 minute, before a further rinse step in tap water. Sections were then transferred and submerged in Scott's tap water (1X), followed by an additional rinse in tap water (3 minutes), before staining in 1% eosin solution (Eosin Y) for 3 minutes. Eosin was then removed in running tap water, dehydrated in an ethanol series (5 seconds - 70% ethanol, 1 minute – 100% ethanol IV, 2 minutes – 100% ethanol V, 3 minutes – 100% ethanol VI), and cleared in xylene (10 minutes – xylene III, 10 minutes – xylene IV). At this stage, the slides were mounted alongside a coverslip using DPX mountant (Atom Scientific), and allowed to air dry. Visual analysis was performed under a light microscope and images captured using Zeiss imaging software.

2.2.9 Molecular biology techniques

2.2.9.1 Restriction digest

Restriction digests were performed according to manufacturer's instructions with the consideration that under appropriate reaction conditions; complete cleavage of 1 µg DNA occurs per hour for every unit of enzyme applied. Where possible, restriction enzymes were purchased from the same manufacturer (ThermoFisher Scientific), with certain exceptions permitted. In the case of double or multiple enzyme restriction digests, ThermoFisher Scientific double restriction digest calculator was used to ascertain buffer compatibility. Standard digests were set up in 20 µL systems as per Table 2.8.

Table 2.8 (A & B) – Reaction systems for single and double restriction digests of plasmid DNA.

A

Single Restriction Digest	
pDNA	1 µg
Enzyme Buffer (1X)	2 µL
Enzyme	0.5 µL
ddH_2O	N/A
TOTAL	20 µL

B

Double Restriction Digest	
pDNA	1 µg
Enzyme Buffer (1X)	2 µL
Enzyme-1	0.5 µL
Enzyme-2	0.5 µL
ddH_2O	N/A
TOTAL	20 µL

2.2.9.2 Agarose gel electrophoresis

DNA products generated from restriction digests and/or PCR amplifications can be resolved, based on their molecular weight, using agarose gel electrophoresis. The specific gel migration distance of a DNA fragment varies inversely with the logarithm of the molecular weight, thus providing a basis for rapid, sensitive and reliable DNA sample identification. Electrophoresis was performed on 1 wt% Medium-Low electroendosmosis (EEO) agarose (Acros Organics) gels in

1X TAE (Tris base, glacial acetic acid, EDTA) buffer. Working buffer (1X TAE) was produced by diluting 50X TAE stock buffer (Table 2.9 A) 1 in 50 in distilled water. DNA staining was carried out using 0.5X SYBR® safe DNA gel stain (Invitrogen). Gels of 7x7cm were cast and run in a Mini-Sub Cell GT Cell (BioRad) horizontal electrophoresis system capable of relaying a field strength of ≥300V. Preceding gel loading, samples were mixed with 1/6 volume of 6X BPB (Bromophenol Blue gel loading buffer (Table 2.9 B). DNA bands were distinguished using a Gel-Doc (UVP, Germany) via UV-illumination & SYBR Green filters. The resulting gel images were then saved for documentation and analysis.

2.2.9.3 DNA extraction from agarose gels

Specific DNA bands, identified by size, were excised from agarose gels and placed in a pre-weighted 1.5 mL Eppendorf tube. The Promega Wizard SV Gel & PCR Clean-Up System was then used for subsequent purification, following manufacturer's instructions.

Table 2.9 (A & B) – Composition of 50X TAE buffer and 6X Bromophenol Blue loading buffer.

A

50X TAE Buffer Composition	
Tris-base	242 g
Glacial Acetic Acid	57.1 mL
0.5M EDTA (pH 8)	100 mL
ddH_2O	N/A
TOTAL	1000 mL

B

6X BPB Gel Loading Buffer	
Bromophenol Blue	0.025%
Glycerol	30%
ddH_2O	70%

2.2.9.4 DNA purification methods

To concentrate or simply purify generated DNA samples, Chloroform extraction & Ethanol precipitation methods were applied. Chloroform extraction involved initially the addition of 1:1 volume of chloroform to the DNA solution. The mixture was then vortexed and subsequently centrifuged (13,000 rpm, 5 minutes). The upper DNA layer was carefully separated from the chloroform and placed in a new 1.5 mL Eppendorf tube. Ethanol precipitation involved firstly the addition of 1/10 3M Sodium Acetate followed by 2.5X volume ice-cold 100% Ethanol. The mixture was thoroughly vortexed before overnight incubation at -70°C. The precipitated solution was placed in a centrifuge (13000 rpm, 10 minutes) and the resulting pellet was washed twice with ice-cold 70% Ethanol. The pellet was then left to air-dry before reconstitution in nuclease-free water.

2.2.9.5 Restriction enzyme mediated ligation (T4 DNA Ligase)

Post extraction and purification, downstream restriction digest DNA products were ligated with pre-cut plasmids in a total volume of 10 µL at 4°C overnight using T4 DNA ligase (Roche Diagnostics GmbH; Mannheim, Germany) (Table 2.10). Concentrations of fragments were calculated using a nanodrop spectrophotometer and as a consequence a ratio of 1:3 (25ng:75ng) vector:insert was generated within the ligation system. Post digest, T4 DNA ligase was inactivated via incubation at 65°C for 20 minutes.

Table 2.10 – T4 DNA ligase reaction system for downstream restriction digest and PCR products.

T4 DNA Ligase Reaction System	
T4 DNA Ligase Buffer (1X)	1 µL
Insert (3X)	75 ng
Vector (1X)	25 ng
T4 DNA Ligase (5U/µL)	1 µL
ddH_2O	N/A
TOTAL	10 µL

2.2.9.6 Culture of E.coli TOP10

E.coli TOP10 was grown at 37°C using liquid Luria Bertani Broth medium (LB, Table 2.11 A) or on LB-agar plates (Table 2.11 B). The active resistance markers for selection of positively transformed colonies was the Ampicillin resistance gene (TEM-1 β-lactamase, bla) or Kanamycin resistance gene (Neomycin phosphotransferase II, NPT II/Neo) respectively. Working concentrations of both antibiotics in liquid and solid media was 50 µg/mL. In the case of the liquid-LB media, an appropriate volume of antibiotic stock solution was added before E.coli inoculation, whilst the LB-agar plates were infused with stock antibiotic pre-casting.

Table 2.11 (A & B) – Composition of Luria-Bertani liquid broth and Luria-Bertani-agar mix.

A

LB Medium	
Tryptone	10 g
Yeast Extract	5 g
NaCl	10 g
ddH_2O	1000 mL

B

LB-Agar	
Tryptone	10 g
Yeast Extract	5 g
NaCl	10 g
Agar	15 g
ddH_2O	1000 mL

2.2.9.7 Preparation of competent E.coli TOP10

Using a 5 mL overnight culture of E.coli TOP10 cells, a further 100 mL LB media was added and subsequently grown to an optical density (OD) OD_{600} = 0.4, using a shaking incubator (37°C, 250 rpm). The cells were transferred to a 50 mL polypropylene centrifuge tube and kept on ice for 10 minutes before centrifugation at 4000 rpm for 10 minutes (4°C). After aspiration of the supernatant, the bacterial pellet was reconstituted in 30 mL ice-cold 80 mM $MgCl_2$ 20 mM $CaCl_2$ ddH_2O solution. After a further 10 minute centrifugation step (4000 rpm, 4°C), the pellet was re-suspended in 2 mL of ice-cold 100 mM $CaCl_2$ 10% glycerol ddH_2O solution. This competent E.coli TOP10 mixture was then separated into 100 µL aliquots and snap-frozen in liquid Nitrogen. Transformation capable stocks were stored at -70°C ready for use.

2.2.9.8 Transformation of E.coli TOP10

30 µL competent E.coli TOP10 was mixed with 5 µL ligation products (as generated in section 2.2.9.5), and incubated on ice for 30 minutes. The transformation mixture was then exposed to heat shock treatment (42°C, 45 seconds) before being immediately cooled on ice for a further 2 minutes. A further 50 µL super optimal medium with catabolic repressor (SOC) medium was then added and the bacteria transferred to a shaking incubator (37°C, 250 rpm) for 45 minutes, allowing outgrowth and production of antibiotic resistance proteins (Table 2.12). The cells (25 µL) were plated on LB-agar plates containing the applicable antibiotic, as shown in the vector maps in section 2.1.5, and incubated overnight. Individually distinct colonies were picked and separately re-suspended in 5 mL LB-media as per overnight culture protocols illustrated in section 2.2.9.6.

Table 2.12 – Composition of SOC medium.

SOC Medium	
Tryptone	2%
Yeast Extract	0.5%
NaCl	10 mM
KCl	2.5 mM
$MgCl_2$	10 mM
$MgSO_4$	10 mM
Glucose	20 mM

2.2.9.9 Minipreparation and maxipreparation of plasmid DNA

Minipreparation of plasmid DNA was performed using the Promega Wizard® SV minipreparation kit (Promega, Madison, WI, USA) according to manufacturer's guidelines. Overnight cultures were formulated with an antibiotic working concentration of 80 μg/μL. Pure plasmid DNA was eluted with 50 μL nuclease-free ddH_2O and stored at -20°C.

Maxipreparation of plasmid DNA was performed using the Qiagen EndoFree Plasmid Maxi kit (Qiagen, Hilden, Germany) according to manufacturer's instructions. Pure plasmid DNA was eluted using 500 μL ddH2O and stored at -20°C.

For determination of DNA concentrations, a spectrophotometer (nanodrop) was used. $A_{260/280}$ measurements (with a A_{260} conversion factor of 1.0 for 50 μg/mL DNA) provided accurate quantification of DNA samples, whereby $A_{260} \geq 1.8$ was considered the baseline for DNA purity with negligible protein contamination.

2.2.9.10 T7 DNA Polymerase Digestion

A typical exonuclease digestion reaction involving T7 DNA polymerase (New England Biolabs, England) generally utilised a 40 μL system as shown in Table 2.13, specifically utilising its high 3' – 5' exonuclease activity. After the mixing of the DNA/oligonucleotide material with the enzyme, the mixture was incubated for 60 minutes and 37°C during which digestion occurred. For enzyme inactivation, a second incubation step was performed at 75°C for 30 minutes.

Table 2.13 – T7 DNA polymerase reaction system for exonuclease mediated double stranded DNA digestion.

T7 DNA Polymerase Reaction System	
DNA Sample	2.5 or 5 μg DNA
T7 DNA polymerase (10U/μL)	1 μL
T4 DNA Ligase Buffer (1X)	4 μL
ddH_2O	N/A
TOTAL	40 μL

2.2.9.11 Polymerase Chain Reaction (PCR)

All PCR reactions were performed using a 5Prime Thermocycler (Techne, Bibby Scientific, UK). KOD is a recombinant form of *Thermococcus kodakaraensis* KOD1 DNA Polymerase with 3'-5' exonuclease-dependent proof-reading capability. In comparison to standard Taq polymerase, KOD maintains 2X faster extension speeds, thus producing blunt ended PCR products in a shorter overall reaction time. KOD Polymerase PCR amplification adhered to manufacturer's instructions with minor modifications.

Table 2.14 (A & B) – KOD Hot Start Polymerase PCR amplification reaction system and cycling parameters. s/kb = seconds per kilobase).

A

Component	Volume	Final Conc
10X Buffer (for KOD Hot Start DNA Pol)	5 µL	1X
25mM $MgSO_4$	3 µL	1.5 mM
dNTPs (2 mM each)	5 µL	0.2 mM
PCR Grade Water	N/A	N/A
Enhancer/DMSO	5 µL	5%
Sense (5') Primer – 10µM (10pmol/µL)	1.5 µL	0.3 µM
Anti-sense (3') Primer – 10µM (10pmol/µL)	1.5 µL	0.3 µM
KOD Hot Start DNA Polymerase (1.0U/µL)	1.0 µL	0.02U/µL
Template DNA	5-10ng	N/A
TOTAL VOLUME	**50 µL**	

B

	Target Size			
Step	**<500bp**	**500-100bp**	**1000-3000bp**	**>3000bp**
1. Polymerase Activation	95°C for 2mins	95°C for 2mins	95°C for 2mins	95°C for 2mins
2. Denaturation	95°C for 20secs	95°C for 20secs	95°C for 20secs	95°C for 20secs
3. Annealing	[Lowest Primer Tm]°C for 10secs			
4. Extension	70°C for 10s/kb	70°C for 15s/kb	70°C for 20s/kb	70°C for 25s/kb
Repeat steps 2-4	20-40 cycles			

Briefly, enzyme activation (removal of dual anti-KOD blocking antibodies) and DNA denaturation steps were performed at 95°C for 2 minutes and/or 20 seconds respectively. 5-10 ng template DNA was used per 50 µL PCR system. Elongation and extension times were tailored according to specific primer T_m and expected PCR product length. The annealing and melting temperatures of each employed primer was calculated using AmplifyX software. For improved amplification in GC-rich target sequences, organic enhancer additives, such as DMSO, were

incorporated in the PCR system. Table 2.14 A & B illustrate the universal PCR parameters applied in this study.

2.2.9.12 Ligation independent cloning

Ligation independent cloning (LIC) relies on the employment of long complimentary overhang sequences between adjacent PCR fragments, enabling stable association and vector transformation without ligation. Successful fragment-fragment fusion requires DNA base overhangs of between 12-25 bp often generated by T4 DNA polymerase. Alternatively, several highly flexible and established commercial LIC kits exist which seamlessly clone multiple DNA fragments together, forming gene expression vectors.

NEBuilder HiFi DNA Assembly Cloning Kit (#E5520) (New England Biolabs; Hitchin, England) enables high fidelity assembly of multiple DNA fragments using a one-step enzyme master mix, resulting in a fully-sealed double stranded DNA molecule capable of a multitude of downstream molecular biology applications.

The NEBuilder HiFi DNA assembly reaction protocol was followed as per manufacturer's instructions (Table 2.15). For a 2-3 fragment assembly system, a total of 0.03-0.2pmol DNA was used. The following formula was used to calculate DNA concentration: Picomoles = (weight (ng)) x 1000 / (base pairs x 650Da)).

Table 2.15 – General NEB HiFi DNA Assembly cloning system for 2-3 or 4-6 DNA fragments.

Recommended Amount of fragments used for HiFi DNA Assembly			
	2-3 Fragment Assembly	4-6 Fragment Assembly	NEB Positive Control
Recommended DNA Molar Ratio	Vector:Insert = 1:2	Vector:Insert = 1:1	
Total amounts of Fragments	0.03-0.2pmols	0.2-0.5pmols	10 µL
NEBuilder HiFi DNA Assembly Master Mix	10 µL	10 µL	10 µL
Deionised H_2O	N/A	N/A	0
Total Volume	20 µL	20 µL	20 µL

Samples were placed in a thermocycler and incubated at 50°C for 15 minutes (2-3 DNA fragments) or 60 minutes (4-6 DNA fragments). The resulting DNA mixture was stored at -20°C for future transformation or placed on ice for immediate use. As such, chemically competent NEB 5-alpha competent E.coli were thawed on ice, to which 2 µL DNA mixture was added. The tube was placed on ice for 30 minutes, heat shocked (42°C, 30seconds), before a further 2 minute incubation on ice. 950 µL room temperature SOC media was then added allowing for bacterial

amplification in a shaking incubator (37°C, 250 rpm) over a duration of 60 minutes. 100 µL cell suspension was plated on LB-agar plates containing the applicable antibiotic, and incubated overnight. Overnight cultures were produced containing individually selected bacterial colonies from the aforementioned plate (80 µg/µL antibiotic working concentration).

2.2.10 Methods of transient cellular transfection

Two reporter expression vectors were either purchased or formulated in-house in order to evaluate successful transfection of both 2D and 3D gene delivery systems. This includes pCAG-eGFP (GeneWiz®, Germany) (Figure 2.1) as a qualitative fluorescence based reporter expression system and pCAG-Met-Luc2 (in-house) (Figure 2.2) as a quantitative luminescence based reporter expression system.

Unless otherwise stated, the formulation of transfection payloads as described in later chapters occurred only after 2D cell monolayer cultures (e.g. C2C21 and Y201) presented with approximately 80% confluency under phase contrast microscopy.

2.2.10.1 Calcium phosphate mediated transfection (Basic co-precipitation)

Transfection capable pDNA-Calcium phosphate nanoparticle complexes were formed via the co-precipitation method, whereby sequential additions of pDNA, $CaCl_2$ and HEPES take place in solution, as per Figure 2.8.

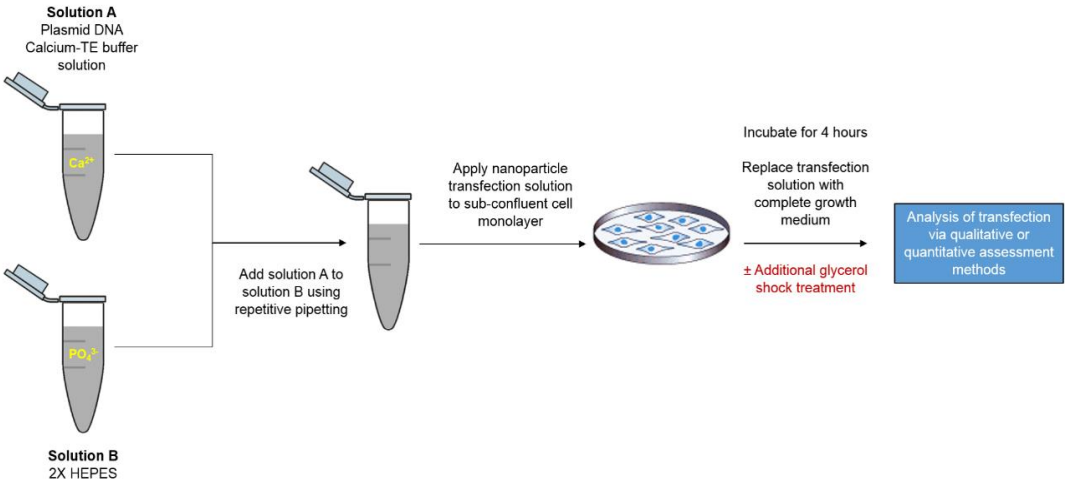

Figure 2.8 – Simplified mechanism of CaP mediated transfection of 2D cell monolayers

Specifically, a plasmid solution (of the desired concentration) was first added to a 250 mM $CaCl_2$-0.1X TE buffer solution and vigorously mixed. An equal amount of phosphate containing 2X HEPES (N-2-hydroxyethylpiperazine-N-2-ethane sulfonic acid) (140 mM NaCl, 1.5 mM Na_2HPO_4, 50 mM HEPES, pH 7.05) was then subsequently added and immediately mixed using repetitive pipetting techniques, to form a heterogeneous nanoparticle transfection mixture. This final transfection solution was then added to appropriate wells containing a semi-confluent cell

monolayer population, at a dilution equivalent to 1/10th total culture volume, before incubation for 4 hours (37°C, 5% CO_2). Upon completion, appropriate wells were either directly media changed with complete medium or underwent glycerol shock treatment. In these cases, transfection solutions were aspirated and gently washed consecutively with PBS, 20% glycerol, PBS, prior to a final addition of complete medium. All transfected culture plates were then further incubated under standard conditions before performance of a transfection assay at the desired timepoint.

2.2.10.2 Polyethylenimine mediated transfection

Based on previously established work, the transfection capability and effectiveness of formulated PEI polyplexes varies according to its cationic character – which is a function of the amount of PEI polymer initially applied to a plasmid solution. This characteristic is more commonly referred to as the ratio between the total number of PEI primary amines (N) and the total number of phosphates in DNA (P), or in short the N/P ratio. As 23.2 mM of nitrogen is present per microliter of a 1 mg/mL PEI stock solution, and 3 nmol of phosphorous is present per microgram of double stranded DNA, the following equation was formulated to ascertain N/P ratios for each polyplex (Equation 2.2).

$$N/P = \frac{(\mu L\ PEI\ working\ solution) \times 23.2\ mM\ Nitrogen\ Residue}{(\mu g\ plasmid\ DNA) \times 3\ nM\ Phosphate} \qquad \textbf{2.2}$$

Polyplexes were subsequently prepared as per Figure 2.9. Briefly, pDNA (of the desired concentration) was added to a specified volume of serum-free media, generating solution X. A specific volume of PEI solution (1 μg/μL) (solution Y) was then added, using repeated pipette mixing techniques, before a 15 minute incubation period, at rest. The resulting polyplexes were then added to appropriate wells containing a semi-confluent cell monolayer population, at a dilution equivalent to 1/10th total culture volume, before incubation for 4 hours (37°C, 5% CO_2). Following this, all wells were directly media changed with complete medium, then re-cultured under standard conditions until eventual performance of a transfection assay, at the desired timepoint.

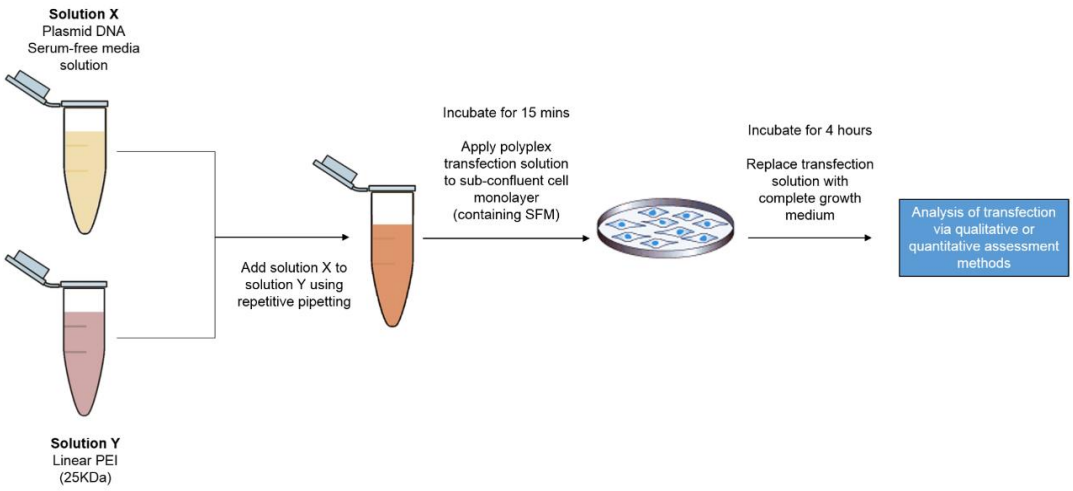

Figure 2.9 – Simplified mechanism of PEI polyplex mediated transfection of 2D cell monolayers

2.2.10.3 Lipofectamine mediated transfection

Briefly, a plasmid solution (of the desired concentration) was first added to a 50 µL volume of serum free media. In tandem, a 2 µL volume of Lipofectamine™ 2000 (Life Technologies) was then separately added to a further 50 µL volume of serum free media, before a 5 minute incubation. After this period, the diluted DNA and lipofectamine solutions were combined, gently mixed using repeated pipette mixing techniques and then incubated again (for 20 minutes at room temperature). The entire DNA-lipid solution (100 µL) was then added to each well containing cells and growth medium (500 µL) and incubated for 4 hours. Upon completion, appropriate wells were directly media changed with complete medium and subsequently re-cultured under standard conditions until eventual performance of a transfection assay, at the desired timepoint.

2.2.11 Assessment of cellular transfection

2.2.11.1 Qualitative assessment of transfection

Successful transfection of a fluorescent reporter plasmid vector such as pCAG-d2-eGFP was visually assessed using fluorescent microscopy in combination with CLSM techniques.

2.2.11.1.1 2D Cell monolayer systems

Transfected cell monolayer cultures were washed twice with PBS before direct imaging using a Leica DM6 CS confocal microscope. Samples were observed initially using brightfield microscopy filters before transfer to fluorescent based optics – including GFP detection channels (excitation filter: 488 nm, emission filter: 509 nm). Images were captured using LAS X Leica software at different cell monolayer locations – providing a detailed picture of transfection mediated fluorescence.

2.2.11.1.2 3D Scaffold systems

Fluorescent microscopy techniques were similarly applied for the evaluation of scaffold based 3D transfection, with modifications. Briefly, seeded scaffolds were transferred to a 96 well plate, rinsed twice with PBS, followed by a 1 hour fixation step in 10% NBF, then PBS washed again removing any residual fixative. A working 4',6-diamidino-2-phenylindole (DAPI) solution was then formulated (0.5 µg/mL in PBS) and applied as 180 µL aliquot to each scaffold for 1 hour in dark conditions. Scaffolds were washed with PBS a final time before transfer onto a glass slide in preparation for fluorescent imaging. Images were produced using LAS X Leica software configured with dual band fluorescence parameters to allow simultaneous capture of both the cytosolic GFP and nucleolar DAPI expression. DAPI detection channel: excitation filter: 358 nm, emission filter: 461 nm.

2.2.11.2 Quantitative assessment of transfection

Successful transfection was also assessed through the use of a luciferase reporter assay – a commonly used tool to study gene expression at the transcriptional level. In contrast to the expensive and time-consuming fluorescence-based detection methods, luciferase assays are a more convenient and inexpensive method which most significantly can produce high throughput quantitative measurements in an almost instantaneous fashion.

The basic principle which forms the basis for this assay type is referred to as bioluminescence, a naturally occurring phenomenon in which luciferin substrates are oxidised to release energy in the form of light. Upon examination of species in which this occurs, such as *Photinus pyralis* (North American firefly) and *Metridia longa* (marine copepod), the exact reactions could be characterised into two types; those catalysed by non-secreted luciferases or those catalysed by secreted luciferases (Figure 2.10).

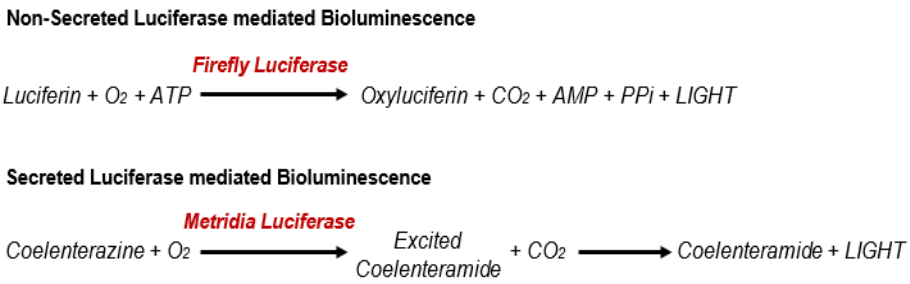

Figure 2.10 – Naturally occurring bioluminescence reactions found in the Photinus pyralis (North American firefly) and Metridia longa (marine copepod) species.

Due to the unique light generating characteristics of these reactions, scientists have sought to isolate the individual components in the hope of repurposing for use as a luminescence reporter system. Recent examples include the non-secreted firefly Luciferase Assay System (Promega) and Ready-To-Glow Secreted Luciferase Reporter Assay (TaKaRa, California, USA), which both

comprise of an expression vector encoding a luciferase reporter gene, and a reagent or substrate which upon chemical reaction with luciferase produces light as a measureable by-product. Crucially, both assays rely on the principle that the intensity of the light produced is directly proportional to the amount of successfully expressed luciferase enzyme within cells. As such, the overall gene expression efficiency of transfection capable payloads can be assessed.

Due to the destructive nature of non-secreted luciferase assays (cell lysis step required), a secreted luciferase assay system was selected for use in this thesis, whereby reporter molecules are naturally secreted into cell media over time. Quantitative measurements of transfection for a single sample could then be evaluated over multiple time-points, more effectively illustrating the overall gene expression profile.

An in-house Secreted Metridia Luciferase Assay or Met-Luc Assay was therefore developed utilising the pCAG-MetLuc2 vector system, notably containing the gene insert encoding *Metridia* Luciferase.

2.2.11.2.1 2D Cell monolayer systems

In order to standardise transfection efficiency, cell culture media was always exchanged 24 hours prior to performance of Met-Luc assay. The assay substrate Coelenterazine (Promega) was subsequently reconstituted in acidified methanol (1 drop conc. HCl in 10 mL Methanol) to generate a 5mg/mL stock substrate solution. A 50 µL transfected cell media sample was then removed from the culture plate on the day of testing and transferred into a specific well of a new 96 well white Maxisorp optiplate (PerkinElmer)) in preparation for luminescence assay. 10 µL working coelenterazine solution (1:500 dilution in sterile PBS) was then added to each well, gently mixed before incubation over a 30 minute period in the dark. Then, using a luminometer microplate reader, light signals for each sample well were measured. Using the values generated from negative control samples (cell only without luciferase), final test readings were equated and illustrated as Fold Luminescence over negative control.

2.2.11.2.2 3D Scaffold systems

The Met-Luc assay protocol outlined in section 2.2.11.2.1 was subsequently applied with ease to scaffold mediated transfection cultures with only few modifications required. As such, in order to again maintain standardised luminescence readings across multiple timepoints, cell seeded scaffolds, on each day preceding the Met-Luc assay, were now transferred to wells of a new round bottom 96 well plate - also containing 200 µL fresh culture media. Then, on the day of assay performance, 50 µL transfected cell media sample was transferred to a well of a 96 well Maxisorp plate in preparation for luminescence assay. The identical protocol as described in section 2.2.11.2.1 was then followed from this point until completion.

2.2.12 Data analysis

2.2.12.1 Statistical analysis

Statistical analysis was performed on numerical data using Graphpad Prism (version 9.2.0, GraphPad Software LLC, San Diego, US). For each dataset, statistical analysis was performed in two-stages. In stage-1, numerical data (containing groups less than 8) was evaluated in terms of normality, with the Shapiro-Wilk normality test being utilised specifically to confirm Gaussian distribution. In stage-2, the means of each group within a dataset was compared. In the case of the comparison of normally distributed data with only two means (i.e 2 groups), an unpaired Student's t-test was used. For data where two means were compared and the data was not normally distributed, a Mann-Whitney U test was used. Furthermore, in the case of the comparison of normally distributed data with multiple means (i.e. greater than 2 groups), an ordinary one-way analysis of variance (ANOVA) with Tukey's multiple comparisons test was used. Finally, in the case of the comparison of not normally distributed data with multiple means, a Kruskal-Wallis ANOVA with Dunn's multiple comparisons test was used.

In all comparison tests performed in stage-2, statistical significance was taken at $P < 0.05$ and was denoted graphically with a single * symbol either directly above the bar chart (showing significance in comparison to the negative control) or using connector lines (showing significance between non-control groups). Additional significance levels were taken at $P < 0.01$, < 0.001, < 0.0001 and were denoted by **, ***, **** symbols respectively. In the context of this thesis, a P value below the 0.05 threshold indicated that the observed difference between a particular set of means was unlikely to have occurred by chance alone (i.e. a real effect or difference was likely present). If no significant difference was observed between a particular set of means, the graph was left unlabelled or in some cases was denoted by a "ns" symbol.

CHAPTER 3

OPTIMISATION OF AGAROSE POLYMER PERCENTAGE FOR POROUS OSTEOCHONDRAL SCAFFOLD FORMATION AND ELECTROPHORETIC DNA PAYLOAD PATTERNING

3 CHAPTER 3: OPTIMISATION OF AGAROSE POLYMER PERCENTAGE FOR POROUS OSTEOCHONDRAL SCAFFOLD FORMATION AND ELECTROPHORETIC DNA PAYLOAD PATTERNING

3.1 Introduction

As has been discussed in chapter 1, for osteochondral tissue engineering (OCTE) approaches to be successful, a 3D biomaterial must be fabricated which possesses physical and biomechanical attributes which resembles that identified within native osteochondral tissue (Berthiaume *et al.*, 2011). Furthermore, due to its primary function as a supportive framework for cellular interaction and bone and cartilage tissue deposition, it must naturally allow for external cellular infiltration, adhesion, proliferation and differentiation. This has generally be exemplified by the production of natural or synthetic 3D biomaterial scaffolds which possess an interconnected and open micro or macroporous structure (inherent pore sizes between 100 μm – 300 μm) with high degrees of porosity and mechanical stability (Lee *et al.*, 2018).

Agarose hydrogels on the other hand are repeating unit polysaccharide systems containing dense networks of polymers with absorbed water and nanosized pores (300-500 nm), the latter of which has been shown to hinder a large proportion of the previously stated cellular processes (Hoffman, 2012; Li *et al.*, 2018). To rectify this, various fabrication strategies can be employed which can adjust agarose hydrogel physical properties (pore size, porosity, mechanical strength) so as to more accurately generate a system which resembles the osteochondral environment as well as facilitate cell ingrowth. These approaches can include; solvent casting, particle leaching and freeze-drying (Annabi *et al.*, 2010). Of these selected methods, freeze-drying is considered most popular on account of its ability to convert hydrogel (i.e. agarose) systems into heterogeneous macro-microporous materials with high speed, high reliability, at relatively low cost (equipment includes standard -80°C freezer and benchtop freeze drying system) (Mirtaghavi *et al.*, 2020). Furthermore, the freeze-drying process is also considered simple and straightforward with no specialist skillset required.

The freeze-drying process, also known as lyophilisation, is a well-established technique extensively employed in the tissue engineering, drug and food packaging industries. It intricately follows a three-stage methodology that encompasses sequential freezing and drying steps. In the initial stage, a liquid-containing material, such as a hydrogel, undergoes controlled cooling under freezing conditions, transforming it into a solid frozen state. Subsequently, in the second stage, this newly formed ice undergoes direct sublimation under vacuum conditions within a freeze-dryer. The final stage involves the simultaneous occurrence of removing any residual water within the material, be it in solid or liquid form, in a process known as secondary drying. Notably, the

last two steps transpire concurrently at different locations within the sample (Flink *et al.*, 2002; Nowak & Jakubczyk, 2020).

As shown in previous works from our group (Figure 1.19 B and C), a simple freeze-drying procedure could induce the macro/microporous conversion of 1 wt% agarose GAM hydrogels into porous agarose scaffolds. Unfortunately, this early data as well as other similar papers showed that lower polymer percentage hydrogels (≤ 1 wt%) were highly susceptible to lyophilisation associated phenomena such as bulk surface area shrinkage and structural chain collapse. Significantly, literary reports have attributed this to firstly the high overall water content found within these hydrogels, of which a substantial portion is removed during lyophilisation, and secondly, due to ice-crystal mediated weakening of agarose fibre architectures, resulting in significant collapse upon ice sublimation (Guastaferro *et al.*, 2021). As a result, low weight percentage agarose scaffold products commonly display physical and mechanical imperfections making them not suitable for application as osteochondral treatment systems. It has however been suggested that these limitations can be easily and straightforwardly ameliorated through simply increasing the inherent agarose percentage of the synthesised hydrogel (i.e ≥ 3 wt%). As shown by Guastaferro *et al*, this results in a more densely packed and mechanically stable helical fibre network in the agarose hydrogel with smaller liquid filled gaps. Subsequently, upon freeze-drying the more robust macrostructure is preserved as the damaging effects of high ice-crystal volumes and crystal growth are substantially restricted (Guastaferro *et al.*, 2021).

Despite acting as a potentially beneficial solution in the context of freeze-drying and scaffold preservation, it must however be considered that the increase in agarose percentage may detrimentally alter several physical properties of the agarose scaffolds ultimately produced (Guastaferro *et al.*, 2021). As literature specifically purports an inverse association between agarose percentage and hydrogel pore size/porosity (Narayanan *et al.*, 2005), if this solution were to be applied, an effective working relationship would likely need to be established across the three stated variables (agarose percentage, detrimental freeze-drying effects, final pore size and porosity), thus facilitating the production of an effective osteochondral agarose scaffold biomaterial with properties which crucially fall within the previously described optimal clinical remits.

An additional factor that must also be considered is that alterations to agarose percentage will result in the requirement for a re-validated F-AGE-1 spatial patterning procedure. Firstly to account for the established fact that plasmid DNA migrates more slowly in higher percentage agarose gels thus rendering the previously optimised F-AGE-1 DNA loading and co-localisation methods inadequate (Yılmaz *et al.*, 2012). Secondly, as illustrated by (Kamitakahara *et al.*, 2012) (Section 1.8.3.1), a more densely packed higher percentage agarose hydrogel network may also facilitate the formation of smaller CaP nanoparticles than what was previously identified within

the 1 wt% proof-of-concept data. This specific area however was the focus of an aligned PhD project within the Feichtinger research group (Daniel White, PhD student).

Ultimately, for the purpose of this PhD project and the formation of an osteochondral GAM system, a functional and structurally stable porous scaffold biomaterial was considered essential and thus this first chapter will seek to explore how this could be achieved. Additionally, this project will also explore for the first time the incorporation of either Fibronectin and PEI into the *in-situ* Feichtinger patterning system. In terms of the former, this chapter will attempt to incorporate Fibronectin as part of the DNA loading solution specifically for the purpose of enhancing cellular adhesion capabilities. In terms of the latter, PEI would be tested as a possible alternative gene delivery vehicle to CaP, a decision taken as a result of its excellent reported cellular transfection ability across multiple cell types and its strong cationic character (Hall *et al.*, 2017).

3.2 Specific materials & methods

3.2.1 Physical characterisation of freeze-dried agarose scaffolds

To elucidate the structural effects of firstly; the freeze-drying process and secondly of increasing agarose polymer content on agarose hydrogels, a combination of qualitative and quantitative methodologies were applied in this study. This included qualitative and quantitative evaluation of the resulting scaffold architecture (including pore structure and size) in 3D (via scanning electron microscopy) and 2D (via histological analysis/tissue sectioning).

3.2.1.1 Scanning Electron Microscopy

Scanning Electron Microscopy (SEM) was used as an important tool to assess the 3D topography of fabricated agarose scaffolds, utilising its specific capability to examine closely the surface structures of samples, both at a gross scale as well as at sub-micrometre resolutions.

3.2.1.1.1 Determination of microarchitecture of agarose Scaffolds

Individual 15 x 15 cm 1 wt% and 3 wt% agarose hydrogel slabs were first fabricated using the protocol set out in section 2.2.2.1.2. Using the in-house designed hydrogel excision tool, individual 1 wt% and 3 wt% hydrogels (6 mm x 4.6 mm) were then isolated from the large gel slabs before specific placement into wells of a 48 well plate. This was then followed by the performance of the freeze-drying procedure, as stated in section 2.2.3, resulting in the bulk transformation of agarose hydrogels into porous scaffolds. From this point on agarose scaffolds were termed either 1%-Blank or 3%-Blank and crucially were deemed ready for direct SEM imaging.

In short, agarose scaffolds were mounted directly onto a 12 mm aluminium SEM stub (Agar Scientific, UK) and then sputter coated with iridium (5 nm) for 5 minutes. Samples were transferred and imaged under vacuum using a Hitachi SU8230 cold field emission SEM (Hitachi, Japan) with following attachments: Oxford Instruments Aztec Energy EDX system with 80 mm X-MAX SDD detector. Imaging was performed at a range of magnifications enabling visual analysis at each architectural level. All scaffolds were stored in a desiccated storage container prior to SEM imaging, thus preventing moisture mediated damage of the scaffold fibres brought about by the SEM working temperature and pressure conditions.

3.2.1.2 2D histology of agarose Scaffolds

To further evaluate pore size characteristics of agarose scaffolds of varying percentage, 1%-Blank and 3%-Blank scaffolds were once again manufactured and then evaluated using simple two-dimensional histological analysis. Through gross evaluation of 2D sections, agarose scaffold pore structure and size was qualitatively and semi-quantitatively assessed.

3.2.1.2.1 Methodology for histological processing and visual analysis

1%-Blank and 3%-Blank agarose scaffolds (n=3 per group) were histologically fixed, processed and sectioned as described in section 2.2.8.1. For each of the three scaffolds per group, a single section (n=1) was taken from its "middle" geometic portion (at approximately 2000-3000 μm). H&E staining, as per section 2.2.8.2, was then used to stain the agarose fibres, thus distinguishing and enhancing the aforementioned 2D pore structure. Images were captured using a light microscope, in tandem with Zeiss image processing software.

3.2.1.2.2 Methodology for basic quantification of pore size

Each image captured was subsequently uploaded to an online software (WebPlotDigitizer) whereby the distance between the two widest points of each pore was determined, as shown in Figure 3.1. For each scaffold section imaged (n=1), all pores were measured and the mean pore size calculated.

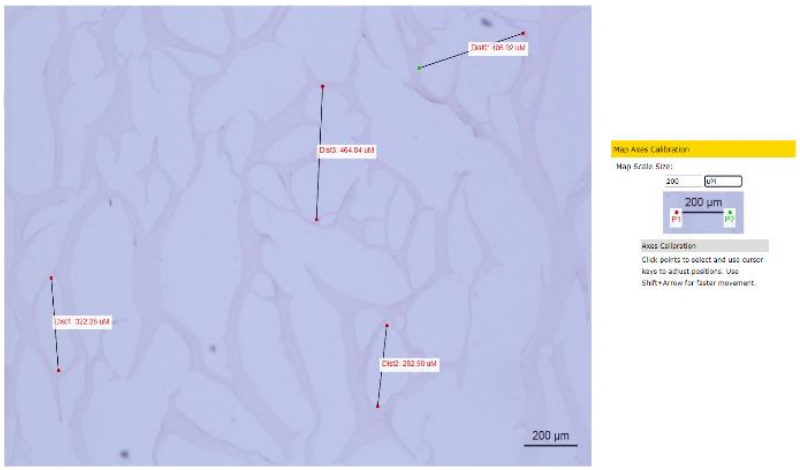

Figure 3.1 – The data extraction process for mean pore size of 2D histologically processed and stained agarose scaffolds. The 200 μm scale bar was incorporated into the WebPlotDigitizer software prior to measurements.

3.2.2 Re-validation of the F-AGE-1 approach in 3 wt% agarose hydrogels

Based on the outcomes of experiments outlined in section 3.2.1, the F-AGE-1 methodology was validated for 3 wt% agarose hydrogels.

This validation process was divided into three incremental stages. Stage-1 consisted of the synthesis and characterisation of *in-situ* CaP nanoparticle precipitates within 3 wt% agarose scaffolds, using the F-AGE-1 method. In this stage, the birds-eye view location or "distance" of the precipitate within the agarose gel was measured to allow for future DNA co-localisation. Then, using these precipitate containing gels, the CaP nanoparticles were imaged via SEM (work performed by Daniel White, Dr Feichtinger supervised PhD student). In stage-2, the

electrophoretic mobility of plasmid DNA and Fibronectin (FN) proteins was assessed within 3 wt% agarose gels. Utilising the most optimal electrophoretic voltage, the time and distance taken to reach the CaP precipitation region was specifically noted. Finally, in stage-3, the entire F-AGE-1 method was performed with co-localisation being confirmed via gel imaging.

For all experimental studies illustrated below, maxipreparations of the pCAG-d2-eGFP plasmid vector was utilised for all nucleic acid master stock solutions.

3.2.2.1 Stage-1: F-AGE-1 mediated CaP synthesis

Briefly, this included the formulation of 3 wt% agarose hydrogels which contained supersaturated levels of a salt precursor (i.e - PO_4^{3-}), to which subsequent introduction of a cationic species (i.e. Ca^{2+}) via electrophoresis was tested specifically for its ability to induce spontaneous crystallisation and precipitation within the agarose gel (The F-AGE-1 Feichtinger core concept).

The detailed experimental procedure used in this validation study is illustrated below in Table 3.1. Each $CaCl_2$ master stock solution was loaded sequentially in a horizontal fashion (n=3) along a single agarose gel row.

After completion of the F-AGE-1 gel loading procedure, the agarose gels were immediately imaged using firstly a digital camera and then a BioSpectrum® 810 imaging system (UVP, Germany) (set to image using the UV-trans-illumination filter, 5 second exposure). Images were subsequently exported to ImageJ software whereby the distance of final precipitate from the back of the original loading well was measured. From this initial value, the "well thickness" (2 mm) was then subtracted away, providing a final distance measurement.

Table 3.1 – Experimental procedure for the synthesis of CaP precipitates within an agarose gel, specifically using the F-AGE-1 approach.

	Brief method description	**Specific materials required**	**Product of each step**	**Detailed Protocol Location**
Step 1	Formulate F-AGE-1 nanoparticle master stock loading solutions (enough for 60 runs)	500 mM $CaCl_2$, 30% Glycerol, ddH_2O	1500 µL $CaCl_2$ master stock loading solutions (0mM-225mM)	2.2.2.1.1
Step 2	Generate concentrated F-AGE-1 buffer solution (Buffer A)	500 mM HEPES, 15 mM Na_2HPO_4, ddH_2O	1000 mL concentrated Buffer A	2.2.2.1.2
Step 3	1 in 20 dilution of concentrated Buffer A solution to generate working/running solution	ddH_2O	2000 mL working Buffer A	2.2.2.1.2

Step 4	Generate 15 x 15 3 wt% agarose gel (with SYBR SAFE DNA stain, 1 in 10,000)	Working Buffer A, ddH_2O, SeaKem LE agarose powder, SYBR SAFE, in-house gel tray, in-house comb inserts	Solidified agarose gel used for payload patterning	2.2.2.1.2
Step 5	Equilibrate agarose gel with running Buffer A within Sub-Cell GT electrophoresis tank	3 wt% agarose gel, 1800 µL working Buffer A, Sub-Cell GT electrophoresis tank	equilibrated agarose gel ready for loading	2.2.2.1.3
Step 6	Performance of the F-AGE-1 gel loading procedure specifically starting at "stage 3"	$CaCl_2$ master stock loading solutions (0mM-225mM), Sub-Cell GT electrophoresis tank, PowerPak 300	Confined crystallisation of CaP nanoparticles	2.2.2.1.3
Step 7	Image capture of CaP nanoparticle precipitates within agarose gels (photographic and UV-trans-illumination)	Standard digital camera, BioSpectrum 810 imaging system	Visual analysis of CaP precipitates including distance of precipitates from loading well	2.2.2.1.3

3.2.2.1.1 CaP precipitate characterisation

SEM imaging was also used for the characterisation of CaP nanoparticle precipitates, formulated using the F-AGE-1 electrophoretic loading method. Specifically, using micron and sub-micron level magnification, the experiment aimed to confirm the presence and morphology of CaP nanoparticles within powderised 3 wt% agarose scaffolds.

This study was carried out by Daniel White (PhD student, University of Leeds) who contributed to experimental performance and analysis. This study followed directly on from the experiment above, whereby post-imaging, the 0 mM $CaCl_2$ and 225mM $CaCl_2$ precipitates were excised using the gel excision protocol (section 2.2.2.1.4) before undergoing a freeze-drying process (section 2.2.3). After freeze-drying, the scaffolds were then powderised with a small pestle and mortar before being transferred to a 1.5 mL Eppendorf tube. A small proportion of the agarose scaffold, in its powderised form, was then mounted directly onto a 12 mm aluminium SEM stub and coated with iridium (5 nm) for 5 minutes. SEM imaging was then performed as previously outlined in section 3.2.1.1.1, specifically using the dual secondary electron (SE) detector modality.

3.2.2.2 Stage-2: pDNA and fibronectin electrophoretic mobility

To ensure proximal co-localisation with CaP complexes within agarose gels, the electrophoretic mobility of two different payloads were assessed (plasmid DNA and bovine fibronectin). Although bovine fibronectin was not included in the F-AGE-1 proof-of-concept investigations, it was purported by this author that due to its negative charge, its electrophoretic mobility and its

usefulness as a cell adhesion enhancer, its presence in combination with pDNA (as a bioconjugate pair) may have a positive enhancing effect to the final GAM system (Hsiao *et al.*, 2017; Musante *et al.*, 1998). Its basic protein structure can be found in Figure 3.2.

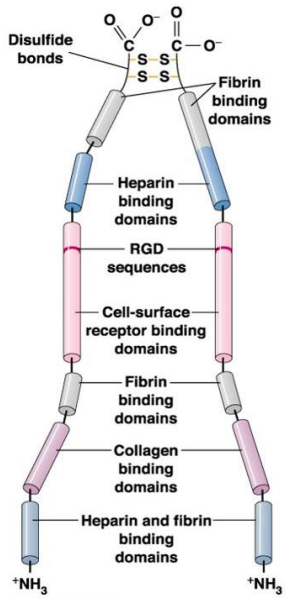

Figure 3.2 – Diagrammatic representation of a bovine fibronectin protein (440KDa dimer). Bovine FN possesses a net charge of -42.0 at pH 7.

This study specifically included measuring the time taken for the pDNA or FN band to reach the previously calculated CaP precipitation region, at a constant voltage (300V). To aid in this selection, equations provided by Dr G Feichtinger and colleagues, which have been used previously to estimate pDNA migration distance in a variety of agarose gel formulations were utilised to good effect (Figure 3.3). Given the location of the F-AGE-1 CaP precipitates, an electrophoresis time of 5 minutes was used and analysed initially for this experiment.

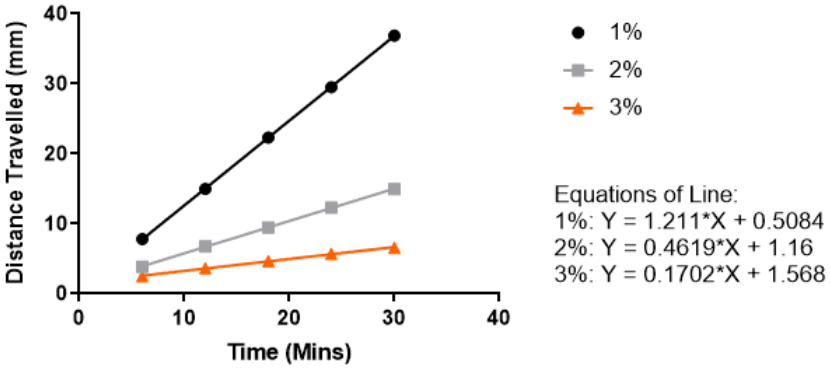

Figure 3.3 – Distance versus time graph for pDNA migration in 1 – 3 wt% agarose gels, at a constant voltage (300V)

Experimentally, steps 1-7 stated in the above table (Table 3.1) were repeated with minor modifications. This included; the preparation and subsequent loading of all DNA and FN master stock loading solutions (as per Table 2.2, Section 2.2.2.1.1). Upon gel loading, the master stock loading solutions were pipetted into five wells (n=1) in a horizontal fashion.

During performance of the F-AGE-1 gel patterning procedure (Section 2.2.2.1.3), only stages 1 and 2 of the protocol were executed before subsequent image analysis. Resulting DNA bands were imaged through exposure to UV-trans-illumination with SYBR Green filter, with specific measurements then taken regarding the distance between the midpoint of the DNA or FN band and the end of the loading well.

3.2.2.3 Stage-3: DNA-CaP co-localisation using F-AGE-1 methodology

Using the results from the above pDNA/FN loading optimisation procedure, the F-AGE-1 process outlined in section 2.2.2.1 was then performed in full, inducing the proximal deposition of pDNA payloads with CaP nanoparticle precipitates, within a 3 wt% agarose hydrogel. All stated DNA and $CaCl_2$ master mix loading solutions were formulated prior to gel patterning whilst each agarose gel contained SYBR SAFE DNA stain. Furthermore, gel loading was performed across a single horizontal row with controls including pDNA master mix only and $CaCl_2$ master mix only (n=3 per group).

The resulting precipitates and band patterns were assessed once all electrophoresis steps were performed, using the same techniques stated in sections 3.2.2.1 and 3.2.2.2.

3.2.3 Creation of a F-AGE method for PEI electrophoretic patterning

Due to the widely successful application of cationic PEI polymers as transfection vehicles for non-viral vector gene delivery, both in 2D cell cultures and in scaffold based systems, the author in this final study sought to investigate the potential incorporation of said polymers within the context of electrophoretic co-localisation in confinement (Boussif *et al.*, 1995; Ding *et al.*, 2022; Zakeri *et al.*, 2018). As linear PEI contains a high positive charge density (protonated amine functional groups), it was hypothesised that comparable electrophoretic mediated spatial control (to that previously identified with inorganic metal cations) could also be achieved within similar agarose hydrogels, leading to proximal pDNA and PEI polyelectrolyte co-localisation and the possible formation of polyplexes.

By utilising fundamental concepts from both F-AGE-1 and Kamitakahara electrophoretic nanoparticle synthesis methods (Kamitakahara *et al.*, 2012), proof-of-concept experiments were subsequently performed to investigate firstly; whether PEI alone possessed effective agarose hydrogel migration potential under a constant electrophoretic potential. Then secondly, whether

proximal DNA-PEI deposition could be achieved within said agarose gels, resulting in co-localisation and the *in-situ* formation of polyplexes.

3.2.3.1 Stage-1: PEI mobility in agarose gels

Unlike the detection of nucleic acids within agarose gels, which possesses a highly reliable and well established gold standard method (agarose gel-DNA dye mediated detection – SYBR SAFE), very little research has been undertaken to establish a similar method for the detection and subsequent characterisation of electrophoretically loaded polymer species within agarose gels (Motohashi, 2019). Interestingly however, in the field of proteomics, staining methods exist for the visualisation of different molecular weight proteins (SDS-PAGE mediated protein analysis), with disulphonated tri-phenylmethane dyes specifically developed for this application (Gauci *et al.*, 2013). Such dyes (e.g. Coomassie Brilliant Blue) act through electrostatic interactions between it and the protonated basic amino acid chains present within the proteins, thus allowing protein specific staining, visualisation and analysis.

Using this same concept, PEI electrophoretically loaded agarose gels were similarly stained with Coomassie Blue with the idea that spatial migration of the PEI polymer within the gel could be visualised and characterised.

Experimentally, ReadyBlue Protein Gel Stain (Merck, UK) was purchased and initially stored at 4°C. A 3 wt% agarose gel was then formulated (in the absence of SYBR SAFE DNA stain) specifically utilising working Buffer B (section 2.2.2.2.2), whilst simultaneously, eight different PEI masterstock loading solutions were also being synthesised (PEI-N/P8-2.5 - PEI-N/P40-5) as per section 2.2.2.2.1, Table 2.5.

To the gel, 30 µL PEI loading solutions were applied to individual wells (n=1). An electrophoretic potential (+ ⟶ - electrode configuration) was then generated using the conditions: 300V for 10 minutes. After completion, the gel was submerged in ReadyBlue Protein Gel Stain and incubated for 2 hours under agitation (150 rpm). Post staining, gels were then imaged using a Gel Doc Imaging system (BioRad) set for detection in the Coomassie Blue filter.

3.2.3.2 Stage-2: PEI-DNA co-localisation using F-AGE polyplex methodology

Upon confirmation of PEI electrophoretic mobility within agarose gels, a proof-of-concept co-localisation investigation was subsequently performed with the hypothesis that pDNA loading followed by reversed PEI loading can induce the formation and deposition of *in-situ* polyplexes.

As such, the F-AGE polyplex method outlined in section 2.2.2.2 was performed to completion. This included the formulation of all stated DNA and PEI master stock loading solutions whilst the agarose gel was produced with the additional SYBR SAFE DNA stain. Furthermore, a single

horizontal gel row was used for gel loading, with pDNA mastermix only and PEI-N/P24 alone acting as controls (n=3 per group).

3.3 Results

3.3.1 Physical characterisation of freeze dried agarose scaffolds

3.3.1.1 Visual analysis of freeze-dried agarose scaffolds

The University of Leeds freeze-drying process (Section 2.2.3) was applied to two different agarose hydrogel formulations (1 wt% and 3 wt% hydrogels). The resulting impact of this process, as illustrated in Figure 3.4, was two-fold – synthesising white glossy porous biomaterials whilst crucially preserving the double helical agarose framework (previously encased buffer components sublimated away). Additionally, scaffolds appeared fully lyophilised after a 12 hour freeze-drying procedure, with no evidence of frozen buffer components remaining within the scaffold bulk.

Significantly, upon individual visual analysis of 1%-Blank scaffolds post-freeze drying, it was found that this particular formulation was, as hypothesised, highly susceptible to lyophilisation mediated damage with large scale shrinkage and chain collapse observed. This culminated in the formation of porous scaffold structures approximately 1.3 fold smaller in size (length and width) (Figure 3.4 A). Furthermore, upon general handling, these scaffolds were also found to be considerably more fragile and brittle with little to no inherent mechanical stability or strength (based on physical examination only).

In contrast, following the freeze-drying of the 3 wt% agarose hydrogel formulation, it was shown that nearly all previously observed lyophilisation mediated damage could be circumvented. Crucially, this includes the maintenance of the desired hydrogel dimensions (approximately 6 mm by 4.6 mm) as well as a stronger and more stable mechanical structure (based on physical examination only) (Figure 3.4 B).

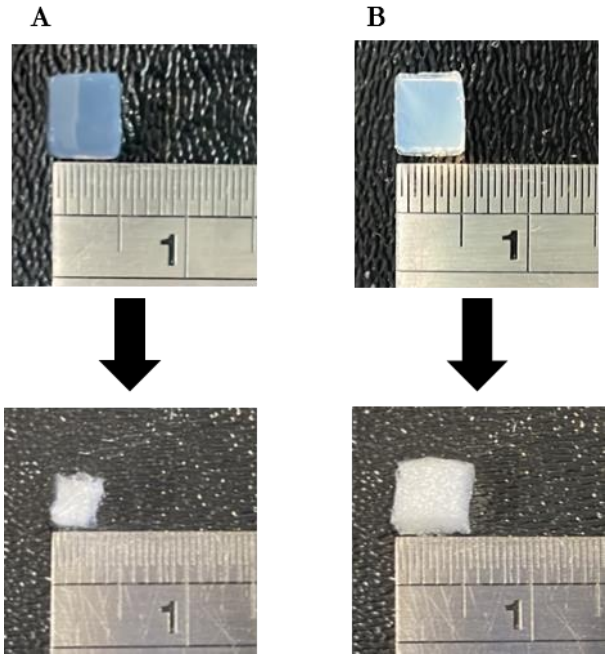

Figure 3.4 – Effect of freeze-drying on 1 wt% (A) and 3 wt% (B) agarose hydrogels.

3.3.1.2 Structural analysis of freeze-dried agarose scaffolds

Despite early success with regards to the protection against harmful freeze-drying mediated effects, it was deemed appropriate to perform more in-depth physical and structural characterisation of the 3%-Blank scaffolds before its selection as a scaffold in further experiments within this PhD project. This included structural analysis under SEM. Through this technique it was anticipated that a greater understanding could be found regarding the differences in freeze-drying resistance illustrated above. Furthermore, based on the resulting micrographs collected, it was hoped an indication of scaffold pore size could be provided. For comparative purposes, 1%-Blank scaffolds were also imaged and analysed.

Firstly, SEM evaluation of said samples at low magnifications confirmed previous visual interpretations, of which purported that agarose hydrogels (1 wt% and 3 wt%) had transformed successfully into porous, interconnected scaffolds upon exposure to a basic freeze-drying process (Figure 3.5 A and C). With such an appearance, it was considered highly likely that significant ice-crystallisation of water and HEPES buffer occurred throughout the gel, leaving large solid regions available to sublimation. Interestingly, upon higher magnification, both scaffold formulations illustrated pores that were considered to be highly irregular with thin walls throughout the scaffold bulk (Figure 3.5 B and D).

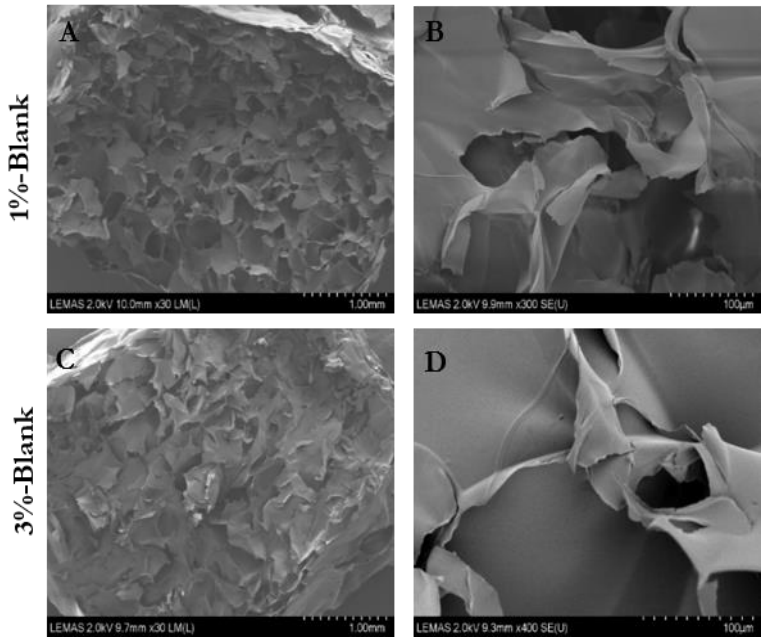

Figure 3.5 – SEM micrograph images of agarose scaffolds after freeze-drying fabrication process. A & B: Representative microstructure of 1%-Blank agarose scaffold, C & D: Representative microstructure of 3%-Blank agarose scaffold.

Unfortunately, despite clear physical differences in terms of structural stability and bulk dimensions between 1%-Blank and 3%-Blank scaffolds, the highly irregular and overlapping nature of the resulting pores meant determining specific pore sizes across the two formulations using SEM was incredibly challenging. Effective pore size measurements could not be obtained

due to the incompatibility of the images with the imageJ BoneJ pore size plug-in (Doube *et al.*, 2010). As a result, an alternative method for pore size assessment was pursued.

3.3.1.3 Agarose scaffold 2D pore size and morphology

Due to study-specific limitations of SEM data collection and analysis, representative 2D histological images of 1%-Blank and 3%-Blank scaffolds were subsequently produced, with a view to provide further evidence of scaffold pore characteristics. Histological sections were analysed qualitatively and quantitatively, as described in section 3.2.1.2.

Based on the images captured, 1%-Blank and 3%-Blank scaffolds (Figure 3.6 A-D) contained highly irregular pores separated by thin agarose fibre walls, as purported from SEM analysis of the bulk scaffolds. It was also found that 3%-Blank scaffolds generally contained a larger number of pores over the analysed scaffold cross-sections, in comparison to 1%-Blank scaffolds. The analysis of the mean pore size diameter revealed a significantly smaller value for the 3%-Blank scaffolds (215 μm ± 132) compared to the 1%-Blank scaffolds (388 μm ± 276) ($P < 0.0001$). It was also found that the 3%-Blank scaffolds contained a smaller median pore size and also the smallest single diameter pore. Crucially, despite possessing lower pore diameters, the 3 wt% scaffolds remain within the previously stated range for osteochondral scaffold systems (Lee *et al.*, 2018).

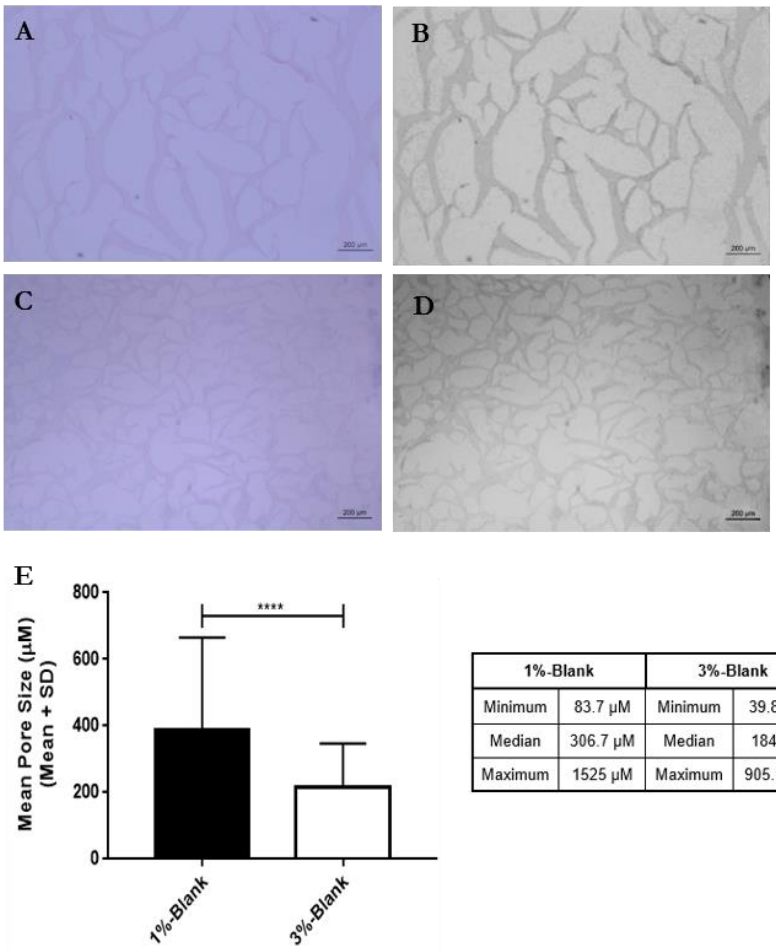

1%-Blank		3%-Blank	
Minimum	83.7 µM	Minimum	39.8 µM
Median	306.7 µM	Median	184 µM
Maximum	1525 µM	Maximum	905.1 µM

Figure 3.6 (A, B, C) – The effect of agarose percentage on 2D pore morphology and mean pore size, using histological processing and imaging concepts. H&E stained (and grey-scale) histological cross-sections of 1%-Blank (A & B) and 3%-Blank (C & D) scaffolds. Prior to staining and imaging, scaffolds were fixed in NBF before processing and sectioning into 10 µm thick slices. Sections were taken from the "middle" portion of the scaffold. E: Mean pore size measurements extracted from 2D histological sections (n=3 per scaffold type). Each pore was measured across its single greatest width. A Mann-Whitney U test was used to compare between the means of each of the scaffold groups. **** = P<0.0001.

3.3.1.4 Final outcome of agarose scaffold characterisation

This small scaffold characterisation study suggests that 3 wt% agarose hydrogels represent a more compatible formulation than the 1 wt% analogue for the lyophilisation-mediated production of porous agarose scaffolds, in the context of osteochondral GAM repair applications. This decision was taken on account of its crucial resistive capabilities to scaffold shrinkage upon exposure to the stressful conditions of freeze-drying as well as its ultimate possession of sufficient micro-porous pore size distributions across its scaffold bulk.

The following sections will now describe the results of the re-validation of the F-AGE-1 spatial patterning approach for 3 wt% hydrogels, as well as the steps involved in the creation of the PEI modified F-AGE methodology.

3.3.2 Spatial patterning using F-AGE-1 approach

3.3.2.1 Synthesis of CaP precipitates

Using the previously illustrated datasets provided by Dr Feichtinger and colleagues as both a guide and as tentative positive controls, the F-AGE-1 spatial patterning method was subsequently re-validated for use in 3 wt% agarose hydrogels. The nanoparticle precipitation step (60V for 6 minutes) utilised in the preliminary work was utilised once more in the 3 wt% gels.

Upon stimulation of an electric potential across the $CaCl_2$ loaded gel (specifically in the + ⟶ - electrode configuration), it was noted that after approximately two minutes, faint white "C-shaped" precipitates appeared to form within the gel structure below loaded wells containing $CaCl_2$ (Figure 3.7 A). As electrophoresis then continued (4-6 minutes), the precipitates initially identified appeared to grow larger and more intense in all cases. In terms of precipitate thickness and intensity, a small $CaCl_2$ concentration dependent effect was observed, with the 225 mM $CaCl_2$ group displaying the thickest and most intense band whilst the 112.5 mM appeared the thinnest with lower overall intensity.

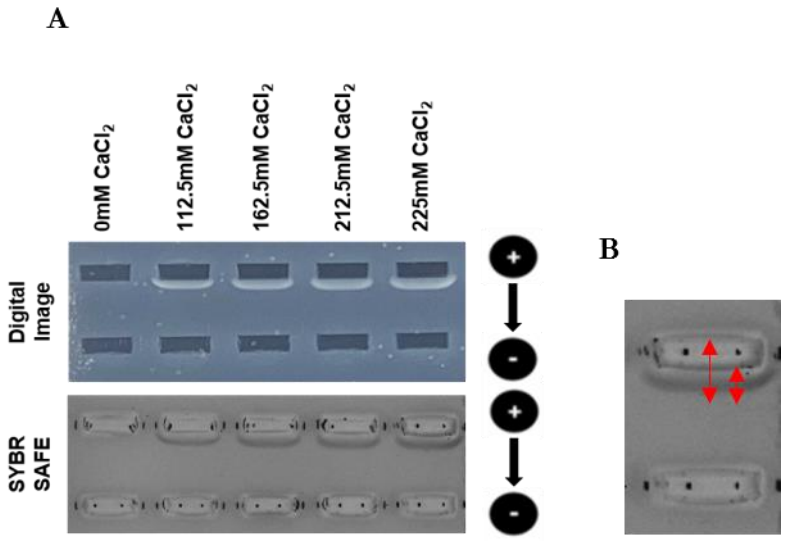

Figure 3.7 (A & B) – Formation of confined CaP precipitates within 3 wt% agarose hydrogels, using the F-AGE-1 method. All wells were exposed to a constant 60V electrophoretic potential for 6 minutes. A: Range of CaP precipitates synthesised from $CaCl_2$ loading solutions ranging from 0mM-225mM. B: Enlarged SYBR SAFE image used to calculate the overall distance of the CaP precipitate from the loading well (i.e. the CaP precipitate region).

Interestingly, such patterns in CaP synthesis generally matched that identified by Feichtinger and colleagues in the proof of concept work utilising 1 wt% gels, with similar thicknesses and precipitate intensities identified over a similar timeframe, despite the increase in agarose gel concentration. Furthermore, similar curved or "C" shape precipitates were presented in this work

as was previously seen, a pattern hypothesised to be as a result of either lateral ion diffusion or specific electric field profile boundaries.

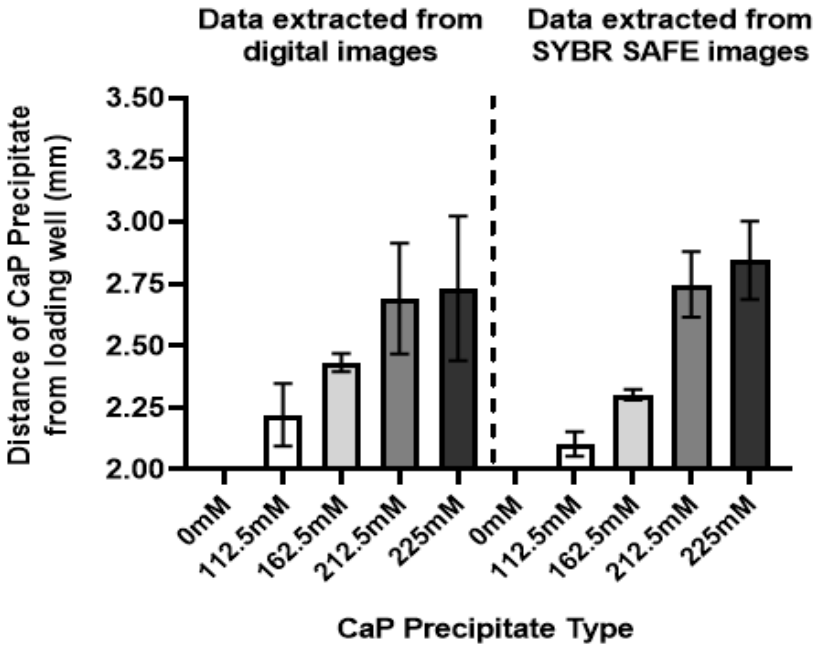

Figure 3.8 – Final distance measurements of the synthesised CaP precipitates after the F-AGE-1 electrophoretic loading process (n=3). ImageJ software was used to calculate total distance measurements between the leading edge of the CaP precipitate and the back of the initial loading well. Once calculated, the length of the well (2mm) was subtracted.

Upon measurement of the distance of the final formulated precipitates from the loading wells, the CaP precipitate regions were found to occur at 2.2-2.75 mm (Figure 3.8). These values were then used for pDNA mobility optimisation in the next section.

3.3.2.1.1 Analysis of CaP precipitates

In a further experiment performed by Daniel White, the 0 mM and 225 mM $CaCl_2$ agarose precipitate hydrogels were analysed via SEM to obtain a greater understanding of particle morphology and size. The images accumulated were illustrated in Figure 3.9.

Analysis of the control 0 mM sample (Figure 3.9 A) provided evidence of the absence of CaP nanoparticles within the agarose fragments. In contrast to the above observations, the 225 mM $CaCl_2$ agarose sample illustrated the existence of distinct populations of visible particles, which exhibited notable differentiation from the surrounding background whilst also displaying uniform and spherical shapes (Figure 3.9 B and C).

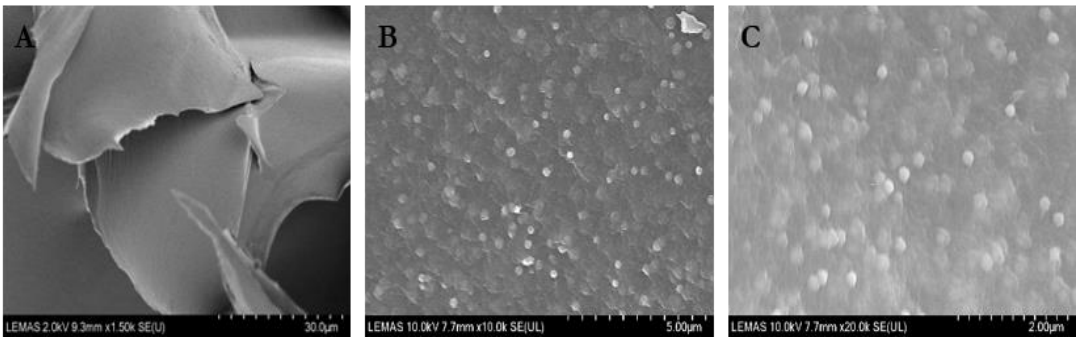

Figure 3.9 (A-C) – Comparative SEM analysis of 3%-Blank versus 3% F-AGE-1 CaP embedded precipitates (225 mM $CaCl_2$). A: 3%-Blank. B & C: 3%-225mM CaP nanoparticle precipitates. Each individual scale-bar tick represents $1/10^{th}$ of the overall bar length (i.e 3 µm, 500 nm, 200 nm).

Additional in-depth characterisation experiments of *in-situ* F-AGE-1 synthesised CaP populations, including X-Ray Diffraction spectra and mean particle diameters, can be found in the PhD thesis by Daniel White (White Rose eThesis depository) entitled "Development of mineralised gene-activated matrices for osteochondral tissue regeneration".

3.3.2.2 Confirmation of pDNA and FN mobility to CaP region

Using the 3 wt% agarose pDNA migration formula, as well as the CaP precipitate distance measurement (2.2-2.4 mm), it was judged that pDNA patterning should be performed over a short duration (5 minutes), at high voltage (300V).

Figure 3.10 illustrates the location of a variety of nucleic acid, bovine fibronectin and nucleic acid-Fibronectin combinations, upon loading and patterning within a 3 wt% agarose gel. Using the aforementioned electrophoretic conditions, all constituents appeared to successfully exit the loading wells and migrate downwards through the gel towards the positive electrode. Significantly after a five minute 300V electrophoretic exposure, all bands appeared within or marginally below the previously calculated CaP region, a factor considered vital as electrophoretic polarity would subsequently be reversed in the later CaP precipitation step, causing marginal upwards migration of nucleic acid components. As a result, pDNA constituents were hypothesised to be proximally located for the following CaP nucleation and precipitation steps (combined co-localisation procedure).

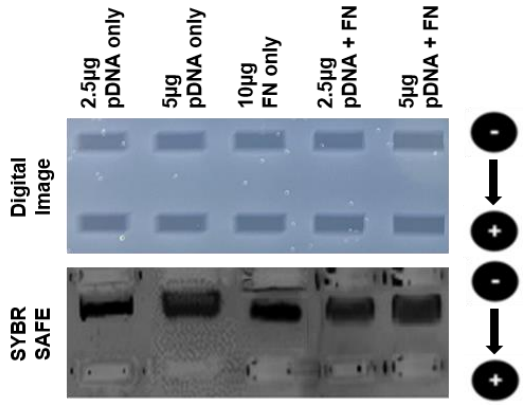

Figure 3.10 – Optimisation of plasmid and Fibronectin migation within 3wt% agarose hydrogels, in the context of F-AGE-1 nanoparticle precipitates and the precipitate region. All wells were exposed to a constant 300V electrophoretic potential for 5 minutes.

3.3.2.3 F-AGE-1 co-localisation

Using the results from sections 3.3.2.1 and 3.3.2.2, the full F-AGE-1 protocol was then performed with the aim of proximally patterning nucleic acid and CaP payloads within specific regions of an 3 wt% agarose gel, allowing for the co-localisation of CaP to DNA or the co-localisation of CaP to DNA-FN composites.

Figure 3.11 illustrates the resulting spatially patterned agarose gels after completion of the F-AGE-1 protocol. Interestingly it was identified by visual observation that pre-loading of wells with nucleic acid payloads alone resulted in marginally fainter CaP precipitates than the controls, whilst the presence nucleic acid-FN payloads resulted in brighter more intense patterning. Significantly, this corresponded with equivalent SYBR SAFE images which showed that pDNA and pDNA-FN payloads were both proximally loaded within the CaP precipitate zones, thus providing supporting evidence of a pDNA-CaP co-localised interaction. Interestingly however, in both cases, no obvious differences were identified in the shape, size or position of the DNA bands when $CaCl_2$ concentration was increased. As a result, it was only possible to infer that co-localisation had occurred in these DNA-CaP and DNA-FN-CaP.

Importantly, all findings matched with those presented previously by the Feichtinger proof-of-concept studies, suggesting successful translation of the F-AGE-1 technique for 3 wt% agarose gels.

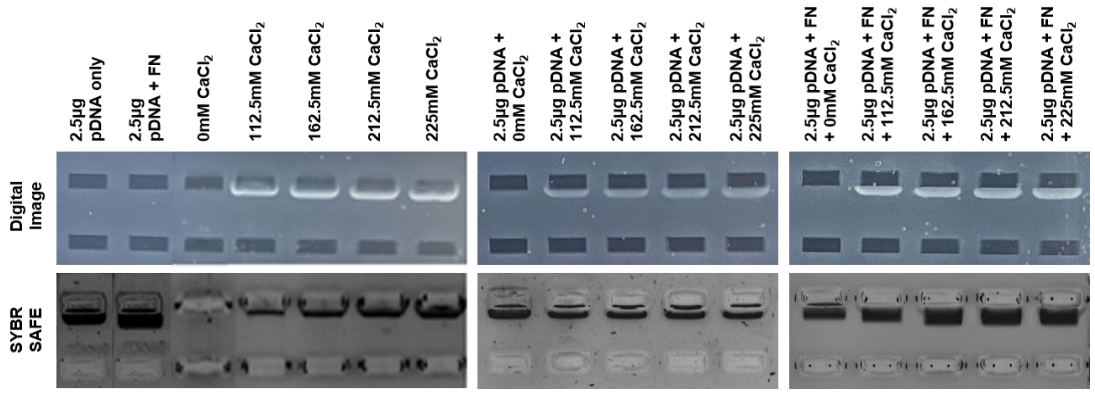

Figure 3.11 – Electrophoretic patterning and co-precipitation of pDNA and CaP nanoparticles within a 3 wt% agarose gel, using the F-AGE-1 approach. All wells were exposed to the F-AGE-1 four stage protocol in which two specific electrophoretic procedures took place. 1) 300V electrophoretic potential for 5 minutes (- ⟶+ electrode configuration). 2) 60V electrophoretic potential for 6 minutes (+ ⟶- electrode configuration).

3.3.3 Spatial patterning using F-AGE polyplex approach

3.3.3.1 Confirmation of PEI mobility within agarose hydrogels

In a proof-of-concept investigation, different concentrations of linear PEI were loaded within 3 wt% agarose gels and exposed to specific electrophoretic stimuli, with the specific intention of classifying polymer mobility within an agarose hydrogel over a specific timeframe and voltage. Due to the novelty of such experiments, Coomassie Blue protein stain was initially tested to visualise and confirm such objectives.

Figure 3.12 shows the resulting agarose gel after PEI loading, electrophoretic exposure and final protein dye staining. Significantly it was confirmed in this test run via Coomassie Blue staining that linear PEI can effectively translocate through a 3 wt% agarose gel, with migration in fact occurring in a unique wave-like pattern downwards towards the negative electrode. Interestingly, observations also suggested that as well as the influence of the electrophoretic voltage applied, migration speed appeared to be concentration dependent, with higher concentration PEI loading samples (e.g. PEI-N/P40-5µg) progressing greater distances within the agarose gel in comparison to lower concentration equivalents (e.g. PEI-N/P8-2.5µg). Based on these results, it was assumed a 10 minute 300V electrophoretic duration could therefore be optimal for subsequent pDNA co-localisation steps.

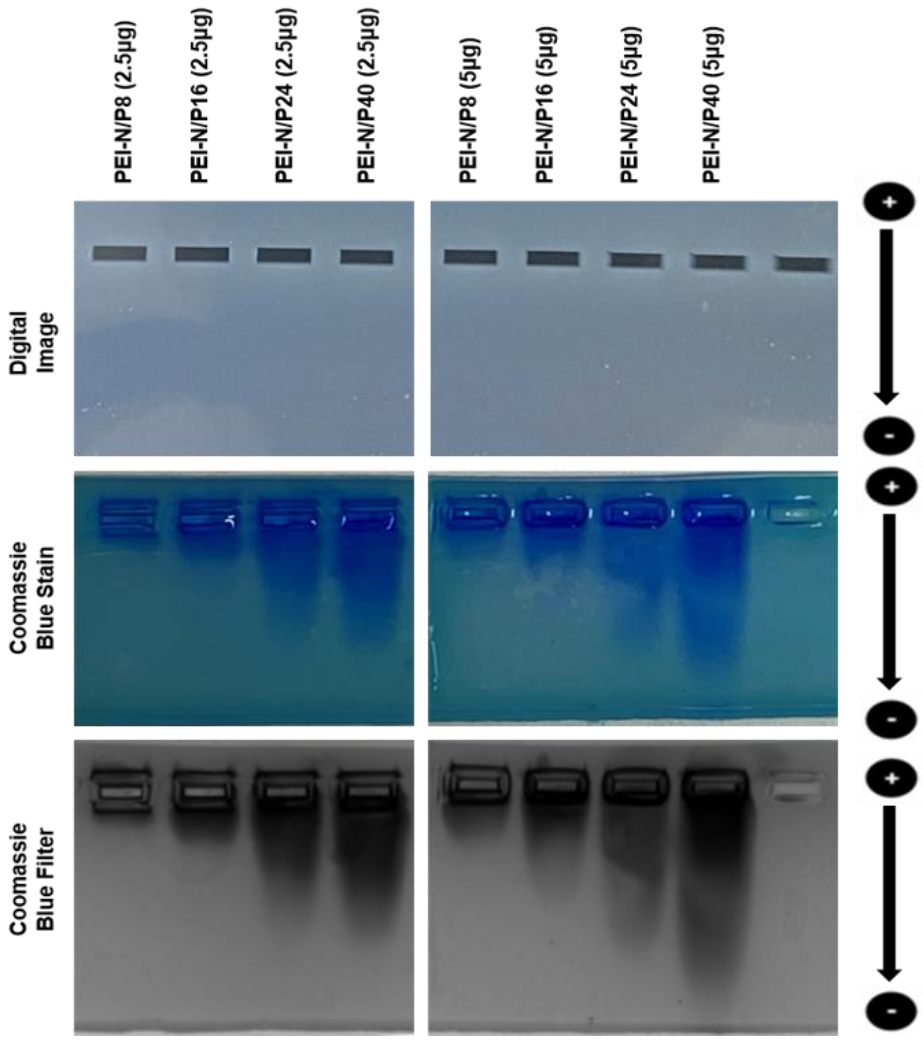

Figure 3.12 – Electrophoretic migration of linear PEI within 3 wt% agarose hydrogels. Gel was exposed to a constant 300V electrophoretic potential for 10 minutes, using a + ⟶- electrode configuration. Post electrophoresis, gels were stained in Ready Blue Protein Gel Stain for 2 hours.

3.3.3.2 PEI-DNA co-localisation

Using the results from section 3.3.3.1, a full AGE-polyplex patterning method was executed with the aim of proximally distributing plasmid and PEI payloads within 3 wt% agarose gels in order to induce the formation of a spatially distinct polyplex populations.

Figure 3.13 illustrates the resulting spatially patterned agarose gels after completion of the F-AGE polyplex protocol. Significantly, over the course the PEI patterning step (stage 4 of the F-AGE polyplex protocol), at approximately 5 minutes, thin faint bands of precipitates began to appear across both the 2.5 µg and 5 µg pDNA containing lanes, with precipitate intensity increasing as concentration of PEI also increased. Interestingly, precipitates in the largest PEI concentration wells appeared first and were also found immobilised at a lower region in the gel.

As PEI concentration then progressively decreased, other precipitates were then observed, each presenting closer to the upper loading well.

Upon analysis of the SYBR SAFE images, it was crucially found that all previously loaded pDNA bands were each now situated in the exact vicinity of the observed PEI precipitate (lower portion of the gel). Moreover, as PEI concentration increased, the thickness of the pDNA band decreased, a phenomenon potentially symptomatic of PEI polymer mediated nucleic acid condensation. This hypothesis was further supported by the location and appearance of the plasmid only control wells, which displayed completely unaffected migration patterns as well as the largest band thickness (remaining in its original supercoiled form) indicating condensation had not occurred.

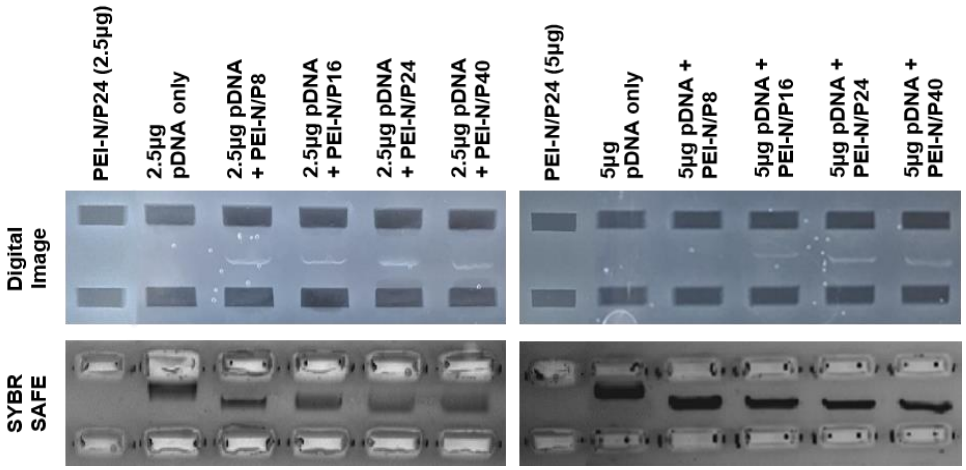

Figure 3.13 – Electrophoretic patterning and polyplex formation within a 3 wt% agarose gel, using the F-AGE polyplex approach. All wells were exposed to the F-AGE polyplex four stage protocol in which two specific electrophoretic procedures took place. 1) DNA patterning: 300V electrophoretic potential for 20 minutes (- ⟶+ electrode configuration). 2) PEI patterning: 300V electrophoretic potential for 10 minutes (+ ⟶- electrode configuration). Both 2.5 µg and 5 µg complexation results illustrated.

3.4 Discussion

3.4.1 Impact of increasing agarose percentage on agarose scaffold structure

In previous works performed by Dr Feichtinger and colleagues involving the freeze-dry mediated fabrication of porous scaffolds from low percentage formulation agarose hydrogels (1 wt%), it was found that the end-stage biomaterial product was unsuitable for use in osteochondral scaffold repair. This was attributed to bulk surface area shrinkage and structural chain collapse, which likely materialised due to damaging ice-crystal growth, causing expansion within the hydrogel pores, thus weakening structural integrity. Here, alternative 3 wt% agarose scaffolds were produced with the assumption that a more suitable osteochondral scaffold product could ultimately be fabricated. This selection was predominantly based on the work by Guastaferro and colleagues, who reported that hydrogels with ≥3 wt% agarose are less susceptible to the detrimental freeze-drying effects previously mentioned (Guastaferro *et al.*, 2021).

Within this study, upon visual analysis of both 1 wt% and 3 wt% agarose hydrogels post freeze-drying (Figure 3.4), it was clear the 3 wt% hydrogel formulation was indeed substantially more resistant to the structural damage associated with freeze-drying process, compared to the 1 wt% analogue. This was illustrated by the clear improvement in dimensional stability in the 3 wt% scaffolds, post freeze-drying, compared to the 1 wt% scaffolds. Significantly, this observed behaviour was consistent with the findings in the detailed study compiled by Guastaferro *et al*, which quantitatively illustrated that such an increases in agarose concentration leads to a large percentage reduction in overall scaffold shrinkage – in their case by approximately 30-40% (Guastaferro *et al.*, 2021).

On closer inspection of the two generated scaffold biomaterials using SEM, the University of Leeds freeze-drying process appeared to induce the complete sublimation of interlocked hydrogel buffer components, resulting in both scaffolds presenting as highly interconnected porous scaffolds at the micron level (Figure 3.5). Both surfaces also appeared highly irregular with pores orientated in a random overlapping distribution separated by thin agarose fibre walls. Regarding the pore orientation, this was thought to have materialised in part due to the non-controlled method of freezing applied within the cryotropic stage of this lyophilisation process (Guastaferro *et al.*, 2021; Loh & Choong, 2013).

However, In terms of specific pore size differences between agarose formulations, the SEM micrograph images failed to provide the author with conclusive readings and thus alternative methods were sought in the form 2D histological sectioning coupled with semi-qualitative image analysis. Crucially, based on the 2D images collected (Figure 3.6) it was found that increasing the agarose biopolymer concentration directly reduced the average pore size of the agarose scaffolds. The reason for this was hypothesised to be as a result of two directly linked factors. Firstly

because of the inherent ability of higher percentage agarose hydrogels to produce a denser nanoscale mesh structure (containing smaller pockets of water/solvent inside the fibre mesh) in comparison to lower biopolymer percentage gels – an advantageous trait commonly utilised in analytical gel electrophoresis for resolving DNA fragments of varying size (Voytas, 2000). Then, as a direct consequence, the higher percentage hydrogels, upon freezing, more effectively restricted the expansion of water/buffer pockets locked within the hydrogel core, limiting the ice crystal growth throughout its bulk. Eventual sublimation of these ice crystals generates a denser framework structure containing pores of smaller diameters, as illustrated in this 2D histological sections provided earlier.

This hypothesis was also suggested by Guastaferro and colleagues which assessed the effect of polymer amount and variable cooling rates on agarose cryogel morphology (Guastaferro *et al.*, 2021). Based on data collected, they too inferred that increases in agarose polymer content resulted in smaller overall pore diameters within cryogels but significantly also showed that this factor can be enhanced or indeed reversed depending on cooling rates applied (2.5°C/min or 0.5°C/min) (Guastaferro *et al.*, 2021; Qian & Zhang, 2011). Although exact cooling rates were not explicitly determined in this study, based on the work by Guastaferro *et al*, it could be concluded that the cryotropic conditions applied here (-80°C for 45 minutes) resulted in a very fast cooling rate – a reason therefore why reported pore diameters were on average smaller in this investigation and why scaffold shrinkage might have only occurred specifically in the 1 wt% gels.

Furthermore, it has also been shown that as a direct consequence of polymer-mediated and cooling rate-mediated pore size adjustments, mechanical properties of the resulting agarose scaffolds such as Young's modulus will likely vary (Choren *et al.*, 2013; Rybacki *et al.*, 2015). Although not explicably assessed in this chapter, an additional trade-off between pore size and mechanical strength clearly exists using this platform, suggesting function-specific scaffold requirements can be more specifically tailored with careful selection of freeze-dry fabrication parameters and agarose percentage.

As such, based on the findings illustrated, the 3 wt% porous agarose scaffold was found to be an acceptable formulation in terms of physical material characteristics, dimensional stability and the preservation of a suitable average pore size diameter for cell attachment and infiltration studies. Before final confirmation as an acceptable scaffold for use as a electrophoretically patterned GAM, the electrophoretic mobility of transfection payloads in the gel must be assessed.

3.4.1 Re-validation of the F-AGE-1 method

The core F-AGE-1 methods formulated and tested in previous work by the Feichtinger research group have tentatively shown their capability for *in-situ* electrophoretic synthesis and deposition

of nanosized CaP crystals, as well as facilitating spatial patterning and co-localisation of nucleic acid payloads with such crystal structures inside agarose hydrogel systems. As increasing the agarose wt% reduces electrophoretic mobility of DNA, the second theme of this chapter therefore sought to re-optimise the previously established F-AGE-1 methodologies (developed for 1 wt% agarose gels), for their use for the higher percentage 3 wt% agarose gel.

Overall, it was found that the F-AGE-1 protocol was generally compatible with the 3 wt% agarose formulation, with only minimal modifications required. In stage-1 of the re-validation process, a large agarose hydrogel slab containing supersaturated levels of Na_2HPO_4 was fabricated. Upon the addition of a $CaCl_2$ loading solution and subsequent generation of an electrophoretic potential, it was found that a chemical reaction was instigated. Specifically, it was found that upon exposure to comparable electrophoretic stimuli used in the proof-of-concept work (60V for 6 minutes), thin white coloured C-shaped precipitates were once again observed directly below the $CaCl_2$ loading wells (a pattern also seen in the 1 wt% methodology). Although large-scale biomineral characterisation was not within the overall remit of this chapter (the objective of the aligned PhD project of Daniel White, PhD student), based on SEM imaging provided in this chapter it was tentatively hypothesised that the precipitates generated from this F-AGE-1 method were likely spherical amorphous calcium phosphate (ACP) granules, with an approximate diameter of 150 nm or less.

This assumption was based predominantly on Ostwalds "step rule" theory, in which less organised and less dense CaP phases (such as ACP) are kinetically more favourable for initial production within confined biomineralisation systems. Thus amorphous CaP was likely induced in this example upon mixing of calcium and phosphate ions during electrophoresis (Figure 3.13). The gradual formation and progression of the precipitate band appeared as a result of the gradual supply of the calcium ions into the system during the electrophoresis process, as previously explained in the "opposite loading" reports by (Kamitakahara *et al.*, 2012). As such, it was reasoned that after approximately two minutes of F-AGE-1 electrophoresis, a large proportion of proximal calcium and phosphate ions (pre-loaded within the gel), became situated and subsequently consumed in the region directly below the loading wells, with pockets of ACP/Posner's clusters likely being synthesised *in-situ*. As concentrations of ions then increase further, supersaturation of the region occurs, leading to the observed formation of C-shaped precipitate bands. Upon continuation of electrophoresis (3-6 minutes), the early precipitation region may then act as a nucleation site for further ACP synthesis and crystal growth, which likely accounts for the observed increases in precipitate size and colour intensity.

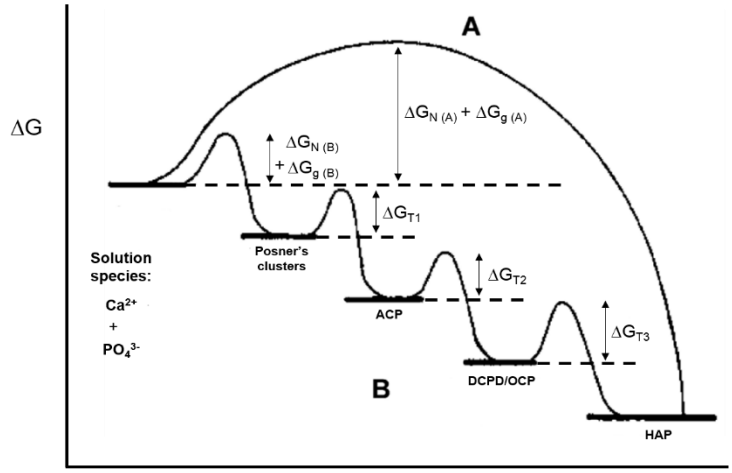

Figure 3.14 – Schematic representation of the CaP synthesis route using Ostwald step rule concepts. Route A represents the traditional crystallisation mechanism whereby HAP is synthesised directly from solution via thermodynamically favourable ion-by-ion pathways, circumventing any intermediate phases. Route B represents a lower energy crystallisation mechanism under kinetic control, whereby step-wise amorphous and metastable phases are sequentially produced prior to HAP. ACP: Amorphous Calcium Phosphate, DCP/OCP: Dicalcium Phopshate and Octacalcium Phosphate, HAP: Hydroxyapatite. Adapted from (Gower, 2008).

In stage-2 of the validation process, the migration of the pDNA and bovine fibronectin within 3 wt% agarose hydrogels was validated such that co-localisation within CaP would then be possible. Using the 3 wt% 300V migration formula as a predictive tool, it was hypothesised that an electrophoretic potential (-⟶+) duration of 5 minutes would be suitable for pDNA migration to the CaP precipitate region of interest. As previously stated, this duration was chosen with specific consideration for the F-AGE-1 CaP precipitation step which in normal circumstances takes place directly after DNA loading and contains a reversal of polarity. Crucially, as shown in the SYBR SAFE images in Figure 3.10, the electrophoresis conditions of 300V for 5 minutes appeared suitable for DNA loading in 3 wt% agarose hydrogels, with all negatively charged species migrating roughly to or just beyond the CaP precipitate region. Interestingly, it was shown that 10 μg fibronectin alone migrated a similar distance to plasmids, whilst a DNA-FN combination generated a thicker and more intense DNA band pattern.

In the final stage of the validation process, the new F-AGE-1 methodology was performed in full using the optimised and validated protocols outlined in stages 1 and 2. Based on the qualitative evidence provided (digital image and SYBR SAFE stain in Figure 3.11), there was clear proof of co-localisation, whereby identifiable CaP precipitates were situated directly within the same location as the SYBR SAFE DNA bands. Interestingly, upon comparisons between the CaP only precipitates and the pDNA-CaP lanes (Figure 3.11 left and middle digital images), it was also shown that the presence of pDNA resulted in an overall reduction in precipitate intensity. This fact may point to a possible co-complexation reaction occurring between the electrophoretically loaded pDNA and the CaP precipitates in these examples. Unfortunately, this could not be fully conclusively corroborated upon analysis of the SYBR SAFE DNA bands,

which appeared identical in shape and location for both the pDNA only lanes and the co-localised pDNA-CaP.

Significantly, as well as matching previous F-AGE system investigations with regards to the confined electrophoretic ACP synthesis, a newer report by Kimura *et al* also probed the impact of gel structure on the size of the electrophoretically synthesised CaP granules created. Crucially, according to TEM image analysis, they concluded that synthesised ACP granules decreased in size upon increasing gel concentration, a hypothesis fundamentally centred around the smaller pore spaces present within such gels restricting ACP growth and particle precipitation (Kimura *et al*., 2018). In the case of the potentially co-localised pDNA-CaP nanoparticles formed using the F-AGE-1 optimised for 3 wt% agarose gels, it could be hypothesised that the range of nanoparticle complexes produced in Figure 3.11 would be likely possess a smaller bulk diameter than those previously analysed in the proof-of-concept work (mean diameter < 232 nm), and as such may possess a greater affinity for cellular uptake and transfection when applied as spatially loaded 3D payloads (Lin *et al*., 2014) (a hypothesis tested in chapter 6).

3.4.2 Creation of a new F-AGE polyplex methodology

As stated in section 3.2.3, the incorporation, synthesis and patterning of PEI polyplexes within a spatially controlled agarose electrophoresis GAM system can be considered a tantalising prospect within the context of gene loaded scaffold systems and was hypothesised that if successful, could not only alleviate multiple limitations currently present within this field but also provide a valid alternative (or enhancement) to the previously developed but yet untested F-AGE-1 DNA-CaP nanoparticle GAMs. With this in mind, the reasoning for the incorporation of PEI particularly related to two unique challenges previously described in the literature review; 1) unwanted polyplex particle aggregation; which is considered a huge impediment for the effective loading of high concentration transfection-active payloads within 3D hydrogel systems and 2) the difficulty of formulating distinct *in-situ* spatial patterning or bi-directional gradients of polyplex payloads within single hydrogel systems. Crucially, through simultaneous synthesis, patterning and confinement of polyplexes within 3 wt% agarose hydrogels, via the F-AGE methodologies, such challenges could potentially be effectively resolved.

As this was a completely new element of research not yet explored by the Feichtinger research group, several basic principles first required testing and validation. This initially included the establishment of electrophoretic mobility and migration speed of linear PEI alone within 3D agarose hydrogel systems – a fundamental factor needed for spatial patterning within F-AGE strategies. Significantly, unlike plasmid DNA or phosphate-nanoparticle precipitates, of which can be easily visualised within agarose hydrogels post electrophoresis, PEI itself has no established visualisation methodologies and as such a novel protocol was developed involving Coomassie Blue protein stain. The use of this dye has been established for the staining of

protonated basic amino acid chains within proteins and the similarly charged PEI should exhibit the same electrostatic interactions with Coomassie Blue (Demoreno *et al.*, 1986). This dye has been shown to effectively penetrate and stain protonated amino acids in other, similar hydrogel systems (polyacrylamide gels versus agarose gels). This was further aided by parallels regarding dye penetration within similar hydrogel-like systems (polyacrylamide gels versus agarose gels) (Kumari *et al.*, 2021).

Crucially, upon direct method translation of Coomassie Blue staining protocols (Merril, 1990), PEI migration within 3 wt% agarose gels could be successfully visualised and characterised, as per **Error! Reference source not found.** A and B. Interestingly the observed staining patterns illustrated wave-like polymer migration towards the negative electrodes, over acceptable time-scales (a finding not yet reported in the literature thus far). It was also observed in **Error! Reference source not found.** A, that PEI migration distances (at a constant voltage) appeared to be directly linked to the well loading concentration of PEI, with greater speed observed when larger quantities of PEI were added to loading wells. This finding proved to be hugely important for subsequent *in-situ* polyplex patterning. The initial testing in this study illustrated PEI's potential compatibility for its incorporation within F-AGE GAM systems.

The next objective was to formulate a full F-AGE polyplex synthesis and patterning protocol, which could proximally control pDNA and linear PEI location within 3 wt% agarose gels, in order to produce *in-situ*, populations of contained, zonally distinct polyplexes. The adaption of the F-AGE process for PEI appeared remarkably successful. Firstly, as shown in Figure 3.13 digital images, thin precipitate bands were only observed for wells containing both PEI and pDNA. As precipitate was not observed in the PEI only and pDNA only controls, this is strong evidence for complexation between PEI and pDNA. Secondly, the DNA bands visible only under the SYBR SAFE filter are proximally located in the same position as the precipitate bands observed in the digital images. Importantly, there was a clear difference in the position of the pDNA band for the combined PEI and pDNA loaded lanes compared to the pDNA only lanes. As shown in the SYBR SAFE images in Figure 3.13, the combination of PEI and pDNA yielded a thinner, more condensed band – a characteristic feature of nucleic acid interaction with cationic polymers such as PEI (Dai *et al.*, 2011). Interestingly, the distance travelled by the band appeared to dependant on the concentration of PEI. This can be seen particularly for the 5 μg pDNA containing lanes in Figure 3.12. In the PEI only migration study a similar relationship between PEI concentration and migration distance was also observed. Further investigations would be required to confirm this relationship.

Critically, the use of higher percentage agarose electrophoretic loading for confined PEI polyplex synthesis appears, albeit in basic proof-of-concept studies, to be a completely novel translation of the previous Watanabe and Kamitakahara electrophoretic biomineralisation methods as well as further advancing on the Feichtinger GAM patterning approaches. Moreover, it importantly

shows considerable potential as a method for not only potentially preserving polyplex transfection activity within 3D hydrogels (via restricted aggregation due to biomaterial confinement) but also allowing for distinct biomaterial payload patterning and gradient formation.

For comparative purposes, the closest analogous report regarding this type of polyplex synthesis within hydrogel systems was those presented by Lei *et al*, in which a caged nanoparticle encapsulation method (or CnE) was applied to preserve polyplex population transfection efficacy within 3D PEG, HA and fibrin hydrogels (Lei *et al*., 2010; Lei *et al*., 2011). In these studies, combinations of high viscosity sucrose and agarose solutions were added to freshly made (dilute) polyplex populations – with the specific aim of restricting Brownian motion behaviours and therefore the formation of larger polyplex aggregates. Using lyophilisation processes, polyplexes were then incorporated as powders during cross-linking and cell-hydrogel formation (NIH 3T3 encapsulated PEG, HA or fibrin hydrogels). Significantly, such hydrogels were then able to illustrate *in-vitro* and *in-vivo* gene transfer after sustained cellular culture, infiltration and hydrogel degradation. However, despite this success, they remained unable to control the spatial distribution of said unaggregated polyplexes, with non-uniform micro-domains present particularly within the final cross-linked gels (Lei *et al*., 2010; Lei *et al*., 2011).

With this in mind, our results provide tentative evidence for a similar caging effect, brought on in this case by the nanosized hydrogel pore confinement properties of agarose hydrogels restricting polyplex aggregation behaviours. Clearly, additional optimisation and characterisation investigations must be performed to fully characterise if polyplex populations were indeed truly formulated using this method, however for this PhD project the F-AGE polyplex strategy provided significant encouragement for at least primary transfection testing, via agarose GAM scaffold creation (as performed in chapter 5).

3.5 Conclusion

In summary, the increased percentage of agarose hydrogel (3 wt%) demonstrated resistance to bulk surface area shrinkage and agarose fibre chain collapse during lyophilisation. The resulting freeze-dried 3% agarose scaffolds exhibited a suitable morphology (porous, 200 μm pores) for 3D tissue engineering biomaterials, featuring a highly interconnected and microporous structure with a pore size distribution ranging from 40 μm to 900 μm. Although the mean pore size was significantly lower than that of 1 wt% agarose scaffolds (215 μm versus 388 μm), it remained within acceptable limits for osteochondral tissue engineering scaffold systems. This was hypothesized to be sufficient for various cellular processes, including infiltration, migration, nutrient transfer, and proliferation. Subsequently, the F-AGE-1 methodology was adapted for use with 3 wt% agarose hydrogels. Protocols were successfully modified to enable simultaneous *in-situ* electrophoretic deposition of inorganic nanosized crystal precipitates and proximally

patterned nucleic acid payloads within the 3 wt% gel. This process was hypothesized to initiate co-localisation, possibly forming pDNA-nanoparticle co-complexes with promising properties, including hypothesized small particle diameters (< 300 nm). Additionally, a novel F-AGE strategy was developed, allowing for the simultaneous *in-situ* electrophoretic deposition of PEI cationic polymers alongside proximally patterned pDNA payloads, representing an entirely unexplored research avenue.

Overall, within the scope of this thesis, this chapter provides essential primary validation data for the generation of a 3D microporous scaffold system as well as two highly promising agarose electrophoretic GAM loading platforms. These agarose GAM platforms now necessitate for further characterisation and testing, particularly in the areas of freeze-dried agarose scaffold cytotoxicity, 3D cellular adhesion, and 3D transfection capability. As such, the respective chapters 4, and 5 will delve into each of these aspects in greater depth, with the ultimate aim of validating both F-AGE-1 co-localised GAM scaffolds and F-AGE polyplex co-localised GAM scaffolds for their ability to perform as transfection capable osteochondral GAM biomaterials.

CHAPTER 4

INVESTIGATION INTO THE CYTOTOXICITY AND CELLULAR ADHESION CAPABILITIES OF POROUS AGAROSE SCAFFOLDS AND THE EFFECTS OF DIFFERENT SURFACE COATING METHODS

4 CHAPTER 4: INVESTIGATION INTO THE CYTOTOXICITY AND CELLULAR ADHESION CAPABILITIES OF POROUS AGAROSE SCAFFOLDS AND THE EFFECTS OF DIFFERENT SURFACE FUNCTIONALISATION METHODS

4.1 Introduction

The pillars of biocompatibility, cytotoxicity and cellular adhesion are considered crucial for the application of GAM scaffolds in osteochondral tissue repair. The terms are often grouped collectively and generally refers to a scaffold's ability to effectively interact with and not destroy living cellular material such that its 3D surfaces may act specifically as stable sites for cellular adherence, migration, proliferation, differentiation and matrix deposition (Krishani *et al.*, 2023). As GAM systems rely on cellular attachment and migration for the successful uptake of its surface bound or immobilised therapeutic DNA payloads, it is therefore essential that these primary cellular adhesion properties are exhibited by the chosen biomaterial framework (O'Brien, 2011).

As discussed in section 1.6.1.2.1, polysaccharide-derived biomaterials such as agarose exhibit multiple characteristics which lend themselves for use in a variety of therapeutic fields, with properties including self-gelling, water solubility, adjustable mechanical properties widely reported cytotoxicity, and favourable economic manufacture. As a result, applications to date have been wide ranging, with successes in areas such as nerve, bone, cartilage and skin tissue engineering (Miguel *et al.*, 2014; Sanchez-Salcedo *et al.*, 2008; Singh *et al.*, 2016; Stokols *et al.*, 2006). However, in many of these examples, there was the apparent requirement for additional coupling materials, functional group modifications or surface coatings, which aim to supplement or enhance the inherent properties of agarose previously discussed. Often this appears particularly motivated by the reported low cellular adherence capabilities of agarose hydrogels alone, which have the potential to severely limit any reparative performance observed upon cellular migration and infiltration (Mercey *et al.*, 2010; Varoni *et al.*, 2012).

In terms of enhancing scaffold mediated cellular adherence, the approaches fall under two main categories, 1) composite manufacture, 2) physical adsorption/surface functionalisation. Composite agarose biomaterials are the most commonly used method in tissue engineering, owing to the ease of additional material incorporation during agarose hydrogel synthesis and its maintenance for self-gelling upon formulation of hybrid blending solutions. Such examples include silk-agarose (Singh *et al.*, 2016), platelet-rich plasma-agarose (Yin *et al.*, 2014) and poly(ethylene) glycol-agarose hybrids (DeKosky *et al.*, 2010) all of which presented elevated cell attachment and biomechanical profiles allowing for effective functional tissue repair. Despite such clear benefits, one potential downside of this approach is the possibility of composite

induced severing of agarose hydrogel electrophoretic and electroendosmosis (EEO) capabilities, which can be only maintained via the delicate chemical constituent relationship between agarose polymer chains and negatively charged sulphate functional groups. As functional electrophoresis is fundamental for this project, agarose hybrids were therefore not considered a viable option as a cell adhesion augmentation approach.

In contrast, physical adsorption techniques can avoid such pitfalls with its specific application as a post hydrogel/scaffold fabrication adhesion augmentation step. In most successful literature cases, the method simply involves the incubation of fabricated scaffolds in solutions containing bioactive molecules, which then attach on the exterior and also penetrate to the interior and affix via physical surface interactions through Van der Waal forces, electrostatic forces, hydrophobic interactions and hydrogen bonds. Crucially, such biomolecule attachment fundamentally alters surface material characteristics which promotes cellular adhesion, increased surface hydrophilicity, positive surface charge density and presentation of binding motifs.

For this thesis three cell attachment/bioactive molecules were considered as contingencies should the inherent cell adhesion characteristics of the freeze-dried agarose scaffolds and electrophoretic GAMs be inadequate, therefore physical adsorption of fibronectin, laponite-PEO, and polydopamine to agarose scaffolds was investigated.

Fibronectin (FN) is a multifunctional modular glycoprotein produced by a range of cell types (hepatocytes, fibroblasts, macrophages) and normally resides within plasma and as part of the extracellular matrix (ECM) which surrounds cells (Palomino-Durand *et al.*, 2021). This protein plays a significant role within the ECM, mediating several physiological processes such as cellular adhesion, regulating phagocytosis, wound healing, cell proliferation and locomotion (Mosher, 1984). In terms of cell adhesion specifically, fibronectin contains unique peptide sequences such as RGD and PHSRN within its modular protein architecture, which are highly specific for integrin cell surface receptor binding (Garcia *et al.*, 2002). Such moieties make this protein a highly pertinent avenue for its use as a grafting/surface coating system whereby cells interact with an exposed protein coating instead of direct biomaterial surface adhesion, thus delivering the desired cell attachment in 3D. This can be seen in reports by Franck *et al* and Arredondo *et al*, in which low adhesion biomaterials such as gel spun silk and polycaprolactone-polyurethane (PCL-PU) were successfully functionalised via a gentle non-damaging fibronectin adsorption strategy, providing hope that agarose scaffolds could be similarly augmented (Arredondo *et al.*, 2021; Franck *et al.*, 2013). It must be clarified that the use of Fibronectin as a surface coating, as stated above, is considered a distinctly separate method to that used in chapter 3 of this thesis, whereby Fibronectin was electrophoretically patterned within the agarose hydrogels.

Laponite® (or LAP) is a commercially available synthetic smectite which is part of the phyllosilicate clay mineral family and can be characterised by its unique crystal structure whereby

two tetrahedral silica sheets sit between a single Mg^{2+} containing octahedral sheet (Tomas *et al.*, 2018). It has an empirical formula of $Na^{+}_{0.7}[(Si_8Mg_{5.5}Li_{0.3})O_{20}(OH)_4]^{-}$ and has both positive and negatively charged regions which allow for the electrostatic formation of nanoplatelets with diameter and thickness of 25 nm and 1 nm respectively (Atrian *et al.*, 2019; Castro-Aguirre *et al.*, 2018). Although it has wide ranging applications such as household cleaning and personal care products (due to its rheological modification and film forming properties), it has been used more recently in the biomedical field, concerning drug delivery, bioimaging and as bioactive tissue engineering coatings (Tomas *et al.*, 2018). As surface coatings, LAP possesses good hydrophilicity, biodegradability, cytotoxicity and importantly allows for the deposition of beneficial films onto scaffold biomaterials, thus augmenting higher adhesion based characteristics. Significantly, one physical adsorption method reported by both Gaharwar *et al* and Orafa *et al* proved highly successful, whereby nanocomposites of LAP-PEO were deposited onto PLA nanofibers, improving overall scaffold hydrophilicity and therefore enhancing downstream MC3T3- E1 and hMSC 3D cell adherence and attachment (Gaharwar *et al.*, 2012; Orafa *et al.*, 2021).

Drawing inspiration from the remarkable bioadhesive properties observed in marine mussels, facilitated in particular by the 3,4-dihydroxy-L-phenylalanine-lysine (DOPA-K) motifs within the mussel foot protein, scientists have successfully synthesized a synthetic analogue known as polydopamine (PDA) (Yu *et al.*, 1999). This innovative biomimetic material exhibits a host of advantageous properties and has revolutionised the field of scaffold surface functionalisation. Notably, its production involves a straightforward self-polymerisation reaction where the base constituent dopamine polymerises under basic conditions and in the presence of oxygen (Tolabi *et al.*, 2022). This process culminates in the formation of an adhesive eumelanin polymer product, characterised by exceptional adhesive strength. The adhesive strength of polydopamine has been attributed to the presence of highly reactive functional groups within its chemical structure, including amines, imines, and catechols (Gao *et al.*, 2019). This unique feature allows polydopamine to serve as a versatile surface coating for a wide range of biomaterial substrates, including synthetic polymers, ceramics, bioinert metals, and polysaccharide hydrogels.

A key facet of polydopamine's versatility lies in its ability to significantly enhance the adhesion capacity of scaffold systems, with the presence of functional groups facilitating the immobilisation of an extensive array of bioactive molecules, growth factors, and extracellular matrix (ECM) proteins onto the scaffold surface (Ku *et al.*, 2010). This transformative capability empowers the PDA-modified scaffold to actively engage in critical cellular signalling processes and tissue regeneration mechanisms. Moreover, polydopamine's inherent cellular adherence and low cytotoxicity ensures that the modified scaffolds provide a conducive environment for fundamental cellular activities, including proliferation, differentiation, and extracellular matrix deposition. The successful works of Tsai *et al* and Wang *et al* and Su *et al* were considered highly

applicable to this thesis and the suitability of PDA as a bioactive/cell adhesion coating for agarose scaffolds was investigated. (Su *et al.*, 2021; Tsai *et al.*, 2011; Wang *et al.*, 2019).

An in-depth investigation regarding the biocompatibility of the agarose scaffolds previously formulated in chapter 3 will therefore greatly aid the progression of the overall Feichtinger electrophoretic GAM patterning platform, elucidating its inherent adhesion capability when biologically relevant cell lines are applied. It will also indicate whether surface functionalisation mechanisms are indeed required. The respective cell line L929 was selected for cytotoxicity testing whilst C2C12 and Y201 cell lines were selected for agarose-cell biomaterial adherence assessments.

4.2 3D scaffold cell adhesion testing specification

The following testing specification was constructed as an experimental blueprint for examining overall cell response, adhesion and viability upon cell seeding within the range of different fabricated agarose scaffolds. The specification is detailed in Table 4.1.

Table 4.1 – 3D scaffold testing specification and testing parameters. Progression through each stage required the provision of reliable data of which conclusively illustrated evidence of each criterion.

	Property	Minimum Requirements or Criteria	Methodology of testing
Stage-1	1.1: Capacity for cell-scaffold adherence	Presentation of large cell numbers on the scaffold surface after initial seeding and staining procedures (48 hours)	LIVE-DEAD staining
	1.2: Maintain viable 3D cell populations	High proportion of live/viable cell populations after 48 hours and 7 days culture	LIVE-DEAD staining
	1.3: Typical/classic 3D cell morphology	All seeded cells appear elongated, interconnected with no signs of stress	LIVE-DEAD staining
Stage-2	2.1: Indication of metabolic activity	Strong indication of cellular metabolism which increases over time (48 hours – 7 days)	AlamarBlue Assay
Stage-3	3.1: Capacity for cell infiltration	Strong evidence of cell permeation throughout the entire geometric scaffold structure	H&E Histological staining
Stage-4	4.1: 3D differentiation potential	Strong support for cell mediated deposition of osteogenic and chondrogenic factors	Osteogenic and chondrogenic histological staining

For the evaluation of potential scaffold biomaterials as 3D GAM systems, effective cell-scaffold adherence and viability, as well as the desired morphological behaviour upon cell interaction, were considered of greatest initial importance As such, these were included within the stage-1 testing specifications for each iteration of agarose scaffolds tested. Although viability was required for longer time periods (up to 28 days) in later studies, the viability at 48 hours and 7 days was considered adequate for initial appraisal of the approach in question. If stage 1 testing outcomes were deemed acceptable, metabolic indicators, as outlined in stage 2, were then evaluated, providing a quantifiable and distinguishable metric for scaffold specific cell health and proliferation. After this, scaffold permeability and infiltration were then evaluated to ensure scaffolds possessed feasible routes of infiltration to therapeutic payloads deposits. Finally,

scaffolds would then be evaluated for their 3D cellular differentiation capacity, considered the final, essential metric required of a osteochondral GAM system.

4.3 Specific materials & methods

4.3.1 Sterility testing

Biomaterial systems used for tissue engineering applications including *in-vitro*, *in-vivo* and clinical testing must adhere to aseptic principles to primarily prevent and restrict the emergence of pathogenic micro-organisms within the system, ensuring safety.

Thioglycolate and tryptone Soya broth mediums were therefore applied to establish bacterial growth capacities of fabricated agarose scaffolds with or without the application of a sterilisation agent. Thioglycolate broth acts as a multi-purpose medium allowing the cultivation of both aerobic and anaerobic organisms, whilst tryptone soya is able to cultivate aerobes, facultative anaerobes and limited fungi.

A working thioglycolate medium was generated by dissolving 2.97g thioglycolate USP (Sigma Aldrich) powder in 100 mL distilled water. The mixture was allowed to dissolve by heat-mixing at 90°C, then aliquotted into glass bottles and autoclaved (121°C, 2.4 bar, 15 minutes). Formulations suitable for sterility testing appeared straw-coloured with a characteristic thin pink upper layer, as seen in Figure 4.1. A working tryptone soya medium was generated by dissolving 15g tryptone soya (Sigma Aldrich) powder in 500 mL distilled water. Upon mixing and subsequent aliquot, the mixture was autoclaved at 121°C for 15 minutes (2.4 bar).

Figure 4.1 – Prepared Thioglycollate broth pre-autoclave sterilisation (left) and post-autoclave sterilisation (right).

4.3.1.1.1 Methodology for testing ethanol mediated agarose GAM Sterilisation

3 wt% agarose hydrogels, 3%-Blank agarose scaffolds, as well as a 3 wt% F-AGE-1 GAM scaffold (AGE1-2.5-225mM), were removed from the F-AGE-1 GAM fabrication process at different stages and, depending on the sample, were either treated with an ethanol sterilisation process or left untreated/un-sterilised. The different fabrication stages were either: 1) hydrogel excision directly from buffer submerged agarose slab or 2) after subjection to freeze-drying procedure.

The stated ethanol sterilisation process included the following steps: scaffolds were removed from freeze-dryer, placed inside individual wells of 48 well plate, then incubated and washed three times with ice-cold 70% ethanol (10 minutes per wash, room temperature). Ensuring residual ethanol was removed, plates were transferred to a -80°C freezer for 1 hour, before freeze-drying overnight.

Consequently, under asceptic conditions, scaffold samples (n=1 per group) were then placed directly into thioglycollate and tryptone soya broths and cultured at 37°C for 48 hours and two weeks, at which point both broths were visually inspected for signs of microbial and/or fungal growth. A negative control (sterile broth without agarose sample) and a positive control (contaminated inoculation loop) were also included.

4.3.2 Contact cytotoxicity

4.3.2.1.1 Assessment of F-AGE-1 electrophoretic GAMs (±FN)

Using the electrophoretic patterning methodologies outlined in chapter 2 section 2.2.2.1, a range of F-AGE-1 electrophoretic GAM hydrogels were formulated (FN± : AGE1-2.5-0mM– AGE1-2.5-225mM). In the FN containing scaffolds, FN was incorporated electrophoretically and thus is situated *in-situ* alongside pDNA-CaP payloads. Next, using freeze-drying and sterilisation methodologies, all hydrogels were converted into sterilised porous agarose scaffolds.

At this stage, samples were individually placed and anchored inside the wells of a 6 well plate, using tailored Steri-strips (3M Steri-Strip SkinClosure 3x75mm, Medisave), as shown in Figure 4.2 A. For the control groups, there was a cell only control, a steri-strip only negative control and a cyanoacrylate adhesive glue positive control (Figure 4.2 B). In the latter, a single drop was deposited in the centre of the well as per the photograph.

A

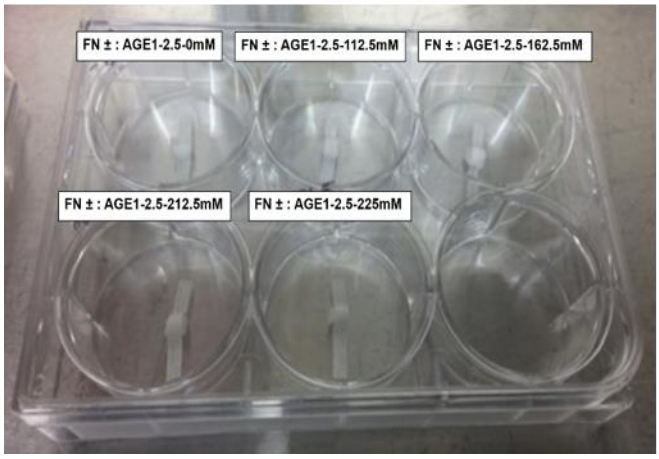

B

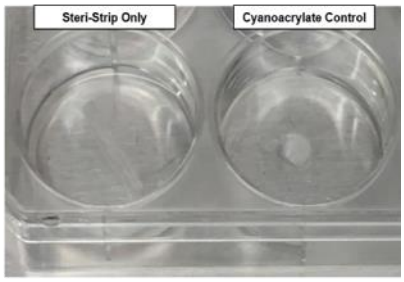

Figure 4.2 (A & B) – Contact Toxicity Sample and Control Layout. A: F-AGE-1 GAM scaffolds were anchored to the 6-well plate surface using a steri-strip. B: Control wells containing a Steri-strip only and a cyanoacrylate adhesive (positive control for cytotoxicity).

L929 cells were passaged and re-suspended to concentrations of $2.5x10^5$ cells/mL before seeding as a 2 mL cell suspension into well plates (n = 3 per group for both FN- and FN+ agarose GAMs as well as each control group). Cells were left to incubate with the agarose GAMs for a duration 48 hours, in 5% CO_2 at 37°C. Following incubation, samples were initially viewed under phase contrast to investigate cell morphology, membrane integrity as well as the presence of dead cells proximal to the scaffold-cell monolayer interface.

Following this, the depleted media was extracted and the sample wells washed twice with PBS (with calcium and magnesium). The PBS was removed and replaced with 2 mL neutral buffered formalin (NBF) 10 minutes. After fixation, Giemsa stain was added to completely cover the cell monolayer and scaffolds and further incubation occurred for 5 minutes. Samples were then carefully washed with tap water to remove excess dye solution and allowed to dry overnight. Finally, the samples were then examined under brightfield microscopy.

4.3.3 Extract toxicity

Using the same sample preparation technique as previously described in section 4.3.2, a range of F-AGE-1 electrophoretic GAM hydrogels (FN± : AGE1-2.5-0mM– AGE1-2.5-225mM) were once more fabricated, freeze-dried and sterilised. Extract solutions for each scaffold sample were then formulated inside sterilised 1.5 mL Eppendorf tubes by immersing scaffolds (n=4) in 1 mL serum free media (SFM) and subsequently incubating them for 72 hours (37°C, 5% CO_2) under constant agitation (250 rpm). For the control groups, an aliquot of 1 mL serum free media (SFM) alone was also taken and agitated using the same conditions.

After 48 hours of extract agitation (of the total 72 hours), a confluent L929 culture was, at this point, passaged and re-suspended to concentrations of $5x10^4$ cells/mL before seeding as a 200 µL cell suspension into flat 96 well plates (n=4 per group for both FN- and FN+ extract subsets, n=6 for negative and cell lysis (positive control) subsets)), as per the plate layout shown in Figure 4.3.

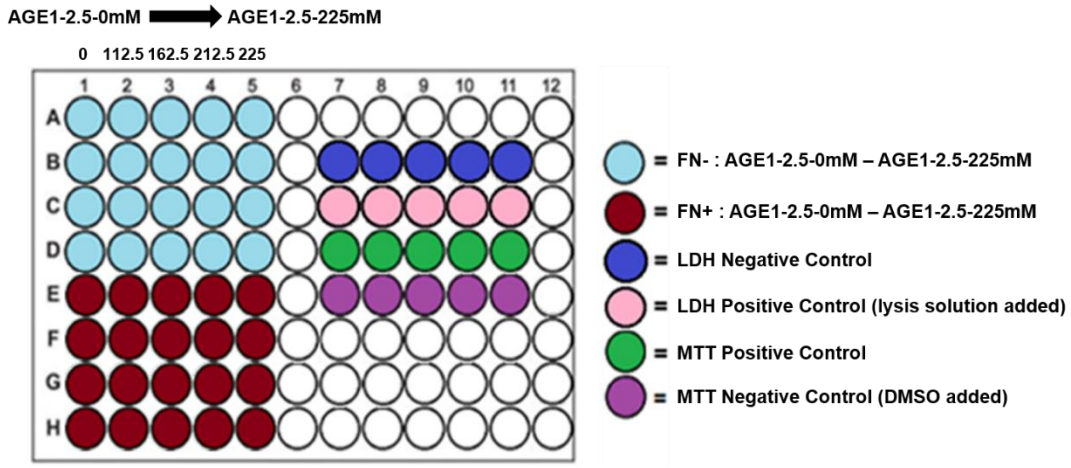

Figure 4.3 – Dual Plate layout for Extract Cytotoxicity (LDH) and Viability testing (MTT). L929 cells were seeded in each coloured well at a density of $5x10^4$ cells/mL. Extract solutions (100 µL) were added 24 hours later.

24 hours later (72 hours total), cell culture media within 96 well plates were aspirated and replaced by 100 µL double strength media alongside either 100 µL test extract or negative control medium. Cell-extract suspensions were then incubated for another 24 hours before LDH and MTT assay execution (as described below).

4.3.3.1.1 Methodology for LDH cytotoxicity assay

Commercial lactate dehydrogenase (LDH) assay kits, such as the CytoTox 96® Non-Radioactive Cytotoxicity kit (Promega), can be employed to allow quantitative assessment of cellular viabilities in the presence of either a drug treatment, a biomaterial or an extract solution. As such, in this study, this kit was applied to elucidate and quantify the cytotoxicity of electrophoretic GAM extracts, utilising the concept that levels of LDH detected within each sample is directly proportional to percentage cell death.

According to manufacturer's instructions, a 50 µL aliquot of sample or control supernatant was transferred to a new flat bottom 96 well plate. Additionally, 10 µL 10X cell lysis solution was applied to positive control wells assigned as the LDH positive control or "maximum LDH release control" and incubated for 45 minutes. 50 µL substrate mix (12 mL Assay Buffer (Promega) added to vial of lyophilized substrate (Promega)) was then added to all samples and gently mixed. The plate was dark adapted for 30 minutes allowing the reaction to progress before incorporating the 50 µL stop solution. Using a Varioskan flash microplate reader (Thermo Scientific) the 96

well plate was read at 490nm with absorbance reading corrected according to background values. The following formula was used to calculate percentage cytotoxicity (equation 4.1):

$$\% \text{ Cytotoxicity} = \frac{\text{Experimental LDH Release } (OD_{490})}{\text{Maximum LDH Release } (OD_{490})} \times 100 \qquad \textbf{4.1}$$

4.3.3.1.2 Methodology for MTT viability assay

In contrast to the LDH assay which assesses cell death via detection of a cell death marker in supernatant, an MTT (3-(4,5-dimethylthiazol-2-yl)-2,5-diphenyltetrazolium bromide) assay measures viable cell proliferation within a cell monolayer, using a tetrazolium specific dye. As such, in this study, the commercial CellTiter 96® Non-Radioactive Cell Proliferation Assay (Promega) kit was also applied.

According to manufacturer's instructions, after sufficient incubation with extract, 15 μL pre-mixed optimised Dye solution (Promega) was added to each sample well of a 96 well. The plate was incubated for 4 hours before the solution was removed. 100 μL or 1 mL of solubilisation solution (Promega) was then applied to the sample wells, sufficiently mixed and incubated again for 1 hour. The colour change within the wells was then quantified through absorbance readings (570 nm) using a plate reader. The following formula was used to calculate percentage viability:

$$\% \text{ Viability} = \frac{\text{Experimental MTT Release } (OD_{570})}{\text{Maximum MTT Release } (OD_{570})} \times 100 \qquad \textbf{4.2}$$

4.3.4 Cellular adhesion assessment of uncoated agarose scaffolds (stage-1)

4.3.4.1 Evaluation of media-pre-conditioning

Using established methods, 3%-Blank agarose scaffolds were fabricated and sterilised. The scaffolds, prior to cell seeding, were either pre-conditioned with complete cell culture medium or left in a dry form before being placed inside each well of a treated 48 well plate (static seeding conditions: method 1 or method 2). A high density C2C12 or Y201 cell solution of 2.5×10^5 Cells was added to each scaffold (n=2 per conditioning method), according to static seeding methodologies outlined in section 2.2.4. Scaffolds were then cultured under static 3D conditions for either 48 hours or 7 days before fluorescent microscopy analysis, via LIVE-DEAD viability assay (section 2.2.6).

4.3.4.2 Evaluation of F-AGE-1 payload patterning (±FN)

F-AGE-1 agarose GAMs (FN±: AGE1-0mM, AGE1-225mM) were fabricated, freeze-dried and ethanol sterilised, as per sections 2.2.2.1, 2.2.3. Using method 2 static seeding conditions, a high

density C2C12 or Y201 cell solution of $2.5x10^5$ cells was subsequently added to each scaffold (n=2 per group), according to static seeding methodologies outlined in section 2.2.4. 3%-Blank was used as the control group. Scaffolds were cultured for 48 hours and 7 days before fluorescent microscopy analysis, via LIVE-DEAD viability assay (section 2.2.6).

4.3.5 Cellular adhesion assessment of surface coated agarose scaffolds (stage-1)

4.3.5.1 Evaluation of FN surface coating

Using the fibronectin coating methodology (chapter 2, section 2.2.4.1), 3%-Blank agarose scaffolds were functionalised with either 25 μg/mL or 50 μg/mL fibronectin (FN) solutions, producing the following scaffold formulations: 3%-FN25 and 3%-FN50. After subsequent lyophilisation and ethanol sterilisation, each scaffold type was seeded with either C2C12 or Y201 cells at a cell density of $2.5x10^5$ cells/scaffold (n=2 per group). Uncoated 3%-Blank scaffolds were used as controls. All of the following 3D culture conditions as well as cell attachment and viability analysis remained consistent with those described in section 4.3.4.1.

4.3.5.2 Evaluation of LAP-PEO surface coating

Using the LAP-PEO dip-diffusion methodology (chapter 2 section 2.2.4.2), 3%-Blank agarose scaffolds were surface functionalised. Agarose scaffolds were submersed and incubated in either 40 mg/mL or 120 mg/mL LAP-PEO solutions for 4 hours before lyophilisation and ethanol sterilisation. At this stage functionalised scaffolds were denoted as LAP40 or LAP120. Each group was then seeded with either C2C12 or Y201 cells at a cell density of $2.5x10^5$ cells/scaffold (n=3 per group). 3D static cell culture conditions and cell attachment and viability analysis remained consistent with those described in section 4.3.4.2.

4.3.5.3 Evaluation of PDA surface coating

Using the PDA coating methodology (chapter 2, section 2.2.4.3), 3%-Blank agarose scaffolds were again functionalised. Using two different PDA concentrations (1 mg/mL or 2 mg/mL) and incubation times ranging from 4 hours to 24 hours, coatings of various densities were deposited onto and within the porous scaffolds, as per Table 4.2.

Table 4.2 – The range of PDA functionalised agarose scaffolds fabricated when different dopamine solution concentrations and immersion times were used.

Scaffold Name	Dopamine Concentration (mg/mL)	Immersion Time (hrs)
3%-Blank	N/A	N/A
3%-PDA4.1	1	4

3%-PDA4.2	2	4
3%-PDA8.1	1	8
3%-PDA8.2	2	8
3%-PDA12.1	1	12
3%-PDA12.2	2	12
3%-PDA24.1	1	24
3%-PDA24.2	2	24

After subsequent washing, lyophilisation and sterilisation, each scaffold group was seeded with either C2C12 or Y201 cells at a cell density of $2.5x10^5$ cells/scaffold (n=2 per group). 3%-Blank scaffolds were used once more as controls. The preceding 3D culture conditions, as well as cell attachment and viability analysis remained consistent with those described initially in section 4.3.4.1.

4.3.6 Cellular adhesion assessment of PDA coated agarose scaffolds (stage-2)

4.3.6.1 Evaluation of PDA surface coating on cellular proliferation (alamarBlue)

4.3.6.1.1 Optimisation of alamarBlue assay parameters

For accurate quantitative measurements of 3D cell metabolism and proliferation on agarose scaffolds, cell seeding density and alamarBlue incubation time must initially be optimised for the scaffold system in question. Crucially, for assay success, the parameters in question must be optimised using a scaffold system which has a proven ability for cell viability and attachment. As this could not be achieved with uncoated agarose scaffolds, the 3%-PDA8.2 PDA scaffold group was selected for use in the following 3D alamarBlue parameter optimisation experiment.

3%-PDA8.2 scaffolds were fabricated and placed in wells of a 48 well plate (static seeding condition 1). Y201 cell solutions of different cell densities were then formulated ($1.25x10^5$, $2.5x10^5$, $3.75x10^5$, $5x10^5$ cells/scaffold) and subsequently seeded using static seeding methodologies (section 2.2.5.1). After 2-3 hours, scaffolds were transferred into round bottom 96 well plates containing 200 µL alamarBlue working solution and incubated over a 6 hour period. Fluorescence intensity was measured at 2, 3, 4 and 6 hours and compared to a fully reduced working alamarBlue sample. Parameters were deemed optimal if percentage alamarBlue reduction over the specified duration was exponential and remained below 50 percent.

4.3.6.1.2 Cell proliferation assay

Using optimised assay parameters from the previous section, Y201 cell proliferation was evaluated on a range of PDA coated agarose scaffolds, with the aim of ascertaining the most effective PDA functionalisation condition. All fabricated groups were evaluated except 3%-PDA4.1, 3%-PDA-24.1 and PDA-24.2. Static seeding 1 conditions were applied before seeding

of each scaffold with C2C12 or Y201 cells at a density of $1.25x10^5$ cells/scaffold. Seeded scaffolds were incubated for either 48 hours or 7 days before alamarBlue assay was performed, according to methods outlined in section 2.2.7.

4.3.7 Cellular adhesion assessment of PDA coated agarose scaffolds (stage-3)

4.3.7.1 Effect of PDA surface coating and seeding density on cellular infiltration

The extent of cellular infiltration into PDA functionalised agarose scaffolds using basic 3D static seeding techniques was assessed using histological processing and staining techniques. Experimentally, 3%-PDA-8.2 scaffolds were statically seeded with Y201 cells at a seeding density of either $2.5x10^5$ or $5x10^5$ cells/scaffold (n=2 per cell density), cultured for 24 hours and then histologically processed and H&E stained, as per section 2.2.7.

To ascertain infiltration capacities, each scaffold post processing was successively sliced in a longitudinal fashion throughout its bulk, with each progressive section (n=3 per geometric section location) then undergoing H&E staining. Through this procedure, a tentative geometric picture of cell seeded agarose scaffolds can be generated. The geometries of acquired sections were assigned according to distance from the first whole longitudinal section generated from the wax block. "Surface" sections were acquired from the first 0-500 μm, "middle" sections were acquired from 2000-3000 μm, "end" sections were acquired from 4500-5000 μm.

4.3.7.2 Optimisation of static seeding procedures

In response to histology data, the static seeding methods were modified to further improve attachment and infiltration efficiency of 3%-PDA-8.2 functionalised scaffolds. Such modifications included the application of an agarose hydrogel layer to the bottom of the well plate. This technique was performed to prevent cell adhesion to surfaces other than the scaffold (Browe *et al.*, 2019; Guler *et al.*, 2023).

In the modified static seeding method, a 3 wt% agarose hydrogel solution was first formulated with sterile deionised water and subsequently autoclaved. Before cooling, 250 μL solution was transferred to each well of a 48 well plate, ensuring complete coverage of the well surface. Wells were subsequently washed twice with PBS and complete media to remove unattached agarose material. This modification to conditions was therefore termed "static seeding conditions method 3".

The cell seeding protocol as described in section 4.3.7.1 was then repeated using both normal 48 well plate wells or agarose treated wells (n=2 per group), with a cell seeding density of $5x10^5$ cells/scaffold. Analysis was performed using H&E staining as per section 4.3.7.1.

4.3.8 Effect of PDA surface coating on cellular differentiation (stage-4)

Prior to examining the supportive capacity of PDA coated agarose scaffolds for osteogenic and chondrogenic differentiation, the inherent tri-lineage differentiation capability of Y201 cells was successfully validated within a 2D cell monolayer context. Results of this experiment are shown in the appendix Figure 8.3

4.3.8.1 Scaffold osteochondral differentiation

3%-PDA-8.2 scaffolds were fabricated and then assigned to one of three differentiation conditions; basal media scaffolds (BS), osteogenic media scaffolds (OS) and chondrogenic media scaffolds (CS) (n=3). Using static seeding conditions method 3, scaffolds were prepared and seeded with a Y201 cell density of $5x10^5$ Cells/Scaffold. After 2-3 hours, 800 µL complete basal media was added to all groups. Following a further 24 hours incubation, media from BS sample groups was exchanged for fresh complete basal media, whilst media from each OS and CS sample groups was exchanged for 800 µL osteogenic and chondrogenic media, respectively (Table 4.3). Cell seeded scaffolds were subsequently cultured for 7, 21 and 28 days under standard conditions (37°C, 5% CO_2) with media replaced every 2-3 days. At each timepoint, the level of scaffold differentiation was evaluated using histological osteochondral differentiation staining procedures.

Table 4.3 – Constituents of osteogenic and chondrogenic media. ITS: Insulin-Transferrin-Selenium.

Osteogenic Medium		**Chondrogenic Medium**	
Supplement Name	**Final Concentration**	**Supplement Name**	**Final Concentration**
Complete DMEM	N/A	SFM (with 2mM L-Glutamine, 100 $U.mL^{-1}$)	N/A
L-Ascorbic acid-2-phosphate (50 mg/mL)	50 µg/mL	L-Ascorbic acid-2-phosphate (50 mg/mL)	50 µg/mL
ß-Glycerophosphate (500 mM stock)	5 mM	L-Proline	40 µg/mL
Dexamethasone (10 µM stock)	10 nM	Dexamethasone (10 µM stock)	100 nM
		ITS-1 (100X)	1X
		hTGF-ß3	10 ng/mL

4.3.8.1.1 Alizarin Red staining

Alizarin Red staining was applied to histological sections to visualise extracellular calcium deposits indicative of cellular differentiation towards an osteogenic lineage. A working staining solution was produced by adding 0.25 g Alizarin Red S powder to 12.5 mL distilled water. The pH was then adjusted via dropwise addition of ammonium hydroxide, filtered and stored in the dark. Sections were dewaxed and dehydrated following the same protocol outlined in section 2.2.8.1. Alizarin Red S working solution was added dropwise to each sample and incubated in the dark for 30 minutes. Excess dye was carefully blotted away. Sections were finally cleared in xylene, mounted using DPX mountant, then imaged using an BX51 inverted microscope (Olympus).

4.3.8.1.2 Safranin O staining

Safranin O staining was applied to histological sections to visualise cartilage-like glycosaminoglycans (GAG) and proteoglycan content. The associated staining pattern is characteristically represented by an increasing intensity of red colour in areas of high GAG content juxtaposed with a fast green countered stain. Working staining solutions of 0.1% w/v Safranin O and 0.02% w/v Fast Green were made by adding 500 mg Safranin O powder (Raymond Lamb, Eastbourne, UK) or 100 mg Fast Green powder (Sigma, UK) to 500 mL distilled water, respectively. Fresh sections (no older than two days) were similarly dewaxed and rehydrated following the protocol outlined in section 2.2.8.1. Slides were subsequently immersed in Weigert haematoxylin for 3 minutes, washed in tap water, and then differentiated in 1% acid-alcohol (5 mL 1% conc. hydrochloric acid in 495 mL 70% ethanol) for 1 minute. After this, slides were placed for 5 minutes in 0.02% aqueous fast green stain, transferred briefly to a 1% acetic acid chamber before being left to drain. A further immersion in 0.1% Safranin O for 4 minutes followed before dehydration in an ethanol series (5 seconds - 70% ethanol, 1 minute – 100% ethanol IV, 2 minutes – 100% ethanol V, 3 minutes – 100% ethanol VI) and a final clearance in xylene (10 minutes – xylene III, 10 minutes – xylene IV). Sections were DPX mounted, visualised and captured as described in section 4.3.8.1.1.

4.3.9 Physical & Chemical characterisation of Polydopamine coatings

4.3.9.1 Scanning Electron Microscopy analysis

3%-Blank, and 3%-PDA-8.2 scaffolds were fabricated and sterilised before standard SEM imaging protocols for bulk scaffold imaging were followed to completion (section 3.2.1.1).

4.4 Results

The following results section will illustrate the outcomes of various agarose scaffold formulations upon extensive sterility, cytotoxicity and cellular adherence testing.

In terms of the adherence testing, experimentation was carried out as per the testing criterion set out in section 4.2. Stage progression was only achieved upon reliable illustration of each testing metric.

4.4.1 Sterility of F-AGE-1 GAMs

Sterility testing was performed on various agarose hydrogels and scaffolds at two timepoints to test if a basic ethanol sterilisation procedure resulted in the appearance of bacterial and/or yeast contamination in containment broths. Visual confirmation of sterility was captured at 48 hours and 14 days, as illustrated in Figure 4.4 and Figure 4.5.

Assessment of sample thioglycollate broths at both timepoints (Figure 4.4) revealed no observable changes or bacterial growth were detected in any samples which underwent ethanol sterilisation. Furthermore, 66% of sample groups which did not undergo a sterilisation procedure also presented as uncontaminated cultures. Conversely group A samples, taken at the wet hydrogel fabrication stage without ethanol sterilisation, illustrated initial pink layer subsidence followed by a turbid, straw coloured bacterial growth, within the O_2-rich layer, at two weeks. This matched comparable observations from positive control groups.

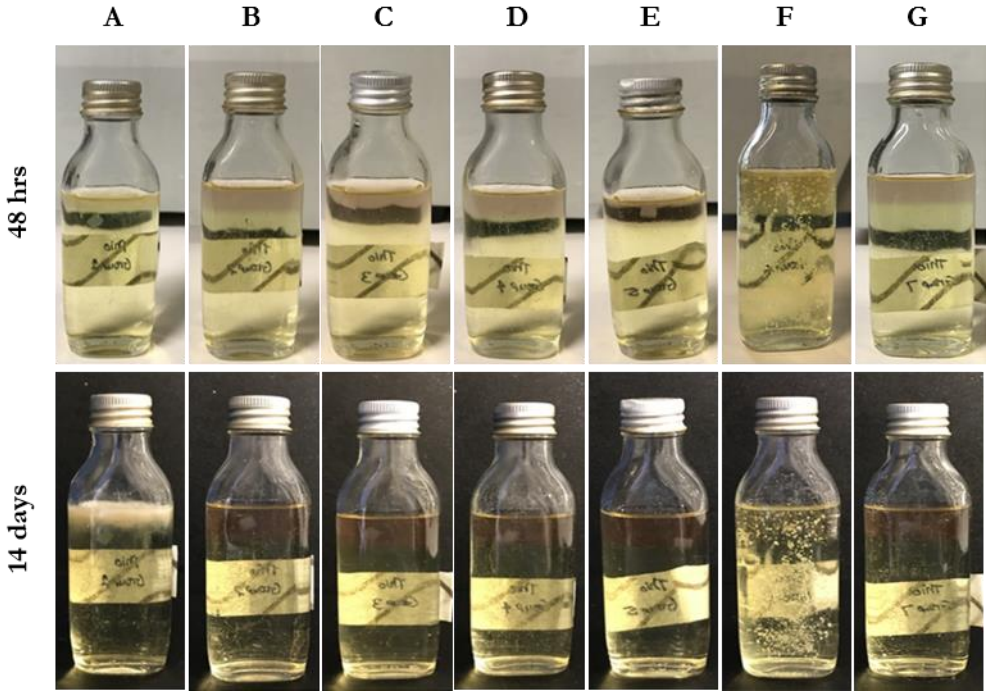

Figure 4.4 – Sterility testing of agarose scaffolds taken at different stages of the fabrication process, using thioglycolate medium. A: 3% Agarose hydrogel (without EtOH), B: 3%-Blank (without EtOH), C: 3%-Blank (with EtOH), D: 3% AGE1-2.5-225mM (without EtOH), E: 3% AGE1-225mM (with EtOH wash), F: Positive Control, G: Negative Control.

Assessment of sample tryptone soya broths at both timepoints (Figure 4.5) similarly illustrated an absence of observable bacterium in all ethanol sterilised sample groups. Formulated agarose hydrogels (group A) and agarose GAM (group D) produced substantial bacterial growth after two weeks, matching turbid string-like infections produced in positive control broths.

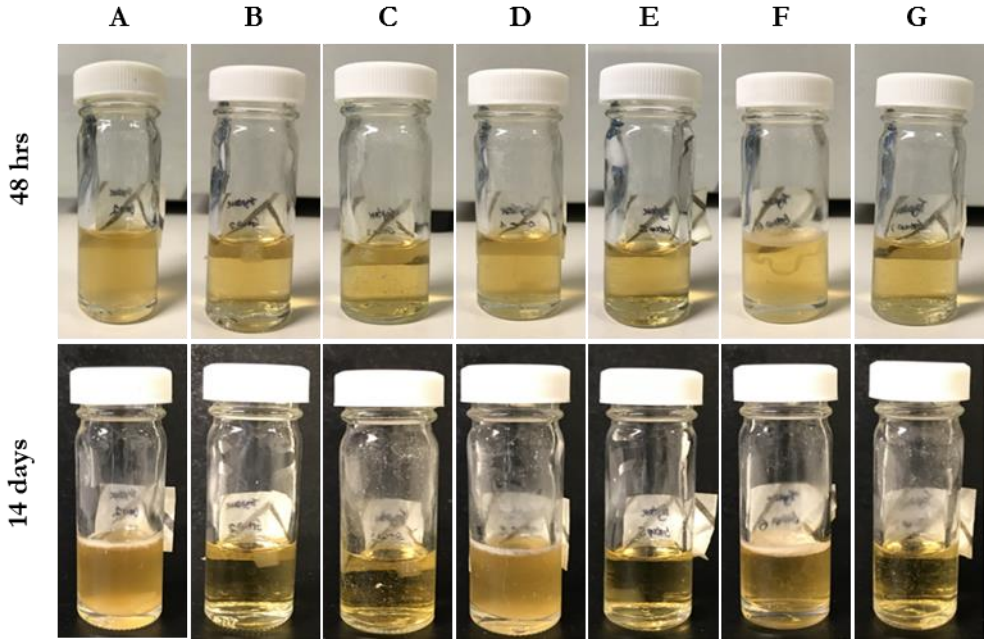

Figure 4.5 – Sterility testing of agarose scaffolds taken at different stages of the fabrication process, using tryptone soya medium. A: 3% Agarose hydrogel (without EtOH), B: 3%-Blank (without EtOH), C: 3%-Blank (with EtOH), D: 3% AGE1-2.5-225mM (without EtOH), E: 3% AGE1-225mM (with EtOH wash), F: Positive Control, G: Negative Control.

4.4.2 Contact toxicity of F-AGE-1 GAMs (± FN)

L929 cells were incubated with a range of fabricated agarose F-AGE-1 GAMs, alongside positive and negative controls, and tissue culture plastic, to evaluate the *in-vitro* cytotoxicity over a 7 Day culture period. Microscopy images captured for each scaffold formulation are shown in Figure 4.6 and Figure 4.7. Steri-strips have been previously shown in the lab to support cell growth so were deemed sufficient as both the anchoring mechanism as well as the negative control (Fermor *et al.*, 2015) whilst cyanoacrylate – which is known to be locally cytotoxic, was used as a positive control.

The cell only and steri-strip only controls were used in this experiment as negative controls for cytotoxicity, and as such provided an example of normal L929 morphology and growth (Figure 4.6 H and F). In comparison, the cyanoacrylate control (Figure 4.6 G), showed clear proximity based cellular cytotoxicity and lack of growth up to the substance layer.

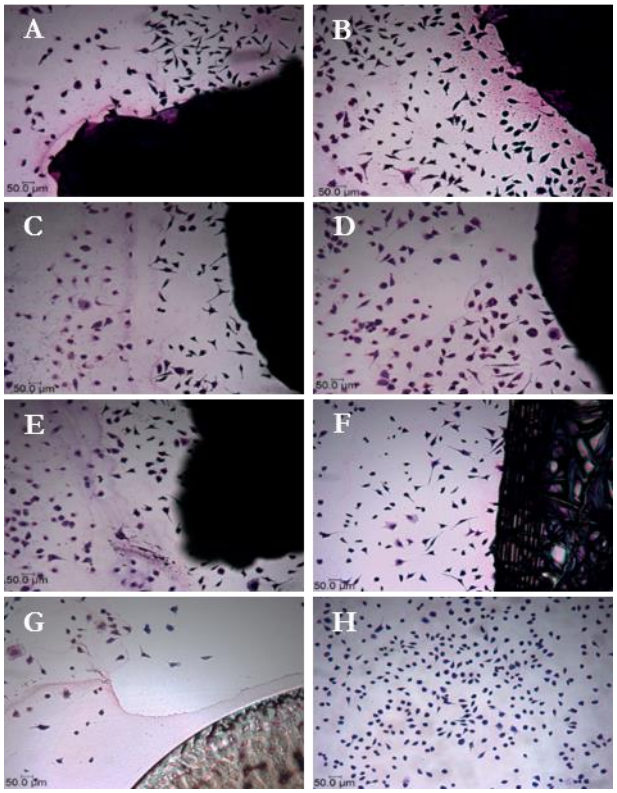

Figure 4.6 – Contact Cytotoxicity assay on a range of electrophoretic agarose GAM scaffolds (FN-). Images A-E show the growth of L929 cells in the presence of electrophoretic agarose GAMs (A: AGE1-0mM, B: AGE1-112.5mM, C: AGE1-162.5mM, D: AGE1-212.5mM, E: AGE1-225mM). Customary cell growth was established in the presence of all scaffolds and made contact with agarose scaffolds in all cases. Growth and contact was also identified in the presence of the steri-strips + cells negative control (F) whilst the cells were severely restricted in the presence of the cyanoacrylate positive control (G). Cells grown on tissue culture plastic alone (H) illustrated sufficient cell numbers and morphology. Scale-bar = 50 μm.

Upon visual analysis of the electrophoretic agarose F-AGE-1 GAM samples (FN ±) (Figure 4.6 and Figure 4.7), normal growth patterns were identified, showing similarities to those cultured with steri-strips and on tissue culture plastic. Furthermore, cells grew up to and made contact in some form with all anchored scaffolds. In one scaffold group (AGE-1-2.5FN-0mM) (Figure 4.7A), a marginal inhibitory zone was identified with cell-scaffold contact not being illustrated. Interestingly, in comparison to the cell only control, L929 cells in the presence of agarose GAMs generally displayed a more heterogeneous morphological profile, with an observable increase in spindle-like cells forming across these cultured populations. As this behaviour was also identified in the steri-strip only group however, this was deemed acceptable. In FN+ containing scaffolds, spindle-shaped cell morphologies were also identified.

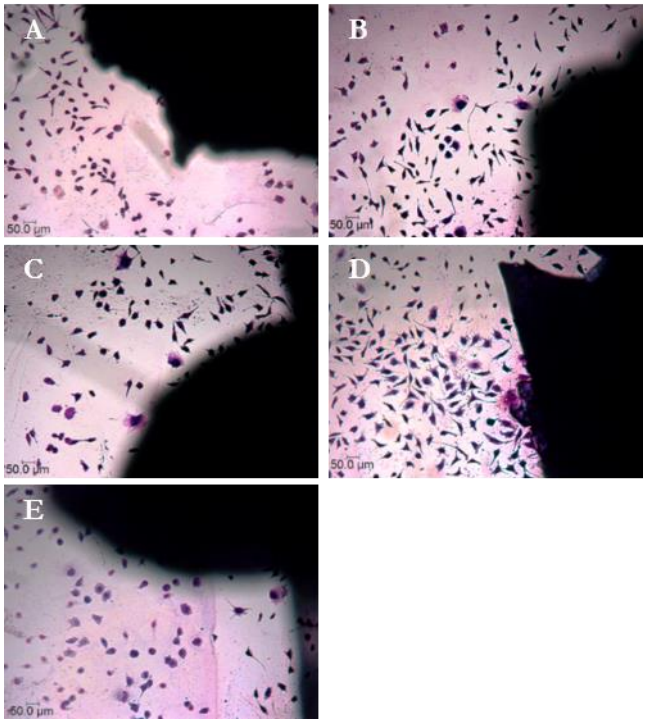

Figure 4.7 – Contact Cytotoxicity assay on a range of electrophoretic agarose GAM scaffolds (FN+). Images A-E show the growth of L929 cells in the presence of electrophoretic agarose GAMs (FN+) (A: AGE1-2.5FN-0mM, B: AGE1-2.5FN-112.5mM, C: AGE1-2.5FN-162.5mM, D: AGE1-2.5FN -212.5mM, E: AGE1-2.5FN-225mM). L929 cells grew normally in the presence of fibronectin containing GAM scaffolds and made contact in all cases with biomaterial perimeters. Scale-bar = 50 µm.

4.4.3 Extract cytotoxicity of F-AGE-1 GAMs (± FN)

After 24 hours exposure to electrophoretic agarose GAM extracts (FN ±), LDH and MTT assays detected only a small loss of L929 viability, in terms of percentage cell death and percentage viability, as illustrated below. Importantly however, Figure 4.8 A illustrates that one group, specifically in the FN+ subset (AGE-1-2.5FN-0mM), produced a statistically significant difference when compared to the negative control ($P = 0.0326$). This further validates the qualitative assertions made in section 4.4.2, specifically regarding the possible inhibitory/cytotoxic zone generated by this specific scaffold type. Despite this, no differences were identified across any of the other tested groups. This latter finding was corroborated with MTT viability counts (Figure 4.8 B), whereby all groups passed the mean percentage viability threshold of 70%, the minimum level of cytotoxicity acceptable for applied biomaterials, as set out in the ISO standard for medical devices (ISO 10993-5:2009 – Biological evaluation of medical devices). Furthermore, no significant differences were identified between any of the tested groups when compared against the SFM extract positive control, thus illustrating all generated GAM extracts possessed similar cytotoxic potential to a media only control.

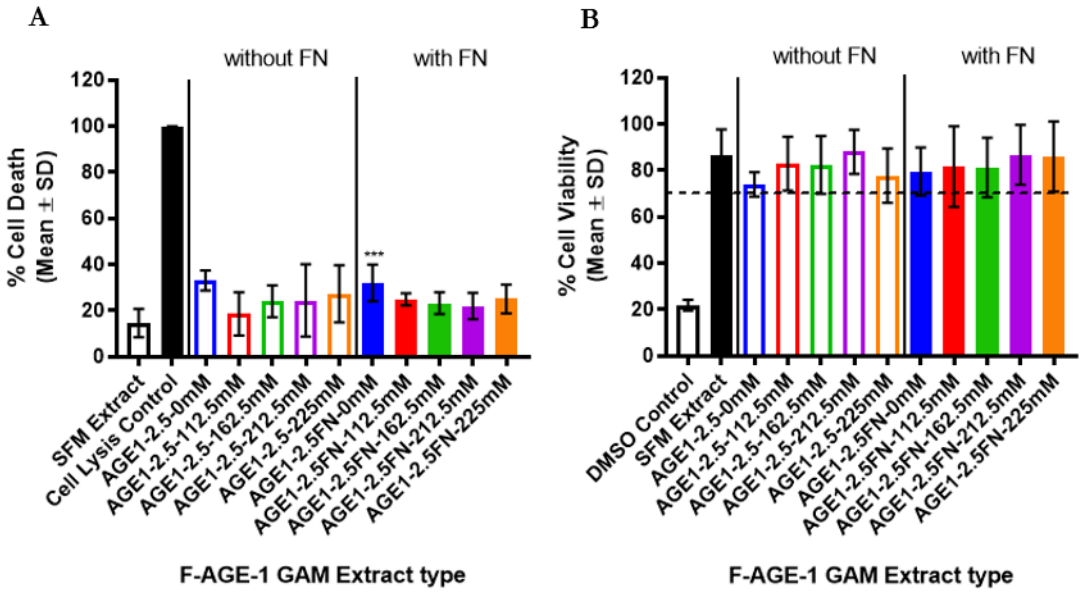

Figure 4.8 (A & B) – Quantitative assessment of percentage L929 cell death and viability after exposure to a range of electrophoretic agarose GAM extracts (FN ±). L929 cells were cultured for 24hrs in the presence of agarose GAM extracts before performance of LDH assay (A) and MTT assay (B) (n=4). SFM extract was used as a negative control (n=6). Data was expressed as mean percentage cell death/cell viability (± SD) when compared to a separate LDH positive control and a MTT negative control. One-way ANOVA with Tukey's multiple comparison test was used after Arc-Sin transformation of the data and compared across the independent variables. *** = $P < 0.001$ compared to SFM extract control.

4.4.4 Cellular behaviour within uncoated agarose scaffolds

As described in section 4.3.4, a variety of unmodified freeze-dried agarose scaffold formulations were first evaluated for their inherent cellular adherence. This included blank agarose control scaffolds, pre-conditioned blank scaffolds and electrophoretically loaded agarose scaffolds (including fibronectin containing payloads).

4.4.4.1 Effect of pre-conditioning on cell attachment

Scaffold pre-conditioning is considered a simple yet effective method within 3D biomaterial cell culture contexts to help facilitate and improve cellular attachment and adhesion, mainly acting via the beneficial presence of pre-deposited serum proteins on scaffold surfaces (Amirikia *et al.*, 2017). Uncoated 3%-Blank agarose scaffolds were therefore tested to evaluate if a similar phenomenon could aid agarose scaffold-cell adherence. As such, scaffolds were either pre-conditioned with complete cell culture medium or left in a dry form, prior to Y201 and C2C12 cell seeding.

At time of seeding, visual inspection indicated pre-conditioned scaffolds remained largely hydrated after the 1 hour dehydration step (Figure 4.9), but unfortunately only allowed absorption of approximately 30 µL cell suspension during seeding (60 µL total). Remaining cell volume in

all cases was noted to percolate directly out of the underside of scaffolds resting on tissue culture plastic. In contrast, dry scaffolds allowed full adsorption of cell suspension during seeding steps, via capillary action, to a near fully hydrated state crucially without leakage.

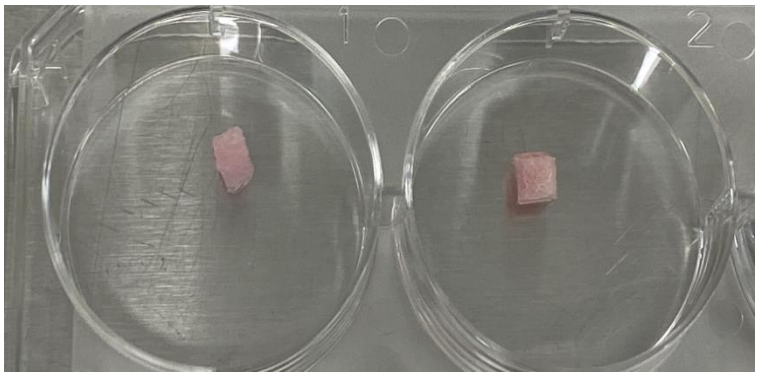

Figure 4.9 – Illustration of the growth media pre-conditioning process on 3%-Blank agarose scaffolds.

The impact of both procedures on scaffold-cell attachment was then assessed using the LIVE-DEAD assay. Following an initial 48-hour period of 3D culture (Figure 4.10), staining of cells within the scaffolds primarily revealed viable C2C12 and Y201 cells situated on the scaffold surfaces, albeit in relatively modest numbers compared to the high initial seeding density of $2.5x10^5$ cells per scaffold. Notably at this early timepoint, pre-conditioned scaffolds, particularly those seeded with Y201 cells, showed a reduction in viable cell count compared to their dry scaffold counterparts. Intriguingly, this decrease did not however correspond with any increase in cell non-viability (as indicated by red staining), implying that the pre-conditioning process did not induce noticeable cytotoxicity or harm to cell viability. It was further observed that the presented cellular morphologies across the seeded scaffolds consistently displayed a characteristic "stressed" or "cobblestone" appearance, appearing as distinct spheroidal cellular structures with no evidence of interconnectivity or elongation (Kim *et al.*, 2009). After prolonged culture (7 days), there was a noticeable decrease in viable cells across all groups, leaving only a small population visibly located to the scaffold surface. Additionally, the spheroidal morphologies observed earlier were sustained.

In light of these observations, and based on the scaffold testing criterion, it was concluded that 1) 3%-Blank scaffolds do not appear to provide a sufficiently bioactive surface capable of large scale cellular adhesion or long term viability and 2) that scaffold pre-conditioning appears ineffective at rectifying such issues. As a result, the pre-conditioning step was eliminated from all subsequent scaffold seeding experiments.

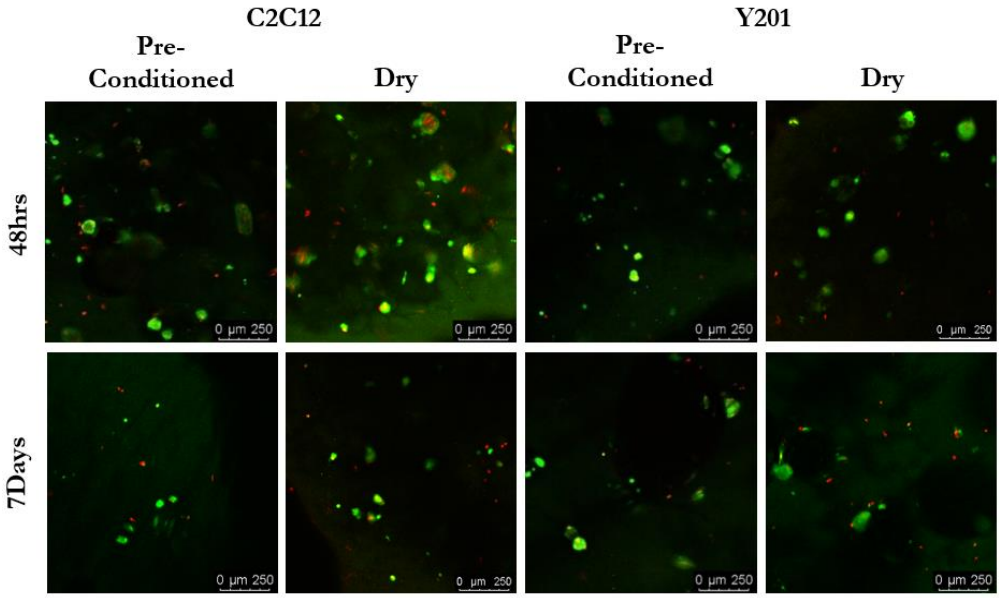

Figure 4.10 – Images of LIVE-DEAD stained C2C12 and Y201 cells following 48 hours and 7 days 3D culture on pre-conditioned or dry 3 wt% agarose scaffolds. Cells were seeded on 3%-Blank scaffolds using static seeding techniques with a density of $2.5x10^5$ Cells/Scaffold. Live cells are stained green and dead cells stained red. Scale bars = 250 µm

4.4.4.2 Effect of FN containing pDNA-nanoparticles on cell attachment

Uncoated 3 wt% F-AGE-1 agarose GAMs (AGE1-2.5-0mM, AGE1-2.5-225mM, AGE1-2.5FN-0mM, AGE1-2.5FN-225mM) alongside 3%-Blank scaffolds were similarly cultured with either C2C12 or Y201 cells before LIVE-DEAD staining at 48 hours and 7 days, as described in section 4.3.4.2.

Upon visual inspection of the F-AGE-1 GAM scaffolds lacking fibronectin (AGE1-2.5-0mM, AGE1-2.5-225mM) (Figure 4.11), similar cell attachment, viability and morphology characteristics were observed as previously outlined in Figure 4.10. It was noted however, that greater cell death occurred in Y201 seeded AGE1-2.5-225mM GAM scaffolds, at 7 days. As this did not appear in the C2C12 samples, it was hypothesised that Y201 cells may possess a greater degree of susceptibility to electrophoretically loaded co-localised payloads and thus the lower viability observed.

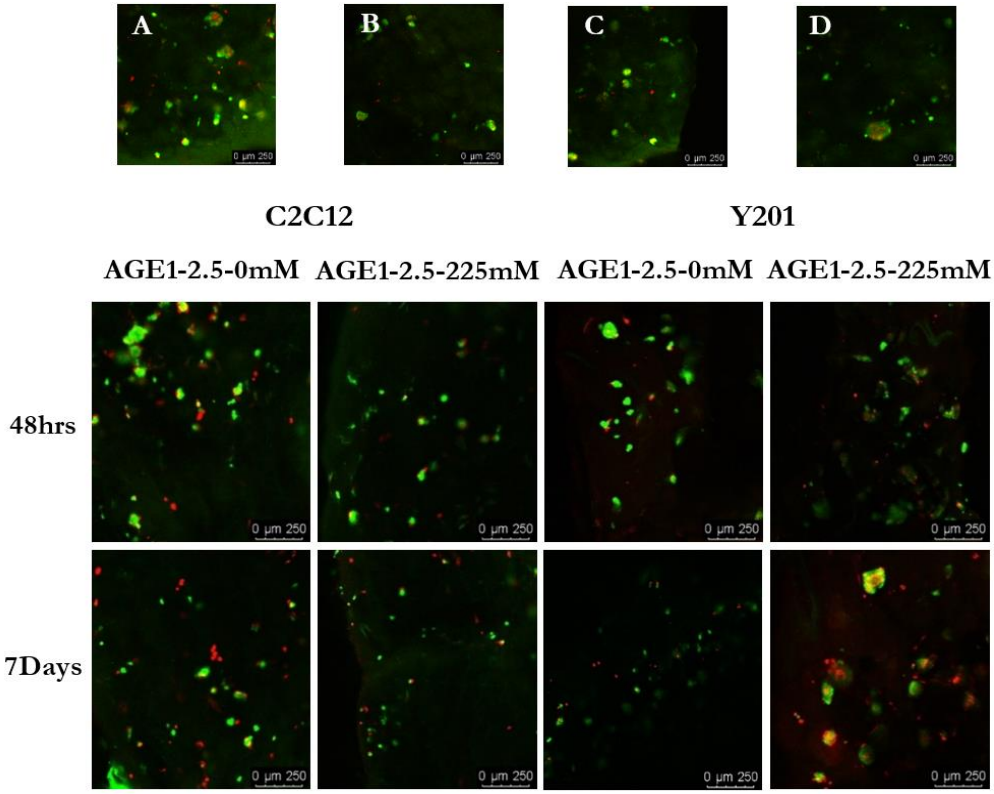

Figure 4.11 – Images of LIVE-DEAD stained C2C12 and Y201 cells following 48 hours and 7 days 3D culture on F-AGE-1 FN- GAMs. Cells were seeded using static seeding techniques with a density of $2.5x10^5$ Cells/Scaffold. GAMs were fabricated containing 2.5 µg pDNA-CaP nanoparticles (F-AGE-1 approach - plasmid used: pCAG-d2-eGFP). Live cells are stained green and dead cells stained red. Images A-B and C-D: 48hr and 7 day 3%-Blank control scaffolds seeded with C2C12 and Y201 cells, respectively. Images were captured specifically at CaP precipitate regions. Scale bars = 250 µm.

When F-AGE-1 GAM scaffolds containing fibronectin (AGE1-2.5FN-0mM, AGE1-2.5FN-225mM) were then examined (Figure 4.12), it was observed that the presence of electrophoretically loaded fibronectin appeared to induce initial positive effects with regards to cell-scaffold surface attachment, with all groups displaying marginally greater cell numbers when stained at 48 hours culture. However, when culture time was increased, such positive effects could not be sustained, with 7 day images revealing lower cell numbers across the groups with more cell death. Electrophoretically loaded FN also had no impact on cellular morphology, with spheroidal phenotypes consistently observed as shown in the previous agarose scaffolds.

Due to these results, it was postulated that the presence of electrophoretically co-localised pDNA-CaP or pDNA-FN-CaP precipitates did not significantly enhance the overall adherence attributes of 3 wt% agarose scaffolds. Crucially, none of the formulations were deemed capable of providing a long-term culture environment conducive to sustaining large 3D populations of C2C12 and Y201 cells, especially in the desired phenotype. As a result, this aspect of the research pertaining to uncoated agarose scaffolds was concluded at the first stage of the adhesion assessment (stage-1), with various methods for scaffold surface functionalisation now actively under development.

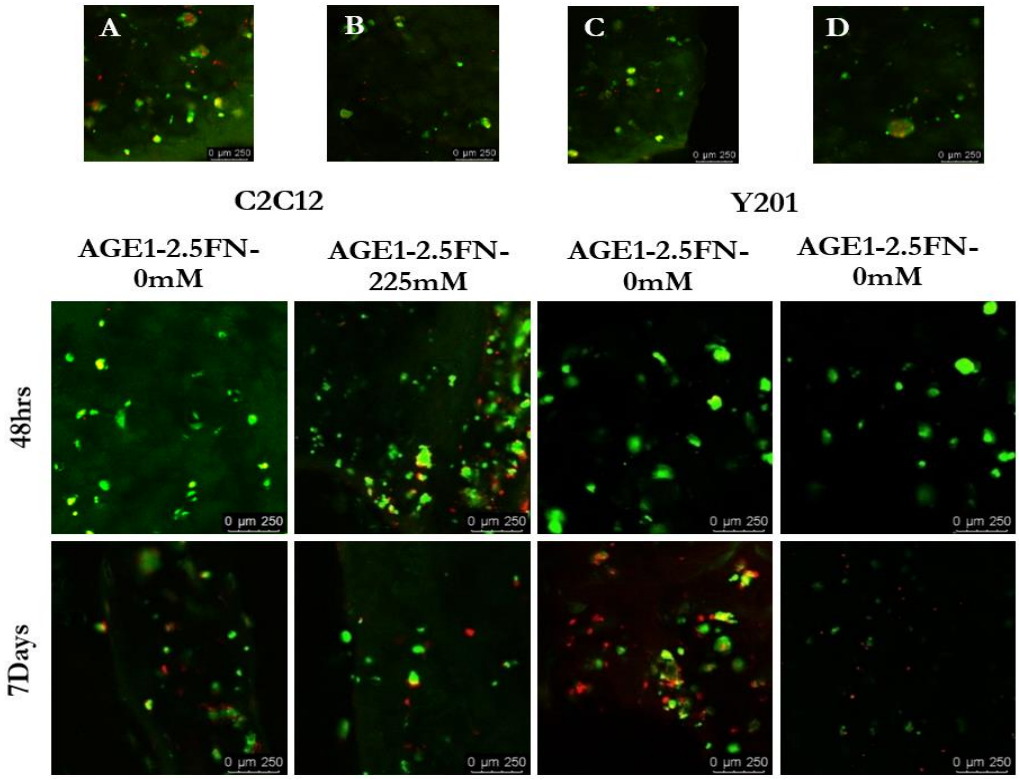

Figure 4.12 – Images of LIVE-DEAD stained C2C12 and Y201 cells following 48 hours and 7 days 3D culture on F-AGE-1 FN+ GAMs. Cells were seeded using static seeding techniques with a density of $2.5x10^5$ Cells/Scaffold. GAMs contained 2.5µg pDNA-CaP nanoparticles conjugated with 10µg FN (F-AGE-1 Approach - plasmid used: pCAG-d2-eGFP). Live cells are stained green and dead cells stained red. Images were captured specifically at CaP precipitate regions. Scale bars = 250 µm

4.4.5 Cellular behaviour within surface coated agarose scaffolds

4.4.5.1 Effect of FN surface coating on cell attachment, viability and morphology

In contrast to GAM scaffolds formulated via FN conjugation within CaP precipitates, alternative surface coated agarose scaffolds were fabricated using two different FN solutions (25 µg/µL and 50 µg/µL). Visual inspection of the cell viability images of all FN coated scaffolds (Figure 4.13) showed C2C12 and Y201 cells were present and viable but again in meagre numbers at 48 hours post seeding.

Viable cell numbers did however appear to remain steady when cultured for a further 5 days, with little obvious depletion. When FN concentration was increased, no visible change in cell numbers was identified, however 7 day images for both C2C12 and Y201 cells did appear less red. FN coatings also had no morphological impact on either cell type, presenting largely as round globular individual cell populations, much like the uncoated 3%-Blank controls.

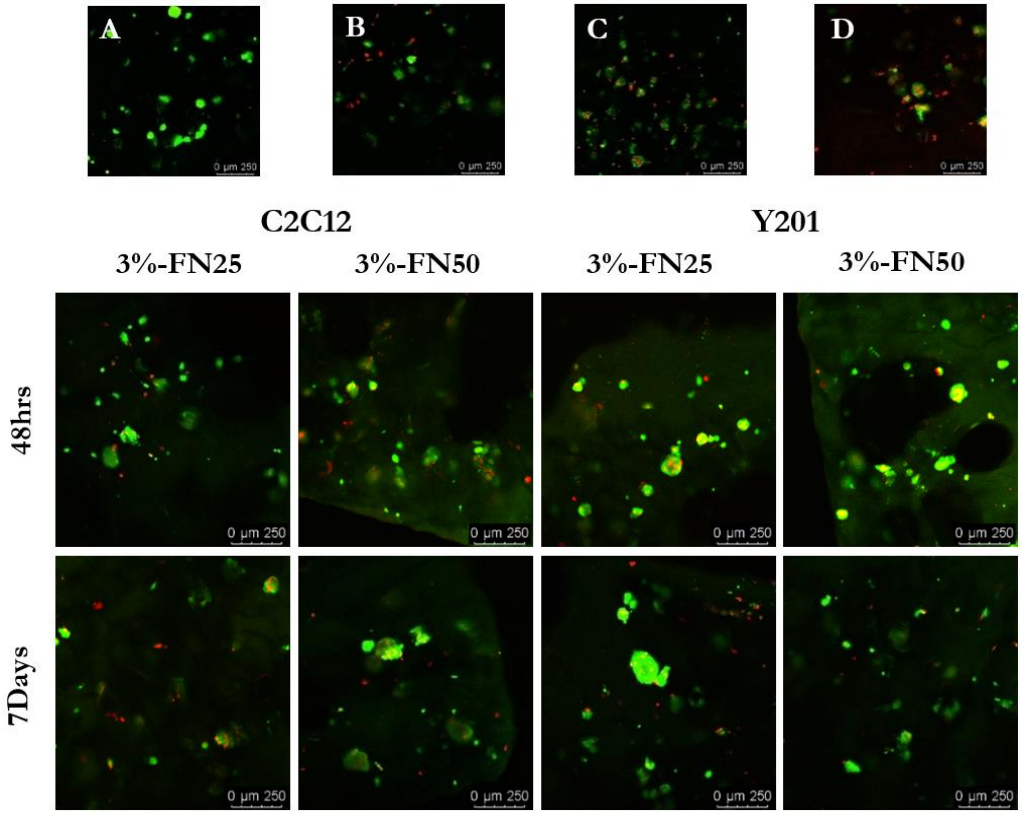

Figure 4.13 – Images of LIVE-DEAD stained C2C12 and Y201 cells following 48 hours and 7 days 3D culture on FN coated 3 wt% agarose scaffolds. Cells were seeded using static seeding techniques with a density of $2.5x10^5$ Cells/Scaffold. 3wt% agarose scaffolds were fabricated and functionalised with either 25 µg/mL or 50 µg/mL fibronectin. Images A & B: 48hr and 7 day uncoated agarose scaffold control (C2C12). Images C & D: 48hr and 7 day uncoated agarose scaffold control (Y201). Scale bars = 250 µm

4.4.5.2 Effect of LAP-PEO surface coating on cell attachment, viability and morphology

In addition to scaffolds coated with FN, an alternate method was developed and tested which deposited LAP nanoplatelets on agarose scaffold surfaces with the aim of improving cell attachment, long term viability and focal cell adhesion. High molecular weight PEO was used to physically crosslink LAP nanoplatelets and form a coating on the agarose scaffold. Two LAP-PEO solutions with concentrations of 40 mg/mL or 120 mg/mL were tested.

Following the surface deposition and freeze-drying process, the scaffolds displayed no obvious visual change in complexion or morphology, remaining white in colour and appearing porous. The presence of a white fluffy-like coating interspersed within the pores and the outer surfaces was noted. Upon handling, the mechanical integrity of the coated scaffolds remained consistent with uncoated controls.

Upon analysis, LAP-PEO scaffold LIVE-DEAD images illustrated a marginal improvement in cell-scaffold adherence after initial culture up to 48 hours, with the appearance of greater overall numbers of viable attached cells (C2C12 and Y201) identified when compared to uncoated

controls (Figure 4.14 A and C). In both cell lines, 40 mg/mL LAP-PEO scaffolds specifically appeared to contain the greatest proportion of attached cells however this apparent advancement did not improve cell morphology, with all cells remaining as distinct spheroids with no interconnectivity. In general, fewer cells were again present on the scaffolds after 7 days across all scaffold groups, indicating cellular adherence and proliferation was not maintained. Additionally, large amounts of LAP-PEO associated background EthD-III staining appeared across all groups at both timepoints (most acute at 7 days), which severely impeded effective viability analysis. The author hypothesises this to be colloidal laponite dispersions which appear as a result of its insolubility in water (Cummins, 2007).

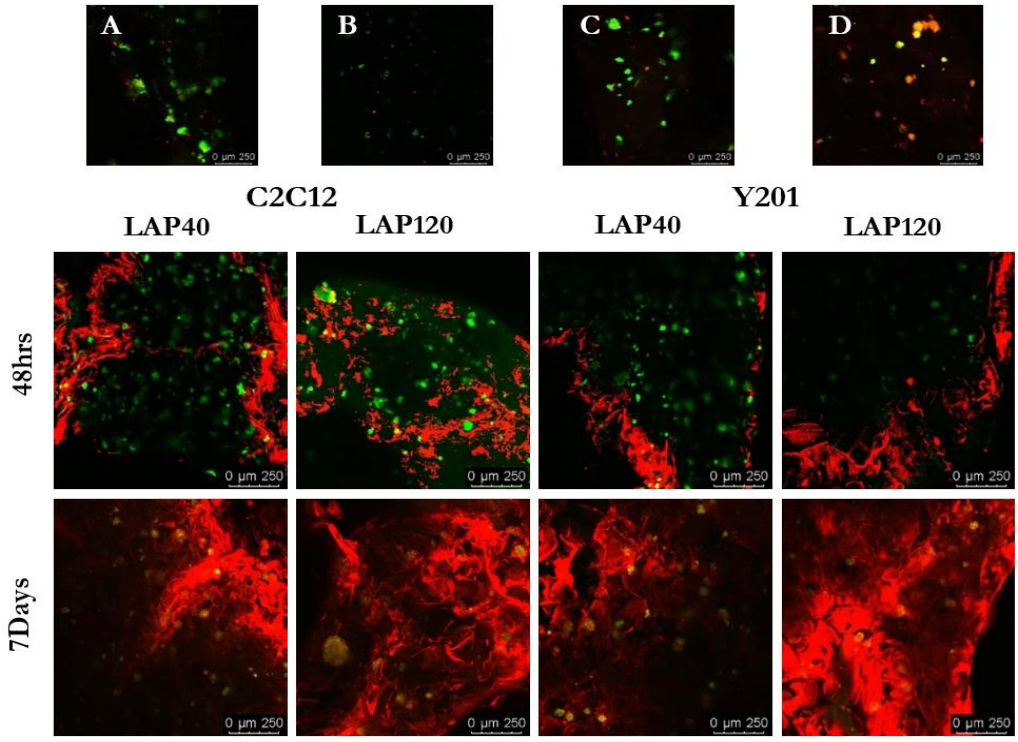

Figure 4.14 – Images of LIVE-DEAD stained C2C12 and Y201 cells following 48 hours and 7 days 3D culture on LAP-PEO coated agarose scaffolds. Cells were seeded using static seeding techniques with a density of $2.5x10^5$ Cells/Scaffold. 3 wt% agarose scaffolds were fabricated and functionalised with either 40 mg/mL or 120 mg/mL LAP-PEO solutions. Images A & B: 48hr and 7 day 3%-Blank control seeded with C2C12. Images C & D: 48hr and 7 day 3%-Blank control seeded with Y201. Scale bars = 250 µm.

4.4.5.3 Effect of PDA surface coating on cell attachment, viability and morphology

Using similar deposition-coating methodologies to the FN and LAP-PEO functionalised scaffolds, 3%-Blank agarose scaffolds were incubated in PDA solutions (1 mg/mL or 2 mg/mL) over the course of a 24 hour period, as described in section 2.2.4.3. C2C12 and Y201 cells were then 3D cultured in the scaffolds over a further 7 day period, and subsequently LIVE-DEAD stained to ascertain viability.

Completion of the PDA deposition protocol revealed a clear visual change in scaffold appearance, with scaffolds transitioning from a white to grey to black colour after 4, 8, 12 and 24 hours respectively (Figure 4.15). Moreover, 2 mg/mL PDA solutions induced a greater colour change for all agarose scaffolds, most noticeably at 4, 8, and 12 hours of immersion time. These findings suggested PDA film density and/or thickness increased with PDA solution concentration and immersion time. Crucially, coatings also remained consistent in colour after ddH_2O washing and subsequent freeze-drying procedures.

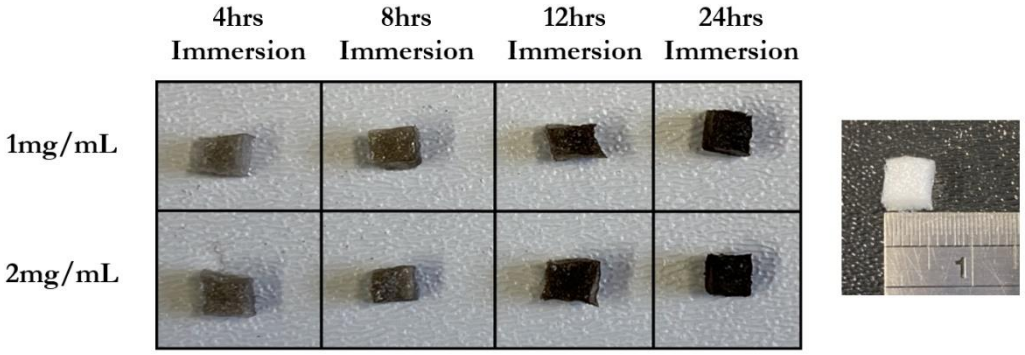

Figure 4.15 – Effect of immersion time and concentration on PDA deposition on agarose scaffolds. 3%-Blank were immersed in 1 mg/mL or 2 mg/mL dopamine solutions of different concentrations for 4, 8, 12 and 24 hours. Unattached PDA was removed with ddH_20 before freeze-drying. The amount of PDA incorporated and overall coating thickness could be controlled by increasing immersion time and PDA solution concentration. Right hand image showing uncoated 3%-Blank scaffold as reference.

Subsequent analysis of the stained 3 wt% PDA scaffold range, after 48 hours initial 3D culture, illustrated positive wholesale transformation across all experimental indictors including improvements to cell-scaffold attachment, the proportion of viable cells present and alterations to cellular morphology (cells presenting as classical elongated and interconnected fibroblast-like cells).

In terms of the effect of PDA immersion time, images initially suggested that coating for 4 hours only marginally improved Y201 and C2C12 cell adhesion and viability, in comparison to uncoated controls, with some instances of cell elongation and interconnectivity (Figure 4.16). When PDA immersion duration was increased further, up to 12 hours, cell adhesion and viability characteristics of the cell seeded scaffolds substantially improved, with large interconnected cell populations now visible on all sides of the biomaterial surface. Beyond this duration (i.e. at 24 hours immersion duration), cell adhesion capabilities appeared to decline with fewer numbers of viable cells detected on the scaffold surfaces, and in some cases cells with the previously described spheroidal phenotypes were observed. Interestingly, these cases were not accompanied with an overall increase in the numbers of dead cells (red staining), suggesting high PDA concentrations may not necessarily cause cytotoxicity. The effect of increasing PDA concentration (1 mg/mL versus 2 mg/mL) appeared to only result in marginal improvements to cell attachment and viability, up to 12 hours (Figure 4.16).

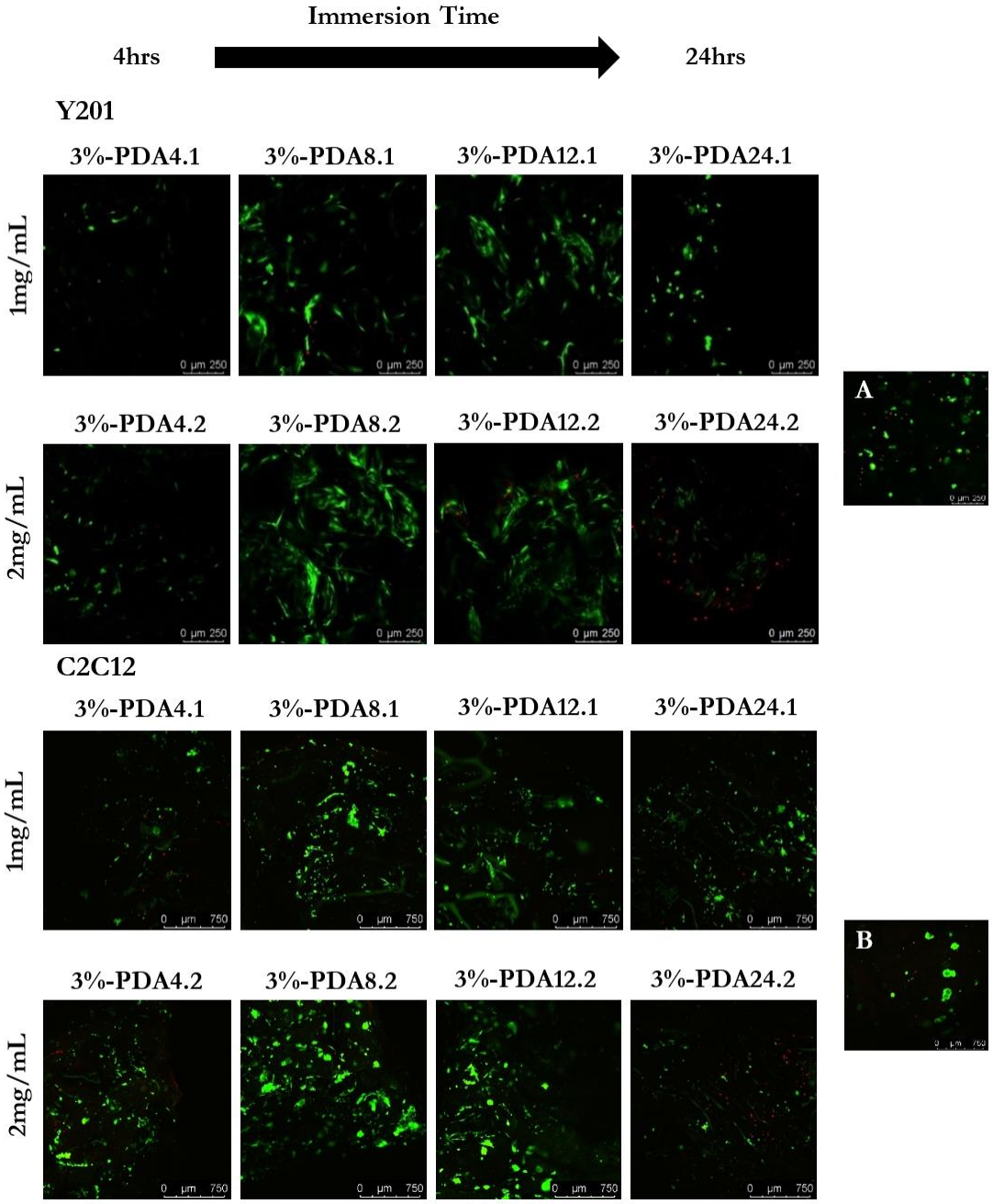

Figure 4.16 – Images of LIVE-DEAD stained Y201 and C2C12 cells following 48 hours 3D culture on Polydopamine (PDA) coated 3 wt% agarose scaffolds. Cells were seeded using static seeding techniques with a density of $2.5x10^5$ Cells/Scaffold. 3%-Blank agarose scaffolds were fabricated and functionalised by immersion in 1 mg/mL or 2 mg/mL PDA solutions over different time periods (4, 8, 12, 24hrs). Live cells are stained green and dead cells stained red. Images A and B: 3%-Blank scaffold controls seeded with Y201 and C2C12, respectively. Scale bars = 250 µm (Y201) and 750 µm (C2C12).

Significantly, after 7 days, clear viable cell populations could still be identified across all PDA coated scaffold groups with little evidence of cellular cytotoxicity (Figure 4.17). The previously classified cell morphologies were also maintained and now appeared highly interconnected over a large proportion of the scaffold surface, likely with permanent focal cell-scaffold adhesions as well as crucial cell-cell contacts.

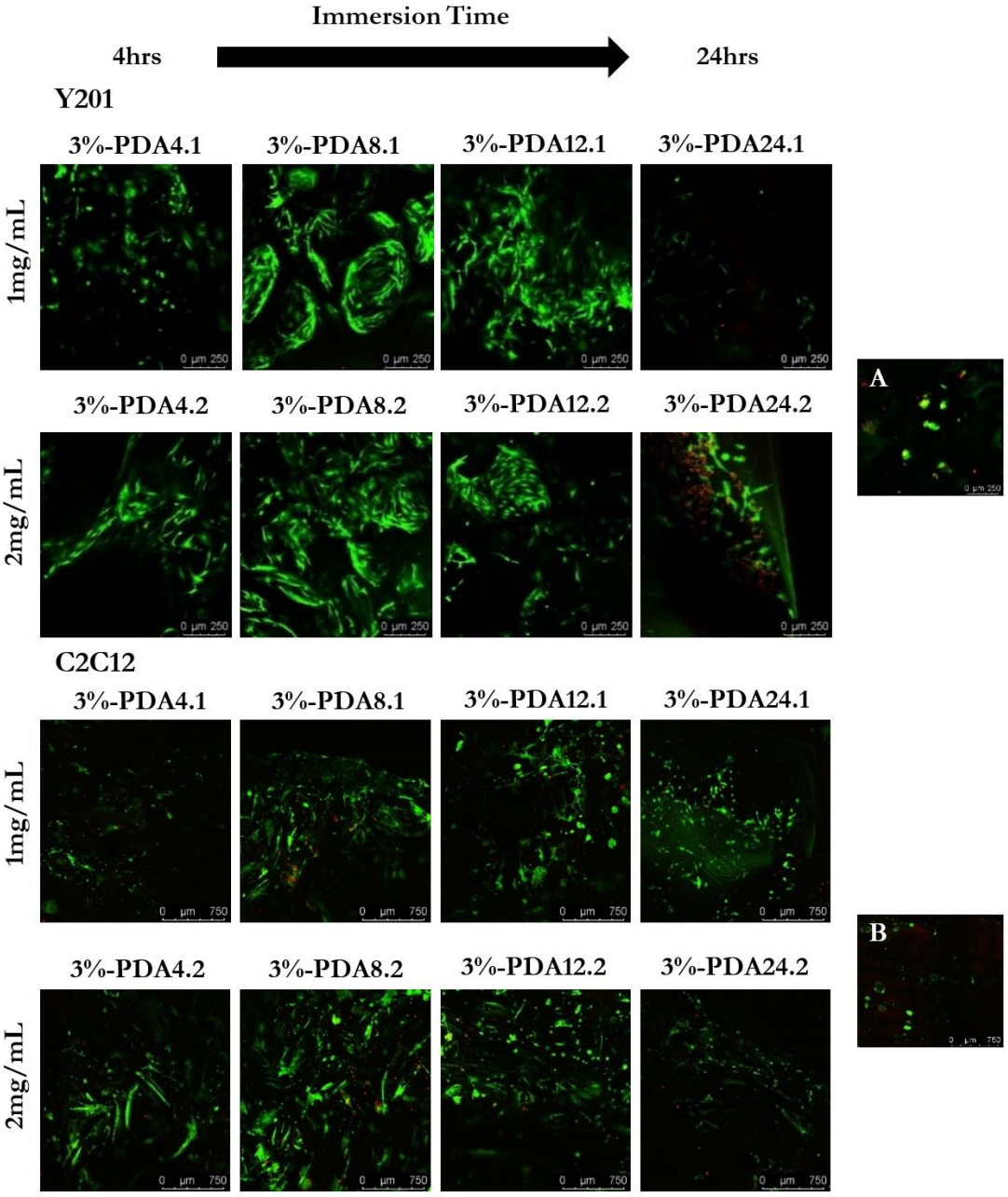

Figure 4.17 – Images of LIVE-DEAD stained Y201 and C2C12 cells following 7 days 3D culture on Polydopamine (PDA) coated 3 wt% agarose scaffolds. Cells were seeded using static seeding techniques with a density of $2.5x10^5$ Cells/Scaffold. 3%-Blank agarose scaffolds were fabricated and functionalised by immersion in 1mg/mL or 2mg/mL PDA solutions over different time periods (4, 8, 12, 24hrs). Live cells are stained green and dead cells stained red. Images A and B: 3%-Blank scaffold controls seeded with Y201 and C2C12, respectively. Scale bars = 250 μm (Y201) and 750 μm (C2C12).

Collation of the above qualitative results (Figure 4.16 and Figure 4.17) comprehensively confirmed the general applicability of PDA coatings for agarose scaffolds, resulting in improved 3D cell attachment and viability as well as drastic changes to cellular morphology. In relation to the cellular adhesion criterion set out in section 4.2, sufficient evidence was provided by most of the PDA formulations with only the 4 hour (1mg/mL) and 24 hour iterations failing to comprehensively illustrate adequate cellular properties for stage-1-stage-2 progression. As a

result, all remaining formulations were recommended for stage-2 cell adhesion investigations, specifically regarding the effect of PDA coating on 3D cell metabolism and proliferation.

4.4.5.4 Effect of PDA surface coating on cellular proliferation

4.4.5.4.1 Optimisation of alamarBlue assay parameters

Quantification of cell proliferation using an alamarBlue assay is most accurately measured when cells are in the exponential phase of growth. As such, experimental parameters including scaffold seeding density and incubation time were first optimised for Y201 cells, as described in section 4.3.6.1.1. As uncoated agarose scaffolds failed to provide a suitable environment for even basic cell attachment, it was essential that optimisation of alamarBlue parameters was performed on a scaffold formulation known to support the measured experimental factors. As such, 8 hours 2 mg/mL (or 3%-PDA8.2) was chosen, with appropriate scaffolds being formulated and sterilised accordingly.

In terms of optimisation of the incubation time, it was identified from Figure 4.18 A that a linear response in percentage reduction in alamarBlue was presented solely when cells were incubated for 4 hours. This was further supported by Figure 4.18 B, which showed that different cell densities could be effectively distinguished at 4 hours of alamarBlue incubation specifically. Moreover, with future long term culture experiments in mind (i.e. over 7 days 3D static culture), an initial seeding density of approximately 125,000 cells/scaffold should be considered, thus containing measured sample reduction to within the measurable limits (<100% reduction). As a result of these findings, a 4 hour incubation period was utilised for subsequent viability and proliferation measurements.

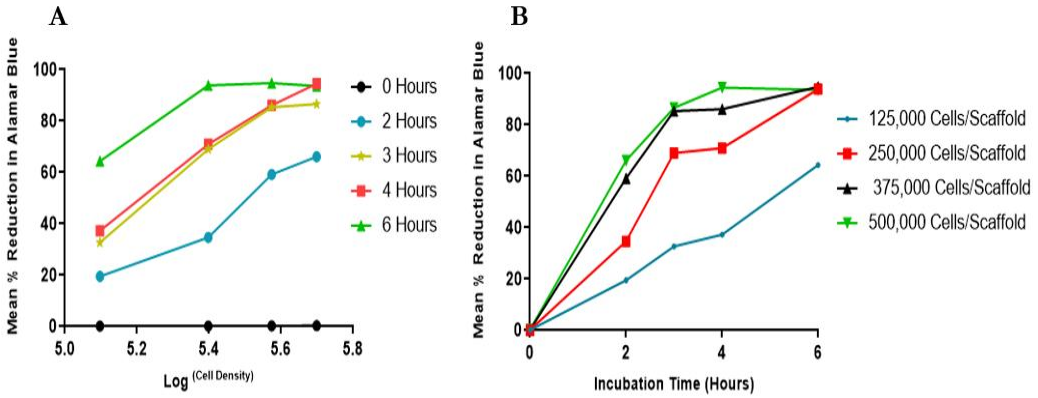

Figure 4.18 – Optimisation of alamarBlue incubation period (A) and Y201 cell seeding density (B) for PDA coated agarose scaffolds. 3%-PDA8.2 scaffolds were selected as the reference biomaterial for which optimisation took place. Scaffolds were seeded under static conditions using a cell density range of 125,000 – 500,000 cells/scaffold. The degree of alamarBlue reduction was measured for a total duration of 6 hours, with separate readings performed every 1-2 hours. Mean percentage reduction in alamarBlue was calculated using a mean reading of a fully reduced alamarBlue sample (n=3).

4.4.5.4.2 PDA coated agarose scaffold cell proliferation assay

AlamarBlue cell proliferation assays were performed on the range of PDA coated 3% agarose scaffolds, as described in section 4.3.6.1. This was done to firstly quantitatively assess the degree to which PDA functionalisation of agarose scaffolds improves cell adhesion and subsequent proliferation compared to uncoated agarose and secondly to reliably inform which specific functionalisation parameters, i.e. PDA solution concentration and immersion time, are most effective and thus deemed optimal for future work.

Y201 cell metabolic activity, as determined by alamarBlue reduction, was initially shown to be low in all tested uncoated control scaffolds (3%-Blank) at both measured timepoints, with an observed drop detected as 3D culture time increased up to 7 days (Figure 4.19). In comparison, detectable metabolic activity of PDA functionalised Y201 seeded scaffolds appeared greatly elevated at 48 hours, which importantly then increased further with 3D culture time (up to 7 days).

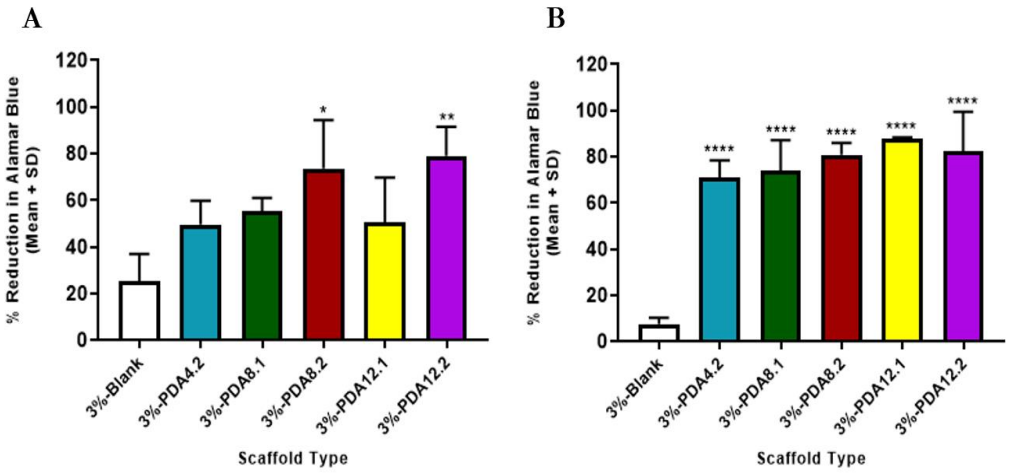

Figure 4.19 (A & B) – Metabolic activity of Y201 cells seeded on a range of PDA coated agarose scaffolds. Cell proliferation within a range of 3 wt% PDA coated scaffolds at (A) 48 hours and (B) 7 days. Cells were seeded using static seeding techniques with a density of $1.25x10^5$ Cells/Scaffold. At each timepoint media was exchanged for working alamarBlue solution and incubated for 4 hours. Mean percentage reduction in alamarBlue was calculated using a fully reduced alamarBlue sample (n=3). Scaffold groups were statistically compared after Arc-Sin transformation using one-way ANOVA (with Tukey's multiple comparisons test). * = $P < 0.05$, ** = $P < 0.01$, **** = $P < 0.0001$

In terms of the most optimal PDA functionalisation condition, Figure 4.19 A and B displayed a time and concentration dependent effect, whereby increases in PDA immersion time as well as PDA solution concentration induced a greater degree of cellular proliferation within the scaffolds over the course of a 7 day culture period. Interestingly, despite large differences in percentage alamarBlue reduction between the 4 hour and 12 hour PDA conditions, no statistically significant differences were found between either of the datasets when each PDA scaffold group was analysed. In the case of the 48 hour timepoint data, statistically significant improvements were found when the 3%-PDA8.2 and 3%-PDA12.2 groups were compared to the uncoated negative

control (P=0.0155, P=0.0067). In contrast, all PDA groups presented as substantially different in the 7 day timepoint when compared to the negative control.

4.4.5.4.3 Final selection of ideal PDA coating parameters

Based on outcomes of initial manufacture as well as qualitative viability images and quantitative metabolic activity (stage-1 and stage-2 testing data for PDA coated agarose scaffolds), it was concluded that PDA coatings were firstly; capable of stable, long term affixation onto and within 3% porous agarose scaffolds, using a standard dip/diffusion coating process and secondly; able to dramatically improve cellular adhesion, viability, survival and proliferation characteristics, upon 3D seeding of two different cell lines. It was further concluded that upon analysis with Y201 seeded cells, cell metabolic activity and proliferation was greatest in coatings cultivated for generally longer periods of time, specifically in the region of 8-12 hours, with extended cultivation periods, such as 24 hours, appearing detrimental.

Given the minimal differences observed in viability, cell attachment and metabolic activity between the 8 hour and 12 hour PDA formulations, final selection was determined simply by practicalities of sample production within the confines of daily laboratory hours. As the 8 hour 2mg/mL agarose scaffolds could be fully functionalised within a single working day, this was deemed most appropriate and as such was subsequently used for all future experimentation.

4.4.5.5 Effect of PDA surface coating on cellular infiltration

Following confirmation of effective cellular attachment, viability and proliferation, further studies were subsequently performed to elucidate the capability of 3%-PDA8.2 scaffolds. This was to allow effective and heterogeneous cellular infiltration, under current static seeded methodologies and determine whether this could be improved via changes to cell seeding densities or by changes to the static seeding methodology. Whole scaffolds were therefore analysed across the material bulk, by typical histological processing and sectioning procedures using H&E staining.

4.4.5.5.1 Influence of cell seeding density

Images obtained from 3%-PDA8.2 scaffolds seeded statically, with either $2.5x10^5$ Y201 cells/scaffold or $5x10^5$ Y201 cells/scaffold (Figure 4.20), appeared to contain populations of cells in each of the geometric groupings, from surface layer sections through to the underlying bottom layer of the scaffold. Furthermore, in both subsets, Y201 cells were found across the geometric layers as interconnected clusters within the agarose pore spaces, displaying classical elongated morphologies with clear evidence of cell-cell and cell-scaffold contacts. When cell seeding density was compared, the appearance within the stained sections suggested more overall cells were present when larger amounts of Y201's were initially seeded, with a greater number of pore spaces filled with Y201 cell clusters, across the entire scaffold bulk.

Based on initial outcomes from this experiment, basic static seeding methodologies (method 1) were deemed largely acceptable as a method for scaffold wide infiltration, and as such only minimal optimisation steps were subsequently performed.

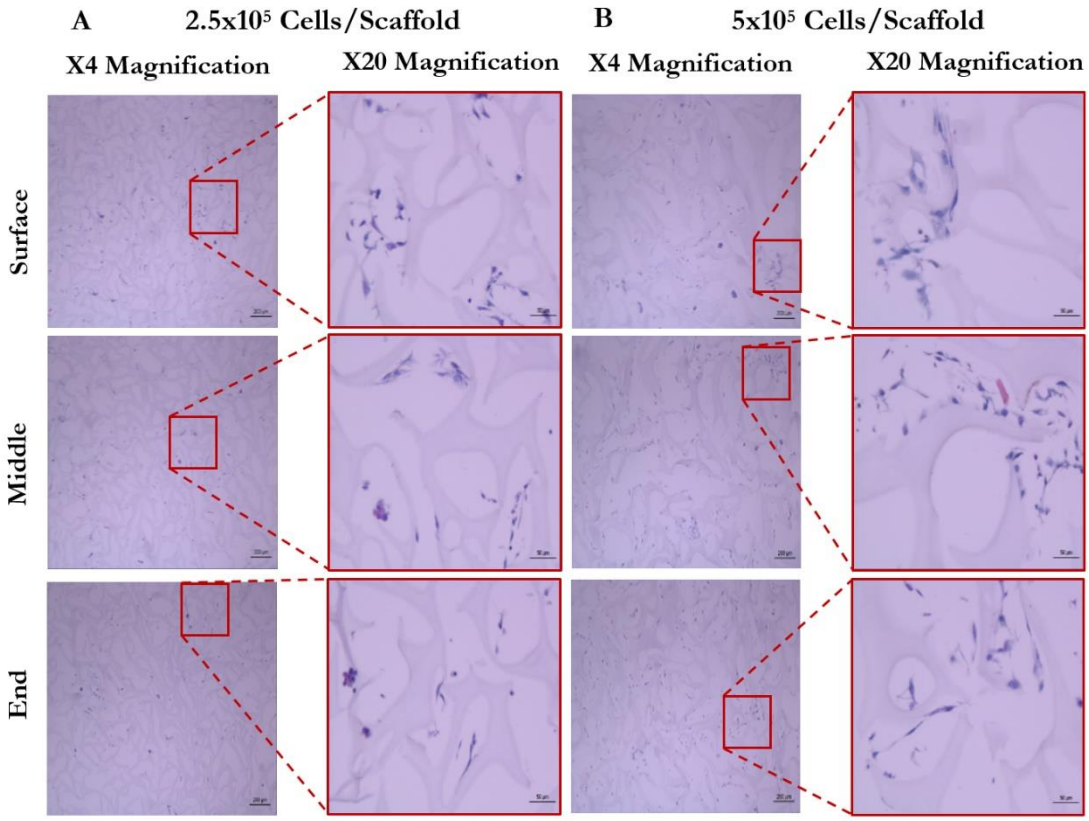

Figure 4.20 – H&E staining of statically seeded 3%-PDA-8.2 PDA coated agarose scaffolds. At 3 different geometric points of interest throughout the scaffold, 10 µm sections were collected and histologically stained to show the degree of 3D cellular infiltration. Y201 cells were seeded at a density of either $2.5x10^5$ (A) or $5x10^5$ cells/scaffold (B) using static seeding techniques and cultured for 48 hours prior to histological processing and staining. Scale bar of X4 images: 200 µm. Scale bar of X20 images: 50 µm.

4.4.5.5.2 Additional optimisation of static seeding procedures

Static seeding methodologies were further optimised to improve cell attachment efficiency and scaffold infiltration through the application of an adhesion resistant agarose layer to the tissue culture plastic well bottom (also known as static seeding method 3), as described in section 4.3.7.2. Through its application, it was hypothesised that cell adhesion towards the PDA coated scaffolds would be favoured, thus restricting attachment and drop-off onto the treated 48 well plate surface. 3%-PDA8.2 scaffolds were cultured for 48 hours followed by histological processing.

Visual analysis via H&E staining confirmed the validity of the new static seeding technique with Y201 cell populations clearly situated across all geometric locations examined. Cells also displayed the expected fibroblastic morphologies, as seen when seeded using seeding methodology 1 (treated 48 well plate), suggesting no apparent morphological impact was induced upon agarose

layer addition. Furthermore, it was also observed that marginal enhancements in cell attachment efficiencies across the entire scaffold bulk occurred when an additional agarose layer was added (Figure 4.21), confirming the experimental hypothesis.

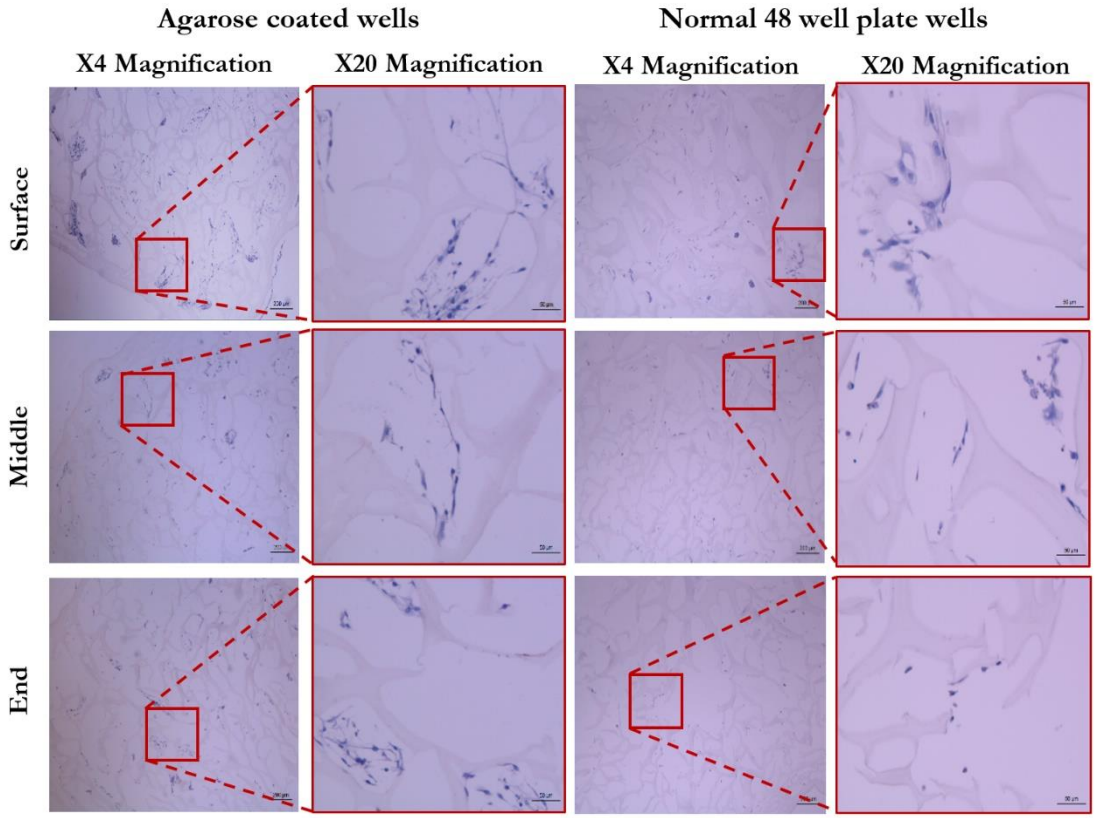

Figure 4.21 – H&E staining of statically seeded PDA coated agarose scaffolds comparing agarose layered 48 well plate methodology versus treated wells. At 3 difference geometric points of interest throughout the scaffold, 10 μm sections were collected and histologically stained to show the degree of 3D cell attachment and infiltration after seeding either in the presence or absence of reportedly adhesion resistant agarose surface layer. Scale bar of X4 images: 200 μm. Scale bar of X20 images: 50 μm.

4.4.5.6 Effect of PDA surface coating on cellular differentiation

Upon optimisation of cell-scaffold infiltration parameters, 3%-PDA8.2 scaffolds were examined with regards to their ability to support and sustain 3D cellular differentiation of Y201 cells towards osteochondral lineages – a key requirement for future application of these scaffolds as GAM repair systems. Furthermore, it was also vital to confirm if the presence of the PDA coating alone possessed any capacity for Y201 lineage commitment.

To ensure comprehensive validation, the Y201 cell line was initially assessed for its tri-lineage differentiation capability in 2D, specifically across the osteogenic, chondrogenic and adipogenic lineages (Appendix Figure 8.3). This was then followed by long term 3D culture of cells within 3%-PDA8.2 scaffolds, specifically for this study, in the presence of either basal media or differentiation media (osteogenic or chondrogenic).

4.4.5.6.1 3D osteochondral differentiation

Following the methods described in section 4.3.8.1, 3%-PDA8.2 scaffolds were seeded with Y201 and evaluated to ascertain their capacity for osteogenic and chondrogenic differentiation. Alizarin red and Safranin O-Fast green staining were utilised as indicators of differentiation commitment (Figure 4.22 and Figure 4.23). Evaluation of agarose scaffolds for their support for adipogenic differentiation was not considered appropriate given the therapeutic context in which these scaffolds are being applied (i.e for osteochondral defects repair).

Initially, visual analysis of negative control scaffolds revealed no inherent detectable ability of PDA coatings to induce seeded Y201 cells towards the osteogenic lineage at any timepoints (Figure 4.22 A). In these samples, seeded cells continued to proliferate and spread throughout the scaffold bulk with no indication of cellular condensation or deposition of calcium and bone nodules. In contrast, cells cultured under osteogenic conditions displayed small quantities of positive alizarin red staining after 21 days, then comprehensively staining after 28 days (Figure 4.22 B). Such red staining specifically appeared to track around the edges of the scaffold pore structure in areas which Y201 cells had formed clusters, suggesting the formation of bone nodules in these scaffold cultures.

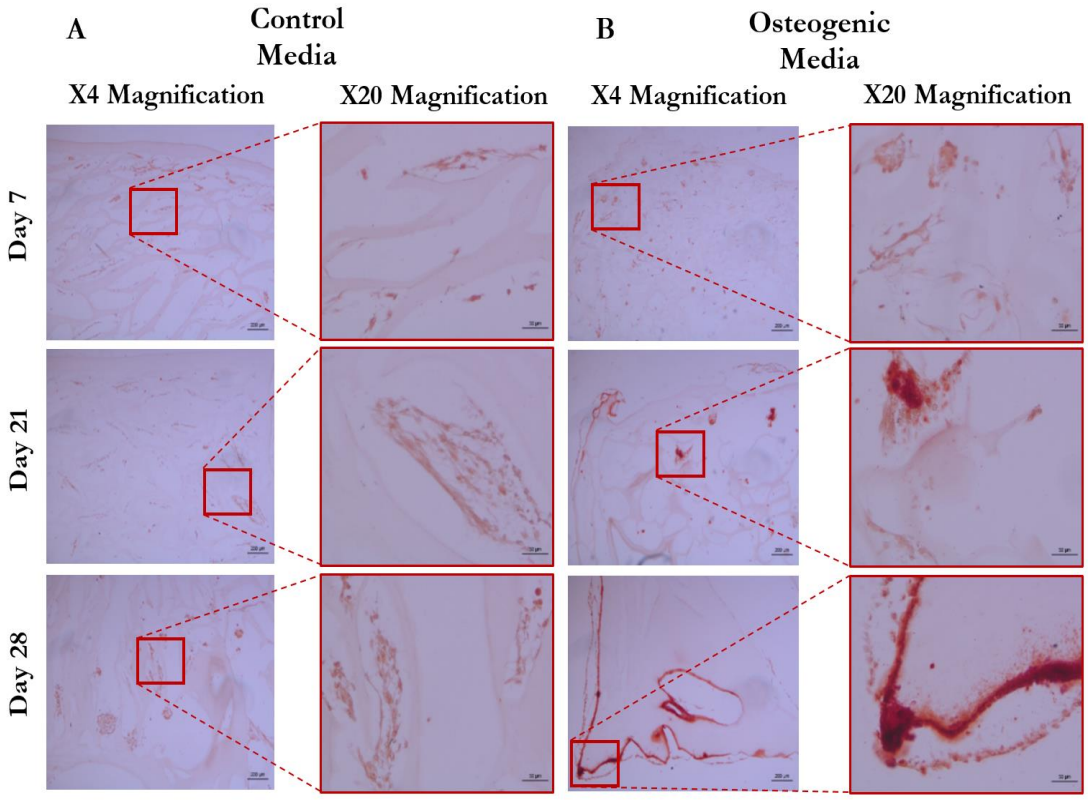

Figure 4.22 – 3D osteogenic differentiation of Y201 seeded PDA agarose scaffolds. Y201 cells were cultured in 3%-PDA8.2 scaffolds under basal or osteogenic conditions for up to 28 days. Sections were stained using alizarin red dye illustrating Ca^{2+} deposition. Scaffold seeding density was $5x10^5$ cells/scaffold. Scale bar of X4 images: 200 µm. Scale bar of X20 images: 50 µm.

Alcian blue staining was performed on chondrogenic sections however significant dye accumulation on agarose scaffold fibres resulted in an indistinguishable colour change between control and chondrogenic samples. As such, Safranin-O-fast green staining was employed.

In a similar fashion to osteogenic control scaffolds, visual analysis of chondrogenic negative control scaffolds revealed no detectable ability of PDA coatings alone to induce seeded Y201 cells towards the chondrogenic lineage at any timepoint (Figure 4.23 A). Sections remained absent of any characteristic red or green staining representing possible proteoglycan deposits. Furthermore, it was noted cell proliferation continued as expected over the sample period with scaffold pores filled with cell clusters across its bulk. In comparison, seeded scaffolds cultured under chondrogenic conditions showed progressive cellular aggregation at 21 and 28 days, forming dense circular populations at pore junctions. Positive staining for safranin O often occurred in regions adjoining these populations, whilst fast green stain was positively identified at cell-cell junctions.

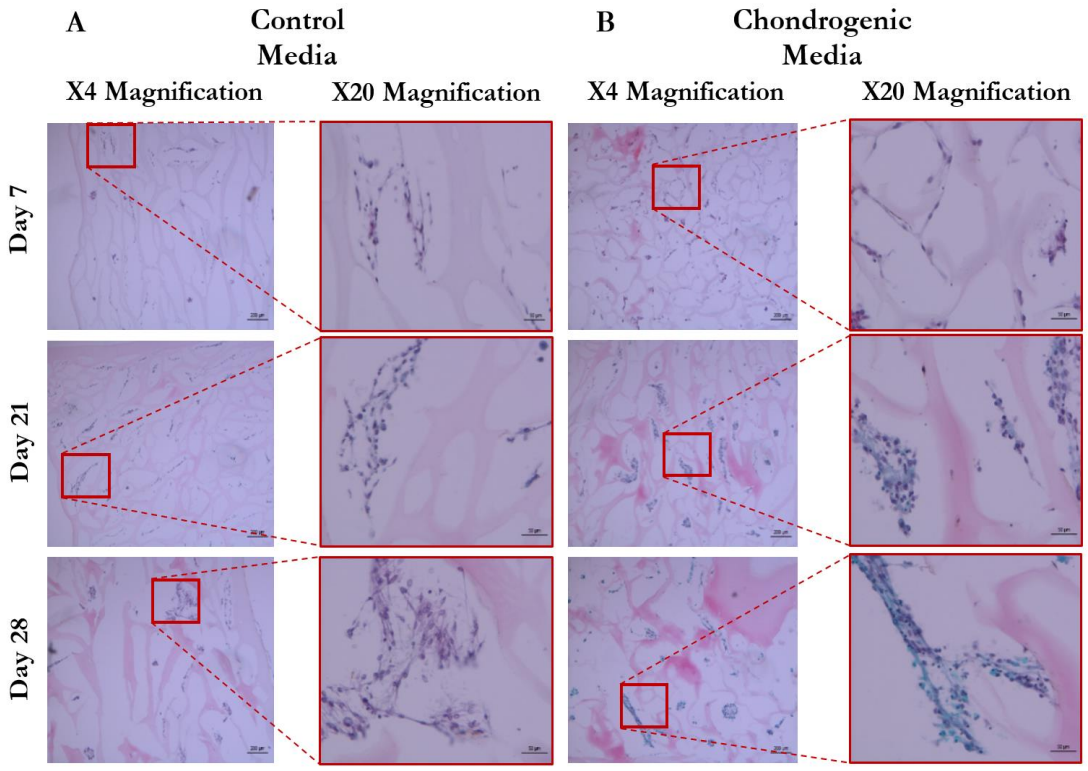

Figure 4.23 – 3D chondrogenic differentiation of Y201 seeded PDA agarose scaffolds. Y201 cells were cultured in 3%-PDA8.2 scaffolds under basal or chondrogenic conditions for up to 28 days. Sections were stained using safranin O-fast green dye illustrating proteoglycan content. Scaffold seeding density was $5x10^5$ cells/scaffold. Scale bar of X4 images: 200 µm. Scale bar of X20 images: 50 µm.

4.4.6 Physical & chemical characterisation of polydopamine coatings

4.4.6.1 Microstructure of PDA coated agarose scaffolds

SEM imaging of PDA functionalised scaffolds was performed to firstly confirm the presence of a deposited PDA coating at the micron scale and secondly to assess its morphological characteristics in comparison to an uncoated scaffold control. Under low magnification, PDA coated scaffolds were indistinguishable from uncoated controls, illustrating the previously characterised interconnected pore microstructure, which also appeared unaffected by additional functionalisation and freeze-drying procedures (Figure 4.24 A & D). However, greater magnification of PDA coated scaffolds revealed wholesale coverage of fibres with a high density PDA film, individually measured in the nanoscale range, accompanied by the presence of PDA agglomerates (Figure 4.24 E & F). In comparison, uncoated agarose fibres remained clean and smooth with no indication of particulates or debris (Figure 4.24 B & C). When these PDA coated regions were analysed under EDX elemental analysis, detectable signals of carbon, oxygen and nitrogen were significantly enhanced in comparison to uncoated agarose (Figure 4.24 G & H). Furthermore, the characteristic sulphur signal present in uncoated agarose decreased to near undetectable levels after PDA coating, suggesting complete coverage by PDA, within the region analysed.

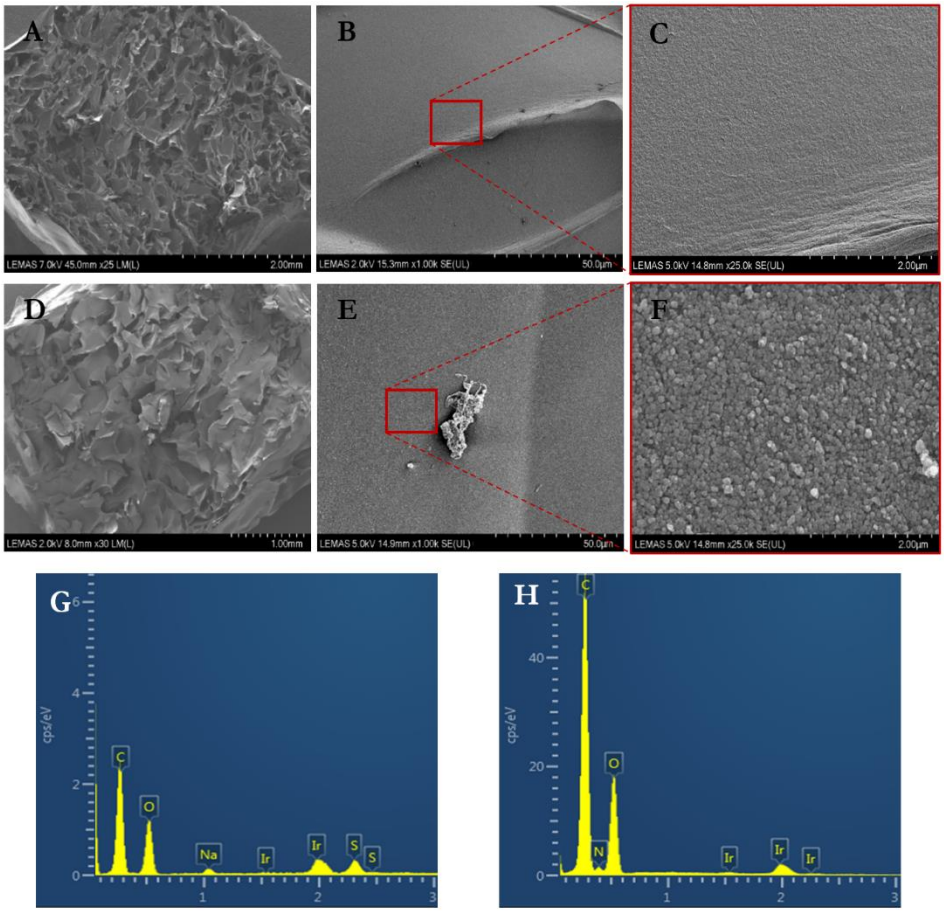

Figure 4.24 (A-H) – SEM micrograph images and EDX analysis of PDA coated agarose scaffolds. A-C: Representative microstructure of 3%-Blank agarose scaffold, D-F: Representative microstructure of 3%-PDA8.2 scaffold. G: EDX analysis of 3%-Blank scaffold, H: EDX analysis of 3%-PDA8.2 scaffold.

4.5 Discussion

4.5.1 Agarose scaffold sterilisation

The first objective of this chapter sought to assess the effectiveness and long-term suitability of a common scaffold sterilisation procedure. Specific attributes of interest for the particular method used included being fast, cheap and easily available, whilst also being able to restrict unwanted biomaterial morphological changes (including the mechanical and chemical properties). Finally, the method should not negatively affect incorporated DNA payloads and their downstream function. Based on these characteristics, the most obvious method chosen for agarose scaffold sterilisation was the use of ethanol – part of the chemical sterilisation family.

When utilised as a step-wise wash procedure, ethanol has in the past, been successfully applied to a range of scaffold based systems including fibrous electrospun biomaterials, hydrogels and porous scaffolds (Rediguieri *et al.*, 2016; Selim *et al.*, 2011; Su *et al.*, 2021). The protocol used in this study was therefore based on these published methodologies and applied accordingly alongside previously established lyophilisation procedures. Upon bacterial broth evaluation, the results suggested ethanol sterilisation was indeed sufficient at preventing microbial growth over a two week period. Of particular note was the apparent partial resistance to bacterial infection in groups which solely underwent a freeze-drying procedure (without an ethanol sterilisation wash). Although more investigations would be required, this finding was in fact backed up in two recent studies which showed that the primary cooling step specifically induces partial microbial inactivation, acting through temperature mediated protein and enzyme denaturation (Dai *et al.*, 2016; Markowicz *et al.*, 2006). As such, overall sterilisation efficiency of agarose scaffolds was likely enhanced by the incorporation of both methods acting in tandem and was therefore deemed acceptable for future experimentation within this thesis.

4.5.2 Agarose scaffold/GAM cytotoxicity

Initial cytotoxicity testing conducted with L929 cells revealed fabricated and sterilised agarose F-AGE-1 GAMs were regarded as not notably toxic to cells. Growth patterns were similar across all GAM groups with no obvious indication of CaP nanoparticle associated cytotoxicity. Furthermore, cell growth up to and in contact with scaffold surfaces did not change upon electrophoretic loading of pDNA-nanoparticle complexes. Observations additionally suggested electrophoretic inclusion of a fibronectin recombinant protein within such GAMs had little effect on contact viability. This was hypothesised to be a result of either; FN inducing little to no visual improvement to contact viability or that FN containing nanoparticle complexes remained immobilised within the freeze-dried agarose matrix over the course of experimentation, thus mitigating its desired effect. Quantitative cytotoxicity analysis revealed small yet non-significant levels of detectable cell death over a 24 hour culture period in which L929 cells were incubated in the presence of GAM extract solutions. The identified cell death was thought to be likely due

in part because of possible residual ethanol remaining within the porous matrix after sterilisation, or carryover of cell passage-seeding related death (Arango *et al.*; Rainer *et al.*, 2010).

Although study results show promise in terms of agarose scaffold cytotoxicity characteristics, it should be clarified this does not guarantee effective cell-scaffold adhesion and attachment when applied in 3D culture environments – a crucial pillar for GAM mediated tissue engineering.

4.5.3 Cellular adhesion capability of uncoated agarose scaffolds

Using standard methods for cell attachment testing, strong evidence was presented which suggested that all of the first generation uncoated agarose scaffold formulations (3%-Blank, F-AGE-1 GAMs (±FN)) were, according to this project's specification, not suitable for short or long term 3D cell culture, with LIVE-DEAD imaging revealing low level surface attachment and long term viability for the two cell lines tested. Additionally, any detectable live cells identified using viability dyes retained distinct round globular morphologies. This evidence supports reports by Cambria *et al* and Evans *et al*, with both purporting agarose biomaterials generally lack the necessary cell adhesion motifs for cell-scaffold focal adhesion and thus successful 3D culture (Cambria *et al.*, 2020; Evans *et al.*, 2022). As a result of this, surface coating methods were therefore applied which aimed to improve agarose scaffold- cell adhesion.

4.5.4 Cellular adhesion capability of FN and LAP-PEO coated scaffolds

Three surface deposition methods (FN, LAP-PEO, PDA) were applied to fabricated agarose scaffolds aiming to improve cell attachment, viability and proliferation characteristics.

It was initially found that direct physical surface adsorption of both FN and LAP-PEO failed to bring any tangible improvements to cell attachment and viability, with scaffolds displaying cell morphologies which retained globular circular conformations after 7 days 3D culture. In the case of FN coated scaffolds, the most likely cause of cell adhesion failure was due to the lack of interaction between the bioinert agarose scaffold and fibronectin molecules. As agarose is only weakly hydrophilic with no inherently charged functional groups, it was reasoned that fibronectin could not adsorb onto and within the scaffold via classical Van der Waals, hydrogen bonding or electrostatic interactions. Therefore, during the PBS and ethanol wash steps in the protocol, as well as in the static seeding procedures, FN molecules were likely easily washed off the scaffold surface, thus providing no improvement in cell attachment and viability compared to the uncoated agarose scaffolds previously tested.

In the case of LAP-PEO coated samples, specific bio-nanocomposite coating methods, such as those reported by Orafa *et al* and Gaharwar *et al*, were adapted with modifications for application as a coating for agarose scaffolds. This involved the replacing of the reported drying and vacuum oven steps with the freeze-drying fabrication procedure used in this thesis (Gaharwar *et al.*, 2012; Orafa *et al.*, 2021). Due to this change, it could be assumed that the cryogenic conditions may

have negatively influenced the reported cell adhesion properties of LAP-PEO, such that cationic interactions may have been disrupted, therefore breaking the delicate interconnectivity of the films. This hypothesis however was at least partially countered by a comprehensive report by Adam *et al* who similarly freeze-dried LAP-PEO solutions but with the aim of characterising its rheological properties. This study reported a similar white fluffy powder to what was identified in this thesis, which possessed similar properties and chemistries to samples not placed under freeze-drying procedures, suggesting lyophilisation mediated damage is unlikely (Adam, 2012). As cell adhesion potential of this LAP-PEO freeze-dried form wasn't evaluated in this stated report, evidence remains scarce supporting the idea lyophilisation was in fact the root cause. Furthermore, as LAP-PEO coatings have widespread reported success for improving biomaterial functionality over a range of cell types and materials, the exact mechanisms for its apparent failure in this case remain up for debate and would require more intense study and characterisation.

Based on FN and LAP-PEO evaluations, it was therefore surmised the inherent bio-inert nature of agarose scaffolds restricts the effective and permanent deposition of adhesion molecules on its surfaces, and as such the biomaterial itself must require either additional chemical modification or intermediary coupling agents to induce the desired cellular adhesion (Evans *et al*., 2022; Meng *et al*., 2012; Zhu *et al*., 2006).

4.5.5 Cellular adhesion capability of PDA coated scaffolds

Polydopamine was alternatively proposed for its ability to form exceptionally well adhered bioactive films on virtually any biomaterial including other bio-inert surfaces such as metals, non-wetting surfaces and 3D scaffolds (Barros *et al*., 2021; Ku *et al*., 2010; Tsai *et al*., 2011). Consequently, previously reported PDA coating procedures were adapted for uncoated agarose scaffold deposition and subsequently applied. Importantly, it was found that several factors during the initial PDA preparation and coating procedure including; reaction temperature, initial dopamine concentration, incubation time, pH, buffer type, can influence the resulting surface characteristics found on the deposited material. Of these factors, dopamine concentration and incubation time were considered paramount, directly controlling coating thickness, density and distribution – characteristics key to inducing scaffold-cell adhesion(Jiang *et al*., 2011).

Upon cell attachment and viability analysis, cellular adherence characteristics of C2C12 and Y201 cells to the PDA scaffolds were dramatically enhanced, illustrating in general a dose-dependent improvement in adherence, viability, and morphology as a function of increasing incubation time and dopamine concentration. This improved surface affinity in both cell types for the functionalised agarose scaffolds was directly attributed to the super hydrophilic environment created by the PDA film. Although still not fully understood, the results here support hypotheses reported by Ku *et al* and Tsai *et al* who purport that catechol and amine functional groups present on the surface of the PDA films covalently bind and immobilise serum proteins present in cell

media (Ku *et al.*, 2010; Tsai *et al.*, 2011). Crucially once bound, these cell adhesive ECM proteins (such as fibronectin and vitronectin) remain in their native conformational state, retaining their interactivity and functional potential as cell adhesion sites (Lee *et al.*, 2009). Integrin cell surface receptors present on cell membranes can then recognise these proteins (specifically the RGD tri-peptide sequence) and establish focal contacts between the seeded cells and the scaffold surface (Mardon & Grant, 1994).

Interestingly, in comparison to other reported studies in which lengthy incubation periods (e.g. 16-24 hours) were required for whole scaffold coating and subsequent cell adhesion, it was found in this study that incubation periods as short as 8 hours were sufficient (Ku & Park, 2010; Ku *et al.*, 2010). This was hypothesised to be due to the highly porous microstructure of freeze-dried agarose scaffolds (chapter 3 scaffold characterisation), whereby polydopamine could diffuse freely into the scaffold bulk during the polymerisation and immersion processes. PDA films likely then could be deposited at speed throughout the entirety of the scaffold bulk, crucially avoiding the need for use of dynamic compression techniques – a method employed by Tsai *et al* to enable dopamine transport into less porous Pellethane scaffolds (Tsai *et al.*, 2011). This fast PDA deposition rate likely instigated overall increases in film thickness or density, possibly a factor contributing to the poorer adhesion characteristics exhibited by the scaffolds incubated for 24 hours over initial 3D culture. Because of this, the author concluded 8 hours with 2 mg/mL dopamine were most suitable conditions for future work (Tierney *et al.*, 2012).

4.5.6 Differentiation capacity of PDA coated scaffolds

In relation to the overall goal of this thesis whereby agarose scaffolds would be used as osteochondral GAM repair systems, it was deemed essential that the functionalised scaffolds were validated with regards to its ability to support not only 3D osteogenic and chondrogenic differentiation, but to also confirm whether PDA, in this context, inherently was capable of directing lineage commitment. As such, osteogenic and chondrogenic differentiation potential of Y201 seeded scaffolds was characterised, using basic histological staining techniques.

Based on the staining pattern of scaffold sections, evidence suggested that PDA films could not instigate Y201 differentiation. Local calcium or GAG deposition – clear histological indicators of osteogenic and chondrogenic differentiation respectively, were not detected. In contrast, when cultured in the presence of differentiation media, clear indications of osteogenic and chondrogenic differentiation could be identified via staining. It was therefore concluded that, via the use of gross histological evaluation techniques only, the PDA functionalised scaffolds supported osteochondral differentiation (in differentiation media) and interestingly appeared deficient with regards to its inherent differentiation capability (in basal media only). It should be noted however that assumptions concerning the latter might not represent the full behavioural relationship occurring between the coating and 3D seeded cells, namely because of limitations in

the histological detection procedures used - of which have the potential to omit or not detect the more subtle cellular changes occurring. Granted, if study time permitted, the power of this hypothesis could likely have been enhanced further with the application of quantitative osteogenic or chondrogenic detection methods such as alkaline phosphatase (ALP) and GAG assays or qPCR gene expression analysis, thus potentially identifying behavioural changes at the cellular and gene level.

In terms of osteogenic differentiation, several examples exist in the literature which suggest PDA films do in fact play a major role in this process. For example, Ghorbani *et al* illustrated upon 7 days culture with MG-63 cells, PDA functionalised electrospun polyurethane-graphene oxide scaffolds alone could significantly enhance ALP activity in comparison to uncoated controls (Ghorbani *et al*., 2019). This behaviour was further corroborated when it was reported by Lee *et al* that ALP activity was enhanced in MC3T3-E1 cells cultured on PDA functionalised titanium (Lee *et al*., 2014). In contrast, in terms of chondrogenic differentiation, little evidence suggests PDA coatings possess an inherent ability to influence cells towards chondrogenesis. Successful examples only exist upon further biomolecule conjugation of PDA functionalised scaffolds enabling growth factor mediated differentiation towards cartilage phenotypes (Tolabi *et al*., 2022; Wei *et al*., 2021).

4.5.7 Physiochemistry of deposited PDA coatings

The cell-surface interaction is recognised as a critical factor influencing the adhesion, proliferation, and differentiation of bone marrow-derived mesenchymal stem cells (BMSCs). Consequently, characterising the surface properties of the developed PDA coated agarose scaffolds becomes crucial for obtaining fundamental insights into the underlying mechanisms governing such interactions. In this regard, numerous studies have highlighted the intrinsic bioinert nature of agarose as a prominent factor contributing to the limited maintenance of stable cell culture (Tang *et al*., 2007; Valdoz *et al*., 2021). Given this understanding, surface modifications that render the agarose surfaces highly hydrophilic hold significant potential in promoting cell adhesion and proliferation.

Commonly, this attribute can be characterised by measuring the water contact angle over a range of PDA coating surfaces, thus determining the degree to which parameters used in this study such as PDA concentration and immersion time (8 hours 2mg/mL) affect overall scaffold wettability. As such, water contact angle experiments were explored for this same purpose, but certain limitations were identified. This included the extremely porous and open nature of the agarose scaffolds, such that the water droplets applied were found to be insufficiently stable at the scaffold surface over the required measurement time. This characteristic specifically caused the droplet to pass directly through the scaffold rather than resting on its surface, restricting the extraction of meaningful contact angle data. Based on literary articles however, in which similar

experiments were performed, e.g. in PDA coated alginate-gelatin hydrogels or poly(caprolactone) scaffolds, it was found that water contact angles were in fact reduced in both cases as a function of PDA coating time and concentration indicating increased hydrophilicity. This can likely be attributed to elevated numbers of amine and catechol residues present in PDA, found at the material surface (Cheng *et al.*, 2016; Ghorbani *et al.*, 2022). As PDA coated agarose scaffolds generally followed this same trend, in terms of cell adhesion, it was therefore hypothesised a similar mechanism of action was in play in this study, with largely hydrophilic surfaces being formed on the agarose scaffold.

Surface chemistry was considered a further essential factor in the successful improvements identified in PDA coated agarose scaffold-cell adhesion. According to SEM images, it was shown that pore structure and size was generally maintained after PDA coating treatment, with little observable differences in bulk scaffold appearance. Furthermore, upon higher magnifications, it was found agarose fibres were largely coated uniformly with spherical PDA particles of sizes below 100 nm in diameter. Small quantities of PDA agglomerates were also identified. Additionally, in uniform PDA regions, the surface chemistry profile was evaluated using energy dispersive X-ray spectroscopy and importantly illustrated the presence of nitrogen atoms, a feature crucially lacking in native agarose scaffold equivalents (Chuah *et al.*, 2015). This was further supported by the removal of the agarose associated sulphur peak as well as higher relative carbon signal, within the PDA coated samples.

4.6 Conclusions

The findings presented in this chapter reveal that lyophilised agarose scaffolds, in their basic form, appear biocompatible but lack the essential attributes required for a biomaterial to be suitable in 3D culture systems. Thus, the need for an effective biomaterial modification strategy to enhance the cell attachment capability of agarose scaffolds became clearly evident. By considering successful literary examples, which circumvent detrimental changes to the novel agarose-mediated electrophoretic loading platforms established (F-AGE-1 and F-AGE polyplex - Chapter 3), led to the consideration of surface functionalisation methodologies as the most suitable approach for elevating overall 3D adhesion. Subsequent evaluation of the stated approaches identified the application of Polydopamine coatings specifically as the most optimal in this regard, significantly improving all the specified characteristics stated within the scaffold design (section 4.2), including cell adhesion, long-term viability, proliferation, infiltration, and migration.

Firstly, the investigation of physically relevant cell lines, such as C2C12 and Y201, revealed their adherence and viability within the PDA-coated scaffolds, as confirmed by LIVE-DEAD staining. These cells exhibited desired morphologies with well-formed focal adhesions on the scaffold surfaces. Over a 5-day period (48 hours to 7 days), cell proliferation was also observed, enabling

the identification of optimal parameters - an 8-hour immersion using 2 mg/mL PDA. With these parameters established, scaffold infiltration and modifications to the static seeding process could then be verified and implemented, respectively.

Secondly, through SEM analysis, it was determined that the aforementioned PDA coatings were uniformly deposited over the porous scaffold, effectively coating the thin agarose fibre walls with nanoparticles.

In conclusion, this work successfully achieved the overall aim of formulating a biocompatible and bioactive agarose scaffold system capable of supporting long-term cell 3D culture, importantly acting as the gateway for subsequent investigations into the 3D transfection capabilities of electrophoretically loaded agarose GAMs, as described in Chapter 5.

CHAPTER 5

3D TRANSFECTION CAPABILITY OF ELECTROPHORETIC LOADED PDA COATED AGAROSE GAMS

5 CHAPTER 5: 3D TRANSFECTION CAPABILITY OF ELECTROPHORETIC LOADED PDA COATED AGAROSE GAMS

5.1 Introduction

Gene therapy is a revolutionary approach which delivers DNA sequences to cells and/or tissues for the purpose of correcting a genetic deficiency or to treat a disease. This ability to foster a targeted and controlled cellular response makes gene therapy systems a highly pertinent avenue of research within the field of tissue engineering. In this regard, the seminal GAM concept proposed by Bonadio in which therapeutic protein encoding non-viral DNA payloads are encapsulated or immobilised within a 3D matrix framework has since become established as the standard blueprint (Bonadio, 2000). Significantly, the utilisation of GAMs facilitates one-time administration of genetic material, directing cells along a predetermined lineage. This is achieved through the sustained expression of transgenes over time, orchestrating a durable *in-vivo* response conducive to effective healing (Avilés *et al.*, 2010). Additionally, by dispersing these genetic complexes uniformly throughout a biomaterial framework, as opposed to concentrating gene therapy solely at the defect site, the scaffold imparts a protective shield to these complexes (Tierney *et al.*, 2012).

It is accepted however, that GAM gene delivery is not straightforward and relies on three essential pillars for its success (El-Sherbiny & Yacoub, 2013). In pillar one, a method must be established which can successfully couple the DNA payload to a biomaterial. This can be achieved either during the biomaterial assembly process (i.e. encapsulation) or after biomaterial assembly via payload adsorption or immobilisation (Bengali & Shea, 2005). In both cases, coupling is reliant on a chemical interaction between the payloads and the biomaterial surfaces, with either non-covalent bonding (e.g. hydrogen bonds, Van Der Waals forces, electrostatic forces) or covalent bonding (e.g. amide bonds) being the primary attachment mechanisms (Tallawi *et al.*, 2015; Yazdi *et al.*, 2020). In pillar two, a biocompatible and bioactive biomaterial surface must be expressed. This factor is essential for gene delivery due to the necessity of cells being viable, conformationally adherent and in a proliferative state when interacting with 3D adsorbed DNA payloads (Oyane *et al.*, 2010). Finally, in pillar three, the impregnated or adsorbed DNA payloads must be gradually released from the biomaterial surface (as a transfection vehicle–DNA vector complex) for subsequent uptake and internalisation by locally adhered cells. Crucially, release kinetics are dependent on the nature of the chemical interaction between said payloads and the biomaterial, with covalent interactions requiring mechanical or enzymatic degradation for effective release (Li & Mooney, 2016). Once released, locally high concentrations of transfection payloads can easily diffuse across the microenvironment created at the cell-scaffold interface, thus ensuring gene delivery and expression (Oyane *et al.*, 2012).

Osteochondral tissue engineering, aimed specifically at repairing the gradient multi-tissue interface across the sub-chondral bone and articular cartilage layers, necessitates sophisticated biomaterials such as GAMs that can guide cellular responses in three dimensions. However, as illustrated in chapter 1, current osteochondral GAM approaches are restricted by their discrete bi-layered design, whereby zonal osteogenicity and chondrogenicity is instigated upon transfection payload delivery (Needham *et al.*, 2014; Yu *et al.*, 2023). Furthermore, due to the requirement of two separate GAM phases which are fused together, it has been identified that mechanical instabilities can be induced with phase separation a likely end result (Seo *et al.*, 2014).

As detailed in chapter 3 and chapter 4, methods for controlling *in-situ* transfection payload patterning (F-AGE-1 and F-AGE polyplex) and methods for improving agarose scaffold cellular adherence (polydopamine) were developed and characterised. Upon amalgamation of these two significant procedures, the resulting PDA coated agarose GAMs serve as a facile strategy for the 3D delivery of non-viral DNA payloads. The research presented in this chapter therefore attempts to assess the third pillar of a 3D GAM system; the inherent 3D transfection capability, with an emphasis on optimising DNA payload properties in the hope of achieving the most effective gene delivery outcome.

5.2 Specific materials & methods

5.2.1 Generation of a luminescence reporter gene expression vector

A previously validated fluorescence reporter plasmid vector termed pCAG-d2-eGFP was kindly provided by Dr G Feichtinger and colleagues. This acted as the primary fluorescent reporter vector, as well as the plasmid vector backbone for additional reporter vector formulations. A pMetLuc2 plasmid was then separately purchased from Clontech/TaKaRa (Palo Alto, USA) encoding the luminescence reporter gene *Metridia* luciferase.

By conducting initial plasmid sequence analysis and then employing a cloning process mediated by restriction enzymes, the GFP reporter gene (originating from pCAG-d2eGFP) was substituted with the Met-Luc reporter gene sourced from the pMetLuc2 plasmid. This led to the creation of a new plasmid, denoted as pCAG-MetLuc2 (refer to Figure 5.1). The experimental procedure involved six key stages, employing various molecular biology techniques outlined in detail in Table 5.1.

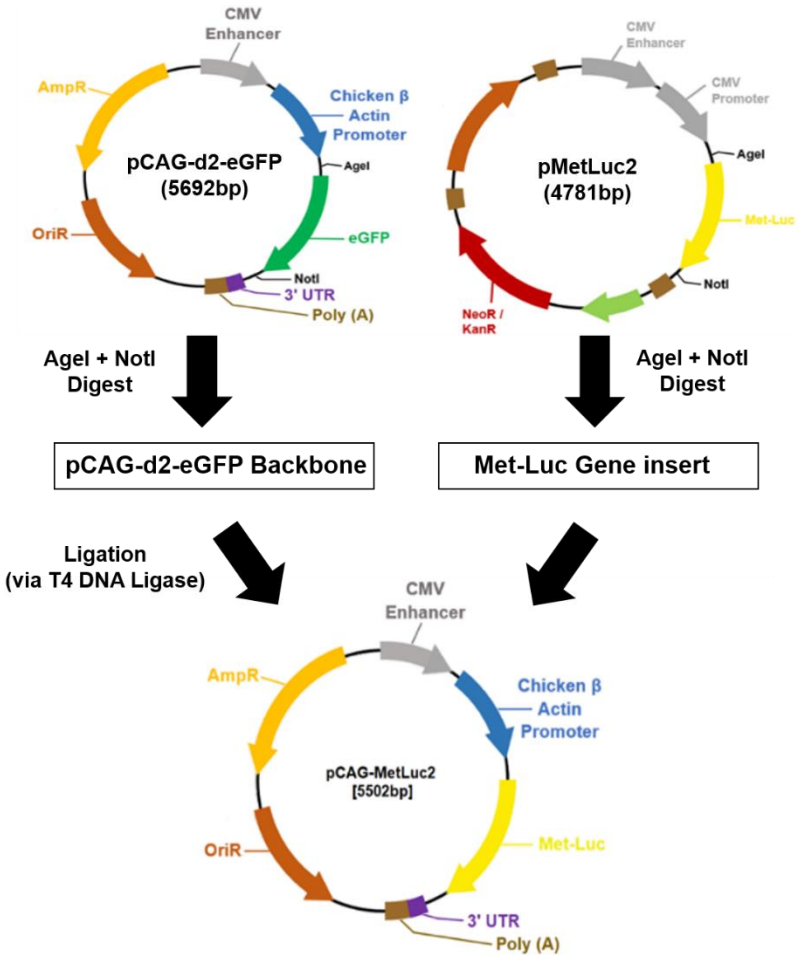

Figure 5.1 – Schematic illustrating the generation of a pCAG-MetLuc2 luminescence reporter vector using restriction enzyme mediated cloning methods.

Table 5.1 – Sequential description of the pCAG-MetLuc2 formulation process

	Brief method description	Specific materials required	Product of each step	Detailed Protocol Location
Step 1	1µg double restriction digest of pCAG-d2-eGFP and pMetLuc2 plasmids	AgeI and NotI restriction enzymes 1 wt% agarose gel DNA ladder	Agarose gel slab containing linearized plasmid fragments	2.2.9.1 2.2.9.2 2.2.9.3
Step 2	Isolation of pCAG backbone and Met-Luc insert from agarose gel	Wizard SV Gel & PCR Clean-Up System	High quality and complementary linear DNA fragments	2.2.9.4
Step 3	Restriction enzyme mediated ligation of pCAG backbone and Met-luc insert using T4 DNA ligase	T4 DNA ligase	Newly circularised plasmid ligation product	2.2.9.5
Step 4	Transformation of circularised ligation product	Competent E.coli TOP10, SOC media, LB agar plates (ampicillin)	Four individual pCAG-MetLuc2 bacterial colonies were selected for minipreparation	2.2.9.8
Step 5	Minipreparation of plasmid DNA	Wizard® SV minipreparation kit (Promega)	High quality pCAG-MetLuc2 samples	2.2.9.9
Step 6	Confirmatory 1µg restriction digest of pCAG-MetLuc2 plasmids	AgeI and NotI (Thermofisher) 1 wt% agarose gel DNA ladder	Linear fragments illustrating pCAG backbone and Met-Luc insert	2.2.9.1 2.2.9.2 2.2.9.3

5.2.2 2D expression of reporter vector library

5.2.2.1 Basic Calcium phosphate and PEI mediated cell monolayer transfection

C2C12 and Y201 cells were separately passaged and re-suspended to a concentration of $0.4x10^5$ cells/well before seeding into 24 well culture plates. Upon approximately 80% confluency (~24 hours post seeding), cells were subsequently transfected with pDNA-nanoparticle complexes or pDNA-PEI polyplexes formulated as per Table 5.2 and Table 5.3, specifically containing either pCAG-d2-eGFP (n=3 per group) or pCAG-MetLuc2 expression vectors (n=4 per group).

Under such parameters, the basic transfection protocols outlined in section 2.2.10 were then followed until completion.

Table 5.2 – Basic 2D CaP transfection parameters for the transfection of C2C12 and Y201 cells cultured within a 24 well plate format.

Modality	CaP:DNA Incubation Solution Volume (per well)	Initial $CaCl_2$ Conc (2.5M stock) (per well)	pDNA Conc (per well)	Final $CaCl_2$ Conc	Culture Volume
24 well plate	50 µL	125 mM	0.625 µg	12.5 mM	500 µL

Table 5.3 – Basic 2D PEI transfection parameters for the transfection of C2C12 and Y201 cells cultured within a 24 well plate format.

Modality	PEI:DNA Incubation Solution Volume (per well)	PEI Conc (1mg/mL stock) (per well)	pDNA Conc (per well)	N/P Ratio	Culture Volume
24 well plate	50 µL SFM	1.94 µg	0.625 µg	24	500 µL

In the case of calcium phosphate mediated transfection, controls were included such as media only (negative control), plasmid only and calcium phosphate only (n=3). In pDNA-nanoparticle complex groups, cells were transfected in both the presence and absence of glycerol shock treatment.

In the case of PEI mediated transfection, controls included media only (negative control) and plasmid only, whilst polyplexes were formulated using a single N/P ratio of 24.

Transfection was ultimately assessed after 48 hours culture (or over the 48 hour time-window) using either qualitative or quantitative assessment methods, as outlined in sections 2.2.10.1.1 and 2.2.10.2.1.

5.2.3 Optimisation of 2D transfection payloads

5.2.3.1 Calcium phosphate mediated transfection

Calcium phosphate mediated transfection of C2C12 and Y201 cells was optimised in the absence of glycerol shock treatment, as the current method is not viable for clinical translation (glycerol cannot be added to GAMs post-implantation). A range of pDNA and $CaCl_2$ concentrations were tested (Table 5.4) for use in solution A of the transfection process (Section 2.2.10.1), all other parameters were maintained.

Cells were cultured in 24 well plates ($0.4x10^5$ cells/well) for 24 hours until 80% confluent. pDNA-CaP nanoparticle complexes (n=3) were added to cells for 4 hours then replaced with complete media. Media only and plasmid only controls (n=3) were included. The CaP transfection procedure was then executed. Met-Luc reporter luminescence was measured per well after 24, 48, 72, 96 and 168 hours to assess transfection efficiency.

Table 5.4 – Optimisation parameters for CaP mediated 2D cell monolayer transfection.

Modality	CaP:DNA Incubation Solution Volume (per well)	Initial $CaCl_2$ Conc (2.5M stock)			Final $CaCl_2$ Conc per well	Culture Volume
		0.5 µg pDNA	1 µg pDNA	2 µg pDNA		
24 well plate	50 µL	0 mM			0 mM	500 µL
24 well plate	50 µL	250 mM			12.5 mM	500 µL
24 well plate	50 µL	500 mM			25.0 mM	500 µL
24 well plate	50 µL	750 mM			37.5 mM	500 µL
24 well plate	50 µL	1000 mM			50.0 mM	500 µL
24 well plate	50 µL	1125 mM			56.25 mM	500 µL

5.2.3.2 PEI mediated transfection

PEI mediated transfection of C2C12 and Y201 cells was also optimised. A range of polyplex formulations were generated (Table 5.5) through modifications to both the pDNA concentration (within solution X) and amount of PEI added (i.e N/P ratio) (solution Y), as previously shown in chapter 2, section 2.2.10.2, all other parameters were maintained.

Cells were seeded and cultured as per section 5.2.3.1, with media only and plasmid only controls (n=3) also being included. The polyplex transfection procedure was then carried out. Met-Luc reporter luminescence was measured per well after 24, 48, 72, 96 and 168 hours to assess transfection efficiency.

Table 5.5 – Optimisation parameters for PEI mediated 2D cell monolayer transfection.

Modality	PEI:DNA Incubation Solution Volume (per well)	PEI Conc (1μg/μL stock) (per well)			N/P Ratio	Culture Volume
		0.5 μg pDNA	1 μg pDNA	2 μg pDNA		
24 well plate	50 μL SFM	0 μg	0 μg	0 μg	0	500 μL
24 well plate	50 μL SFM	0.37 μg	0.75 μg	1.5 μg	8	500 μL
24 well plate	50 μL SFM	1.55 μg	3.1 μg	6.2 μg	24	500 μL
24 well plate	50 μL SFM	2.07 μg	4.14 μg	8.28 μg	32	500 μL
24 well plate	50 μL SFM	2.59 μg	5.17 μg	10.34 μg	40	500 μL

5.2.4 3D transfection control study (external application method)

Using the principle of external application of transfection capable DNA complexes, a basic scaffold transfection control model was generated which enabled the evaluation of PDA coated agarose scaffolds as platforms for 3D transfection (Figure 5.2).

Using optimised functionalisation parameters from chapter 4, PDA coated scaffolds (3%-PDA8.2) were first fabricated and sterilised and then placed into agarose coated 48 well plates, in preparation for seeding. C2C12 and Y201 cells were simultaneously passaged and re-suspended to a concentration of $5x10^5$ cells/scaffold before undergoing static seeding methodologies (section 2.2.5.1). Cell seeded scaffolds were consequently incubated for between 2-3 hours before wells were flooded with 800 μL complete growth media.

Following an initial 24 hour culture period, cell seeded scaffolds were then prepared for transfection using external application of either DNA containing CaP nanoparticles or PEI polyplexes.

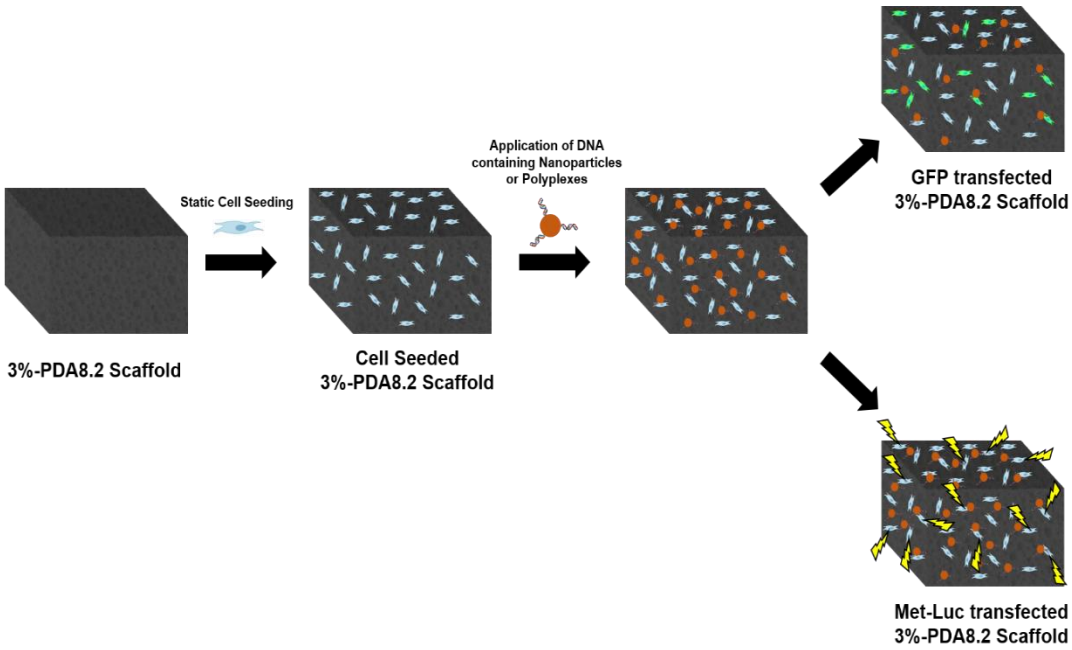

Figure 5.2 – Schematic illustrating the proposed external application method for 3D transfection of a pre-seeded PDA coated agarose scaffold, using either GFP containing or Met-Luc containing transfection complexes.

5.2.4.1.1 External application of calcium phosphate complexes

Scaffold containing media was firstly replaced with 900 µL complete media. Then, using the two best performing $CaCl_2$ concentrations from 2D monolayer transfection (25 mM and 56.25 mM) (section 5.2.3.1), CaP nanoparticle complexes consisting of 2.5 µg or 5 µg pCAG-MetLuc2 were formulated, as per Table 5.6. 100 µL of each nanoparticle complex solution was then gently applied to the surface of pre-seeded scaffolds and incubated for 4 hours (n=4 per group). After completion, transfection medium was replaced with fresh growth media and the well plate transferred to an incubator for longer term culture (37°C, 5% CO_2).

Alongside each nanoparticle solution, media only (negative control) and plasmid only controls were tested (n=4). Transfection was then assessed over a 7 day culture period using scaffold specific quantitative Met-Luc transfection assays, as per section 2.2.11.2.2.

Table 5.6 – Optimisation parameters for CaP mediated external application onto cell seeded agarose scaffolds.

Modality	CaP:DNA Incubation Solution Volume (per well)	Initial $CaCl_2$ Conc (2.5M stock)		Final $CaCl_2$ Conc per well	Culture Volume
		2.5 µg pDNA	5 µg pDNA		
Scaffold in 48 well plate	100 µL	0 mM		0 mM	1 mL
Scaffold in 48 well plate	100 µL	500 mM		25.0 mM	1 mL
Scaffold in 48 well plate	100 µL	1125 mM		56.25 mM	1 mL

5.2.4.1.2 External application of PEI polyplexes

Scaffold containing media was initially replaced with 900 µL serum free media (SFM). A range of polyplexes were then formulated consisting of 2.5 µg and 5 µg pCAG-MetLuc2 or pCAG-eGFP with N/P ratio's ranging from N/P8 – N/P40, as per Table 5.7. 100 µL of each polyplex solution was then gently applied to the surface of pre-seeded scaffolds and incubated for 4 hours (n=4 per group). After completion, transfection medium was replaced with fresh media and the well plate transferred to an incubator for longer term culture (37°C, 5% CO_2).

Alongside each polyplex solution, media only (negative control) and plasmid only controls were also tested (n=4). Transfection was then assessed over a 7 day culture period using scaffold specific quantitative Met-Luc transfection assays as well as qualitative fluorescence microscopy, as per sections 2.2.11.1.2 and 2.2.11.2.2.

Table 5.7 – Optimisation parameters for PEI mediated external application onto cell seeded agarose scaffolds.

Modality	PEI:DNA Incubation Solution Volume (per well)	PEI Conc (1µg/µL stock) (per well)		N/P Ratio	Culture Volume
		2.5 µg pDNA	5 µg pDNA		
24 well plate	100 µL SFM	0 µg	0 µg	0	1 mL
24 well plate	100 µL SFM	2.59 µg	5.17 µg	8	1 mL

24 well plate	100 µL SFM	7.76 µg	15.5 µg	24	1 mL
24 well plate	100 µL SFM	12.93 µg	25.86 µg	40	1 mL

5.2.5 3D GAM transfection study (F-AGE-1 and F-AGE polyplex GAMs)

Using the full processes outlined in chapter 2 section 2.2.2, a range of electrophoretically loaded agarose hydrogels were formulated via Feichtinger patterning and excision protocols. For high throughput quantitative analysis of 3D transfection, the pCAG-MetLuc2 luminescence reporter system was used as the GAM vector of choice for all patterning methods. All hydrogels were freeze-dried directly after gel excision and were then functionalised post scaffold fabrication with a polydopamine (PDA) coating (8 hour, 2mg/mL) prior to cell seeding, as validated in chapter 4.

5.2.5.1 PDA coated F-AGE-1 GAMs

2.5 µg and 5 µg loaded PDA coated F-AGE-1 GAM scaffolds were ethanol sterilised and then placed into agarose treated 48 well plates as per static seeding method 3 (n=4 for each group - Table 5.8 A and B).

C2C12 and Y201 cells were simultaneously passaged and re-suspended to a concentration of $5x10^5$ cells/scaffold before seeding onto each scaffold (60 µL cell suspension – static seeding method 3 (section 2.2.5.1)). Cell populations were then incubated for 2-3 hours to allow sufficient scaffold attachment before all wells were flooded with 800 µL growth media, placed into an incubator and cultured under standard conditions (37°C, 5% CO_2).

Alongside each agarose GAM group, media only scaffolds (negative control) and plasmid only scaffolds were also tested (n=4). Over the course of a 7 day culture period, scaffold mediated transfection was then quantitatively assessed using Met-Luc assays, as described in section 2.2.11.2.2.

Furthermore, an additional set of F-AGE-1 agarose GAM scaffolds (n=1) were also formulated specifically for LIVE-DEAD staining (see Table 5.8). Scaffold seeding conditions remained the same as previously described above. Imaging, as per section 2.2.6, took place at the 48 hour timepoint directly before the first Met-Luc transfection assay.

Table 5.8 – The range of F-AGE-1 agarose GAM scaffolds formulated for the 3D transfection study. All scaffolds were functionalised post electrophoretic loading using previously optimised polydopamine coating conditions. pCAG-MetLuc2 expression vector was used in all cases.

F-AGE-1 Methodology		
PDA coated		
Scaffold Name	**pDNA Conc**	**LIVE-DEAD stained at 48 hours**
3%-Blank / Negative Control	N/A	✓
AGE1-2.5-0mM	2.5 µg	✗
AGE1-2.5-112.5mM	2.5 µg	✓
AGE1-2.5-162.5mM	2.5 µg	✗
AGE1-2.5-212.5mM	2.5 µg	✗
AGE1-2.5-225mM	2.5 µg	✓
AGE1-5-0mM	5 µg	✗
AGE1-5-112.5mM	5 µg	✓
AGE1-5-162.5mM	5 µg	✗
AGE1-5-212.5mM	5 µg	✗
AGE1-5-225mM	5 µg	✓

5.2.5.2 PDA coated F-AGE polyplex GAMs

2.5 µg and 5 µg loaded PDA coated F-AGE polyplex GAM scaffolds were ethanol sterilised and placed into agarose treated 48 well plates, as per static seeding method 3 (n=4 for each group - Table 5.9). C2C12 and Y201 cells were similarly passaged and re-suspended to a concentration of $5x10^5$ cells/Scaffold before static seeding onto each scaffold. As the proceeding steps are exactly the same as above, the protocol outlined in section 5.2.5.1 was continued from this stage until completion.

Likewise, additional sets of F-AGE polyplex agarose scaffolds (n=1) were also formulated specifically for LIVE-DEAD staining (see Table 5.9). Scaffold seeding conditions remained consistent with the above 3D transfection study whilst imaging was again performed at 72 hours.

Table 5.9 – A range of agarose GAM scaffolds formulated using the F-AGE polyplex electrophoretic patterning method. All scaffolds were functionalised post electrophoretic loading using previously optimised polydopamine coating conditions. pCAG-MetLuc2 expression vector was used in all cases.

F-AGE Polyplex Method			
PDA coated			
Scaffold Name	**pDNA Conc**	**N/P Ratio**	**LIVE-DEAD stained at 48 hours**
3%-Blank / Negative Control	N/A	N/A	✓
AGE-2.5-N/P0	2.5 µg	0	✗
AGE-2.5-N/P8	2.5 µg	8	✓
AGE-2.5-N/P16	2.5 µg	16	✗
AGE-2.5-N/P24	2.5 µg	24	✗
AGE-2.5-N/P40	2.5 µg	40	✓
AGE-5-N/P0	5 µg	0	✗
AGE-5-N/P8	5 µg	8	✓
AGE-5-N/P16	5 µg	16	✗
AGE-5-N/P24	5 µg	24	✗
AGE-5-N/P40	5 µg	40	✓

5.3 Results

5.3.1 Generation of pCAG-MetLuc2 reporter plasmid

For effective insertion of the *Metridia* Luciferase gene into the pCAG-d2-eGFP vector, the donor (pMetLuc2) and recipient plasmid (pCAG-d2-eGFP) sequences were initially analysed using SnapGene software for complementary single cutter restriction sites upstream and downstream of the gene insert. AgeI and NotI restriction enzymes were consequently selected, producing cohesive end products incapable of re-ligation as well as limiting potential sequence reversal of insert.

Upon actual double digestion of pCAG-d2-eGFP and pMetLuc2 plasmids, two linearised fragments were generated from each plasmid – including the pCAG backbone of 4828 bp and a MetLuc insert of 674 bp, as shown in the agarose gel image (Figure 5.3 A). These fragments were purified from the gels and subsequently ligated, transformed and miniprepped in order to generate four distinct pCAG-MetLuc2 clones (pCAG-MetLuc2 (I-IV)).

A secondary comparative digest of these clones versus the source plasmids (AgeI and NotI) confirmed the presence of both fragments (Figure 5.3 B), with matching DNA fragments at 4828 bp and 647 bp, thus illustrating successful plasmid assembly.

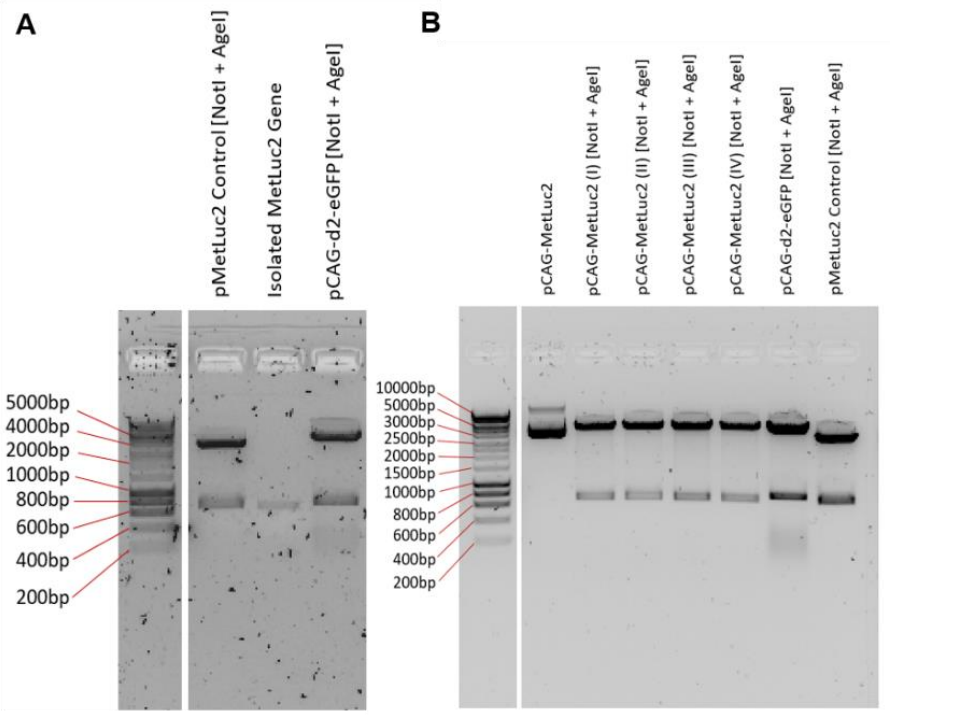

Figure 5.3 (A & B) – Synthesis of pCAG-MetLuc2 using restriction ligation methods. A) Double restriction digest of 1 µg pMetLuc2 Control donor plasmid and pCAG-eGFPd2 recipient plasmid using the NotI and AgeI restriction enzymes. B) Confirmatory double restriction digest of the final pCAG-MetLuc2 vector using NotI and AgeI restriction enzymes. Size Ladder = Hyperladder 1 kb.

5.3.2 Analysis of fluorescence and luminescence reporter expression

5.3.2.1 Basic calcium phosphate mediated 2D cell monolayer transfection

Using basic calcium phosphate transfection protocols found in the literature, pDNA-nanoparticle complexes containing either a fluorescent reporter vector pCAG-d2-eGFP or the newly generated pCAG-MetLuc2 luminescence vector were formulated and validated in terms of their expression within 2D cell monolayer models (C2C12 and Y201 cell lines) (Jordan *et al.*, 1996; Sambrook, 2001).

C2C12 and Y201 transfection using these nanoparticles was initially assessed qualitatively using CLSM techniques as illustrated in Figure 5.4. Upon excitation at 48 hours using the GFP channel, the negative control and pDNA only groups illustrated no detectable intracellular fluorescence in both cell lines. In contrast, in the pDNA-nanoparticle groups, in particular with glycerol shock, clear evidence of intracellular fluorescent protein production was displayed, thus implying that not only was successful transfection achieved, but also that the pCAG-d2-eGFP plasmid was indeed functional. Crucially, little evidence of transfection induced cell death was identified.

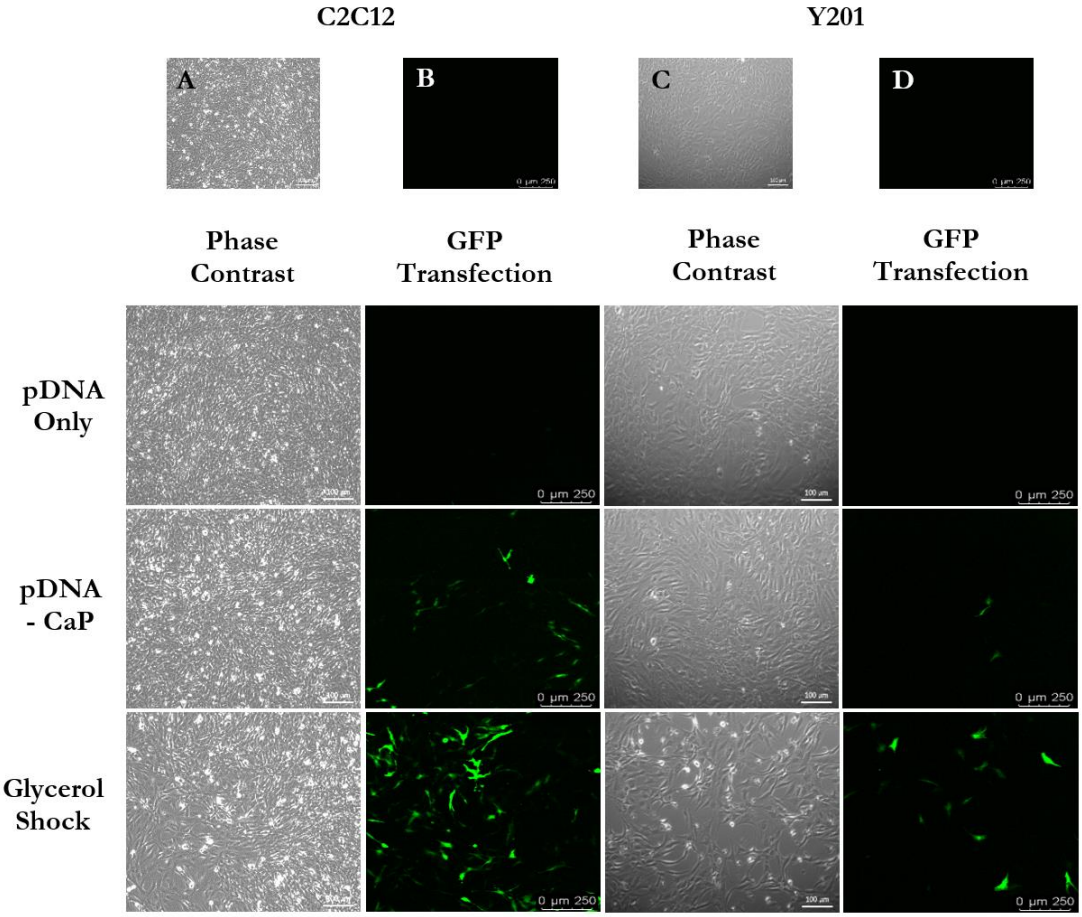

Figure 5.4 – Qualitative assessment of basic calcium phosphate mediated 2D cell monolayer transfection (C2C12 & Y201). Cells were seeded using static seeding techniques with a density of $0.4x10^5$ cells/well before transfection with nanoparticles containing 0.625 µg pCAG-eGFP. A & C) Phase contrast image of C2C12 and Y201 negative control groups respectively. B & D) Fluorescence image of C2C12 and Y201 negative control group respectively. Scale bars = 100 µm (phase contrast) and 250 µm (FITC filter).

To validate the above findings and to ensure homogeneity across both qualitative and quantitative transfection assay techniques, C2C12 and Y201 2D cell monolayer transfection using basic nanoparticle complexes was then re-assessed using the pCAG-MetLuc2 vector system, thus providing an equivalent numerical dataset in which statistical analysis of the independent variable could be performed (Figure 5.5).

Firstly, in the context of validating the efficacy of the met-luc reporter system as a quantitative measure of transfection, basic observations of both datasets heavily indicate that successful transfection was again achieved, using the CaP co-precipitiation method and that the newly synthesised luminescence reporter vector (pCAG-MetLuc2) could effectively express the met-luc gene insert, within both cell types. Additionally, based on these findings, post translational luciferase secretion into the surrounding cell media was also effective.

Secondly, it further shows that the in-house met-luc assay can successfully and reliably translate overall enzymatic yield produced by cells into meaningful and quantifiable transfection data, by means of fold luminescence values. In short, a functioning in-house met-luc reporter assay system was developed.

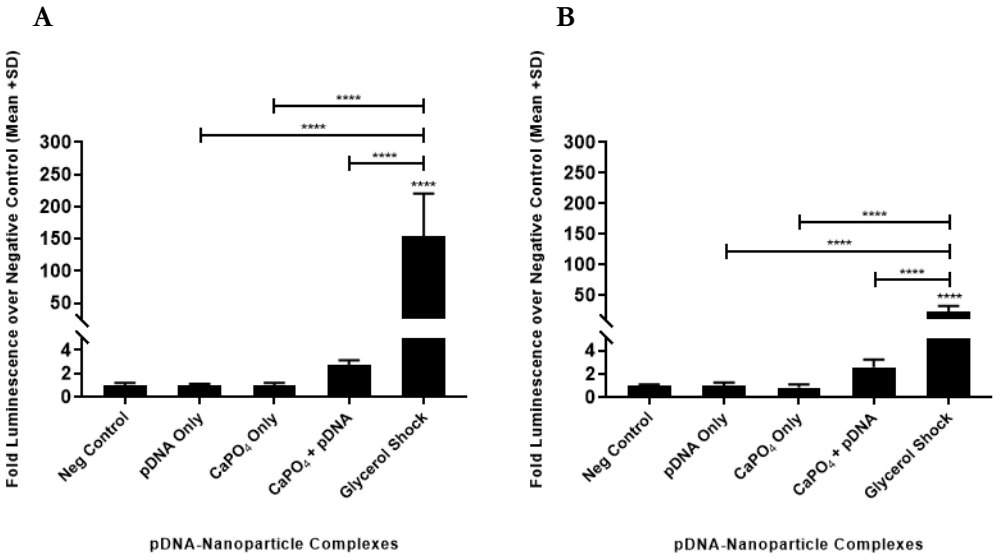

Figure 5.5 (A & B) – Quantitative assessment of basic calcium phosphate mediated C2C12 and Y201 2D cell monolayer transfection. A: Fold luminescence detected from C2C12 cells 48 hours after exposure to pDNA-nanoparticle complexes. B: Fold luminescence detected from Y201 cells 48 hours after exposure to pDNA-nanoparticle complexes. Data was expressed as Fold Luminescence over negative control (Mean + SD). One-way ANOVA with Tukey's multiple comparison test was used to compare across the independent variables. **** = $P < 0.0001$.

In terms of transfecton behaviour, a similar pattern of reporter gene expression was identified, with pDNA-nanoparticle groups, in particular with glycerol shock groups inducing the greatest detectable expression. Interestingly however, only the glycerol shock group alone experienced significantly higher increases in luciferase expression in comparison to the negative control.

Furthermore, when both transfection capable groups were compared, further significant differences were identified ($P<0.0001$).

In short, both qualitative and quantitative methods importantly conveyed a mutual agreement with regards to overall transfection behaviour, thus establishing a good degree of confidence in either method of assessment. Furthermore, it could be concluded that when calcium phosphate nanoparticle complexes were applied alone (in absence of glycerol), they appeared to produce mediocre or non-significant expression profiles for what is usually required of a effective 2D transfection system. Upon reflection, this was deemed unsurprising considering the basic nature of this initial calcium phosphate transfection methodology. Subsequent optimisation of the transfection vehicles was therefore considered essential to improve all aspects of the nanoparticle complex transfection pathway, with the overall goal of generating expression profiles which performed comparbly as a minimum, to those presented in glycerol shock groups.

5.3.2.2 Basic PEI mediated 2D cell monolayer transfection

In a similar fashion, using basic PEI transfection protocols, polyplexes containing a fluorescent reporter vector or the newly generated pCAG-MetLuc2 luminescence vector were also evaluated in terms of their expression within 2D cell monolayer models (C2C12 and Y201 cell lines).

C2C12 and Y201 transfection using these polyplexes was assessed qualitatively using CLSM techniques and as such was illustrated in Figure 5.6. Upon subsequent excitation using the GFP channel, the negative control and pDNA only groups once again illustrated no detectable intracellular fluorescence in both cell lines. The N/P24 polyplex formulation however induced substantial cellular GFP production upon payload delivery, in both datasets, thus implying successful transfection and expression using these polyplex vehicles.

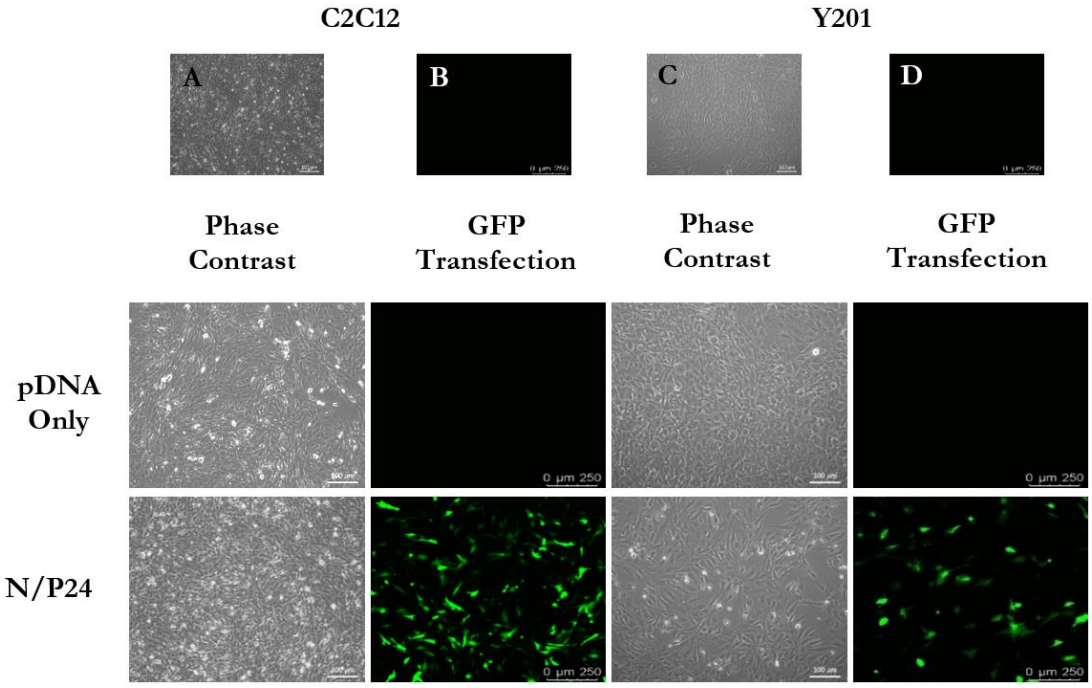

Figure 5.6 – Qualitative assessment of basic PEI mediated 2D cell monolayer transfection (C2C12 & Y201). Cells were seeded using static seeding techniques with a density of $0.4x10^5$ cells/well before transfection with nanoparticles containing 0.625 µg pCAG-eGFP. A & C) Phase contrast image of C2C12 and Y201 negative control groups respectively. B & D) Fluorescence image of C2C12 and Y201 negative control group respectively. Scale bars = 100 µm (phase contrast) and 250 µm (FITC filter).

As with section 5.3.2.1, the findings outlined above were then validated qualitatively for both cell lines and are illustrated in Figure 5.7.

Upon analysis of polyplex transfection behaviour for both cell lines, it was clearly shown that very large significant increases in fold luminescence (in comparison to negative control) occur when cells underwent polyplex mediated transfection. This was also the case for both cell lines upon comparisons with pDNA only groups ($P<0.0001$).

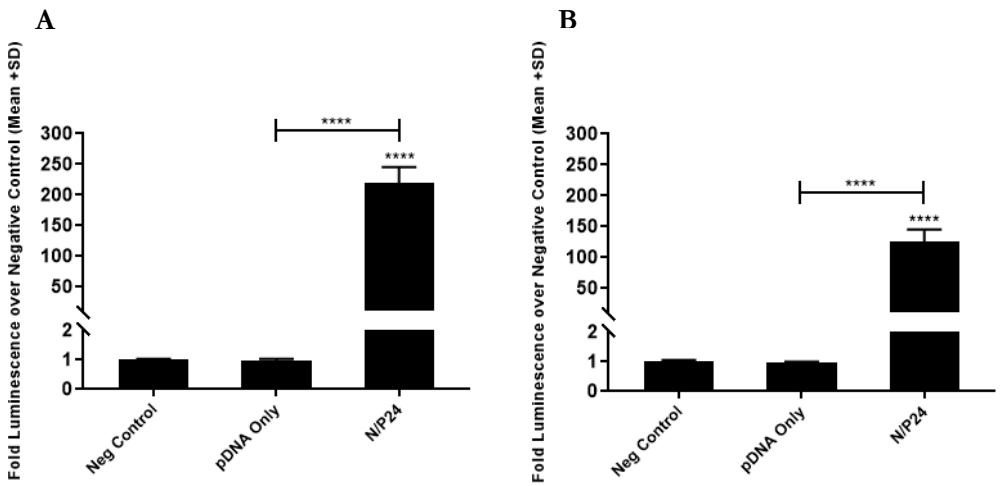

Figure 5.7 (A & B) – Quantitative assessment of basic PEI mediated C2C12 and Y201 2D cell monolayer transfection. A: Fold luminescence detected from C2C12 cells 48 hours after exposure to polyplexes. B: Fold luminescence detected from Y201 cells 48 hours after exposure to polyplexes. Data was expressed as Fold Luminescence over negative control (Mean + SD). One-way ANOVA with Tukey's multiple comparison test was used to compare across the independent variables. **** = $P < 0.0001$.

Overall, the data presented in this section, along with those shown in section 5.3.2.1, illustrated that the pCAG-d2-eGFP and pCAG-MetLuc2 expression vectors were effective at inducing the expression of reporter proteins, at a cellular level. Furthermore, there was also a significant level of agreement between qualitative and quantitative assessment strategies when evaluating the application of both polyplexes and calcium phosphate nanoparticle complexes on 2D cell monolayer models. This finding is of critical importance as it validates the use of either assessment method for future experimentation whilst also providing a foundation for specific transfection capacities of polyplex or nanoparticle mediated transfection. This crucially included the major finding that both gene delivery methods, in their basic form, were generally capable of inducing some form of 2D cellular transfection, over a 48-hour period.

It was however considered essential to continue experimentation for both methods, specifically modifying formulation parameters such as pDNA concentration and N/P ratio (or $CaCl_2$ concentration) so as to optimise and maximise the transfection potential for each strategy. Such optimisation steps were thought to be highly beneficial for the downstream testing of electrophoretic agarose GAM systems, with outcomes in 2D being highly translatable into 3D systems.

5.3.3 Optimisation of 2D cell monolayer transfection methodologies

For optimisation purposes, two different independent variable parameters for each of the transfection methodologies (Calcium phosphate mediated and PEI mediated) were identified and then evaluated – the pDNA concentration (for both methods) and also either initial $CaCl_2$ concentration or the N/P ratio. By using a low-high range for each of these variables, in conjunction with quantitative methods of transfection assessment, an optimal set of cell line

specific conditions was then identified which most effectively instigated transfection over the course of 7 days.

Selection of said parameters was achieved via time-course assessment of fold luminescence measurements as well as analysis of the total fold luminescence produced termed "cumulative fold luminescence over negative control". Total fold luminescence was calculated by measuring the total area under the curve (AUC) for each individual group, across the timecourse.

5.3.3.1 Calcium phosphate nanoparticle payloads

The following datasets are presented in two sections: first, the optimisation of pDNA concentration (at the original $CaCl_2$ concentration of 12.5 mM), followed by the optimisation of $CaCl_2$ concentration using the best-performing pDNA concentrations.

5.3.3.1.1 Optimisation of pDNA concentration

Evaluations of the 7 day timecourse data for C2C12 (Figure 5.8 A) revealed modifications to the pDNA concentration had little effect on the transfection capabilities of pDNA-CaP complexes, with meagre levels of Met-Luc gene expression identified in all tested formulations. The expression pattern in these cases generally appeared to peak during the 48 hour time-window (<5 AUC units), before then proceeding to gradually decline, up to the final measurement taken at 7 days.

When equivalent C2C12 AUC values were calculated from the curves, a dose-dependent relationship between Met-Luc expression and pDNA concentration was however presented, with the 2 µg formulations inducing the greatest cumulative gene expression. Although this increase was statistically significant in comparison to the negative control (P=0.0003), the differences in gene expression between each of the pDNA concentrations however appeared non-significant.

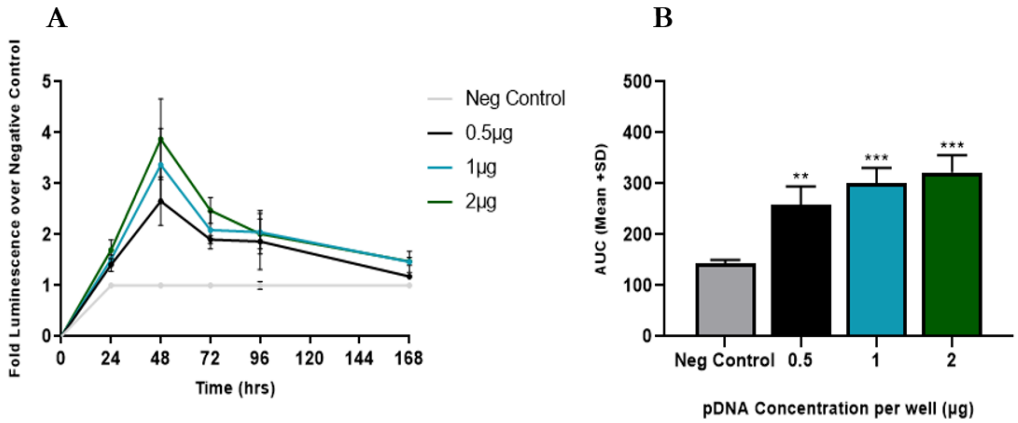

Figure 5.8 (A & B) – Evaluation of the effect of pDNA concentration on the transfection capability of calcium phosphate nanoparticle complexes when applied to C2C12 cell monolayers. A: 7 Day time course Met-Luc assay of CaP mediated cell monolayer transfection using 0.5-2 µg pCAG-MetLuc2. B: Effect of pDNA concentration on cumulative CaP mediated Met-Luc expression, calculated using area under the curve measurements. Data was expressed as Fold Luminescence over negative control (Mean ±SD) or Area under Curve (AUC) (Mean +SD). One-Way ANOVA with Tukey's multiple comparisons test was used to compare between groups. ** = $P < 0.01$, *** = $P < 0.001$.

The 7 day timecourse data for Y201 (Figure 5.9 A) revealed similar findings, with no obvious improvements in gene expression observed upon the application of pDNA-CaP complexes containing increasing concentrations of pDNA. Gene expression also appeared lower in this cell line, with no clear time-window in which expression appeared to peak. By 7 days, only marginal expression was found.

When the Y201 AUC values were calculated from the curves (Figure 5.9 B), the 1 µg nanoparticle complexes specifically produced the greatest cumulative expression, and was the only condition which produced a significant increase in expression when compared to the negative control (P=0.0279).

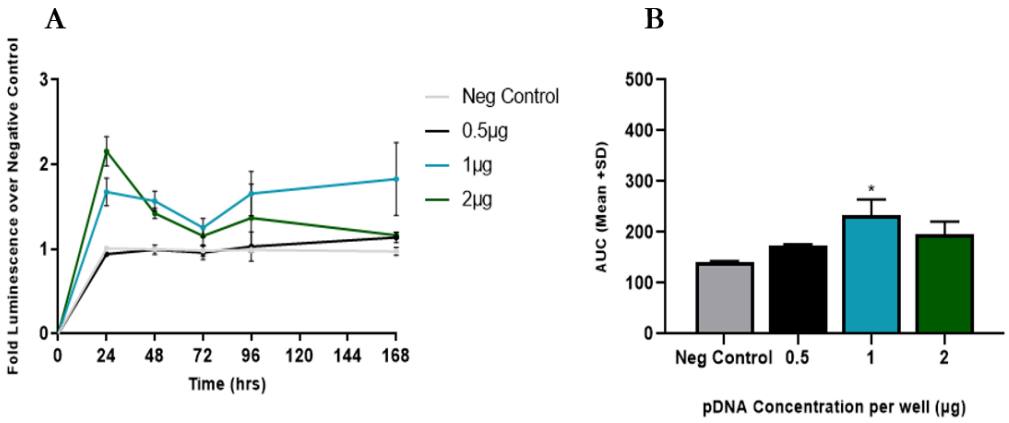

Figure 5.9 (A & B) – Evaluation of the effect of pDNA concentration on the transfection capability of calcium phosphate nanoparticle complexes when applied to Y201 cell monolayers. A: 7 Day time course Met-Luc assay of CaP mediated cell monolayer transfection using 0.5-2µg pCAG-MetLuc2. B: Effect of pDNA concentration on cumulative CaP mediated Met-Luc expression, calculated using area under the curve measurements. Data was expressed as Fold Luminescence over negative control (Mean ±SD) or Area under Curve (AUC) (Mean +SD). One-Way ANOVA with Tukey's multiple comparisons test was used to compare between groups. * = $P < 0.05$.

Overall, alterations to pDNA loading concentrations for nanoparticle complexation resulted in only marginal improvements to cumulative reporter gene expression in both cell lines, with gene expression remaining far below that identified after glycerol shock treatment (pre-optimised levels). Nevertheless, for C2C12 and Y201 cells, 2 µg and 1 µg appeared optimal at this stage, respectively.

5.3.3.1.2 Optimisation of $CaCl_2$ concentration

The following results subsequently displayed the effect of modifications to $CaCl_2$ concentration on gene expression, specifically in the context of the best performing pDNA concentrations as stated in the previous section (C2C12 – 2 µg, Y201 – 1 µg).

Evaluations of the 7 day timecourse data for C2C12 (Figure 5.10 A) revealed positive changes to the Met-Luc expression profiles upon alterations to the $CaCl_2$ concentration. Specifically, in these cases, gene expression levels appeared larger and more sustained, with larger expression peaks

generally being observed during the 48 hour or 72 hour time-window (~15 fold increase over negative control) before eventually declining at 7 days.

When C2C12 AUC values were calculated from the equivalent curves (Figure 5.10 B), no particular trend was illustrated. Despite this, peak values were specifically identified within the 56.25 mM group. Such increases in total Met-Luc expression were deemed statically significant in this group, as well as in the 25 mM, 37.5 mM groups, when compared to the negative control. However, a lack of significance was found when the differences in cumulative Met-Luc expression were compared between each of these three best performing groups.

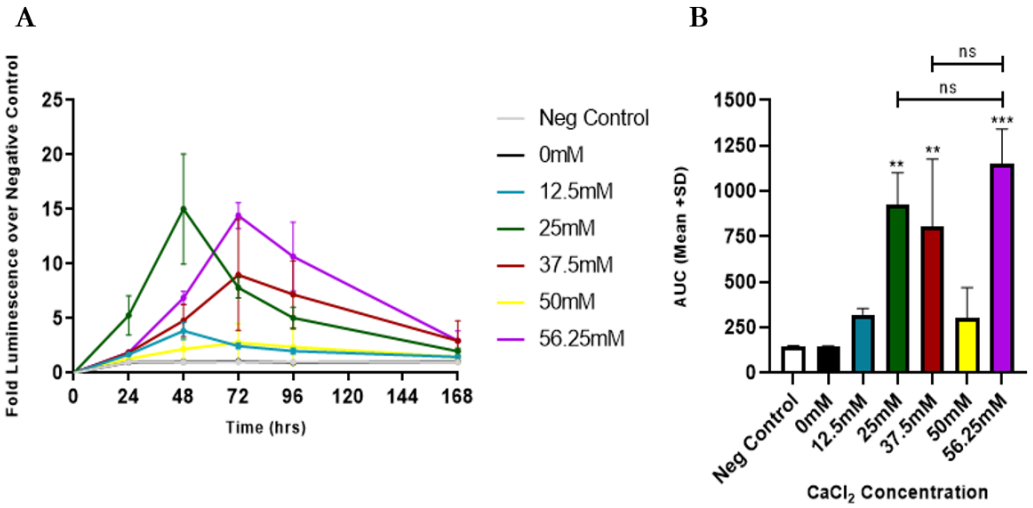

Figure 5.10 (A & B) – Evaluation of the effect of $CaCl_2$ concentration on the transfection capability of calcium phosphate nanoparticle complexes when applied to C2C12 cell monolayers. A: 7 Day time course Met-Luc assay of CaP mediated cell monolayer transfection using complexes formulated with initial $CaCl_2$ concentrations ranging from 0mM-56.25mM. B: Effect of $CaCl_2$ concentrations on cumulative CaP mediated Met-Luc expression, calculated using area under the curve measurements. Data was expressed as Fold Luminescence over negative control (Mean ±SD) or Area under Curve (AUC) (Mean +SD). One-Way ANOVA with Tukey's multiple comparisons test was used to compare between groups. ** = $P < 0.01$, *** = $P < 0.001$.

Unfortunately, upon application of these same nanoparticle complex types to Y201 cell monolayers (Figure 5.11 A), only marginal increases in gene expression were identified. Significantly, in these cases, expression profiles generally remained low (<5 fold change) in all groups, with the 56.25 mM formulation appearing most effective.

When cumulative Met-Luc values were calculated (Figure 5.11 B), this finding was substantiated, with the 56.25 mM group displaying the largest overall quantity of reporter gene produced (354 AUC). The increase in total Met-Luc expression was statistically significant in comparison to the negative control ($P<0.0001$), however crucially lacked significance when compared to the next best performing group (50 mM).

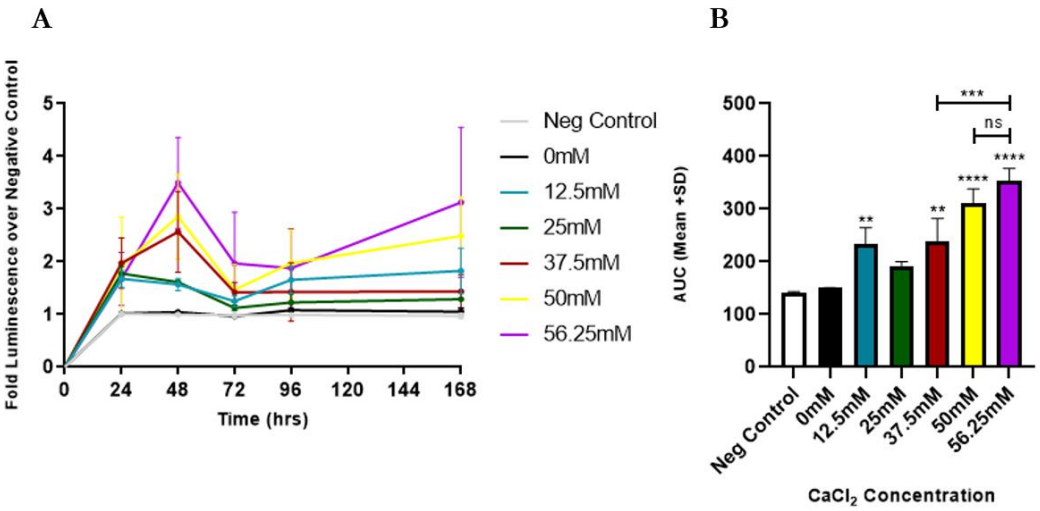

Figure 5.11 (A & B) – Evaluation of the effect of $CaCl_2$ concentration on the transfection capability of calcium phosphate nanoparticle complexes when applied to Y201 cell monolayers. A: 7 Day time course Met-Luc assay of CaP mediated cell monolayer transfection using complexes formulated with initial $CaCl_2$ concentrations ranging from 0mM-56.25mM. B: Effect of $CaCl_2$ concentrations on cumulative $CaPO_4$ mediated Met-Luc expression, calculated using area under the curve measurements. Data was expressed as Fold Luminescence over negative control (Mean ±SD) or Area under Curve (AUC) (Mean +SD). One-Way ANOVA with Tukey's multiple comparisons test was used to compare between groups. ** = $P < 0.01$, *** = $P < 0.001$.

Overall, alterations to $CaCl_2$ concentrations during nanoparticle complex formulation resulted in a considerable positive effect on both peak Met-Luc expression as well as total Met-Luc produced by cells, over the course of a 7 day time period. It was therefore found in both cell lines, that a pDNA-nanoparticle formulation containing a final 56.25 mM $CaCl_2$ concentration was considered optimal and was therefore taken forward for future studies.

Based on the outcomes of each optimisation step within the calcium phosphate mediated transfection study, it was generally found that alterations to pDNA concentration and $CaCl_2$ concentration could amplify nanoparticle transfection capabilities to some regard (approximately 4 fold in the case of C2C12), however unfortunately remaining largely below the expression displayed in that of pre-optimised glycerol shock treatment groups. In the case of C2C12, glycerol shock induced 10 fold greater Met-Luc expression (154.1 versus 15 fold luminescence over negative control) whilst Y201 glycerol shock induced 4 fold greater Met-Luc expression (15 versus 3.5 fold luminescence over negative control). As a result of this, the current co-precipitation CaP transfection method used in 2D cell monolayer transfection was found to be insufficient in terms of vector gene delivery and therefore highly unlikely to be capable of a long term therapeutic response in its current form.

5.3.3.2 PEI mediated transfection

The PEI optimisation results were also divided into two sections, firstly in terms of the optimisation of pDNA concentration (using the original N/P ratio - 24), and secondly by the

optimisation in terms of the N/P ratio (using the best performing pDNA concentrations for each cell line).

5.3.3.2.1 Optimisation of pDNA concentration

Based on the 7 day timecourse data for C2C12 (Figure 5.12 A), it was observed that that modifications to pDNA concentration within polyplexes has a large effect on the daily amount of reporter protein expressed by cells. Specifically, daily Met-Luc expression appeared most optimal at the midpoint pDNA concentration (1 µg), producing a substantial burst release expression profile which peaked during the 48 hour time-window, before eventually diminishing at 7 days.

C2C12 AUC values (Figure 5.12 B) substantiated this finding, clearly detailing that the 1 µg polyplex group induces the greatest cumulative Met-Luc expression over the 7 days post transfection. Such amplification in the levels of met-luc expressed was also considered significant with regards to the negative control ($P<0.0001$) as well as when compared to the other polyplex groups (0.5 µg, $P=0.0005$ and 2 µg, $P<0.0001$).

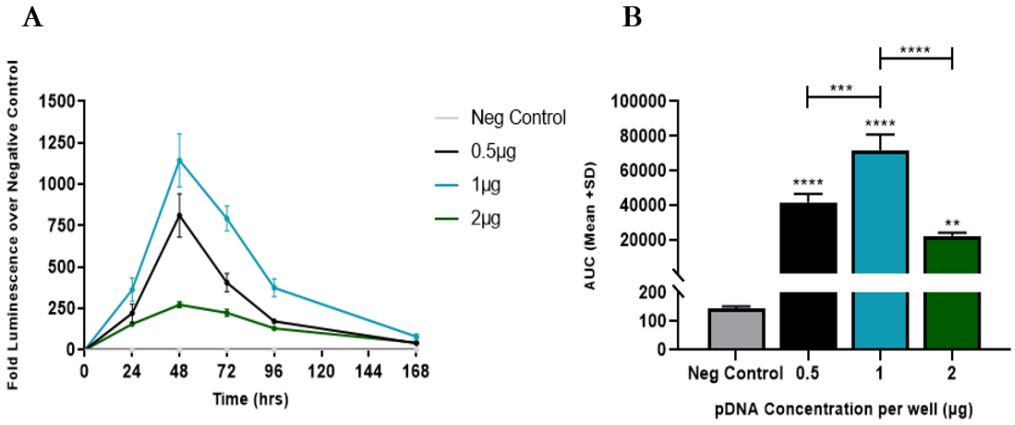

Figure 5.12 (A & B) – Evaluation of the effect of pDNA concentration on the transfection capability of PEI polyplexes when applied to C2C12 cell monolayers. A: 7 Day time course Met-Luc assay of PEI mediated cell monolayer transfection using 0.5-2 µg pCAG-MetLuc2. B: Effect of pDNA concentration on cumulative polyplex mediated Met-Luc expression, calculated using area under the curve measurements. Data was expressed as Fold Luminescence over negative control (Mean ±SD) or Area under Curve (AUC) (Mean +SD). One-Way ANOVA with Tukey's multiple comparisons test was used to compare between groups. ** = $P < 0.01$, *** = $P < 0.001$, **** = $P < 0.0001$.

Time course distributions of Y201 transfection (Figure 5.13 A) illustrated a similar trend with regards to the effect of pDNA modification, albeit at a much lower expression range in comparison to C2C12. Once more, the 1 µg polyplex formulation appeared most optimal for daily Met-Luc expression, however interestingly producing expression profiles which were considerably more gradual, over the course of the 7 days. As a result, expression peaks were generally presented at the 72-96 hour time-windows, before then declining at 7 days.

Upon calculation and analysis of Y201 AUC values (Figure 5.13 B), this hypothesis was further substantiated with the 1 µg polyplex group displaying the greatest cumulative level of reporter gene expression. Such increases in cellular expression were considered statistically significant when compared to the negative control and also to the 0.5 µg polyplex group, however interestingly a lack of significance was found when compared to the 2 µg group.

At this stage, it was therefore concluded that changes to pDNA concentration during the formulation of polyplexes has a substantial effect on the transfection capability in 2D cell monolayer settings, with optimal concentrations in both cell lines occurring at the midpoint of the range tested (i.e 1 µg).

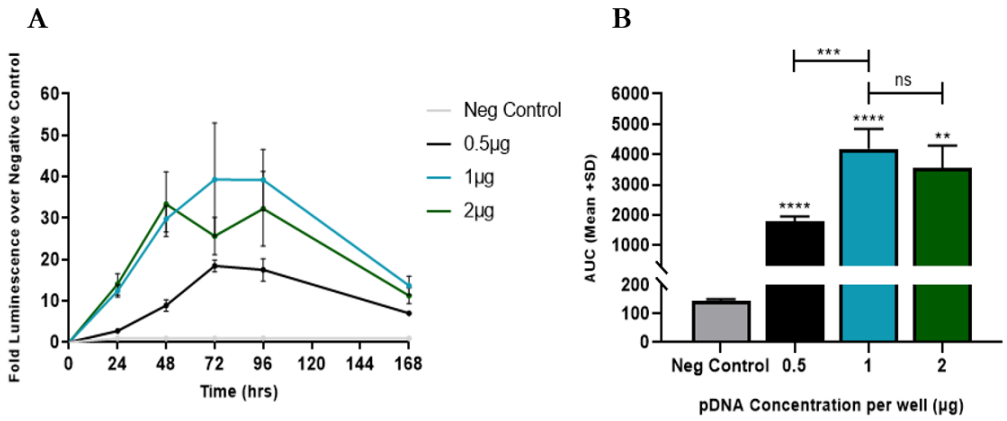

Figure 5.13 (A & B) – Evaluation of the effect of pDNA concentration on the transfection capability of PEI polyplexes when applied to Y201 cell monolayers. A: 7 Day time course Met-Luc assay of PEI mediated cell monolayer transfection using 0.5-2 µg pCAG-MetLuc2. B: Effect of pDNA concentration on cumulative polyplex mediated Met-Luc expression, calculated using area under the curve measurements. Data was expressed as Fold Luminescence over negative control (Mean ±SD) or Area under Curve (AUC) (Mean +SD). One-Way ANOVA with Tukey's multiple comparisons test was used to compare between groups. ** = $P < 0.01$, *** = $P < 0.001$, **** = $P < 0.0001$.

5.3.3.2.2 Optimisation of N/P ratio

The following results subsequently displayed the effect of modifications to N/P ratio on gene expression, specifically in the context of the best performing pDNA concentrations (C2C12 – 1 µg, Y201 – 1 µg).

Evaluations of the subsequent 7 day timecourse data for C2C12 (Figure 5.14 A) revealed changes to N/P ratio generally had little effect on the gene expression profile of polyplexes, with N/P16, 24 and 32 all presenting similar distributions over the course of the 7 days of measurement. Interestingly, at minimum and maximum N/P ratios, reporter gene expression was considerably reduced, suggesting optimal Met-Luc enzyme expression converges on an N/P ratio midpoint – between 16 - 32 specifically. However, due to significant overlap of the line graphs within this midpoint range, AUC cumulative values of Met-Luc were required for definitive selection of a single optimal condition.

The resulting quantitative C2C12 AUC data (Figure 5.14 B) illustrates firstly that an N/P ratio of 24 produced the single greatest cumulative Met-Luc expression. Secondly, it can be substantiated that optimal N/P ratio's for this cell line converge over the 16-32 range, with the total AUC values of the N/P16, 24 and 32 polyplex groups all falling within a range of approximately 2000 units. Furthermore, analysis revealed the differences in the total cumulative Met-Luc expression between these groups was not deemed statistically significant.

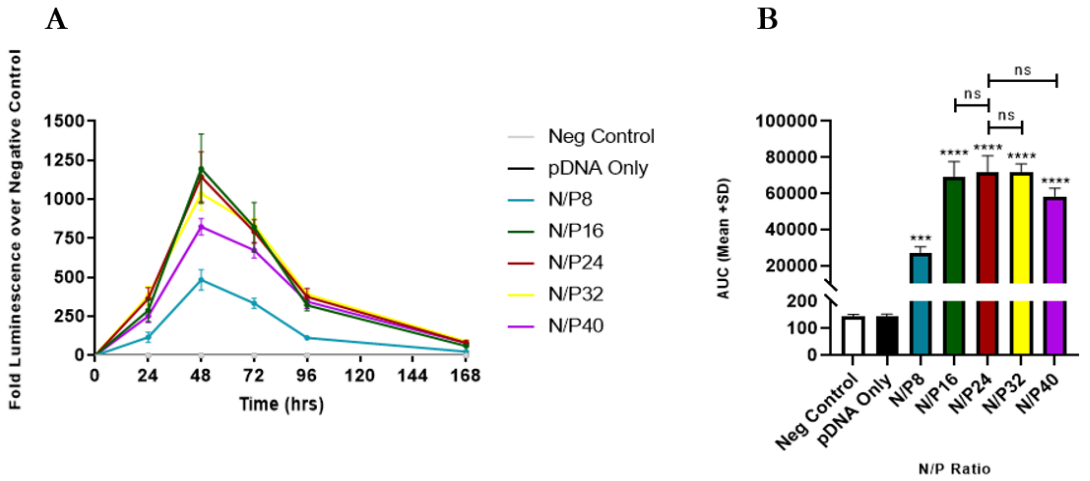

Figure 5.14 (A & B) – Evaluation of the effect of N/P ratio on the transfection capability of PEI polyplexes when applied to C2C12 cell monolayers. A: 7 Day time course Met-Luc assay of PEI mediated cell monolayer transfection using polyplexes formulated with N/P ratios ranging from 8-40. B: Effect of N/P ratio on cumulative PEI mediated Met-Luc expression, calculated using area under the curve measurements. Data was expressed as Fold Luminescence over negative control (Mean ±SD) or Area under Curve (AUC) (Mean +SD). One-Way ANOVA with Tukey's multiple comparisons test was used to compare between groups. ns = no significant difference, *** = $P < 0.001$, **** = $P < 0.0001$.

Expression profiles of transfected Y201 cells (Figure 5.15 A) revealed a similar expression pattern as described in C2C12, albeit with lower overall Met-Luc produced at each of the measured timepoints. However in contrast to the data illustrated in Figure 5.14 A, less overlap was identified within the distributions and crucially revealed that an N/P ratio of 24 generally induced the largest daily met-luc expression, at each of the timepoints.

This hypothesis was corroborated by Y201 AUC cumulative data (Figure 5.15 B), which showed N/P24 polyplexes produced the greatest total reporter gene expression. Interestingly, upon analysis, polyplexes formulated using N/P24 ratios produced increases in total Met-Luc expression which were deemed statistically significant in all groups except N/P32.

Overall, for C2C12 and Y201 cells, the N/P24 ratio was taken forward and considered most optimal for polyplex mediated transfection.

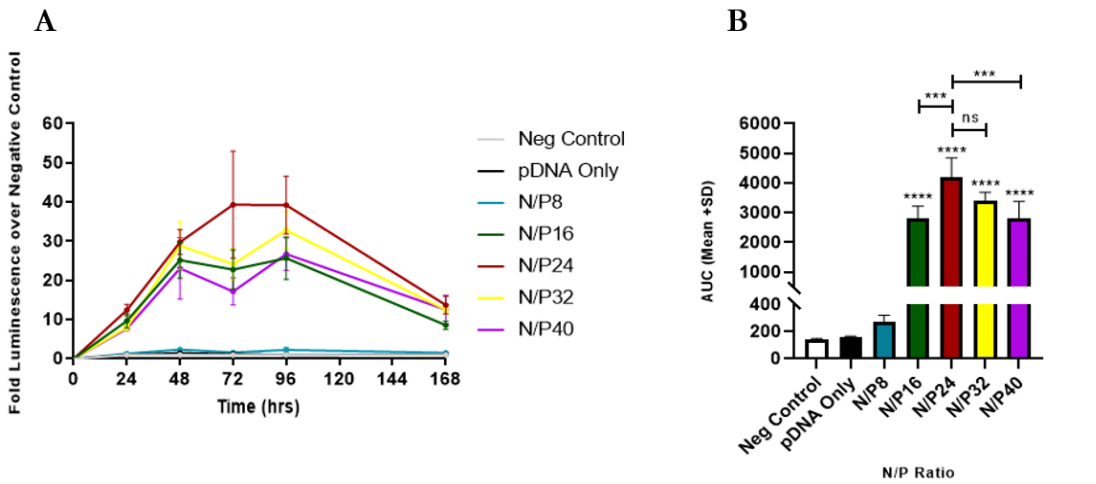

Figure 5.15 (A & B) – Evaluation of the effect of N/P ratio on the transfection capability of PEI polyplexes when applied to Y201 cell monolayers. A: 7 Day time course Met-Luc assay of PEI mediated cell monolayer transfection using polyplexes formulated with N/P ratios ranging from 8-40. B: Effect of N/P ratio on cumulative PEI mediated Met-Luc expression, calculated using area under the curve measurements. Data was expressed as Fold Luminescence over negative control (Mean ±SD) or Area under Curve (AUC) (Mean +SD). One-Way ANOVA with Tukey's multiple comparisons test was used to compare between groups. ns = no significant difference, *** = $P < 0.001$, **** = $P < 0.0001$.

Table 5.10 – Final optimised conditions for calcium phosphate and PEI mediated 2D cell monolayer transfection in C2C12 and Y201 cell lines.

Transfection Method	Cell Line	Optimal N/P Ratio Concentration	Optimal pDNA Concentration
CaP Transfection	C2C12	56.25mM	2µg
CaP Transfection	Y201	56.25mM	1µg
PEI Transfection	C2C12	N/P24	1µg
PEI Transfection	Y201	N/P24	1µg

5.3.4 Validation of 3D scaffold transfection control study

Using the knowledge obtained from section 5.3.3 as well as literary examples, scaffold mediated transfection in its basic form (i.e using the external application method) was then tested to ascertain firstly; whether a cell seeded PDA functionalised agarose scaffold could support localised cellular transfection, and secondly; whether both quantitative and qualitative methods of transfection assessment were capable of detecting said transfection, in a 3D environment.

5.3.4.1 Quantitative assessment of 3D nanoparticle transfection

CaP nanoparticle complexes, prepared as detailed in section 5.2.4.1.1, were applied to cell-seeded scaffolds. A 7-day time-course assay was constructed for both C2C12 and Y201 seeded scaffolds In general, the luminescence changes observed in the time course line graphs tentatively indicated

successful secretion of Met-Luc into the scaffold growth media from adhered cells, allowing reliable transfection data to be obtained using the established Met-Luc assay procedure.

In terms of transcription performance, CaP-mediated transfection in C2C12 and Y201 seeded scaffolds (Figure 5.16 and Figure 5.17) gave low luminescence values across both the 2.5 µg and 5 µg pDNA concentrations. The fold luminescence values peaked at approximately 5 in both cases, suggesting only a small amounts of met-luc was produced by any of the adhered cells.

Based on these preliminary results, the method of CaP external nanoparticle application was ineffective in instigating the necessary 3D transfection profiles required. In fact, it performed worse to those identified in optimized 2D cell monolayer models where glycerol treatment was also excluded. Therefore, nanoparticle complexes were replaced with the more promising polyplex transfection strategy.

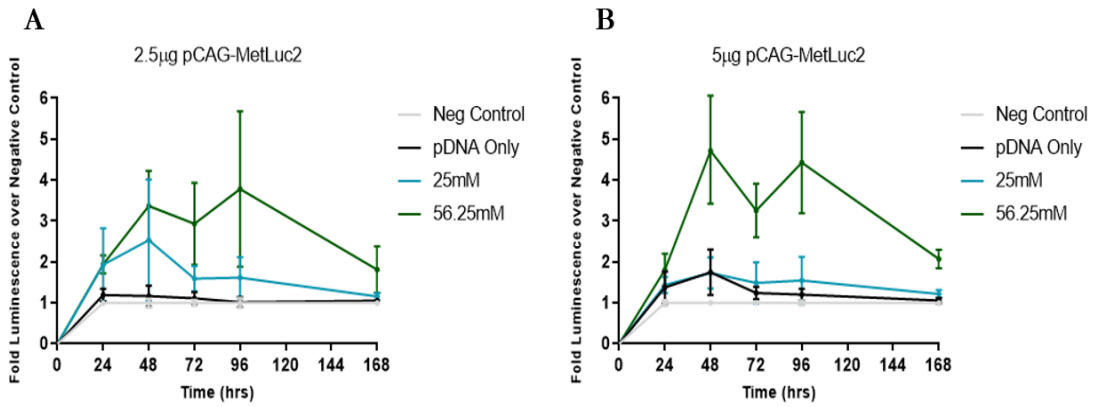

Figure 5.16 (A & B) – Calcium phosphate mediated C2C12 3D scaffold transfection using external application method (No glycerol shock treatment). A & B: 7 Day time course Met-Luc assay of CaP mediated C2C12 scaffold transfection using either 2.5 µg or 5 µg pCAG-MetLuc2. Cell media was exchanged 24 hours prior to Met-Luc assay measurements performed on days 1, 2, 3, 4 & 7. Data was expressed as Fold Luminescence over negative control (Mean ±SD).

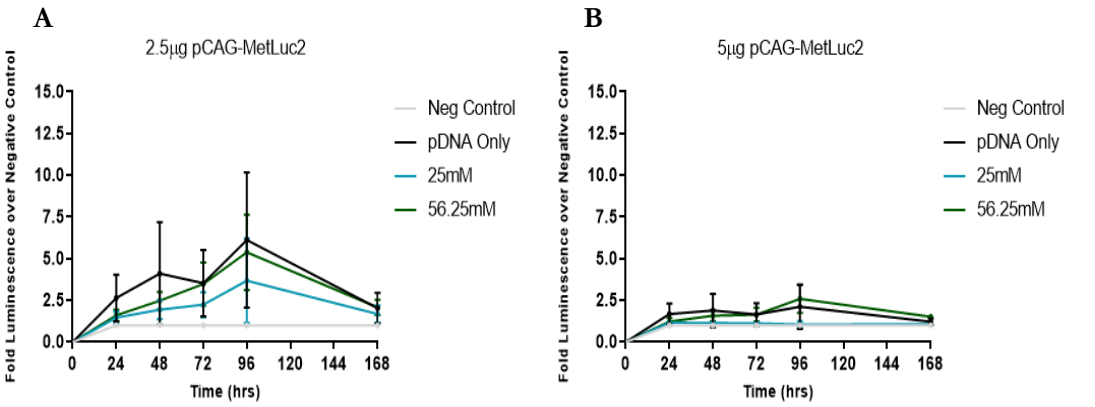

Figure 5.17 (A & B) – Calcium phosphate mediated Y201 3D scaffold transfection using external application method (No glycerol shock treatment). A & B: 7 Day time course Met-Luc assay of CaP mediated Y201 scaffold transfection using either 2.5 µg or 5 µg pCAG-MetLuc2. Cell media was exchanged 24 hours prior to Met-Luc assay measurements performed on days 1, 2, 3, 4 & 7. Data was expressed as Fold Luminescence over negative control (Mean ±SD).

5.3.4.2 Quantitative assessment of 3D PEI transfection

The external application PEI optimisation results were once again divided into two sections, initially in terms of the optimisation of pDNA concentration (using the original N/P ratio - 24), and then by the optimisation in terms of the N/P ratio (using the best performing pDNA concentrations for each cell line).

5.3.4.2.1 Optimisation of pDNA concentration

Immediate observations from Figure 5.18 and Figure 5.19 importantly corroborated previous results which indicated cellular Met-Luc was secreted by both cell types whilst adhered to or within a 3D agarose scaffold environment. Furthermore, it was shown that the previously validated Met-Luc assay system could also continue to detect the secreted gene product when in the presence of a PDA coated scaffold material and that the final luminescence values produced were left unaffected as a result.

Subsequent analysis of the 7 day time-course transfection data for C2C12 seeded cells (Figure 5.18 A) revealed that external application of polyplexes onto cell-laden scaffolds resulted in substantial amounts of 3D cell transfection. Specifically, this presented as a classical burst release expression pattern whereby peak expression occurred during the 48 hour time-window before rapidly declining to marginal levels at 96 hours. In terms of pDNA optimisation, both polyplex formulations produced similar expression profiles, with 5 µg appearing marginally more effective than the equivalent 2.5 µg group.

Upon calculation of C2C12 AUC values (Figure 5.18 B), it was confirmed that the 5 µg polyplex formulation induced the greatest scaffold based cumulative gene expression over the 7 days of culture and measurement. Despite this, such increases were not large enough to produce statistically significant differences when compared to the 2.5 µg group.

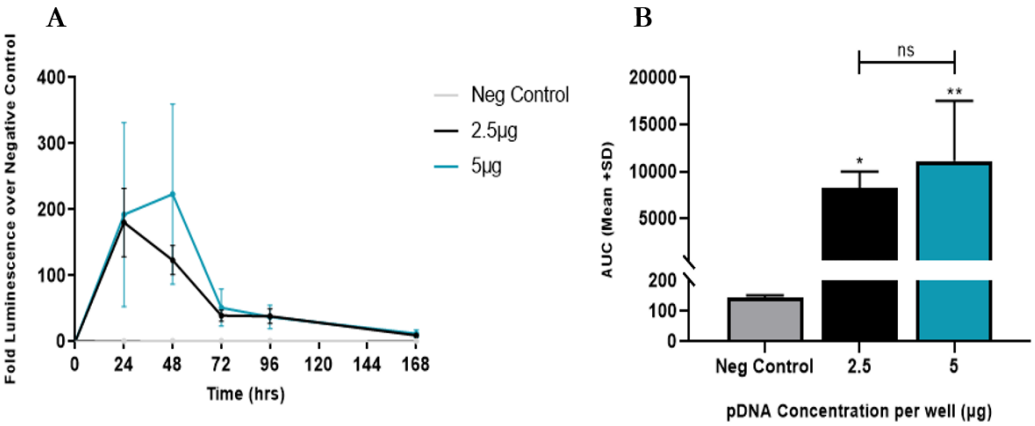

Figure 5.18 (A & B) – Evaluation of the effect of pDNA concentration on the 3D transfection capability of PEI polyplexes when applied, using the external application method, to C2C12 seeded scaffolds. A: 7 Day time course Met-Luc assay of PEI mediated cell monolayer transfection using 2.5 or 5 µg pCAG-MetLuc2. B: Effect of pDNA concentration on cumulative polyplex mediated Met-Luc expression, calculated using area under the curve measurements. Data was expressed as Fold Luminescence over negative control (Mean ±SD) or Area under Curve (AUC) (Mean +SD). One-Way ANOVA with Tukey's multiple comparisons test was used to compare between groups. ns = no significant difference, * = $P < 0.05$, ** = $P < 0.01$.

Interestingly, analysis of the 7 day time-course transfection data for Y201 seeded cells (Figure 5.19 A) revealed good overall 3D transfection in this cell line after external application of polyplexes. Specifically, these samples presented with more prolonged transfection expression profiles, albeit over a lower overall expression range, in comparison to C2C12. Furthermore, it was also identified that a lower polyplex pDNA concentration was considered more optimal for cellular transfection, with the 2.5 µg group displaying higher fold luminescence at every timepoint measured.

This was substantiated by Y201 AUC values (Figure 5.19 B), which confirmed total Met-Luc expression was higher in the 2.5 µg polyplex group in comparison to the 5 µg group. Crucially however, it was identified once more that when the specific polyplex groups were compared (2.5 µg versus 5 µg), a lack of statistical significance was found.

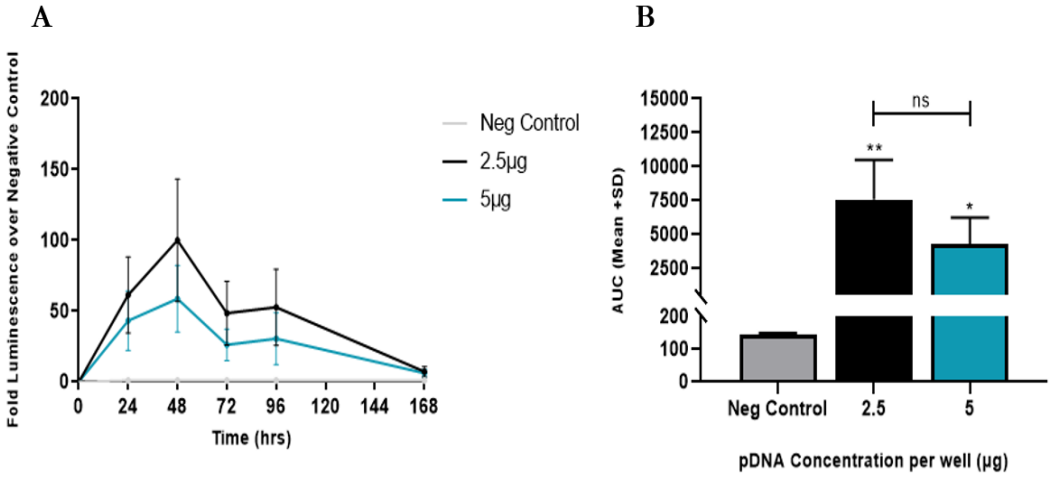

Figure 5.19 (A & B) – Evaluation of the effect of pDNA concentration on the 3D transfection capability of PEI polyplexes when applied, using the external application method, to Y201 seeded scaffolds. A: 7 Day time course Met-Luc assay of PEI mediated cell monolayer transfection using 2.5 or 5 µg pCAG-MetLuc2. B: Effect of pDNA concentration on cumulative polyplex mediated Met-Luc expression, calculated using area under the curve measurements. Data was expressed as Fold Luminescence over negative control (Mean ±SD) or Area under Curve (AUC) (Mean +SD). One-Way ANOVA with Tukey's multiple comparisons test was used to compare between groups. ns = no significant difference, * = $P < 0.05$, ** = $P < 0.01$.

5.3.4.2.2 Optimisation of N/P ratio

The following results subsequently displayed the effect of modifications to N/P ratio on 3D scaffold transfection, specifically in the context of the best performing pDNA concentrations (C2C12 – 5 µg, Y201 – 2.5 µg).

Evaluations of the subsequent 7 day timecourse data for C2C12 seeded cells (Figure 5.20 A) revealed identical burst release expression profiles were present across each N/P ratio range tested. Interestingly, in terms of Met-Luc expression, when N/P ratio was either increased or decreased, a negative effect was observed, thus confirming therefore that N/P24 was likely the optimal ratio in this scenario for this cell line.

C2C12 AUC values (Figure 5.20 B) further substantiated this assertion, illustrating the N/P24 polyplex group produced the greatest cumulative 3D Met-Luc expression over the 7 day timecourse. Such increases in expression were not deemed statistically significant when compared to any other polyplex group.

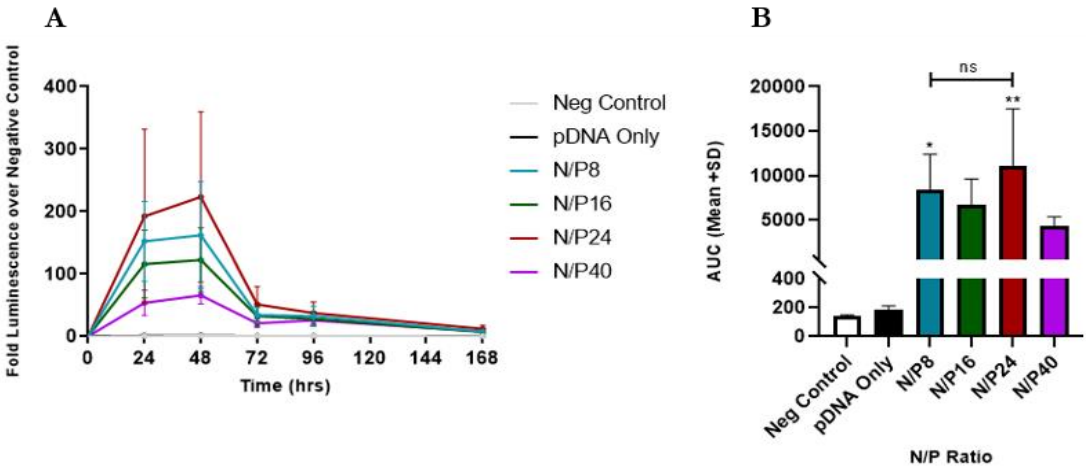

Figure 5.20 (A & B) – Evaluation of the effect of N/P ratio on the 3D transfection capability of PEI polyplexes when applied, using the external application method, to C2C12 seeded scaffolds. A: 7 Day time course Met-Luc assay of PEI mediated cell monolayer transfection using polyplexes formulated with N/P ratios ranging from 8-40. B: Effect of N/P ratio on cumulative PEI mediated Met-Luc expression, calculated using area under the curve measurements. Data was expressed as Fold Luminescence over negative control (Mean ±SD) or Area under Curve (AUC) (Mean +SD). Kruskal-Wallis with Dunns multiple comparisons test was used to compare between groups. ns = no significant difference, * = $P < 0.05$, ** = $P < 0.01$.

Similarly, in the equivalent Y201 7 day time course (Figure 5.21 A), the expression patterns of each N/P ratio group remained largely the same, upon either an increase or decrease in the amount of PEI, with peak daily Met-Luc expression displayed consistently at the 48 hour time-window before preceding to decline at 7 days. However, in terms of Met-Luc expression, it was found that a dose-dependent relationship was present over the range of N/P ratios tested, explicitly illustrating as N/P ratio was increased, the amount of Met-Luc produced per day also increased.

The resulting quantitative Y201 AUC data (Figure 5.21 B) further substantiated this hypothesis and furthermore illustrated that the difference in cumulative Met-Luc expression produced was in fact statistically significant, when compared to all N/P ratio groups. As such, it was assumed in the case of pre-seeded Y201 transfection, N/P ratio appeared to induce a greater overall effect on 3D cellular transfection.

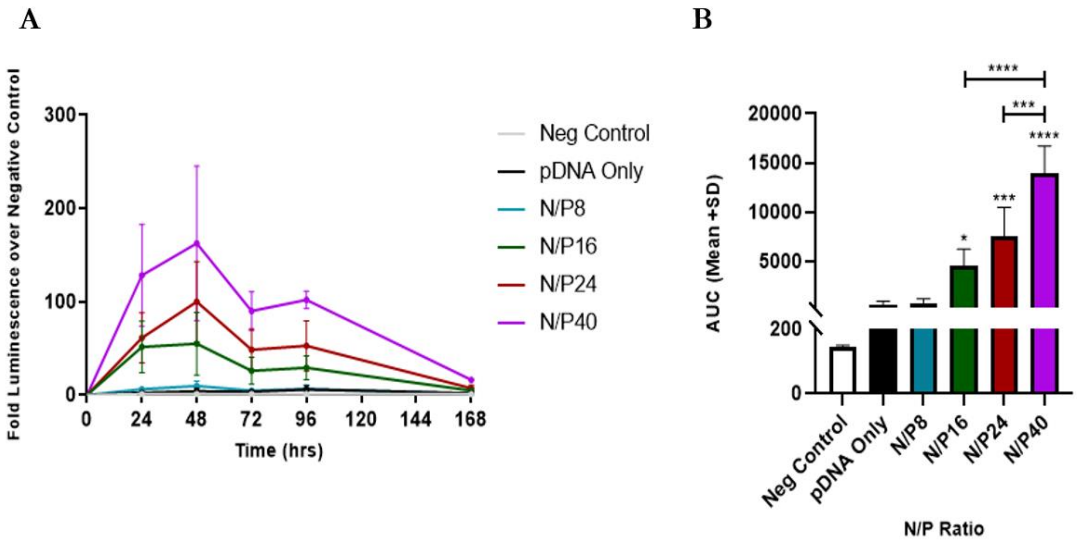

Figure 5.21 (A & B) – Evaluation of the effect of N/P ratio on the 3D transfection capability of PEI polyplexes when applied, using the external application method, to Y201 seeded scaffolds. A: 7 Day time course Met-Luc assay of PEI mediated cell monolayer transfection using polyplexes formulated with N/P ratios ranging from 8-40. B: Effect of N/P ratio on cumulative PEI mediated Met-Luc expression, calculated using area under the curve measurements. Data was expressed as Fold Luminescence over negative control (Mean ±SD) or Area under Curve (AUC) (Mean +SD). One-Way ANOVA with Tukey's multiple comparisons test was used to compare between groups. ns = no significant difference, * = $P < 0.05$, *** = $P < 0.001$, **** = $P < 0.0001$.

Table 5.11 – Final optimised conditions for PEI mediated external application method in C2C12 and Y201 seeded scaffolds.

Transfection Method	Cell Line	Optimal N/P Ratio Concentration	Optimal pDNA Concentration
PEI Mediated External Application Transfection Method	C2C12	N/P24	5 µg
PEI Mediated External Application Transfection Method	Y201	N/P40	2.5 µg

Based on the two main outcomes of the optimisation steps, within the PEI polyplex mediated external application method (3D transfection control), it was reaffirmed that in 3D scaffold transfection contexts, pDNA concentration and N/P ratio are key factors which influence cellular transfection. It was also shown that, much like the 2D cell monolayer transfection models, the PEI polyplex external application 3D method was much superior in both scaffold seeded cell lines for the payload delivery and cellular transfection, over the equivalent nanoparticle external application method. Interestingly however, unlike the considerable difference in total cumulative Met-Luc expression seen between C2C12 and Y201 cell lines in the 2D transfection models, the 3D transfection control illustrated only a small difference in performance and expression, upon seeding and transfection within agarose scaffolds.

In conclusion, the PEI external application method was successfully validated as a possible 3D scaffold transfection method, crucially acting as a viable control or reference for future agarose GAM studies such as the F-AGE-1, F-AGE polyplex electrophoretic GAM scaffolds.

5.3.4.3 Qualitative assessment of 3D PEI transfection

In a final validation experiment, the experimental procedures for the PEI-mediated external application transfection method were replicated, utilising in this case the GFP fluorescence reporter system. Fluorescent images were generated illustrating localised intracellular GFP production from successfully transfected cell laden scaffolds (Figure 5.22).

Based on the generated images, it was verified initially through DAPI nuclear staining that both cell types remained adhered to the surface of the PDA-coated agarose scaffolds in both the control groups and after the application of polyplex transfection payloads.

Much like the C2C12 2D cell monolayer transfection model, negative control and pDNA only scaffold groups here failed to produce any detectable cellular GFP in regions which contained DAPI positive cells, thus indicating a lack of 3D transfection. Conversely, considerable GFP expression was detected across the N/P24 polyplex scaffold group surface, with green GFP signal appearing regularly across the scaffold and largely in direct association with blue DAPI positive regions. Furthermore, much like the Met-Luc results outlined in Figure 5.20, the higher N/P ratio (N/P40) exhibited sub-optimal levels of 3D transfection, characterised by fewer discernible DAPI-stained cells and notably diminished detectable GFP expression among the seeded C2C12 cells.

Concerning the Y201-seeded cells subjected to externally applied polyplexes, a parallel trend was identified in the control groups, with no detectable GFP fluorescence in any captured image. Interestingly, within both scaffold groups exposed to polyplex payloads (N/P24 and N/P40), DAPI-positive regions were more frequently observed as larger cell clusters. Nevertheless, effective 3D transfection persisted, as these clusters - particularly prominent in the N/P40 group - contained multiple GFP positive cells. This observation significantly aligns with the conclusions drawn from the quantitative datasets of both C2C12 and Y201 cells.

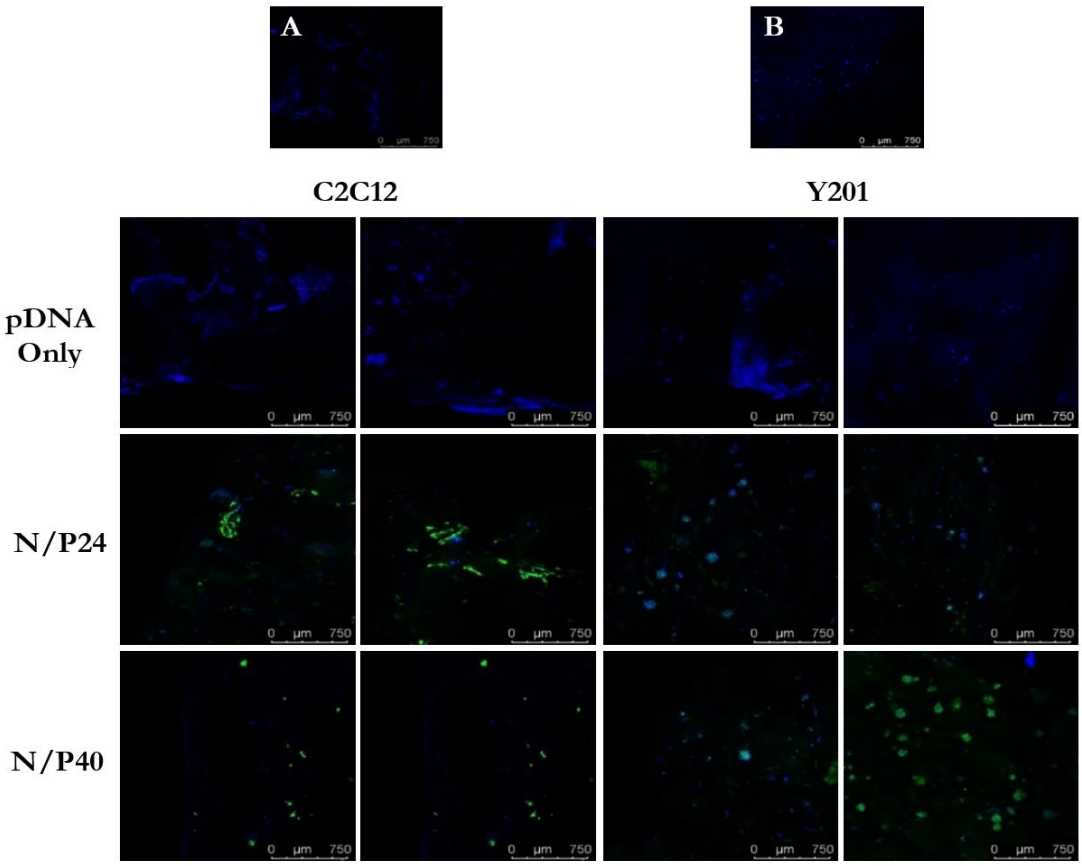

Figure 5.22 – Fluorescent images of PEI mediated 3D scaffold transfection using the external application method. C2C12 or Y201 Cells were seeded using static seeding techniques with a density of $5x10^5$ Cells/Scaffold. After 24hrs, seeded scaffolds were transfected with N/P24 or N/P40 polyplexes containing either 2.5 µg (C2C12) or 5 µg (Y201) pCAG-eGFP. At 48hrs post-transfection, scaffolds were then stained with 0.5 µg/mL DAPI nuclear dye and imaged under the GFP excitation filter. A & B: Media only/negative control scaffolds, seeded with C2C12 and Y201 respectively. Scale bars = 750 µm.

5.3.5 Analysis of 3D GAM transfection capabilities

Upon successful validation of the external application method (sections 5.3.4.2 and 5.3.4.3 specifically), agarose GAMs generated using the F-AGE-1 and F-AGE polyplex electrophoretic loading methods (chapter 3), were subsequently tested for their ability to induce 3D scaffold transfection. As described in section 5.2.5, 3D transfection was assessed using quantitative methods of assessment, over a 7 day culture period, with Met-Luc assay measurements performed over the 48 hour, 72 hour and 7 day time-windows, providing a gauge of early transfection performance. To substantiate the Met-Luc assay results, agarose GAM scaffolds were also imaged at an early timepoint via LIVE-DEAD stain, thus providing an indication of 3D cell viability at the first point of transfection assay performance.

5.3.5.1 F-AGE-1 agarose GAMs

Prior to transfection assessment, it was noted based on 48 hour LIVE-DEAD staining of a selection of cell seeded F-AGE-1 GAM scaffolds, that 3D cell attachment and 3D cell viability was generally consistent with results previously illustrated in chapter 4. Crucially, in both datasets

(Figure 5.23 and Figure 5.25), C2C12 and Y201 cells appeared successfully adhered to the F-AGE-1 GAM scaffolds with no obvious visual differences observed between scaffolds containing transfection payloads versus the 3%-PDA8.2 negative controls. Furthermore, no visual differences in viability were identified when the calcium concentration within the transfection payloads increased (112.5-225 mM). Importantly, in terms of cellular morphology, both cell types also possessed elongated conformations whilst on the GAM surface with evidence of cell-cell contacts and interconnectivity.

Yet, despite this fact, the subsequent C2C12 and Y201 transfection data acquired from F-AGE-1 GAMs (Figure 5.24 and Figure 5.26) revealed no tangible increases in fold luminescence occurring during each of the three time-windows, when scaffolds contained an electrophoretically loaded nanoparticle complex (2.5 or 5 μg pDNA concentration). Statistical analysis further substantiated this with outputs revealing any small increases in gene expression identified in the AGE-1 GAM groups possessed virtually no statistically significant difference when compared to the blank negative control groups, with the exception of AGE-1-2.5-162.5mM (Figure 5.26 A – 72hrs $P = 0.0234$) and AGE-1-5-162.5mM (Figure 5.26 B – 7 days $P = 0.0374$). This exception was however discounted due to its peak value remaining far below acceptable 3D transfection levels previously identified in the PEI external application method.

Such assumptions were also consistent when the pDNA concentration per nanoparticle complex was increased from 2.5 μg to 5 μg, illustrating alterations to pDNA concentration also had no significant effect on the transfection capability of the GAM systems. Based on these findings alone, the PDA coated F-AGE-1 nanoparticle GAMs appeared unable to induce even small levels scaffold mediated reporter gene expression within the testing parameters set.

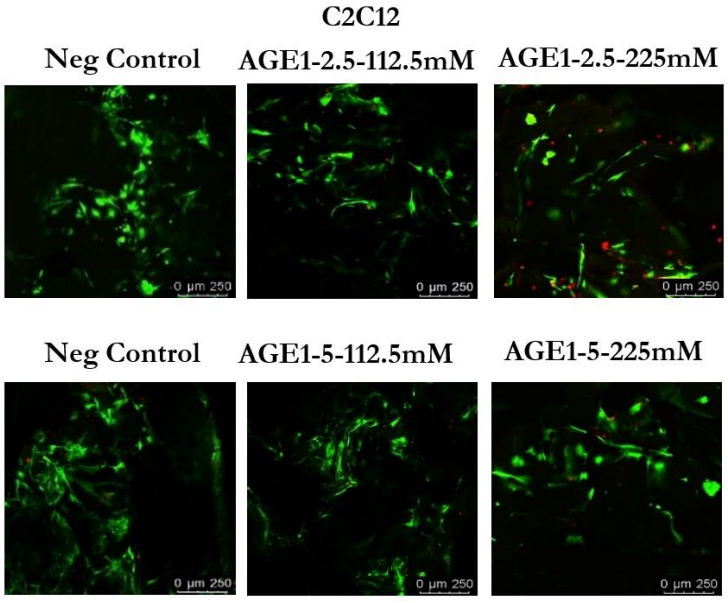

Figure 5.23 – Images of LIVE-DEAD stained C2C12 cells following 48 hours 3D culture on selected F-AGE-1 GAMs. Cells were seeded using static seeding techniques with a density of $5x10^5$ Cells/Scaffold. Live cells are stained green and dead cells stained red. Images were captured specifically at CaP precipitate regions. Scale bars = 250 μm

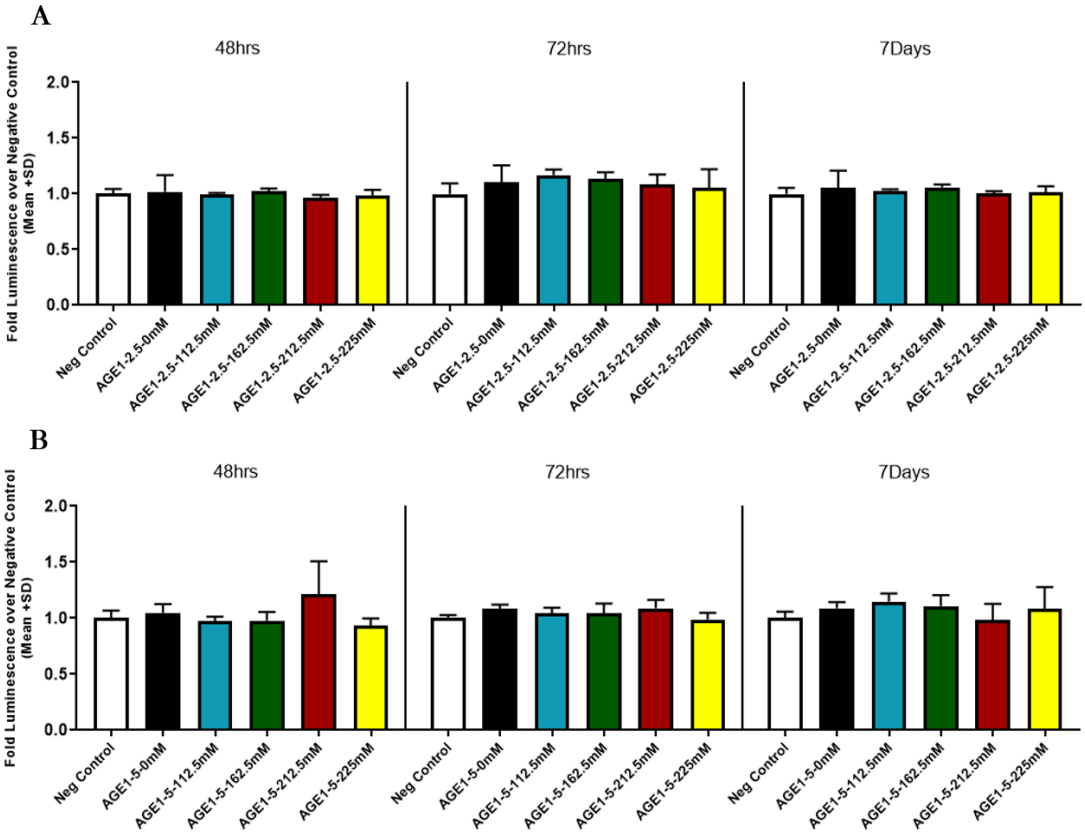

Figure 5.25 (A & B) – Quantitative assessment of the transfection capability of F-AGE-1 Nanoparticle GAM scaffolds after seeding with C2C12 cells. A: F-AGE-1 agarose GAMs containing 2.5 µg pCAG-MetLuc2 vector. B: F-AGE-1 agarose GAMs containing 5 µg pCAG-MetLuc2 vector. Data was expressed as Fold Luminescence over negative control (Mean +SD). One-Way ANOVA with Tukey's multiple comparisons test was used to compare between groups.

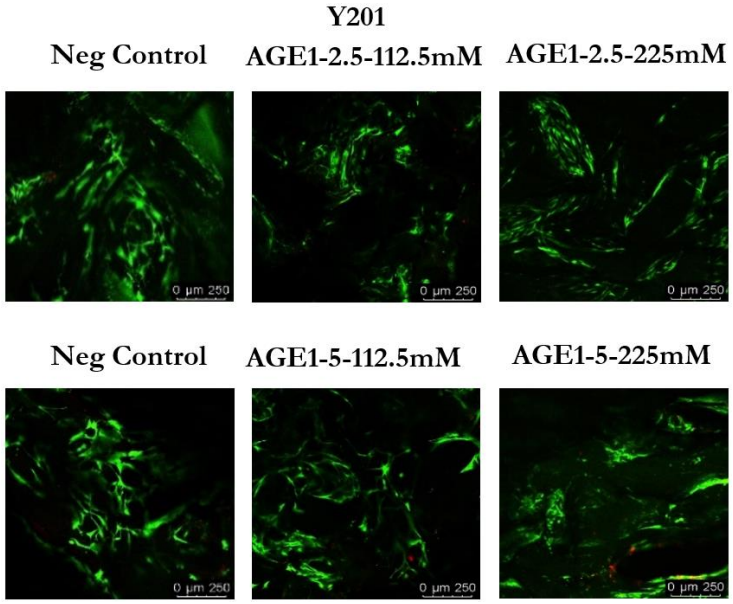

Figure 5.24 – Images of LIVE-DEAD stained Y201 cells following 48 hours 3D culture on selected F-AGE-1 GAMs. Cells were seeded using static seeding techniques with a density of $5x10^5$ Cells/Scaffold. Live cells are stained green and dead cells stained red. Images were captured specifically at CaP precipitate regions. Scale bars = 250 µm

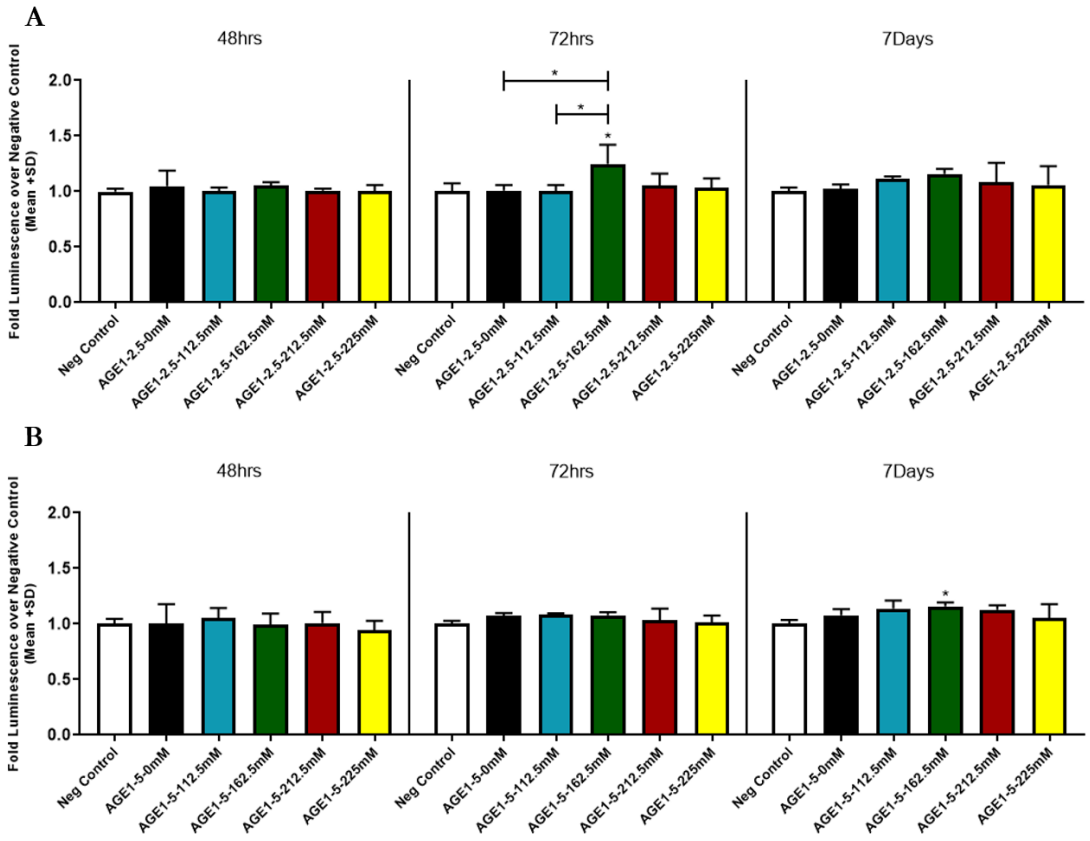

Figure 5.26 (A & B) – Quantitative assessment of the transfection capability of F-AGE-1 Nanoparticle GAM scaffolds after seeding with Y201 cells. A: F-AGE-1 agarose GAMs containing 2.5 µg pCAG-MetLuc2 vector. B: F-AGE-1 agarose GAMs containing 5 µg pCAG-MetLuc2 vector. Data was expressed as Fold Luminescence over negative control (Mean +SD). One-Way ANOVA with Tukey's multiple comparisons test or Kruskal-Wallis test with Dunns multiple comparisons test (Bar chart A - 7 day timepoint) was used to compare between groups. * = $P < 0.05$.

5.3.5.2 F-AGE polyplex GAMs

Much like the F-AGE-1 GAM scaffolds at 48 hours post cell seeding, the selected F-AGE polyplex GAMs similarly induced very small levels of observable cytotoxicity, with large numbers of viable adherent cells present on the scaffold surfaces (Figure 5.27 and Figure 5.29). Interestingly, observable viability also remained high even upon substantial increases in transfection payload N/P ratio, as shown by the large amount of live cells identified in the N/P40 F-AGE polyplex GAM formulations. Furthermore, both cell types presented with elongated fibroblast-like morphologies with good interconnectivity and cell-cell contacts.

However, when transfection behaviour was analysed for both cell lines (Figure 5.28 and Figure 5.30), it was again revealed that there was little to no discernable statistically significant increases in fold luminescence that occurs in any of the tested F-AGE polyplex GAM scaffolds, when compared against the negative control, over the course of the 7 day experiment.

Furthermore, this apparent absence of gene expression was consistent across the GAM groups regardless of pDNA concentration or N/P ratio, suggesting all electrophoretically loaded

polyplex payloads were, in the early period after cell seeding, incapable of inducing scaffold based cellular transfection.

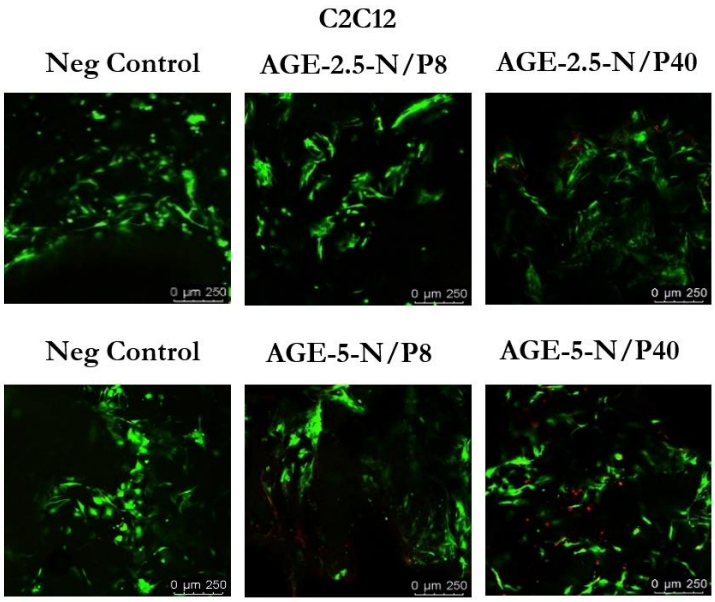

Figure 5.27 – Images of LIVE-DEAD stained C2C12 cells following 48 hours 3D culture on selected F-AGE polyplex GAMs. Cells were seeded using static seeding techniques with a density of $5x10^5$ Cells/Scaffold. Live cells are stained green and dead cells stained red. Images were captured specifically at PEI precipitate regions. Scale bars = 250 µm.

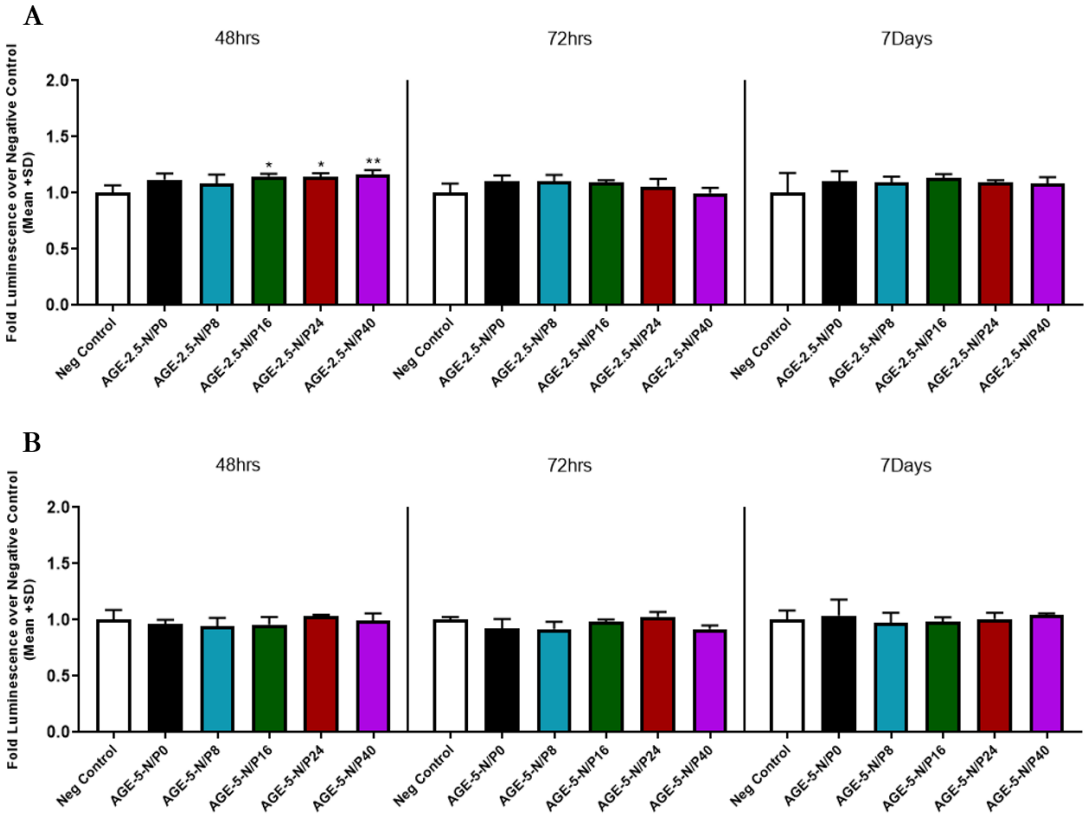

Figure 5.28 (A & B) – Quantitative assessment of the transfection capability of F-AGE Polyplex GAM scaffolds after seeding with C2C12 cells. A: AGE-2 polyplex GAMs containing 2.5 µg pCAG-MetLuc2 vector. B: F-AGE polyplex GAMs containing 5 µg pCAG-MetLuc2 vector. Data was expressed as Fold Luminescence over negative control (Mean +SD). One-Way ANOVA with Tukey's multiple comparisons test or Kruskal-Wallis test with Dunns multiple comparisons test was used to compare between groups. * = $P < 0.05$, ** = $P < 0.01$.

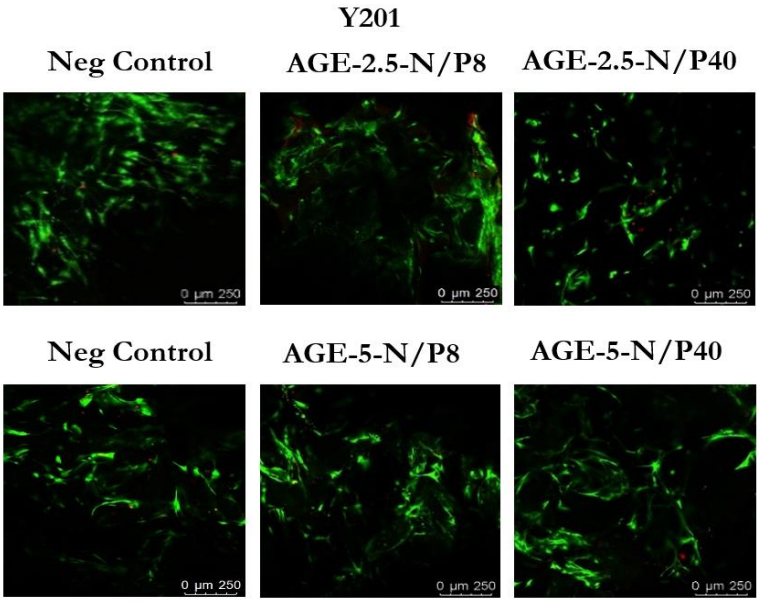

Figure 5.30 – Images of LIVE-DEAD stained Y201 cells following 48 hours 3D culture on selected F-AGE polyplex GAMs. Cells were seeded using static seeding techniques with a density of $5x10^5$ Cells/Scaffold. Live cells are stained green and dead cells stained red. Images were captured specifically at PEI precipitate regions. Scale bars = 250 µm.

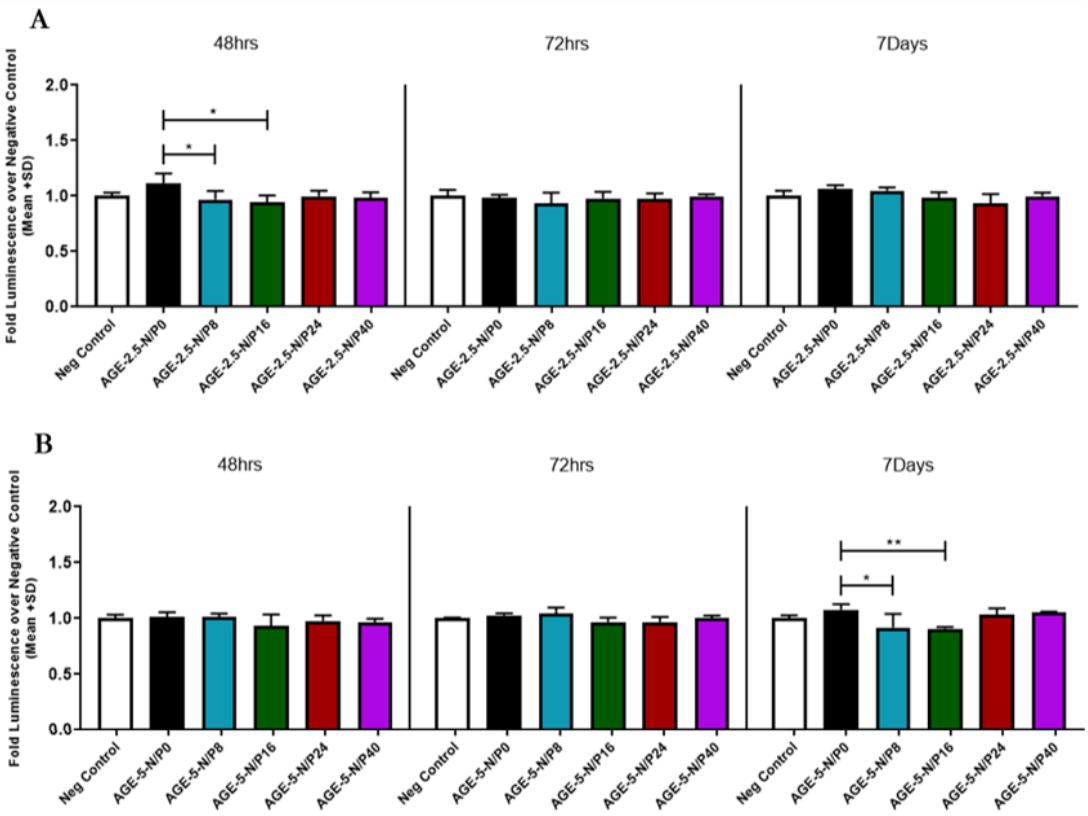

Figure 5.29 (A & B) – Quantitative assessment of the transfection capability of F-AGE Polyplex GAM scaffolds after seeding with Y201 cells. A: F-AGE polyplex GAMs containing 2.5 µg pCAG-MetLuc2 vector. B: AGE polyplex GAMs containing 5 µg pCAG-MetLuc2 vector. Data was expressed as Fold Luminescence over negative control (Mean +SD). One-Way ANOVA with Tukey's multiple comparisons test or Kruskal-Wallis test with Dunns multiple comparisons test (Bar chart A 7 days and bar chart B 48 hrs) was used to compare between groups. * = $P < 0.05$, ** = $P < 0.01$

5.4 Discussion

5.4.1 Selection of a suitable gene expression plasmid vector system

Prior to optimisation of CaP and PEI payloads used in this chapter, it was firstly deemed vital to select an appropriate plasmid expression system which, no matter the transfection vehicle, would be capable of inducing the expression of the encoding gene of interest at high levels over a prolonged period of culture.

In the field of gene therapy, a multitude of plasmid expression systems exist, with each consisting of different promoter elements. Significantly, variations in the inherent chemistry of said promoter elements play vital roles in not only the efficiency of gene transcription but also the strength and time at which the process occurs (Estes *et al.*, 2015). As such, when designing a GAM system, careful consideration should be undertaken when selecting the vector of choice, with particular plasmid systems likely possessing functional characteristics which align more or less favourably with the objectives stated forthwith in this chapter.

Commonly, the most used vector system in the field is the pCMV system, specifically for its ability to instigate very intense gene expression in a variety of mammalian cells (Mark *et al.*, 2022). Although effective, it is widely accepted that the duration of said expression is extremely short, with yields often diminishing within 48 hours, a fact hypothesised to be as a result of its specific in-built promoter element as well as downstream transcriptional silencing and elevated DNA methylation (Y. Y. Dou *et al.*, 2021; Yang *et al.*, 2017). As prolonged expression is paramount in the context of scaffold mediated gene expression, an alternative vector system was sought specifically for this study.

Based on the outcomes of previous unpublished works by the Feichtinger research group, as well as a recent report by Dou *et al*, it was found that the alternative plasmid expression system, known as the pCAG vector, possessed several improved expression characteristics which supplant CMV vectors for use specifically in the context of GAM gene delivery (Y. Y. Dou *et al.*, 2021). Such characteristics include the capability of the pCAG vector to exhibit significantly higher reporter gene expression (MFI - Mean Fluorescence intensity) and more effective transfection efficiency in comparison to equivalent vectors like CMV, in certain cell lines (HEK293F – 48 hours - $2.73x10^5$ versus $2.19x10^5$ MFI, 81.3% versus 59.1%) (Y. Y. Dou *et al.*, 2021). Inherently, this finding can be attributed to the unique CAG promoter element which the pCAG vector carries (a CMV early enhancer coupled with chicken beta-actin promoter and rabbit beta-globin splice acceptor) and through its action allows more favourable interactions between transcriptional processes, leading to the aforementioned boost in gene expression and stability (Miyazaki *et al.*, 1989).

With considerably greater alignment between the characteristics of the pCAG system and the specific aims and objectives stated in this chapter, the pCAG-d2-eGFP plasmid vector, developed

and generously provided by Dr G Feichtinger, was selected for use as the base expression vector platform from which all future gene expression was driven.

5.4.2 Development of effective reporter gene expression systems as tools for transfection assessment

At the start of this chapter, the Feichtinger expression vector library for evaluation of the 2D and 3D transfection processes consisted initially of just the pCAG-d2-eGFP plasmid, which naturally encodes for the expression of the fluorescent GFP protein. Although highly advantageous in terms of visualising the location of successful transfection within a system, it, in most cases, solely functions as a qualitative measurement tool, crucially without the ability to quantify how much protein is being expressed by cells at a specific point in time. In contrast, the application of luciferase reporter systems are able to mitigate such limitations, specifically by means of the luciferin-luciferase (or coelenterazine-luciferase) reaction, which produces quantifiable light-emitting reaction products. Such products not only indicate evidence of successful transfection but do so over a large quantifiable dynamic range, specifically allowing the disclosure of sensitive changes occurring at the transcriptional level. Significantly, such characteristics were deemed fundamental when aiming to specifically evaluate a variety of different 2D transfection payload formulations or unique 3D GAM delivery systems.

As such, an additional reporter plasmid was purchased which specifically encoded for the secreted luciferase enzyme known as *metridia* luciferase (pMetLuc2). As this plasmid vector lacked the pCAG promoter expression system, it simply acted as a gene insert donor, allowing the eventual synthesis of the new plasmid system: pCAG-MetLuc2, via restriction enzyme mediated ligation and cloning processes (Figure 2.2).

The pCAG-MetLuc2 vector enabled qualitative and quantitative analyses of 2D and 3D transfection vehicles and therefore robust optimisation of transfection methods.

5.4.3 Validation of reporter library and quantitative / qualitative methods of transfection assessment

Each of the developed expression vectors (pCAG-d2-eGFP and pCAG-MetLuc2) were applied to basic CaP or PEI 2D cell monolayer transfection systems, with the aim of achieving three specific objectives (Guo *et al.*, 2017; Roberts *et al.*, 2015). Firstly, ensuring that each vector possessed the ability to drive cellular reporter gene expression in two different cell lines. Secondly; to validate that both qualitative and quantitative assessment methods proposed for use in this study were physically capable of detecting said expression (CLSM and in-house developed Met-Luc assay). Thirdly, validation of qualitative and quantitative data against one another.

Through the application of basic calcium phosphate (original co-precipitation method) and PEI mediated transfection protocols, each objective was determined. In both cases, assessment of

transfection took place at 48 hours post-exposure, a duration considered optimal by Guo *et al* for the capture of cellular reporter protein maturation/secretion (Guo *et al*., 2017). Furthermore, given the nature of the tested cell lines utilised, as well as the potential cytotoxic effects of the PEI polymer, a midpoint N/P ratio of 24 was selected for polyplex transfection (Tong *et al*., 2013; Yang *et al*., 2016).

Evaluations of both calcium phosphate and PEI transfection datasets quickly confirmed that the pCAG-d2-eGFP and pCAG-MetLuc2 vectors were sufficiently capable of inducing the production of functional GFP fluorescence proteins and luciferase enzymes in C2C12 and Y201 cells respectively. This demonstrates not only the effectiveness of the pCAG promoter elements for transcriptional induction, but also that the enclosed gene inserts are likely devoid of any lack of function base mutations that could for example cause downstream reporter protein dis-function.

These same results also similarly proved that alongside CLSM techniques, the newly formulated and largely untested in-house Met-Luc assay was also compatible in 2D cell monolayer transfection contexts, with detectable and consistent luminescence values generated from luciferase containing supernatant media extracts. To the best of the author's knowledge, the quantitative Met-Luc assessment method illustrated here remains one of very few examples of a cheap non-commercial alternative for the fast non-destructive measurement of 2D cellular transfection within supernatant extract samples (Tie & Stafford, 2017), significantly illustrating comparable data as to those produced by the commercial Ready-to-Glow assay kit (Clontech/TaKaRa).

Finally, from comparisons between qualitative and quantitative datasets for each cell line, high levels of symmetry existed across equivalent samples, with the visual effectiveness of each transfection vehicle, as shown in the GFP results, importantly reflected in subtle quantitative changes when expressed according to fold luminescence (over negative control).

5.4.4 Selection of the ideal 2D transfection vehicle

In general, there is a lack of consensus with regards to the ideal transfection vehicle for BM-MSC's and similar cell lines such as C2C12 and Y201, with a multitude of different inorganic, lipid and polymer based systems all reported to have varying degrees of success, specifically in terms of their transfection efficiency (Lo *et al*., 2019; Tierney *et al*., 2012). This study therefore sought to identify and optimise two specific transfection vehicles for their use initially in 2D cell monolayer transfection systems, with those being; CaP nanoparticle complexes and PEI polyplexes. Such experiments were considered a vital early building block in this chapter not only with regards to the full exploitation and maximisation of the transfection vehicles performance themselves, but also furthering the understanding of their methods of action such that smooth translation into 3D GAM contexts can then be achieved with minimal disruption.

In terms of CaP mediated transfection, the well-established co-precipitation synthesis method was applied once more in this optimisation study, crucially without additional glycerol shock treatments, with the aim of modifying DNA concentration and $CaCl_2$ parameters so as to synthesise more effective transfection capable precipitates. Based on the accumulated datasets as a whole, it could be concluded that optimisation of the stated parameters resulted in only marginal improvements in the transfection capabilities of the pDNA-CaP co-precipitates, within C2C12 and Y201 cell monolayers. Specifically, even in the cases of the best performing formulations (C2C12: 2 μg, 56.25 mM - Y201: 1 μg, 56.25 mM), transfection efficacy failed to match those illustrated in the pre-optimised glycerol shock groups.

Compared to similar reports involving the use of the co-precipitation transfection method, this overall lack of high level transfection efficacy was often substantiated, with several limiting factors being repeatedly identified in the above synthesis and application method. Such factors included the unrestricted agglomeration of CaP precipitates within the PO_4^{2-}-$CaCl_2$ complexation system, both at the initial point of nucleation and synthesis, as well as post application to cells within growth media, leading in many cases to unwanted micro-crystal formation and thus poorer transfection (Jordan *et al.*, 1996; Orrantia & Chang, 1990). Similarly, it could also be suggested that lower Ca:P ratio's (similar in magnitude to that of normal calcium phosphate compounds) appear to result in a larger overall particle size distributions specifically within the precipitates synthesised, further impacting transfection efficacy (Olton *et al.*, 2007). In this study, the fact that CaP formulations synthesised from lower $CaCl_2$ concentrations induced lower cumulative reporter gene expression, it could be assumed similar limitations were present, thus lending credence to the above theory.

That said, due to obvious limitations in the range of data collected (2D transfection data only presented here), inferences relating to the actual CaP co-precipitate synthesis and behaviour in this study were therefore somewhat restricted, with further information such as particle size measurements and zeta potential (via dynamic light scattering and zetasizer testing) likely required to aid the discussion further. Nevertheless, the outcomes of this CaP study, in terms of the most optimal pDNA concentration and $CaCl_2$ concentration remained highly beneficial and informed the choices made with regards to future 3D transfection methodologies and GAM mediated scaffolds.

In contrast, through optimisation of equivalent parameters for PEI mediated 2D transfection, it could be concluded that the polyplexes formulated in this study were highly effective in terms of inducing strong transfection, crucially in both C2C12 and Y201 culture systems. Clear expression profile patterns were also presented, indicating cellular expression was most often highest over the first 48-96 hours of culture, post vehicle exposure, before eventually declining at the 7 day time-window. By comparing the cumulative Met-Luc expression, the optimum PEI conditions were subsequently found, in this case; 1 μg N/P24, for both cell types. Interestingly, in the

context of pCAG expression vector performance, this appeared to contrast findings by Dou *et al* which showed sustained expression at 3-4 weeks post exposure, although this was in a different cell line (HEK293 cells - an extremely proliferative and robust cell line), having been transfected with the optimised commercial Lipofectamine 2000 reagent (Y. Y. Dou *et al*., 2021).

A secondary outcome from these experiments was the illustration that gene expression was magnitudes higher in C2C12 cells in comparison to Y201 cells, a finding also tentatively displayed in CaP transfection data. As this occurred in both transfection systems, it was hypothesised to mainly be as a result of cell line specific behaviour instead of transfection system-cell line incompatibilities. Although not wholly unexpected given the primary stem-cell like nature of Y201 cells (being an immortalised cell line derived from a bone marrow MSC source), it remained an interesting finding with regards to the therapeutic magnitude required of a transfection payload for BM-MSC induced differentiation and repair (James *et al*., 2015).

5.4.5 3D transfection control study (external application method)

The successful outputs relayed from the 2D cell monolayer studies led to the subsequent investigation of the capability of PDA coated agarose scaffolds to support similar levels of gene expression, upon transfection payload delivery. As a proof-of-concept study, external application methodologies were therefore employed, whereby CaP or PEI polyplex payloads were delivered onto cell-laden agarose scaffolds and the resulting gene expression measured. Two main objectives were sought, which included; firstly the confirmation that the previously validated qualitative and quantitative transfection assessment methods could be used in a 3D scaffold transfection context, and secondly whether cells seeded within a PDA coated agarose scaffold could successfully be transfected with a particular transfection payload (CaP or PEI polyplexes).

In terms of the first objective, based on the initial C2C12 and Y201 luminescence data collected after cell laden scaffolds were exposed to CaP and PEI payloads, it was determined with a reasonable degree of confidence that Met-Luc assays could reliably detect secreted Met-Luc reporter from transfected cells adhered to PDA functionalised agarose scaffolds, importantly producing reliable expression distribution patterns, which matched in most cases to those illustrated in 2D transfection models. This was particularly significant given the problematic finding discovered during method development which suggested excess PDA leaching into cell culture media caused luminescence quenching upon Met-Luc assay performance. As a result of this, additional washing steps (overnight deionised water wash) were implemented within the PDA functionalisation procedure prior to scaffold seeding, crucially leading to the subsidence of this phenomenon and thus the successful detection of 3D Met-Luc activity.

In this case of qualitative assessment via CSLM methods however, no such issues were identified upon translation into a 3D assessment platform, with visual determination of GFP expression

clearly identified, as shown in Figure 5.22. The inclusion of DAPI nuclear staining was however considered instrumental to enable the deduction of successful transfection.

5.4.5.1 Transfection potential of externally applied CaP nanoparticles

With the assessment methods successfully verified, transfection behaviours could then effectively be evaluated. Overall, upon exposure of cell laden agarose scaffolds to pDNA-nanoparticle payloads, it was found that very small levels of successful gene expression could be detected across the majority of formulations tested. By and large, this small scale gene expression only occurred in C2C12 pre-seeded scaffolds, which were exposed to nanoparticle formulations synthesised from the 56.25 mM $CaCl_2$ groups. Even in these optimal groups however, expression patterns appeared lower than hoped, with peak fold luminescence values of approximately 5 being displayed in both the 2.5 μg and 5 μg formulations.

Conversely, in the case of Y201 seeded scaffolds, nanoparticle complex exposure led to considerably worse 3D expression profiles in all cases, with the additional and surprising finding that the pDNA only group was most effective in comparison to pDNA-nanoparticle complexes. This particular increase was however negligible considering the magnitude of fold change in luminescence versus the negative control.

Although there is a consensus in the field that the majority of 3D mediated transfection/gene delivery systems produce on average less transfection than equivalent 2D methodologies it was particularly noticeable the lack of any tangible reporter gene expression produced by the nanoparticle external application method, across both seeded scaffold constructs (Truong *et al.*, 2019). As the same co-precipitation method was applied here, it was therefore assumed many of the limitations discussed in section 5.2.3.1 were again present, resulting in the generally poor outcomes displayed.

Furthermore, it was also hypothesised that the mechanism of action of the external application method likely compounded these limitations further. For instance, despite suspensions being applied directly to the cell laden scaffolds, it was hypothesised that due to colloidal pDNA-CaP suspension kinetics and Brownian motion, the complexes likely dispersed quickly away from the scaffolds, perhaps settling at the bottom of the well plates under gravity, and thus restricting the in-contact duration time prior to its eventual removal and media exchange (after the 4 hour incubation) (Khan *et al.*, 2016). Alternatively, due to the suggestion that sedimentation may be an essential characteristic of CaP mediated gene delivery (concentrating pDNA on the cell surface), the method of external application of pDNA-CaP nanoparticles to a high surface area scaffold system may be restrictive, conceivably leading to the poor transfection profiles described (Luo & Saltzman, 2000).

5.4.5.2 Transfection potential of externally applied polyplexes

Crucially however, upon exposure of cell laden agarose scaffolds to polyplex payloads, it was found much higher levels of reporter gene expression were observed, over the majority of polyplex formulations, and also across both cell lines. In the case of both C2C12 and Y201 laden scaffolds, classical burst release gene expression profiles were displayed specifically peaking during the 48 hour time-window prior to a rapid decline towards 7 days.

Furthermore, in contrast to 2D cell monolayer transfection, optimal pDNA concentrations and N/P ratios for 3D transfection via external application appeared cell line specific in this study (C2C12: 2.5 μg – N/P24, Y201: 5 μg – N/P40), thus signifying the impact changes to the culture environment has on cellular transfection mechanisms, particularly with regards to the suitability of the 3D scaffold for cell line specific metabolism and uptake (Luo *et al.*, 2015). Interestingly, as optimal gene expression from the Y201 laden scaffolds now appeared equivalent to C2C12 values (Figure 5.20 and Figure 5.21) (a finding not displayed in 2D transfection systems), it could therefore be surmised Y201 cells may, in this scenario, display more preferential characteristics for transfection, specifically within a PDA agarose scaffold environment. Unfortunately, as this is the only known study in which Y201 cells were added to PDA functionalised scaffolds, this finding could not be substantiated.

As the mechanism of action was mostly the same as the external application of nanoparticle complexes, the enhancement in gene expression identified in this study was likely therefore a culmination of two factors. Firstly, it was hypothesised that due to their apparent smaller hydrodynamic diameters, polyplexes may have remained more effectively diffuse within the cell media solution post application, in turn resulting in lower sedimentation rates and thus a greater in-contact duration time with the cell-laden scaffolds (Pedraza *et al.*, 2008; Pezzoli *et al.*, 2017). Secondly, as a result of the potentially high cationic charge densities presented by the formulated polyplexes, faster and more stable electrostatic interactions could consequently be formed with negatively charged cell membranes of scaffold adhered cells, thus improving the 3D transfection processes further (Amin *et al.*, 2013).

Overall, based on quantitative and qualitative transfection data, particularly from the PEI external application method, PDA agarose scaffolds were sufficiently validated as a platform from which 3D gene delivery should be possible, crucially acting as a reference or positive control for which future GAM studies may be compared against whilst also informing GAM formulation conditions such as plasmid loading concentration, CaP ratio or N/P ratio. Such foundations paved the way for the effective evaluation of the transfection capabilities of the F-AGE-1 and F-AGE polyplex GAM scaffolds.

5.4.6 Transfection capabilities of F-AGE GAM systems

As stated, for surface mediated GAM delivery to be successful, three underlying pillars must be present within the 3D scaffold system. Firstly, an effective method of transfection payload incorporation within or on the biomaterial, secondly the provision of a biocompatible, bioactive 3D support structure or surface and thirdly the effective release and uptake of said payloads to locally adhered cells (El-Sherbiny & Yacoub, 2013). Significantly, with the first and second pillars having previously been characterised and successfully optimised in chapters 3 and 4 respectively, it was now deemed necessary to test, validate and optimise the final pillar within 3D GAM culture contexts. As such, PDA functionalised F-AGE-1 and F-AGE polyplex GAMs were formulated in their entirety, containing either DNA-CaP or polyplex payloads. Pillar three was then tentatively evaluated via a proof of concept 3D transfection experiment, specifically over a 7 day culture period.

Based on the transfection studies outlined in section 5.3.5, it was illustrated that F-AGE-1 and F-AGE polyplex GAM scaffolds containing either electrophoretically loaded pDNA-CaP nanoparticle complexes or electrophoretically loaded PEI polyplexes were completely ineffective at inducing any tangible gene expression in GAM adhered cells. This finding was consistent in both cell lines (C2C12 and Y201) over a 7 day 3D culture period, in which Met-Luc assays were performed on three separate days (48, 72 and 7 day time-windows). Furthermore, no significant increases in expression occurred upon modifications to pDNA loading concentration (2.5 or 5 μg), calcium chloride concentration (0-225 mM) or PEI concentration (N/P 8-40).

As 3D cell viability and cell morphology on the F-AGE-1 and F-AGE polyplex GAMs appeared consistent with unloaded negative controls, it was theorised that the lack the transfection capability likely centred around the successful synthesis, patterning, manufacture and condition of the transfection payloads themselves rather than scaffold cytotoxicity, adherence, scaffold penetration, or due to any cell line specific issues. Three main working theories have since been generated which propose possible reasons for this phenomenon and generally fall under the following categories; limitations regarding vector encapsulation, limitations regarding release kinetics, and/or lyophilisation/freeze-drying mediated damage. Detailed considerations of each of the proposed challenges is presented in the general discussion in chapter 7.

5.5 Conclusions

This study aimed to characterise transfection capabilities in electrophoretically loaded PDA-functionalised agarose GAM scaffolds. However to achieve this goal, transfection vehicle performance (CaP and PEI) in 2D monolayer cultures first needed to be validated. Reporter vectors (pCAG-d2-eGFP and pCAG-Met-Luc2) were therefore successfully formulated and tested for expression in C2C12 and Y201 cells, confirming both the functionality of the vectors and the successful use of qualitative (fluorescence microscopy) and quantitative assessment (Met-

Luc assay) methods. Through further optimisation investigations within the 2D cell monolayer context, optimum transfection parameters including $CaCl_2$, pDNA concentration, and N/P ratio were then established.

Upon translation into 3D scaffold culture settings (external application control method), it was found polydopamine coated agarose scaffolds acted as effective platforms for externally applied surface mediated transfection, with PEI polyplexes being particularly effective. Moreover, in these cases reporter gene expression remained higher in C2C12 cells in comparison to Y201, an indication that phenotypic differences in 2D were also present in 3D scaffold contexts. Unfortunately, when all formulations of the PDA coated F-AGE agarose GAMs were applied for similar 3D transfection testing, gene expression was found to be negligible, likely highlighting fundamental incompatibilities with the previously established F-AGE approaches, which requires greater investigation to understand the intricacies of failure and thus application of appropriate solutions.

Despite the results illustrated, parallel work remained ongoing regarding the use of alternative DNA vector systems for incorporation within the F-AGE agarose GAM patterning platforms. This particularly focused on the development of dumbbell hairpin vectors (also known as covalently closed hairpin loop vectors (CCHLV)) which possess uniquely favourable conformations for said electrophoretic incorporation. The final experimental chapter in this thesis (chapter 6) will illustrate the progress made regarding their synthesis and initial testing.

CHAPTER 6:

DESIGN, SYNTHESIS AND TESTING OF MINIMALISTIC DUMBBELL DNA EXPRESSION VECTORS FOR AGAROSE GAM INCORPORATION

6 CHAPTER 6: DESIGN, SYNTHESIS AND TESTING OF MINIMALISTIC DUMBBELL DNA EXPRESSION VECTORS FOR AGAROSE GAM INCORPORATION

6.1 Introduction

The capacity for successful gene delivery performance of a GAM loaded therapeutic nucleic acid payload is dependent not only on the chemical transfection vehicle which the DNA vector is coupled to, but is also dependent on the structure and inherent properties of the DNA vector itself. As previously discussed, artificial plasmid vectors are considered the current gold standard expression system for such non-viral GAMs, and through its action it is possible to introduce any feasible transgene into a eukaryotic cell population for the specific purpose of inducing a transient gene expression response (Hassan *et al.*, 2016). However, despite its success and wide use, such vector systems are not without limitations, particularly in terms of their size, possession of several potentially detrimental bacterial elements and latent immunogenicity, all of which prohibit either gene delivery performance or downstream safe clinical translation (Mairhofer & Grabherr, 2008).

Conventional plasmids consist of three major components: 1) prokaryotic bacterial backbone region (ori, antibiotic resistance genes, selectable markers), 2) spacer sequences and 3) the eukaryotic transcriptional unit (transgene, promoter, intron, termination/poly(A) signals) (Jechlinger, 2006). Packaging this substantial amount of genetic material unfortunately makes plasmids very large molecules (0.8 – 120 kb with an average diameter of approximately 100-200 nm), particularly in comparison to viruses and RNA (De La Vega *et al.*, 2013). In gene therapy contexts, such a large size can negatively modulate gene transfer efficiency, whereby larger plasmids are less effective at nuclear entry (via NPC) in comparison to smaller iterations (Kreiss *et al.*, 1999). Furthermore, size related instability can also cause highly detrimental DNA integration events (Ertl & Thomsen, 2003). Alongside size related issues, the presence of prokaryotic elements is itself considered problematic. Although required for plasmid production in bacteria, the presence of antibiotic resistance genes raises substantial safety concerns when applied in humans, with the potential for horizontal gene transfer into pathogenic bacteria not wholly out of the realms of possibility (Vandermeulen *et al.*, 2011). Besides, these prokaryotic sequences are also heavily rich in unmethylated CpG dinucleotides (or CpG motifs), which are capable of binding to Toll-like receptors and inducing detrimental immune responses during the gene delivery process (Klinman, 2004). Ultimately, as the bacterial backbone does not possess any therapeutic benefits for the gene therapy process, it is commonly suggested wholesale elimination of these elements would bring a multitude of benefits. This desire has therefore led to the exploration of alternative nucleic vector designs, among which minimalistic dumbbell DNA vectors have gained significant recent attention.

Minimalistic dumbbell DNA vectors or covalently closed hairpin loop vectors (CCHLV) are a novel, alternative class of non-viral DNA vectors which have been developed and tentatively utilised in fields such as immunisation/vaccine development and tumour gene therapies (Schmidt *et al.*, 2005). These vectors were first postulated in 2001 by Wittig & Schakowski *et al*, and were deemed the smallest, most consolidated vector system capable of controlled effective protein encoding expression. The system is characterised as a plasmid derived, double stranded, linear, end-sealed (dumbbell) DNA molecule consisting solely of a gene expression cassette (promoter sequence, therapeutic transgene, polyA signal), significantly omitting unnecessary plasmid material not utilised in transgene transfection (such as bacterial backbone, spacers, CpG sequences) (Figure 6.1) (Schakowski *et al.*, 2001).

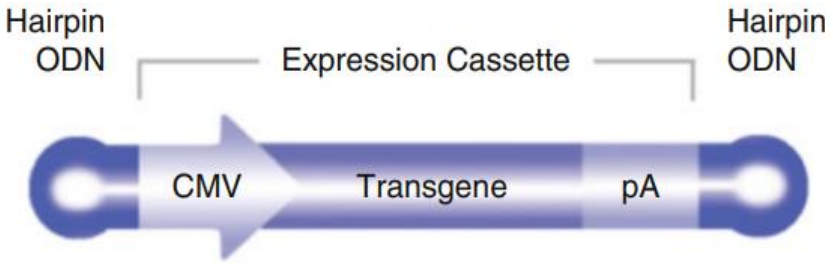

Figure 6.1 – Diagrammatic representation of a conventional CCHLV. Hairpin oligodeoxynucleotides are used to covalently close the linear double stranded gene expression cassette, of which consists solely of a enhancer-promoter region (e.g. CMV), a transgenes, and a poly(A) signal. Taken from (Schmidt *et al.*, 2015) with permission from Springer Nature under licence number 5670840528372.

In terms of CCHLV synthesis, it is generally observed that these vectors can be generated via three distinct *in-vitro* enzymatic mechanisms; 1) the enzymatic ligation assisted by nucleases (ELAN) strategy, 2) the PCR amplification strategy and 3) the protelomerase, or prokaryotic telomerase strategy. Each mechanism is illustrated in Figure 6.2.

The ELAN approach was the first synthesis method to be established and has since become the most frequently utilised of all the stated strategies (Yu *et al.*, 2015). This strategy utilises a conventional artificial plasmid as the starting vector, specifically containing a gene expression cassette (GEC), a prokaryotic backbone, and two specific type II restriction endonuclease recognition sites (upstream and downstream of the GEC region). In the first ELAN step, two equivalent restriction endonucleases are applied, inducing the digestion of the plasmid vector in two specific locations. As a result, a linearised GEC DNA product forms with terminal 5' and 3' cohesive end sequences specific to the enzyme utilised. After the digestion and purification, 10-20 bp oligonucleotide hairpin loops (containing complementary overhang sequences to the GEC product) are applied into the reaction alongside a ligase enzyme. At this stage, a CCHLV product is tentatively formed. To ensure a stable and effective hairpin ligation has taken place, as well as to remove unbound hairpin oligonucleotides, the system is subjected to T7 DNA polymerase treatment, which exhibits strong 3'-5' exonuclease activity (Engler *et al.*, 1983). As T7 DNA

polymerase primarily acts on single-stranded DNA regions (i.e. exposed cohesive ends), a successfully synthesised CCHLV product would remain undigested after such an exposure. In the final ELAN step, the CCHLV is purified using standard DNA purification methods, such as phenol extraction, column-based purification, or high-performance liquid chromatography.

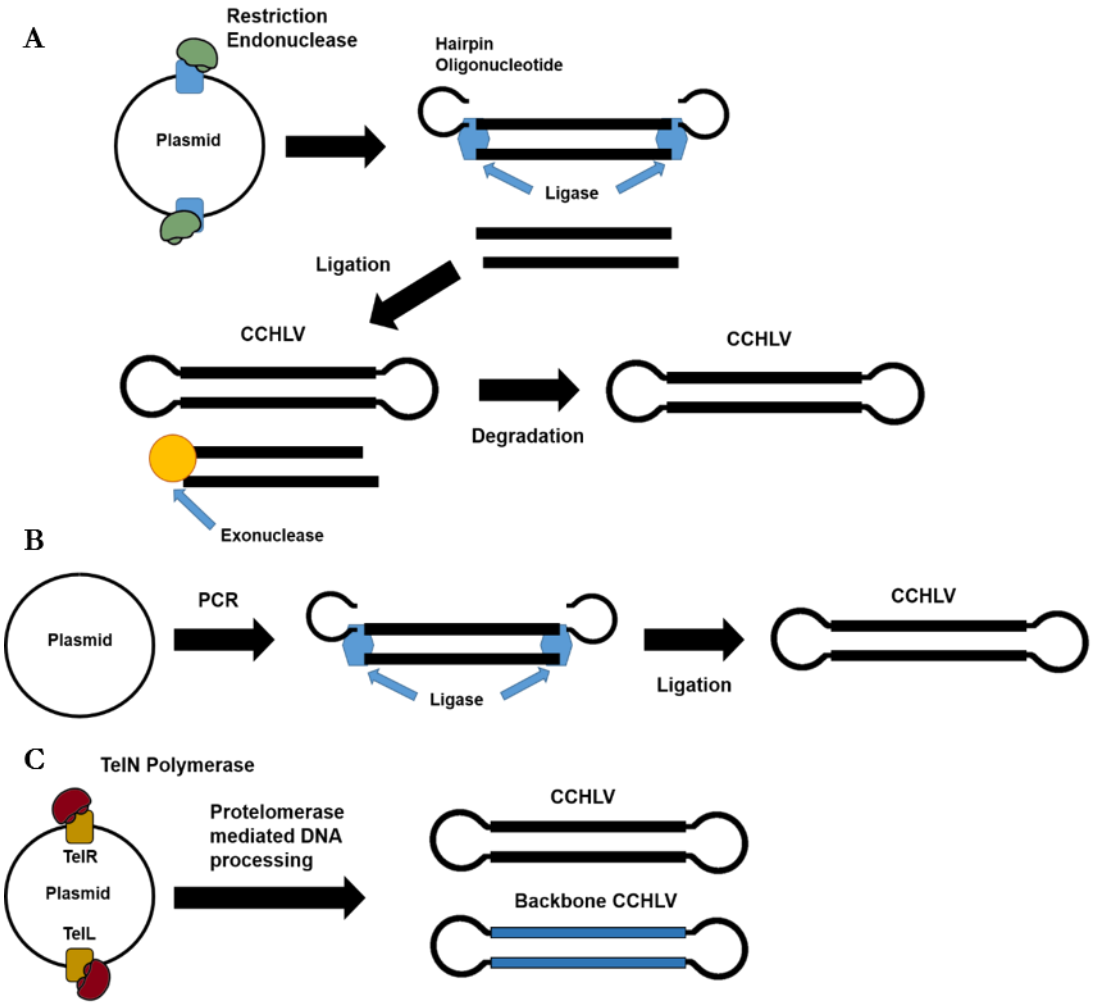

Figure 6.2 (A-C) – The different synthesis strategies employed for the production of CCHLVs. A: The ELAN synthesis strategy. Includes the targeted restriction endonuclease mediated (multiple) digestion of a plasmid vector followed by hairpin oligonucleotide ligation. Exonuclease digestion is used in a second step to simultaneously remove the bacterial backbone region whilst leaving the CCHLV unaffected. B: PCR synthesis strategy. Includes PCR mediated amplification and subsequent ligation with hairpin oligonucleotides. C: TelN protelomerase mediated CCHLV synthesis strategy. Includes the utilisation of the TelN protelomerase from bacteriophage N15 (FN15 TelN), of which performs double strand cleavage on a plasmid at specific target sequences (telL, telR). Post cleavage, 3' complementary overhangs are present which enables TelN mediated ligation and the formation of a hairpin end-sealed CCHLV. Adapted from (Rodríguez, 2004).

In comparison to the current established plasmid vectors, these alternative CCHLV systems possess several characteristics which are highly advantageous within the realm of gene therapy and in the context of the F-AGE electrophoretic platforms developed in this thesis. As highlighted in the CCHLV structure diagram (Figure 6.1), these vectors are importantly devoid of all bacterial plasmid regions, only containing sequences that are necessary for transgene

expression. The downstream effect of this is three-fold; firstly the overall size of the vector is reduced, secondly the potentially harmful prokaryotic genes (such as the antibiotic resistance genes, the selective markers and the ori) are removed, and thirdly the vector no longer possesses large quantities of CpG motifs (Hodges *et al.*, 2004). Regarding the reduction in size, it can therefore be hypothesised that the CCHLVs are likely to be more compatible for size-dependent diffusion into the nucleus via the NPC. Furthermore, being smaller they are also considered more stable than pDNA vectors and thus possess a lower probability of inducing a random DNA integration event (Jiang *et al.*, 2016). Additionally, the absence of prokaryotic sequences crucially imbues CCHLVs with enhanced safety profiles and lower overall immunogenicity (Schnödt *et al.*, 2016).

Significantly, in early pre-clinical trials involving the use of purified CCHLVs, the above claims were tentatively verified with increased gene delivery efficiencies (3-17 fold improvement) observed in comparison to equivalent plasmid controls (Schakowski *et al.*, 2007; Schakowski *et al.*, 2001). In light of this improved transfection capability, it was considered highly pertinent to initiate exploration regarding the use of novel CCHLVs as the primary DNA vector within GAM systems – a tantalising combination that has not yet, to this authors knowledge, been investigated in any regard. This would include optimisation of CCHLV synthesis and basic 2D and 3D CCHLV transfection testing. Furthermore, as CCHLVs are linear DNA vectors, it was hypothesised that CCHLVs might be remarkably suited for F-AGE mediated electrophoretic patterning, where unlike plasmid vectors, they would always migrate through agarose hydrogels in a single linear conformation. As a result, *in-situ* co-localisation and co-complexation with CaP or PEI payloads could be more effectively controlled, leading to high encapsulation efficiencies of final transfection payloads.

The methodologies for CCHLV synthesis used in this chapter were based on the ELAN strategy first reported by Schakowski and colleagues (Schakowski *et al.*, 2007). In these reports, a dual RE ELAN strategy was employed in a two-tube reaction process, enabling the downstream formation of CCHLV vectors which were capable of enhanced gene expression. Although reported as a reliable and successful strategy, upon method specific scrutiny, several potentially solvable limitations could be identified, which restricted its potential use in large scale CCHLV production. This included the number of RE enzymes used (2 – EcoRI and BamHI), the number of and amount of hairpin oligonucleotides required (2 – 200-fold molar excess per hairpin) and the cost of specialist CCHLV and GEC isolation equipment (two rounds of purification via anion exchange chromatography). As such, this author sought to formulate a new method to solve several of the stated limitations mentioned previously, using a cheaper, more effective and streamlined ELAN CCHLV synthesis method. Once achieved, its potential use as an enhanced DNA vector system would be investigated.

6.2 Specific materials & methods

6.2.1 Custom oligonucleotides & primers

Table 6.1 – DNA base sequences and associated characteristics of hairpin oligonucleotides used in this study. (*P indicates the presence of a 5' terminal phosphate modification on end base).

Hairpin Oligonucleotides			
Name / ID	**Base Sequence (5'-3')**	**T_a**	**Purpose**
EcoRI_Hairpin (*±P)	AAT-TCG-GCC-GGC-CGT-TTT-CGG-CCG-GCC-G	62°C	Complimentary MunI overhang for GEC attachment
5'_Esp3I_Hairpin (*P)	ATC-GCG-GCC-GGC-CGT-TTT-CGG-CCG-GCC-G	53°C	Complimentary 5' Esp3I overhang for GEC attachment
3'_Esp3I_Hairpin (*P)	TTG-CCG-GCC-GGC-CGT-TTT-CGG-CCG-GCC-G	58°C	Complimentary 3' Esp3I overhang for GEC attachment
5'_Esp3I_Hairpin_EdU (*P)	ATC-GCG-GCC-GGC-CGT-5TT-CGG-CCG-GCC-G	53°C	Complimentary 5' Esp3I overhang for GEC attachment Linear alkyne modification (Thymidine base) for biomolecule conjugation (5) = Ethynyl-2'-deoxyuridine (EdU) modified Thymidine
3'_Esp3I_Hairpin_EdU (*P)	TTG-CCG-GCC-GGC-CGT-5TT-CGG-CCG-GCC-G	58°C	Complimentary 3' Esp3I overhang for GEC attachment Linear alkyne modification (Thymidine base) for biomolecule conjugation (5) = Ethynyl-2'-deoxyuridine (EdU) modified Thymidine

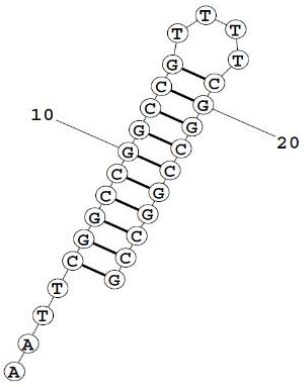

Figure 6.3 – Structural conformation of the hairpin DNA oligonucleotide from the F-ELAN-II approach. EcoRI_Hairpin. DNA folding at 95°C for 5 minutes using a PCR thermocycler machine (Techne Prime, England).

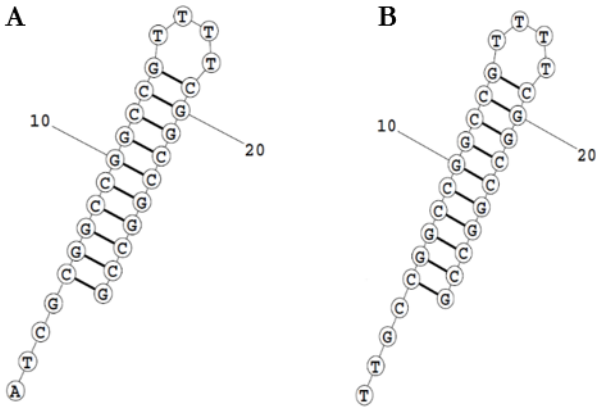

Figure 6.4 (A & B) – Structural conformation of the hairpin DNA oligonucleotides from the F-ELAN-IIS approach. A: 5'_Esp3I_Hairpin. B: 3'_Esp3I_Hairpin. DNA folding at 95°C for 5 minutes using a PCR thermocycler machine (Techne Prime, England).

Table 6.2 – Name (ID), base sequence, and annealing temperatures (Ta) of synthesis primers used in this study.

Synthesis Primers			
Name / ID	**Base Sequence (5'-3')**	**T_a**	**Purpose**
NEBf_GEC	GCT-GCG-TCT-CCC-GAT-TCC-CCG-AAA-AGT-GCC-ACC-TG	62°C	PCR mediated amplification of GEC region within pCAG-MetLuc2(forward sequence) Insertion of specific Esp3I recognition site
NEBr_GEC	ATC-GTC-TCG-GCA-AGA-TTT-GCC-CAA-TTG-CTC-CCA-TA	59°C	PCR mediated amplification of GEC region within pCAG-MetLuc2(forward sequence) (reverse sequence) Insertion of specific Esp3I recognition site
NEBf_pCAG	GCA-AAT-CTT-GCC-GAG-ACG-ATC-TCG-GAA-GGA-CAT-ATG-GG	53°C	PCR mediated amplification of pCAG-MetLuc2 backbone region (forward sequence) Insertion of specific Esp3I recognition site
NEBr_pCAG	GGG-GAA-TCG-GGA-GAC-GCA-GCG-ACC-AGG-TGG-CAC-TTT-TC	58°C	PCR mediated amplification of pCAG-MetLuc2 backbone region (reverse sequence) Insertion of specific Esp3I recognition site

6.2.2 Covalently closed hairpin loop vector (CCHLV) synthesis

6.2.2.1 F-ELAN-II synthesis method

This study utilised a modified version of the ELAN type II strategy to produce a functioning reporter CCHLV expression system. This approach was termed Feichtinger or F-ELAN-II and significantly utilised a single restriction enzyme and two-tube synthesis approach. The pCAG-

MetLuc2 plasmid was selected as the base expression vector due to its strong synthetic promoter sequences which have been proven to drive high level transgene expression in mammalian cells (Y. Y. Dou *et al.*, 2021). Crucially, two synonymous MunI restriction sites were located upstream and downstream of the pCAG-MetLuc2 gene expression cassette, thus enabling quick and effective linearization of the plasmid vector, specifically exposing the gene expression cassette (GEC) region.

Based on the knowledge that MunI cuts double stranded plasmid DNA at unique C^AATTG sites, a complimentary EcoRI/MunI hairpin oligonucleotide was subsequently purchased (EcoRI_Hairpin – 28bp (Eurogentec, Belgium)), enabling covalent attachment and dumbbell vector formation upon ligation (Table 6.1 and Figure 6.3). Although both iterations were ultimately purchased, the EcoRI_Hairpin oligonucleotide was initially synthesised in the absence of a 5' terminal phosphate, a decision taken to avoid hairpin-hairpin multimerisation. Basic ligation and exonuclease digestion processes were then performed in order to generate and confirm the formation of a covalently closed hairpin loop vector system, as shown in the Figure 6.5 workflow.

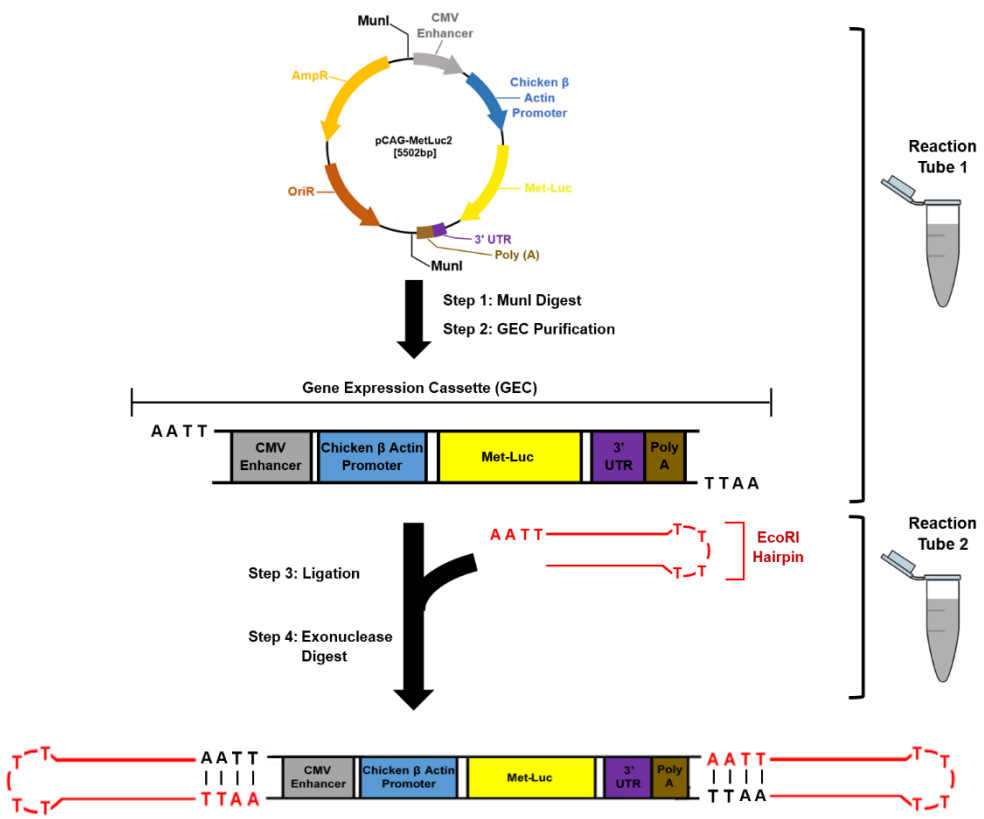

Figure 6.5 – Simplified workflow for synthesis of CCHLV using the F-ELAN-II approach.

The detailed experimental procedure used in this study is illustrated below in Table 6.3, whereby eleven major steps were performed in a sequential fashion. This included initial pCAG-MetLuc2 digestion (10 µg), followed by GEC isolation, GEC-EcoRI_Hairpin ligation, exonuclease

digestion and final CCHLV purification. In order to confirm the success of each of the stated procedures (those specifically highlighted in grey), a 2 µL aliquot was removed from the main reaction mixture and loaded within a 1 wt% agarose gel (stained previously with SYBR SAFE gel stain). Each gel was then analysed via UV illumination with specific emphasis on the presence, size and location of the various DNA bands generated.

Table 6.3 – Detailed MunI F-ELAN-II approach for the synthesis of a CCHLV vector.

	Brief method description	**Specific materials required**	**Product of each step**	**Detailed Protocol Location**
Step 1	10 µg double restriction digest of pCAG-MetLuc2 (overnight digest)	MunI and PscI restriction enzymes (5 units per enzyme required – 40 µL system) 1X Tango Buffer	Unique recognition and double stranded excision of pCAG-MetLuc2 vector	2.2.9.1
Step 2	Separation of digested pCAG-MetLuc2 linear fragments using agarose gel electrophoresis	1 wt% agarose gel DNA ladder	Confirmation of plasmid excision, presence of GEC in digest sample	2.2.9.2
Step 3	Isolation of GEC	Wizard SV Gel & PCR Clean-Up System	High quality linear DNA fragment. 20 µL elution volume (ddH_20)	2.2.9.3 2.2.9.4
Step 4	Calculate GEC sample concentration and yield	Nanodrop spectrophotometer	N/A	2.2.9.10
Step 5	Beer-Lambert law calculation for concentrations of EcoRI hairpin required (80X, 200X, 1000X excess versus 2.5µg GEC)	Nanodrop spectrophotometer	2.5 µg GEC (2684 bp) = 1.433pmol 80X Excess = 114.64pmol 200X Excess = 286.6pmol 1000X Excess = 1433pmol	N/A
Step 6	EcoRI Hairpin folding procedure (95°C for 5 minutes)	PCR thermocycler	Correctly folded oligonucleotide hairpin	6.2.1
Step 7	Overnight GEC-EcoRI hairpin ligation	T4 DNA ligase (40 µL system, 7.5 units used) 1X T4 DNA ligase buffer	Ligation products including CCHLV	2.2.9.5
Step 8	Inactivation of T4 DNA ligase (65°C, 20mins)	PCR thermocycler	Post ligation inactivation to avoid downstream activity	2.2.9.5

Step 9	T7 DNA Polymerase Digest (37°C, 60mins)	T7 DNA Polymerase (40 µL system, 10 units used)	Removal of unligated DNA products CCHLV product remains unaffected	2.2.9.10
Step 10	Inactivation of T7 DNA Polymerase (75°C, 30mins)	PCR thermocycler	Post digest inactivation to avoid downstream activity	2.2.9.10
Step 11	CCHLV purification via Chloroform extraction and ethanol precipitation (250µL ddH_2O reconstitution final volume)	Chloroform, 100% ethanol, Sodium acetate	CCHLV vector & Excess EcoRI hairpin products	2.2.9.4

6.2.2.2 F-ELAN-IIS synthesis method

Based on the outcomes of CCHLV synthesis via F-ELAN-II (MunI) methodologies, several method specific limitations were present which restricted the efficiency and yield of final CCHLV products. As a result, the alternate F-ELAN-IIS method was created with the intention that such limitations could be avoided. The new synthesis strategy utilised the concept of smart cohesive end base sequence design to produce unique GEC and hairpin oligonucleotide fragments, which crucially were resistant to self-ligation, thus promoting CCHLV formation when in the presence of complimentary hairpins. This was achieved mainly through the novel use of a type IIS restriction enzyme termed Esp3I.

Type IIS restriction enzymes differ widely from standard type II enzymes in terms of protein structure and overall functionality. Structurally, type IIS restriction enzymes, such as Esp3I or FokI, are larger proteins partitioned into two domains; the recognition domain and catalytic domain (linked by a polypeptide connector) as opposed to the single domain observed in type II enzymes such as HindIII or MunI. Upon DNA sequence recognition, the protein conformation is such that the catalytic domain resides spatially distinct (several base pairs) from the recognition site, leading to upstream or downstream shifts in overall cleavage site locations (Szybalski *et al.*, 1991). As a result, type IIS has the capability of asymmetric sequence recognition and also fundamentally possesses the capacity to produce DNA fragments with terminal non-palindromic, self-incompatible cohesive ends (Figure 6.6).

Figure 6.6 – Recognition sequence and downstream cleavage site of Esp3I Type IIS restriction enzyme.

It was therefore theorised that dual insertion of separate Esp3I recognition and cleavage sequences upstream and downstream of the pCAG-MetLuc2 gene expression cassette, would allow for the formation of a GEC, uniquely resistant to self-ligation and concatamerisation. Furthermore, simultaneous synthesis of 5' and 3' hairpins which shared such complementarity with the aforementioned GEC would also convey such properties.

Crucially, due to the lack of any 5' and 3' Esp3I recognition sites within the original pCAG-MetLuc2 plasmid, several methods were therefore employed which allowed for its correct insertion, specifically in two locations upstream and downstream of the gene expression cassette.

6.2.2.2.1 Design and modelling of Esp3I GEC and Esp3I hairpin oligonucleotides

To ensure that successful CCHLV synthesis could be achieved whilst simultaneously restricting any unwanted DNA ligation conformations, unique base sequences had to be developed for both the 5' and 3' cohesive ends for the hypothesised GEC and hairpin oligonucleotides respectively. Within these unique base sequences (4 bp), it was imperative that they possessed a non-palindromic sequence structure as well as a complete resistance to self-compatibility. As a result, the following sequences shown in Table 6.4 were designed.

Using standard DNA base pairing models, it was then possible to demonstrate each viable DNA ligation product, and how such sequences can avoid their synthesis (Figure 6.7).

Table 6.4 – Hypothesised cohesive end base sequences designed specifically to avoid unwanted ligation products upon exposure of GEC and hairpin oligonucleotides to T4 DNA Ligase.

Linear DNA fragment	5' Cohesive End Base Sequence	3' Cohesive End Base Sequence
GEC	5' – CGAT – 3'	5' – AACG – 3'
5'_Esp3I_Hairpin	5' – ATCG – 3'	N/A
3'_Esp3I_Hairpin	N/A	5' – TTGC – 3'

6.2.2.2.2 Insertion of Esp3I recognition sequences into pCAG-MetLuc2

Precise 5' and 3' Esp3I recognition sites flanking the GEC region were inserted into the source plasmid pCAG-MetLuc2 using ligation independent cloning (LIC) strategies outlined in section 2.2.8.12. Initially, four synthesis primers (NEBf_GEC, NEBr_GEC, NEBf_pCAG, NEBr_pCAG) were designed, as per Table 6.2. These were firstly capable of amplifying both the GEC and pCAG backbone regions of the pCAG-MetLuc2 plasmid, and secondly able to insert of specific designed Esp3I recognition and cleavage sites flanking the expression cassette region. Furthermore, both resulting blunt ended PCR fragments (GEC-MetLuc_PCR, pCAG_PCR) were modelled such that they contained a shared 5' and 3' 20 bp homology region, allowing downstream fragment annealing for plasmid vector reconstruction (NEB HiFi DNA fragment assembly) (Figure 6.8). The online NEBuilder tool was used to aid in primer design.

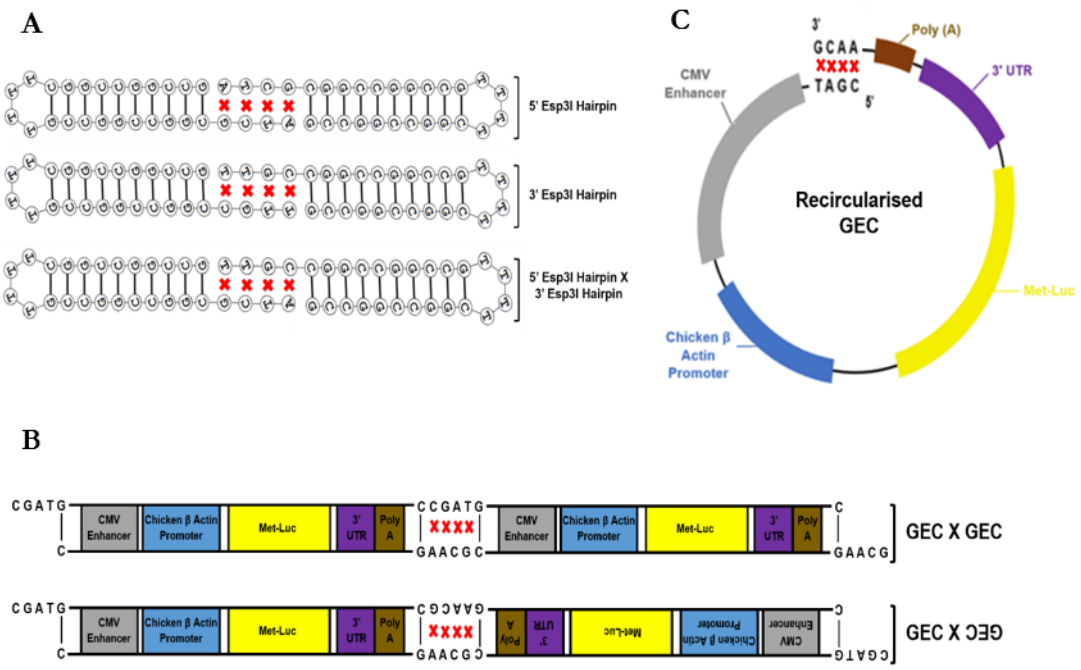

Figure 6.7 – Hypothesised ligation products resulting from pre-designed 5' and 3' Esp3I GEC or pre-designed 5' and 3' Esp3I_Hairpin (P) upon exposure to T4 DNA ligase. Red X indicates incompatible base pairing.

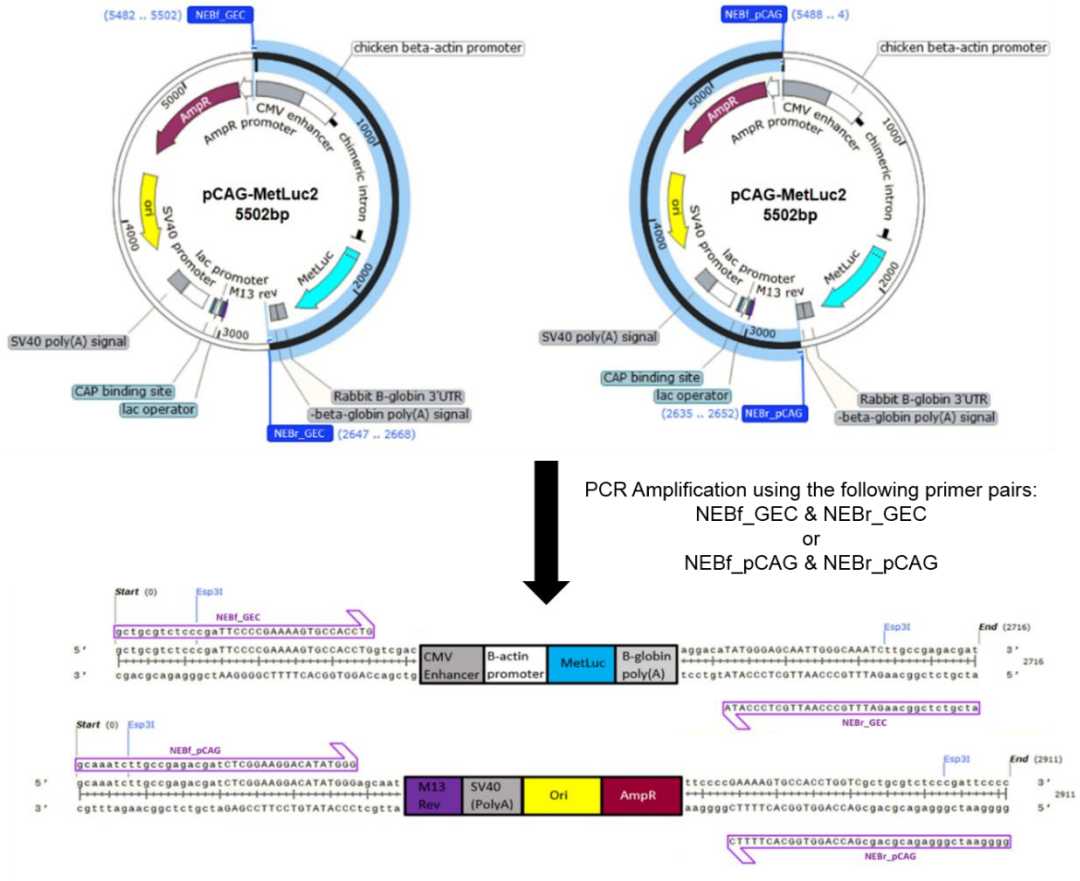

Figure 6.8 – Modelled pCAG-MetLuc mediated PCR products using the synthesis primers NEBf_GEC, NEBr_GEC, NEBf_pCAG, NEBr_pCAG. Predicted GEC-PCR product size: 2716 bp, Predicted pCAG Backbone PCR product size: 2911 bp.

To achieve this, the KOD Hot Start DNA Polymerase PCR protocol outlined in section 2.2.8.11 was carried out, without any modifications. This included the performance of two separate 50 µL PCR reactions, using 10 ng pCAG-MetLuc2 (acting as the template DNA) alongside either the NEBf_GEC and NEBr_GEC or the NEBf_CAG and NEBr_CAG primer pairs. Primer melting temperatures of 60.5°C and 63.7°C were used respectively.

After amplification, 2 µL aliquots were removed for agarose gel electrophoresis and analysis. The remaining mixture (~50 µL) was then digested overnight with 1 µL DpnI (10U/µL) (Thermofisher), to remove surplus cell-derived plasmid template from PCR reaction, prior to final purification steps (2.2.8.4). The mass of each purified PCR fragment was then measured using a nanodrop spectrophotometer.

To ensure the presence of the desired Esp3I sequences within each PCR fragment, an additional double digest was performed at this stage. This included Esp3I (+ dithiothreitol (DTT)) and PscI/XbaI digestion in the presence of 500 ng PCR products, followed by analysis via agarose gel electrophoresis (1 wt%).

To then assemble the two PCR fragments into a circularised plasmid vector, the NEBuilder HiFi DNA Assembly reaction protocol (section 2.2.9.12) was followed, using a 1:2 pCAG_PCR:GEC-MetLuc_PCR molar ratio (0.01 pmol total DNA). Ampicillin antibiotic (80 µg/µL) was used for overnight cultures and within LB-agar plates. Figure 6.9 represents a diagrammatic illustration of the PCR-plasmid assembly process.

In the final stage, standard minipreparation protocols were performed to isolate and purify the final pCAG-MetLuc2 (Esp3I) plasmid. Two clones were purified and subsequently tested for the existence of correct Esp3I insertion sites, as well as the presence of correct backbone sequence structure. This included a single Esp3I (+DTT) digest (500 ng) and a double Esp3I (+DTT) and PscI digest (500 ng each), followed by analytical agarose gel electrophoresis (1 wt%).

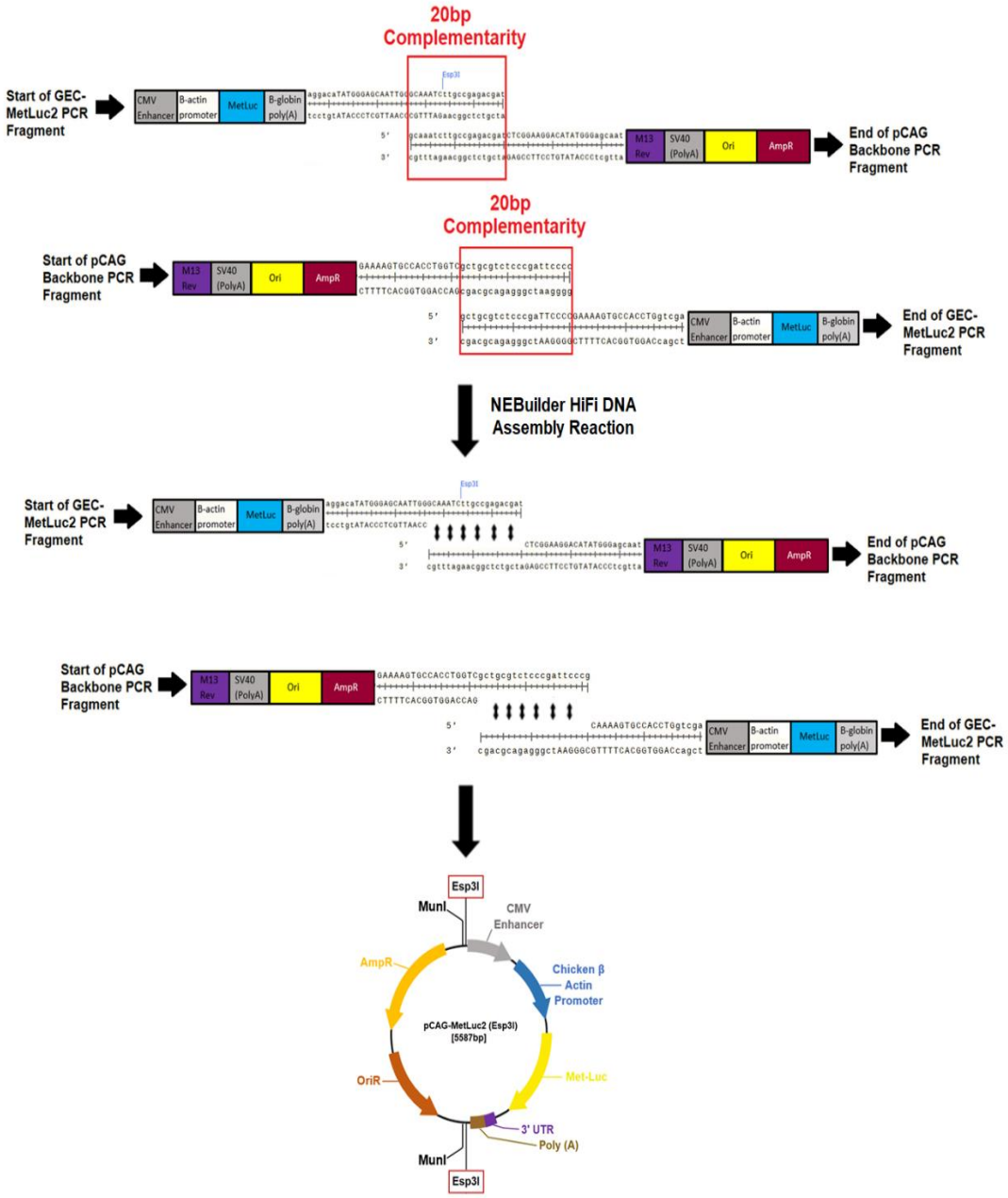

Figure 6.9 – Modelled PCR product DNA assembly and pCAG-MetLuc2 (Esp3I) plasmid formation using the NEB HiFi DNA Assembly Reaction kit.

6.2.2.2.3 CCHLV synthesis

As a result of hypothesised incompatible non-palindromic cohesive ends being present on both the GEC and hairpin oligonucleotides, CCHLV synthesis using the Esp3I restriction enzyme crucially allowed for the production of hairpin vectors within a single-tube method approach, avoiding the inefficient DNA isolation steps previously used in the MunI approach. This was possible only if the Esp3I restriction enzyme remained active during the ligation reaction, such that reformation of the pCAG-MetLuc2 (Esp3I) plasmid (in the presence of DNA ligase) would result in secondary Esp3I site recognition and re-cleavage back into the linear products.

A single restriction endonuclease digest (Esp3I (+DTT)) of pCAG-MetLuc2 (Esp3I) was therefore performed, generating linear DNA products including the GEC (containing pre-designed 5' and 3' cohesive ends). 5'_Esp3I_Hairpin & 3'_Esp3I_Hairpin oligonucleotides (with 5' terminal phosphate modification) were then applied to GEC in a variety of excesses (10X, 20X, 80X), in presence of T4 DNA ligase (5U/µL). Successfully ligated CCHLV were validated upon T7 DNA polymerase (10U/µL) treatment whilst unligated linear DNA products were digested completely. Final synthesis products were then purified as previously stated. This process was summarised in the Figure 6.10 workflow and the full step-wise approach is given in Table 6.5. Each major synthesis step (highlighted in grey) was ratified via 2 µL aliquot loading within analytical agarose gels.

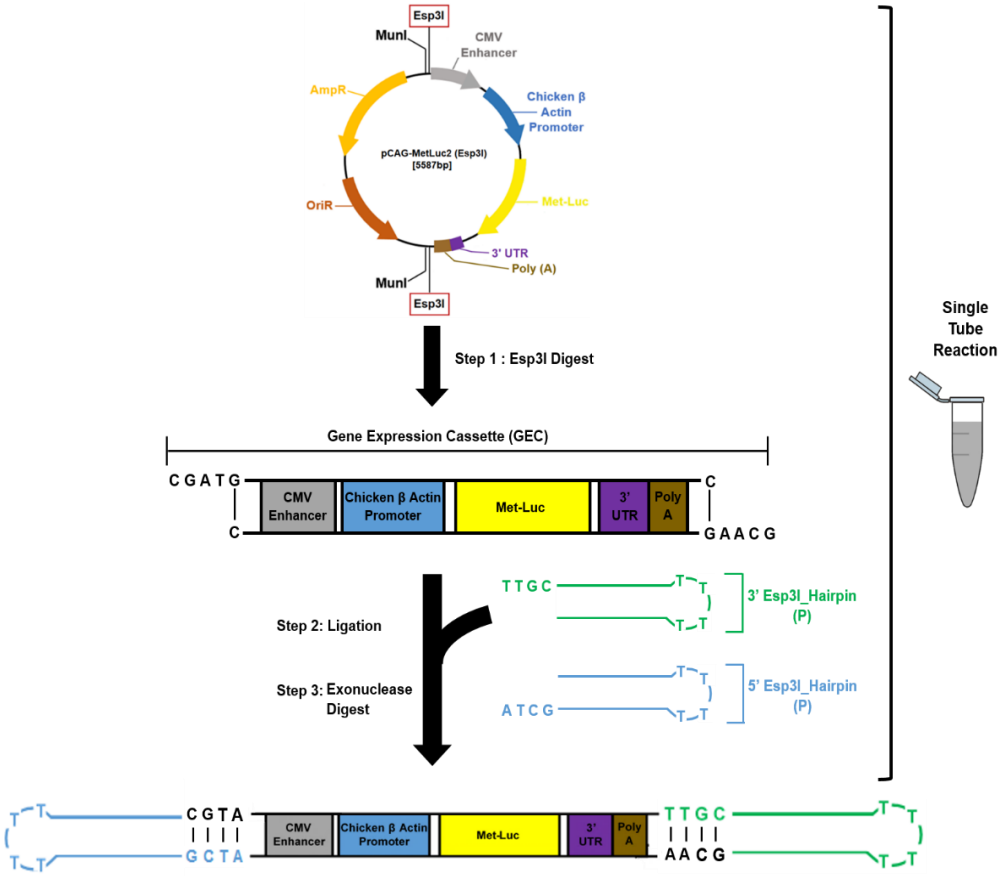

Figure 6.10 – Simplified workflow for synthesis of CCHLV using the single tube F-ELAN-IIS approach.

Table 6.5 – Detailed Esp3I mediated F-ELAN-IIS approach for the synthesis of a CCHLV vector.

	Brief method description	Specific materials required	Product of each step	Detailed Protocol Location

Step 1	10µg single restriction digest of pCAG-MetLuc2 (overnight digest)	Esp3I (+DTT) restriction enzyme (5 units required - 40µL system) 1X Tango Buffer	Unique recognition and double stranded excision of pCAG-MetLuc2 vector	2.2.9.1
Step 2	Calculate hypothesised GEC sample concentration/yield if 100% digestion occurred	N/A	N/A	N/A
Step 3	Beer-Lambert law calculation for concentrations of 5'_Esp3I_Hairpin and 3'_Esp3I_Hairpin required (10X, 20X, 80X excess versus 4.8µg GEC)	Nanodrop spectrophotometer	4.8µg GEC (2692bp) = 2.754pmol 10X Excess = 27.54pmol 20X Excess = 55.07pmol 80X Excess = 220.29pmol	N/A
Step 4	5'_Esp3I_Hairpin and 3'_Esp3I_Hairpin folding procedure (95°C for 5 minutes)	PCR thermocycler	Correctly folded oligonucleotide hairpins	6.2.1
Step 5	Overnight 5'_Esp3I_Hairpin-GEC-3'_Esp3I_Hairpin ligation	T4 DNA ligase (40 µL system, 7.5 units used) 1X T4 DNA ligase buffer	Ligation products including CCHLV	2.2.9.5
Step 6	Inactivation of T4 DNA ligase (65°C, 20mins)	PCR thermocycler	Post ligation inactivation to avoid downstream activity	2.2.9.5
Step 7	T7 DNA Polymerase Digest (37°C, 60mins)	T7 DNA Polymerase (40 µL system, 10 units used)	Removal of unligated DNA products CCHLV product remains unaffected	2.2.9.10
Step 8	Inactivation of T7 DNA Polymerase (75°C, 30mins)	PCR thermocycler	Post digest inactivation to avoid downstream activity	2.2.9.10
Step 9	CCHLV purification via Chloroform extraction and ethanol precipitation (250µL ddH_2O reconstitution final volume)	Chloroform, 100% ethanol, Sodium acetate	Fully purified CCHLV vector	2.2.9.4

6.2.3 2D Transfection capability of CCHLV

Successfully purified Met-Luc encoding CCHLVs were then assessed for their transfection capability, in comparison to standard plasmid vectors. Transfection was evaluated in a basic 2D cell monolayer format (C2C12 and Y201) using three different transfection reagents; Calcium phosphate (no glycerol shock), lipofectamine and PEI. Met-Luc expression was measured over a 72 hour duration, with assays performed daily. As the DNA vectors used in this experiment were

of different sizes (pCAG-MetLuc2: 5587 bp, CCHLV-MetLuc: 2752 bp), direct comparisons were made using equimolar ratios (picomoles DNA per well) instead of actual DNA concentration added.

Experimentally, C2C12 and Y201 cells were separately passaged and re-suspended to a concentration of $0.4x10^5$ cells/well before seeding into 24 well culture plates (n=4 per transfection group). Upon approximately 80% confluency (~24 hours post seeding), a range of pDNA or CCHLV transfection payloads were then formulated, as per Table 6.6, Table 6.7 and Table 6.8. Under such parameters, the basic transfection protocols outlined in chapter 2 section 2.2.10 were then followed for each method, until completion.

For each transfection payload method, controls were included such as media only (negative control) and plasmid only (n=4).

Transfection was assessed daily using quantitative assessment methods, as outlined in section 2.2.10.2.1.

Table 6.6 – 2D CaP transfection parameters for the transfection of C2C12 and Y201 cells with pDNA-CaP complexes or CCHLV-CaP complexes.

Vector	CaP:DNA /CCHLV Incubation Solution Volume (per well)	Initial $CaCl_2$ Conc (2.5M stock) (per well)	pDNA Conc (per well)	Number of moles DNA/CCHLV (per well)	Final $CaCl_2$ Conc	Culture Volume
pDNA (5587bp)	50 µL	500 mM	1 µg	0.275 pmol	25 mM	500 µL
CCHLV (2752bp)	50 µL	500 mM	500 ng	0.275 pmol	25 mM	500 µL

Table 6.7 – 2D PEI transfection parameters for the transfection of C2C12 and Y201 cells with pDNA-PEI polyplexes or CCHLV-CaP polyplexes.

Vector	PEI:DNA Incubation Solution Volume (per well)	PEI Conc (1μg/μL stock) (per well)	N/P Ratio	pDNA Conc (per well)	Number of moles DNA/CCHLV (per well)	Culture Volume
pDNA (5587bp)	50 μL SFM	3.10	24	1 μg	0.275 pmol	500 μL
CCHLV (2752bp)	50 μL SFM	1.55	24	500 ng	0.275 pmol	500 μL

Table 6.8 – 2D Lipofectamine transfection parameters for the transfection of C2C12 and Y201 cells with pDNA-lipoplexes or CCHLV-lipoplexes.

Vector	Lipofectamine :DNA Incubation Solution Volume (per well)	Volume Lipofectamine added	pDNA Conc (per well)	Number of moles DNA/CCHLV (per well)	Culture Volume
pDNA (5587bp)	100 μL SFM	2 μL	1 μg	0.275 pmol	500 μL
CCHLV (2752bp)	100 μL SFM	2 μL	500 ng	0.275 pmol	500 μL

6.3 Results

6.3.1 CCHLV Synthesis (F-ELAN-II MunI Strategy)

6.3.1.1 Confirmation of source plasmid MunI recognition sites & GEC isolation

Figure 6.11 illustrates the outcome of a double restriction digest of two clones of the plasmid pCAG-MetLuc2, using the MunI and PscI enzymes. A further restriction enzyme (PscI) was added to effectively differentiate the GEC fragment (circled in red) from the pCAG bacterial backbone (a single MunI digest generating two fragments of correlative size; 2818 bp and 2684bp respectively) allowing downstream purification via gel excision and silica-based columns. The double digest was successful in both cases, with MunI and PscI splicing the plasmid at four separate recognition sequences. As such, four linear fragments were produced; 2684 bp, 1788 bp, 798 bp, 232 bp, the largest of which, represented the expression cassette region.

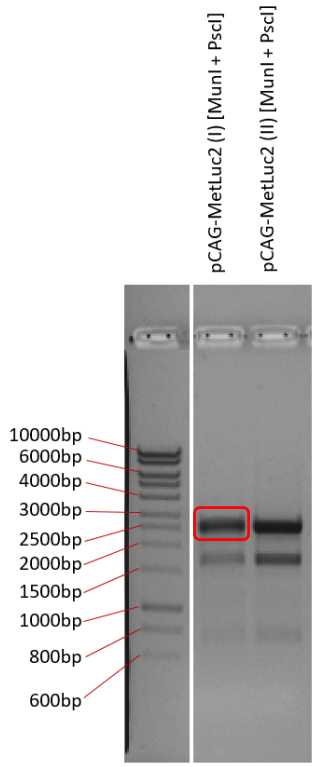

Figure 6.11 – Example of GEC DNA fragment purification from agarose gels using Wizard® SV Gel and PCR Clean-Up System (Promega). 1 wt% agarose gel (with SYBR SAFE), run at 90V for 30 minutes. Size ladder = Hyperladder 1 kb. Red highlighted band = GEC fragment.

Post digest, the GEC fragment was then excised from the agarose gel and purified using the Wizard SV Gel & PCR Clean-Up System (Promega). Upon protocol optimisation, a maximum GEC recovery efficiency of 60% was achieved from a 10 µg pCAG-MetLuc2 double digest (100% recovery of GEC = 4.9 µg).

6.3.1.2 Synthesis of CCHLV

CCHLV production steps described in section 6.2.2.1 were followed to completion. 2 μL aliquots were taken at three different stages of the synthesis process for analytical gel electrophoresis (pre-T4 DNA ligase, post-T4 DNA ligase, post-T7 DNA polymerase). Figure 6.12 A & B illustrates the DNA products formed using 5' terminal phosphate deficient EcoRI_Hairpin oligonucleotides whilst Figure 6.12 C & D illustrates DNA products formed using 5' terminal phosphate containing oligonucleotide hairpins.

In lane 2 of Figure 6.12 A, upon T4 DNA ligase addition to GEC alone, the appearance of DNA bands showed significant change. As opposed to a single DNA fragment at 2684 bp, multiple intense thinner bands were now present, located at approximately 1700 bp (single band), 2800 bp and 4000 bp (double band), and approximately 6000 bp and 8000 bp (feint double band). Upon addition of EcoRI_Hairpin (80X excess) into the system (lane 4), observable changes were only displayed on the 2800 bp band whereby its intensity appeared to have marginally increased. As no further changes occurred in the other bands, it could be assumed the 80X excess concentration had minimal impact on the many ligation products generated.

Interestingly, upon further increases in EcoRI_hairpin concentration (200X, 1000X excess) (lane 5 and 6), the previously illustrated banding pattern began to alter. Specifically, a dose-dependent decrease in intensity occurred in the various bands above and below the GEC/CCHLV region (1700 bp single band and 6000 bp and 8000bp double bands, respectively). Moreover, the double banding pattern located in the GEC region (2700 - 4000 bp) also changed upon increases in EcoRI_Hairpin, forming a solid single band at the highest EcoRI hairpin concentration, illustrating tentative GEC-EcoRI_Hairpin attachment within these conditions.

However, upon exposure to T7 DNA polymerase (Figure 6.12 B), all DNA bands originally present within the GEC/CCHLV region were promptly degraded, suggesting the DNA products produced by ligation were not in fact true CCHLV (due to the absence of exonuclease resistance). Yet, the survival of two single DNA bands at 1700 bp and 6000 bp (in GEC + ligase – 80X, 200X excess lanes) implied production of alternative exonuclease resistant constructs; likely reformed plasmid vectors and/or mini-circles.

Figure 6.12 (C & D) illustrates the DNA products formed using 5' terminal phosphate modified EcoRI_Hairpin oligonucleotides. The band pattern associated with GEC + ligase remains similar in these gels, with single and double bands appearing at 1700 bp and 2800-4000 bp respectively. The extra double band at 6000-8000 bp was present although faint in some cases. In the post-ligation gel (Gel C), the band pattern matches that previously identified in Gel A, with dose-dependent decreases in intensity seen in upper and lower band patterns as EcoRI_Hairpin concentration increases.

Gel D however, illustrates several marked differences in DNA patterning as a result of the 5' terminal phosphate modification, namely the presence of an exonuclease resistant product in the expected CCHLV region (2750 bp) in all lanes containing EcoRI_Hairpin (P). This attribute, in conjunction with a correct approximation of molecular weight, implies successful CCHLV synthesis under these conditions. Moreover, as the system becomes ultra-saturated with increasing levels of hairpin, dose-dependent decreases occur in unwanted exonuclease resistant bands, improving CCHLV yields further. This culminates in 1000X excess EcoRI_Hairpin lane (Gel D – lane 6), where only two DNA bi-products are produced, the CCHLV and dimerized hairpin.

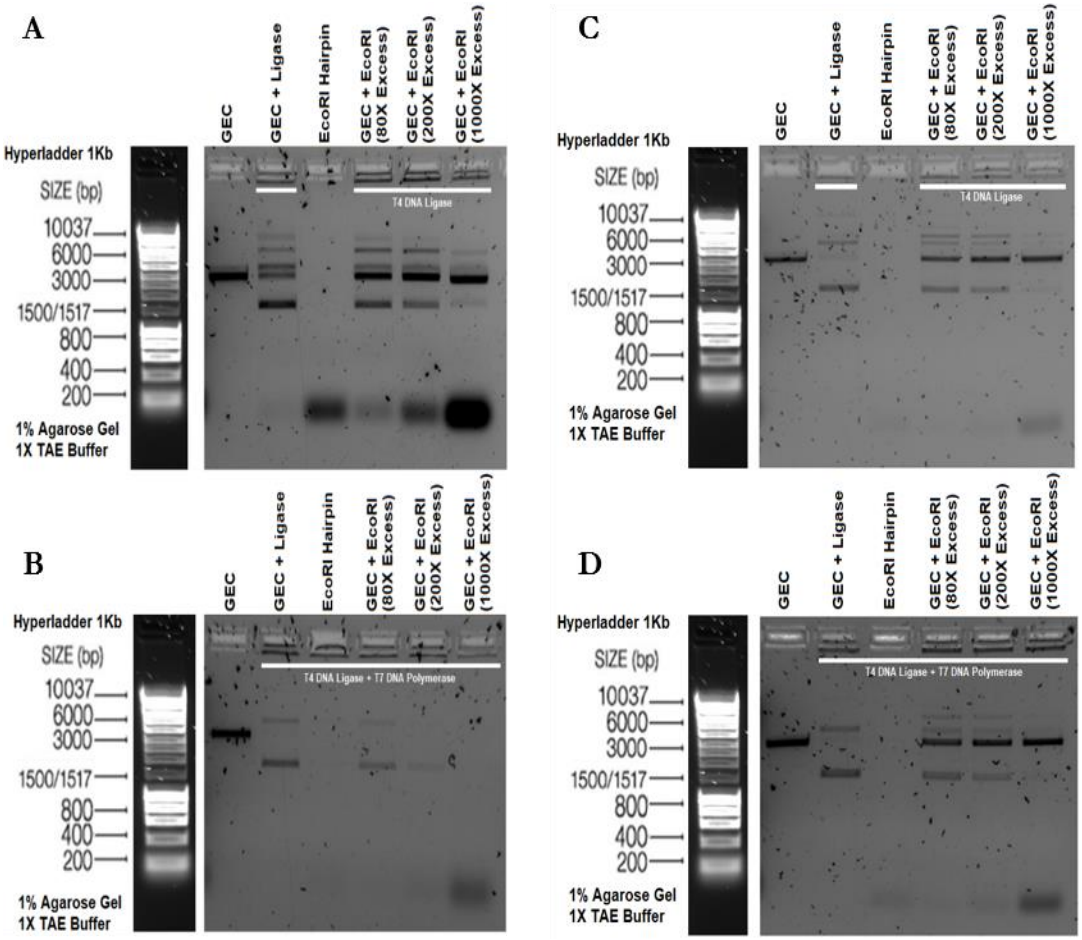

Figure 6.12 (A, B, C, D) – Synthesis of CCHLV using the MunI mediated F-ELAN-II strategy. A: Unphosphorylated EcoRI_Hairpin mediated CCHLV formation, after T4 DNA ligase treatment only, B: Unphosphorylated EcoRI_Hairpin mediated CCHLV formation, after T4 DNA ligase & T7 DNA Polymerase treatment, C: Phosphorylated EcoRI_Hairpin (P) mediated CCHLV formation, after T4 DNA ligase treatment, D: Phosphorylated EcoRI_Hairpin (P) mediated CCHLV formation, after T4 DNA ligase & T7 DNA polymerase treatment. 1 wt% agarose gel (with SYBR SAFE), run at 90V for 20 minutes. Size ladder = Hyperladder 1 kb.

6.3.2 CCHLV Synthesis (F-ELAN-IIS Esp3I Strategy)

6.3.2.1 Insertion of Esp3I recognition sequences

In order to generate a GEC with non-palindromic cohesive ends, specifically designed recognition sites were inserted into the source plasmid pCAG-MetLuc2 using PCR based DNA fragment assembly. The synthesis primers NEBf_GEC, NEBr_GEC, NEBf_pCAG, NEBr_pCAG were used to generate two blunt ended PCR products, which possessed the desired and hypothesised Esp3I cohesive ends, whilst also sharing a 20 bp homology region – crucial for ligation independent cloning and plasmid formation.

Figure 6.13 A illustrates the first stage of this process, whereby blunt ended PCR products were initially generated, containing the aforementioned Esp3I recognition sites. GEC and pCAG PCR products were analysed using agarose gel electrophoresis, pre and post DpnI exposure, as per section 0.

The GEC-MetLuc_PCR and pCAG_PCR products generated using the pre-designed primers resulted in the production of two linear DNA products each represented as a single intense DNA band in the region of 2700 bp and 2900 bp respectively (lane 3 and 4). Crucially, little difference was observed in the band patterns pre and post DpnI treatment (lane 5 and 6), signifying the sole presence of PCR mediated DNA products, which lacked adeno-methylated GATC sites (unlike plasmid material – lane 2). Multiple faint DNA bands did however appear below the PCR bands in both cases, implying a small degree of non-specific primer attachment and amplification may have occurred, potentially as a result of imperfect annealing time and/or temperature.

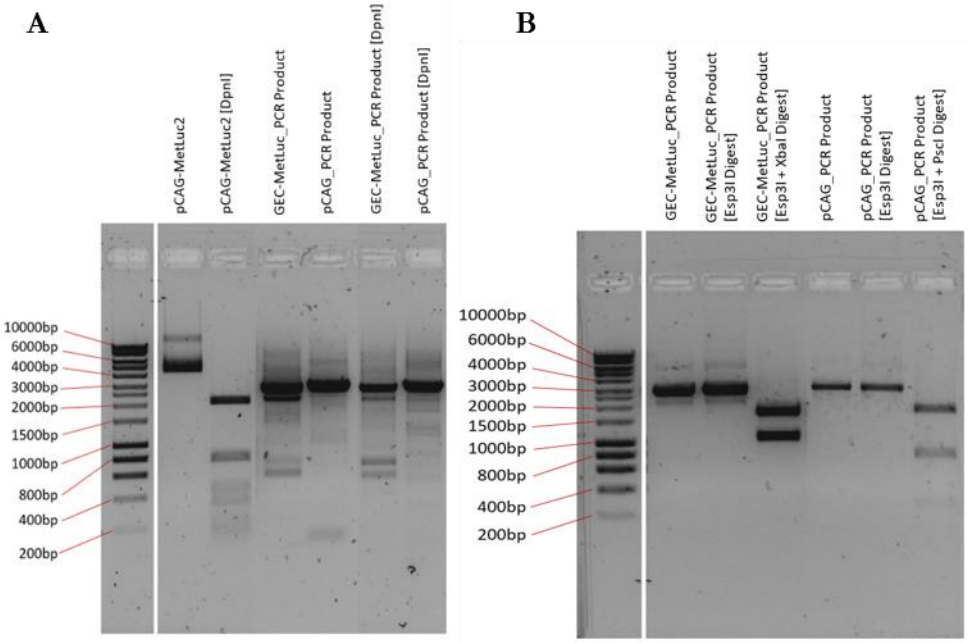

Figure 6.13 (A & B) – Confirmation of successful PCR amplification of pCAG-MetLuc2 using NEBf_GEC, NEBr_GEC, NEBf_pCAG, NEBr_pCAG synthesis primers. Gel A illustrates the PCR products produced before and after DpnI digestion. Gel B illustrates various confirmatory restriction digests on the generated PCR products. 1 wt% agarose gel (with SYBR SAFE), run at 90V for 30 minutes. Size ladder = Hyperladder 1 kb.

Figure 6.13 B on the other hand, illustrates the restriction digests of the purified PCR fragments with specific restriction enzymes only present in the GEC or pCAG PCR regions (Esp3I, XbaI, PscI), thus allowing the confirmation of successful Esp3I sequence insertion for each PCR product.

Due to the close proximity of Esp3I sites to the 5' and 3' terminal ends, only marginal differences can be identified between the Esp3I digested PCR products and their respective blunt ended fragments (lanes 1 & 2 – 2696 bp versus 2716 bp, lanes 4 & 5 – 2891 bp versus 2911 bp). However, in lane 3, two intense bands were identified after GEC-MetLuc_PCR digestion with Esp3I and XbaI, at approximately 1000 bp and 1600 bp. As XbaI was modelled to be a single cutter for this DNA region, the creation of two bands of this size categorically demonstrates the presence of Esp3I sites within this PCR product, with the 5' Esp3I acting as a left cutter to XbaI and 3' Esp3I acting as a right cutter to XbaI.

Similarly, in lane 6, three bands were identified after Esp3I and PscI digestion of pCAG_PCR at approximately 1800 bp, 800 bp and 250 bp. As PscI was modelled to be a dual sequence cutter, failure of Esp3I insertion would lead to two bands as opposed to the three identified, again confirming the presence of functioning restriction sites at the desired location.

Based on these findings, it can therefore be assumed GEC-MetLuc_PCR and pCAG_PCR fragments suitably matched the modelled size and characteristics expected from successful PCR amplification enabling subsequent downstream DNA assembly and plasmid production.

In the second stage of this Esp3I insertion process, the two GEC-MetLuc_PCR and pCAG_PCR fragments generated were subsequently assembled back into a circularised plasmid vector, a process made possible through the employment of the NEBuilder HiFi DNA Assembly reaction kit, which was described in section 2.2.9.12.

Figure 6.14 illustrates the result of successful PCR fragment assembly, transformation, outgrowth and purification of the final pCAG-MetLuc2 (Esp3I) plasmid. Specifically, the presence of a host of NEB 5-alpha Competent E. coli colonies on an ampicillin LB-agar plate (Figure 6.14 A) suggests the existence of an active ampicillin resistance gene present within the plasmid backbone, i.e successful incorporation of the pCAG bacterial elements donated via pCAG_PCR fragment. Figure 6.14 B illustrates minipreparation of four plasmid clones, characteristically presenting as a double band pattern whereby an intense supercoiled band is coupled below a band of nicked pDNA.

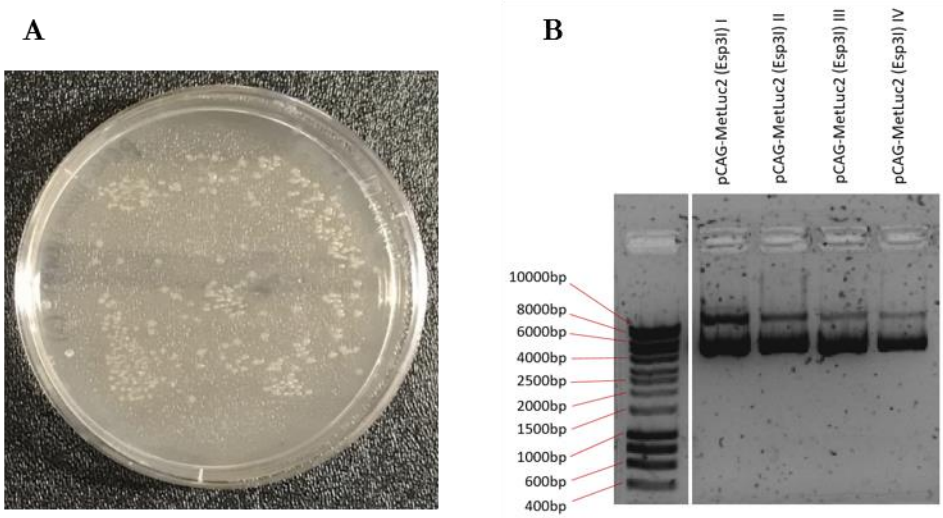

Figure 6.14 (A & B) – Transformation and Minipreparation of pCAG-MetLuc2 (Esp3I) after HiFi DNA Fragment Assembly. A: NEB 5-alpha Competent E. coli transformed with pCAG-MetLuc2 (Esp3I). Ampicillin LB-agar plates used. B: Analytical agarose gel of four isolated pCAG-MetLuc2 (Esp3I) plasmids. 1 wt% agarose gel (with SYBR SAFE), run at 90V for 15 minutes. Size ladder = Hyperladder 1kb.

6.3.2.2 Confirmation of pCAG-MetLuc2 (Esp3I) Esp3I recognition Sites & GEC Isolation

To sanction pCAG-MetLuc2 (Esp3I) as the new source plasmid for CCHLV synthesis, a confirmatory single and double restriction digest was first performed on two pCAG-MetLuc2 (Esp3I) clones, using Esp3I (+DTT) and PscI restriction enzymes.

A single Esp3I digest (as shown in Figure 6.15 A - lane 1 and 2) generates a single dense DNA band at approximately 2800 bp. As a projected dual cutter, two DNA bands were modelled pre-digest, however due to size similarities between each fragment as well as a short electrophoresis duration, it can be assumed that the single band seen was simply an amalgamation of both.

This assumption was subsequently confirmed by analysis of the band patterns generated by Esp3I and PscI digestion in lanes 3 and 4. Three clear linear DNA fragments can be identified at approximately 2700 bp, 1800 bp, 800 bp, which matched pre-digest models for digestion with Esp3I and PscI. As both are dual cutters, a fourth band at 262 bp was expected, however as a result of its small size, the band intensity fell below detectable levels. The largest band at approximately 2700 bp was therefore the GEC of interest (circled in red), containing the specifically designed non-palindromic non-complimentary 5' and 3' cohesive ends (Figure 6.15 B).

Due to successful Esp3I mediated restriction digestion, the single Esp3I restriction digest shown in Figure 6.15 A - lane 1 was subsequently up-scaled for CCHLV synthesis, whereby 10 µg pCAG-MetLuc2 (Esp3I) was linearised in a single 40 µL reaction system. It was also deemed DNA purification steps post Esp3I digest were unnecessary as long as Esp3I remained active

throughout the ligation procedure, thus re-cleaving pCAG-MetLuc2 (Esp3I) plasmids upon their potential re-ligation. Furthermore, based on modelling, no other DNA products were hypothesised to be possible, according to standard base complementarity.

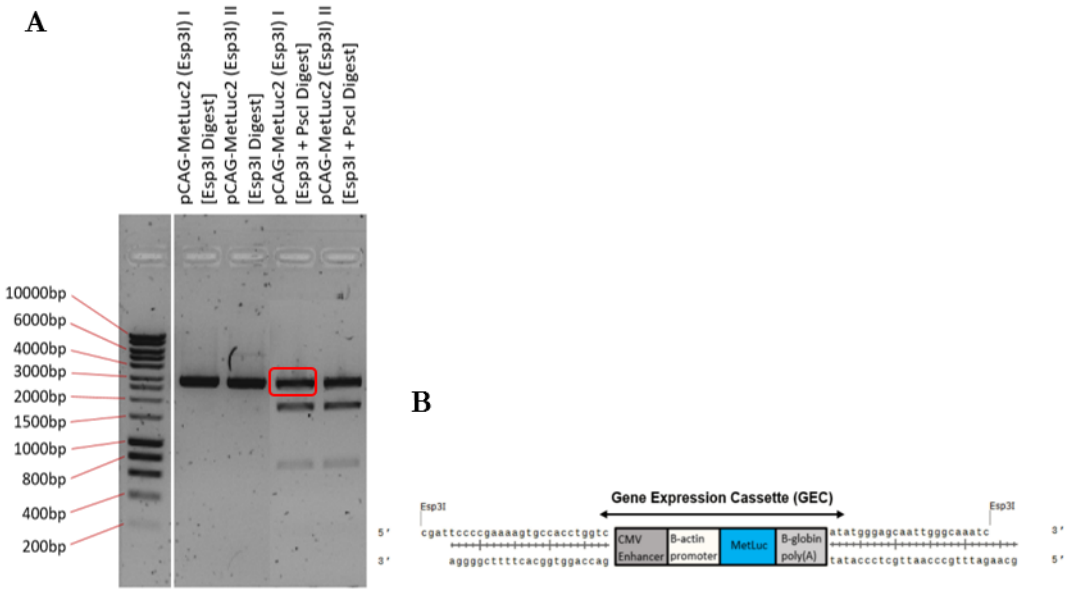

Figure 6.15 (A & B) – Confirmation of 5' and 3' Esp3I recognition sites flanking the gene expression cassette region of pCAG-MetLuc2 (Esp3I). 1 wt% agarose gel (with SYBR SAFE), run at 90V for 30 minutes. Size ladder = Hyperladder 1 kb. Red highlighted band = Esp3I GEC fragment (B).

6.3.2.3 Synthesis of CCHLV

CCHLV production steps described in section 6.2.2.2.3 were followed to completion. 2 µL aliquots were taken at the three different stages of the synthesis process for analytical gel electrophoresis (pre- T4 DNA ligase, post-T4 DNA ligase, post-T7 DNA polymerase).

Figure 6.16 (A & B) illustrates the DNA products formed upon mixing the GEC in the presence of excess 5'_Esp3I_Hairpin (P) and 3'_Esp3I_Hairpin (P) oligonucleotides and DNA ligase. It was firstly noted in gel A, the apparent lack of impact of T4 DNA ligase on the Esp3I generated GEC, with no unwanted DNA products produced alongside the expected linear GEC, as represented by a single band at approximately 2700 bp.

This band pattern continued in lanes 6, 7 and 8 containing excess hairpin oligonucleotides, whereby only a single DNA band is generated (of marginally larger molecular weight). No further contaminating DNA products were identified above or below this band. Interestingly, previously identified hairpin DNA bands (at < 200 bp) disappeared after mixing with the GEC in the presence of DNA ligase, with them now only faintly appearing at the highest 80X excess level. Such increases in size, as well as the disappearance of hairpin only bands, suggests successful attachment of all 5'_Esp3I_Hairpin (P) and 3'_Esp3I_Hairpin oligonucleotides to their corresponding GEC cohesive ends.

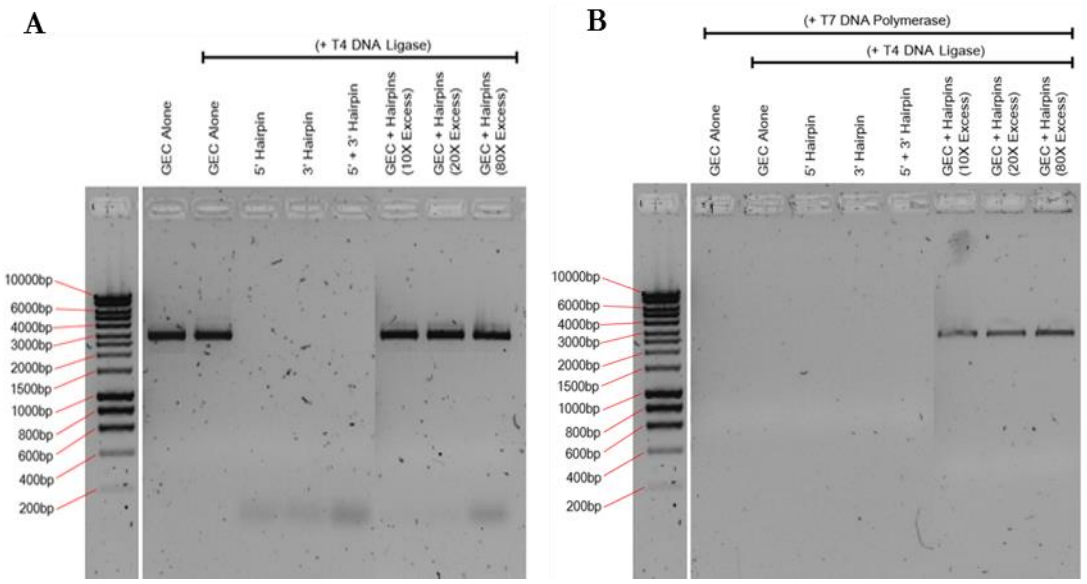

Figure 6.16 (A & B) – Synthesis of CCHLV using the Esp3I ELAN strategy. A: Phosphorylated 5'_Esp3I_Hairpin (P) & 3'_Esp3I_Hairpin mediated CCHLV formation, after T4 DNA ligase treatment only, B: Phosphorylated 5'_Esp3I_Hairpin (P) & 3'_Esp3I_Hairpin mediated CCHLV formation, after T4 DNA ligase & T7 DNA polymerase treatment. 1 wt% agarose gel (with SYBR SAFE), run at 90V for 30 minutes. Size ladder = Hyperladder 1 kb.

Figure 6.16 B illustrates the DNA products synthesised after exposure to a 3'-5' exonuclease enzyme. Lanes 1-5 illustrate widespread DNA removal by T7 DNA polymerase, with a complete lack of DNA products present in any lane, proving all lane specific products formed post ligation were not covalently closed/exonuclease-resistant or had any capacity for recircularization (i.e. no pCAG-MetLuc2 (Esp3I) plasmid was present).

Significantly, in lanes 6 - 8, in which hairpin oligonucleotides were present in the system in excess (10X, 20X, 80X), a single marginally fainter DNA band was identified in the GEC/CCHLV region in each well, after exposure to T7 DNA polymerase. Such resistance to exonuclease digestion, alongside correct approximate molecular weight, proved that CCHLV vectors were successfully synthesised, crucially with no other DNA constructs present whilst also at very low Esp3I hairpin-GEC ratios/excesses.

CCHLV was then purified using phenol-chloroform based extraction methods and reconstituted in volumes suitable for downstream transfection (approximately 10-20 µL ddH_2O). Importantly, after purification procedures, no excess 5'_Esp3I_Hairpin (P) and 3'_Esp3I_Hairpin (P) oligonucleotide carryover occurred (Figure 6.17). In terms of the overall CCHLV yields using the ELAN Type IIS protocol (initial 10 µg pCAG-MetLuc2 (Esp3I) digest – with 20X excess hairpins), it was found that a maximum of 3 µg final purified DNA product could be synthesised, per run, with no major contamination.

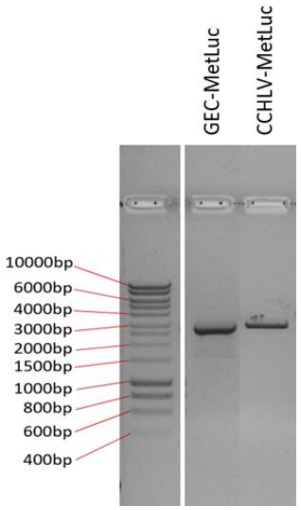

Figure 6.17 – Purified GEC and CCHLV (250ng) after Esp3I mediated synthesis and downstream DNA purification methods. 1 wt% agarose gel (with SYBR SAFE), run at 90V for 30 minutes. Size ladder = Hyperladder 1 kb.

6.3.3 2D transfection potential of CCHLV

CCHLV and plasmid transfection payloads were formulated as described in section 6.2.3 before subsequent application to C2C12 and Y201 cell monolayers. Upon *in-vitro* cell culture, the resulting Met-Luc gene expression was then captured daily, over a three day transfection study, as seen in Figure 6.18 and Figure 6.19.

Luciferase activity was unanimously detected in both cell lines upon application of CCHLV transfection payloads, thus indicating vectors were expression capable. By far the highest levels of reporter transgene expression was detected when the lipofectamine and PEI transfection payload methodologies were utilised, with CaP generally performing sub-optimally, in most cases.

Transfection efficiencies of C2C12 applied CCHLV vectors (Figure 6.18), as measured quantitatively by luciferase protein production, were found to be significantly higher only in the PEI format when compared to the corresponding plasmid vector (24 hours: $P = 0.0148$, 48 hours: $P = 0.0169$, 72 hours: $P = 0.0001$). However, in the cases of CaP and lipofectamine payloads applied to C2C12, mean transfection efficiencies were not significantly different between CCHLV and pDNA vectors (CaP - 24 hours: $P = 0.4515$, 48 hours: $P = 0.8035$, 72 hours: $P = 0.1394$) (Lipofectamine - 24 hours: $P = 0.3605$, 48 hours: $P = 0.5571$, 72 hours: $P = 0.0503$).

In contrast, transfection efficiencies of Y201 applied CCHLV vectors (Figure 6.19), were found to be significantly lower in the PEI and lipofectamine formats when compared to the corresponding plasmid vector (PEI – All timepoints: $P < 0.0001$) (Lipofectamine - 24 hours: $P = 0.0105$, 48 hours: $P = 0.0081$). Alternatively, in the case of CaP payloads applied to Y201 cells, mean transfection efficiencies were not significantly different between the two specific vector formulations (CaP - 24 hours: $P = 0.1259$, 48 hours: $P = 0.5659$, 72 hours: $P = 0.9943$).

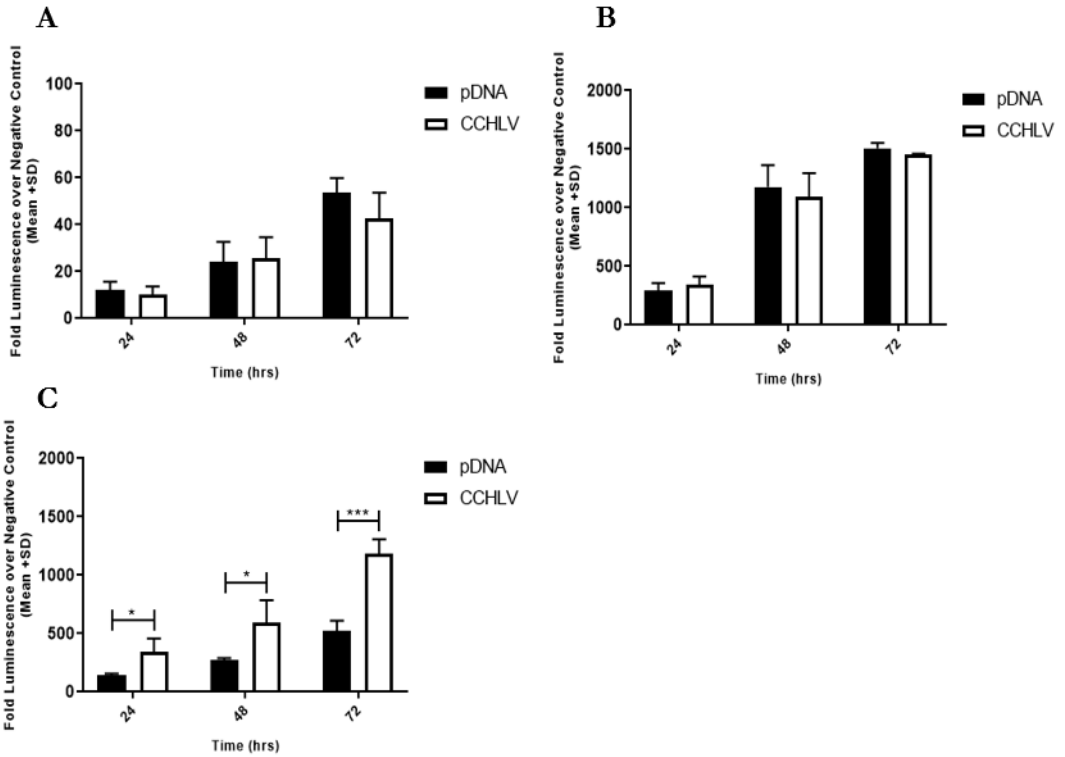

Figure 6.19 (A-C) – Comparison of the 2D transfection capabilities of CCHLV versus pDNA vectors, upon transfection of C2C12 with a variety of transfection payloads. Fold luminescence detected from C2C12 cells after transfection with pDNA or CCHLV payloads formulated with (A) CaP, (B) Lipofectamine, and (C) PEI. Data was expressed as Fold Luminescence over negative control (Mean + SD). Unpaired T-test was used to compare between the two vector groups. * = P < 0.05, *** = P < 0.001.

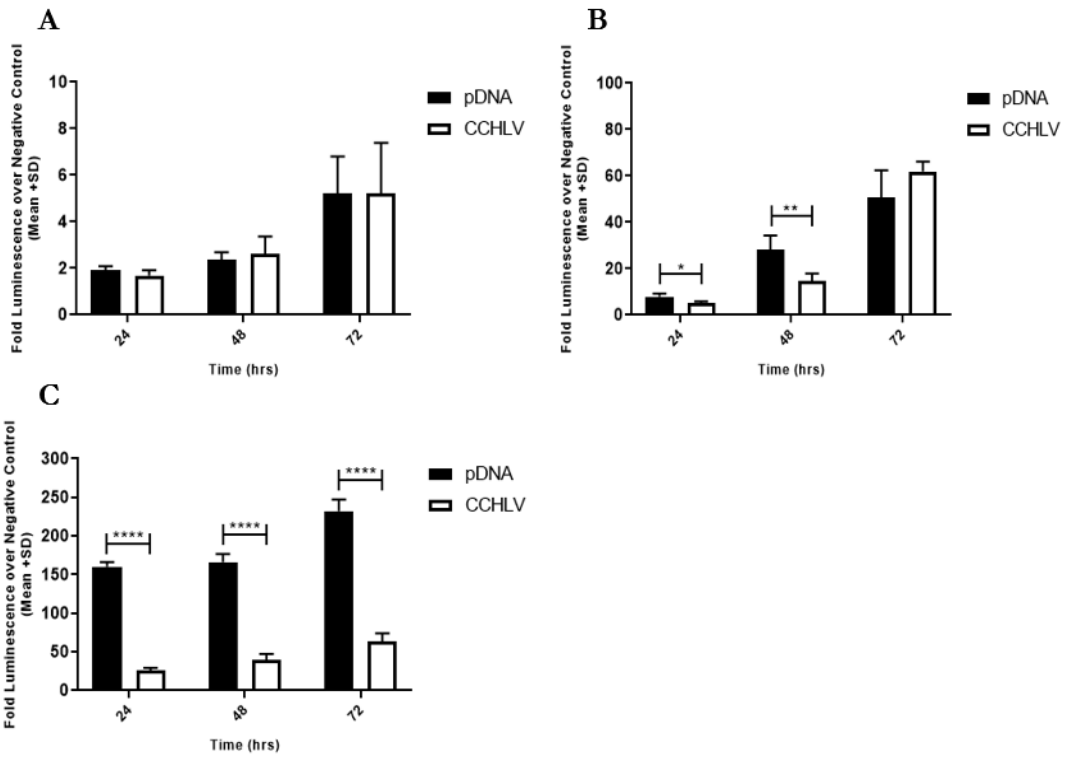

Figure 6.18 (A-C) – Comparison of the 2D transfection capabilities of CCHLV versus pDNA vectors, upon transfection of Y201 with a variety of transfection payloads. Fold luminescence detected from C2C12 cells after transfection with pDNA or CCHLV payloads formulated with (A) CaP, (B) Lipofectamine, and (C) PEI. Data was expressed as Fold Luminescence over negative control (Mean + SD). Unpaired T-test was used to compare between the two vector groups. * = P < 0.05, *** = P < 0.001.

6.4 Discussion

6.4.1 CCHLV synthesis using the modified F-ELAN-II method

The methodologies for CCHLV synthesis used in this chapter were based on the ELAN strategy first reported by Schakowski and colleagues (Schakowski *et al.*, 2007). In this report, a dual RE ELAN strategy was employed, in a two-tube reaction process, enabling the downstream formation of CCHLV vectors which were capable of gene expression. Although reported as a reliable and successful strategy, upon method specific scrutiny, several potentially solvable limitations could be identified, which restricted its potential use in large scale CCHLV production. This included the number of RE enzymes used (2 – EcoRI and BamHI), the number of and amount of hairpin oligonucleotides required (2 – 200-fold molar excess per hairpin) and the cost of specialist CCHLV and GEC isolation equipment (two rounds of purification via anion exchange chromatography). As such the F-ELAN-II method was initially formulated with the aim of solving several of the stated limitations in a more effective, cheaper and streamlined CCHLV synthesis method.

The underlying concept for the F-ELAN-II synthesis approach illustrated in this chapter initially utilised a single RE, single unphosphorylated hairpin oligonucleotide approach for the production of CCHLV vectors. The objective being that successful CCHLV synthesis could be achieved with the same speed and better efficiency whilst using a streamlined cost reduced methodology. Such streamlining was achieved by reducing the number of RE and hairpin oligonucleotides required (from two to one, in both cases), as well as utilising an alternate low cost commercial DNA purification kit – in the form of agarose gel DNA purification columns. The latter of which was considered superior to anion exchange chromatography (AEC) in terms of speed, reliability and cost (e.g. expensive diethylaminoethyl resins used in AEC).

Due to the fact that a single dual cutter restriction enzyme (MunI) was utilised in the F-ELAN-II approach, the downstream linear GEC product formed was predicted to contain 5' overhang complementarity, with strong potential for circularisation or concatamerisation, upon exposure to DNA ligase enzymes. To avoid such products, the ligation system here was saturated with the complimentary hairpin oligonucleotides with molar excesses in the region of 80 or 200-fold. Furthermore, as a single complimentary hairpin oligonucleotide was also used (EcoRI_Hairpin), this too possessed dimerization potential. To prevent this phenomenon, and encourage CCHLV assembly, oligonucleotide synthesis was completed in the absence of a terminal phosphate, thus restricting phosphodiester bond formation between hairpin dimers. As restriction enzyme mediated digestion of plasmids perpetually produces linear fragments with 5' phosphate terminal overhangs, the ligation process between the MunI digested GEC and the hairpin was expected to proceed as desired.

In order to formulate large quantities of CCHLV for 2D and 3D GAM transfection studies, substantial amounts of GEC must first be isolated after RE digestion. In the F-ELAN-II method described in this chapter, the Wizard SV Gel & PCR Clean-Up System was selected for such GEC purifications, whereby specific DNA fragments are excised and subsequently bound to silica membrane columns in the presence of chaotropic salts. According to evidence supplied by the manufacturer, percentage recovery of 1000-3000 bp DNA fragments was stated to be in the region of 92-95%. However, upon experimental execution of said procedures (including optimisation steps), GEC yields post MunI and PscI digestion were actually considerably lower, with maximum yields of approximately 60% (or 2.94 μg) reported from a 10 μg pCAG-MetLuc2 restriction digest. An alternative purification approach, utilising a large scale continuous elution electrophoresis system (MiniPrep Cell (BioRad) system) was therefore explored as a solution, specifically using methods reported by Rodriguez *et al*, however the GEC yields conveyed were generally poorer than the silica column method, whilst also being dramatically more time-consuming (Rodriguez & Akman, 1998). As such, the semi-superior commercial silica membrane kit continued for all subsequent GEC isolation procedures despite lower yields than anticipated.

In terms of CCHLV synthesis using the F-ELAN-II method, initial findings suggested that its successful construction was not possible with oligonucleotide hairpins lacking terminal 5' phosphate modifications. In these cases, explicitly in the large excess groups (1000X), the apparent CCHLV product was completely degraded by the exonuclease actions of the T7 DNA polymerase, thus signifying constructs crucially lacked a fully covalently closed structure representative of CCHLVs. The author theorises that the absence of terminal phosphates on the hairpins resulted in incomplete phosphodiester bond formation between the two sets of oligonucleotides (GEC and EcoRI_Hairpin), with the resulting construct instead held weakly via hydrogen bonding between complementary bases. It was therefore likely T7 DNA polymerase could then recognise these regions as "single stranded nicks" leading to activation of its exonuclease functionality and the overall digestion of the CCHLV product. Such behaviour also corroborates an additional theory proposed by Wuite *et al* which suggests incorrectly or unfavourably bound DNA results in changes to the tension within the backbone, leading to DNA polymerase recognition and removal (Wuite *et al*., 2000).

To rectify this, the F-ELAN-II synthesis strategy was modified and re-tested with phosphorylated EcoRI_Hairpins, with clear improvements subsequently observed. Significantly, upon T7 polymerase exposure, exonuclease resistant DNA constructs were now synthesised within the expected CCHLV region (i.e. successful CCHLV formation). Unfortunately, despite substantial saturation of the reaction with hairpin oligonucleotides (at acceptable molar excesses such as 80X and 200X), CCHLV synthesis remained inefficient with various exonuclease resistant ligation products also present. As previously stated, this outcome was not wholly unexpected and was likely due to the complimentary base overhangs present within MunI digested GEC. Subsequent

modelling suggests that at least four ligation products could feasibly be synthesised from the GEC, in the presence of T4 DNA ligase. This includes the formation of both forward-forward and forward-reverse linear GEC concatamers and re-circularised GEC and mini-circle GEC, the latter of which conveyed conformational exonuclease resistance (Figure 6.12 C and D – 1700 bp, 6000 bp DNA bands).

It was therefore concluded that such products were the direct consequence of firstly; the complimentary nature of dual MunI cohesive ends, and secondly the palindromic sequence pattern. Furthermore, as a result of the terminal phosphate modification, TTAA self-dimerisation of the EcoRI_Hairpin now also presented within the final reaction system, producing an additional exonuclease resistant product, whilst further blocking the desired CCHLV synthesis pathway (Figure 6.20).

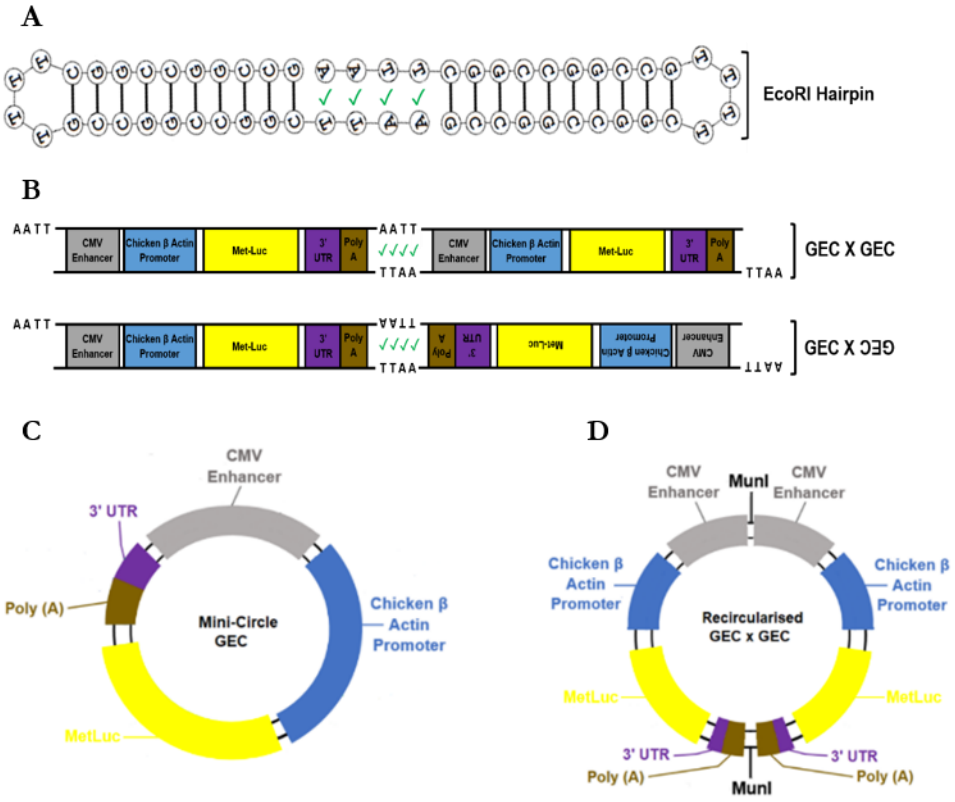

Figure 6.20 (A-D) – Hypothesised ligation products resulting from a MunI digested GEC or complimentary EcoRI_Hairpin (P) upon exposure to T4 DNA ligase. Green ✓ indicates compatible base pairing.

Based on these findings, it could therefore be said that the single RE F-ELAN-II method (MunI) performed poorly in comparison to the original Schakowski synthesis protocol, with this iteration proving considerably more detrimental for CCHLV production efficiency (Schakowski *et al.*, 2007; Schakowski *et al.*, 2001). This was especially highlighted by the need for ultra-saturation of the ligation system with EcoRI hairpins (1000X excess) in order to compel CCHLV formation over the more thermodynamically favourable self-ligation products. Additionally, as

contaminating exonuclease resistant hairpin dimers remained in the system post exonuclease exposure, further purification steps were required to isolate the final pure CCHLV product – of which substantial vector loss would have likely occurred.

As a result, the F-ELAN-II strategy was abandoned in favour of the newly devised F-ELAN-IIS method, with the aim that the various shortcomings stated previously could be overcome.

6.4.2 CCHLV synthesis using the modified F-ELAN-IIS method

The F-ELAN-IIS CCHLV synthesis method was subsequently designed to overcome the efficiency barriers demonstrated by F-ELAN-II MunI mediated synthesis, with a particular emphasis on prevention of unwanted self-compatible, palindromic ligation products. The unique downstream splicing mechanism of Type IIS RE, such as Esp3I, gave the author complete control over GEC cohesive end design (and by-definition hairpin oligonucleotide design) to create a deft CCHLV-promoting synthesis mechanism. The proposed strategic design therefore generated four 4 bp length sequences (5' and 3' GEC overhang, 5' Esp3I Hairpin and 3' Esp3I hairpin) which displayed non-palindromicity as well as unanimous resistance to self-compatibility. Subsequent modelling of said sequences within the pCAG-MetLuc2 expression system, after Esp3I digestion and T4 DNA ligase exposure (Figure 6.7), confirmed their applicability to the above hypothesis.

Experimental results using this strategy conclusively substantiated this rationale for CCHLV production with categorical and highly efficient results identified. In particular, this included the formation of a completely pure exonuclease resistant CCHLV product from a GEC fragment exposed to excess hairpin oligonucleotide, molar quantities as low as 10-20 fold. Significantly, in these cases, gel analysis revealed that the pre-designed 5' and 3' GEC cohesive ends prevented the formation of all types of self-ligation products, whilst dimerization of equivalent 5'_Esp3I_Hairpins and 5'_Esp3I_Hairpins were also restricted. As a result, CCHLV synthesis progressed unburdened with remarkable efficiency. Crucially, in comparison to methods presented by Schakowski *et al*, as well as a multitude of other more recent ELAN based reports, the F-ELAN-IIS strategy appears to surpass these, specifically in terms of its production efficiency and the molar ratios of hairpin oligonucleotide required for effective CCHLV synthesis (current gold standard: 80X excess) (Schakowski *et al.*, 2007; Schakowski *et al.*, 2001; Schmidt, 2005).

As discussed previously, most reports utilising the ELAN method for CCHLV synthesis rely on Anion Exchange Chromatography or silica based columns for GEC purification (as part of the two-tube reaction process), practices which can be expensive and time-consuming. In contrast, the F-ELAN-IIS method achieved effective CCHLV synthesis without this step entirely, proceeding as a single tube step-wise reaction system. This was only possible because ligation was

performed in the presence of an active Esp3I restriction enzyme (i.e - it was not inactivated post plasmid-RE digestion), thus ensuring any reformed plasmids (formed between the GEC and the pCAG backbone) were effectively re-cleaved over the course of the ligation reaction. It was therefore assumed that in the F-ELAN-IIS strategy, most of the available GEC was in fact covalently capped by the hairpin oligonucleotides, leaving only the linearised/re-cleaved pCAG backbone as a waste bi-product –which was effectively degraded by T7 DNA polymerase.

Crucially, the removal of this purification step allowed the F-ELAN-IIS method to circumvent all previously stated purification mediated limitations, ensuring that the greatest proportion of GEC was available for downstream hairpin ligation, unlike the F-ELAN-II method. This was considered vital upon scaled-up manufacture of CCHLVs, whereby costly DNA wastage could be minimised, whilst simultaneously shortening production duration and reducing overall operating overheads.

As such, the F-ELAN-IIS strategy was considered a completely novel, highly effective and efficient method for the production of CCHLV, with characteristics considered uniquely compatible with cGMP standards and its use in clinical settings. Crucially, as of the time of writing, this was the first known example by which CCHLV synthesis was achieved whilst utilising a single type IIS restriction enzyme strategy. Moreover, with several advantageous features with regards to the efficiency and cost of CCHLV synthesis, it has remarkable potential to displace the current gold standard ELAN strategies for production of this particular type of linear DNA vector.

6.4.3 CCHLV transgene expression versus plasmid vectors

The success observed with the F-ELAN-IIS synthesis strategy in Figure 6.16 led to the investigation into the capabilities of the synthesised CCHLVs, to induce encoded transgene expression in two different cell lines (C2C12 and Y201), with a specific emphasis on their performance in comparison to equivalent pDNA vectors. In this study, three different 2D *in-vitro* transfection strategies including; inorganic CaP, cationic polymers (linear PEI) and cationic lipoplexes (Lipofectamine 2000), were used – a decision made since these methods had been optimised previously for 2D cell monolayer transfection (chapter 6 or by other Feichtinger colleagues) and also because of strong reported evidence of their application within successful *in-vivo* transfection models (Lungwitz *et al.*, 2005). The Met-Luc reporter gene insert was used for all tested DNA vectors, thus allowing reliable quantitative assessment of vector mediated gene expression and direct statistical analysis between each vector construct.

Upon performance of said study, it was revealed that the synthesised CCHLV constructs were explicitly expression capable, with substantial Met-Luc expression detected in both of the tested cell types over a 72 hour transfection timecourse. Such data provided strong evidence that the

dumbbell vector constructs produced were 1) capable of co-complexation and condensation with a variety of cationic transfection characters thus allowing DNA delivery and cellular uptake and 2) that upon nuclear delivery the CCHLVs could be effectively transcribed and translated in order for reporter gene expression and secretion. Furthermore, it was also broadly observed that regardless of the cell line, lipofectamine and PEI mediated transfection appeared superior over CaP mediated strategies, whilst in all cases peak transgene expression was usually displayed during the 72 hour time-window.

Interestingly, in terms of vector performance, the detected Met-Luc expression induced by CCHLVs was considered highly variable, with fluctuating gene expression profiles observed depending on the cell type to which the construct was applied and also the transfection vehicle utilised.

In the case of C2C12 cells, it was found that formulated CCHLVs were generally as effective, or under certain conditions more effective at inducing reporter gene expression than equivalent pDNA vectors, when using the stated methods of transfection (inorganic nanoparticles, cationic lipids, cationic polymers). This culminated in the major finding that upon PEI transfection (Figure 6.18 C), statistically significant enhancements in gene expression were identified in all CCHLV groups versus equivalent plasmid DNA (24, 48 and 72 hours post-transfection).

In contrast, upon CCHLV exposure in Y201 cells, the opposite effect was displayed in terms of quantity of reporter gene expressed, such that the formulated CCHLVs were, in a substantial amount of payload formulations, less effective at inducing reporter gene expression than equivalent pDNA vectors. This decrease in transfection performance was illustrated most clearly across the PEI and lipofectamine datasets (Figure 6.19 B and C) whereby statistically significant differences in reporter gene expression were identified (with the exception of Figure 6.19 B Lipofectamine - 72hrs).

Overall, such results accurately reflect the current state-of-play with regards to the gene expression performance of other similarly reported CCHLV vector systems currently under investigation, with transfection capabilities differing widely upon their application with alternate cell types and transfection vehicles. This was particularly highlighted by the conflicting reports by both Schakowski *et al* and Zanta *et al* (Schakowski *et al*., 2001; Zanta *et al*., 1999). In the extensive study by the former, CCHLV vectors were developed (via ELAN type II synthesis methodologies) before complexation with PEI or Lipofectamine and their subsequent application upon two different human colon adenocarcinoma cell lines (SW480 and HT-29). Transfection was then quantified according to GFP reporter gene expression, as measured by flow cytometry. Based on the published datasets, it was reported thereafter that hairpin mediated gene expression was significantly enhanced (two to four-fold higher in comparison to plasmid equivalent) upon complexation with Lipofectamine transfection vehicles (both cell lines) whilst

was equivalent when complexed with PEI (Schakowski *et al.*, 2001). Based on this evidence, the authors stipulated considerable benefits were present upon applying vectors of reduced size, in a dumbbell-like conformation.

As similar findings (albeit with C2C12 favouring cationic PEI complexes) were illustrated in Figure 6.18, tentative support could be provided regarding its theorized methods of action, specifically for the enhancement of vector gene expression. Such notions stated by Schakowski *et al* include the idea that successful transfection is obstructed specifically on the account of the nuclear envelope, which preferentially favours smaller DNA constructs for nucleolar uptake and entry, over larger equivalent payloads, such as pDNA (Li & Huang, 2000; Ohno *et al.*, 1998). In the case of the CCHLVs developed in this study, as they are markedly smaller in size compared to the corresponding plasmid vectors (e.g. a 2-fold size reduction), the identified enhancement of gene expression within transfected C2C12s thus holds substantial credibility. This was further supported by both Huang *et al* and Chang *et al,* in which researchers exposed cationic lipid or cationic polymer mini-circle payloads to C2C12 cell monolayers, illustrating significantly higher expression in the smaller sized mini-circle vectors in comparison to the larger equivalent plasmids (Chang *et al.*, 2008; Huang *et al.*, 2009).

Despite the substantial positive evidence regarding minimally sized DNA vectors as discussed above, the opposing report by Zanta *et al* provides an interesting alternative argument regarding their gene expression potential. This included the observations that upon CCHLV-PEI payload exposure to murine fibroblasts (NIH 3T3), reported transgene expression (24 hours later) was in fact 1-2 logs less efficient in comparison to plasmid equivalent (Zanta *et al.*, 1999). Unfortunately, with only one timepoint utilised (24 hours post transfection) and no reasoning supplied by Zanta *et al* regarding these less favourable findings, it was this author's opinion that in their results (and possibly in the case of the Y201 dataset in Figure 6.19) such expression profiles could be explained simply by the different cell type specific vector trafficking machinery present – which may have been less efficient at recognising and subsequently transporting the linear vector constructs towards the nucleolar compartments of NIH 3T3 and Y201 cells (Durymanov & Reineke, 2018). Unfortunately, as our study was the first known report for CCHLV transfection of an MSC-like cell type, it remains up for debate whether such hypotheses are legitimate for our context, with more in-depth investigations naturally required over a range of cell types including primary cells.

Interestingly, in comparison to Schakowski *et al*, this report did ensure direct vector comparisons according to equi-molar or mass corrected DNA amounts (a practice also used in this chapter) and as such may present a more comparable point of reference, with the latter likely presenting elevated data especially given the amount of CCHLV used versus plasmid.

Possibly of even greater interest, however, was a further finding within the Zanta report; in which CCHLV mediated transgene expression could be significantly enhanced upon conjugation of nuclear localisation sequence (NLS) peptides to the hairpin loop structures. Such was the impact of these sequences, that the NLS modified CCHLVs now outperformed the equivalent plasmid vector constructs (1-2 logs more efficient), after 24 hours post transfection (Zanta *et al.*, 1999). Mechanistically, this enhancement was theorised to be as a result of elevated cytosolic importin receptor recognition of the NLS containing CCHLV constructs (SV40 T large antigen NLS-sequence (or NLS^{T})), which facilitated more efficient vector translocation to the nucleolar compartments and uptake through the nuclear pore complex (NPC) (Hebert, 2003).

Importantly, findings such as these open up further avenues for the F-ELAN-IIS CCHLVs designed in this chapter, presenting the realistic prospect of a bioconjugated vector iteration whereby the construct can be uniquely tailored for optimal DNA delivery and gene expression, especially in cell types potentially considered sub-optimal for linear DNA vector delivery (such as Y201s). Tentative investigations regarding this area of research were subsequently initiated with Esp3I hairpin oligonucleotides containing a linear alkyne modification (Ethynyl-2'-deoxyuridine (EdU)) being synthesised. Through the inclusion of this functional moiety, stable CCHLV modifications such as NLS peptides or cell receptor-specific aptamers could therefore be achieved - specifically utilising simple click chemistry concepts such as the Copper-catalysed azide–alkyne cycloaddition (CuAAC) reaction system (appendix section 8.6) (Fantoni *et al.*, 2021).

Overall, the conflicting findings presented both in this preliminary study and in the studies by Schakowski *et al* and Zanta *et al* exemplify the shear complexities involved in the process of non-viral DNA vector delivery, importantly illustrating that the stated modifications to the structure, size and conformation of the DNA vectors do not always correlate with improvements to the expression characteristics, especially when experimental conditions such as cell type are altered. Furthermore, it must also be mentioned that direct comparisons between different sized vector constructs is generally an extremely difficult task given the selected use of associated chemical transfection vehicles, such as cationic polymers, lipids and inorganic nanoparticles, for DNA vector uptake and internalisation. Within these cases, specific limitations exist with regards to simply reporting transgene expression as a function of the DNA vector utilised, even if equimolar amounts are applied. This is because reported transgene expression is also synonymous and highly dependent on the transfection vehicle applied, with performance outcomes differing as a result of varied concentrations and its unique interactions with the DNA, thus achieving optimal vector expression whilst attempting to maintain both an equivalent DNA molar ratio and transfection vehicle concentration, which is rarely accomplished. This is exemplified in the PEI datasets presented, which despite sharing the same N/P ratio (N/P24), the formulated transfection complexes actually contain different amounts of PEI (pDNA: 3.10 μg, CCHLV: 1.55 μg).

It is therefore this author's opinion, that unanimous agreement regarding the effectiveness of CCHLV vectors can only be achieved through further study, with a particular emphasis on use of a standardised protocol for comparing DNA vectors of different sizes. Such standardisation should look to limit the compounding factors regarding chemical transfection reagent use either through its complete removal (in favour of naked DNA transfection techniques such as electroporation) or through the use of a single consistent experimental methodology (i.e. the maximal gene expression produced by DNA vector-transfection complexes irrespective of DNA mass). Once achieved, potential downstream use of these vectors within scaffold-based GAM systems may become a reality.

6.5 Conclusion

Taken as a whole, this chapter serves as an interesting proof-of-concept study for the potential use of CCHLV constructs within 3D GAM systems, particularly in the case of the F-AGE agarose GAMs previously developed in this thesis. Significantly, in terms of the production mechanism, it initially revealed that the most commonly used CCHLV synthesis strategy (ELAN mechanism) can be substantially improved both in terms of DNA vector production efficiency and cost through the completely novel use of type IIS restriction enzymes – such as Esp3I. With this restriction enzyme and alongside smartly designed non-palindromic, self-incompatible four base overhang sequences, a CCHLV production pathway could be obtained, which utilises as little as 10-20-fold excess oligonucleotide hairpin per run. As the current best performing literature report (ELAN) utilises a minimum of 80-fold excess hairpin, this represented a highly significant finding which could drastically benefit this field of research.

In the second part of the chapter, it was then demonstrated in a small transfection study, that CCHLVs can, under certain circumstances, more effectively induce a greater degree of 2D transgene expression in comparison to corresponding plasmid vectors. Although not wholly unanimous, these findings point towards the use of CCHLVs as a potential next generation DNA vector, with this thesis ultimately recommending substantial future work is needed before its application within biomaterial GAM contexts, clinical investigations and beyond. Such recommendations explicitly refer to cell type specific optimisation of CCHLV constructs either through large scale transfection reagent studies or via bioconjugation of synthetic targeting molecules (NLS peptides or aptamers).

CHAPTER 7

GENERAL DISCUSSION

7 CHAPTER 7: GENERAL DISCUSSION

7.1 Summary of thesis aim and main outcomes

The aim of this research thesis was to characterise the cellular responses and gene delivery capabilities of a range of porous agarose GAM scaffolds developed using the novel F-AGE spatial patterning platform. The ultimate goal is to produce a gradiented agarose GAM device to support osteochondral tissue repair.

This thesis first sought in chapter 3 to optimise agarose hydrogel properties (i.e agarose polymer percentage), to create a final porous agarose scaffold product which possesses suitable osteochondral-like physical and structural properties yet remained impervious to the detrimental side-effects of freeze-drying. Based on the side-by-side characterisation of 1 wt% and 3 wt% freeze-dried formulations, it was found that increases in polymer concentration had an overall positive effect on the end stage scaffold products produced. In this regard, 3 wt% agarose scaffolds were observed to possess high porosity and interconnectivity with good resistance to lyophilisation damage. Furthermore, despite a significant reduction in mean pore size, 3 wt% scaffolds remained within acceptable limits for cellular seeding and culture investigations (Lee *et al.*, 2018). The F-AGE-1 method was then translated and revalidated in 3 wt% agarose scaffolds. Through such translation, the F-AGE-1 biomineralisation/co-localisation platforms exhibited largely similar electrophoretic synthesis behaviours to that observed in the previous 1 wt% proof-of-concept work. This was achieved through agarose polymer concentration mediated modifications to the nucleic loading schemes, whereby higher and longer voltage potentials were applied to enforce the necessary proximal deposition within specific inorganic precipitate regions. Within this same chapter, it was further illustrated that F-AGE platforms have applicability for the synthesis and patterning of transfection payloads, namely cationic polymer species. As a result, a new F-AGE polyplex method was developed for the *in-situ* confined synthesis of PEI-pDNA polyplexes, explicitly utilising novel electrophoretic concepts in combination with biomaterial confinement principles. It was qualitatively illustrated a reaction took place between pDNA and PEI (hypothesised to be co-complexation), resulting in the potential *in-situ* formation of polyplexes.

The porous 3 wt% F-AGE-1 and F-AGE polyplex scaffolds were then assessed according to standard cytotoxicity guidelines as well as an extensive scaffold-cellular adhesion testing specification (chapter 4), with the aim of investigating characteristics such as sterility, cytotoxicity, cell adhesion, viability, morphology, proliferation, infiltration and differentiation using two relevant cell lines (C2C12 and Y201). Through testing, it was found that GAMs could be made sterile (only when freeze-dried and washed with ethanol) and also possessed low cytotoxicity profiles. Unfortunately, in terms of cellular adhesion, the porous agarose GAMs were deficient, with poor outcomes represented across all stage-1 testing metrics, especially in terms of surface

attachment, long term viability (7 days 3D culture) and morphology (spheroidal/globular morphologies). Upon Polydopamine surface functionalisation however, scaffold bioactivities became unanimously enhanced, with cell viabilities, attachment and morphology all improved for both C2C12 and Y201 cell lines. Through the testing of additional parameters such as cell metabolism, scaffold infiltration and 3D cell differentiation (adhesion testing stages 2, 3, and 4), further supporting evidence of was accumulated. As a result, a final PDA coating condition of 8 hours in 2 mg/mL PDA solution (or 3%-PDA8.2) was selected and utilised for future investigations concerning GAM scaffold transfection (chapter 5).

Various PDA functionalised F-AGE agarose GAM scaffolds were then developed and evaluated for their 3D transfection capability. Such agarose GAMs ranged from F-AGE-1 pDNA-CaP containing scaffolds and F-AGE pDNA-PEI containing scaffolds. Furthermore, GAMs were tested across both C2C12 and Y201 cell lines using two different pDNA concentrations (2.5 μg and 5 μg). Despite adequate 3D cell viability across the different agarose GAM scaffolds, it was found all groups (F-AGE-1, F-AGE polyplex GAMs) appeared transfection deficient, with no significant scaffold mediated reporter gene expression identified over a 7 day culture period, when compared to blank scaffold controls. With such poor transfection behaviours, it was therefore proposed that inherent faults were present at one or multiple points across the Feichtinger GAM synthesis and production routes, likely leading to payload loss of function or inactivation.

Finally, a pilot study run in parallel to the main Feichtinger AGE research was performed, investigating the synthesis of alternative nucleic acid vector systems known as covalently closed hairpin loop vectors (CCHLV). These systems are of significant interest due to their potential for effective gene delivery when utilised in GAM scaffolds. This was based on the pool of evidence in the literature, purporting such vectors exhibit superior gene delivery and safety over current plasmid systems. (Schakowski *et al.*, 2007; Schakowski *et al.*, 2001). In this final chapter it was the objective to initially improve the efficiency of the current established CCHLV synthesis route; commonly known as the enzymatic ligation assisted by nucleases (ELAN) based strategy. The second objective was to compare CCHLV transfection performance to equivalent plasmid vectors in 2D cell monolayer systems. Of the two synthesis methods developed in this thesis, the F-ELAN-IIS was considered to have potential, with our preliminary study suggesting CCHLV production efficiency was improved 4-8 fold when the adapted approach was applied, specifically in terms of amount of oligonucleotide hairpin utilised per synthesis run. This has the potential for considerable improvements on scale-up manufacture and cost savings. Interestingly, when such vectors were isolated and applied in 2D transfection contexts, it was found the CCHLVs were capable of significantly greater gene expression in comparison to equivalent plasmids, under certain conditions.

7.2 Porous electrophoretically loaded agarose scaffolds for osteochondral GAM tissue engineering

7.2.1 Porous agarose scaffold development

In order to produce a monophasic scaffold biomaterial which is more suitable for the repair of osteochondral defects, compositional changes were made to the starting agarose hydrogel formulation. In place of the 1 wt% hydrogels previously utilised and tested in the Feichtinger proof-of-concept investigations, a 3 wt% agarose hydrogel was in this case developed. This was specifically selected on account of previous work illustrating that 1 wt% formulations were incompatible with a conventional freeze-drying process and further from supporting evidence by works from Guastaferro and colleagues (Guastaferro *et al.*, 2021). Basic qualitative assessment of this new formulation, upon exposure to the same freeze-drying process, demonstrated a comparable hydrogel-scaffold conversion process was initiated, resulting in the generation of a macroporous 3 wt% agarose scaffold. More importantly however, in contrast to the 1 wt% hydrogels, the 3 wt% formulation produced a scaffold which maintained dimensional stability and illustrated no visual sign of agarose fibre collapse or shrinkage. This was deemed vital as this was considered the major issue identified in early F-AGE approach testing. Furthermore, the findings tallied with the in-depth study performed by Guastaferro *et al*, whereby detrimental freeze-drying mediated shrinkage was substantially reduced upon similar agarose compositional changes (Guastaferro *et al.*, 2021).

Despite these benefits, it was however shown that the effect of increasing agarose percentage was paradoxical with regards to eventual scaffold pore size. This was evident when 1 wt% and 3 wt% scaffold cross-sections were analysed (SEM and histology), with the 3 wt% possessing significantly smaller mean pore diameters (215 μm ± 132) in comparison to the 1 wt% equivalent (388 μm ± 276). Ultimately, although hypothesised to be marginally more restrictive for cellular ingrowth, this final 3 wt% pore size, determined in this characterisation study, remained in line with current non-agarose based osteochondral GAM systems such as the collagen type II/I-nHA scaffold by Lee *et al* and thus was considered acceptable for all future work concerning this thesis (Lee *et al.*, 2017).

Interestingly, in other studies in which 3 wt% agarose hydrogels were freeze-dried, a large variation in final scaffold pore size distribution can be found. This is specifically exemplified in reports by Stokols *et al*, Li *et al* and Guastaferro *et al*, who each generated 3 wt% agarose scaffolds illustrating specific pore sizes of 100-150 μm, 50-100 μm and 300-400 μm (or > 400 μm when using a ultra-slow cooling rate), respectively (Guastaferro *et al.*, 2021; Li *et al.*, 2022; Stokols *et al.*, 2006). Upon protocol analysis, it was found that each report possessed markedly different freeze-drying protocols, crucially with highly variable freezing temperature conditions/steps. In the case of Stokols *et al*, a uniaxial temperature freezing system was utilised whereby liquid nitrogen cooled

dry ice was placed underneath a 3 wt% agarose hydrogel to induce freezing (45 minute incubation) (Stokols *et al.*, 2006). Although the freezing rate was not explicitly stated, due to the presence of liquid nitrogen it was assumed to be rapid and thus resulted in smaller apparent scaffold pores. In contrast, Guastaferro produced 3 wt% porous scaffolds using a cryostat controlled freezing device set to -50°C (specific freezing rates of 2.5 or 0.1 °C/min stated). At both rates, agarose scaffolds were formed with much larger pores than those identified in Stokols study and in this thesis (difference of approximately 200 μm) (Guastaferro *et al.*, 2021). These contrasting findings indicate that alongside agarose percentage, a faster freezing temperature and/or freezing rate may act as an additional contributing factor for agarose scaffold pore formation. The reason for this, centred around the idea that hydrogels subjected to lower temperatures induced the rapid formation of a higher number of ice cystal nuclei, which prevent the excessive growth of very large individual ice crystals. These smaller ice crystals subequently lead to finer structures during sublimation, contributing to the formation of smaller final pores (Guastaferro *et al.*, 2021). Although not considered within the remit of this project, further studies involving the use of temperature/freezing rate as a pore size mediator (above or below -80 °C in the University of Leeds freeze-drying method) would therefore hold huge potential within the context of scaffold based tissue engineering, allowing even greater control of scaffold properties depending on the desired tissue repair type. This would be significant, given that scaffold pore size characteristics contribute to several fundamental processes which mediate successful GAM medaited tissue repair. This includes regulating cellular infiltration, attachment and proliferation, nutrient and oxygen diffusion, waste removal, cellular communication, transfection payload release and mechanical support (Abbasi *et al.*, 2020; Loh & Choong, 2013; Lu *et al.*, 2001).

It can therefore be expected that the above factors would be altered (either positively or negatively), as a result of the smaller pore size characteristics presented by the fabricated 3 wt% agarose scaffolds. Although explicit comparisons were not performed in this thesis, it is evidenced in similar reports that a decrease in pore size is marginally prohibitive for cellular migration, adhesion and proliferation, a result attributed to larger 3D surface areas and reduced permeability (Murphy *et al.*, 2010; O'Brien *et al.*, 2007). As GAMs rely on these factors for nucleic acid payload delivery, it was deemed essential that validatory investigations were performed with this new scaffold formulation (chapter 4) (Oyane *et al.*, 2012). In contrast, such pore size decreases have shown highly beneficial utility with regards to DNA payload release from GAM scaffold systems and overall mechanical properties. In terms of the DNA payload release, this stems from the previously mentioned increase in scaffold surface area (and decrease in permeability), which in this case can enforce greater constraints on internal payload diffusion away from the GAM or drug loaded system (Zhang *et al.*, 2021). By slowing transfection payload release (via a decrease in pore size), the window for cellular uptake is extended, thus ensuring therapeutic reponses can be sustained over a period of weeks rather than days or hours. How this specifically relates to the agarose F-AGE GAMs developed in this thesis project will be discussed further in section 7.2.4.2.

Additionally, it is commonly accepted that smaller pore sizes exponentially improve mechanical properties of scaffold systems (Hollister, 2005). Although not within the experimental remit of this PhD project, the decrease in the agarose scaffold pore size observed was therefore hypothesised to induce a positive effect on scaffold characteristics such as compressive modulus, creep resistance, fracture toughness. Interestingly, in reports testing similar freeze-dried hydrogel formulations (agarose and hyaluronan), it was shown that the mechanical characteristics of these scaffolds are at least one order below that observed in natural cartilage (0.2–6.44 MPa) whilst several orders below that in sub-chondral bone (0.1–0.9 GPa) (Tatman *et al.*, 2015; Zhang *et al.*, 2020). An example of this was the porous 2 wt% agarose scaffolds produced and tested by Mancino and colleagues. They reported under different cooling conditions (-12°C, -19°C, -25°C) the macroporous systems possessed a maximum compressive moduli of only 3.7 KPa (Mancino *et al.*, 2023). Moreover, a similar 1 wt% hyaluronan scaffold when tested produced a meagre 0.2-2KPa. As the mechanical properties of the 3 wt% scaffolds were not assessed in this study, they may also possess mechanically inferior characteristics and thus result in sub-optimal load transmission to infiltrating cells post-surgical GAM implantation (Stella *et al.*, 2010). Herein, lies one of the key remaining unresolved factors surrounding the use of hydrogel systems for the regeneration of osteochondral defects. With mechanical strength and appropriate cellular infiltration presenting as vital yet opposing component factors for biomaterials, a compromise remains the most optimal solution.

Novel methods for improving biomechanical properties without detrimentally affecting cell infiltration should therefore be of particular significance in any future works which concern this system. This may include agarose gel solutions being incorporated with proven mechanical enhancers (such as halloysite nanotubes) or with other beneficial composites such as chitosan (Bhat *et al.*, 2011; Suner *et al.*, 2019), although extra care must be taken to not disrupt the key underlying electrophoretic properties needed for gradient payload production. Alternatively, the method of surgical scaffold implantation below the host tissue surface line may ultimately be necessary to allow sufficient protection from high joint stresses experienced within the osteochondral articulating joint space, if sufficient inherent mechanical properties of the agarose scaffolds cannot be achieved (Kosik-Koziol *et al.*, 2020).

Although enforced due to inconclusive SEM scaffold imaging, a limitation of our presented pore size data remains the rudimentary 2D pore size measurement method utilised. Despite largely consistent results across repeat sample sets, the method possessed a limited analytical range across only a 2D cross-sectional plain, thus providing only a partial representative picture of pore size, morphology and distribution within 1 wt% and 3 wt% agarose scaffolds. Additionally, this also meant characteristics such as pore continuity remained unidentified. Furthermore, the process of data collection was also highly time-consuming and subject to interpretational bias whilst the sample preparation procedure may potentially have resulted in the exposure to

structurally detrimental histological processing solutions and conditions (NBF, xylene, 50°C). In light of these factors, it was deemed useful to seek a supplementary assessment method that encompassed the complete 3D architecture, ensuring total bulk analysis whilst maintaining experimental congruity with previous results (Mancino *et al.*, 2023). Tentative investigations were therefore attempted regarding the use of Low Field NMR for pore size, volume and 3D porosity analysis of biomaterial scaffolds – a novel method translated from the field of geological petrophysics for the study of pore formation within rock samples (Halib *et al.*, 2014; Hossain *et al.*, 2011). Unfortunately, due to the small size of the 1 wt% and 3 wt% scaffolds (6mm by 4.6mm), data collection (in the form of T_2 relaxation curves) was found to be extremely challenging when testing the individual agarose scaffolds with inadequate measurable volumes of liquid isopropanol present within the testing chamber. An alternative stacked scaffold approach (6 agarose scaffolds placed on top of each other) was subsequently attempted to combat this issue but results remained largely inconclusive (appendix section 8.4).

7.2.2 Electrophoresis mediated transfection payload co-localisation and complexation

The objective of the second part of chapter 3, was to effectively translate the previously established F-AGE-1 pDNA-CaP spatial patterning approach from 1 wt% to 3 wt% agarose hydrogel formulations. The translation process was largely successful and required only minimal modifications, with pDNA migration behaviour being specifically identified as the characteristic most affected by the agarose formulation change (pDNA payloads migrate 7X slower in 3 wt% agarose gels versus 1 wt% - according to work produced by Dr Feichtinger). Crucially, through a substantial elevation in electrophoretic voltage conditions (300V for 5 minutes), it was found proximal deposition of pDNA payloads within desired CaP precipitation regions (as performed in the Feichtinger proof-of-concept studies) could be once again achieved. This was further confirmed upon full performance of the updated 3 wt% F-AGE-1 methodology, whereby SYBR SAFE DNA imaging revealed that DNA bands were co-located directly within the region in which a CaP precipitate had formed. Interestingly, this was accompanied with a loss of precipitate intensity (duller white precipitates), a possible further indicator of co-complexation alongside said co-localisation. Unfortunately, with no observable changes found in SYBR SAFE DNA band thickness, shape or location, this element could not be further verified. Although this qualitative analysis strategy can largely be considered a non-specific method of co-localisation and co-complexation confirmation, it was deemed acceptable if coupled with downstream 3D transfection data, with successful transfection providing the required supplementary evidence for the possible *in-situ* pDNA-CaP interactions stated above.

A straightforward confirmatory method for large scale particle characterisation and confirmation of co-complexation, would be to extract the *in-situ* electrophoretically synthesised co-complexes

from the 3 wt% agarose hydrogels. With a purified sample of pDNA-CaP complexes, it would then be possible to perform comprehensive structural analysis (such as X-Ray diffraction analysis and dynamic light scattering) as well as a confirmatory 2D cell monolayer transfection study. This work was the focus of an ongoing aligned Feichtinger lab group PhD project (Daniel White, University of Leeds), with two specific isolation methods being electrophoretic transport with membrane fractionation and agarose enzymatic degradation both being utilised and tested. In the case if the former approach, it has been surmised that through pH changes, synthesised pDNA-CaP particles could possess a negative zeta potential and thus be electrophoretically transported out of the agarose gels and collected via a membrane diffusion layer (Zhu *et al.*, 2007). In preliminary findings from the aforementioned PhD project, it was found that particle containing solutions could be transported out of the agarose gels, but upon ultracentrifugation (180,000 x g for 3 hours) resulted in a hardened CaP containing pellet which could not be disrupted or re-solubilised with any feasible method. The enzymatic degradation approach (beta agarase) was shown to have been complicated by the high melting and gelation points of the SeaKem LE agarose powder utilised to form the original electrophoresis hydrogels. By applying beta agarase to melted agarose it was possible to form an agarose based slurry which could in part allowed CaP nanoparticle extraction (although reformation of the gel structure was shown to often occur). Unfortunately, a large proportion of undigested agarose remained present in the solution after gradient-based ultracentrifugation and thus remained unsuitable for the characterisation testing previously mentioned. With no feasible particle isolation method being produced throughout the length of this PhD project, the previously used qualitative agarose gel analysis method remained the quickest and most viable option available for assessment of payload co-localisation/co-complexation and thus sufficed for achieving the aims set out in this chapter (Unpublished data, Daniel White, University of Leeds).

The final part of chapter 3 illustrated one of the most interesting elements of this PhD project, where it was shown for the first time that alternative transfection payloads (such as pDNA-PEI) could be simultaneously synthesised and patterned *in-situ* within agarose hydrogels, via a F-AGE based approach. This was particularly significant given that in standard 2D cell monolayer transfection contexts (as illustrated in chapter 5), PEI mediated gene delivery has been shown to induce substantially higher transfection efficiency in comparison to established inorganic CaP transfection vehicles (Chernousova & Epple, 2017). Through the specific inclusion of the cationic polymer PEI (linear 25KDa) within F-AGE agarose GAM scaffold systems, it was therefore hypothesised that gene delivery to local infiltrating cells would be dramatically enhanced in comparison to the current F-AGE-1 CaP containing agarose GAM equivalents.

In terms of the adaptations required for the inclusion of PEI within an F-AGE platform, the most crucial finding was that PEI was indeed capable of electrophoretic migration, with Coomassie Blue staining revealing rapid wave-like polymer movement through the nanopore

structure of the 3 wt% agarose hydrogels, specifically towards the negative electrode. Following this, two different electrophoretic conditions were then tested, with 300V for 10 minutes proving the most optimal for PEI migration across a smaller distance of 7 mm. Ultimately, the full F-AGE polyplex methodology was then developed and tested with a similar sequential two stage loading procedure as previously utilised in the F-AGE-1 approach. As shown, thin PEI polyplex precipitates were generated as a result of pDNA and PEI proximal co-localisation, thus fundamentally illustrating successful DNA-PEI interaction. Interestingly, as PEI concentration or N/P ratio increased it was further identified via SYBR SAFE images that DNA bands appeared more condensed, becoming thinner in comparison to the plasmid only control. This visual illustration of increasing pDNA-PEI condensation as a function of N/P ratio, matches in part with the literary consensus surrounding polyplex synthesis in solution, whereby the hydrodynamic diameter of particles decreases with increasing concentrations of PEI (Diaz *et al.*, 2021). Unfortunately, due to the previously described limitations in *in-situ* particle extraction methodologies, exact size and zeta potential comparisons between the polyplexes made in this study and those synthesised using a standard aqueous solution method could not be made.

Taking all this data together, evidence was provided for the successful use of two separate agarose gel electrophoresis platforms (F-AGE-1 and F-AGE polyplex) for the simultaneous *in-situ* synthesis and patterning of either pDNA-CaP transfection payloads or pDNA-PEI payloads. The benefits of both approaches directly relate to the ability to spatially control the location of a transfection complex within a 3D hydrogel matrix, specifically through simple electrophoretic attractive forces. It was also hypothesised that due to the utilisation of a confined nanoporous hydrogel environment as the reaction system for payload co-localisation and complexation, the size, morphology and aggregative ability of the final transfection complexes was heavily controlled. Unfortunately, this could not be confirmed due to insufficient agarose-payload extraction protocols available. Future work should now focus on investigating this aspect fully, with transfection complex extraction from agarose hydrogels being the primary aim in order to confirm or reject the above hypothesis. If successful, a full characterisation study could then be performed on the formulated payloads, elucidating crucial information such as size, zeta potential, encapsulation efficiency and transfection capability.

7.2.3 Agarose scaffold cytotoxicity and 3D adherence

As the Feichtinger developed agarose GAMs were conceptualised as an acellular scaffold treatment system, it was therefore considered paramount that the structural 3D biomaterial framework was biocompatible and bioactive, such that endogenous infiltrating cell populations may successfully infiltrate, adhere, proliferate and differentiate on its surface over an extended length of time. Furthermore, given that process of 3D GAM surface mediated gene transfer has been shown to be largely reliant on highly effective cell-scaffold adhesion, the above

characteristics bear even greater importance for successful GAM transfection performance (Oyane *et al.*, 2012). Such properties were validated for 3 wt% agarose scaffolds and agarose F-AGE GAMs in chapter 4, via the execution of a large scale adhesion assessment study with a four stage criterium being defined.

The choice of cells for these studies were two specific cell lines; C2C12 Mouse Muscle Myoblast cells and Y201 (hTERT) human BM-MSCs. In terms of the former, C2C12 cells possessed robust proliferative capacities which was advantageous for 3D cell seeding studies involving high seeding densities with multiple repeats (Katayama *et al.*, 2023). Furthermore, C2C12 cells have also been shown to exhibit good attachment to various substrates, including natural and synthetic scaffold materials, as well as demonstrating long term viability under appropriate 3D cell culture conditions (Kumari & Kumar, 2017; Xu *et al.*, 2014; Yeong *et al.*, 2010). Regarding the latter (Y201), this cell line was specifically selected due to its strong phenotypic resemblance to primary BM-MSCs, making it a highly relevant *in-vitro* cell model which bears excellent translational applicability for future *in-vivo* and clinical studies (James *et al.*, 2015). Significantly, due to its hTERT mediated immortalisation characteristic, the limitations of primary cells (such as cellular senescence, inter-donor variability and cell sourcing challenges) could also be avoided.

Despite the good cytotoxicity characteristics afforded by agarose hydrogel/scaffold systems, both blank 3 wt% scaffolds and F-AGE-1 pDNA-CaP payload containing scaffolds illustrated low level adhesion behaviours upon static seeding with C2C12 and Y201 cells (high density cell solutions applied statically). The developed scaffolds failed to meet essential testing characteristics, with 1) low numbers of viable surface bound cells present after 48 hours 3D culture, 2) low numbers of viable surface bound cells present after 7 days 3D culture, and 3) cells appearing globular or spheroidal with no sign of elongation or interconnectivity. Although disappointing, this was not unexpected, as several potential limitations regarding the inherent incapacity of 3D agarose systems for cellular attachment and proliferation were identified in Chapter 1. This result was also in line with work by Li *et al*, who compared 3 wt% freeze-dried agarose scaffolds alongside decellularised rat spinal cord for their capacity to act as biomaterials for spinal cord injury. Through 3D static cell seeding of fluorescently labelled bone marrow stromal cells ($1x10^6$ cells/scaffold), they too illustrated very low cell numbers with no evidence of large scale attachment, proliferation and fibroblast-like morphologies. Furthermore, they also showed via cell counting, that decellularised spinal cords possessed significantly greater numbers of attached cells at four different timepoints over a 12 day culture period (Figure 7.1) (Li *et al.*, 2022). Although not explicitly stated in this report, it can be assumed that the overarching literary hypothesis regarding agarose biomaterials lacking the necessary cell adhesion motifs (such as cell attachment proteins, RGD binding sequences) required for stable cellular contact sites, likely holds true for our freeze-dried sample iterations (Tang *et al.*, 2007; Valdoz *et al.*, 2021).

In an attempt to overcome the limited scaffold-cell adhesion observed and to provide the 3D agarose system with a proven cell attachment molecule, a new iteration of the F-AGE-1 GAM scaffolds was developed specifically containing the recombinant protein bovine fibronectin (FN) within the pDNA-CaP payloads. Unfortunately, despite this inclusion, upon cell seeding of F-AGE-1 FN GAMs it was generally found this also made very little difference to scaffold-cell adhesion capabilities.

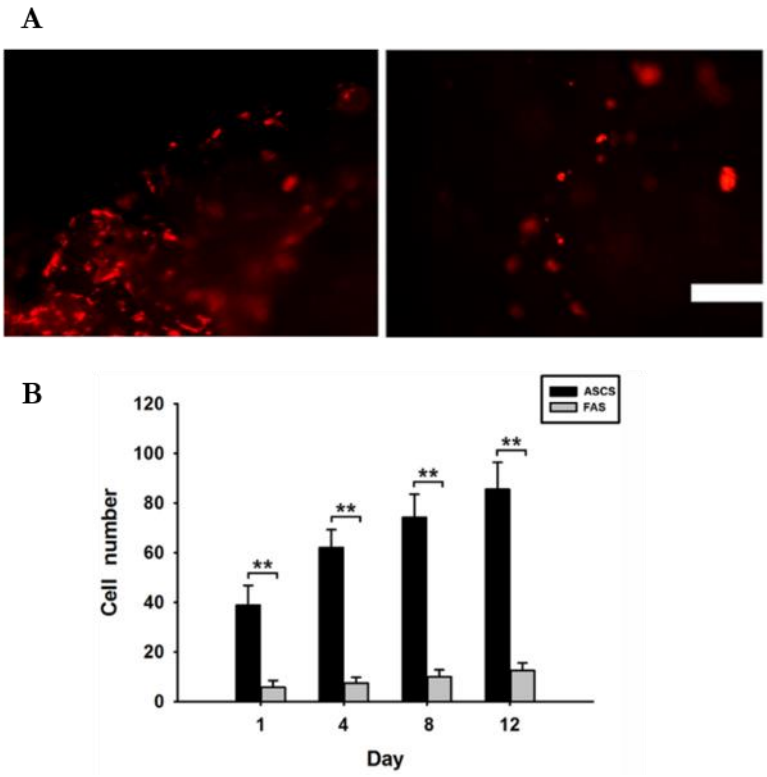

Figure 7.1 (A & B) – Cell attachment and proliferation analysis of fluorescently labelled bone marrow stromal cells seeded onto decellularised rat spinal cord (ASCs) and freeze-dried agarose scaffold (FAS) A: Fluorescence microscopy analysis. B: Cell counting assay. ** = $P < 0.01$. Images taken from (Li *et al.*, 2022).

Following this result, the decision was made to begin testing three different downstream surface functionalisation methods (fibronectin coating, LAP-PEO coating, PDA coating), all of which have previously demonstrated cell attachment enhancement abilities (Franck *et al.*, 2013; Gaharwar *et al.*, 2012; Orafa *et al.*, 2021; Su *et al.*, 2021). Out of the three methods tested, agarose scaffolds coated in PDA showed the greatest improvement in 3D cell adhesion. In comparison to the agarose-PDA method protocol outlined in Su *et al*, in which PDA was incorporated into agarose gels during gelation, this investigation utilised a dip-diffusion soaking method for effective surface functionalisation onto pre-made porous scaffolds (Su *et al.*, 2021). The reason for this selection was to ensure the electrophoretic capabilities of agarose gels remained unaffected at the point of F-AGE transfection payload spatial patterning. PDA functionalisation (1 mg/mL or 2 mg/mL, for 8-12 hours) induced substantial Y201 and C2C12 cell attachment

onto the surfaces of the agarose scaffolds, with large numbers of viable cells present after 48 hours and 7 days 3D culture. Furthermore, significant alterations in cell morphology were noted, with surface bound cells now appearing elongated and interconnected in comparison to the individual, spherical globular cell structures observed in the uncoated agarose control. As reported by Ku *et al* and Tsai *et al*, the ability of PDA to immobilise serum proteins as well as its overall super-hydrophilic environment, remain the primary candidates for why this positive effect was observed (Ku *et al*., 2010; Tsai *et al*., 2011). Upon proliferation studies (stage-2 cell adhesion testing), it was then quantitatively illustrated that metabolic activity of cells on all PDA coated agarose scaffolds increased over a 7 day culture period (48 hours versus 7 days), whereas cells seeded onto blank agarose scaffolds in fact decreased over the same time span. Crucially, through analysis of this data, specific selection of the most optimal conditions for enhanced scaffold adhesion capability could be made – i.e 8 hours 2mg/mL (3%-PDA8.2). The 3D cellular penetration and migration properties of these PDA functionalised scaffolds were also important, especially in terms of facilitating cellular interactions with *in-situ* electrophoretically loaded transfection payloads. Therefore, a 3D histological study was carried out, whereby various scaffold cross-sections were taken from different cell seeded scaffold regions before undergoing H&E staining. Importantly, utilising static seeding methodologies only, it was found that cell populations were present and in acceptable numbers throughout the entire scaffold bulk. Although this author co-developed and manufactured a dynamic seeding system specifically for the enhancement of scaffold penetration and migration, it was found based on these results that basic static seeding methods were generally sufficient for bulk scaffold coverage in this agarose formulation (dynamic seeding system illustrating in appendix section 8.7). At this stage, it was summarised that the results provided in our study were highly analogous to those reported by Su *et al*, with very similar improvements in agarose-cell adhesion being observed, albeit with two different cell lines being tested in 3D culture. Interestingly, through fluorescence imaging of cell attachment indicators such as intracellular filamentous-actin and integrin-β1, they were additionally able to correlate increased PDA concentration with more stable cell-scaffold interactions (Su *et al*., 2021). Although not performed in this study due to the high degree of symmetry between these reports, it was hypothesised that a similar behaviour was likely at play in our iteration.

In summary, use of polydopamine coatings has shown considerable potential in improving cell adhesion, proliferation, and differentiation, crucial factors for successful tissue regeneration. Moreover, its simplicity of application and cost-effectiveness make it an attractive option for larger-scale biomedical manufacture and application. However, pre-clinical and clinical translation of polydopamine associated biomaterial systems remains in their preliminary or planning stages. One notable limitation is the potential for batch-to-batch variability in coating properties, which can arise from disparities in synthesis conditions (Cai *et al*., 2023), ensuring consistency in coating characteristics is therefore considered paramount for reproducibility and

reliability in clinical settings. Furthermore, the long-term *in-vivo* stability of polydopamine coatings and their potential degradation over time remains largely unknown and thus requires further evaluation, particularly in the context of implantable medical devices or long-lasting tissue engineering constructs.

Upon concluding the 3D cell adhesion studies performed in chapter 4, a PDA coating was considered vital for the successful adhesion, proliferation and penetration of Y201 and C2C12 cells into porous agarose scaffolds. Through this finding, it was hypothesised that conditions were now optimal for scaffold mediated gene delivery via the presence of *in-situ* electrophoretically loaded transfection payloads (F-AGE-1 and F-AGE polyplex GAM scaffolds).

7.2.4 3D transfection capability of F-AGE agarose GAMs

Up to this point, several essential components of a 3D GAM scaffold system were either tested and validated or optimised to an acceptable level in chapters 3, 4 and 5. Consequently, the initial aim of chapter 6 was then to combine these findings in order to generate two novel biocompatible, bioactive, transfection capable 3D agarose GAM systems (F-AGE-1 agarose GAMs and F-AGE polyplex agarose GAMs). Once fabricated, the aim was ultimately to test both systems specifically for their *in-vitro* 3D gene delivery capability. Crucially, prior to testing of agarose GAMs, transfection capabilities of CaP and PEI was validated in a 2D cell monolayer format and a 3D transfection control experiment.

A range of F-AGE-1 pDNA-CaP and F-AGE polyplex scaffolds were produced. After successful spatial patterning and freeze-drying, scaffolds were subjected to the optimised PDA coating procedure, thus generating a PDA coated agarose GAM scaffold system. A 3D transfection study was undertaken in both C2C12 and Y201 cell lines, with transfection analysis occurring over a 7 day culture period. Furthermore, a LIVE-DEAD fluorescence assay was used as a control experiment post agarose GAM cell seeding. Upon application of the LIVE-DEAD stain to F-AGE-1 and F-AGE polyplex GAMs, it was re-affirmed that previously optimised cell seeding procedures were effective in this case, with large quantities of viable cells (C2C12 and Y201) present on the scaffold surfaces. Furthermore, this data showed highly consistent behaviours to that identified in the PDA optimisation work in chapter 4, with good initial adhesion (cell attachment, cell viability, and appropriate cell morphology). As the only modification made to these newer scaffold systems was the inclusion of electrophoretically deposited transfection payloads, it was confidently hypothesised that cell infiltration and penetration throughout the scaffold bulk was also achieved as previously shown. Unfortunately, in terms of the 3D GAM transfection study, it was found that no reporter gene expression was produced by any of the F-AGE-1 agarose GAMs or the F-AGE polyplex scaffolds at any of the measured transfection assay timepoints (48 hours, 72 hours and 7 days). This unanimous result was consistent when

agarose GAMs were seeded with either C2C12 or Y201 and also remained the same upon increases in pDNA concentration (2.5 μg or 5 μg).

Based on both the LIVE-DEAD agarose GAM images and 3D transfection results, it was apparent that one or multiple inherent issues were present within both scaffold systems which prevented even low levels of reporter gene transfer. Through extensive method scrutiny, several working theories have since been postulated which may have contributed. These are discussed further in the following sections.

7.2.4.1 Potential issues with transfection payload encapsulation/co-complexation efficiency

As illustrated in the early chapter 5 2D cell monolayer investigations, transfection payloads in the absence of a chemical transfection vehicle (such as CaP or PEI), were shown to not be capable of inducing tangible reporter gene expression in either C2C12 or Y201s. This was likely attributed to several extracellular and intracellular barriers such as resident serum nucleases, the negatively charged plasma membrane, endosomal and lysosomal vesicle enzymes which restrict plasmid vector delivery and expression (Pouton & Seymour, 1998; Varkouhi *et al.*, 2011). As similarly low levels of transfection were illustrated in 3D agarose GAM transfection study, it was possible that F-AGE-1 and F-AGE polyplex approaches may not have resulted in effective encapsulation/co-complexation, specifically between electrophoretically loaded pDNA and CaP/PEI. In this scenario the agarose GAMs would've likely contained *in-situ* but uncomplexed transfection payloads, which would possess very poor gene delivery capabilities (Nie *et al.*, 2009). As the development of complex extraction methods in the simultaneous Dr Feichtinger supervised PhD project proved unsuccessful, a potential drawback in this study was the reliance of qualitative agarose gel imaging (digital photograph and SYBR SAFE Gel stain) for F-AGE-1 method optimisation and co-localisation confirmation. This was generally found to be sub-optimal, with non-specific and highly subjective visual data being produced. Furthermore, due to the restriction of image capture from a vertical viewpoint, this resulted in a potentially skewed analysis whereby apparent co-localisation may have actually been pDNA bands appearing within agarose hydrogels below or above the CaP precipitate region. As no visual changes in actual DNA band patterns could be ascertained, this notion may hold true to some extent within the F-AGE-1 approach.

However, in the case of the F-AGE polyplex method, co-complexation failure was deemed highly unlikely, specifically given the sole appearance of PEI precipitates only when pDNA and PEI loading solutions were proximally deposited within agarose hydrogels via electrophoresis. Given the stronger co-complexation evidence, the fact that F-AGE polyplex GAMs also failed to induce a gene response in 3D transfection studies, potentially indicates that encapsulation/co-complexation may not be the issue. To fully confirm whether encapsulation/co-complexation did occur, a large scale 20-30 day DNA release and encapsulation study should be performed on

F-AGE-1 and F-AGE polyplex GAM scaffolds. Through short and long term scaffold incubation in both a stable buffer system (e.g PBS or TRIS buffer) and a complex dissociative buffer system (e.g. EDTA for CaP-pDNA, heparin for PEI-pDNA), the percentage of free and encapsulated pDNA molecules released from fabricated agarose GAMs could be indirectly calculated (measurements being performed using a Picogreen DNA assay) (Bisht *et al.*, 2005; Nguyen *et al.*, 2008).

7.2.4.2 Potential issues with transfection payload release kinetics

The developed F-AGE agarose GAM scaffolds were hypothesised to facilitate 3D scaffold transfection via surface mediated gene transfer mechanisms. Shen *et al* however states that for this to be achieved, the scaffold surface must not only enable cell adhesion and growth (without inducing cytotoxic effects), but also sufficiently release adhered or immobilised DNA molecules/transfection payloads into surrounding medium. With this release, regions of high local payload concentration are formed in solution at the scaffold surface, thus encouraging DNA uptake by surface attached cells (Shen *et al.*, 2004). In the context of this thesis, a sub-optimal payload release mechanism from the agarose GAM surfaces may have attributed to the poor transfection data observed. This includes the possibilities that transfection payload release was either too fast, too slow or in fact did not take place at all. Based on the literature regarding agarose hydrogel based DNA release, evidence may indicate a slow release model might hold more relevance for the agarose GAMs produced in this project. Specifically, in a similar report by Meilander *et al*, a 0.75 wt% agarose hydrogel encapsulated with 125 μg pDNA (complexed with a cationic peptide vehicle) illustrated only 40% and 50% payload release when incubated in PBS solution for 10 days and 1 month, respectively (Meilander *et al.*, 2003). This apparent release profile compares poorly with other established works by Tierney and colleagues, who demonstrated 100% polyplex release from a transfection capable collagen based GAM after 2-3 weeks (Tierney *et al.*, 2012). Within clinical contexts, this faster release profile was deemed substantially more optimal for GAM systems, given that an early and powerful gene delivery response is required within the first days and weeks to induce high quality tissue repair (Ji *et al.*, 2011). However, it must be stated in contrast to Meilander, our agarose GAMs were subjected to a lyophilisation process, which converted agarose hydrogel nanopores to a larger micron size. Given it is well established that drug loaded biomaterials with larger pore diameters have enhanced drug/payload release rates, it remains probable that *in-situ* electrophoretically loaded transfection payloads formed in our study will have released within a faster timeframe (Zhang *et al.*, 2021). Herein, lies a further complexity concerning GAM based systems, with transfection payload release profiles needing to be adapted and optimised specifically to match with cellular infiltration and migration behaviours.

One further variable which may have had an additional negative effect on agarose GAM transfection payload release is the presence of the additional PDA surface coating. As *in-situ* electrophoretic patterning was performed prior to scaffold functionalisation, it can therefore be reasoned that the highly adhesive coating may have entrapped or "masked" the transfection payloads, thus preventing effective release and exposure to scaffold infiltrating cells. Through largely the same encapsulation/release study as stated in the previous section (additional uncoated versus PDA coated groups also analysed), its effect on transfection payload release could also be answered.

7.2.4.3 Potential issues with lyophilisation/freeze-drying

As illustrated in chapter 3, lyophilisation was an essential process required for the conversion of agarose hydrogels into macroporous scaffolds, crucially imbuing the resulting biomaterial with various structural and biomechanical characteristics which more favourably enable its application within 3D cell culture contexts (i.e larger pore sizes of approximately 215 μm). Despite this beneficial conversion process, there is additional evidence that states its fundamental processes (e.g. the freezing and drying steps) can have a substantial destabilising or disruptive effect on the chemical transfection payloads (Anchordoquy & Koe, 2000; Kasper *et al.*, 2011). To this end, various examples have since been reported which confirm an overall negative relationship between the lyophilisation process and downstream transfection capabilities of gene delivery payloads, specifically illustrating a multitude of separate freezing related and drying related limitations, as shown in (Trenkenschuh & Friess, 2021). Intriguingly, in such studies, prolonged exposure of aqueous polyplex formulations to the frozen state has been shown to induce significant aggregation. This has been shown to be attributed in part to the rapid freeze-concentration occurring within the exposed solution (Armstrong & Anchordoquy, 2004). In this example, polyplex payloads appear to consolidate within residual unfrozen liquid fractions of the sample, facilitating the enhancement of unwanted particle-particle interactions due to their close-proximity (Randolph, 1997). As a result, previous electrostatic repulsive forces between polyplexes are likely overcome by more attractive inter-particle forces, leading to the aforementioned uncontrolled aggregation of the system. A process which may be further exacerbated by synchronous freezing mediated increases in polyplex ionic strength, promoting charge shielding and further aggregation (Bhattacharjee, 2016). Other factors such as internal and external ice crystal formation can also play a role in destabilising transfection payloads simply due to the exposure to severe mechanical stresses. Furthermore, depending on the buffer system in which the payloads are dissolved (e.g. sodium phosphate buffer), it has been found that severe pH changes can occur as temperature is reduced, thus inducing surface charge alterations and eventual colloidal instability (Kolhe *et al.*, 2010; Trenkenschuh & Friess, 2021).

On top of freezing mediated damage, further evidence has also been reported that the sublimation process (primary and secondary drying) can also play a harmful role, particularly in

electrostatically stabilised nanoparticles such as lipids. The cause and effects of the freeze-drying process can be found summarised in Figure 7.2. As agarose GAM hydrogels were subjected to three sequential freeze-drying processes (1st – directly after F-AGE patterning procedure, 2nd – after PDA coating, 3rd – after ethanol sterilisation), a substantial lyophilisation mediated negative effect could have rendered the final electrophoretically loaded payloads severely damaged and thus resulted in the poor 3D gene delivery capabilities illustrated.

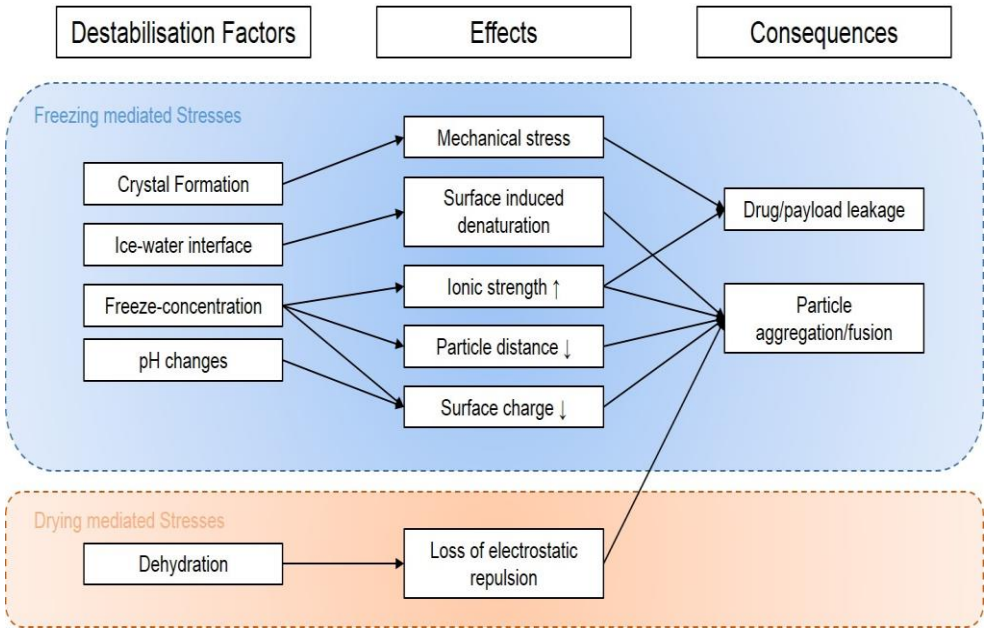

Figure 7.2 – Destabilisation factors and consequences on transfection payload stability during freeze-drying process. Adapted from (Trenkenschuh & Friess, 2021).

One novel solution to this problem, as proposed by Kasper and colleagues, could be through the coupling of pDNA-PEI polyplex payloads with known cryoprotective and lyoprotective stabilisers, such as sucrose, trehalose, β-cyclodextrin. Significantly, in this stated report, it was shown that after lyophilisation (followed by reconstitution after 6 weeks storage), stabiliser modified polyplex solutions were highly resistant to the previously stated aggregative behaviour and as a result were able to maintain high transfection capabilities when applied in cell monolayer contexts (Kasper *et al.*, 2011). The reason for this, they propose, was due to the vitrification mechanism associated with such stabilisers, whereby polyplex payloads are effectively immobilised or "caked" within a rigid, amorphous sugar matrix, thus restricting the diffusion, leakage and aggregation mediated damage associated when DNA-transfection vehicle solutions are freeze-dried (Mensink *et al.*, 2017; Trenkenschuh & Friess, 2021). Using this study as a model, future work should be pursued which attempts to couple a cryoprotective and lyoprotective stabiliser within F-AGE fabricated agarose GAM scaffolds. If achieved, the effects surrounding freeze-drying mediated transfection payload deactivation could be hypothetically minimised and thus recapitulate 3D transfection capabilities.

In conclusion, this section has highlighted three specific hypotheses which may have singularly or collectively contributed to the poor 3D transfection capabilities identified with the developed F-AGE-1 and F-AGE polyplex agarose GAM scaffolds. In-depth investigations should now be undertaken which test each individual hypothesis and the resulting outcomes (i.e whether the hypothesis is accepted or rejected) will greatly aid further progression of this device towards the clinic.

7.3 Development of CCHLVs for use in agarose GAMs

Despite the ever growing popularity of non-viral GAM systems as effective strategies for tissue repair, the reliance on plasmid vectors as the DNA vector of choice remains a limiting factor for its clinical application. Strangely however, only one example currently exists which has attempted to formulate a GAM system containing an alternate, more clinically relevant and safer DNA cargo, with this being the minicircle loaded PLGA scaffold developed by Keeney and colleagues (Keeney *et al.*, 2016). As covalently closed hairpin loop vectors (CCHLV) have shown remarkable potential for enhanced gene delivery, as well as a similarly impressive safety profile, this thesis sought for the first time to generate a CCHLV loaded GAM, specifically within the AGE patterning platforms tested previously (Schakowski *et al.*, 2001).

In order to progress closer towards this larger overall goal, chapter 6 consisted of a proof-of-concept study. The two aims of this study were to 1) produce an effective and efficient CCHLV synthesis strategy based on the ELAN concept, 2) assess the 2D gene delivery capabilities of the newly synthesised DNA vectors, with particular emphasis towards CCHLV performance in comparison to equivalent plasmids (Schakowski *et al.*, 2001). Regarding the first aim, the reason an ELAN synthesis strategy was selected over the PCR mediated methodologies, was based on a combination of cost considerations, commercial scale-up potential and the risk of base sequence mutations. When considering the PCR method, it specifically relies on a bottom-up type approach, whereby final CCHLV yield is determined by the amount of GEC product produced from a standard Taq or KOD polymerase PCR amplification process. As standard PCR reactions generally produce yields of only 1 µg per run, this was considered a low return given experimental set up time, consumables costs and the amount of CCHLV vector required for future GAM incorporation (~2.5-10 µg per GAM) (Cha & Thilly, 1993; Tierney *et al.*, 2013). Furthermore, as polymerase enzymes possess a mutation risk (Taq polymerase: $1.8x10^{-4}$ error rate), unintended loss of function mutations within GEC regions could occur (Potapov & Ong, 2017). In contrast, the ELAN approach utilises a top-down approach, whereby final CCHLV yield is determined primarily by the quantity of source plasmid applied within the primary restriction enzyme digestion step. As a result, large-scale batch E.coli fermentation can be utilised (maxi-preparation/gigapreparation/industrial scale bioreactors), producing plasmid yields in the milligram to gram range without the high risk of sequence mutation. This was considered vital for downstream vector application in gene therapy contexts as well as for large scale commercial

manufacturing. Two ELAN synthesis approaches were produced, termed the Feichtinger-enzymatic ligation assisted by nucleases type II (F-ELAN-II) and Feichtinger-enzymatic ligation assisted by nucleases type IIS (F-ELAN-IIS). Naturally, these approaches utilised singular type II or type IIS restriction enzymes respectively.

One of the first findings when testing the F-ELAN-II CCHLV synthesis approach was the preferential production of unwanted exonuclease resistant ligation products (such as recircularised plasmids, mini-circles and hairpin dimers), when GEC and hairpin oligonucleotide material was combined in the presence of ligase. This was attributed specifically to the complementary overhang sequences present on the GEC and hairpins, which severely restricted the efficiency of CCHLV production. Raising the hairpin concentration up to X1000 excess was shown to rectify this, but predominantly this was considered a substantially inefficient and costly solution.

This ultimately led to the creation of the F-ELAN-IIS method. To this author's knowledge, this was the first time a type IIS restriction enzyme had been utilised within an ELAN strategy for the formation of a CCHLV. Through its unique downstream recognition site, it allowed the author complete control over 5' and 3' GEC overhang sequences and hairpin oligonucleotide sequences – the previous contributors to the inefficiency observed within the F-ELAN-II approach. By selecting two separate non-palindromic, non-complimentary four base sequences (representing the 5' and 3' GEC overhangs), a facile system was then created which facilitated the sole production of a CCHLV construct. Remarkably, it was found that a completely pure CCHLV product could be generated using a single tube method, with a hairpin excess as low as 10-20 fold. This surpassed all currently used ELAN type II approaches, with the current best solution utilising 80 fold excess of oligonucleotide hairpins (Schakowski *et al.*, 2007; Schakowski *et al.*, 2001; Schmidt, 2005).

Considering these data, the F-ELAN-IIS method has the potential to become the new accepted gold standard ELAN synthesis strategy and could feasibly revolutionise the CCHLV research field through its efficiency and cost-effectiveness. To substantiate these claims, a large-scale statistically powered yield efficiency investigation should be performed, with both the F-ELAN-IIS and the current gold standard ELAN synthesis methods run in tandem (Schakowski *et al.*, 2007; Schakowski *et al.*, 2001; Schmidt, 2005). By ensuring the same amount of starting DNA material is provided at the beginning of the synthesis pathway, downstream CCHLV yields can be collated and statistically analysed for each approach. Separately to this, a costs of goods analysis would also be recommended. This would be crucial for understanding the economic viability and competitiveness of a newly developed F-ELAN-IIS synthesis strategy compared to the existing gold standard. Elements of the synthesis process that would be compared include raw material procurement, labour costs, equipment costs, manufacturing time and final yield produced. By achieving a system wide lower cost and better yield method, patient access to gene therapies can

be enhanced. In combination, these two studies could effectively illustrate both the research and clinical potential of the F-ELAN-IIS strategy and thus recommend its wide-spread adoption within the non-viral gene therapy field.

From a gene delivery and transfection perspective, the CCHLVs appeared to illustrate both cell dependent and transfection vehicle dependent behaviours. For C2C12 cells, CCHLVs were found to induce equivalent or in some cases (e.g. the PEI group) significantly greater amounts of gene expression, in comparison to plasmid controls. In contrast, when exposed to Y201 cells (Figure 7.19), the opposite effect was generally illustrated, with pDNA vectors outperforming CCHLVs when applied in equimolar quantities. The reason for this difference likely centres around different cell specific attributes, with tissue origin, cell cycle dependency, cell specific endocytosis pathways, cell specific promoter/enhancer sequences all playing roles in vector delivery to nucleolar components and thus the final gene expression observed (Yang *et al.*, 2022). Future works should now look to expand on this study, with a particular emphasis on elevating transfection potential of CCHLV constructs within so called "hard to transfect" cell lines such as Y201s and primary BM-MSCs.

Unfortunately, due to time constraints and the transfection issues of the F-AGE-1 and F-AGE polyplex agarose GAM scaffolds, the evaluation of CCHLV systems as gene delivery vehicles within agarose GAM scaffolds could not be undertaken in this PhD project. Despite this, the successful optimisation of the ELAN CCHLV synthesis (F-ELAN-IIS), is an extremely significant and exciting result.

7.4 Clinical translation and feasibility of electrophoretically patterned agarose GAMs

As highlighted in Chapter 1, osteochondral defects represent a significant clinical challenge imparted through the limited reparative capacities of local cartilage tissue systems as well as the underlying gradient-like architectures which are present within the natural osteochondral unit (Karuppal, 2017; Wang *et al.*, 2022). While various current generation treatment modalities such as microfracture, mosaicplasty, ACI and cell-free tissue engineering scaffolds have been employed as reparative solutions, their efficacy in achieving durable, functional, and hierarchical neo-tissue remains largely sub-optimal for this context. Although the root cause of such neo-tissue inferiorities varies for each modality, there is a common consensus in the field that they are all generally lacking in terms of the simultaneous provision of complex structural frameworks and supply of regulatory/directive bioactive stimuli to endogenous cellular populations (Madry *et al.*, 2020). The clinical necessity therefore for gradient patterned gene loaded scaffolds in osteochondral repair arises from the pressing need to overcome these limitations and achieve the robust, long-lasting natural tissue regeneration that is desperately required. In terms of the novel agarose F-AGE GAM osteochondral system tested in this thesis, there are several advantageous

properties within its manufacture and overall design which aids in its downstream clinical and commercialisation potential.

Firstly, due to agarose's use as a gel electrophoresis filling material in molecular biology laboratories worldwide as well as being derived from a naturally occurring and abundant resource (Seaweed – *Rhodophyceae* species), it is considered to be a highly accessible and low cost base material (agarose powder unit costs per 100g at £276.00 (SeaKem® LE (Lonza, UK)), especially when compared to other commonly used biomaterials such as Collagen, Silk and Self-assembling Peptides (Jiang *et al.*, 2023). Significantly, for many prospective tissue engineering/GAM scaffold based approaches aiming for eventual large scale manufacture, having such low raw material sourcing costs is considered a paramount pre-requisite and thus the utilisation of agarose polysaccharides in this approach can effectively negate such a clinical translational barrier (Gonçalves *et al.*, 2021).

Additionally, based on this research, the F-AGE patterning systems (F-AGE-1 and F-AGE polyplex) utilised for *in-situ* payload incorporation appear highly reliable and repeatable, whilst crucially producing very large quantities of GAM scaffolds from minimal production runs. When considering a single 3 wt% 15 x 15 cm gel slab utilises 3.9 g agarose powder, and 240 individual agarose GAMs can be manufactured per slab, this equates to as little as £0.042 per GAM (excluding buffers, DNA payload materials, PDA coating, freeze-drying, sterilisation and man-power costs). This high throughput low cost characteristic particularly sets this projects F-AGE agarose GAMs apart from other current osteochondral GAM systems produced by Chen *et al*, Lee *et al* and Needham *et al*, who all utilise singular mold cross-linking/fibrin glue based strategies which are more difficult to manufacture in bulk at industrial scales (Chen *et al.*, 2011; Lee *et al.*, 2017; Needham *et al.*, 2014).

Significantly, upon completion of all manufacturing and processing steps, the F-AGE agarose GAMs developed in this project are crucially in a lyophilised/dry state. This characteristic is extremely beneficial for implantable medicical devices for a number of reasons specifically related to improved commercialisation and clinical feasibility (Nwankwo *et al.*, 2023). Firstly, through the act of removing all water from the biomaterial matrix, it is generated found that such systems can more effectively maintain their original/desired physical structural integrity, avoiding the risk of fibre damage and collapse from inherently entrapped moisture particles. This naturally results in a more commercially viable off-the-shelf product, crucially with longer term expiration dates (Sharma *et al.*, 2021). Importantly, lyophilised systems also confer the requirement for inexpensive low energy storage facilities, whereby room temperature or refrigurated temperature systems can be utilised instead of costly ultra-low temperature storage such as liquid nitrogen. And finally, lyophilised biomaterials are well-suited for transportation and distribution, offering enhanced stability and resilience to environmental stressors during transit (Merivaara *et al.*, 2021). The removal of water from the biomaterial matrix reduces the risk of physical degradation or

microbial contamination during shipping, thereby ensuring the integrity and efficacy of the material upon arrival at the clinical site (Dai *et al.*, 2016; Markowicz *et al.*, 2006). Additionally, the lightweight nature of a potentailly lyophilised GAM system facilitates cost-effective transportation and reduces logistical complexities associated with handling and storage.

Unfortunately, despite the commercial advantages stated above, the F-AGE GAM approach does inherently possess various fundamental flaws which significantly lowers its overall feasibility and likelihood of commercial adoption. One example of this for instance is the poor cellular adhesion capabilities of unmodified agarose biomaterials and the necessity of PDA surface functionalisation (Bloch *et al.*, 2005). Such modification steps, whilst acceptable in smaller academic studies, may become problematic in commercial settings whereby its presence can result in extended manufacturing timescales, batch-batch variabilities and additional cost outlays. As an implantable medical device, any PDA coated GAM system would also require unanimous compliance with UK, EU or US statutory regulations and ISO standards – a trait which as of 2023 has not yet been granted to any PDA modified scaffold-like system (Witkowska *et al.*, 2023).

A further problem to consider was the necessity of physical biomaterial conversion techniques, such as freeze-drying, for the specific conversion of nanoporous agarose hydrogel GAMs into macroporous scaffolds (Guastaferro *et al.*, 2021). By generating pore structures through this largely uncontrollable and temperamental method (ice formation-sublimation), there is an increased risk that significant batch-batch variabilities between individual GAM products can occur. This characteristic being once more unfavourable in terms of biomaterial reproducibility within clinical and commercial manufacturing contexts. In this regard, there has been a clear recent trend away from conventional biomaterial manufacturing and processing techniques in favour of more advanced controllable additive manufacturing methodologies (Suamte *et al.*, 2023). With methods such as stereolithography, fused deposition modelling and laser-assisted 3D bioprinting now offering ultra-precise and repeatable machinability and the flexibility for topologically optimised geometric structures, it is clear more commercially feasible manufacturing approaches exist which could supplant that used in this work (Chou *et al.*, 2016; C. R. Dou *et al.*, 2021; Schubert *et al.*, 2014).

Lastly, as a result of the incorporation of genetic material, such as plasmid DNA vectors, into a 3D scaffold system, a further complexity is introduced to the already expansive and exhaustive regulatory and commercial landscape. This can be exemplified by the fact that under European Medicines Agency guidelines, a GAM system can be considered as both a GMTP (gene therapy medicinal product) and as a cATMP (combined Advanced Therapeutic Medicinal Product) under Article 2(1) of Regulation (EC) No. 1394/2007, and thus must adhere to additional time-consuming testing specifications not previously required of scaffold only approaches. Moreover, the FDA in contrast considers such products to be classified under the "combination products" label which covers an entirely separate testing specification (Wilkinson *et al.*, 2021). Such

differences across EU and US regulatory jurisdictions in terms of classifications and compliance therefore instigates the requirements for separate, independent pre-clinical and clinical trials, which naturally commands considerable monetary investment and time. Interestingly, the GAM commercialisation landscape within the Russian Federation however appears more conducive to clinical acceleration, as shown by the rapid approval and clinical trial testing of "Neovasculgen R " and "Neovasculgen R -Nucleostim GAM combination device" (HSCI, Russia) for the treatment of chronic lower limb ischemia (Deev *et al.*, 2017). Through an apparent phased translational pathway in which a previously approved gene therapy can be combined and repurposed within a biomaterial GAM system, such dogmatic regulations may in fact be rapidly fast-tracked in some instances. In wider scientific contexts, the recent rapid FDA approval and successful roll out of RNA-based COVID-19 vaccines suggests RNA/DNA based therapeutics do in fact possess powerful clinical potential and its worldwide acceptance may now act as the doorway for more GAM biomaterial based devices entering clinical readiness in the future (Laird *et al.*, 2021).

7.5 Conclusion

To conclude, this project describes the continued development of an early stage agarose GAM scaffold platform in which electrophoretic mechanisms are innovatively used to simultaneously synthesise and spatially pattern DNA transfection payloads *in-situ*. The specific aim of this project was to comprehensively characterise and optimise the biological responses and gene delivery capabilities of the developed electrophoretically patterned agarose GAMs. This was ultimately achieved with two specific electrophoresis platforms (F-AGE-1 and F-AGE polyplex), which allowed for the downstream fabrication of agarose GAM scaffolds incorporated with pDNA-CaP payloads and pDNA-PEI payloads, respectively. The outcomes of this work in relation to the six project objectives are shown below:

1) **To determine the structural and physical effect of freeze-drying on different agarose formulations.**
    - 1 wt% and 3 wt% agarose hydrogels were subjected to a freeze-drying process with resulting porous scaffolds compared for their resistance to lyophilisation mediated damage and pore size. The 3 wt% hydrogel formulation was specifically found to be optimal and sufficient across both respective testing measures.

2) **To determine if the primary F-AGE-1 agarose gel electrophoresis approach can be successfully translated into higher percentage agarose gels.**
    - Using qualitative gel image and SEM analysis it was shown that the F-AGE-1 platform remained effective at synthesising *in-situ* CaP nanoparticle precipitates

within 3 wt% agarose hydrogels. Furthermore, through optimisation of pDNA migration conditions, it was possible to co-locate said payloads with CaP precipitates thus inducing a potential co-complexation reaction.

3) **To design and validate a new iteration of the agarose gel electrophoresis approach which could synthesise and spatially deposit pDNA-PEI transfection payloads *in-situ*.**
    - Through modifications to the F-AGE-1 platform, it was illustrated for the first time that linear PEI polymers can also be electrophoretically deposited alongside pDNA payloads within agarose hydrogels, with a precipitate-like pDNA-PEI compound being explicitly synthesised *in-situ*.
4) **To determine and if necessary optimise the cytotoxicity and cellular adherence characteristics of agarose GAM scaffolds.**
    - *In-vitro* analysis of the F-AGE-1 agarose GAMs demonstrated good cytotoxicity but showed characteristic signs of low inherent cellular adhesion. Through subsequent application of a surface coating (polydopamine), characteristics such as cell attachment, viability, cell morphology and metabolic activity could be substantially enhanced. Long term examination revealed osteogenic and chondrogenic potential of polydopamine functionalised scaffolds, thereby establishing the potential of these GAMs for osteochondral tissue repair.
5) **To characterise the 3D gene delivery capabilities of developed agarose GAM scaffolds.**
    - A variety of PDA coated F-AGE-1 and F-AGE polyplex agarose GAM scaffolds were fabricated and tested for their functionality as 3D gene delivery systems. However, no apparent 3D gene transfection was detected over a 7 day period upon seeding and culture with C2C12 and Y201 cell lines. Additional testing is required to ascertain the mechanism for this outcome.
6) **To explore the potential of covalently closed hairpin loop vector (CCHLV) systems as an alternative nucleic acid vector for agarose GAM incorporation.**
    - A remarkable type IIS restriction enzyme modified ELAN strategy (F-ELAN-IIS) was developed which enabled functional CCHLVs to be produced more efficiently and at lower cost (in comparison to the current established ELAN type II synthesis method). Furthermore, under specific conditions (such as cell type, transfection vehicle) CCHLVs possessed better transfection efficiencies in comparison to plasmid vectors.

7.5.1 Future work

This discussion chapter has highlighted suggestions to improve experimental procedures and identified further exploratory studies necessary for the continued development of this novel agarose GAM system towards clinical readiness. The following section will now clearly list the higher priority recommendations.

i. Biomechanical characterisation of 3 wt% agarose scaffolds

Scaffold tissue engineering mediated regeneration of osteochondral defects is dependent on the provision of a mechanically stable biomaterial construct (i.e. one that can withstand and dissipate clinically relevant mechanical loads. For any newly formulated GAM therapeutic (such as the agarose GAMs developed here), a comprehensive biomechanical characterisation study is essential. Initial indentation creep testing of 3 wt% agarose scaffolds followed by finite element modelling should be performed (Abdelgaied *et al.*, 2015; Pawaskar *et al.*, 2010). Through testing alongside native bone and cartilage tissue controls, in a low load set-up (percentage deformation below 20% - according to biphasic model assumptions), valuable insights into agarose scaffold compressive modulus and permeability could be ascertained. Using this data, experimental plans can then be constructed which either investigate necessary biomechanical enhancement strategies or directly test *in-vitro* and *in-vivo* scaffold functionality, specifically in the context of the impact of non-native biomechanical properties on cellular signalling and downstream joint restoration.

ii. Transfection payload extraction from agarose hydrogels

One major limitation identified throughout the duration of this research project was the lack of an effective transfection payload extraction method once *in-situ* electrophoretic synthesis and spatial deposition within agarose hydrogels had been completed. With such a method, more extensive and specific characterisation of the resulting payloads would have been possible (e.g. size, shape, encapsulation efficiency and transfection verification studies). As described in section 0, two methodologies have been proposed and examined within an on-going aligned PhD project which may solve this issue. These methods have been termed: electrophoretic transport with membrane fractionation, and isolation via agarose enzymatic degradation. This work should be expanded with additional recommendations for both the stated methods. In terms of the electrophoretic transport with membrane fractionation, a separate study should be performed which tests the applicability of continuous elution electrophoresis systems, such as the BioRad Mini Prep Cell machine, which has excellent utility in protein purification from agarose gels. With good literary evidence for its applied use in plasmid purification, this system may hold potential for isolation of co-complexed pDNA-CaP or pDNA-PEI transfection payloads (Rodriguez & Akman, 1998). In terms of the enzymatic method, this author recommends the utilisation of novel thermostable β-agarase enzymes (J. Li *et al.*, 2014). Due to the stated limitation observed in temperature

dependent re-gelation of agarose GAM scaffolds during extraction, it is believed that a thermostable agarose degrading enzyme which effectively degrades molten agarose solutions could hold the key to allow effective extraction of transfection payloads away from agarose components.

iii. Further investigation into release and encapsulation kinetics

For a GAM system to induce transfection, it is accepted that 1) a large reservoir of successfully co-complexed transfection payloads must be present (i.e pDNA vectors electrostatically bound to either CaP or PEI) and 2) that these payloads can then be effectively released from the surface of the biomaterial on which they are immobilised. A comprehensive DNA release study experiment has the ability to measure/quantify both of these characteristics. The logical next step for future works would be to execute a long term release study (0-30 days) for both F-AGE-1 and F-AGE polyplex GAM scaffolds, determining whether either of the above stated factors contributed to the low 3D gene delivery capacities observed in this project. To ascertain encapsulation efficiency, scaffold GAMs should be incubated in both stable and dissociative buffer systems as described in section 7.2.4.2. Furthermore, to elucidate the potential inhibitory release effect of a PDA coating, both uncoated and PDA coated GAMs should be tested and examined simultaneously.

iv. Assessment of the effect of freeze-drying on *in-situ* synthesised transfection payloads

To affirm the effects of freeze-drying on the electrophoretically patterned *in-situ* transfection payloads generated via the F-AGE approaches, it is essential once more that an effective agarose gel extraction procedure is developed (future experiment ii). By achieving this goal, a downstream study can then be carried out in which transfection payloads are isolated from either non-freeze dried or freeze-dried agarose GAMs. Then, by applying these isolates to a 2D cell monolayer transfection model, the lyophilisation effect can be easily evaluated.

If freeze-drying is confirmed to have a significant detrimental effect on gene delivery capabilities (as proposed by (Armstrong & Anchordoquy, 2004)), a new theme of research should be introduced within the Feichtinger lab group concerning strategies which combat or mitigate this problem. In a similar fashion to reported works by Kasper and colleagues, future investigations should likewise test a range of promising stabiliser compounds (such as sucrose or hydroxypropylbetadextrin) which can be added to aqueous solutions of formulated polyplexes, prior to freeze-drying (Kasper *et al.*, 2011). Once an optimal transfection preserving formulation has been achieved, attempts should then be made to incorporate these formulations within the F-AGE patterning platforms. This author believes specific care should be taken to ensure the stabiliser compounds are biocompatible, are regulatory approved and inherently charged, making them capable of migration through agarose gels under an electric field.

v. Further investigation and optimisation of CCHLVs

This thesis has demonstrated the significant potential of CCHLVs for improved gene delivery in cell lines such as C2C12s, specifically in comparison to plasmid equivalents. Naturally, the next step would be to formulate a similar CCHLV conjugate construct (e.g. NLS bound or aptamer bound) which has a comparable effect in Y201 and primary BM-MSCs. To achieve this, the primary click chemistry investigations presented in appendix 8.6 should be continued. In these experiments, early stage progress was made regarding the use of alkyne modified hairpin oligonucleotides (in this case an EdU functional group) in proof-of-concept click chemistry reactions. An azide containing alexa fluorophore was successfully conjugated to an EdU containing hairpin oligonucleotide, specifically via a stable CuAAc click reaction. Due to this success, the next step would be to apply the same click chemistry protocol with an azide modified NLS peptide or an azide modified aptamer molecule. In the case of the latter, an aptamer specific to the CD29 cell surface receptor could be highly relevant and hypothetically induce greater dumbbell mediated gene expression in Y201 and BM-MSC specific cell types (Ip *et al.*, 2007). A direct comparison between CCHLVs versus Aptamer conjugated CCHLVs would then provide beneficial data for advancing this type of vector development.

In the longer term, fully optimised CCHLV containing therapeutic osteochondral inducing genes (such as TGFβ, BMP, SOX9, RUNX2) should be introduced within the agarose F-AGE GAM system, with the ultimate aim of characterising *in-vitro* 3D gene delivery and cellular differentiation potential. This should be a substantial month-long study involving multi-timepoint qPCR analysis, specifically for the gene expression measurement of both chondrogenic and osteogenic markers (Aggrecan, Cartilage Oligomeric Matrix Protein, Collagen I, collagen II, collagen X, alkaline phosphatase). Results from this experiment would be highly beneficial in elucidating gene mediated cellular responses, allowing comparisons to similar osteochondral GAM studies such as that performed by (Lee *et al.*, 2017).

APPENDIX

8 APPENDIX

8.1 Equipment

Table 8.1 – Equipment: A list of general equipment used and the suppliers.

Equipment	Model	Supplier
Agarose gel comb	-	In-house
Agarose gel electrophoresis tank (large)	Sub Cell GT	BioRad
Agarose gel electrophoresis tank (small)	Mini-Sub Cell GT	BioRad
Agarose gel tray (15 x 15 cm)	-	In-house
Agarose gel tray (7 x 7 cm)	-	BioRad
Autoclave	MVA C40 Benchtop	Priorclave
Automatic cell counter	Countess II (Brightfield)	Invitrogen
Automatic Pipettes	Gilson P2-1000	Anachem Ltd
Balances	GX-2000	A&D
Bench top centrifuge	5415R	Eppendorf
Centrifuge	Harrier 15/80	Sanyo Biomedical Europe
Class II safety cabinet	Heraeus 85	Kendro
CO_2 Incubator	MCO-20AIC	Sanyo Biomedical Europe
Confocal Laser Scanning Microscope	TCS SP8	Leica
Digital microscope camera	AXIOCAM MRc5	Zeiss
Freeze drier	ModulyoD-230	Thermo Savant
Freezer (-20°C)	Electrolux 3000	Jencons PLC
Freezer(-80°C)	Various	Sanyo Biomedical
Fridge	Electrolux ER8817C	Jencons PLC
Fume hood	N/A	Whiteley fume extraction solutions
Gel electrophoresis power pack	Powerpac 300	BioRad
Gel imager	BioSpectrum® 810	UVP
Gel imager	Gel doc XR	BioRad
Histology hot plate	E18.1	Raymond A Lamb
Histology Moulds (32 x 23 x 14 mm)	3803085E	LeiceBiosystems
Histology water bath	MH8515	Barnstead Electrothermal
Hydrogel excision tool	-	In-house

Liquid nitrogen dewar	BIO65	Jencons PLC
Magnetic stirrer	-	Fisher Scientific
Microbalance, 7 figure digital	ABJ220-4NM	KERN
Microplate Spectrophotometer	Multiskan	Thermo Fisher Scientific
Microscope, upright light	AXIO Imager.M2	Zeiss
Microtome semi-automatic	RM2255	Leica Biosystems
Nanodrop Spectrophotometer	ND-1000	Labtech International
Pestle and mortar	-	Victor
pH meter	3510 pH meter	Jenway
Pipette boy	Acu	Integra biosciences
Plate Shaker	IKA KS130 basic	Jencons PLC
Scanning Electron Microscope	SU8230	Hitachi
Slide holders	E102	Raymond A Lamb
Thermocyler	5Prime	Techne
Tissue processor	TP1020	Leica
Vacuum pump	-	-
Vortexer	Topmix FB15024	Fisher Scientific
Water bath	Grant JB Nova	Wolf laboratories
Water purifier	Option 7	ELGA
Wax dispenser	E66	Raymond A Lamb
Wax oven	GPWAX-SO-HYD	Jim Engineering Ltd

8.2 Consumables

Table 8.2 – Consumables: A list of general consumables used and the suppliers.

Consumables	Model	Supplier
3M Steri-Strip Skin Closure	-	Medisave
Cell counting chamber slide	Countess (disposable)	Invitrogen
Cell culture flasks	T75, T175	Thermo Fisher Scientific Ltd
Centrifuge tubes	50 mL	Corning
Coverslips	(22 x 64 mm)	Scientific Laboratory Supplies Ltd
Cryovials	Cryolife	Nunc International Corporation
Falcon tube	Conical (50 mL)	Corning
Histology cassettes	EMB-130-020R	Thermo Fisher Scientific Ltd

Histology cover slips (50 x 70 mm)	3800198G	Leica Biosystems
Histology slides (superfrost plus 25 x 75mm)	10149870	Fisher Scientific
Microtome blades (Feather N35)	3808311E	Leica Biosystems
Microtubes	1.5 mL and 2 mL	Eppendorf
OptiplateTM	96-well	PerkinElmerTM
PCR Tubes & Caps	0.2mL (8-strip)	Thermo Fisher Scientific
Petri dish	100 mm x 15 mm	Fisher Scientific
Pipette tips	10, 20, 200, 1000 µL	Star Labs
Plastic syringes	1, 2, 5, 10, 20, 50 mL	Scientific Laboratory Supplies Ltd
Scalpel blade	Size 10, 22	Fisher Scientific
Serological pipettes	5, 10, 25, 50mL	Sigma Aldrich
Sterile filters	20 and 70 µm	
Sterile loop	-	Fisher Scientific
Stripettes	1, 2, 5, 10, 25 mL	Sigma-Aldrich Ltd
Tissue Culture Flask	T25, T75, T175	Tissue Culture Flask
Well plates (flat-bottomed)	6, 12, 24, 48, 96-well plates	Nunc International Corporation

8.3 Chemicals, reagents and enzymes

Table 8.3 – Chemicals used in this study

Chemical/Reagent	Supplier
Absolute Ethanol	Sigma-Aldrich
Agarose powder (Medium-Low electroendoosmosis)	Acros Organics
Agarose powder (SeaKem® LE)	Lonza
AlamarBlue	BioRad
Ampicillin	Sigma Aldrich
Bovine plasma fibronectin	Invitrogen
Bromophenol Blue	Sigma Aldrich
Calcium chloride	VWR International
Chloroform	Sigma
CO_2 in air 5% (v/v)	British Oxygen Company

Coelenterazine	Promega
Cyanoacrylate contact adhesive	Scotch Super Glue Liquid
DAPI (4'-6-diamidino-2-phenylindoledihydrochloride)	Sigma Aldrich
Dexamethasone	Merck Life Science
dimethylsulfoxide	Sigma Aldrich
Disodium hydrogen phosphate	
Dithiothreitol	Thermo Fisher Scientific
DNAase/RNase free water	5 Prime
Dopamine-HCl	Sigma
DPX mountant	Atom Scientific
Dulbecco's modified eagle medium (DMEM)	Sigma Aldrich
EDTA (disodium ethylenediaminetetraacetic acid)	Thermo Fisher Scientific
Eosin	VWR International
Fast Green	Sigma
Fetal Bovine Serum (FBS)	Sera Labs
Giemsa stain	VWR International
Glacial acetic acid	Sigma Aldrich
Glycerol	Scientific Laboatory Supplies
Haematoxylin (Mayer's)	Atom Scientific
Haematoxylin (Weigert's)	Atom Scientific
HEPES	Lonza
Hydrochloric acid (1M,6M)	Thermo Fisher Scientific
Insulin, transferrin and selenous acid (ITS) premix	BD Biosciences
Isopropanol	Thermo Fisher Scientific
ITS	Corning
Laponite® RD	BYK
L-Ascorbic acid-2-phosphate	Sigma Aldrich
L-Glutamine (200 mM)	Sigma Aldrich
Lipofectamine™ 2000	Life Technologies
L-Proline	Fisher Scientific
Magnesium chloride hexahydrate	Thermo Fisher Scientific
Magnesium sulphate	Thermo Fisher Scientific

Neutral Buffered Formalin (10% v/v)	Thermo Fisher Scientific
Nuclease free water	VWR International
Paraffin wax	Raymond A Lamb
Penicillin (5000 U/mL)/streptomycin (5mg/mL)	Sigma Aldrich
Phosphate Buffered Saline (no calcium, no magnesium)	Gibco
Polyethylene oxide	Sigma Aldrich
Polyethylenimine (linear 25KDa)	Alfa Aesar
Potassium chloride	Sigma Aldrich
Ready Blue Gel stain	Merck
Safranin O	Acros
Scotts's tap water	Atom Scientific
Sodium acetate	Sigma Aldrich
Sodium chloride	Thermo Fisher Scientific
Sodium hydroxide	Thermo Fisher Scientific
ß-Glycerophosphate	Sigma Aldrich
SYBR® SAFE DNA gel stain	Invitrogen
Thioglycollate medium USP	Sigma Aldrich
Transforming growth factor-beta 1	Peprotech
Trizma base	Sigma Aldrich
Trypan blue	Invitrogen
Trypsin-EDTA solution (0.5%; w/v)	Sigma Aldrich
Tryptone soya broth	Sigma Aldrich
Viability/Cytotoxicity Assay Kit for Animal Live & Dead Cells (LIVE-DEAD)	Biotium
Xylene	Atom Scientific

Table 8.4 – Restriction enzymes used in this study.

Name / ID	Concentration	Type	Recognition sequence	Supplier
AgeI	10 U/µL	Type II	A^CCGGT	Thermo Fisher Scientific
MunI	10 U/µL	Type II	GC^GGCCGC	
NotI	10 U/µL	Type II	C^AATTG	
PscI	10 U/µL	Type II	A^CATGT	
XbaI	10 U/µL	Type II	T^CTAGA	
Esp3I	10 U/µL	Type IIS	CGTCTC(1/5)^	

8.4 Chapter 3 – supplementary information

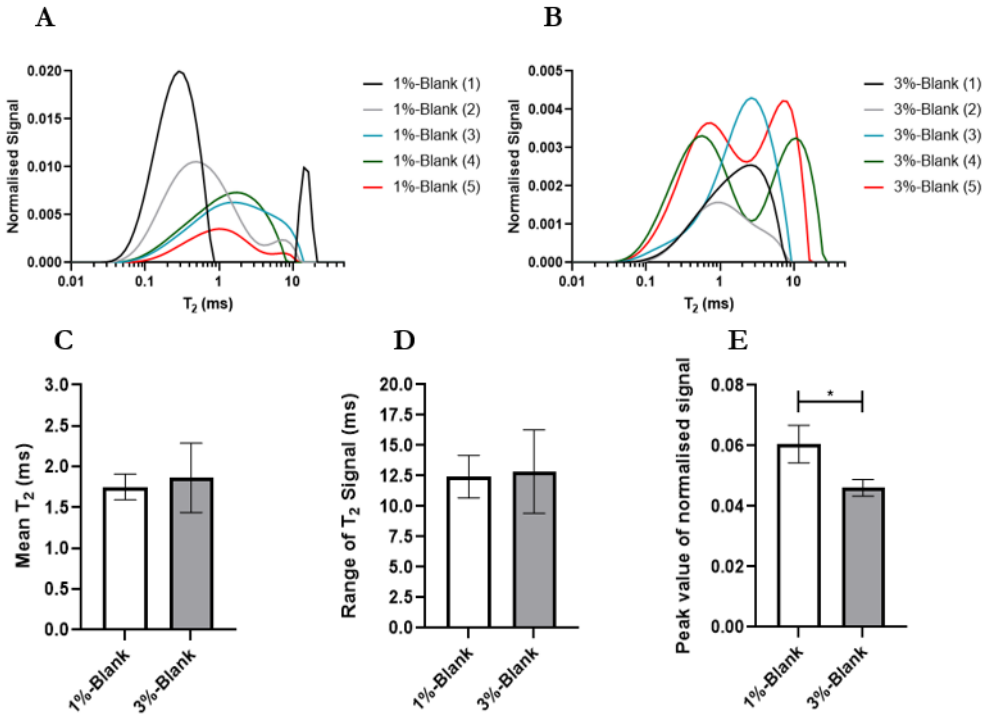

Figure 8.1 (A-E) – T2 distribution curves and associated analysis of different percentage agarose scaffolds, using NMR petrophysics concepts. The values of T2 in which the signal peaks are proportional to the volume of the pores within the agarose scaffolds. A: T_2 distribution curves of 1%-Blank scaffolds. B: T_2 distribution curves of 3%-Blank scaffolds. C: Mean T_2, D: T_2 signal range, E: Peak T_2 signal. Data was analysed using an unpaired t-test or Mann-Whitney U test, depending on normality. All error bars represent standard error, n=5. * = $P < 0.05$.

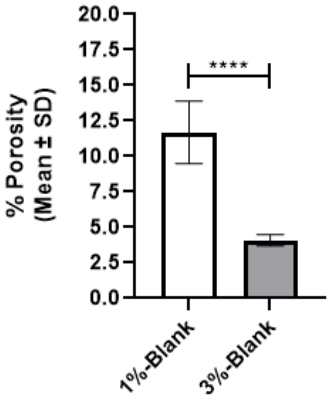

Figure 8.2 – Comparison of agarose scaffold porosity, as calculated using total T_2 signal magnitude values. Data was analysed using a unpaired t test. Error bars represent standard deviation, n=5. **** = $P < 0.0001$.

8.5 Chapter 4 – supplementary information

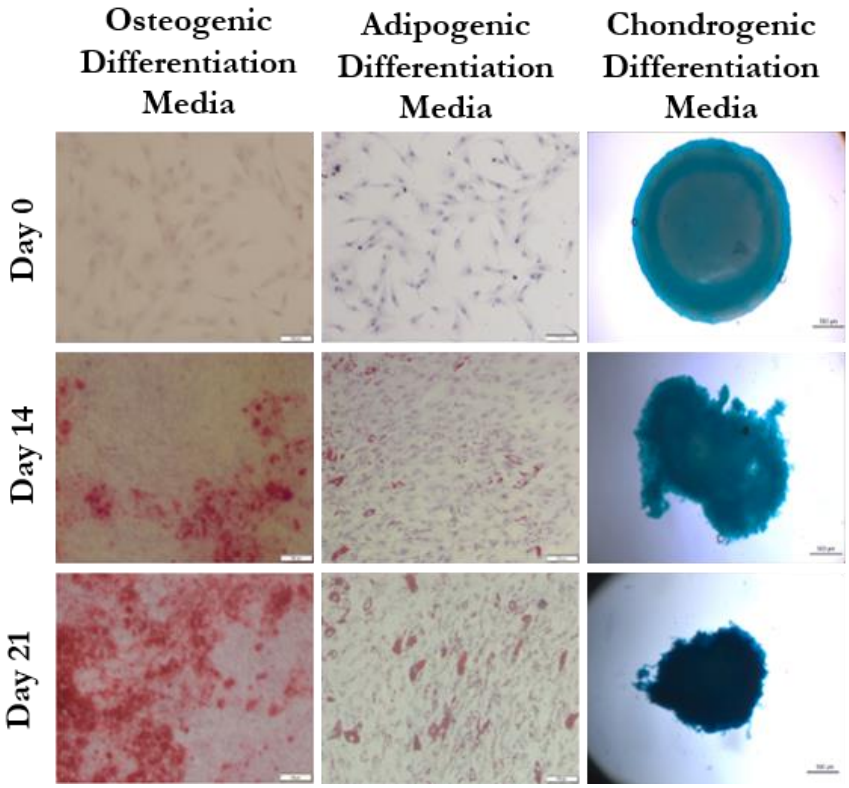

Figure 8.3 – Comparison of Y201 tri-lineage differentiation potential. Light microscopy images of Y201 cell monolayer and pellet cultures were captured after 3 week culture. Differentiation was characterised via staining with Alizarin Red, Oil Red O and Alcian Blue, respectively. Osteogenic and adipogenic image scale bars represent 100 µm. Chondrogenic image scale bars represent 500 µm.

8.6 Chapter 6 – supplementary information

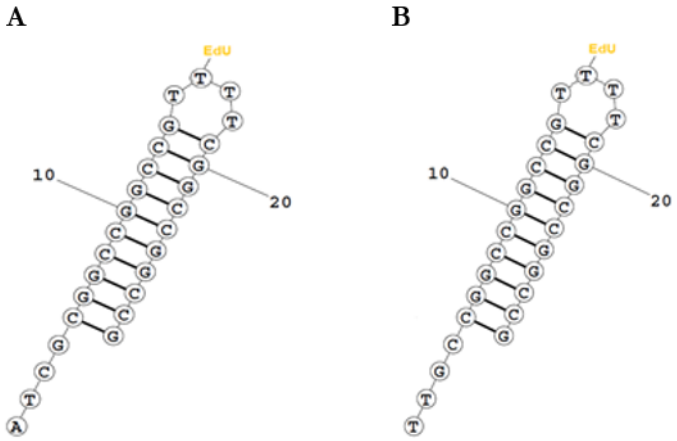

Figure 8.4 (A & B) – Structural conformation of the Ethynyl-2'-deoxyuridine (EdU) modified hairpin oligonucleotides. A: 5'_Esp3I_Hairpin_EdU. B: 3'_Esp3I_Hairpin_EdU. DNA folding at 95°C for 5 minutes using a PCR thermocycler machine (Techne Prime, England).

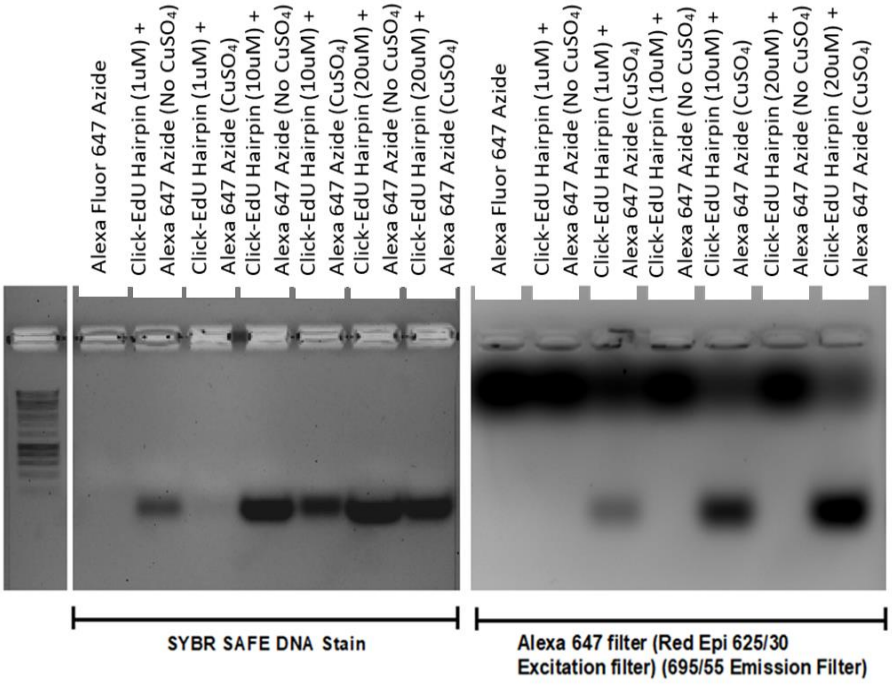

Figure 8.5 – Confirmation of successful click chemistry mediated CuAAC reactions between an azide containing alexaFluor molecule and an alkyne containing oligonucleotide hairpins (5'_Esp3I_Hairpin_EdU 3'_Esp3I_Hairpin_EdU). $CuSO_4$ was used as the catalyst, Sodium-L-ascorbate used as a reducing agent. Reaction conditions (final concentrations per tube): 8 µM Alexa Fluor 647 Azide, 2 mM $CuSO_4$, 100 mM Sodium-L-ascorbate, 1 µM or 10 µM or 20 µM 5'_Esp3I_Hairpin_EdU 3'_Esp3I_Hairpin_EdU.

8.7 Dynamic seeding machine

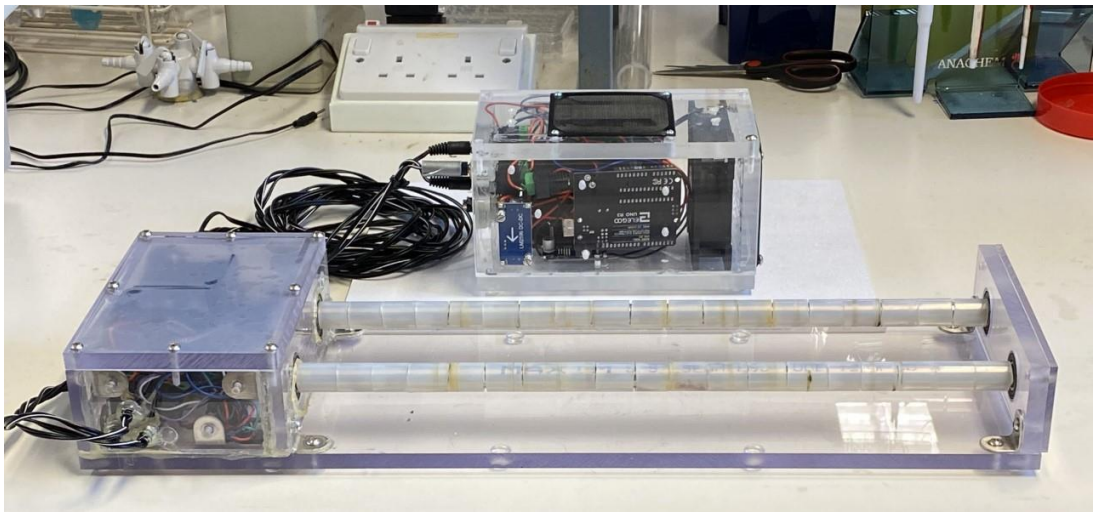

Figure 8.6 – An in-house dynamic seeding rig developed and manufactured in partnership with Daniel White, PhD student. Consists of two 316-stainless steel rollers wrapped in silicone held by ball stainless steel ball bearings. An electronics enclosure houses a 2-phase stepper motor (42 Ncm) - that drives a single roller - and DC power connections. The stepper motor drives a single roller at pre-defined rotational speeds.

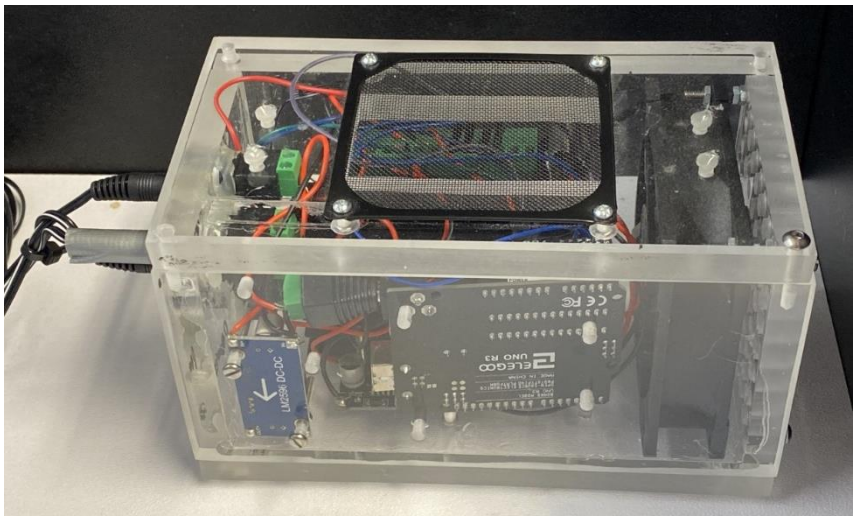

Figure 8.7 – Control unit for the dynamic seeding rig housing a TB6600 stepper motor driver controller, Arduino Uno, infrared receiver, and cooling fan. An infrared remote sends a signal to the infrared receiver which instructs a rotational speed (5 – 10 rpm) to the stepper motor via the Arduino Uno and motor driver. A 12 V DC power supply (180 W) supplies power to the control unit.

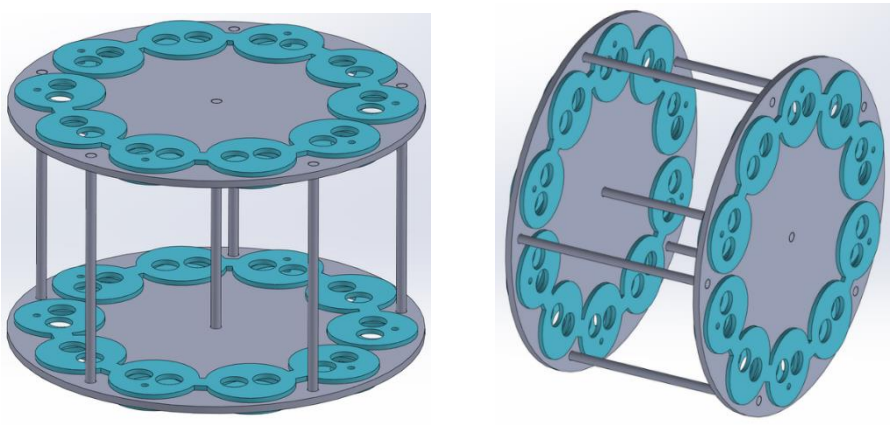

Figure 8.8 – 3D-CAD model of a pair roller plates (grey) for the dynamic seeder with 1.5 mL microcentrifuge adapters (blue) fitted.

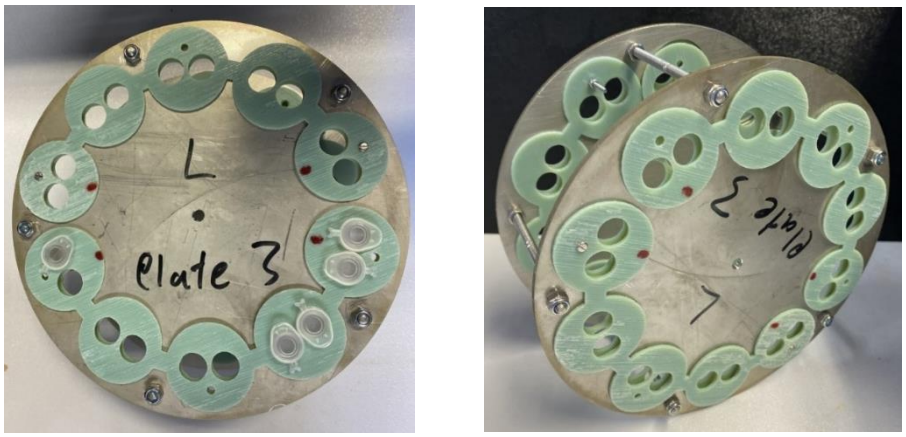

Figure 8.9 – A pair of 316-stainless steel roller plates with 1.5 mL microcentrifuge tubes adapters (green) 3D-printed in Vero® by an Objet1000 Plus (Stratasys, Minnesota, USA).

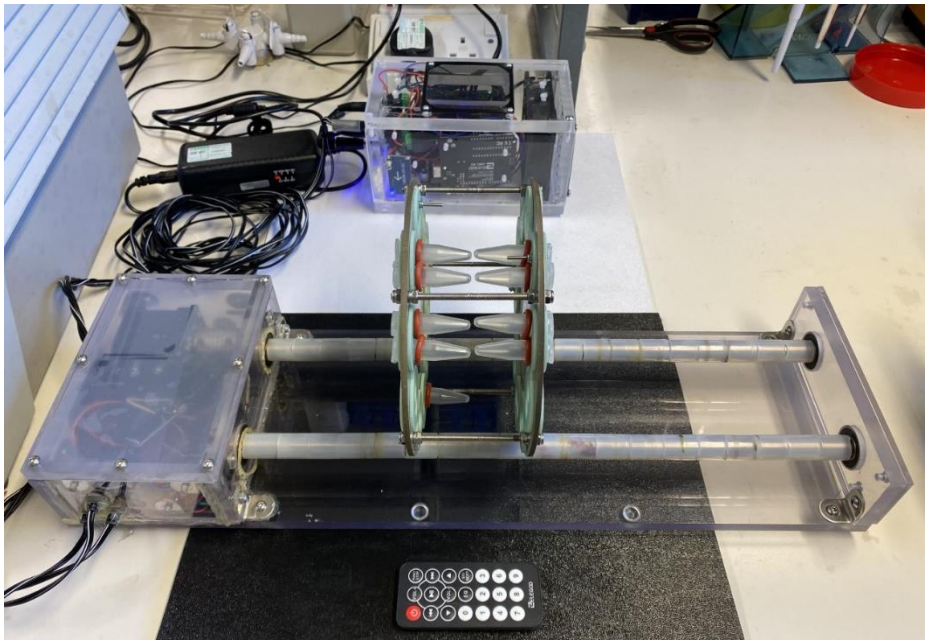

Figure 8.10 – An assembly of the dynamic seeding rig with a pair of roller plates. 1.5 mL microcentrifuge tubes are fitted into the rollers with small O-rings to prevent tubes slipping out of the adapters. The dynamic seeder rollers have a maximum capacity of 4 pairs of roller plates.

9 REFERENCES

Abbasi, N., Hamlet, S., Love, R. M., & Nguyen, N. T. (2020). Porous scaffolds for bone regeneration. *Journal of Science-Advanced Materials and Devices*, *5*(1), 1-9. https://doi.org/10.1016/j.jsamd.2020.01.007

Abdelgaied, A., Stanley, M., Galfe, M., Berry, H., Ingham, E., & Fisher, J. (2015). Comparison of the biomechanical tensile and compressive properties of decellularised and natural porcine meniscus. *Journal of Biomechanics*, *48*(8), 1389-1396. https://doi.org/10.1016/j.jbiomech.2015.02.044

Adam, O. (2012). Design, structuration and rheological properties of Laponite based polymeric nanocomposites. In: Other. Université du Maine, 2012. English. ffNNT : 2012LEMA1014ff.

Agerbaek, M. O., Eriksen, E. F., Kragstrup, J., Mosekilde, L., & Melsen, F. (1991). A reconstruction of the remodelling cycle in normal human cortical iliac bone. *Bone and Mineral*, *12*(2), 101-112. https://doi.org/10.1016/0169-6009(91)90039-3

Akizuki, S., Mow, V. C., Muller, F., Pita, J. C., Howell, D. S., & Manicourt, D. H. (1986). Tensile properties of human knee-joint cartilage: Influence of ionic conditions, weight bearing and fibrillation of the tensile modulus. *Journal of Orthopaedic Research*, *4*(4), 379-392. https://doi.org/10.1002/jor.1100040401

Al-Dosari, M. S., & Gao, X. (2009). Nonviral Gene Delivery: Principle, Limitations, and Recent Progress. *Aaps Journal*, *11*(4), 671-681. https://doi.org/10.1208/s12248-009-9143-y

Alcaide-Ruggiero, L., Cugat, R., & Domínguez, J. M. (2023). Proteoglycans in Articular Cartilage and Their Contribution to Chondral Injury and Repair Mechanisms. *International Journal of Molecular Sciences*, *24*(13), Article 10824. https://doi.org/10.3390/ijms241310824

Alves da Silva, M. L., Crawford, A., Mundy, J. M., Correlo, V. M., Sol, P., Bhattacharya, M., . . . Neves, N. M. (2010). Chitosan/polyester-based scaffolds for cartilage tissue engineering: Assessment of extracellular matrix formation. *Acta Biomaterialia*, *6*(3), 1149-1157. https://doi.org/https://doi.org/10.1016/j.actbio.2009.09.006

Ambekar, R. S., & Kandasubramanian, B. (2019). Progress in the Advancement of Porous Biopolymer Scaffold: Tissue Engineering Application. *Industrial & Engineering Chemistry Research*, *58*(16), 6163-6194. https://doi.org/10.1021/acs.iecr.8b05334

Amin, Z. R., Rahimizadeh, M., Eshghi, H., Dehshahri, A., & Ramezani, M. (2013). The Effect of Cationic Charge Density Change on Transfection Efficiency of Polyethylenimine. *Iranian Journal of Basic Medical Sciences*, *16*(2), 150-156.

Amirikia, M., Shariatzadeh, S. M. A., Jorsaraei, S. G. A., & Mehranjani, M. S. (2017). Impact of pre-incubation time of silk fibroin scaffolds in culture medium on cell proliferation and attachment. *Tissue & Cell*, *49*(6), 657-663. https://doi.org/10.1016/j.tice.2017.09.002

An, H. M., Liu, Y. B., Yi, J. F., Xie, H. B., Li, C., Wang, X., & Chai, W. (2022). Research progress of cartilage lubrication and biomimetic cartilage lubrication materials. *Frontiers in Bioengineering and Biotechnology*, *10*, Article 1012653. https://doi.org/10.3389/fbioe.2022.1012653

Anchordoquy, T. J., & Koe, G. S. (2000). Physical stability of nonviral plasmid-based therapeutics. *Journal of Pharmaceutical Sciences*, *89*(3), 289-296. https://doi.org/10.1002/(sici)1520-6017(200003)89:3<289::aid-jps1>3.3.co;2-e

Anderson, H. C., & Reynolds, J. J. (1973). PYROPHOSPHATE STIMULATION OF CALCIUM UPTAKE INTO CULTURED EMBRYONIC BONES - FINE-STRUCTURE OF MATRIX VESICLES AND THEIR ROLE IN CALCIFICATION. *Developmental Biology*, *34*(2), 211-227. https://doi.org/10.1016/0012-1606(73)90351-5

Annabi, N., Nichol, J. W., Zhong, X., Ji, C. D., Koshy, S., Khademhosseini, A., & Dehghani, F. (2010). Controlling the Porosity and Microarchitecture of Hydrogels for Tissue Engineering. *Tissue Engineering Part B-Reviews*, *16*(4), 371-383. https://doi.org/10.1089/ten.teb.2009.0639

Ansari, S., Khorshidi, S., & Karkhaneh, A. (2019). Engineering of gradient osteochondral tissue: From nature to lab. *Acta Biomaterialia*, *87*, 41-54. https://doi.org/10.1016/j.actbio.2019.01.071

Arabi, F., Mansouri, V., & Ahmadbeigi, N. (2022). Gene therapy clinical trials, where do we go? An overview. *Biomedicine & Pharmacotherapy*, *153*, Article 113324. https://doi.org/10.1016/j.biopha.2022.113324

Arango, M. C., Osorio, Y. M., Osorno, J. B., Parra, S. B., & Alvarez-Lopez, C. Effect of Ethanol Post-Treatments over Sericin Scaffolds for Tissue Engineering Applications. *Journal of Polymers and the Environment*. https://doi.org/10.1007/s10924-022-02647-3

Aravamudhan, A., M. Ramos, D., Nada, A., & Kumbar, S. (2014). Chapter 4 - Natural Polymers: Polysaccharides and Their Derivatives for Biomedical Applications. In S. Kumbar, C. Laurencin, & M. Deng (Eds.), *Natural and Synthetic Biomedical Polymers* (pp. 67-89). Elsevier. https://doi.org/https://doi.org/10.1016/B978-0-12-396983-5.00004-1

Armstrong, T. K., & Anchordoquy, T. J. (2004). Immobilization of nonviral vectors during the freezing step of lyophilization. *Journal of Pharmaceutical Sciences*, *93*(11), 2698-2709. https://doi.org/10.1002/jps.20177

Arredondo, R., Poggioli, F., Martinez-Diaz, S., Piera-Trilla, M., Torres-Claramunt, R., Tio, L., & Monllau, J. C. (2021). Fibronectin-coating enhances attachment and proliferation of mesenchymal stem cells on a polyurethane meniscal scaffold. *Regenerative Therapy*, *18*, 480-486. https://doi.org/10.1016/j.reth.2021.11.001

Asensio, G., Benito-Garzón, L., Ramírez-Jiménez, R. A., Guadilla, Y., Gonzalez-Rubio, J., Abradelo, C., . . . Rojo, L. (2022). Biomimetic Gradient Scaffolds Containing Hyaluronic

Acid and Sr/Zn Folates for Osteochondral Tissue Engineering. *Polymers*, *14*(1), Article 12. https://doi.org/10.3390/polym14010012

Atala, A. (2007). Engineering tissues, organs and cells. *Journal of Tissue Engineering and Regenerative Medicine*, *1*(2), 83-96. https://doi.org/10.1002/term.18

Atkins, G. J., & Findlay, D. M. (2012). Osteocyte regulation of bone mineral: a little give and take. *Osteoporosis International*, *23*(8), 2067-2079. https://doi.org/10.1007/s00198-012-1915-z

Atrian, M., Kharaziha, M., Emadi, R., & Alihosseini, F. (2019). Silk-Laponite (R) fibrous membranes for bone tissue engineering. *Applied Clay Science*, *174*, 90-99. https://doi.org/10.1016/j.clay.2019.03.038

Augat, P., & Schorlemmer, S. (2006). The role of cortical bone and its microstructure in bone strength. *Age and Ageing*, *35*, 27-31. https://doi.org/10.1093/ageing/afl081

Avilés, M. O., Lin, C. H., Zelivyanskaya, M., Graham, J. G., Boehler, R. M., Messersmith, P. B., & Shea, L. D. (2010). The contribution of plasmid design and release to in vivo gene expression following delivery from cationic polymer modified scaffolds. *Biomaterials*, *31*(6), 1140-1147. https://doi.org/10.1016/j.biomaterials.2009.10.035

Bajaj, S., Shoemaker, T., Hakimiyan, A. A., Rappoport, L., Pascual-Garrido, C., Oegema, T. R., . . . Chubinskaya, S. (2010). Protective effect of P188 in the Model of Acute Trauma to Human Ankle Cartilage: The Mechanism of Action. *Journal of Orthopaedic Trauma*, *24*(9), 571-576. https://doi.org/10.1097/BOT.0b013e3181ec4712

Bakan, F., Kara, G., Cakmak, M. C., Cokol, M., & Denkbas, E. B. (2017). Synthesis and characterization of amino acid-functionalized calcium phosphate nanoparticles for siRNA delivery. *Colloids and Surfaces B-Biointerfaces*, *158*, 175-181. https://doi.org/10.1016/j.colsurfb.2017.06.028

Barros, N. R., Chen, Y., Hosseini, V., Wang, W. Y., Nasiri, R., Mahmoodi, M., . . . Kim, H. J. (2021). Recent developments in mussel-inspired materials for biomedical applications. *Biomaterials Science*, *9*(20), 6653-6672. https://doi.org/10.1039/d1bm01126j

Bartha, L., Vajda, A., Duska, Z., Rahmeh, H., & Hangody, L. (2006). Autologous osteochondral mosaicplasty grafting. *Journal of Orthopaedic & Sports Physical Therapy*, *36*(10), 739-750. https://doi.org/10.2519/jospt.2006.2182

Bashir, S., Hina, M., Iqbal, J., Rajpar, A. H., Mujtaba, M. A., Alghamdi, N. A., . . . Ramesh, S. (2020). Fundamental Concepts of Hydrogels: Synthesis, Properties, and Their Applications. *Polymers*, *12*(11), Article 2702. https://doi.org/10.3390/polym12112702

Baumann, C. A., Hinckel, B. B., Bozynski, C. C., & Farr, J. (2019). *Articular Cartilage: Structure and Restoration*. Springer International Publishing. https://doi.org/10.1007/978-3-030-01491-9_1

Behr, J.-P. (1997). The Proton Sponge: a Trick to Enter Cells the Viruses Did Not Exploit. *CHIMIA*, *51*(1-2), 34. https://doi.org/10.2533/chimia.1997.34

Bengali, Z., & Shea, L. D. (2005). Gene delivery by immobilization to cell-adhesive substrates. *Mrs Bulletin*, *30*(9), 659-662. https://doi.org/10.1557/mrs2005.193

Bentley, G. (2004). A prospective, randomised comparison of autologous chondrocyte implantation versus mosaicplasty for osteochondral defects in the knee - Reply [Letter]. *Journal of Bone and Joint Surgery-British Volume*, *86B*(4), 619-620.

Bentley, G., Biant, L. C., Vijayan, S., Macmull, S., Skinner, J. A., & Carrington, R. W. J. (2012). Minimum ten-year results of a prospective randomised study of autologous chondrocyte implantation versus mosaicplasty for symptomatic articular cartilage lesions of the knee. *Journal of Bone and Joint Surgery-British Volume*, *94B*(4), 504-509. https://doi.org/10.1302/0301-620x.94b4.27495

Bernhardt, A., Paul, B., & Gelinsky, M. (2018). Biphasic Scaffolds from Marine Collagens for Regeneration of Osteochondral Defects. *Marine Drugs*, *16*(3), Article 91. https://doi.org/10.3390/md16030091

Berthiaume, F., Maguire, T. J., & Yarmush, M. L. (2011). Tissue Engineering and Regenerative Medicine: History, Progress, and Challenges. *Annual Review of Chemical and Biomolecular Engineering, Vol 2*, *2*, 403-430. https://doi.org/10.1146/annurev-chembioeng-061010-114257

Betz, O. B., Betz, V. M., Schroder, C., Penzkofer, R., Gottlinger, M., Mayer-Wagner, S., . . . Muller, P. E. (2013). Repair of large segmental bone defects: BMP-2 gene activated muscle grafts vs. autologous bone grafting [Article]. *Bmc Biotechnology*, *13*, 8, Article 65. https://doi.org/10.1186/1472-6750-13-65

Bhat, S., Tripathi, A., & Kumar, A. (2011). Supermacroprous chitosan-agarose-gelatin cryogels: in vitro characterization and in vivo assessment for cartilage tissue engineering. *Journal of the Royal Society Interface*, *8*(57), 540-554. https://doi.org/10.1098/rsif.2010.0455

Bhattacharjee, S. (2016). DLS and zeta potential - What they are and what they are not? *Journal of Controlled Release*, *235*, 337-351. https://doi.org/10.1016/j.jconrel.2016.06.017

Bhosale, A. M., & Richardson, J. B. (2008). Articular cartilage: structure, injuries and review of management [Review]. *British Medical Bulletin*, *87*(1), 77-95. https://doi.org/10.1093/bmb/ldn025

Billinghurst, R. C., Dahlberg, L., Ionescu, M., Reiner, A., Bourne, R., Rorabeck, C., . . . Poole, A. R. (1997). Enhanced cleavage of type II collagen by collagenases in osteoarthritic articular cartilage. *Journal of Clinical Investigation*, *99*(7), 1534-1545. https://doi.org/10.1172/jci119316

Bisht, S., Bhakta, G., Mitra, S., & Maitra, A. (2005). pDNA loaded calcium phosphate nanoparticles: highly efficient non-viral vector for gene delivery. *International Journal of Pharmaceutics*, *288*(1), 157-168. https://doi.org/10.1016/j.ijpharm.2004.07.035

Bittner, S. M., Smith, B. T., Diaz-Gomez, L., Hudgins, C. D., Melchiorri, A. J., Scott, D. W., . . . Mikos, A. G. (2019). Fabrication and mechanical characterization of 3D printed vertical uniform and gradient scaffolds for bone and osteochondral tissue engineering. *Acta Biomaterialia*, *90*, 37-48. https://doi.org/10.1016/j.actbio.2019.03.041

Bloch, K., Lozinsky, V. I., Galaev, I. Y., Yavriyanz, K., Vorobeychik, M., Azarov, D., . . . Vardi, P. (2005). Functional activity of insulinoma cells (INS-1E) and pancreatic islets cultured in agarose cryogel sponges. *Journal of Biomedical Materials Research Part A*, *75A*(4), 802-809. https://doi.org/10.1002/jbm.a.30466

Bocciarelli, D. S. (1970). MORPHOLOGY OF CRYSTALLITES IN BONE. *Calcified Tissue Research*, *5*(3), 261-+. https://doi.org/10.1007/bf02017554

Bonadio, J. (2000). Tissue engineering via local gene delivery. *Journal of Molecular Medicine-Jmm*, *78*(6), 303-311. https://doi.org/10.1007/s001090000118

Bonadio, J., Smiley, E., Patil, P., & Goldstein, S. (1999). Localized, direct plasmid gene delivery in vivo: prolonged therapy results in reproducible tissue regeneration. *Nat Med*, *5*(7), 753-759. https://doi.org/10.1038/10473

Boskey, A. L. (2015). Bone composition: relationship to bone fragility and antiosteoporotic drug effects (vol 2, 447, 2013). *Bonekey Reports*, *4*, Article 710. https://doi.org/10.1038/bonekey.2015.79

Bottini, M., Mebarek, S., Anderson, K. L., Strzelecka-Kiliszek, A., Bozycki, L., Simao, A. M. S., . . . Buchet, R. (2018). Matrix vesicles from chondrocytes and osteoblasts: Their biogenesis, properties, functions and biomimetic models. *Biochimica Et Biophysica Acta-General Subjects*, *1862*(3), 532-546. https://doi.org/10.1016/j.bbagen.2017.11.005

Bougault, C., Aubert-Foucher, E., Paumier, A., Perrier-Groult, E., Huot, L., Hot, D., . . . Mallein-Gerin, F. (2012). Dynamic Compression of Chondrocyte-Agarose Constructs Reveals New Candidate Mechanosensitive Genes. *Plos One*, *7*(5), Article e36964. https://doi.org/10.1371/journal.pone.0036964

Boussif, O., Lezoualch, F., Zanta, M. A., Mergny, M. D., Scherman, D., Demeneix, B., & Behr, J. P. (1995). A VERSATILE VECTOR FOR GENE AND OLIGONUCLEOTIDE TRANSFER INTO CELLS IN CULTURE AND IN-VIVO - POLYETHYLENIMINE. *Proceedings of the National Academy of Sciences of the United States of America*, *92*(16), 7297-7301. https://doi.org/10.1073/pnas.92.16.7297

Boyce, B. F., & Xing, L. P. (2007). Biology of RANK, RANKL, and osteoprotegerin. *Arthritis Research & Therapy*, *9*, Article S1. https://doi.org/10.1186/ar2165

Boyce, B. F., & Xing, L. P. (2008). Functions of RANKL/RANK/OPG in bone modeling and remodeling. *Archives of Biochemistry and Biophysics*, *473*(2), 139-146. https://doi.org/10.1016/j.abb.2008.03.018

Brittberg, M., Lindahl, A., Nilsson, A., Ohlsson, C., Isaksson, O., & Peterson, L. (1994). TREATMENT OF DEEP CARTILAGE DEFECTS IN THE KNEE WITH

AUTOLOGOUS CHONDROCYTE TRANSPLANTATION. *New England Journal of Medicine*, *331*(14), 889-895. https://doi.org/10.1056/nejm199410063311401

Brittberg, M., & Winalski, C. S. (2003). Evaluation of cartilage injuries and repair. *Journal of Bone and Joint Surgery-American Volume*, *85A*, 58-69. https://doi.org/10.2106/00004623-200300002-00008

Browe, D. C., Mahon, O. R., Diaz-Payno, P. J., Cassidy, N., Dudurych, I., Dunne, A., . . . Kelly, D. J. (2019). Glyoxal cross-linking of solubilized extracellular matrix to produce highly porous, elastic, and chondro-permissive scaffolds for orthopedic tissue engineering. *Journal of Biomedical Materials Research Part A*, *107*(10), 2222-2234. https://doi.org/10.1002/jbm.a.36731

Buckwalter. J, M. H., Grodzinsky. A. (2005). Articular cartilage and osteoarthritis. *Instructional course lectures*, *54*, 465-480.

Buckwalter. J. A, a. M. H. (1998). Articular cartilage: tissue design and chondrocyte-matrix interactions. *Instructional course lectures*, *47*, 477-486. https://doi.org/10.2106/00004623-199704000-00021

Cai, S., Cheng, Y., Qiu, C., Liu, G., & Chu, C. (2023). The versatile applications of polydopamine in regenerative medicine: Progress and challenges. *Smart Materials in Medicine*, *4*, 294-312. https://doi.org/https://doi.org/10.1016/j.smaim.2022.11.005

Cambria, E., Brunner, S., Heusser, S., Fisch, P., Hitzl, W., Ferguson, S. J., & Wuertz-Kozak, K. (2020). Cell-Laden Agarose-Collagen Composite Hydrogels for Mechanotransduction Studies. *Frontiers in Bioengineering and Biotechnology*, *8*, Article 346. https://doi.org/10.3389/fbioe.2020.00346

Canovas, F., & Dagneaux, L. (2018). Quality of life after total knee arthroplasty. *Orthopaedics & Traumatology-Surgery & Research*, *104*(1), S41-S46. https://doi.org/10.1016/j.otsr.2017.04.017

Cao, L., Yang, F., Liu, G. W., Yu, D. G., Li, H. W., Fan, Q. M., . . . Dai, K. R. (2011). The promotion of cartilage defect repair using adenovirus mediated Sox9 gene transfer of rabbit bone marrow mesenchymal stem cells. *Biomaterials*, *32*(16), 3910-3920. https://doi.org/10.1016/j.biomaterials.2011.02.014

Casper, J., Schenk, S. H., Parhizkar, E., Detampel, P., Dehshahri, A., & Huwyler, J. (2023). Polyethylenimine (PEI) in gene therapy: Current status and clinical applications. *J Control Release*, *362*, 667-691. https://doi.org/10.1016/j.jconrel.2023.09.001

Castro, N. J., O'Brien, J., & Zhang, L. G. (2015). Integrating biologically inspired nanomaterials and table-top stereolithography for 3D printed biomimetic osteochondral scaffolds. *Nanoscale*, *7*(33), 14010-14022. https://doi.org/10.1039/c5nr03425f

Castro-Aguirre, E., Auras, R., Selke, S., Rubino, M., & Marsh, T. (2018). Impact of Nanoclays on the Biodegradation of Poly(Lactic Acid) Nanocomposites. *Polymers*, *10*(2), Article 202. https://doi.org/10.3390/polym10020202

Cha, R. S., & Thilly, W. G. (1993). SPECIFICITY, EFFICIENCY, AND FIDELITY OF PCR. *Pcr-Methods and Applications*, *3*(3), S18-S29.

Chang, C. W., Christensen, L. V., Lee, M., & Kim, S. W. (2008). Efficient expression of vascular endothelial growth factor using minicircle DNA for angiogenic gene therapy. *Journal of Controlled Release*, *125*(2), 155-163. https://doi.org/10.1016/j.jconrel.2007.10.014

Chen, G. Q., Deng, C. X., & Li, Y. P. (2012). TGF-β and BMP Signaling in Osteoblast Differentiation and Bone Formation. *International Journal of Biological Sciences*, *8*(2), 272-288. https://doi.org/10.7150/ijbs.2929

Chen, J. N., Chen, H. A., Li, P., Diao, H. J., Zhu, S. Y., Dong, L., . . . Zhang, J. F. (2011). Simultaneous regeneration of articular cartilage and subchondral bone in vivo using MSCs induced by a spatially controlled gene delivery system in bilayered integrated scaffolds. *Biomaterials*, *32*(21), 4793-4805. https://doi.org/10.1016/j.biomaterials.2011.03.041

Chen, L., Wei, L., Su, X. D., Qin, L. L., Xu, Z. H., Huang, X., . . . Hu, N. (2023). Preparation and Characterization of Biomimetic Functional Scaffold with Gradient Structure for Osteochondral Defect Repair. *Bioengineering-Basel*, *10*(2), Article 213. https://doi.org/10.3390/bioengineering10020213

Chen, R. Y., Pye, J. S., Li, J. R., Little, C. B., & Li, J. J. (2023). Multiphasic scaffolds for the repair of osteochondral defects: Outcomes of preclinical studies. *Bioactive Materials*, *27*, 505-545. https://doi.org/10.1016/j.bioactmat.2023.04.016

Cheng, Y. L., Chen, Y. W., Wang, K., & Shie, M. Y. (2016). Enhanced adhesion and differentiation of human mesenchymal stem cell inside apatite-mineralized/poly(dopamine)-coated poly(epsilon-caprolactone) scaffolds by stereolithography. *Journal of Materials Chemistry B*, *4*(38), 6307-6315. https://doi.org/10.1039/c6tb01377e

Chernousova, S., & Epple, M. (2017). Live-cell imaging to compare the transfection and gene silencing efficiency of calcium phosphate nanoparticles and a liposomal transfection agent. *Gene Therapy*, *24*(5), 282-289. https://doi.org/10.1038/gt.2017.13

Chimutengwende-Gordon, M., Donaldson, J., & Bentley, G. (2020). Current solutions for the treatment of chronic articular cartilage defects in the knee. *Efort Open Reviews*, *5*(3), 156-163. https://doi.org/10.1302/2058-5241.5.190031

Choren, J. A., Heinrich, S. M., & Silver-Thorn, M. B. (2013). Young's modulus and volume porosity relationships for additive manufacturing applications. *Journal of Materials Science*, *48*(15), 5103-5112. https://doi.org/10.1007/s10853-013-7237-5

Chou, Y. C., Lee, D., Chang, T. M., Hsu, Y. H., Yu, Y. H., Liu, S. J., & Ueng, S. W. N. (2016). Development of a Three-Dimensional (3D) Printed Biodegradable Cage to Convert Morselized Corticocancellous Bone Chips into a Structured Cortical Bone Graft.

International Journal of Molecular Sciences, *17*(4), Article 595. https://doi.org/10.3390/ijms17040595

Chuah, Y. J., Koh, Y. T., Lim, K., Menon, N. V., Wu, Y., & Kang, Y. (2015). Simple surface engineering of polydimethylsiloxane with polydopamine for stabilized mesenchymal stem cell adhesion and multipotency. *Scientific Reports*, *5*, Article 18162. https://doi.org/10.1038/srep18162

Cigan, A. D., Roach, B. L., Nims, R. J., Tan, A. R., Albro, M. B., Stoker, A. M., . . . Ateshian, G. A. (2016). High seeding density of human chondrocytes in agarose produces tissue-engineered cartilage approaching native mechanical and biochemical properties. *Journal of Biomechanics*, *49*(9), 1909-1917. https://doi.org/10.1016/j.jbiomech.2016.04.039

Clar, C., Cummins, E., McIntyre, L., Thomas, S., Lamb, J., Bain, L., . . . Waugh, N. (2005). Clinical and cost-effectiveness of autologous chondrocyte implantation for cartilage defects in knee joints: systematic review and economic evaluation. *Health Technology Assessment*, *9*(47), III-+.

Cohen, N. P., Foster, R. J., & Mow, V. C. (1998). Composition and dynamics of articular cartilage: Structure, function, and maintaining healthy state. *Journal of Orthopaedic & Sports Physical Therapy*, *28*(4), 203-215. https://doi.org/10.2519/jospt.1998.28.4.203

Costa, A., Hood, I. V., & Berger, J. M. (2013). Mechanisms for Initiating Cellular DNA Replication. *Annual Review of Biochemistry, Vol 82*, *82*, 25-+. https://doi.org/10.1146/annurev-biochem-052610-094414

Costantini, M., Jaroszewicz, J., Kozon, L., Szlazak, K., Swieszkowski, W., Garstecki, P., . . . Guzowski, J. (2019). 3D-Printing of Functionally Graded Porous Materials Using On-Demand Reconfigurable Microfluidics. *Angewandte Chemie-International Edition*, *58*(23), 7620-7625. https://doi.org/10.1002/anie.201900530

Crolla, J. P., Lawless, B. M., Cederlund, A. A., Aspden, R. M., & Espino, D. M. (2022). Analysis of hydration and subchondral bone density on the viscoelastic properties of bovine articular cartilage. *Bmc Musculoskeletal Disorders*, *23*(1), Article 228. https://doi.org/10.1186/s12891-022-05169-0

Cucchiarini, M., & Madry, H. (2019). Biomaterial-guided delivery of gene vectors for targeted articular cartilage repair. *Nature Reviews Rheumatology*, *15*(1), 18-29. https://doi.org/10.1038/s41584-018-0125-2

Cummins, H. Z. (2007). Liquid, glass, gel: The phases of colloidal Laponite. *Journal of Non-Crystalline Solids*, *353*(41-43), 3891-3905. https://doi.org/10.1016/j.jnoncrysol.2007.02.066

D'Lima, D. D., Fregly, B. J., Patil, S., Steklov, N., & Colwell, C. W. (2012). Knee joint forces: prediction, measurement, and significance. *Proceedings of the Institution of Mechanical Engineers Part H-Journal of Engineering in Medicine*, *226*(H2), 95-102. https://doi.org/10.1177/0954411911433372

D'Lima, D. D., Hashimoto, S., Chen, P. C., Colwell, C. W., & Lotz, M. K. (2001). Human chondrocyte apoptosis in response to mechanical injury. *Osteoarthritis and Cartilage*, *9*(8), 712-719. https://doi.org/10.1053/joca.2001.0468

D'Mello, S. R., Elangovan, S., Hong, L., Ross, R. D., Sumner, D. R., & Salem, A. K. (2015). A Pilot Study Evaluating Combinatorial and Simultaneous Delivery of Polyethylenimine-Plasmid DNA Complexes Encoding for VEGF and PDGF for Bone Regeneration in Calvarial Bone Defects. *Current Pharmaceutical Biotechnology*, *16*(7), 655-660. https://doi.org/10.2174/1389201016071504271127 53

da Silva, M. A., Crawford, A., Mundy, J., Martins, A., Araújo, J. V., Hatton, P. V., . . . Neves, N. M. (2009). Evaluation of Extracellular Matrix Formation in Polycaprolactone and Starch-Compounded Polycaprolactone Nanofiber Meshes When Seeded with Bovine Articular Chondrocytes. *Tissue Engineering Part A*, *15*(2), 377-385. https://doi.org/10.1089/ten.tea.2007.0327

Dai, Z., Ronholm, J., Tian, Y. P., Sethi, B., & Cao, X. D. (2016). Sterilization techniques for biodegradable scaffolds in tissue engineering applications. *Journal of Tissue Engineering*, *7*, Article 2041731416648810. https://doi.org/10.1177/2041731416648810

Dai, Z. J., Gjetting, T., Mattebjerg, M. A., Wu, C., & Andresen, T. L. (2011). Elucidating the interplay between DNA-condensing and free polycations in gene transfection through a mechanistic study of linear and branched PEI. *Biomaterials*, *32*(33), 8626-8634. https://doi.org/10.1016/j.biomaterials.2011.07.044

Dallas, S. L., Prideaux, M., & Bonewald, L. F. (2013). The Osteocyte: An Endocrine Cell . . . and More. *Endocrine Reviews*, *34*(5), 658-690. https://doi.org/10.1210/er.2012-1026

De La Vega, J., Ter Braak, B., Azzoni, A. R., Monteiro, G. A., & Prazeres, D. M. F. (2013). Impact of Plasmid Quality on Lipoplex-Mediated Transfection. *Journal of Pharmaceutical Sciences*, *102*(11), 3932-3941. https://doi.org/10.1002/jps.23709

De Laroche, R., Simon, E., Suignard, N., Williams, T., Henry, M. P., Robin, P., . . . Querellou, S. (2018). Clinical interest of quantitative bone SPECT-CT in the preoperative assessment of knee osteoarthritis. *Medicine*, *97*(35), Article e11943. https://doi.org/10.1097/md.0000000000011943

Deev, R., Plaksa, I., Bozo, I., & Isaev, A. (2017). Results of an International Postmarketing Surveillance Study of pl-VEGF165 Safety and Efficacy in 210 Patients with Peripheral Arterial Disease. *American Journal of Cardiovascular Drugs*, *17*(3), 235-242. https://doi.org/10.1007/s40256-016-0210-3

DeKosky, B. J., Dormer, N. H., Ingavle, G. C., Roatch, C. H., Lomakin, J., Detamore, M. S., & Gehrke, S. H. (2010). Hierarchically Designed Agarose and Poly(Ethylene Glycol) Interpenetrating Network Hydrogels for Cartilage Tissue Engineering. *Tissue Engineering Part C-Methods*, *16*(6), 1533-1542. https://doi.org/10.1089/ten.tec.2009.0761

Demoor, M., Ollitrault, D., Gomez-Leduc, T., Bouyoucef, M., Hervieu, M., Fabre, H., . . . Galera, P. (2014). Cartilage tissue engineering: Molecular control of chondrocyte differentiation for proper cartilage matrix reconstruction. *Biochimica Et Biophysica Acta-General Subjects*, *1840*(8), 2414-2440. https://doi.org/10.1016/j.bbagen.2014.02.030

Demoreno, M. R., Smith, J. F., & Smith, R. V. (1986). MECHANISM STUDIES OF COOMASSIE BLUE AND SILVER STAINING OF PROTEINS. *Journal of Pharmaceutical Sciences*, *75*(9), 907-911. https://doi.org/10.1002/jps.2600750919

Dhandayuthapani, B., Yoshida, Y., Maekawa, T., & Kumar, D. S. (2011). Polymeric Scaffolds in Tissue Engineering Application: A Review. *International Journal of Polymer Science*, *2011*, Article 290602. https://doi.org/10.1155/2011/290602

Di Luca, A., Ostrowska, B., Lorenzo-Moldero, I., Lepedda, A., Swieszkowski, W., Van Blitterswijk, C., & Moroni, L. (2016). Gradients in pore size enhance the osteogenic differentiation of human mesenchymal stromal cells in three-dimensional scaffolds. *Scientific Reports*, *6*, Article 22898. https://doi.org/10.1038/srep22898

Di Luca, A., Szlazak, K., Lorenzo-Moldero, I., Ghebes, C. A., Lepedda, A., Swieszkowski, W., . . . Moroni, L. (2016). Influencing chondrogenic differentiation of human mesenchymal stromal cells in scaffolds displaying a structural gradient in pore size. *Acta Biomaterialia*, *36*, 210-219. https://doi.org/10.1016/j.actbio.2016.03.014

Di Micco, M. A., Patwari, P., Siparsky, P. N., Kumar, S., Pratta, M. A., Lark, M. W., . . . Grodzinsky, A. J. (2004). Mechanisms and kinetics of glycosaminoglycan release following in vitro cartilage injury. *Arthritis and Rheumatism*, *50*(3), 840-848. https://doi.org/10.1002/art.20101

Diaz, I. L., Jérôme, V., Freitag, R., & Perez, L. D. (2021). Development of poly(ethyleneimine) grafted amphiphilic copolymers: Evaluation of their cytotoxicity and ability to complex DNA. *Journal of Bioactive and Compatible Polymers*, *36*(6), 447-463, Article 08839115211053925. https://doi.org/10.1177/08839115211053925

Dilley, J. E., Bello, M. A., Roman, N., McKinley, T., & Sankar, U. (2023). Post-traumatic osteoarthritis: A review of pathogenic mechanisms and novel targets for mitigation. *Bone Reports*, *18*, Article 101658. https://doi.org/10.1016/j.bonr.2023.101658

Ding, R. Y., Liu, Y. J., Cheng, D. W., Yang, G., Wu, W. J., Du, H. R., . . . Xu, J. G. (2022). A novel gene-activated matrix composed of PEI/plasmid-BMP2 complexes and hydroxyapatite/chitosan-microspheres promotes bone regeneration. *Nano Research*, *15*(7), 6348-6360. https://doi.org/10.1007/s12274-022-4292-8

Ding, X. M., Zhu, M. F., Xu, B. S., Zhang, J. M., Zhao, Y. H., Ji, S. L., . . . Yang, Q. (2014). Integrated Trilayered Silk Fibroin Scaffold for Osteochondral Differentiation of Adipose-Derived Stem Cells. *Acs Applied Materials & Interfaces*, *6*(19), 16696-16705. https://doi.org/10.1021/am5036708

Dole, N. S., Mazur, C. M., Acevedo, C., Lopez, J. P., Monteiro, D. A., Fowler, T. W., . . . Alliston, T. (2017). Osteocyte-Intrinsic TGF-β Signaling Regulates Bone Quality through Perilacunar/Canalicular Remodeling. *Cell Reports*, *21*(9), 2585-2596. https://doi.org/10.1016/j.celrep.2017.10.115

Dong, C. J., & Lv, Y. G. (2016). Application of Collagen Scaffold in Tissue Engineering: Recent Advances and New Perspectives. *Polymers*, *8*(2), Article 42. https://doi.org/10.3390/polym8020042

Dormer, N. H., Singh, M., Wang, L., Berkland, C. J., & Detamore, M. S. (2010). Osteochondral interface tissue engineering using macroscopic gradients of bioactive signals. *Ann Biomed Eng*, *38*(6), 2167-2182.

Dorozhkin, S. V. (2010). Nanosized and nanocrystalline calcium orthophosphates. *Acta Biomaterialia*, *6*(3), 715-734. https://doi.org/10.1016/j.actbio.2009.10.031

Dou, C. R., Perez, V., Qu, J., Tsin, A., Xu, B., & Li, J. Z. (2021). A State-of-the-Art Review of Laser-Assisted Bioprinting and its Future Research Trends. *Chembioeng Reviews*, *8*(5), 517-534. https://doi.org/10.1002/cben.202000037

Dou, Y. Y., Lin, Y., Wang, T. Y., Wang, X. Y., Jia, Y. L., & Zhao, C. P. (2021). The CAG promoter maintains high-level transgene expression in HEK293 cells. *Febs Open Bio*, *11*(1), 95-104. https://doi.org/10.1002/2211-5463.13029

Doube, M. a. M., M., Kłosowski, M., Arganda-Carreras, I., Cordelières, F., Dougherty, R., Jackson, J., . . . Shefelbine, S. (2010). BoneJ: Free and extensible bone image analysis in ImageJ. *Bone*, *47*(6), 1076-1079. https://doi.org/https://doi.org/10.1016/j.bone.2010.08.023

Durymanov, M., & Reineke, J. (2018). Non-viral Delivery of Nucleic Acids: Insight Into Mechanisms of Overcoming Intracellular Barriers. *Frontiers in Pharmacology*, *9*, Article 971. https://doi.org/10.3389/fphar.2018.00971

El-Sherbiny, I. M., & Yacoub, M. H. (2013). Hydrogel scaffolds for tissue engineering: Progress and challenges. *Glob Cardiol Sci Pract*, *2013*(3), 316-342. https://doi.org/10.5339/gcsp.2013.38

Endoh, M., Koibuchi, N., Sato, M., Morishita, R., Kanzaki, T., Murata, Y., & Kaneda, Y. (2002). Fetal gene transfer by intrauterine injection with microbubble-enhanced ultrasound. *Molecular Therapy*, *5*(5), 501-508. https://doi.org/10.1006/mthe.2002.0577

Engler, M. J., Lechner, R. L., & Richardson, C. C. (1983). REPLICATION OF BACTERIOPHAGE-T7 DEOXYRIBONUCLEIC-ACID .23. 2 FORMS OF THE DNA-POLYMERASE OF BACTERIOPHAGE-T7. *Journal of Biological Chemistry*, *258*(18), 1165-1173.

Ertl, P. F., & Thomsen, L. L. (2003). Technical issues in construction of nucleic acid vaccines. *Methods*, *31*(3), 199-206. https://doi.org/10.1016/s1046-2023(03)00134-8

Escoffre, J. M., Portet, T., Wasungu, L., Teissié, J., Dean, D., & Rols, M. P. (2009). What is (Still not) Known of the Mechanism by Which Electroporation Mediates Gene Transfer and Expression in Cells and Tissues. *Molecular Biotechnology*, *41*(3), 286-295. https://doi.org/10.1007/s12033-008-9121-0

Escoffre, J. M., Teissie, J., & Rols, M. P. (2010). Gene Transfer: How Can the Biological Barriers Be Overcome? *Journal of Membrane Biology*, *236*(1), 61-74. https://doi.org/10.1007/s00232-010-9275-0

Estes, B., Hsu, Y. R., Tam, L. T., Sheng, J., Stevens, J., & Haldankar, R. (2015). Uncovering Methods for the Prevention of Protein Aggregation and Improvement of Product Quality in a Transient Expression System. *Biotechnology Progress*, *31*(1), 258-267. https://doi.org/10.1002/btpr.2021

Evans, C., Morimitsu, Y., Nishi, R., Yoshida, M., & Takei, T. (2022). Novel hydrophobically modified agarose cryogels fabricated using dimethyl sulfoxide. *Journal of Bioscience and Bioengineering*, *133*(4), 390-395. https://doi.org/10.1016/j.jbiosc.2021.12.009

Evers, B. J., Van den Bosch, M. H. J., Blom, A. B., van der Kraan, P. M., Koëter, S., & Thurlings, R. M. (2022). Post-traumatic knee osteoarthritis; the role of inflammation and hemarthrosis on disease progression. *Frontiers in Medicine*, *9*, Article 973870. https://doi.org/10.3389/fmed.2022.973870

F.Boschetti, F., Peretti, G., Colombo, M., Cattaneo, S., Pietrabissa, R., F. Gervaso, F., & Fraschini, G. (2004). *Direct and indirect measurement of human articular cartilage permeability, in: 49th*

Annu. Meet. Orthop. Res. Soc., n.d., p. 293. https://api.semanticscholar.org/CorpusID:12354143

Fantoni, N. Z., El-Sagheer, A. H., & Brown, T. (2021). A Hitchhiker's Guide to Click-Chemistry with Nucleic Acids. *Chemical Reviews*, *121*(12), 7122-7154. https://doi.org/10.1021/acs.chemrev.0c00928

Feichtinger, G. A. (2016). Changing the Face of Modern Medicine: Stem Cells and Gene Therapy Florence, Italy October 18–21, 2016 Abstracts. *Human Gene Therapy*, *27*(11), A1-A185. https://doi.org/10.1089/hum.2016.29035.abstracts , note = PMID: 27749099

Feray, B. (2017). Gene Delivery by Hydroxyapatite and Calcium Phosphate Nanoparticles: A Review of Novel and Recent Applications. In T. Jagannathan (Ed.), *Hydroxyapatite*. IntechOpen. https://doi.org/10.5772/intechopen.71062

Fermor, H. L., Russell, S. L., Williams, S., Fisher, J., & Ingham, E. (2015). Development and characterisation of a decellularised bovine osteochondral biomaterial for cartilage repair. *Journal of Materials Science-Materials in Medicine*, *26*(5), Article 186. https://doi.org/10.1007/s10856-015-5517-0

Finnson, K. W., Chi, Y., Bou-Gharios, G., Leask, A., & Philip, A. (2012). TGF-beta signaling in cartilage homeostasis and osteoarthritis. *Fbs*, *4*(1), 251--268 , doi = 210.2741/s2266.

Finnson, K. W., Parker, W. L., ten Dijke, P., Thorikay, M., & Philip, A. (2008). ALK1 opposes ALK5/Smad3 signaling and expression of extracellular matrix components in human chondrocytes. *Journal of Bone and Mineral Research*, *23*(6), 896-906. https://doi.org/10.1359/jbmr.080209

Flink, J., Knudsen, H., & Jouan, N. (2002). *An introduction to freeze drying*. Jouan Nordic Allerød.

Forster, H., & Fisher, J. (1996). The influence of loading time and lubricant on the friction of articular cartilage. *Proc Inst Mech Eng H*, *210*(2), 109-119. https://doi.org/10.1243/pime_proc_1996_210_399_02

Fox. A, B. A., Rodeo.S. (2009). The Basic Science of Articular Cartilage: Structure, Composition, and Function. *Sports health*, *1*, 461-468. https://doi.org/10.1177/1941738109350438

Franck, D., Gil, E. S., Adam, R. M., Kaplan, D. L., Chung, Y. G., Estrada, C. R., & Mauney, J. R. (2013). Evaluation of Silk Biomaterials in Combination with Extracellular Matrix Coatings for Bladder Tissue Engineering with Primary and Pluripotent Cells. *Plos One*, *8*(2), Article e56237. https://doi.org/10.1371/journal.pone.0056237

Fraser, S. A., Crawford, A., Frazer, A., Dickinson, S., Hollander, A. P., Brook, I. M., & Hatton, P. V. (2006). Localization of type VI collagen in tissue-engineered cartilage on polymer scaffolds. *Tissue Engineering*, *12*(3), 569-577. https://doi.org/10.1089/ten.2006.12.569

Gaharwar, A. K., Kishore, V., Rivera, C., Bullock, W., Wu, C. J., Akkus, O., & Schmidt, G. (2012). Physically Crosslinked Nanocomposites from Silicate-Crosslinked PEO: Mechanical Properties and Osteogenic Differentiation of Human Mesenchymal Stem Cells. *Macromolecular Bioscience*, *12*(6), 779-793. https://doi.org/10.1002/mabi.201100508

Gao, B., Chen, L. H., Zhao, Y. L., Yan, X., Wang, X. Y., Zhou, C. R., . . . Xue, W. (2019). Methods to prepare. dopamine/polydopamine modified alginate hydrogels and their special improved properties for drug delivery. *European Polymer Journal*, *110*, 192-201. https://doi.org/10.1016/j.eurpolymj.2018.11.025

Garcia, A. J., Schwarzbauer, J. E., & Boettiger, D. (2002). Distinct activation states of alpha 5 beta 1 integrin show differential binding to RGD and synergy domains of fibronectin. *Biochemistry*, *41*(29), 9063-9069. https://doi.org/10.1021/bi025752f

Gauci, V. J., Padula, M. P., & Coorssen, J. R. (2013). Coomassie blue staining for high sensitivity gel-based proteomics. *Journal of Proteomics*, *90*, 96-106. https://doi.org/10.1016/j.jprot.2013.01.027

Gelehrter, T., Collins, F., & Ginsburg, D. (1998). Gene Therapy. In P. Kelly (Ed.), *Principles of Medical Genetics* (2nd ed., pp. 311-328). Williams & Wilkins.

Ghorbani, F., Kim, M., Monavari, M., Ghalandari, B., & Boccaccini, A. R. (2022). Mussel-inspired polydopamine decorated alginate dialdehyde-gelatin 3D printed scaffolds for bone tissue engineering application. *Frontiers in Bioengineering and Biotechnology*, *10*, Article 940070. https://doi.org/10.3389/fbioe.2022.940070

Ghorbani, F., Zamanian, A., & Aidun, A. (2019). Bioinspired polydopamine coating-assisted electrospun polyurethane-graphene oxide nanofibers for bone tissue engineering application. *Journal of Applied Polymer Science*, *136*(24), Article 47656. https://doi.org/10.1002/app.47656

Gibson, L. J. (1985). THE MECHANICAL-BEHAVIOR OF CANCELLOUS BONE. *Journal of Biomechanics*, *18*(5), 317-&. https://doi.org/10.1016/0021-9290(85)90287-8

Glyn-Jones, S., Palmer, A. J. R., Agricola, R., Price, A. J., Vincent, T. L., Weinans, H., & Carr, A. J. (2015). Osteoarthritis [Article]. *Lancet*, *386*(9991), 376-387. https://doi.org/10.1016/s0140-6736(14)60802-3

Goldring, M. B., & Goldring, S. R. (2010). Articular cartilage and subchondral bone in the pathogenesis of osteoarthritis [Article; Proceedings Paper]. *Skeletal Biology and Medicine*, *1192*, 230-237. https://doi.org/10.1111/j.1749-6632.2009.05240.x

Goldring, M. B., & Marcu, K. B. (2009). Cartilage homeostasis in health and rheumatic diseases. *Arthritis Research & Therapy*, *11*(3), Article 224. https://doi.org/10.1186/ar2592

Goldring, S. R. (2015). The osteocyte: key player in regulating bone turnover. *Rmd Open*, *1*, Article UNSP e000049. https://doi.org/10.1136/rmdopen-2015-000049

Gonçalves, A. M., Moreira, A., Weber, A., Williams, G. R., & Costa, P. F. (2021). Osteochondral Tissue Engineering: The Potential of Electrospinning and Additive Manufacturing. *Pharmaceutics*, *13*(7), Article 983. https://doi.org/10.3390/pharmaceutics13070983

Gorbachova, T., Melenevsky, Y., Cohen, M., & Cerniglia, B. W. (2018). Osteochondral Lesions of the Knee: Differentiating the Most Common Entities at MRI. *Radiographics*, *38*(5), 1478-1495. https://doi.org/10.1148/rg.2018180044

Gower, L. B. (2008). Biomimetic Model Systems for Investigating the Amorphous Precursor Pathway and Its Role in Biomineralization. *Chemical Reviews*, *108*(11), 4551-4627. https://doi.org/10.1021/cr800443h

Graham, F. L. (1988). A NEW TECHNIQUE FOR THE ASSAY OF INFECTIVITY OF HUMAN ADENOVIRUS-5 DNA [Article]. *Current Contents/Clinical Medicine*(46), 16-16.

Guastaferro, M., Baldino, L., Reverchon, E., & Cardea, S. (2021). Production of Porous Agarose-Based Structures: Freeze-Drying vs. Supercritical CO2 Drying. *Gels*, *7*(4), Article 198. https://doi.org/10.3390/gels7040198

Guilak, F., Alexopoulos, L. G., Upton, M. L., Youn, I., Choi, J. B., Cao, L., . . . Haider, M. A. (2006). The pericellular matrix as a transducer of biomechanical and biochemical signals in articular cartilage. *Skeletal Development and Remodeling in Health, Disease, and Aging*, *1068*, 498-512. https://doi.org/10.1196/annals.1346.011

Guler, S., Eichholz, K., Chariyev-Prinz, F., Pitacco, P., Aydin, H. M., Kelly, D. J., & Vargel, I. (2023). Biofabrication of Poly(glycerol sebacate) Scaffolds Functionalized with a Decellularized Bone Extracellular Matrix for Bone Tissue Engineering. *Bioengineering-Basel*, *10*(1), Article 30. https://doi.org/10.3390/bioengineering10010030

Guo, H. Q., & Torzilli, P. A. (2016). Shape of chondrocytes within articular cartilage affects the solid but not the fluid microenvironment under unconfined compression. *Acta Biomaterialia*, *29*, 170-179. https://doi.org/10.1016/j.actbio.2015.10.035

Guo, L., Wang, L. Y., Yang, R. H., Feng, R., Li, Z. G., Zhou, X., . . . Xu, X. H. (2017). Optimizing conditions for calcium phosphate mediated transient transfection. *Saudi Journal of Biological Sciences*, *24*(3), 622-629. https://doi.org/10.1016/j.sjbs.2017.01.034

Halib, N., Amin, M., Ahmad, I., Abrami, M., Fiorentino, S., Farra, R., . . . Grassi, M. (2014). Topological characterization of a bacterial cellulose-acrylic acid polymeric matrix. *European Journal of Pharmaceutical Sciences*, *62*, 326-333. https://doi.org/10.1016/j.ejps.2014.06.004

Hall, A., Lächelt, U., Bartek, J., Wagner, E., & Moghimi, S. M. (2017). Polyplex Evolution: Understanding Biology, Optimizing Performance. *Molecular Therapy*, *25*(7), 1476-1490. https://doi.org/10.1016/j.ymthe.2017.01.024

Han, Y. C., Wang, X. Y., Dai, H. L., & Li, S. P. (2012). Nanosize and Surface Charge Effects of Hydroxyapatite Nanoparticles on Red Blood Cell Suspensions. *Acs Applied Materials & Interfaces*, *4*(9), 4616-4622. https://doi.org/10.1021/am300992x

Hardee, C. L., Arevalo-Soliz, L. M., Hornstein, B. D., & Zechiedrich, L. (2017). Advances in Non-Viral DNA Vectors for Gene Therapy. *Genes*, *8*(2), Article 65. https://doi.org/10.3390/genes8020065

Hassan, S., Keshavarz-Moore, E., & Ward, J. (2016). A Cell Engineering Strategy to Enhance Supercoiled Plasmid DNA Production for Gene Therapy. *Biotechnology and Bioengineering*, *113*(9), 2064-2071. https://doi.org/10.1002/bit.25971

He, X. F., Li, W., Zhu, L. M., & Zhang, J. W. (2018). Investigation for effects of iNOS on biologics function of chondrocytes in rats with post-traumatic osteoarthritis. *European Review for Medical and Pharmacological Sciences*, *22*(21), 7140-7147.

Hebert, E. (2003). Improvement of exogenous DNA nuclear importation by nuclear localization signal-bearing vectors: a promising way for non-viral gene therapy? *Biology of the Cell*, *95*(2), 59-68. https://doi.org/10.1016/s0248-4900(03)00007-8

Hildner, F., Albrecht, C., Gabriel, C., Redl, H., & van Griensven, M. (2011). State of the art and future perspectives of articular cartilage regeneration: a focus on adipose-derived stem cells and platelet-derived products [Review]. *Journal of Tissue Engineering and Regenerative Medicine*, *5*(4), E36-E51. https://doi.org/10.1002/term.386

Ho, K. K. W., Chau, W. W., Lau, L. C. M., Ng, J. P., Chiu, K. H., & Ong, M. T. Y. (2023). Long-term survivorship and results in lower limb arthroplasty: a registry-based comparison study. *Bmc Musculoskeletal Disorders*, *24*(1), Article 307. https://doi.org/10.1186/s12891-023-06398-7

Hodges, B. L., Taylor, K. M., Joseph, M. F., Bourgeois, S. A., & Scheule, R. K. (2004). Long-term transgene expression from plasmid DNA gene therapy vectors is negatively affected by

CpG dinucleotides. *Molecular Therapy*, *10*(2), 269-278. https://doi.org/10.1016/j.ymthe.2004.04.018

Hoffman, A. S. (2012). Hydrogels for biomedical applications. *Advanced Drug Delivery Reviews*, *64*, 18-23. https://doi.org/10.1016/j.addr.2012.09.010

Hollister, S. J. (2005). Porous scaffold design for tissue engineering. *Nature Materials*, *4*(7), 518-524. https://doi.org/10.1038/nmat1421

Holmen, S. L., Vanbrocklin, M. W., Eversole, R. R., Stapleton, S. R., & Ginsberg, L. C. (1995). EFFICIENT LIPID-MEDIATED TRANSFECTION OF DNA INTO PRIMARY RAT HEPATOCYTES. *In Vitro Cellular & Developmental Biology-Animal*, *31*(5), 347-351.

Hossain, Z., Grattoni, C. A., Solymar, M., & Fabricius, I. L. (2011). Petrophysical properties of greensand as predicted from NMR measurements. *Petroleum Geoscience*, *17*(2), 111-125. https://doi.org/10.1144/1354-079309-038

Hou, X. D., Zhang, L., Zhou, Z. F., Luo, X., Wang, T. L., Zhao, X. Y., . . . Zheng, L. P. (2022). Calcium Phosphate-Based Biomaterials for Bone Repair. *Journal of Functional Biomaterials*, *13*(4), Article 187. https://doi.org/10.3390/jfb13040187

Howell, M., Liao, Q. T., & Gee, C. W. (2021). Surgical Management of Osteochondral Defects of the Knee: An Educational Review. *Current Reviews in Musculoskeletal Medicine*, *14*(1), 60-66. https://doi.org/10.1007/s12178-020-09685-1

Hsiao, C. T., Cheng, H. W., Huang, C. M., Li, H. R., Ou, M. H., Huang, J. R., . . . Kuo, J. C. (2017). Fibronectin in cell adhesion and migration via N-glycosylation. *Oncotarget*, *8*(41), 70653-70668. https://doi.org/10.18632/oncotarget.19969

Huang, M., Chen, Z. Y., Hu, S. J., Jia, F. J., Li, Z. J., Hoyt, G., . . . Wu, J. C. (2009). Novel Minicircle Vector for Gene Therapy in Murine Myocardial Infarction. *Circulation*, *120*(11), S230-S237. https://doi.org/10.1161/circulationaha.108.841155

Hunter, D. J., McDougall, J. J., & Keefe, F. J. (2008). The symptoms of osteoarthritis and the genesis of pain. *Rheumatic Disease Clinics of North America*, *34*(3), 623-+. https://doi.org/10.1016/j.rdc.2008.05.004

Hunziker, E. B. (2002). Articular cartilage repair: basic science and clinical progress. A review of the current status and prospects [Review]. *Osteoarthritis and Cartilage*, *10*(6), 432-463. https://doi.org/10.1053/joca.2002.0801

Hunziker, E. B., & Driesang, I. M. K. (2003). Functional barrier principle for growth-factor-based articular cartilage repair. *Osteoarthritis and Cartilage*, *11*(5), 320-327. https://doi.org/10.1016/s1063-4584(03)00031-1

Hunziker, E. B., Lippuner, K., Keel, M. J. B., & Shintani, N. (2015). An educational review of cartilage repair: precepts & practice - myths & misconceptions - progress & prospects. *Osteoarthritis and Cartilage*, *23*(3), 334-350. https://doi.org/10.1016/j.joca.2014.12.011

Ip, J. E., Wu, Y. J., Huang, J., Zhang, L. N., Pratt, R. E., & Dzau, V. J. (2007). Mesenchymal stem cells use integrin β1 not CXC chemokine receptor 4 for myocardial migration

and engraftment. *Molecular Biology of the Cell*, *18*(8), 2873-2882. https://doi.org/10.1091/mbc.E07-02-0166

James, S., Fox, J., Afsari, F., Lee, J., Clough, S., Knight, C., . . . Genever, P. (2015). Multiparameter Analysis of Human Bone Marrow Stromal Cells Identifies Distinct Immunomodulatory and Differentiation-Competent Subtypes. *Stem Cell Reports*, *4*(6), 1004-1015. https://doi.org/10.1016/j.stemcr.2015.05.005

Jechlinger, W. (2006). Optimization and delivery of plasmid DNA for vaccination. *Expert Review of Vaccines*, *5*(6), 803-825. https://doi.org/10.1586/14760584.5.6.803

Jeon, S. Y., Park, J. S., Yang, H. N., Woo, D. G., & Park, K. H. (2012). Co-delivery of SOX9 genes and anti-Cbfa-1 siRNA coated onto PLGA nanoparticles for chondrogenesis of human MSCs [Article]. *Biomaterials*, *33*(17), 4413-4423. https://doi.org/10.1016/j.biomaterials.2012.02.051

Ji, W., Sun, Y., Yang, F., van den Beucken, J., Fan, M. W., Chen, Z., & Jansen, J. A. (2011). Bioactive Electrospun Scaffolds Delivering Growth Factors and Genes for Tissue Engineering Applications. *Pharmaceutical Research*, *28*(6), 1259-1272. https://doi.org/10.1007/s11095-010-0320-6

Jiang, F., Xu, X. W., Chen, F. Q., Weng, H. F., Chen, J., Ru, Y., . . . Xiao, A. F. (2023). Extraction, Modification and Biomedical Application of Agarose Hydrogels: A Review. *Marine Drugs*, *21*(5), Article 299. https://doi.org/10.3390/md21050299

Jiang, J. H., Zhu, L. P., Zhu, L. J., Zhu, B. K., & Xu, Y. Y. (2011). Surface Characteristics of a Self-Polymerized Dopamine Coating Deposited on Hydrophobic Polymer Films. *Langmuir*, *27*(23), 14180-14187. https://doi.org/10.1021/la202877k

Jiang, X. O., Yu, H., Teo, C. R., Tan, G. S. X., Goh, S. C., Patel, P., . . . Patzel, V. (2016). Advanced Design of Dumbbell-shaped Genetic Minimal Vectors Improves Non-coding and Coding RNA Expression. *Molecular Therapy*, *24*(9), 1581-1591. https://doi.org/10.1038/mt.2016.138

Jiang, Y. H., Lou, Y. Y., Li, T. H., Liu, B. Z., Chen, K., Zhang, D., & Li, T. (2022). Review Article Cross-linking methods of type I collagen-based scaffolds for cartilage tissue engineering. *American Journal of Translational Research*, *14*(2), 1146-1159.

Jin, M., Shi, J. L., Zhu, W. Z., Yao, H., & Wang, D. A. (2021). Polysaccharide-Based Biomaterials in Tissue Engineering: A Review. *Tissue Engineering Part B-Reviews*, *27*(6), 604-626. https://doi.org/10.1089/ten.teb.2020.0208

Jordan, M., Schallhorn, A., & Wurm, F. M. (1996). Transfecting mammalian cells: Optimization of critical parameters affecting calcium-phosphate precipitate formation. *Nucleic Acids Research*, *24*(4), 596-601. https://doi.org/10.1093/nar/24.4.596

Julin, J., Jämsen, E., Puolakka, T., Konttinen, Y. T., & Moilanen, T. (2010). Younger age increases the risk of early prosthesis failure following primary total knee replacement for osteoarthritis A follow-up study of 32,019 total knee replacements in the Finnish

Arthroplasty Register. *Acta Orthopaedica*, *81*(4), 413-419. https://doi.org/10.3109/17453674.2010.501747

Kamitakahara, M., Kimura, K., & Ioku, K. (2012). Synthesis of nanosized porous hydroxyapatite granules in hydrogel by electrophoresis. *Colloids Surf B Biointerfaces*, *97*, 236-239.

Kane, R., & Ma, P. X. (2013). Mimicking the nanostructure of bone matrix to regenerate bone. *Materials Today*, *16*(11), 418-423. https://doi.org/10.1016/j.mattod.2013.11.001

Karuppal, R. (2017). Current concepts in the articular cartilage repair and regeneration. *Journal of Orthopaedics*, *14*(2), A1-A3. https://doi.org/10.1016/j.jor.2017.05.001

Kasper, F. K., Jerkins, E., Tanahashi, K., Barry, M. A., Tabata, Y., & Mikos, A. G. (2006). Characterization of DNA release from composites of oligo(poly(ethylene glycol) fumarate) and cationized gelatin microspheres in vitro. *Journal of Biomedical Materials Research Part A*, *78A*(4), 823-835. https://doi.org/10.1002/jbm.a.30736

Kasper, J. C., Schaffert, D., Ogris, M., Wagner, E., & Friess, W. (2011). Development of a lyophilized plasmid/LPEI polyplex formulation with long-term stability-A step closer from promising technology to application. *Journal of Controlled Release*, *151*(3), 246-255. https://doi.org/10.1016/j.jconrel.2011.01.003

Katayama, T., Chigi, Y., & Okamura, D. (2023). The ensured proliferative capacity of myoblast in serum-reduced conditions with Methyl-β-cyclodextrin. *Frontiers in Cell and Developmental Biology*, *11*, Article 1193634. https://doi.org/10.3389/fcell.2023.1193634

Katta, J., Jin, Z. M., Ingham, E., & Fisher, J. (2008). Biotribology of articular cartilage-A review of the recent advances. *Medical Engineering & Physics*, *30*(10), 1349-1363. https://doi.org/10.1016/j.medengphy.2008.09.004

Keeney, M., Chung, M. T., Zielins, E. R., Paik, K. J., McArdle, A., Morrison, S. D., . . . Yang, F. (2016). Scaffold-mediated BMP-2 minicircle DNA delivery accelerated bone repair in a mouse critical-size calvarial defect model. *Journal of Biomedical Materials Research Part A*, *104*(8), 2099-2107. https://doi.org/10.1002/jbm.a.35735

Kenkre, J. S., & Bassett, J. H. D. (2018). The bone remodelling cycle. *Annals of Clinical Biochemistry*, *55*(3), 308-327. https://doi.org/10.1177/0004563218759371

Kennedy, O. D., Laudier, D. M., Majeska, R. J., Sun, H. B., & Schaffler, M. B. (2014). Osteocyte apoptosis is required for production of osteoclastogenic signals following bone fatigue in vivo. *Bone*, *64*, 132-137. https://doi.org/10.1016/j.bone.2014.03.049

Khan, M. A., Wu, V. M., Ghosh, S., & Uskokovic, V. (2016). Gene delivery using calcium phosphate nanoparticles: Optimization of the transfection process and the effects of citrate and poly(L-lysine) as additives. *Journal of Colloid and Interface Science*, *471*, 48-58. https://doi.org/10.1016/j.jcis.2016.03.007

Kim, H. K. W., Moran, M. E., & Salter, R. B. (1991). THE POTENTIAL FOR REGENERATION OF ARTICULAR-CARTILAGE IN DEFECTS CREATED BY CHONDRAL SHAVING AND SUBCHONDRAL ABRASION - AN

EXPERIMENTAL INVESTIGATION IN RABBITS [Article]. *Journal of Bone and Joint Surgery-American Volume*, *73A*(9), 1301-1315. https://doi.org/10.2106/00004623-199173090-00004

Kim, S., English, A. E., & Kihm, K. D. (2009). Surface elasticity and charge concentration-dependent endothelial cell attachment to copolymer polyelectrolyte hydrogel. *Acta Biomaterialia*, *5*(1), 144-151. https://doi.org/10.1016/j.actbio.2008.07.033

Kim, T. K., & Eberwine, J. H. (2010). Mammalian cell transfection: the present and the future. *Analytical and Bioanalytical Chemistry*, *397*(8), 3173-3178. https://doi.org/10.1007/s00216-010-3821-6

Kimura, K., Kamitakahara, M., Yokoi, T., & Ioku, K. (2018). Formation Process of Hydroxyapatite Granules in Agarose Hydrogel by Electrophoresis. *Crystal Growth & Design*, *18*(4), 1961-1966. https://doi.org/10.1021/acs.cgc1.7b01154

Kish, G., Módis, L., & Hangody, L. (1999). Osteochondral mosaicplasty for the treatment of focal chondral and osteochondral lesions of the knee and talus in the athlete -: Rationale, indications, techniques, and results. *Clinics in Sports Medicine*, *18*(1), 45-+. https://doi.org/10.1016/s0278-5919(05)70129-0

Klatt, A. R., Klinger, G., Neumüller, O., Eidenmüller, B., Wagner, I., Acbenbach, T., . . . Bartnik, E. (2006). TAK1 downregulation reduces IL-1β induced expression of MMP13, MMP1 and TNF-alpha. *Biomedicine & Pharmacotherapy*, *60*(2), 55-61. https://doi.org/10.1016/j.biopha.2005.08.007

Klinman, D. M. (2004). Immunotherapeutic uses of CpG oligodeoxynucleotides. *Nature Reviews Immunology*, *4*(4), 248-257. https://doi.org/10.1038/nri1329

Kolhe, P., Amend, E., & Singh, S. K. (2010). Impact of Freezing on pH of Buffered Solutions and Consequences for Monoclonal Antibody Aggregation. *Biotechnology Progress*, *26*(3), 727-733. https://doi.org/10.1002/btpr.377

Kosik-Koziol, A., Heljak, M., & Swieszkowski, W. (2020). Mechanical properties of hybrid triphasic scaffolds for osteochondral tissue engineering. *Materials Letters*, *261*, Article 126893. https://doi.org/10.1016/j.matlet.2019.126893

Kreiss, P., Cameron, B., Rangara, R., Mailhe, P., Aguerre-Charriol, O., Airiau, M., . . . Pitard, B. (1999). Plasmid DNA size does not affect the physicochemical properties of lipoplexes but modulates gene transfer efficiency. *Nucleic Acids Res*, *27*(19), 3792-3798. https://doi.org/10.1093/nar/27.19.3792

Krishani, M., Shin, W. Y., Suhaimi, H., & Sambudi, N. S. (2023). Development of Scaffolds from Bio-Based Natural Materials for Tissue Regeneration Applications: A Review. *Gels*, *9*(2), Article 100. https://doi.org/10.3390/gels9020100

Ku, S. H., & Park, C. B. (2010). Human endothelial cell growth on mussel-inspired nanofiber scaffold for vascular tissue engineering. *Biomaterials*, *31*(36), 9431-9437. https://doi.org/10.1016/j.biomaterials.2010.08.071

Ku, S. H., Ryu, J., Hong, S. K., Lee, H., & Park, C. B. (2010). General functionalization route for cell adhesion on non-wetting surfaces. *Biomaterials*, *31*(9), 2535-2541. https://doi.org/10.1016/j.biomaterials.2009.12.020

Kumari, J., & Kumar, A. (2017). Development of polymer based cryogel matrix for transportation and storage of mammalian cells. *Scientific Reports*, *7*, Article 41551. https://doi.org/10.1038/srep41551

Kumari, M., Bhardwaj, B., Kumar, D., Bhattacharyya, R., & Banerjee, D. (2021). Coomassie Brilliant Blue Can Visualize a Protein Band Without Destaining: A Quick Visualization Protocol on the Agarose Gel. *Indian Journal of Clinical Biochemistry*, *36*(2), 248-249. https://doi.org/10.1007/s12291-020-00874-w

Laird, N. Z., Acri, T. M., Tingle, K., & Salem, A. K. (2021). Gene- and RNAi-activated scaffolds for bone tissue engineering: Current progress and future directions. *Advanced Drug Delivery Reviews*, *174*, 613-627. https://doi.org/10.1016/j.addr.2021.05.009

Lam, A. P., & Dean, D. A. (2010). Progress and prospects: nuclear import of nonviral vectors. *Gene Therapy*, *17*(4), 439-447. https://doi.org/10.1038/gt.2010.31

Langer, R., & Vacanti, J. P. (1993). Tissue engineering. *Science*, *260*(5110), 920-926. https://doi.org/10.1126/science.8493529

Lawson, A. C., & Czernuszka, J. T. (1998). Collagen-calcium phosphate composites. *Proceedings of the Institution of Mechanical Engineers Part H-Journal of Engineering in Medicine*, *212*(H6), 413-425. https://doi.org/10.1243/0954411981534187

Ledo, A. M., Senra, A., Rilo-Alvarez, H., Borrajo, E., Vidal, A., Alonso, M. J., & Garcia-Fuentes, M. (2020). mRNA-activated matrices encoding transcription factors as primers of cell differentiation in tissue engineering. *Biomaterials*, *247*, Article 120016. https://doi.org/10.1016/j.biomaterials.2020.120016

Lee, H., Rho, J., & Messersmith, P. B. (2009). Facile Conjugation of Biomolecules onto Surfaces via Mussel Adhesive Protein Inspired Coatings. *Advanced Materials*, *21*(4), 431-+. https://doi.org/10.1002/adma.200801222

Lee, J. J., Park, I. S., Shin, G. S., Lyu, S. K., Ahn, S. G., Bae, T. S., & Lee, M. H. (2014). Effects of Polydopamine Coating on the Bioactivity of Titanium for Dental Implants. *International Journal of Precision Engineering and Manufacturing*, *15*(8), 1647-1655. https://doi.org/10.1007/s12541-014-0515-6

Lee, K. A., Ng, H. Y., Wei, L., & Shen, Y. (2018). 3D functional scaffolds for cartilage tissue engineering. In K. Ying Deng and Jordan (Ed.), *Functional 3D Tissue Engineering Scaffolds* (pp. 391-421). Woodhead Publishing. https://doi.org/https://doi.org/10.1016/B978-0-08-100979-6.00016-1

Lee, Y. H., Wu, H. C., Yeh, C. W., Kuan, C. H., Liao, H. T., Hsu, H. C., . . . Wang, T. W. (2017). Enzyme-crosslinked gene-activated matrix for the induction of mesenchymal stem cells

in osteochondral tissue regeneration. *Acta Biomater*, *63*, 210-226. https://doi.org/10.1016/j.actbio.2017.09.008

Lees, S., & Prostak, K. (1988). THE LOCUS OF MINERAL CRYSTALLITES IN BONE. *Connective Tissue Research*, *18*(1), 41-54. https://doi.org/10.3109/03008208809019071

Lei, Y. G., Huang, S. X., Sharif-Kashani, P., Chen, Y., Kavehpour, P., & Segura, T. (2010). Incorporation of active DNA/cationic polymer polyplexes into hydrogel scaffolds. *Biomaterials*, *31*(34), 9106-9116. https://doi.org/10.1016/j.biomaterials.2010.08.016

Lei, Y. G., Rahim, M., Ng, Q., & Segura, T. (2011). Hyaluronic acid and fibrin hydrogels with concentrated DNA/PEI polyplexes for local gene delivery. *Journal of Controlled Release*, *153*(3), 255-261. https://doi.org/10.1016/j.jconrel.2011.01.028

Leng, P., Ding, C. R., Zhang, H. N., & Wang, Y. Z. (2012). Reconstruct large osteochondral defects of the knee with hIGF-1 gene enhanced Mosaicplasty. *Knee*, *19*(6), 804-811. https://doi.org/10.1016/j.knee.2012.03.009

Leonard, A. C., & Mechali, M. (2013). DNA Replication Origins. *Cold Spring Harbor Perspectives in Biology*, *5*(10), Article a010116. https://doi.org/10.1101/cshperspect.a010116

Lepage, S. I. M., Robson, N., Gilmore, H., Davis, O., Hooper, A., St John, S., . . . Koch, T. G. (2019). Beyond Cartilage Repair: The Role of the Osteochondral Unit in Joint Health and Disease. *Tissue Engineering Part B-Reviews*, *25*(2), 114-125. https://doi.org/10.1089/ten.teb.2018.0122

Lerner, U. H. (2012). Osteoblasts, Osteoclasts, and Osteocytes: Unveiling Their Intimate-Associated Responses to Applied Orthodontic Forces. *Seminars in Orthodontics*, *18*(4), 237-248. https://doi.org/https://doi.org/10.1053/j.sodo.2012.06.002

Lesage, C., Lafont, M., Guihard, P., Weiss, P., Guicheux, J., & Delplace, V. (2022). Material-Assisted Strategies for Osteochondral Defect Repair. *Advanced Science*, *9*(16), Article 2200050. https://doi.org/10.1002/advs.202200050

Li, B., Li, F. F., Ma, L., Yang, J. Z., Wang, C. F., Wang, D. A., & Gao, C. Y. (2014). Poly(lactide-co-glycolide)/Fibrin Gel Construct as a 3D Model to Evaluate Gene Therapy of Cartilage in Vivo. *Molecular Pharmaceutics*, *11*(7), 2062-2070. https://doi.org/10.1021/mp5000136

Li, C., & Arakawa, T. (2019). Agarose native gel electrophoresis of proteins. *International Journal of Biological Macromolecules*, *140*, 668-671. https://doi.org/10.1016/j.ijbiomac.2019.08.066

Li, C. C., Ouyang, L. L., Armstrong, J. P., & Stevens, M. M. (2021). Advances in the Fabrication of Biomaterials for Gradient Tissue Engineering. *Trends in Biotechnology*, *39*(2), 150-164. https://doi.org/10.1016/j.tibtech.2020.06.005

Li, C. Y., Song, J. A., Wang, Y. P., Shi, Y., Ji, J. Y., Lin, Q., & Liu, Y. M. (2022). Adhesion and proliferation of bone marrow stromal cells on acellular spinal cord scaffolds. *International Journal of Neuroscience*. https://doi.org/10.1080/00207454.2022.2155155

Li, J., Chen, Y. C., Tseng, Y. C., Mozumdar, S., & Huang, L. (2010). Biodegradable calcium phosphate nanoparticle with lipid coating for systemic siRNA delivery. *Journal of Controlled Release*, *142*(3), 416-421. https://doi.org/10.1016/j.jconrel.2009.11.008

Li, J., Sha, Y. J., Seswita-Zilda, D., Hu, Q. S., & He, P. Q. (2014). Purification and Characterization of Thermostable Agarase from Bacillus sp BI-3, a Thermophilic Bacterium Isolated from Hot Spring. *Journal of Microbiology and Biotechnology*, *24*(1), 19-25. https://doi.org/10.4014/jmb.1308.08055

Li, J. Q., Wang, Q. K., Gu, Y. B., Zhu, Y., Chen, L., & Chen, Y. F. (2017). Production of Composite Scaffold Containing Silk Fibroin, Chitosan, and Gelatin for 3D Cell Culture and Bone Tissue Regeneration. *Medical Science Monitor*, *23*, 5311-5320. https://doi.org/10.12659/msm.905085

Li, J. Y., & Mooney, D. J. (2016). Designing hydrogels for controlled drug delivery. *Nature Reviews Materials*, *1*(12), Article 16071. https://doi.org/10.1038/natrevmats.2016.71

Li, S., & Huang, L. (2000). Nonviral gene therapy: promises and challenges. *Gene Therapy*, *7*(1), 31-34. https://doi.org/10.1038/sj.gt.3301110

Li, X. M., Sun, Q. Q., Li, Q., Kawazoe, N., & Chen, G. P. (2018). Functional Hydrogels With Tunable Structures and Properties for Tissue Engineering Applications. *Frontiers in Chemistry*, *6*, Article 499. https://doi.org/10.3389/fchem.2018.00499

Liacini, A., Sylvester, J., Li, W. Q., Huang, W. S., Dehnade, F., Ahmad, M., & Zafarullah, M. (2003). Induction of matrix metalloproteinase-13 gene expression by TNF-α is mediated by MAP kinases, AP-1, and NF-κB transcription factors in articular chondrocytes. *Experimental Cell Research*, *288*(1), 208-217. https://doi.org/10.1016/s0014-4827(03)00180-0

Lin, C. W., Jan, M. S., Kuo, J. H. S., Hsu, L. J., & Lin, Y. S. (2012). Protective role of autophagy in branched polyethylenimine (25K)- and poly(L-lysine) (30-70K)-induced cell death. *European Journal of Pharmaceutical Sciences*, *47*(5), 865-874. https://doi.org/10.1016/j.ejps.2012.09.007

Lin, K. L., Wu, C. T., & Chang, J. (2014). Advances in synthesis of calcium phosphate crystals with controlled size and shape. *Acta Biomaterialia*, *10*(10), 4071-4102. https://doi.org/10.1016/j.actbio.2014.06.017

Lin, W. F., Liu, Z., Kampf, N., & Klein, J. (2020). The Role of Hyaluronic Acid in Cartilage Boundary Lubrication. *Cells*, *9*(7), Article 1606. https://doi.org/10.3390/cells9071606

Link, J. M., Salinas, E. Y., Hu, J. C., & Athanasiou, K. A. (2020). The tribology of cartilage: Mechanisms, experimental techniques, and relevance to translational tissue engineering. *Clinical Biomechanics*, *79*, Article 104880. https://doi.org/10.1016/j.clinbiomech.2019.10.016

Linnemann, A. K., & Krawetz, S. A. (2009). Silencing by nuclear matrix attachment distinguishes cell-type specificity: association with increased proliferation capacity. *Nucleic Acids Research*, *37*(9), 2779-2788. https://doi.org/10.1093/nar/gkp135

Liu, Z. H., Jiao, Y. P., Wang, Y. F., Zhou, C. R., & Zhang, Z. Y. (2008). Polysaccharides-based nanoparticles as drug delivery systems. *Advanced Drug Delivery Reviews*, *60*(15), 1650-1662. https://doi.org/10.1016/j.addr.2008.09.001

Lo, C. W., Lin, Z. H., Ueno, M., Romero-Lopez, M., Maruyama, M., Kohno, Y., . . . Goodman, S. B. (2019). Optimization and Characterization of Calcium Phosphate Transfection in Mesenchymal Stem Cells. *Tissue Engineering Part C-Methods*, *25*(9), 543-552. https://doi.org/10.1089/ten.tec.2019.0147

Loh, Q. L., & Choong, C. (2013). Three-Dimensional Scaffolds for Tissue Engineering Applications: Role of Porosity and Pore Size. *Tissue Engineering Part B-Reviews*, *19*(6), 485-502. https://doi.org/10.1089/ten.teb.2012.0437

Loozen, L. D., Wegman, F., Öner, F. C., Dhert, W. J. A., & Alblas, J. (2013). Porous bioprinted constructs in BMP-2 non-viral gene therapy for bone tissue engineering. *Journal of Materials Chemistry B*, *1*(48), 6619-6626. https://doi.org/10.1039/c3tb21093f

Losina, E., & Katz, J. N. (2012). Total knee arthroplasty on the rise in younger patients: Are we sure that past performance will guarantee future success? *Arthritis and Rheumatism*, *64*(2), 339-341. https://doi.org/10.1002/art.33371

Lu, L. C., Zhu, X., Valenzuela, R. G., Currier, B. L., & Yaszemski, M. J. (2001). Biodegradable polymer scaffolds for cartilage tissue engineering. *Clinical Orthopaedics and Related Research*(391), S251-S270.

Lukacs, G. L., Haggie, P., Seksek, O., Lechardeur, D., Freedman, N., & Verkman, A. S. (2000). Size-dependent DNA mobility in cytoplasm and nucleus. *Journal of Biological Chemistry*, *275*(3), 1625-1629. https://doi.org/10.1074/jbc.275.3.1625

Lungwitz, U., Breunig, M., Blunk, T., & Göpferich, A. (2005). Polyethylenimine-based non-viral gene delivery systems. *European Journal of Pharmaceutics and Biopharmaceutics*, *60*(2), 247-266. https://doi.org/10.1016/j.ejpb.2004.11.011

Luo, D., & Saltzman, W. M. (2000). Synthetic DNA delivery systems. *Nature Biotechnology*, *18*(1), 33-37. https://doi.org/10.1038/71889

Luo, J., Li, C. X., Chen, J. L., Wang, G., Gao, R., & Gu, Z. W. (2015). An efficient method for in vitro gene delivery via regulation of cellular endocytosis pathway. *International Journal of Nanomedicine*, *10*, 1667-1677. https://doi.org/10.2147/ijn.s77527

Maaloum, M., Pernodet, N., & Tinland, B. (1998). Agarose gel structure using atomic force microscopy: Gel concentration and ionic strength effects. *Electrophoresis*, *19*(10), 1606-1610. https://doi.org/10.1002/elps.1150191015

MacIntosh, A. C., Kearns, V. R., Crawford, A., & Hatton, P. V. (2008). Skeletal tissue engineering using silk biomaterials. *Journal of Tissue Engineering and Regenerative Medicine*, *2*(2-3), 71-80. https://doi.org/10.1002/term.68

Madry, H., van Dijk, C. N., & Mueller-Gerbl, M. (2010). The basic science of the subchondral bone [Article; Proceedings Paper]. *Knee Surgery Sports Traumatology Arthroscopy*, *18*(4), 419-433. https://doi.org/10.1007/s00167-010-1054-z

Madry, H., Venkatesan, J. K., Carballo-Pedrares, N., Rey-Rico, A., & Cucchiarini, M. (2020). Scaffold-Mediated Gene Delivery for Osteochondral Repair. *Pharmaceutics*, *12*(10), Article 930. https://doi.org/10.3390/pharmaceutics12100930

Magalhaes, J., Crawford, A., Hatton, P. V., Blanco, F. J., & Roman, J. S. (2014). Poly(2-ethyl-(2-pyrrolidone) methacrylate) and hyaluronic acid-based hydrogels for the engineering of a cartilage-like tissue using bovine articular chondrocytes. *Journal of Bioactive and Compatible Polymers*, *29*(6), 545-559. https://doi.org/10.1177/0883911514555609

Mahajan, S., & Tang, T. (2019). Polyethylenimine-DNA Ratio Strongly Affects Their Nanoparticle Formation: A Large-Scale Coarse-Grained Molecular Dynamics Study. *Journal of Physical Chemistry B*, *123*(45), 9629-9640. https://doi.org/10.1021/acs.jpcb.9b07031

Maia, C. R., Annichino, R. F., Munhoz, M. D., Machado, E. G., Marchi, E., & Castano-Betancourt, M. C. (2023). Post-traumatic osteoarthritis: the worst associated injuries and differences in patients' profile when compared with primary osteoarthritis. *Bmc Musculoskeletal Disorders*, *24*(1), Article 568. https://doi.org/10.1186/s12891-023-06663-9

Mairhofer, J., & Grabherr, R. (2008). Rational vector design for efficient non-viral gene delivery: Challenges facing the use of plasmid DNA. *Molecular Biotechnology*, *39*(2), 97-104. https://doi.org/10.1007/s12033-008-9046-7

Maitra, A. (2005). Calcium phosphate nanoparticles: second-generation nonviral vectors in gene therapy. *Expert Review of Molecular Diagnostics*, *5*(6), 893-905. https://doi.org/10.1586/14737159.5.6.893

Maitz, M. F. (2015). Applications of synthetic polymers in clinical medicine. *Biosurface and Biotribology*, *1*(3), 161-176. https://doi.org/https://doi.org/10.1016/j.bsbt.2015.08.002

Makadia, H. K., & Siegel, S. J. (2011). Poly Lactic-co-Glycolic Acid (PLGA) as Biodegradable Controlled Drug Delivery Carrier. *Polymers*, *3*(3), 1377-1397. https://doi.org/10.3390/polym3031377

Mancino, R., Caccavo, D., Barba, A. A., Lamberti, G., Biasin, A., Cortesi, A., . . . Abrami, M. (2023). Agarose Cryogels: Production Process Modeling and Structural Characterization. *Gels*, *9*(9). https://doi.org/10.3390/gels9090765

Mansour, J. M. (2003). Biomechanics of cartilage. *Kinesiology: the mechanics and pathomechanics of human movement*, *2*, 66-79.

Mardon, H. J., & Grant, K. E. (1994). THE ROLE OF THE 9TH AND 10TH TYPE-III DOMAINS OF HUMAN FIBRONECTIN IN CELL-ADHESION. *Febs Letters*, *340*(3), 197-201. https://doi.org/10.1016/0014-5793(94)80137-1

Mark, J. K. K., Lim, C. S. Y., Nordin, F., & Tye, G. J. (2022). Expression of mammalian proteins for diagnostics and therapeutics: a review. *Molecular Biology Reports*, *49*(11), 10593-10608. https://doi.org/10.1007/s11033-022-07651-3

Markowicz, A., Koellensperger, E., Steffens, G. C. M., Frentz, M., Schrage, N., & Pallua, N. (2006). The impact of vacuum freeze-drying on collagen sponges after gas plasma sterilization. *Journal of Biomaterials Science-Polymer Edition*, *17*(1-2), 61-75. https://doi.org/10.1163/156856206774879135

Maroudas, A., & Venn, M. (1977). CHEMICAL COMPOSITION AND SWELLING OF NORMAL AND OSTEOARTHROTIC FEMORAL-HEAD CARTILAGE .2. SWELLING. *Annals of the Rheumatic Diseases*, *36*(5), 399-406. https://doi.org/10.1136/ard.36.5.399

Martin, I., Miot, S., Barbero, A., Jakob, M., & Wendt, D. (2007). Osteochondral tissue engineering. *Journal of Biomechanics*, *40*(4), 750-765. https://doi.org/https://doi.org/10.1016/j.jbiomech.2006.03.008

Martin, R. B., & Ishida, J. (1989). THE RELATIVE EFFECTS OF COLLAGEN FIBER ORIENTATION, POROSITY, DENSITY, AND MINERALIZATION ON BONE STRENGTH. *Journal of Biomechanics*, *22*(5), 419-&. https://doi.org/10.1016/0021-9290(89)90202-9

Meilander, N. J., Pasumarthy, M. K., Kowalczyk, T. H., Cooper, M. J., & Bellamkonda, R. V. (2003). Sustained release of plasmid DNA using lipid microtubules and agarose hydrogel. *Journal of Controlled Release*, *88*(2), 321-331. https://doi.org/10.1016/s0168-3659(03)00007-5

Meng, Z. X., Zeng, Q. T., Sun, Z. Z., Xu, X. X., Wang, Y. S., Zheng, W., & Zheng, Y. F. (2012). Immobilizing natural macromolecule on PLGA electrospun nanofiber with surface entrapment and entrapment-graft techniques. *Colloids and Surfaces B-Biointerfaces*, *94*, 44-50. https://doi.org/10.1016/j.colsurfb.2012.01.017

Mensink, M. A., Frijlink, H. W., Maarschalk, K. V., & Hinrichs, W. L. J. (2017). How sugars protect proteins in the solid state and during drying (review): Mechanisms of stabilization in relation to stress conditions. *European Journal of Pharmaceutics and Biopharmaceutics*, *114*, 288-295. https://doi.org/10.1016/j.ejpb.2017.01.024

Mercey, E., Obeid, P., Glaise, D., Calvo-Munoz, M. L., Guguen-Guillouzo, C., & Fouque, B. (2010). The application of 3D micropatterning of agarose substrate for cell culture and in situ comet assays. *Biomaterials*, *31*(12), 3156-3165. https://doi.org/10.1016/j.biomaterials.2010.01.020

Merivaara, A., Zini, J., Koivunotko, E., Valkonen, S., Korhonen, O., Fernandes, F. M., & Yliperttula, M. (2021). Preservation of biomaterials and cells by freeze-drying: Change of paradigm. *Journal of Controlled Release*, *336*, 480-498. https://doi.org/10.1016/j.jconrel.2021.06.042

Merril, C. (1990). Gel-staining techniques. In P. D. Murray (Ed.), *Guide to Protein Purification* (Vol. 182, pp. 477-488). Academic Press. https://doi.org/https://doi.org/10.1016/0076-6879(90)82038-4

Miguel, S. P., Ribeiro, M. P., Brancal, H., Coutinho, P., & Correia, I. J. (2014). Thermoresponsive chitosan-agarose hydrogel for skin regeneration. *Carbohydrate Polymers*, *111*, 366-373. https://doi.org/10.1016/j.carbpol.2014.04.093

Mikos, A. G., Bao, Y., Cima, L. G., Ingber, D. E., Vacanti, J. P., & Langer, R. (1993). PREPARATION OF POLY(GLYCOLIC ACID) BONDED FIBER STRUCTURES FOR CELL ATTACHMENT AND TRANSPLANTATION. *Journal of Biomedical Materials Research*, *27*(2), 183-189. https://doi.org/10.1002/jbm.820270207

Miller, A. M., & Dean, D. A. (2009). Tissue-specific and transcription factor-mediated nuclear entry of DNA. *Advanced Drug Delivery Reviews*, *61*(7-8), 603-613. https://doi.org/10.1016/j.addr.2009.02.008

Mirtaghavi, A., Luo, J. K., & Muthuraj, R. (2020). Recent Advances in Porous 3D Cellulose Aerogels for Tissue Engineering Applications: A Review. *Journal of Composites Science*, *4*(4), Article 152. https://doi.org/10.3390/jcs4040152

Mithoefer, K., McAdams, T., Williams, R. J., Kreuz, P. C., & Mandelbaum, B. R. (2009). Clinical Efficacy of the Microfracture Technique for Articular Cartilage Repair in the Knee An Evidence-Based Systematic Analysis. *American Journal of Sports Medicine*, *37*(10), 2053-2063. https://doi.org/10.1177/0363546508328414

Mithoefer, K., Peterson, L., Zenobi-Wong, M., & Mandelbaum, B. R. (2015). Cartilage issues in football-today's problems and tomorrow's solutions. *British Journal of Sports Medicine*, *49*(9), 590-U548. https://doi.org/10.1136/bjsports-2015-094772

Miyazaki, J., Takaki, S., Araki, K., Tashiro, F., Tominaga, A., Takatsu, K., & Yamamura, K. (1989). Expression vector system based on the chicken beta-actin promoter directs efficient production of interleukin-5. *Gene*, *79*(2), 269-277, Article 1989.

Moghimi, S. M., Symonds, P., Murray, J. C., Hunter, A. C., Debska, G., & Szewczyk, A. (2005). A two-stage poly(ethylenimine)-mediated cytotoxicity: Implications for gene transfer/therapy. *Molecular Therapy*, *11*(6), 990-995. https://doi.org/10.1016/j.ymthe.2005.02.010

Mohamed, A. M. (2008). An overview of bone cells and their regulating factors of differentiation. *Malays J Med Sci*, *15*(1), 4-12.

Mohan, N., Gupta, V., Sridharan, B., Sutherland, A., & Detamore, M. S. (2014). The Potential of Encapsulating "Raw Materials" in 3D Osteochondral Gradient Scaffolds. *Biotechnology and Bioengineering*, *111*(4), 829-841. https://doi.org/10.1002/bit.25145

Mosher, D. F. (1984). PHYSIOLOGY OF FIBRONECTIN. *Annual Review of Medicine*, *35*, 561-575. https://doi.org/10.1146/annurev.me.35.020184.003021

Motohashi, K. (2019). Development of highly sensitive and low-cost DNA agarose gel electrophoresis detection systems, and evaluation of non-mutagenic and loading dye-type DNA-staining reagents. *Plos One*, *14*(9), Article e0222209. https://doi.org/10.1371/journal.pone.0222209

Murphy, C. M., Haugh, M. G., & O'Brien, F. J. (2010). The effect of mean pore size on cell attachment, proliferation and migration in collagen-glycosaminoglycan scaffolds for bone tissue engineering. *Biomaterials*, *31*(3), 461-466. https://doi.org/10.1016/j.biomaterials.2009.09.063

Murphy, C. M., O'Brien, F. J., Little, D. G., & Schindeler, A. (2013). CELL-SCAFFOLD INTERACTIONS IN THE BONE TISSUE ENGINEERING TRIAD [Article]. *European Cells & Materials*, *26*, 120-132. https://doi.org/10.22203/eCM.v026a09

Musante, L., Candiano, G., & Ghiggeri, G. M. (1998). Resolution of fibronectin and other uncharacterized proteins by two-dimensional polyacrylamide electrophoresis with thiourea. *Journal of Chromatography B*, *705*(2), 351-356. https://doi.org/10.1016/s0378-4347(97)00545-8

Narayanan, J., Xiong, J. Y., & Liu, X. Y. (2005, Jul 03-08). Determination of agarose gel pore size: Absorbance measurements vis a vis other techniques.*Journal of Physics Conference Series* [International conference on materials for advanced technologies (icmat 2005)]. 3rd International Conference on Materials for Advanced Technologies (ICMAT-2005)/9th International Conference on Advanced Materials (ICAM 2005), Singapore, SINGAPORE.

Natenstedt, J., Kok, A. C., Dankelman, J., & Tuijthof, G. J. (2015). What quantitative mechanical loading stimulates in vitro cultivation best? *J Exp Orthop*, *2*(1), 15. https://doi.org/10.1186/s40634-015-0029-x

Needham, C. J., Shah, S. R., Dahlin, R. L., Kinard, L. A., Lam, J., Watson, B. M., . . . Mikos, A. G. (2014). Osteochondral tissue regeneration through polymeric delivery of DNA encoding for the SOX trio and RUNX2. *Acta Biomaterialia*, *10*(10), 4103-4112. https://doi.org/10.1016/j.actbio.2014.05.011

Ng, K. W., Kugler, L. E., Doty, S. B., Ateshian, G. A., & Hung, C. T. (2009). Scaffold degradation elevates the Collagen content and dynamic compressive modulus in engineered articular cartilage. *Osteoarthritis and Cartilage*, *17*(2), 220-227. https://doi.org/10.1016/j.joca.2008.06.013

Nguyen, D. N., Raghavan, S. S., Tashima, L. M., Lin, E. C., Fredette, S. J., Langer, R. S., & Wang, C. (2008). Enhancement of poly(orthoester) microspheres for DNA vaccine delivery by blending with poly(ethylenimine). *Biomaterials*, *29*(18), 2783-2793. https://doi.org/10.1016/j.biomaterials.2008.03.011

Nguyen, T. P. T., Li, F. Y., Shrestha, S., Tuan, R. S., Thissen, H., Forsythe, J. S., & Frith, J. E. (2021). Cell-laden injectable microgels: Current status and future prospects for cartilage regeneration. *Biomaterials*, *279*, Article 121214. https://doi.org/10.1016/j.biomaterials.2021.121214

Nie, H., Ho, M. L., Wang, C. K., Wang, C. H., & Fu, Y. C. (2009). BMP-2 plasmid loaded PLGA/HAp composite scaffolds for treatment of bone defects in nude mice. *Biomaterials*, *30*(5), 892-901. https://doi.org/10.1016/j.biomaterials.2008.10.029

Nowak, D., & Jakubczyk, E. (2020). The Freeze-Drying of Foods-The Characteristic of the Process Course and the Effect of Its Parameters on the Physical Properties of Food Materials. *Foods*, *9*(10), Article 1488. https://doi.org/10.3390/foods9101488

Nwankwo, C. S., Okpomor, E. O., Dibagar, N., Wodecki, M., Zwierz, W., & Figiel, A. (2023). Recent Developments in the Hybridization of the Freeze-Drying Technique in Food Dehydration: A Review on Chemical and Sensory Qualities. *Foods*, *12*(18), Article 3437. https://doi.org/10.3390/foods12183437

O'Brien, F. J. (2011). Biomaterials & scaffolds for tissue engineering [Article]. *Materials Today*, *14*(3), 88-95. https://doi.org/10.1016/s1369-7021(11)70058-x

O'Brien, F. J., Harley, B. A., Waller, M. A., Yannas, I. V., Gibson, L. J., & Prendergast, P. J. (2007). The effect of pore size on permeability and cell attachment in collagen scaffolds for tissue engineering. *Technol Health Care*, *15*(1), 3-17.

Oftadeh, R., Perez-Viloria, M., Villa-Camacho, J. C., Vaziri, A., & Nazarian, A. (2015). Biomechanics and Mechanobiology of Trabecular Bone: A Review. *Journal of Biomechanical Engineering-Transactions of the Asme*, *137*(1), Article 010802. https://doi.org/10.1115/1.4029176

Ogura, T., Merkely, G., Bryant, T., Winalski, C. S., & Minas, T. (2019). Autologous Chondrocyte Implantation "Segmental-Sandwich" Technique for Deep Osteochondral Defects in the Knee: Clinical Outcomes and Correlation With Magnetic Resonance Imaging Findings. *Orthopaedic Journal of Sports Medicine*, *7*(5), Article 2325967119847173. https://doi.org/10.1177/2325967119847173

Oh, Y. K., Suh, D., Kim, J. M., Choi, H. G., Shin, K., & Ko, J. J. (2002). Polyethylenimine-mediated cellular uptake, nucleus trafficking and expression of cytokine plasmid DNA. *Gene Therapy*, *9*(23), 1627-1632. https://doi.org/10.1038/sj.gt.3301735

Ohno, M., Fornerod, M., & Mattaj, I. W. (1998). Nucleocytoplasmic transport: The last 200 nanometers [Review]. *Cell*, *92*(3), 327-336. https://doi.org/10.1016/s0092-8674(00)80926-5

Olton, D., Li, J. H., Wilson, M. E., Rogers, T., Close, J., Huang, L., . . . Sfeir, C. (2007). Nanostructured calcium phosphates (NanoCaPs) for non-viral gene delivery: Influence of the synthesis parameters on transfection efficiency [Article]. *Biomaterials*, *28*(6), 1267-1279. https://doi.org/10.1016/j.biomaterials.2006.10.026

Olton, D. Y. E., Close, J. M., Sfeir, C. S., & Kumta, P. N. (2011). Intracellular trafficking pathways involved in the gene transfer of nano-structured calcium phosphate-DNA particles. *Biomaterials*, *32*(30), 7662-7670. https://doi.org/10.1016/j.biomaterials.2011.01.043

Orafa, Z., Irani, S., Zamanian, A., Bakhshi, H., Nikukar, H., & Ghalandari, B. (2021). Coating of Laponite on PLA Nanofibrous for Bone Tissue Engineering Application. *Macromolecular Research*, *29*(3), 191-198. https://doi.org/10.1007/s13233-021-9028-1

Orimo, H. (2010). The Mechanism of Mineralization and the Role of Alkaline Phosphatase in Health and Disease. *Journal of Nippon Medical School*, *77*(1), 4-12. https://doi.org/10.1272/jnms.77.4

Orrantia, E., & Chang, P. L. (1990). INTRACELLULAR-DISTRIBUTION OF DNA INTERNALIZED THROUGH CALCIUM-PHOSPHATE PRECIPITATION. *Experimental Cell Research*, *190*(2), 170-174. https://doi.org/10.1016/0014-4827(90)90181-9

Oyane, A., Murayama, M., Yamazaki, A., Sogo, Y., Ito, A., & Tsurushima, H. (2010). Fibronectin-DNA-apatite composite layer for highly efficient and area-specific gene transfer. *Journal of Biomedical Materials Research Part A*, *92A*(3), 1038-1047. https://doi.org/10.1002/jbm.a.32449

Oyane, A., Wang, X. P., Sogo, Y., Ito, A., & Tsurushima, H. (2012). Calcium phosphate composite layers for surface-mediated gene transfer. *Acta Biomaterialia*, *8*(6), 2034-2046. https://doi.org/10.1016/j.actbio.2012.02.003

Ozmeriç, A., Alemdaroğlu, K. B., & Aydoğan, N. H. (2014). Treatment for cartilage injuries of the knee with a new treatment algorithm. *World J Orthop*, *5*(5), 677-684. https://doi.org/10.5312/wjo.v5.i5.677

Pahle, J., & Walther, W. (2016). Vectors and strategies for nonviral cancer gene therapy. *Expert Opinion on Biological Therapy*, *16*(4), 443-461. https://doi.org/10.1517/14712598.2016.1134480

Palomino-Durand, C., Pauthe, E., & Gand, A. (2021). Fibronectin-Enriched Biomaterials, Biofunctionalization, and Proactivity: A Review. *Applied Sciences-Basel*, *11*(24), Article 12111. https://doi.org/10.3390/app112412111

Pan, J., Zhou, X. Z., Li, W., Novotny, J. E., Doty, S. B., & Wang, L. Y. (2009). In Situ Measurement of Transport between Subchondral Bone and Articular Cartilage [Article]. *Journal of Orthopaedic Research*, *27*(10), 1347-1352. https://doi.org/10.1002/jor.20883

Parisi, C., Salvatore, L., Veschini, L., Serra, M. P., Hobbs, C., Madaghiele, M., . . . Di Silvio, L. (2020). Biomimetic gradient scaffold of collagen-hydroxyapatite for osteochondral

regeneration. *Journal of Tissue Engineering*, *11*, Article 2041731419896068. https://doi.org/10.1177/2041731419896068

Park, S. J., Goodman, M. B., Pruitt, B. L., & Ieee. (2005, May 12-15). Measurement of mechanical properties of Caenorhabditis elegans with a piezoresistive microcantilever system.*IEEE Engineering in Medicine and Biology Society Annual Conference (EMBS)* [2005 3rd ieee/embs special topic conference on microtechnology in medicine and biology]. 3rd IEEE/EMBS Special Topic Conference on Microtechnology in Medicine and Biology, Oahu, HI.

Parveen, S., Krishnakumar, K., & Sahoo, S. (2006). New era in health care: tissue engineering. *J Stem Cells Regen Med*, *1*(1), 8-24. https://doi.org/10.46582/jsrm.0101003

Pawaskar, S. S., Fisher, J., & Jin, Z. M. (2010). Robust and General Method for Determining Surface Fluid Flow Boundary Conditions in Articular Cartilage Contact Mechanics Modeling. *Journal of Biomechanical Engineering-Transactions of the Asme*, *132*(3), Article 031001. https://doi.org/10.1115/1.4000869

Pedraza, C. E., Bassett, D. C., McKee, M. D., Nelea, V., Gbureck, U., & Barralet, J. E. (2008). The importance of particle size and DNA condensation salt for calcium phosphate nanoparticle transfection [Article]. *Biomaterials*, *29*(23), 3384-3392. https://doi.org/10.1016/j.biomaterials.2008.04.043

Pezzoli, D., Giupponi, E., Mantovani, D., & Candiani, G. (2017). Size matters for in vitro gene delivery: investigating the relationships among complexation protocol, transfection medium, size and sedimentation. *Scientific Reports*, *7*, Article 44134. https://doi.org/10.1038/srep44134

Place, E. S., George, J. H., Williams, C. K., & Stevens, M. M. (2009). Synthetic polymer scaffolds for tissue engineering. *Chemical Society Reviews*, *38*(4), 1139-1151. https://doi.org/10.1039/b811392k

Poole, C. A., Flint, M. H., & Beaumont, B. W. (1987). CHONDRONS IN CARTILAGE - ULTRASTRUCTURAL ANALYSIS OF THE PERICELLULAR MICROENVIRONMENT IN ADULT HUMAN ARTICULAR CARTILAGES. *Journal of Orthopaedic Research*, *5*(4), 509-522. https://doi.org/10.1002/jor.1100050406

Potapov, V., & Ong, J. L. (2017). Examining Sources of Error in PCR by Single-Molecule Sequencing. *Plos One*, *12*(1), Article e0169774. https://doi.org/10.1371/journal.pone.0169774

Pouton, C. W., & Seymour, L. W. (1998). Key issues in non-viral gene delivery. *Advanced Drug Delivery Reviews*, *34*(1), 3-19. https://doi.org/10.1016/s0169-409x(98)00048-9

Qian, L., & Zhang, H. F. (2011). Controlled freezing and freeze drying: a versatile route for porous and micro-/nano-structured materials. *Journal of Chemical Technology and Biotechnology*, *86*(2), 172-184. https://doi.org/10.1002/jctb.2495

Qiao, Z. Y., Hou, C. Y., Zhao, W. J., Zhang, D., Yang, P. P., Wang, L., & Wang, H. (2015). Synthesis of self-reporting polymeric nanoparticles for in situ monitoring of endocytic microenvironmental pH. *Chemical Communications*, *51*(63), 12609-12612. https://doi.org/10.1039/c5cc03752b

Quinn, T. M., Häuselmann, H. J., Shintani, N., & Hunziker, E. B. (2013). Cell and matrix morphology in articular cartilage from adult human knee and ankle joints suggests depth-associated adaptations to biomechanical and anatomical roles. *Osteoarthritis and Cartilage*, *21*(12), 1904-1912. https://doi.org/10.1016/j.joca.2013.09.011

Rainer, A., Centola, M., Spadaccio, C., Gherardi, G., Genovese, J. A., Licoccia, S., & Trombetta, M. (2010). Comparative study of different techniques for the sterilization of poly-L-lactide electrospun microfibers: effectiveness vs. material degradation. *International Journal of Artificial Organs*, *33*(2), 76-85.

Ramzan, F., Salim, A., & Khan, I. (2023). Osteochondral Tissue Engineering Dilemma: Scaffolding Trends in Regenerative Medicine. *Stem Cell Reviews and Reports*, *19*(6), 1615-1634. https://doi.org/10.1007/s12015-023-10545-x

Randolph, T. W. (1997). Phase separation of excipients during lyophilization: Effects on protein stability. *Journal of Pharmaceutical Sciences*, *86*(11), 1198-1203. https://doi.org/10.1021/js970135b

Rediguieri, C. F., Sassonia, R. C., Dua, K., Kikuchi, I. S., & Pinto, T. D. A. (2016). Impact of sterilization methods on electrospun scaffolds for tissue engineering. *European Polymer Journal*, *82*, 181-195. https://doi.org/10.1016/j.eurpolymj.2016.07.016

Redman, S. N., Oldfield, S. F., & Archer, C. W. (2005). Current strategies for articular cartilage repair. *Eur Cell Mater*, *9*, 23-32; discussion 23-32. https://doi.org/10.22203/ecm.v009a04

Robert, H. (2011). Chondral repair of the knee joint using mosaicplasty. *Orthopaedics & Traumatology-Surgery & Research*, *97*(4), 418-429. https://doi.org/10.1016/j.otsr.2011.04.001

Roberts, K., Walter, P., Green, M. R., & Sambrook, J. (2015). *Molecular Cloning A Laboratory Manual Fourth Edition*

Rodriguez, H., & Akman, S. A. (1998). Large scale isolation of genes as DNA fragment lengths by continuous elution electrophoresis through an agarose matrix. *Electrophoresis*, *19*(5), 646-652. https://doi.org/10.1002/elps.1150190506

Rodríguez, E. G. (2004). Nonviral DNA vectors for immunization and therapy:: design and methods for their obtention. *Journal of Molecular Medicine-Jmm*, *82*(8), 500-509. https://doi.org/10.1007/s00109-004-0548-x

Roeder, R. K., Converse, G. L., Kane, R. J., & Yue, W. M. (2008). Hydroxyapatite-reinforced polymer biocomposites for synthetic bone substitutes. *Jom*, *60*(3), 38-45. https://doi.org/10.1007/s11837-008-0030-2

Roman, M. D., Russu, O., Mohor, C., Necula, R., Boicean, A., Todor, A., & Fleaca, S. R. (2022). Outcomes in revision total knee arthroplasty (Review). *Experimental and Therapeutic Medicine*, *23*(1), Article 29. https://doi.org/10.3892/etm.2021.10951

Rybacki, E., Reinicke, A., Meier, T., Makasi, M., & Dresen, G. (2015). What controls the mechanical properties of shale rocks? - Part I: Strength and Young's modulus. *Journal of Petroleum Science and Engineering*, *135*, 702-722. https://doi.org/10.1016/j.petrol.2015.10.028

Sahay, G., Alakhova, D. Y., & Kabanov, A. V. (2010). Endocytosis of nanomedicines. *Journal of Controlled Release*, *145*(3), 182-195. https://doi.org/10.1016/j.jconrel.2010.01.036

Sakurai, F., Nishioka, T., Saito, H., Baba, T., Okuda, A., Matsumoto, O., . . . Hashida, M. (2001). Interaction between DNA-cationic liposome complexes and erythrocytes is an important factor in systemic gene transfer via the intravenous route in mice: the role of the neutral helper lipid. *Gene Therapy*, *8*(9), 677-686. https://doi.org/10.1038/sj.gt.3301460

Salati, M. A., Khazai, J., Tahmuri, A. M., Samadi, A., Taghizadeh, A., Taghizadeh, M., . . . Mozafari, M. (2020). Agarose-Based Biomaterials: Opportunities and Challenges in Cartilage Tissue Engineering. *Polymers*, *12*(5), Article 1150. https://doi.org/10.3390/polym12051150

Sambrook, J. (2001). *Molecular cloning : a laboratory manual*. Third edition. Cold Spring Harbor, N.Y. : Cold Spring Harbor Laboratory Press, [2001] ©2001.

Samrot, A. V., Sathiyasree, M., Rahim, S. B. A., Renitta, R. E., Kasipandian, K., Shree, S. K., . . . Chinni, S. V. (2023). Scaffold Using Chitosan, Agarose, Cellulose, Dextran and Protein for Tissue Engineering-A Review. *Polymers*, *15*(6), Article 1525. https://doi.org/10.3390/polym15061525

Sanchez-Salcedo, S., Nieto, A., & Vallet-Regi, M. (2008). Hydroxyapatite/beta-tricalcium phosphate/agarose macroporous scaffolds for bone tissue engineering. *Chemical Engineering Journal*, *137*(1), 62-71. https://doi.org/10.1016/j.cej.2007.09.011

Saris, D. B. F., Vanlauwe, J., Victor, J., Almqvist, K. F., Verdonk, R., Bellemans, J., . . . Grp, E. X. T. S. (2009). Treatment of Symptomatic Cartilage Defects of the Knee: Characterized Chondrocyte Implantation Results in Better Clinical Outcome at 36 Months in a Randomized Trial Compared to Microfracture. *American Journal of Sports Medicine*, *37*, 10S-19S. https://doi.org/10.1177/0363546509350694

Scanzello, C. R., & Goldring, S. R. (2012). The role of synovitis in osteoarthritis pathogenesis. *Bone*, *51*(2), 249-257. https://doi.org/10.1016/j.bone.2012.02.012

Schakowski, F., Gorschluter, M., Buttgereit, P., Marten, A., Lilienfeld-Toal, M. V., Junghans, C., . . . Schmidt-Wolf, I. G. H. (2007). Minimal size MIDGE vectors improve transgene expression in vivo. *In Vivo*, *21*(1), 17-23.

Schakowski, F., Gorschluter, M., Junghans, C., Schroff, M., Buttgereit, P., Ziske, C., . . . Schmidt-Wolf, I. G. H. (2001). A novel minimal-size vector (MIDGE) improves transgene expression in colon carcinoma cells and avoids transfection of undesired DNA [Article]. *Molecular Therapy*, *3*(5), 793-800. https://doi.org/10.1006/mthe.2001.0322

Schenker, M. L., Mauck, R. L., Ahn, J., & Mehta, S. (2014). Pathogenesis and Prevention of Posttraumatic Osteoarthritis After Intra-articular Fracture. *Journal of the American Academy of Orthopaedic Surgeons*, *22*(1), 20-28. https://doi.org/10.5435/jaaos-22-01-20

Schmidt, M. (2005). MIDGE Vectors and dSLIM Immunomodulators: DNA-based Molecules for Gene Therapeutic Strategies. In: Knä blein J, Muller (eds) Modern Biopharmaceutical. Wiley-VCH Verlag, Weinheim, pp 1-29. In B. W. Voltz, B. (Ed.).

Schmidt, M., Volz, B., Großmann, P., Heinrich, K., & Wittig, B. (2015). MIDGE Technology for the Production of a Fourfold Gene-Modified, Allogenic Cell-Based Vaccine for Cancer Therapy. In W. Walther & U. Stein (Eds.), *Gene Therapy of Solid Cancers: Methods and Protocols* (pp. 39-51). Springer New York. https://doi.org/10.1007/978-1-4939-2727-2_3

Schmidt, M., Volz, B., & Wittig, B. (2005). MIDGE Vectors and dSLIM Immunomodulators: DNA-based Molecules for Gene Therapeutic Strategies. In *Modern Biopharmaceuticals* (pp. 183-211). https://doi.org/https://doi.org/10.1002/9783527620982.ch7

Schnödt, M., Schmeer, M., Kracher, B., Krüsemann, C., Espinosa, L. E., Grünert, A., . . . Büning, H. (2016). DNA Minicircle Technology Improves Purity of Adeno-associated Viral Vector Preparations. *Molecular Therapy-Nucleic Acids*, *5*, Article e355. https://doi.org/10.1038/mtna.016.60

Schubert, C., van Langeveld, M. C., & Donoso, L. A. (2014). Innovations in 3D printing: a 3D overview from optics to organs. *British Journal of Ophthalmology*, *98*(2), 159-161. https://doi.org/10.1136/bjophthalmol-2013-304446

Selim, M., Bullock, A. J., Blackwood, K. A., Chapple, C. R., & MacNeil, S. (2011). Developing biodegradable scaffolds for tissue engineering of the urethra. *Bju International*, *107*(2), 296-302. https://doi.org/10.1111/j.1464-410X.2010.09310.x

Seo, S., Mahapatra, C., Singh, R., Knowles, J., & Kim, H. (2014). Strategies for osteochondral repair: Focus on scaffolds. *Journal of Tissue Engineering*, *5*, 2041731414541850. https://doi.org/10.1177/2041731414541850

Shah. M, K. K., Meislin. R, Bosco. J. (2007). Articular cartilage restoration of the knee. *Bulletin of the NYU hospital for joint diseases*, *65*, 51-60.

Sharma, A., Khamar, D., Cullen, S., Hayden, A., & Hughes, H. (2021). Innovative Drying Technologies for Biopharmaceuticals. *International Journal of Pharmaceutics*, *609*, Article 121115. https://doi.org/10.1016/j.ijpharm.2021.121115

Shen, H., Tan, J., & Saltzman, W. M. (2004). Surface-mediated gene transfer from nanocomposites of controlled texture. *Nature Materials*, *3*(8), 569-574. https://doi.org/10.1038/nmat1179

Shepherd, D. E. T., & Seedhom, B. B. (1999). Thickness of human articular cartilage in joints of the lower limb. *Annals of the Rheumatic Diseases*, *58*(1), 27-34. https://doi.org/10.1136/ard.58.1.27

Shi, S. L., Chan, A. G., Mercer, S., Eckert, G. J., & Trippel, S. B. (2014). Endogenous versus Exogenous Growth Factor Regulation of Articular Chondrocytes. *Journal of Orthopaedic Research*, *32*(1), 54-60. https://doi.org/10.1002/jor.22444

Siddiqui, N., Asawa, S., Birru, B., Baadhe, R., & Rao, S. (2018). PCL-Based Composite Scaffold Matrices for Tissue Engineering Applications. *Molecular Biotechnology*, *60*(7), 506-532. https://doi.org/10.1007/s12033-018-0084-5

Silver, F. H., Bradica, G., & Tria, A. (2002). Elastic energy storage in human articular cartilage: estimation of the elastic modulus for type II collagen and changes associated with osteoarthritis. *Matrix Biology*, *21*(2), 129-137, Article Pii s0945-053x(01)00195-0. https://doi.org/10.1016/s0945-053x(01)00195-0

Singh, Y. P., Bhardwaj, N., & Mandal, B. B. (2016). Potential of Agarose/Silk Fibroin Blended Hydrogel for in Vitro Cartilage Tissue Engineering. *Acs Applied Materials & Interfaces*, *8*(33), 21236-21249. https://doi.org/10.1021/acsami.6b08285

Slattery, C., & Kweon, C. Y. (2018). Classifications in Brief: Outerbridge Classification of Chondral Lesions. *Clinical Orthopaedics and Related Research*, *476*(10), 2101-2104. https://doi.org/10.1007/s11999.0000000000000255

Sokolova, V. V., Radtke, I., Heumann, R., & Epple, M. (2006). Effective transfection of cells with multi-shell calcium phosphate-DNA nanoparticles. *Biomaterials*, *27*(16), 3147-3153. https://doi.org/10.1016/j.biomaterials.2005.12.030

Steadman. JR, R. W., Singleton. S, Briggs. K. (1997). Microfracture technique for full-thickness chondral defects: Technique and clinical results. *Operative Techniques in Orthopaedics*, *7*(4), 300 - 304. https://doi.org/https://doi.org/10.1016/S1048-6666(97)80033-X

Stella, J. A., D'Amore, A., Wagner, W. R., & Sacks, M. S. (2010). On the biomechanical function of scaffolds for engineering load-bearing soft tissues. *Acta Biomaterialia*, *6*(7), 2365-2381. https://doi.org/10.1016/j.actbio.2010.01.001

Stellwagen, N. C., & Stellwagen, E. (2009). Effect of the matrix on DNA electrophoretic mobility. *Journal of Chromatography A*, *1216*(10), 1917-1929. https://doi.org/10.1016/j.chroma.2008.11.090

Stokols, S., Sakamoto, J., Breckon, C., Holt, T., Weiss, J., & Tuszynski, M. H. (2006). Templated agarose scaffolds support linear axonal regeneration. *Tissue Engineering*, *12*(10), 2777-2787. https://doi.org/10.1089/ten.2006.12.2777

Su, T., Zhang, M. Y., Zeng, Q. K., Pan, W. H., Huang, Y. J., Qian, Y. N., . . . Shen, J. L. (2021). Mussel-inspired agarose hydrogel scaffolds for skin tissue engineering. *Bioactive Materials*, *6*(3), 579-588. https://doi.org/10.1016/j.bioactmat.2020.09.004

Suamte, L., Tirkey, A., Barman, J., & Jayasekhar Babu, P. (2023). Various manufacturing methods and ideal properties of scaffolds for tissue engineering applications. *Smart Materials in Manufacturing*, *1*, 100011. https://doi.org/https://doi.org/10.1016/j.smmf.2022.100011

Suchanek, W., & Yoshimura, M. (1998). Processing and properties of hydroxyapatite-based biomaterials for use as hard tissue replacement implants. *Journal of Materials Research*, *13*(1), 94-117. https://doi.org/10.1557/jmr.1998.0015

Suner, S. S., Demirci, S., Yetiskin, B., Fakhrullin, R., Naumenko, E., Okay, O., . . . Sahiner, N. (2019). Cryogel composites based on hyaluronic acid and halloysite nanotubes as scaffold for tissue engineering. *International Journal of Biological Macromolecules*, *130*, 627-635. https://doi.org/10.1016/j.ijbiomac.2019.03.025

Surowiec, R. K., Allen, M. R., & Wallace, J. M. (2022). Bone hydration: How we can evaluate it, what can it tell us, and is it an effective therapeutic target? *Bone Rep*, *16*, 101161. https://doi.org/10.1016/j.bonr.2021.101161

Swieszkowski, W., Tuan, B. H. S., Kurzydlowski, K. J., & Hutmacher, D. W. (2007). Repair and regeneration of osteochondral defects in the articular joints. *Biomolecular Engineering*, *24*(5), 489-495. https://doi.org/10.1016/j.bioeng.2007.07.014

Szybalski, W., Kim, S. C., Hasan, N., & Podhajska, A. J. (1991). CLASS-IIS RESTRICTION ENZYMES - A REVIEW. *Gene*, *100*, 13-26. https://doi.org/10.1016/0378-1119(91)90345-c

Tallawi, M., Rosellini, E., Barbani, N., Cascone, M. G., Rai, R., Saint-Pierre, G., & Boccaccini, A. R. (2015). Strategies for the chemical and biological functionalization of scaffolds for cardiac tissue engineering: a review. *Journal of the Royal Society Interface*, *12*(108), Article 20150254. https://doi.org/10.1098/rsif.2015.0254

Tang, S. Q., Yang, W., & Mao, X. (2007). Agarose/collagen composite scaffold as an anti-adhesive sheet. *Biomedical Materials*, *2*(3), S129-S134. https://doi.org/10.1088/1748-6041/2/3/s09

Tatman, P. D., Gerull, W., Sweeney-Easter, S., Davis, J. I., Gee, A. O., & Kim, D. H. (2015). Multiscale Biofabrication of Articular Cartilage: Bioinspired and Biomimetic Approaches. *Tissue Engineering Part B-Reviews*, *21*(6), 543-559. https://doi.org/10.1089/ten.teb.2015.0142

te Nijenhuis, K. (1997). Agarose. *Thermoreversible Networks: Viscoelastic Properties and Structure of Gels*, 194-202.

Thomas, A. C., Hubbard-Turner, T., Wikstrom, E. A., & Palmieri-Smith, R. M. (2017). Epidemiology of Posttraumatic Osteoarthritis. *Journal of Athletic Training*, *52*(6), 491-496. https://doi.org/10.4085/1062-6050-51.5.08

Tian, J. J., Paterson, T. E., Zhang, J. J., Li, Y. X., Ouyang, H., Asencio, I. O., . . . Li, Z. (2023). Enhanced Antibacterial Ability of Electrospun PCL Scaffolds Incorporating ZnO Nanowires. *International Journal of Molecular Sciences*, *24*(19), Article 14420. https://doi.org/10.3390/ijms241914420

Tie, J. K., & Stafford, D. W. (2017). Functional Study of the Vitamin K Cycle Enzymes in Live Cells. *Enzymology at the Membrane Interface: Intramembrane Proteases*, *584*, 349-394. https://doi.org/10.1016/bs.mie.2016.10.015

Tierney, E. G., Duffy, G. P., Cryan, S. A., Curtin, C. M., & O'Brien, F. J. (2013). Non-viral gene-activated matrices Next generation constructs for bone repair. *Organogenesis*, *9*(1), 22-28. https://doi.org/10.4161/org.24329

Tierney, E. G., Duffy, G. P., Hibbitts, A. J., Cryan, S. A., & O'Brien, F. J. (2012). The development of non-viral gene-activated matrices for bone regeneration using polyethyleneimine (PEI) and collagen-based scaffolds. *Journal of Controlled Release*, *158*(2), 304-311. https://doi.org/10.1016/j.jconrel.2011.11.026

Tolabi, H., Bakhtiary, N., Sayadi, S., Tamaddon, M., Ghorbani, F., Boccaccini, A. R., & Liu, C. (2022). A critical review on polydopamine surface-modified scaffolds in musculoskeletal regeneration. *Front Bioeng Biotechnol*, *10*, 1008360. https://doi.org/10.3389/fbioe.2022.1008360

Tolmachov, O. (2009). Designing plasmid vectors. *Methods Mol Biol*, *542*, 117-129. https://doi.org/10.1007/978-1-59745-561-9_6

Tomas, H., Alves, C. S., & Rodrigues, J. (2018). Laponite (R) : A key nanoplatform for biomedical applications? *Nanomedicine-Nanotechnology Biology and Medicine*, *14*(7), 2407-2420. https://doi.org/10.1016/j.nano.2017.04.016

Tomioka, Y., Arakawa, T., Akuta, T., Nakagawa, M., & Ishibashi, M. (2022). Analysis of proteins by agarose native gel electrophoresis in the presence of solvent additives. *International Journal of Biological Macromolecules*, *198*, 26-36. https://doi.org/10.1016/j.ijbiomac.2021.12.084

Tong, H. J., Wang, C. D., Huang, Y., Shi, Q., Fernandes, J. C., Dai, K. R., . . . Zhang, X. L. (2013). Polyethylenimine(600)-beta-cyclodextrin: a promising nanopolymer for nonviral gene delivery of primary mesenchymal stem cells. *International Journal of Nanomedicine*, *8*, 1935-1946. https://doi.org/10.2147/ijn.s43074

Trenkenschuh, E., & Friess, W. (2021). Freeze-drying of nanoparticles: How to overcome colloidal instability by formulation and process optimization. *European Journal of Pharmaceutics and Biopharmaceutics*, *165*, 345-360. https://doi.org/10.1016/j.ejpb.2021.05.024

Truong, N. F., Lesher-Perez, S. C., Kurt, E., & Segura, T. (2019). Pathways Governing Polyethylenimine Polyplex Transfection in Microporous Annealed Particle Scaffolds.

Bioconjugate Chemistry, *30*(2), 476-486. https://doi.org/10.1021/acs.bioconjchem.8b00696

Tsai, W. B., Chen, W. T., Chien, H. W., Kuo, W. H., & Wang, M. J. (2011). Poly(dopamine) coating of scaffolds for articular cartilage tissue engineering. *Acta Biomaterialia*, *7*(12), 4187-4194. https://doi.org/10.1016/j.actbio.2011.07.024

U Song, S., Cha, Y.-D., Han, J.-U., Oh, I.-S., Baek Choi, K., Yi, Y., . . . Lee, K. (2005). *Hyaline Cartilage Regeneration Using Mixed Human Chondrocytes and Transforming Growth Factor-β 1 - Producing Chondrocytes* (Vol. 11). https://doi.org/10.1089/ten.2005.11.1516

Uchida, M., Li, X. W., Mertens, P., & Alpar, H. O. (2009). Transfection by particle bombardment: Delivery of plasmid DNA into mammalian cells using gene gun. *Biochimica Et Biophysica Acta-General Subjects*, *1790*(8), 754-764. https://doi.org/10.1016/j.bbagen.2009.05.013

Valdoz, J. C., Johnson, B. C., Jacobs, D. J., Franks, N. A., Dodson, E. L., Sanders, C., . . . Van Ry, P. M. (2021). The ECM: To Scaffold, or Not to Scaffold, That Is the Question. *Int J Mol Sci*, *22*(23). https://doi.org/10.3390/ijms222312690

van der Kraan, P. M., & van den Berg, W. B. (2007). Osteophytes: relevance and biology. *Osteoarthritis and Cartilage*, *15*(3), 237-244. https://doi.org/10.1016/j.joca.2006.11.006

Vandermeulen, G., Marie, C., Scherman, D., & Préat, V. (2011). New Generation of Plasmid Backbones Devoid of Antibiotic Resistance Marker for Gene Therapy Trials. *Molecular Therapy*, *19*(11), 1942-1949. https://doi.org/10.1038/mt.2011.182

Varkouhi, A. K., Scholte, M., Storm, G., & Haisma, H. J. (2011). Endosomal escape pathways for delivery of biologicals. *Journal of Controlled Release*, *151*(3), 220-228. https://doi.org/10.1016/j.jconrel.2010.11.004

Varoni, E., Tschon, M., Palazzo, B., Nitti, P., Martini, L., & Rimondini, L. (2012). Agarose Gel as Biomaterial or Scaffold for Implantation Surgery: Characterization, Histological and Histomorphometric Study on Soft Tissue Response [Article]. *Connective Tissue Research*, *53*(6), 548-554. https://doi.org/10.3109/03008207.2012.712583

Vaughan, E. E., DeGiulio, J. V., & Dean, D. A. (2006). Intracellular trafficking of plasmids for gene therapy: Mechanisms of cytoplasmic movement and nuclear import. *Current Gene Therapy*, *6*(6), 671-681. https://doi.org/10.2174/156652306779010688

Vermeulen, L. M. P., De Smedt, S. C., Remaut, K., & Braeckmans, K. (2018). The proton sponge hypothesis: Fable or fact? *European Journal of Pharmaceutics and Biopharmaceutics*, *129*, 184-190. https://doi.org/10.1016/j.ejpb.2018.05.034

Voytas, D. (2000). Agarose Gel Electrophoresis. *Current Protocols in Molecular Biology*, *51*(1), 2.5A.1-2.5A.9. https://doi.org/https://doi.org/10.1002/0471142727.mb0205as51

Vyas, C., Mishbak, H., Cooper, G., Peach, C., Pereira, R. F., & Bartolo, P. (2020). Biological perspectives and current biofabrication strategies in osteochondral tissue engineering. *Biomanufacturing Reviews*, *5*(1), 2. https://doi.org/10.1007/s40898-020-00008-y

Wang, H., Lin, C. C., Zhang, X. R., Lin, K. L., Wang, X. D., & Shen, S. G. (2019). Mussel-Inspired Polydopamine Coating: A General Strategy To Enhance Osteogenic Differentiation and Osseointegration for Diverse Implants. *Acs Applied Materials & Interfaces*, *11*(7), 7615-7625. https://doi.org/10.1021/acsami.8b21558

Wang, W. Y., Ye, R. X., Xie, W. Q., Zhang, Y. Y., An, S. B., Li, Y. S., & Zhou, Y. (2022). Roles of the calcified cartilage layer and its tissue engineering reconstruction in osteoarthritis treatment. *Frontiers in Bioengineering and Biotechnology*, *10*, Article 911281. https://doi.org/10.3389/fbioe.2022.911281

Washbourne, P., & McAllister, A. K. (2002). Techniques for gene transfer into neurons. *Current Opinion in Neurobiology*, *12*(5), 566-573. https://doi.org/10.1016/s0959-4388(02)00365-3

Watanabe, J., & Akashi, M. (2006). Novel biomineralization for hydrogels: electrophoresis approach accelerates hydroxyapatite formation in hydrogels. *Biomacromolecules*, *7*(11), 3008-3011, Article 2006. https://doi.org/10.1021/bm060488h

Watanabe, J., & Akashi, M. (2007). *Patent WO2007061001A1: Composite of gel carrier and hydroxyapatite and method for producing the same*. https://patents.google.com/patent/WO2007061001A1/en

Watanabe, J., & Akashi, M. (2008). Anisotropic hydroxyapatite formation inside agarose gels by integration of electrophoretic and alternate soaking approaches. *Journal of Biomaterials Science-Polymer Edition*, *19*(12), 1625-1635. https://doi.org/10.1163/156856208786440505

Wei, P. R., Xu, Y., Zhang, H. K., & Wang, L. M. (2021). Continued sustained insulin-releasing PLGA nanoparticles modified 3D-Printed PCL composite scaffolds for osteochondral repair. *Chemical Engineering Journal*, *422*, Article 130051. https://doi.org/10.1016/j.cej.2021.130051

Wei, W. Y., & Dai, H. L. (2021). Articular cartilage and osteochondral tissue engineering techniques: Recent advances and challenges. *Bioactive Materials*, *6*(12), 4830-4855. https://doi.org/10.1016/j.bioactmat.2021.05.011

Weiner, S., & Traub, W. (1986). Organisation of hydroxyapatite crystals within collagen fibrils. *Febs Letters*, *206*(2), 262-266. https://doi.org/10.1016/0014-5793(86)80993-0

Welzel, T., Radtke, I., Meyer-Zaika, W., Heumann, R., & Epple, M. (2004). Transfection of cells with custom-made calcium phosphate nanoparticles coated with DNA. *Journal of Materials Chemistry*, *14*(14), 2213-2217. https://doi.org/10.1039/b401644k

Wilkinson, P., Bozo, I. Y., Braxton, T., Just, P., Jones, E., Deev, R. V., . . . Feichtinger, G. A. (2021). Systematic Review of the Preclinical Technology Readiness of Orthopedic Gene Therapy and Outlook for Clinical Translation. *Frontiers in Bioengineering and Biotechnology*, *9*, Article 626315. https://doi.org/10.3389/fbioe.2021.626315

Witkowska, M., Golusinska-Kardach, E., Golusinski, W., & Florek, E. (2023). Polydopamine-Based Material and Their Potential in Head and Neck Cancer Therapy-Current State of

Knowledge. *International Journal of Molecular Sciences*, *24*(5), Article 4890. https://doi.org/10.3390/ijms24054890

Wolanski, M., Donczew, R., Zawilak-Pawlik, A., & Zakrzewska-Czerwinska, J. (2015). oriC-encoded instructions for the initiation of bacterial chromosome replication. *Frontiers in Microbiology*, *5*, Article 735. https://doi.org/10.3389/fmicb.2014.00735

Wong, S. P., & Harbottle, R. P. (2013). Genetic modification of dividing cells using episomally maintained S/MAR DNA vectors. *Molecular Therapy-Nucleic Acids*, *2*, Article e115. https://doi.org/10.1038/mtna.2013.40

Wu, P., Chen, H. J., Jin, R. H., Weng, T. T., Ho, J. K., You, C. G., . . . Han, C. M. (2018). Non-viral gene delivery systems for tissue repair and regeneration. *Journal of Translational Medicine*, *16*, Article 29. https://doi.org/10.1186/s12967-018-1402-1

Wu, X. R., Cheng, X. L., Kang, M. Y., Dong, R. P., Zhao, J. W., & Qu, Y. (2023). Natural polysaccharide-based hydrogel bioprinting for articular cartilage repair. *Frontiers in Materials*, *10*, Article 1204318. https://doi.org/10.3389/fmats.2023.1204318

Wuite, G. J. L., Smith, S. B., Young, M., Keller, D., & Bustamante, C. (2000). Single-molecule studies of the effect of template tension on T7 DNA polymerase activity [Article]. *Nature*, *404*(6773), 103-106.

Xiang, S. D., Scholzen, A., Minigo, G., David, C., Apostolopoulos, V., Mottram, P. L., & Plebanski, M. (2006). Pathogen recognition and development of particulate vaccines: Does size matter? *Methods*, *40*(1), 1-9. https://doi.org/10.1016/j.ymeth.2006.05.016

Xu, J. Z., Xie, Y., Zhang, H. B., Ye, Z. O. Y., & Zhang, W. J. (2014). Fabrication of PLGA/MWNTs composite electrospun fibrous scaffolds for improved myogenic differentiation of C2C12 cells. *Colloids and Surfaces B-Biointerfaces*, *123*, 907-915. https://doi.org/10.1016/j.colsurfb.2014.10.041

Xu, Z. P. G. (2022). Strategy for Cytoplasmic Delivery Using Inorganic Particles. *Pharmaceutical Research*, *39*(6), 1035-1045. https://doi.org/10.1007/s11095-022-03178-1

Yang, C. R., Shang, X. Y., Cheng, L., Yang, L., Liu, X. F., Bai, C. L., . . . Li, G. P. (2017). DNMT 1 maintains hypermethylation of CAG promoter specific region and prevents expression of exogenous gene in fat-1 transgenic sheep. *Plos One*, *12*(2), Article e0171442. https://doi.org/10.1371/journal.pone.0171442

Yang, H. N., Park, J. S., Jeon, S. Y., & Park, K. H. (2015). Carboxymethylcellulose (CMC) formed nanogels with branched poly(ethyleneimine) (bPEI) for inhibition of cytotoxicity in human MSCs as a gene delivery vehicles. *Carbohydrate Polymers*, *122*, 265-275. https://doi.org/10.1016/j.carbpol.2014.12.073

Yang, J., Shi, G. X., Bei, J. Z., Wang, S. G., Cao, Y. L., Shang, Q. X., . . . Wang, W. J. (2002). Fabrication and surface modification of macroporous poly(L-lactic acid) and poly(L-lactic-co-glycolic acid) (70/30) cell scaffolds for human skin fibroblast cell

culture. *Journal of Biomedical Materials Research*, *62*(3), 438-446. https://doi.org/10.1002/jbm.10318

Yang, S. Z., Shi, H. J., Chu, X. R., Zhou, X. L., & Sun, P. N. (2016). A rapid and efficient polyethylenimine-based transfection method to prepare lentiviral or retroviral vectors: useful for making iPS cells and transduction of primary cells. *Biotechnology Letters*, *38*(9), 1631-1641. https://doi.org/10.1007/s10529-016-2123-2

Yang, X., Wen, X. W., Dai, J., Chen, Y. M., Ding, W. C., Wang, J., . . . Ruan, G. (2022). Probing the Intracellular Delivery of Nanoparticles into Hard-to-Transfect Cells. *Acs Nano*, *16*(6), 8751-8765. https://doi.org/10.1021/acsnano.1c07648

Yazdi, M. K., Taghizadeh, A., Taghizadeh, M., Stadler, F. J., Farokhi, M., Mottaghitalab, F., . . . Mozafari, M. (2020). Agarose-based biomaterials for advanced drug delivery. *Journal of Controlled Release*, *326*, 523-543. https://doi.org/10.1016/j.jconrel.2020.07.028

Yeong, W. Y., Sudarmadji, N., Yu, H. Y., Chua, C. K., Leong, K. F., Venkatraman, S. S., . . . Tan, L. P. (2010). Porous polycaprolactone scaffold for cardiac tissue engineering fabricated by selective laser sintering. *Acta Biomaterialia*, *6*(6), 2028-2034. https://doi.org/10.1016/j.actbio.2009.12.033

Yılmaz, M., Ozic, C., & Gok, I. (2012). Principles of Nucleic Acid Separation by Agarose Gel Electrophoresis. In M. Sameh (Ed.), *Gel Electrophoresis*. IntechOpen. https://doi.org/10.5772/38654

Yin, Z. W., Yang, X. F., Jiang, Y. Q., Xing, L. Z., Xu, Y., Lu, Y. M., . . . Gui, J. C. (2014). Platelet-rich plasma combined with agarose as a bioactive scaffold to enhance cartilage repair: An in vitro study. *Journal of Biomaterials Applications*, *28*(7), 1039-1050. https://doi.org/10.1177/0885328213492573

Yokota, H., Leong, D., & Sun, H. (2011). Mechanical Loading: Bone Remodeling and Cartilage Maintenance. *Current Osteoporosis Reports*, *9*(4), 237-242. https://doi.org/10.1007/s11914-011-0067-y

Yu, H., Jiang, X. O., Tan, K. T., Hang, L. T., & Patzel, V. (2015). Efficient production of superior dumbbell-shaped DNA minimal vectors for small hairpin RNA expression. *Nucleic Acids Research*, *43*(18), Article e120. https://doi.org/10.1093/nar/gkv583

Yu, L., Cavelier, S., Hannon, B., & Wei, M. (2023). Recent development in multizonal scaffolds for osteochondral regeneration. *Bioactive Materials*, *25*, 122-159. https://doi.org/10.1016/j.bioactmat.2023.01.012

Yu, M. E., Hwang, J. Y., & Deming, T. J. (1999). Role of L-3,4-dihydroxyphenylalanine in mussel adhesive proteins. *Journal of the American Chemical Society*, *121*(24), 5825-5826. https://doi.org/10.1021/ja990469y

Zakeri, A., Kouhbanani, M. A. J., Beheshtkhoo, N., Beigi, V., Mousavi, S. M., Hashemi, S. A. R., . . . Movahedpour, A. (2018). Polyethylenimine-based nanocarriers in co-delivery of drug

and gene: a developing horizon. *Nano Reviews & Experiments*, *9*, Article 1488497. https://doi.org/10.1080/20022727.2018.1488497

Zanetti, A. S., Sabliov, C., Gimble, J. M., & Hayes, D. J. (2013). Human adipose-derived stem cells and three-dimensional scaffold constructs: A review of the biomaterials and models currently used for bone regeneration. *Journal of Biomedical Materials Research Part B-Applied Biomaterials*, *101B*(1), 187-199. https://doi.org/10.1002/jbm.b.32817

Zanta, M. A., Belguise-Valladier, P., & Behr, J. P. (1999). Gene delivery: A single nuclear localization signal peptide is sufficient to carry DNA to the cell nucleus. *Proceedings of the National Academy of Sciences of the United States of America*, *96*(1), 91-96. https://doi.org/10.1073/pnas.96.1.91

Zarrintaj, P., Manouchehri, S., Ahmadi, Z., Saeb, M. R., Urbanska, A. M., Kaplan, D. L., & Mozafari, M. (2018). Agarose-based biomaterials for tissue engineering. *Carbohydrate Polymers*, *187*, 66-84. https://doi.org/10.1016/j.carbpol.2018.01.060

Zhang, B., Gleadall, A., Belton, P., McDonagh, T., Bibb, R., & Qi, S. (2021). New insights into the effects of porosity, pore length, pore shape and pore alignment on drug release from extrusionbased additive manufactured pharmaceuticals. *Additive Manufacturing*, *46*, Article 102196. https://doi.org/10.1016/j.addma.2021.102196

Zhang, B., Huang, J., & Narayan, R. J. (2020). Gradient scaffolds for osteochondral tissue engineering and regeneration. *Journal of Materials Chemistry B*, *8*(36), 8149-8170. https://doi.org/10.1039/d0tb00688b

Zhang, Y., Wang, F. Y., Tan, H. B., Chen, G. X., Guo, L., & Yang, L. (2012). Analysis of the Mineral Composition of the Human Calcified Cartilage Zone. *International Journal of Medical Sciences*, *9*(5), 353-360. https://doi.org/10.7150/ijms.4276

Zhou, H., He, Y., Xiong, W., Jing, S. L., Duan, X. X., Huang, Z. Y., . . . Ye, Q. S. (2023). MSC based gene delivery methods and strategies improve the therapeutic efficacy of neurological diseases. *Bioactive Materials*, *23*, 409-437. https://doi.org/10.1016/j.bioactmat.2022.11.007

Zhou, L. B., Van Osch, G., Malda, J., Stoddart, M. J., Lai, Y. X., Richards, R. G., . . . Qin, L. (2020). Innovative Tissue-Engineered Strategies for Osteochondral Defect Repair and Regeneration: Current Progress and Challenges. *Advanced Healthcare Materials*, *9*(23), Article 2001008. https://doi.org/10.1002/adhm.202001008

Zhou, Y. G., Chyu, J., & Zumwalt, M. (2018). Recent Progress of Fabrication of Cell Scaffold by Electrospinning Technique for Articular Cartilage Tissue Engineering. *International Journal of Biomaterials*, *2018*, Article 1953636. https://doi.org/10.1155/2018/1953636

Zhu, A. P., Fang, N., Chan-Park, M. B., & Chan, V. (2006). Adhesion contact dynamics of 3T3 fibroblasts on poly (lactide-co-glycolide acid) surface modified by photochemical immobilization of biomacromolecules. *Biomaterials*, *27*(12), 2566-2576. https://doi.org/10.1016/j.biomaterials.2005.11.039

Zhu, X. D., Fan, H. S., Li, D. X., Xiao, Y. M., & Zhang, X. D. (2007). Protein adsorption and zeta potentials of a biphasic calcium phosphate ceramic under various conditions. *Journal of Biomedical Materials Research Part B-Applied Biomaterials*, *82B*(1), 65-73. https://doi.org/10.1002/jbm.b.30706